UNIVERSITY OF OKLAHOMA

GRADUATE COLLEGE

APPLIED PETROLEUM SOURCE ROCK EVALUATION AND HIGH-RESOLUTION SEQUENCE STRATIGRAPHY FOR UNCONVENTIONAL RESERVOIRS IN LA LUNA FORMATION (CENOMANIAN- SANTONIAN) NORTHWEST MARACAIBO BASIN, VENEZUELA.

A DISSERTATION

SUBMITTED TO THE GRADUATE FACULTY

in partial fulfillment of the requirements for the

Degree of

DOCTOR OF PHILOSOPHY

By

ANDREINA DE LOS ANGELES LIBORIUS PARADA
Norman, Oklahoma
2019

Downloaded from SHAREOK. Persistent Handle URL: https://hdl.handle.net/11244/319563

APPLIED PETROLEUM SOURCE ROCK EVALUATION AND HIGH-RESOLUTION SEQUENCE STRATIGRAPHY FOR UNCONVENTIONAL RESERVOIRS IN LA LUNA FORMATION (CENOMANIAN- SANTONIAN) NORTHWEST MARACAIBO BASIN, VENEZUELA.

A DISSERTATION APPROVED FOR THE
CONOCOPHILLIPS SCHOOL OF GEOLOGY AND GEOPHYSICS

BY

Dr. Roger Slatt, Chair

Dr. Paul Philp

Dr. Richard Elmore

Dr. Deepak Devegowda

Dr. Michael Engel

© Copyright by ANDREINA DE LOS ANGELES LIBORIUS PARADA 2019
All Rights Reserved.

To God almighty and family,

especially to my mom Pilar and my grandparents Julio and Nena.

To my best friend and future husband Lennon.

Words cannot express how much I love you all.

To Venezuela, I want to see you smile again.

Acknowledgments

Many people helped me through this dissertation for the past five years, and without them, it would not have been possible to complete. My first and foremost bit of gratitude goes to my advisors, Dr. Roger Slatt Dr. and Dr. Paul Philp for the continuous support and funding of my master and Ph.D. study research. I am grateful for their patience, motivation, and immense knowledge. I have enjoyed the challenging material and hands-on experience in the field and the lab. Their guidance helped me to turn into an integrated geologist; thank you for all the advices during my research and writing of this dissertation. I could not have imagined having a better two advisors and mentors for my graduate studies (Master and Doctoral degrees).

Dr. Slatt, thank you for taking me as a student when I was a recent graduate from Venezuela. I will be forever in your debt because you changed my life. Thank you for showing me that you can be brilliant, passionate and still be humble and kind to others. Thank you for your life advice and for treating me like family.

Dr. Philp, thank you for the opportunity you gave me when I mentioned three years ago that I wanted to learn about geochemistry. Thank you for pushing me to be a better student and to embrace the fear of working in something new and challenging as organic geochemistry. I could have never done it if it were not for your mentoring.

I would also like to extend my gratitude to Dr. Michael Engel, Dr. Richard Elmore and Dr. Deepak Devegowda for serving on my dissertation committee, for their individual guidance and instruction during my time at OU, not to mention their time and dedication in reviewing this manuscript.

Thank you to Dr. Omar Guerrero for guidance and mentorship in the realization of this work, thank you for your guidance in the field and for all your support every time I needed it.

Thank you to the OU Organic Geochemistry group, especially to Mr. Jon Allen and Mr. Larry Hyde for the tremendous help during my lab work experience. Thank you for all the procedures that you both taught me in the lab, for your patience, dedication, and constructive criticism. Both of you are exceptional and essential for our geochemical group. Likewise, nothing would be the same without you guys: Cecilia, Ann, Lydia, Yağmur, Britney, Tarah, Carl, Greg, and Emilio; thank you for the support and friendship.

Thank you to our dear Dr. Silvana Barbanti for taking the time of guiding me in and out of lab work.

Thank you to the Institute for Reservoir Characterization for these five years of learning experiences, presentations, field-work, and mentorship, especially to Jing, Dani, Henry, and David Duarte, I have learned a lot from all of you, I will miss you guys!

I also want to thank the generous assistance that Brian Cardott gave me during the vitrinite reflectance measurements in the organic petrographic lab. Thank you for your patience and for providing me valuable feedback on my results.

I also gratefully acknowledge the AAPG Grants-in-Aid, the ConocoPhillips School of Geology and Geophysics and the Oklahoma Memorial Union Board of Trustees for awarding me Student Grants. These contributions significantly supported my work.

Thank you to the personnel of INTEVEP, especially to Dr. Uzcategui and Dr. Baquero, I am grateful for providing me all the data support during my research. Nicanor Mendez and Elber Molina, thank you for their help at the beginning of his project and, for your support during the

fieldwork stage. And last but not least, thank you to the personnel of La Concepcion for all the support during my core description.

I will always be thankful to PALADIN GEOLOGICAL SERVICES, especially to Andrew Sneddon, for the realization of all the XRD and XRF analysis done for this project. I am very thankful for all the support you gave me in the past two years.

Thank you to my colleagues Emilio Torres, Carl Symcox, Javier Tellez and Henry Galvis. I think of you as mentors, I will always be grateful for sharing your experience during my classes and my research. I learned a lot from you guys!

OU also gave me the opportunity to meet these fantastic friends: Elizabeth Da Silva, Gabriel Machado, Carolina Mayorga, Jing Zhang, Emilio Torres, David Lubo, and Carl Symcox. Thank you for your friendship, for sharing moments of happiness but also moments of frustration, (because grad-school sometimes is not that easy) for giving me their loyalty and support every time I need it.

Finally, and most importantly, I want to thank the motor of my life: my family. I cannot express with words how thankful I am with God to have you as a family! Thank you for being so caring and so supportive through my life. To my mother, who has been my best friend and my mentor, you are the reason that keeps me motivated in life. Thank you for all the sacrifices you have done for me.

To my grandparents, for being the sweetest part of my life, for treating me as another daughter and loving me unconditionally.

To Luis, thank you for being so caring and patient with me. Thank you for your support and for not only being my little brother but my friend.

To my aunt Nena, my uncle Jesus, Julio and my cousin Kike; thank you for all your support and unconditional love!

And lastly, to Lennon for being my partner in science and love, my best friend and my support. For always being there and being my mentor/coach during the hard times and for making me so happy in the good ones, you are a blessing in my life, and I am more than glad to be able to call you family in a couple of months, I love you!

Table of Contents

Table of Contents ix

List of Tables xvii

List of Figures xix

Abstract xxxii

CHAPTER I: 1

1. INTRODUCTION 1

1.1 Geologic Framework 5

1.1.1 Regional Geology 5

1.1.2 Paleogeography and paleo-climate of La Luna Formation 11

1.1.3 Isotopic analysis of La Luna Formation and relationship with Oceanic Anoxic Events (OAE) in the Maracaibo Basin. 13

1.2 Objectives 17

CHAPTER II 18

2. METHODOLOGY 18

2.1 Study area and sample location 18

2.1.1 Fieldwork and core samples: 21

2.2 Reservoir Characterization 25

2.2.1 X-Ray Fluorescence 25

2.2.2 X-Ray Diffraction 26

2.2.3 Petrographic thin sections 27

2.3 Source Rock Characterization 28
2.3.1 Preliminary sample treatment 28
2.3.2 Rock-Eval pyrolysis and Total Organic Carbon 29
2.3.3 Vitrinite Reflectance 30
2.3.4 Extraction of soluble organic matter 31
2.3.5 Maltene Fractionation 32
2.3.6 Gas Chromatography (GC) 33
2.3.7 Gas Chromatography-Mass Spectrometry (GC-MS) 33
2.3.8 Quantitative Biomarker Analysis 34
CHAPTER III 36
RESERVOIR CHARACTERIZATION 36
3.1. Lithofacies Characterization 36
3.1.1 La Luna IE core 39
3.1.2 La Luna IA core 47
3.1.3 La Luna IS core 57
3.2 Mineralogical and elemental description of La Luna Formation, NW and SW Maracaibo Basin 63
3.2.1 Southwestern-northeastern trend in the Maracaibo Basin: 64
3.2.2 Northwestern-southeastern trend Maracaibo Basin 70
3.3 Elemental Chemostratigraphy 76
3.3.1 Elements associated with detrital input and clay content 77
3.3.2 Elements associated with carbonate input 84
3.3.3 Elements associated with paleo-redox/anoxic input 85

CHAPTER IV 87

SOURCE ROCK CHARACTERIZATION 87

4.1 Total Organic Carbon (TOC) and Rock-Eval Pyrolysis 87

4.1.1 Organic Richness 87

4.1.2 Organic matter type 90

4.1.3 Thermal Maturity 97

4.2 Gas Chromatography (GC) 103

4.2.1 *n*-Alkane distributions 103

4.2.2 Pristane and Phytane 108

4.3 Biomarker Analysis and Evaluation of Organic Matter Source and Depositional Environments 112

4.3.1 Steranes 112

4.3.1.1 Regular steranes 115

4.3.1.2 Diasteranes or “rearranged steranes.” 121

4.3.1.3 Pregnane and homopregnane 122

4.3.2 Terpanes 126

4.3.2.1 The tricyclic terpanes 127

4.3.2.2 The tetracyclic terpanes 139

4.3.2.3 The Pentacyclic Terpanes 140

4.3.3 Aryl Isoprenoids 149

4.3.4 Monoaromatic Steroid Hydrocarbons 154

4.3.4 Dibenzothiophene, phenanthrene and pristane, phytane as indicators of the depositional environment 157

4.4 Evaluation of thermal maturity based on biomarker distribution 158
4.4.1 Steranes (m/z 217) 158
4.4.2 Terpanes (m/z 191) 160
4.4.2.1 Hopanes 160
4.4.2.2 Moretanes 161
4.4.2.3 Ts and Tm 164
4.4.2.4 Monoaromatic and Triaromatic Steroids 166
4.4.2.5 Phenanthrenes 168
4.4.2.6 Maturity assessment based on dibenzothiophene and its methyl-homologs 172
CHAPTER 5 175
5.1 Sequence stratigraphy framework 175
5.1.2 Sub-regional sequence stratigraphy and the relative hydrocarbon potential 176
5.1.3 Brittleness index 188
5.2 Biomarkers, relationship with sequence stratigraphy and prospective organo-facies 190
6. CONCLUSIONS 204
7. REFERENCES 208
8. APPENDIX 233
7.1. Total Organic Carbon (TOC) and Rock-Eval (RE) parameters for La Luna Formation samples 234
7.1.1. La Luna IX *core (cont.)* 234
7.1.2. La Luna IE core 237
7.1.3. La Luna stratotype 239
7.1.4. La Luna IA core 240

7.1.5. La Luna IS core 242
7.2. Photomicrographs of La Luna Formation bitumen for measured vitrinite equivalent values. 244
7.2.1. Photomicrographs from the La Luna Formation IA and bitumen vitrinite reflectance values before the conversion to vitrinite reflectance equivalent. 244
7.2.2. Photomicrographs from the La Luna Formation IS and bitumen vitrinite reflectance values before the conversion to vitrinite reflectance equivalent. 245
7.2.3. Photomicrographs from the La Luna Formation IS and bitumen vitrinite reflectance values before the conversion to vitrinite reflectance equivalent. 246
7.2.4. Photomicrographs from the La Luna Formation IS and bitumen vitrinite reflectance values before the conversion to vitrinite reflectance equivalent. 247
7.3. Geochemical ratios of *n*-alkanes and isoprenoids for the saturate fractions of the La Luna Formation bitumen samples 248
7.3.1. La Luna IX core 248
7.3.2. La Luna IA core 250
7.3.3. La Luna IS core 251
7.3.4. La Luna stratotype 252
7.4. Gas chromatograms of the saturate fractions for the La Luna Formation samples analyzed in this study 253
7.4.1. La Luna IX core. 253
7.4.2. La Luna IA core 265
7.4.3. La Luna IS core 273
7.4.4. La Luna stratotype 277

7.5. Abbreviations and formulas used for calculation of geochemical biomarker ratios 280

7.5.1. *n*-alkanes 280

7.5.2. Steranes 280

7.5.3. Hopanes 281

7.5.4. Aryl Isoprenoids 282

7.5.5. Aromatics 282

7.6. Geochemical ratios of steranes for the branched and cyclic fractions (B&C) of the La Luna Formation bitumen 284

7.6.1. La Luna IX core 284

7.6.2. La Luna IA core 286

7.6.3. La Luna IS core 288

7.6.4. La Luna stratotype 289

7.7. Geochemical ratios of terpanes for the branched and cyclic fractions (B&C) of the La Luna bitumen (ND) not determined) 290

7.7.1. La Luna IX core 290

7.7.2. La Luna IA core 292

7.7.3. La Luna IS core 293

7.7.4. La Luna stratotype 294

7.8 Aryl isoprenoids ratio (AIR) for the branched and cyclic fractions (B&C) of the La Luna bitumen (ND = not determined) 295

7.8.1. La Luna IX core 295

7.8.2. La Luna IA core 296

7.8.3. La Luna IS core 296

7.9. Geochemical ratios for aromatic biomarkers of the La Luna Formation bitumen (ND= not determined) 298
7.9.1. La Luna IX core 298
7.9.2. La Luna IA core 300
7.9.3. La Luna IS core 301
7.10. Biomarker quantification results for steranes (Concentrations are expressed as in ppm W/W) 302
7.10.1. La Luna IX core 302
7.10.2. La Luna IA core 306
7.10.3. La Luna IS core 308
7.10.4. La Luna stratotype 310
7.11. Biomarker quantification results for for terpanes (Concentrations are expressed as in ppm W/W) 311
7.11.1. La Luna IX core 311
7.11.2. La Luna IA core 315
7.11.3. La Luna IS core 317
7.11.4. La Luna stratotype 319
7.12. Quantitative biomarker analysis results for aryl isoprenoids (Concentrations are expressed as in ppm W/W) 320
7.12.1. La Luna IX core 320
7.12.2. La Luna IA core 324
7.12.3. La Luna IS core 326
7.12.1. La Luna stratotype 327

7.13. Quantitative biomarker analysis results for monoaromatic steroids (Concentrations are expressed as in ppm W/W) 328
7.13.1. La Luna IX core 328
7.13.2. La Luna IA core 332
7.13.3. La Luna IS core 334
7.13.4. La Luna stratotype 336
7.14. Quantitative biomarker analysis results for phenanthrenes and triaromatic steroids (Concentrations are expressed as in ppm W/W) 337
7.14.1. La Luna IX core 337
7.14.2. La Luna IA core 341
7.14.3. La Luna IX core 343
7.14.4. La Luna stratotype 345

List of Tables

Table 1. Summary of samples used for geochemical and petrographic analysis..... 24

Table 2. Summary of key chemostratigraphic elements and proxies as indicators of the depositional environment..... 26

Table 3. Vitrinite reflectance equivalent values (on average) of La Luna Formation samples. . 101

Table 4. Pristane/Phytane ratios and their relationship with other indicators of redox conditions and the environment of sedimentation..... 109

Table 5. Summary table of *n*-alkanes analyses from the saturated fraction of La Luna Formation bitumens..... 110

Table 6. Identification of steranes in the partial m/z 217.3 fragmentogram of the B&C hydrocarbon fractions. 116

Table 7. Sterane homologs and their association with the different depositional environments.118

Table 8 Identification of terpanes in the partial m/z 191.3 fragmentograms of the branched and cyclic fractions of La Luna Formation samples..... 134

Table 9. Identification of monoaromatic steroids (MAS) in the partial m/z 253.3 156

Table 10. Identification of triaromatic steroids (TAS) in the partial m/z 231.3 169

Table 11. Identification of phenanthrenes in the partial mass chromatograms of m/z 178.3, 192.3, 206.3..... 171

Table 12. Average of the calculated vitrinite reflectance (Rc) for La Luna Formation samples from MPI-1 values. 172

Table 13. Measured vitrinite reflectance calculated by the 4-Methyldibenzothiophene (4-MDBT) over the 1-Methyldibenzothiophene (1-MDBT) ratio. 174

Table 14. Average constituent minerals in the rock and total organic carbon used for the Brittleness Index equation..... 189

List of Figures

Figure 1. Prospective Area for Shale Exploration in the Maracaibo Basin 2

Figure 2. Distribution of Jurassic rocks: 1) in Perijá Range; 2) as part of the economic basement of Maracaibo Basin; 3) in the Andes; 4) in Barinas-Apure and eastern Venezuela Basins (Apure-Mantecal and Espino Graben). It is believed that they are involved in deep thrusting within eastern Venezuela's interior range 7

Figure 2. Distribution of Jurassic rocks: 1) in Perijá Range; 2) as part of the economic basement of Maracaibo Basin; 3) in the Andes; 4) in Barinas-Apure and eastern Venezuela Basins (Apure-Mantecal and Espino Graben). It is believed that they are involved in deep thrusting within eastern Venezuela's interior range 7

Figure 3. Stratigraphic column of the Cretaceous in Maracaibo Basin, Venezuela 8

Figure 4. Paleo-environmental distribution during the Cenomanian-Campanian at the northern edge of the Guayana Shield. Typical units of these sets of facies indicated 9

Figure 5. $\delta^{13}C$ organic carbon isotopic composition of organic matter (‰PDB); % carbonates (as $CaCO_3$); % TOC (expressed on a carbonate-free basis); H.I. = hydrogen index (from pyrolysis Rock-Eval, mg HC/g TOC); silica/alumina data of the La Luna Formation at Quebrada Maraca. 14

Figure 6. Stable carbon isotopic composition of bulk organic matter and generalized stratigraphy of the ALP-6 core 15

Figure 7. Map of Venezuela bordered by Colombia on the west, Brazil on the south, Guyana on the east, the Dutch Lesser Antilles to the north and Trinidad and Tobago to the north-east 18

Figure 8. La Luna stratotype outcrop displaying the Lower (A), Middle (B) and Upper (C) La Luna in Flanco Perijanero, Maracaibo-Venezuela..... 19
Figure 9. Cores used for the study of unconventional reservoirs in La Luna Formation, Venezuela located along northwest, Venezuela. (A) La Luna IX, (B) La Luna IA; (C) La Luna IE and (D) La Luna IS. 20
Figure 10. Flowchart for source rock evaluation of unconventional gas shales..... 22
Figure 11 Map showing the core and outcrop location of La Luna Formation in Northwestern Venezuela. The dash yellow line represents the Maracaibo Basin The La Luna IE core represents the dark yellow circle; the pale green circle represents the La Luna IX core, red circle by the La Luna IA and pink circle represents La Luna IS. 23
Figure 12. Photographs of La Luna IX core and its most characteristic facies. (A and B) represents facies I (Dark Laminated mudstone) by an alternation of a discontinuous planal-parallel mudstone and wackestone-packstone containing uniserial foraminifera and shell fragments. (C) Presence of bentonites in a clay-rich matrix. (D) Recrystallized foraminifera and small quartz grains in an organic-rich matrix. (E) Recrystallization of forams, spicules of Echinoderms and small quartz grains in an organic matrix. (F) Recrystallization of uniserial foraminifera, pellets, aragonite and small quartz grains in an organic to micrite cement. (G) Diagenetic-altered foraminifera filled with organic matter in a micrite- cement. (H)Packstone-grainstone with high amounts of organic rich-foraminifera and shell fragments in a siderite cement (cross-polarized light) with a high abundance of glauconite and phosphates. 38
Figure 13. Facies I (Dark gray, massive mudstone). (A) Sharp contact of Maraca and La Luna Formation showing the Early Albian-Cenomanian unconformity. (B) Massive calcite-filled veins (shown almost perpendicular through the interval). 40

Figure 14. LLIE core interval displaying gradually lithological changes (calcareous to organic-rich mudstone). 40
Figure 15. Fossiliferous wackestone facies in LLIE core..... 41
Figure 16. Volcanic ash pulses in the LLIE core (dashed- yellow lines) 42
Figure 17. Facies IV (Massive mudstone with limestone concretions and packstone). 43
Figure 18. Facies V (Siliceous- calcareous laminated mudstone interbedded with black chert filled with calcite veins)..... 44
Figure 19. (A and B) Representation of the LLIE core and thin section microphotography depicting dolomitization in interbedded layers of facies V. 45
Figure 20. Photographs of La Luna IE core and its most characteristic facies..... 46
Figure 21. Representation of Facies I (Dark gray laminar mudstone) in LLIA core. (A) Interval is showing the unconformity of Maraca Formation (Cogollo Group) with La Luna Formation displaying a series of conchiferous bivalves. (B) Presence of small calcite nodules recrystallized with anhydrite. (C) Organic-rich interval is showing calcite-filled vertical fractures..... 48
Figure 22. Representation of Facies II (Calcareous-marlstone with the presence of pyrite layers) in LLIA core. 49
Figure 23. Representation of Facies III (Volcanic Ash facies) in LLIA core displaying a fissile yellowish color with coarse particles of volcanic ash..... 50
Figure 24. Photographs of La Luna IA core and its most characteristic facies. 50
Figure 25. Representation of Facies IV (Laminated mudstone with limestone concretions and packstone) in LLIA core representing the MFS and the most organic-rich lithofacies..... 51
Figure 26. Representation of Facies V (Siliceous- calcareous laminated mudstone interbedded with black chert filled with calcite veins).. 52

Figure 27. Perpendicular deposition angle of almost 45 degrees perpendicular to the underlying and overlaying massive sediments. 52
Figure 28. Representation of Facies V (Siliceous- calcareous laminated mudstone interbedded with black chert filled with calcite veins 53
Figure 29. Photographs of La Luna IA core and its most characteristic facies. 54
Figure 30. (A) Presence of an organic-rich matrix along small micritized foraminifera (B) vertical stylolite (16798'-16796') possibly related to the bedding at right angles. 55
Figure 31. Bioturbation and cyclicity of small intervals of dolomitization almost parallel and with a cross lamination like structure at the end of the La Luna Formation IA core. 56
Figure 32. Photographs of La Luna IE core and its most characteristic facies. 57
Figure 33. Core interval displaying the significant cyclicity represented for two main facies in La Luna IS core. 58
Figure 34. Representation of Facies I (Dark gray laminar mudstone). 59
Figure 35. (A) Representation of the LLIE core and thin section microphotography displaying the fissile character in an organic-rich matrix. (B) The separation of the layers presented in thin sections is due to the high fissile character of the rock, the presence of organic-rich filled foraminifera and glossifungites. 59
Figure 36. Representation of Facies I (Dark gray laminar mudstone). 60
Figure 37. Representation of Facies II (Calcareous-marlstone with the presence of pyrite layers). 61
Figure 38. Representation of facies II (Calcareous-marlstone with the presence of pyrite layers) displaying of a micritization cement rich in uniserial and multiserial foraminifera recrystallized to calcite (yellow-dashed lines). 61

Figure 39. Representation of Facies III (Volcanic Ash facies) in LLIS core displaying a fissile yellowish color with coarse particles of volcanic ash. 62
Figure 40. Estimated location and representation of the evaluated cores and stratotype in the study area. 65
Figure 41. A. Whisker distribution of the principal mineralogical components (quartz, carbonate and clay); B. XRD-derived depth profile depicting the normalized percentage of quartz, carbonate and clay. C. XRD-derived depth profile depicting the relative mineralogy of the Lower, Middle and Upper La Luna Formation in La Luna stratotype. 66
Figure 42. Whisker distribution of the principal mineralogical components (quartz, carbonate and clay); B. XRD-derived depth profile depicting the normalized percentage of quartz, carbonate and clay. C. XRD-derived depth profile depicting the relative mineralogy of the Lower, Middle and Upper La Luna Formation in core La Luna IX. 67
Figure 43. Whisker distribution of the principal mineralogical components (quartz, carbonate and clay); B. XRD-derived depth profile depicting the normalized percentage of quartz, carbonate and clay. C. XRD-derived depth profile depicting the relative mineralogy of the Lower, Middle and Upper La Luna Formation in core La Luna IE. 68
Figure 44. Whisker distribution of the principal mineralogical components (quartz, carbonate and clay); B. XRD-derived depth profile depicting the normalized percentage of quartz, carbonate and clay. C. XRD-derived depth profile depicting the relative mineralogy of the Lower, Middle and Upper La Luna Formation in core La Luna IA 71
Figure 45. Whisker distribution of the principal mineralogical components (quartz, carbonate and clay); B. XRD-derived depth profile depicting the normalized percentage of quartz, carbonate

and clay. C. XRD-derived depth profile depicting the relative mineralogy of the Lower, Middle and Upper La Luna Formation in core La Luna IS. 72
Figure 46. Overall mineralogical composition of La Luna Formation in the trend NE-SW Maracaibo Basin using the ternary plot classification from Gamero-Diaz et al., 2012. 75
Figure 47. Gamma Ray, XRD and chemostratigraphic profile of the Lower, Middle and Upper La Luna Formation in core La Luna IX showing the overall elements of this study in parts per million (ppm). 80
Figure 48. Gamma Ray, XRD and chemostratigraphic profile of the Lower, Middle and Upper La Luna Formation in core La Luna IE showing the overall elements of this study in parts per million (ppm). 81
Figure 49. Gamma Ray, XRD and chemostratigraphic profile of the Lower, Middle and Upper La Luna Formation in core La Luna IA showing the overall elements of this study in parts per million (ppm).. 82
Figure 50. Gamma Ray, XRD and chemostratigraphic profile of the Lower, Middle and Upper La Luna Formation in core La Luna IS showing the overall elements of this study in parts per million (ppm). 83
Figure 51. Pyrogram that represents the distribution of Organic Matter in Rock. From Philp, 2014..... 88
Figure 52. Organic richness histogram determined by TOC content in the outcrop and subsurface samples located in the Maracaibo Basin. 91
Figure 53. Modified Van-Krevelen diagram for the La Luna Formation samples. 92
Figure 54. Rock-Eval Remaining Hydrocarbon Potential (S2) vs. TOC plot for determination of kerogen type and maturity of La Luna samples..... 94

Figure 55. Hydrogen index histogram determined by S_2/TOC content in the outcrop and subsurface samples located in the Maracaibo Basin. 95
Figure 56. S1 vs. TOC plot (Hunt 1995) indicating migrated versus indigenous hydrocarbons of La Luna subsurface and outcrop samples. 96
Figure 57. Kerogen type and maturity assessment via integration of HI and Tmax data. 98
Figure 58. Ro histogram determined by the following formula (0.018*Tmax)-7.16 by Jarvie et al., 2001. 99
Figure 59. Photomicrographs from the La Luna Formation IX and bitumen vitrinite reflectance values before the conversion to vitrinite reflectance equivalent. 102
Figure 60. Gas chromatograms of the saturated hydrocarbon fractions from bitumen extracts of the LLIX and LLIA core 104
Figure 61. Gas chromatograms of the saturated hydrocarbon fractions from bitumen extracts of the LLIS and La Luna stratotype core 105
Figure 62. Plot of pristane/*n*-C_{17} versus phytane/*n*-C_{18} showing redox conditions, maturity, and depositional environments for samples of the La Luna Formation 111
Figure 63. Partial fragmentograms of the m/z 217 ion showing steranes distribution in the branched and cyclic hydrocarbon fractions of the La Luna Formation in LLIX core. 113
Figure 64. Partial fragmentograms of the m/z 217.3 ion showing distribution of steranes in the branched and cyclic hydrocarbon fractions of the LLIA and LLIS samples 114
Figure 65. Partial fragmentograms of the m/z 217.3 ion showing distribution of steranes in the branched and cyclic hydrocarbon fractions of the Perija samples. 115
Figure 66. Ternary diagram of C_{27}, C_{28}, and C_{29} regular steranes for the La Luna samples in the Maracaibo Basin. 119

Figure 67. Geochemical logs of the C_{30} index for the LLIX, LLIA, LLIS and La Luna stratotype samples..... 120

Figure 68 Geochemical logs of the C_{27} diasterane/ C_{27} sterane index for the LLIX, LLIA, LLIS and La Luna stratotype samples..... 123

Figure 69 Geochemical logs of the pregnane/sterane ratio for the LLIX, LLIA, LLIS and La Luna stratotype samples..... 125

Figure 70 Plot of $\Sigma C_{21\text{-}22}/\Sigma C_{27\text{-}29}$ Steranes vs. ΣC_{27} diasteranes /Σregular C_{27} Steranes 126

Figure 71. Partial fragmentograms of the m/z 191.3 ion showing distribution of terpanes in the branched and cyclic hydrocarbon fractions of the LLIX samples. 128

Figure 72. Partial fragmentograms of the m/z 191.3 ion showing distribution of terpanes in the branched and cyclic hydrocarbon fractions of the of the LLIA and LLIS samples..... 129

Figure 73. Partial fragmentograms of the m/z 191.3 ion showing distribution of terpanes in the branched and cyclic hydrocarbon fractions of the La Luna stratotype samples 130

Figure 74 Geochemical logs of the sterane/ 17 α-H ratio for the LLIX, LLIA, LLIS and La Luna stratotype samples..... 131

Figure 75. Gamma ray and geochemical logs of the $C_{20}TT/C_{23}TT$; $C_{26}TT/C_{25}TT$ and C_{23}/C_{30}Hopane ratios for LLIX..... 135

Figure 76. Gamma ray and geochemical logs of the $C_{20}TT/C_{23}TT$; $C_{26}TT/C_{25}TT$ and C_{23}/C_{30}Hopane ratios for LLIA..... 136

Figure 77. Gamma ray and geochemical logs of the $C_{20}TT/C_{23}TT$; $C_{26}TT/C_{25}TT$ and C_{23}/C_{30}Hopane ratios for LLIS. 137

Figure 78. Geochemical logs of the $C_{20}TT/C_{23}TT$; $C_{26}TT/C_{25}TT$ and C_{23}/C_{30}Hopane ratios for La Luna stratotype..... 138

Figure 79. The plot of C_{22}/C_{21} versus C_{24}/C_{23} tricyclic terpanes showing the source rock depositional environments for the La Luna Formation bitumens. 139
Figure 80. Geochemical logs of the C_{24}TT/30H for La Luna stratotype. 141
Figure 81. Geochemical logs of the 30-NorH/30H for La Luna stratotype. 142
Figure 82. Plot of 30-Nor/C_{30} hopane versus $C_{35}S/C_{34}S$ homohopanes indicating that most of the La Luna samples are in the marine carbonates and marls range. 144
Figure 83. Geochemical logs of the 31R/30H for La Luna stratotype. 145
Figure 84. Plot of C_{26}/C_{25} versus $C_{31}R/C_{30}$ hopane displaying the marine origin of the La Luna samples 146
Figure 85. Homohopanes distribution for bitumens from the La Luna Formation. 147
Figure 86. Geochemical logs of the 31R/30H for La Luna stratotype. 148
Figure 87. Summed mass chromatograms of m/z 133, 134 of the B&C fractions showing the aryl isoprenoids distributions of the La Luna samples. 151
Figure 88. AIR versus Pr/Ph plot for the La Luna samples. 152
Figure 89. Gamma ray log and geochemical logs of the Pr/Ph aryl-isoprenoids ratio for the LLIA. 153
Figure 90. Partial fragmentograms of the m/z 253.3 ion showing distribution of the monoaromatic steroids (MAS) in the B&C fractions of the LLIS samples 154
Figure 91. Ternary diagram of C_{27}, C_{28}, and C_{29} monoaromatic steroids for La Luna samples. 155
Figure 92. Ratio of dibenzothiophene to phenanthrene (DBT/P) plotted against the ratios of pristane to phytane (Pr/Ph) to determine shale depositional environments in La Luna Formation. 157

Figure 93. C29(ααα20S/ ααα20S + ααα20R) vs. depth showing the maturity variation through the La Luna subsurface wells. 159
Figure 94. Plot of C_{29} ββ/(ββ+αα) steranes vs. C_{29} 20S/(20S+20R) steranes displaying variations of thermal maturity for the La Luna samples (Light blue area is represented by endpoints of isomerization reactions 160
Figure 95. C_{31} 22S/(22S+22R) logs vs. depth in the subsurface and outcrop La Luna samples. 162
Figure 96. C_{30} moretanes/hopanes logs vs. depth are showing the maturity variation the subsurface and outcrop La Luna samples. 163
Figure 97. Ts/Ts+Tm logs vs. depth showing the maturity variation the subsurface and outcrop La Luna samples. 165
Figure 98. Plot of diasteranes/(diasteranes+regular) C_{27} Steranes versus Ts/(Ts+Tm) ratios displaying a variation in thermal maturity, source, and redox potential for the La Luna samples 166
Figure 99. Partial fragmentograms of the m/z 231.3 ion showing the distribution of the triaromatic steroids (TAS) in the aromatic fractions of sample LLIS 168
Figure 100. Summed mass chromatograms of m/z 178.3, 192.3, 206.3 ions showing the distribution of phenanthrenes compounds in the aromatic fractions of LLIS sample. 170
Figure 101. Maturity effect on the distributions of 4-Methyldibenzothiophene (4-MDBT) with respect to the 1-Methyldibenzothiophene (1-MDBT) in La Luna Formation samples. 173
Figure 102. La Luna stratotype. Black dashed lines show the erosional contact of the Maraca and overlying La Luna Formation. This image represents the Lower-Middle la Luna formation. ... 177
Figure 103. Generalized planktonic foraminiferal biozones, and stage boundaries for the La Luna Formation and surrounding units in La Luna IX. 181

Figure 104. Sequence stratigraphy cycles of the La Luna Formation based on Gamma Ray, TOC and relative hydrocarbon potential (RHP) vs depth for LLIX (HST, highstand systems tract; TST, transgressive systems tract, MFS, maximum flooding surface; FS flooding surface, SB/TSE, Sequence boundary and transgressive surface of erosion). 182
Figure 105. Sequence stratigraphy cycles of the La Luna Formation based on Gamma Ray, TOC and relative hydrocarbon potential (RHP) vs. depth for LLIA (HST, Highstand systems tract; TST, Transgressive systems tract, MFS, maximum flooding surface; SB/TSE, Sequence boundary and the transgressive surface of erosion). 183
Figure 106. Sequence stratigraphy cycles of the La Luna Formation based on Gamma Ray, TOC and relative hydrocarbon potential (RHP) vs. depth for LLIE (HST, Highstand systems tract; TST, transgressive systems tract, MFS, maximum flooding surface; SB/TSE, Sequence boundary and the transgressive surface of erosion). 184
Figure 107. Sequence stratigraphy cycles of the La Luna Formation based on Gamma Ray, TOC and relative hydrocarbon potential (RHP) vs. depth for LLIS (HST, Highstand systems tract; TST, transgressive systems tract, MFS, maximum flooding surface; SB/TSE, Sequence boundary and the transgressive surface of erosion). Dashed lines are the proposed surfaces for this core due to the low sampling density. 185
Figure 108. N-S Stratigraphic cross section in La Luna 1X well using the second MFS (green line) as a stratigraphic datum. 186
Figure 109. SW-NE Stratigraphic cross section in La Luna 1X well using the second MFS (green lines) as a stratigraphic datum..... 187

Figure 110. GR, BI, sea level curve, 4th order sequence stratigraphic framework and geochemical logs of La Luna Formation IX in Maracaibo Basin displaying the best organo-facies for prospective unconventional reservoirs. 195
Figure 111. GR, BI, sea level curve, 4th order sequence stratigraphic framework and geochemical logs of La Luna Formation IA in Maracaibo Basin displaying the best organo-facies for prospective unconventional reservoirs. 196
Figure 112. GR, BI, sea level curve, 4th order sequence stratigraphic framework and geochemical logs of La Luna Formation IS in Maracaibo Basin displaying the best organo-facies for prospective unconventional reservoirs 197
Figure 113. Depositional model through one eustatic sea level cycle represented by the deposition of the shallow-water platform of Maraca Formation (Cogollo Group) suggesting a paleo-karst development and subaerial exposure before deposition of the La Luna 198
Figure 114. Depositional model of the La Luna Formation through one eustatic sea level cycle represented by the initial worldwide transgression that represents the major time of organic matter accumulation in the La Luna Formation and the OAE-2 in the Cenomanian- Turonian Boundary. 199
Figure 115. Depositional model of the La Luna Formation through one eustatic sea level cycle representing the highest period of sea level cycle (MFS). 200
Figure 116. Depositional model of the La Luna Formation through one eustatic sea level cycle represented by the development of the upwelling currents that brought all these nutrients towards the ocean surface generating higher productivity (plankton blooms) and higher quality of organic matter generated. 201

Figure 117. Depositional model of the La Luna Formation through one eustatic sea level cycle represented by the final deposition of the La Luna Formation. 202
Figure 118. Depositional model of the La Luna Formation through one eustatic sea level cycle represented by a regression that is represented by the shale facies of the overlying Colón and Mito Juan Formations. 203

Abstract

Since the early 2000s, the exploitation of unconventional reservoirs has become very important around the world because of their high potential source of energy and their high economic value. Venezuela possesses a world-class, hydrocarbon source rock from one of the most prolific places for oil accumulation in the world. This source rock, the La Luna Formation, (Cretaceous in age) is located in eastern Venezuela's Maracaibo Basin. One of the theories that makes La Luna one of the best source rocks in the world is its deposition in an extensive transgressive and dysaerobic setting that created the optimal conditions for the productivity and preservation of the organic matter. Local variations in depositional and diagenetic conditions have manifestly affected the preservation and dilution of organic matter to some degree, generating small-scale variability in the depositional environments, and thus creating a higher-quality source rock within the depositional sequence that can be more prospective than others.

To understand the variability of the depositional conditions, variations in organic matter source, thermal maturity, depositional environments, the use of organic, inorganic geochemical and geological parameters were crucial in this study.

Four cores and one outcrop located along the Northwestern Maracaibo Basin provided the database for this study. The methodology used was based on the integration of a comprehensive multiscale characterization for source rocks that encompasses reservoir and source rock evaluation to unravel the stratigraphic origin of the petroleum system.

Eight facies identified in one of the most preserved and complete cores (La Luna IX) of the Maracaibo Basin showed a good relationship with what was observed and analyzed in the outcrop. Based on lithofacies characterization and inorganic analysis using X-ray Diffraction (XRD) and X-Ray Fluorescence (XRF), more cores were evaluated along the basin displaying

essential variations in the mineralogical and elemental content of different La Luna Formation lithofacies. The analyses allowed construction of a proposed depositional model for the La Luna Formation in the Maracaibo Basin. Based upon 153 analyses from all the subsurface and outcrop samples, the average total organic carbon (TOC) values ranged between 3.85 and 9.10 wt.%. Rock-Eval pyrolysis and biomarker data showed the La Luna Formation is dominated by Type IIS kerogen, indicating an oil and gas prone marine organic matter origin.

Pristane, phytane (Pr/Ph) and other biomarker ratios suggest anoxic conditions during deposition of the La Luna Formation. Distributions of regular steranes, hopanes, monoaromatic steroid hydrocarbons (MAS) and tentative identification of gammacerane suggest a hypersaline and marine carbonate depositional environment. Thermal maturity parameters indicate that most of the cores (with the exception LLIE) are within the oil window. Liquid hydrocarbons in the study area occur in the northwest and southwest areas, and condensates and dry/wet gases occur in the northeast.

The lithofacies association, the sequence-stratigraphic framework, relative hydrocarbon potential (RHP), and biomarker analysis identified the depositional environment as an epicontinental sea developed in a shallow marine, upper shelf euxinic environment represented by a series of third order sequences of Highstand and Transgressive System Tracts overlying the erosional top of the underlying Cogollo Group (Maraca Formation). According to lithofacies, well log interpretation, and organo-facies, the La Luna Formation deposition is paleo-topographically controlled in some areas by the karstic-like shallow-water platform of the Early Cretaceous, analogous to the Hunton- Woodford Formation in the USA midcontinent (Slatt et al., 2012).

This combined source rock evaluation composed of geological and geochemical parameters indicated an excellent potential as an unconventional reservoir for oil and gas in the

study area. Geochemical analysis confirmed the excellent quality of the organo-facies with higher productivity and preservation indicating that the most prospective intervals for mixed hydrocarbons in La Luna Formation are located in the Upper La Luna in the northwest Maracaibo Basin.

Conversely, paleo-topographic controls and variation in lithofacies illustrate that the Lower La Luna as the most prospective area for hydrocarbons towards the southwest Maracaibo Basin. By the application of a higher density sampling and the use of the biomarkers, current results enhance the previous work done by Liborius (2015).

These stark differences show the tremendous value that biomarkers provide in the exploration of prospective source rocks. Not only do they help to identify paleoenvironmental changes and redox conditions, but they also depict the best organo-facies and accurate maturity parameters of the rock.

CHAPTER I:

1. INTRODUCTION

The exploration and exploitation of unconventional reservoirs (especially shale gas, shale oil, tight gas, and tight oil) is currently undergoing a worldwide boom. Many countries are increasing their reserves by the discovery of this relatively new energy resource. The United States was the promoter of this unconventional resource, increasing their production significantly (Mouawad, 2009). The economic success of the unconventional reservoirs in the United States since 2000 has led to their rapid development around the world. Countries like Russia, Canada, China, and Australia have shown many recent developments of unconventional reservoirs.

The Cretaceous units of northern South-America (especially the La Luna Formation, located in Colombia and Venezuela) have one of the most significant potentials for prospective unconventional shale gas and oil. Based on the shale resource assessments for the Cretaceous Colombian Basins, the U.S Energy Information Administration (2015) estimates for Colombia are approximately 6.8 billion barrels and 55 Trillion Cubic Feet (TCF) of risked, Technically Recoverable Resource (TRR). Additionally, for western Venezuela, the estimation is approximately 13.4 billion barrels of oil and 167 TCF of gas making the Maracaibo Basin a predominant oil/gas area for the well-known La Luna Formation. The prospective area for shale exploration in the Maracaibo Basin is shown in figure 1.

La Luna Formation has been considered for a long time the main focus of study for conventional oil production since it is the most important source rock in the Maracaibo Basin and Venezuela. However, recent works on this Upper Cretaceous shale as an unconventional reservoir are very few, and La Luna is now being considered an unconventional shale prospect as well as a major hydrocarbon source rock.

Several studies have demonstrated the stratigraphic and geochemical heterogeneities present in shales and shale-gas systems. The understanding of these changes is essential to improve the efficiency of hydrocarbon prediction and production in unconventional reservoirs. Consequently, the primary objective of this work was to complete a petroleum source rock evaluation and a high-resolution sequence-stratigraphic characterization of the La Luna Formation in the western Maracaibo Basin in order to evaluate and recognize stratigraphic patterns or cycles in organic matter deposition.

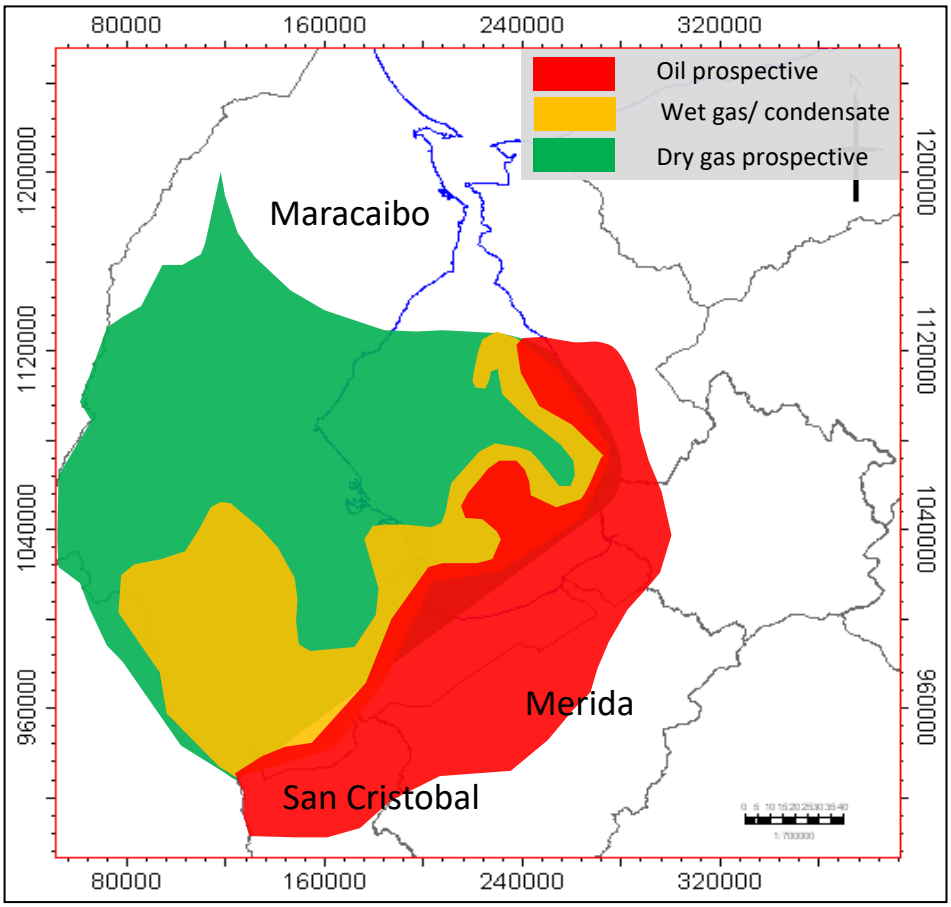

Figure 1. Prospective Area for Shale Exploration in the Maracaibo Basin (Modified from U.S Energy Information Administration, 2015).

An extensive literature has been published for La Luna Formation in the Maracaibo Basin. Talukdar et al. (1986), in their integrated basin study based on organic richness, organic matter

type and maturity, denoted the La Luna Formation as the most important source rock in the Maracaibo basin. Their estimations are based on hydrogen index and TOC, calculated an average of 290 million barrels of oil per each km^3 of the La Luna oil source at the end of the oil window.

Villamil (2002) proposed that La Luna Formation is a widespread rock unit that has different names locally, which creates confusion in the regional understanding of northern South America geology. La Luna extends from the central part of Ecuador where it is known as Chonta Formation to Colombia where it is known as Villeta, Chipaque, Gachetá, La Luna and San Rafael Formations. It extends to western Venezuela, where it is known as La Luna and Navay in the Barinas-Apure basins. It is found in eastern Venezuela and is known as Querecual. The La Luna is known as Naparima Hill in Trinidad, Guyana, Suriname, and northern Brazil, but it does not produce much oil because it has not been buried deep enough to reach the appropriate thermal maturity.

Quero et al (2007) evaluated the La Luna Formation in Táchira state, Venezuela, to determine organic matter type, depositional environment, and thermal maturity. The samples were separated into SARA (Saturate, Aromatic, Resins and Asphaltenes) fractions and analyzed by GC-MS (Gas Chromatography-Mass Spectrometry). The n-alkane distributions revealed mixed marine and terrestrial organic matter, and pristane/phytane ratios indicating suboxic-dysoxic conditions.

In 2012, Petróleos de Venezuela Sociedad Anónima along with Universidad de Los Andes-Venezuela began several projects on gas-shale exploration along outcrops in the North Andean flank. Lopez (2013b); Pachano (2013) & Monsalve (2014) did a sedimentological and geochemical characterization for the Colon Formation (Late Cretaceous, campanian in age). Results from the preliminary analysis based on Rock-Eval parameters and mineralogy have shown good geochemical properties for the development of gas-shale reservoirs.

The School of Geology and Geophysics at the University of Oklahoma has been involved with the study of unconventional deposits in many parts of the world, including La Luna Formation in Colombia and Venezuela. Torres (2013) conducted outcrop studies in the southern and middle parts of the Middle Magdalena Basin (MMB), Colombia to assess the gas shale and oil potential of La Luna Formation. The Salada and Galembo members have reached the dry gas window for hydrocarbon generation in this area of the MMB. Gomez (2014) also conducted an integrated geological characterization and distribution of the Salada Member in the central region of the MMB suggesting that the facies studied are considered as good to excellent source rocks.

Liborius and Slatt (2015) undertook a stratigraphic and geochemical characterization of La Luna Formation from one outcrop and a 345-foot core along the northwest of Lago de Maracaibo Basin. Based upon biostratigraphy, petrography, geochemical analysis, and facies characterization, the deposits were identified as third order sequences of Highstand and Transgressive system tracts.

Slatt and Rodriguez (2012) stated the importance of biomarkers and their relationship with the sequence stratigraphic framework. They developed a predictive model for evaluating the efficacy of Paleozoic and Mesozoic gas-shale plays in north America. In their model, they proposed that biomarkers and sequence stratigraphy are related by the abundance or depletion of certain compounds that can be very characteristic of a highstand or transgressive system tract, oxic and anoxic environments, and water depth indicators

Because certain biomarkers are specific to a type of organism (e.g., algal, bacterial, higher plant), the depositional environment of a unit of interest has implications when building a sequence stratigraphic framework in a basin (Calvert & Pedersen, 1993; Peters et al., 2000; Rodriguez, 2007; Slatt & Rodriguez, 2012).

For example, an indicator of oxygenation is the pristane and phytane ratio (ten Haven et al., 1987). Low values of this ratio (lower than 1) are usually related to anoxic conditions and can usually be associated to areas where a transgressive systems tract is formed. Furthermore, isoprenoids, aryl isoprenoids, and sulfur compounds are useful for interpretation of water depth, depositional setting, and source materials, respectively. Some authors have found a high abundance of C_{27} steranes near the condensed section and a high concentration of C_{29} steranes in the highstand systems tract (Fleck et al., 2002).

In this study, the variability of the lithofacies was determined from cores located in different positions of the northwest Maracaibo Basin. The integration of X-Ray Fluorescence (XRF), X-Ray Diffraction (XRD), rigorous sequence stratigraphy and organic geochemistry helped to create a depositional model and identify the vertical variability and the high definition of the most abundant and prospective organic-rich intervals in La Luna Formation in the Maracaibo Basin.

1.1 Geologic Framework

1.1.1 Regional Geology

The Maracaibo Basin is the most important petroliferous basin in Venezuela and is one of the most prolific hydrocarbon basins in the world; its extension goes over 14,210 square miles in western Venezuela (Escalona & Mann, 2006). It is located towards the north by the Gulf of Venezuela and to the west by the Sierra de Perija. Its main source rock is the La Luna Formation of Late Cretaceous age, with facies extending to western Venezuela and Colombia.

The Andes uplifted in several phases, resulting in the generation, migration, and accumulation of oil. The formation of the Maracaibo basin began 160 Ma ago with the North American, South American, and Caribbean plates playing critical roles in the evolution of the

basin. The Maracaibo Basin has developed into the present-day foreland basin via multiple tectonic stages throughout time, specifically Late Jurassic, Late Cretaceous, Paleocene-Eocene, and the Oligocene-Holocene stages (Escalona & Mann, 2006).

No Triassic rocks have been found in Venezuela so far. The lower Jurassic is represented by Volcánicas de la Ge (Sierra de Perijá) and Volcánicas de Guacamayas (Macizo El Baúl), which predated red bed sedimentation of La Quinta Formation and the extension process related to the Gulf of Mexico or Proto-Caribe opening.

Acuna et al. (1997) describe the rifting of Pangea as the formation of several structural features that later influenced the evolution of the Venezuelan sedimentary basins (Figure 2). The Proto-Caribe opening induced the development of northeast-oriented extension valleys or grabens, also controlled by linear, north-northeast– striking normal faults (Maze et al., 1984; Lugo & Mann, 1995). Among these valleys are the Apure-Mantecal, Espino, Andes-Perijá and Maracaibo grabens. All these grabens were filled during the Jurassic Period by red bed (continental) sediments, diverse volcanics, and occasional shallow-marine clastics and limestones.

In fact, in western Venezuela, the Early Cretaceous was controlled initially by the Jurassic graben faults systems, evidenced by the variable thicknesses of Rio Negro Formation clastics, from more than 2 kilometers near the south of Machiques. Later the subsidence stabilized, and there was an extensive transgression of an open sea over the western Venezuelan shelf causing carbonate sedimentation of the Cogollo Group.

The lateral clastic equivalent of these carbonates in the Cratón or Guayana Province Margins is the equivalent to the Aguardiente Formation (Acuna et al., 1997). The stratigraphic column of the Cretaceous in the Maracaibo Basin, Venezuela is shown in figure 3.

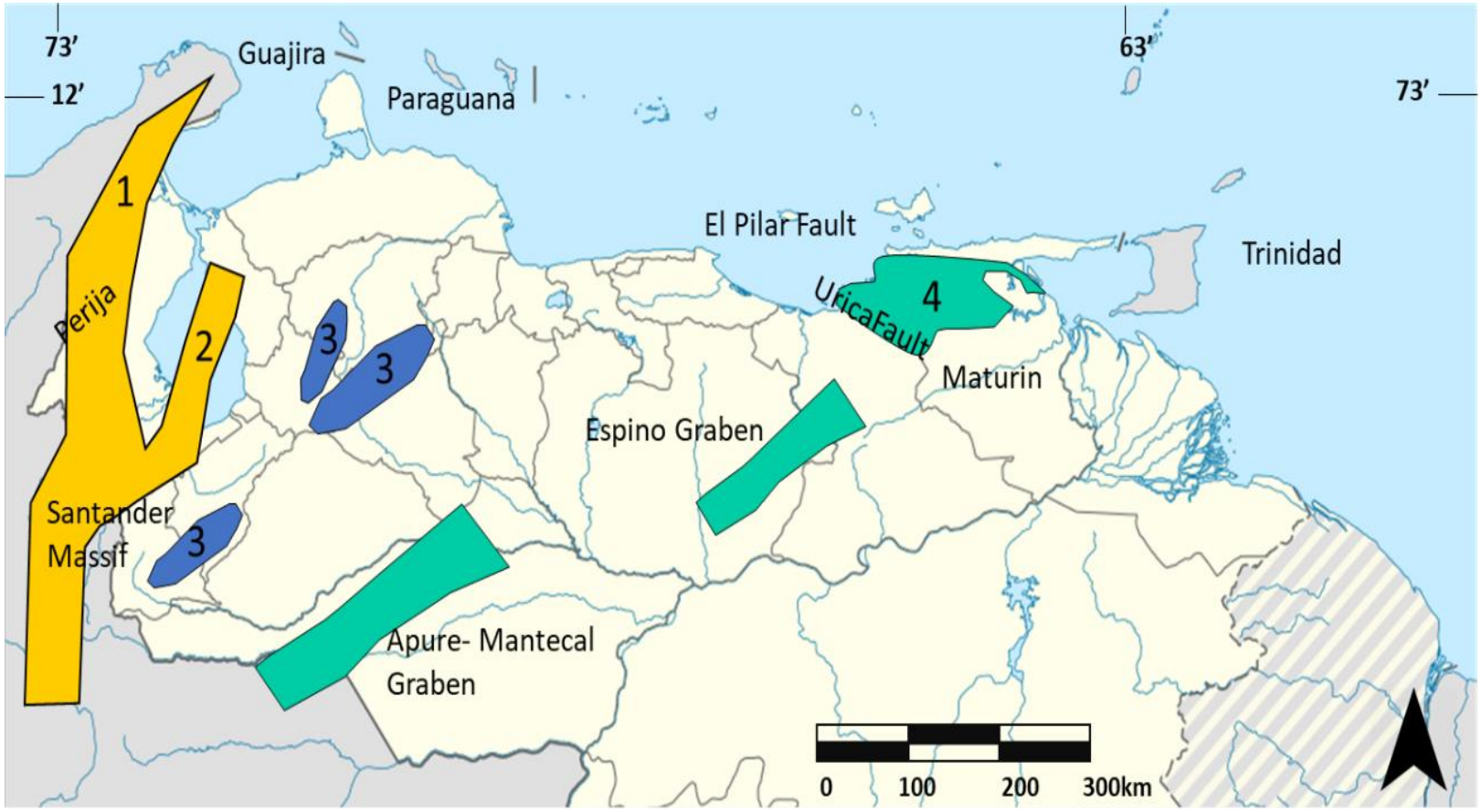

Figure 2. Distribution of Jurassic rocks: 1) in Perijá Range; 2) as part of the economic basement of Maracaibo Basin; 3) in the Andes; 4) in Barinas-Apure and eastern Venezuela Basins (Apure-Mantecal and Espino Graben). It is believed that they are involved in deep thrusting within eastern Venezuela's interior range (Modified after Bartok, 1993; Passalacqua et al., 1995 and Lugo & Mann, 1995).

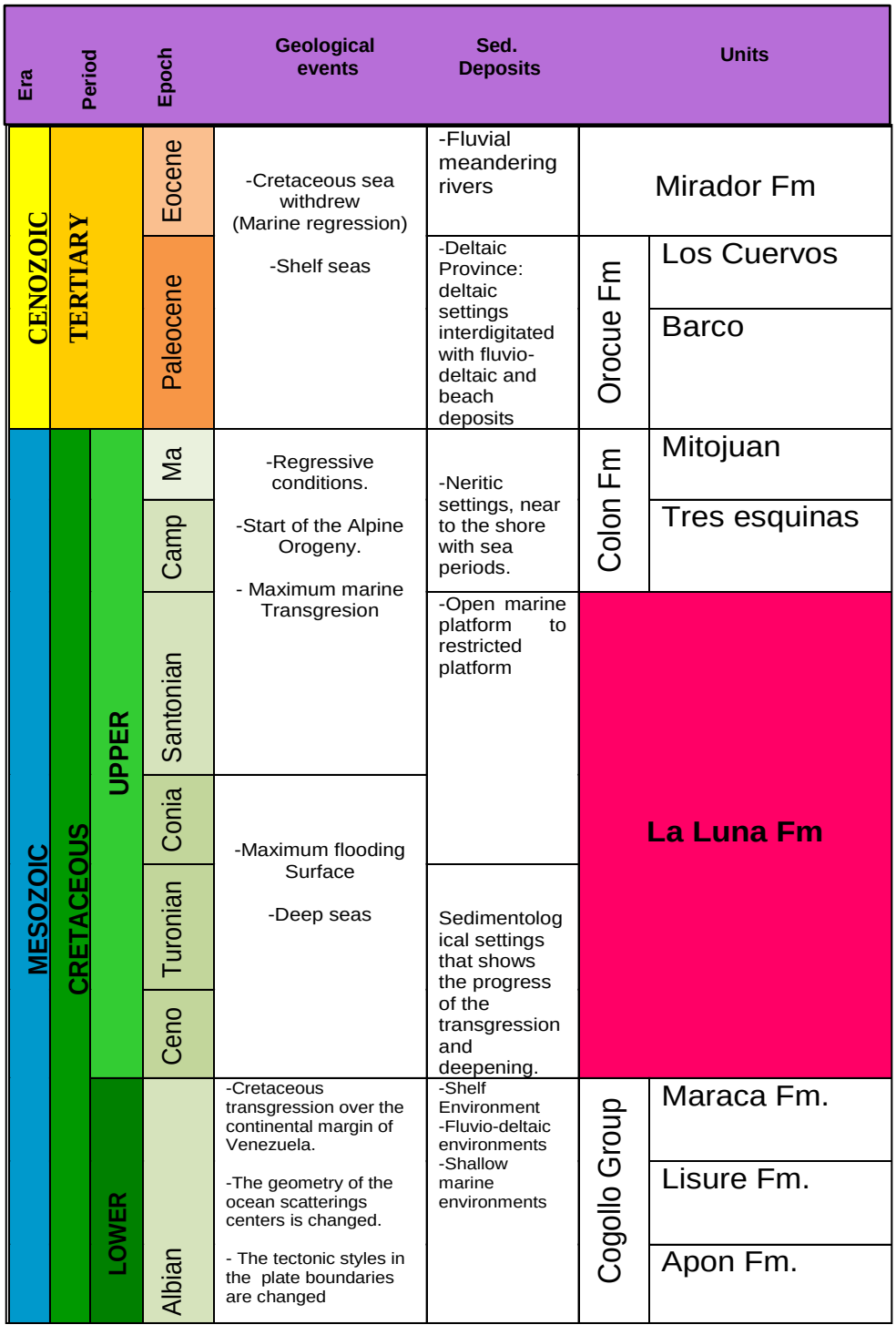

Figure 4. Stratigraphic column of the Cretaceous in Maracaibo Basin, Venezuela (Modified after González et al., 1980).

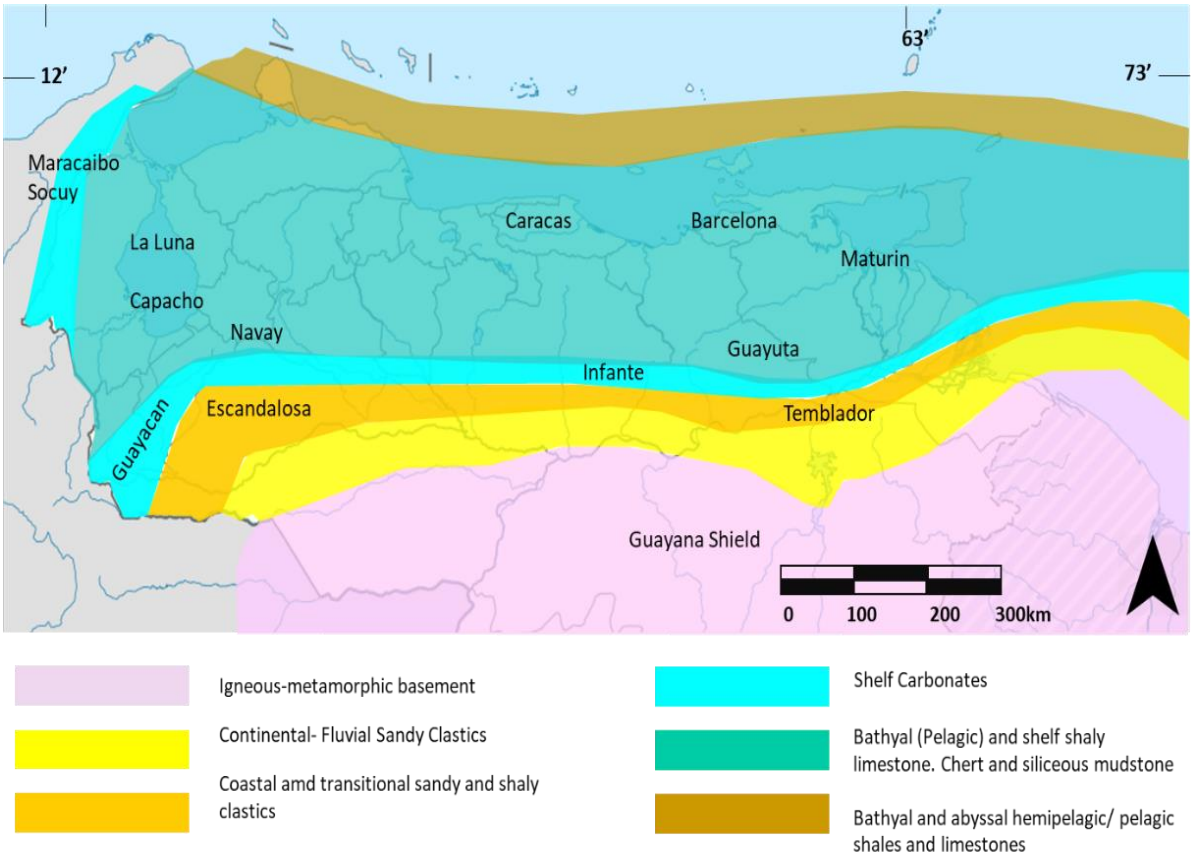

Figure 5. Paleo-environmental distribution during the Cenomanian-Campanian at the northern edge of the Guayana Shield. Typical units of these sets of facies indicated. Taken from Acuna et al., 1997.

The Early Cretaceous- Paleocene was characterized by a "mixed clastic-carbonate platform and a thermal subsidence and tectonic quiescence of the passive margin leading to a period of sediment accumulation and absence of deformation" (Escalona & Mann, 2006). The paleo-environmental distribution and stratigraphic units during the Late Cretaceous are shown in Figure 4 which encompass the correlation for these units in Venezuela. A marine invasion began at the end of the Lower Cretaceous, moving from east to west and invading the south of Venezuela, which had been emerging and undergoing erosion since Late Jurassic and possibly Paleozoic times.

This marine invasion is related to the worldwide transgressive pulse of the Late Cretaceous developed in America and Europe through the sedimentation of organic-rich limestones, shales, and cherts; these rocks in Venezuela known as the Querecual- San Antonio (Guayuta Group), Mucaria, Navay, and La Luna Formations (Acuna et al., 1997).

The maximum transgression and lack of oxygen are believed to have occurred between the Cenomanian- Santonian (100.5-83.6 Ma) in which La Luna Formation deposited in a shelf- slope setting (Liborius and Slatt, 2016). In Perijá and the Maracaibo Basin, La Luna Formation grades vertically to glauconitic limestones (Socuy Member), and dark shales with thin sandstones defined as the Colon and Mito Juan Formations.

The Late Cretaceous in Venezuela ends in the Maastrichtian, with units that are regressive related to the deeper environments of the source rock. Lugo & Mann (1995) and Parnaud et al. (1995) describe some structures present in the Maracaibo Basin because of the tectonic uplift of the western and Central Cordillera of Colombia during the Cretaceous Period that possibly caused the increment of subsidence in the Late Cretaceous in where the Colon Formation was deposited.

In Northwestern Maracaibo, the Paleocene-Eocene Epoch was characterized by a complex foreland wedge filled by clastic sediments due to the oblique convergence between the Caribbean plate and the northwestern margin of South- America. (Lugo & Mann, 1995). This deposition represents the most prolific hydrocarbon reservoirs in the Maracaibo Basin (Misoa Formation). Meandriform rivers and fluvial deposits are characteristic of the Eocene Epoch.

Escalona & Mann (2003) stated that the isostatic rebound affected the central and eastern parts of the Maracaibo Basin forming the Eocene unconformity (that also represents the main seal above the Eocene Reservoirs) eroding the central and northeastern parts of the basin until the end of the Oligocene.

The Miocene–Holocene period is characterized by the uplift of the Venezuelan Andes and the erosion of the Sierra de Perija towards the west and southeast flanks of the Maracaibo Basin (Shagam, 1984). Escalona & Mann (2003) attribute the formation of the north-south–trending Maracaibo syncline to the final stage of this uplift and convergence also stating that it controls the present-day geographic configuration of the basin and the location of its marginal oil seeps.

1.1.2 Paleogeography and paleo-climate of La Luna Formation

The initiation and the end of anoxic conditions in the Maracaibo Basin follows a complex relationship of paleo-bathymetry, paleoclimate, and paleoceanography (Erlich et al., 2000). Even within the Cretaceous, two critical regional transgressions caused the development of pelagic marine facies in western Venezuela; a marine transgression is insufficient to explain the uniformity and continuity of the organic-rich deposits during the Albian-Cenomanian and Cenomanian-Turonian (Erlich et al., 2000).

Erlich et al. (2000) states that the Turonian-Campanian positive Santa Marta and Santander massifs and the ancestral Merida Andes paleo-bathymetric highs (caused by the uplift of the Central Cordillera of Colombia) developed a poor circulation (anoxia) and a limited ventilation within the Maracaibo and Barinas/Apure basins during the deposition of the La Luna and the Navay Formation. Anoxia was also enhanced by high evaporation and low precipitation rates (high salinity bottom water) and high levels of marine algal productivity (Erlich et al., 2000). Anoxia was not necessarily a requirement for the accumulation of organic carbon-rich sediments in western Venezuela (Pedersen & Calvert, 1990) since normal marine productivity levels characterized the La Luna and Navay formations during their deposition (Erlich et al., 2000).

La Luna Formation was deposited in mid-shelf to upper-slope environments on the Late Cretaceous passive continental margin of northern South America (Macellari & De-Vries 1987;

Erlich et al., 2000). Productivity is one major factor in the source rock formation, but preservation is equally important. Preservation will depend mainly on both the nature of organic matter and the nature of the depositional and post-depositional environment. Both are equally important to preserve the TOC since good preservation is no good without the organic matter production (Philp, personal communication, 2015).

Macellari & De-Vries (1987) and Martinez & Hernandez (1992) state, in an extensive review of literature related to productivity vs. preservation, the lateral and stratigraphic heterogeneity of La Luna Formation suggests the existence of temporal variations in nutrient-rich upwelling currents during deposition. However, Perez-Infante et al. (1996) indicate that "primary productivity may have had only a minor influence on the final TOC since the parameter does not change markedly in those intervals where an increase in primary productivity can be expected". Total organic carbon interpretation in the La Luna Formation is more likely controlled by local environmental factors related to the preservation and degradation of organic matter than to productivity. Since preservation is the most prominent factor in the La Luna Formation, this leads to a higher organic matter quality and a higher TOC.

Erlich et al. (2000) described the deposition of the Socuy and Tres Esquinas member (Upper La Luna) during the Late Cretaceous, as a change in the paleoclimate and paleoceanography in western Venezuela. An increment in bottom water oxygenation generated the development of burrowing, reducing in this way, the preservation of organic matter. Also, the increment in tectonic activity and global climate change contributed to higher rainfall rates and intensified wind-driven upwelling causing a frequent overturn of anoxic water in western Venezuela. He also states that Phosphatic fish and reptile bone beds found within the Tres Esquinas

Member are the result of explosive dinoflagellate productivity (red tides), induced by intensified upwelling and episodic fluvial supply of nutrients.

1.1.3 Isotopic analysis of La Luna Formation and relationship with Oceanic Anoxic Events (OAE) in the Maracaibo Basin.

Biostratigraphy and carbon-isotope stratigraphy have been used to correlate and characterize the temporal and spatial patterns of deposition in organic-rich sediments of La Luna Formation. Documented carbon isotopic analysis on La Luna started more than 35 years ago when Scholle & Arthur (1980) proposed the potential of carbon isotopic fluctuations as a stratigraphic tool in the Late Cretaceous sediments of the Maracaibo Basin. The findings of large positive excursions of $\delta^{13}C$ in the carbonates of the Aptian- Albian and Cenomanian-Turonian boundary and some smaller excursions in other periods found in several sections was the starting point of these studies in the La Luna Formation.

Perez-Infante et al. (1996) started to evaluate not only the biostratigraphic and isotopic relationship of La Luna Formation but also the lithologic and the geochemical data to assess the global and local controls influencing the deposition of the La Luna Formation in western Venezuela. He found a marked and positive $\delta^{13}C$ organic isotopic excursion (-27.6‰ to -29‰ VPDB standard) in the middle part of the section (Figure 5).

Results from Perez-Infante (1996) are unrelated to local paleo-environmental changes in bio-productivity and oxygen depletion. The interesting part is that the isotopic excursion did not show any association with the biomarker data, meaning that the isotopic excursion could have been generated by the controls on local fluctuations in organic-matter input and preservation. As it is noticeable in Figure 5, the isotopic profile and positive excursion are not associated with any

marked change in lithology, TOC or HI, suggesting that dysoxic- anoxic bottom waters were already locally established in the basin.

Alternatively, Davis et al. (1999) presented a $\delta^{13}C$ curve from a core located in the northwestern Maracaibo Basin (Figure 6). The analysis trend represents a possible excursion in the carbon isotopic composition of bulk organic matter that can be associated with an event of widespread oxygen limitation during the Aptian-Albian (Ocean Anoxic Event 1B) which enhanced the global burial rate of reduced relative to oxidized sediments. This event makes up the Cogollo Group, the underlying member of La Luna Formation.

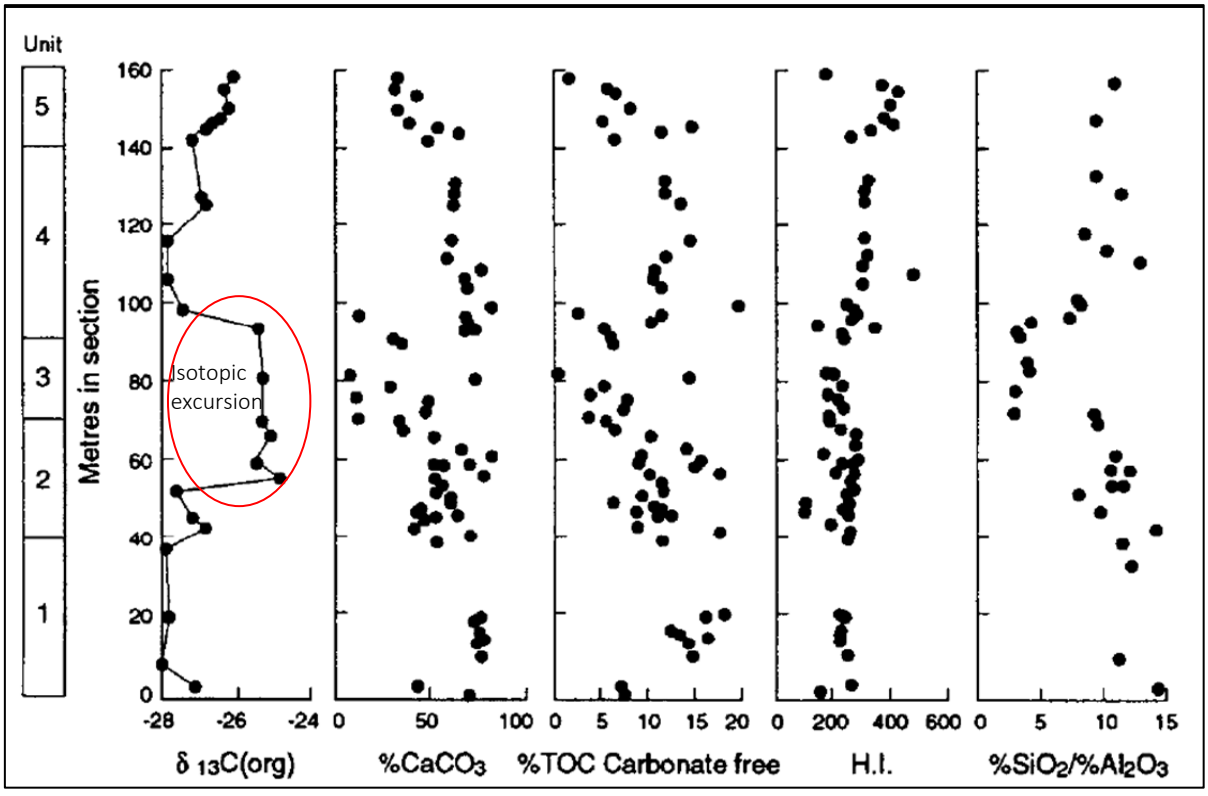

Figure 6. $\delta^{13}C$ organic carbon isotopic composition of organic matter (‰PDB); % carbonates (as $CaCO_3$); % TOC (expressed on a carbonate-free basis); H.I. = hydrogen index (from pyrolysis Rock-Eval, mg HC/g TOC); silica/alumina data of the La Luna Formation at Quebrada Maraca. Only values for marls and shales are plotted (From Perez-Infante, 1996).

The isotopic excursion associated with the OAE1B also resulted from a similar event during the Cenomanian-Turonian that was indicated by a significant isotopic excursion in the La Luna. Interestingly, the isotopic analysis also shows no relationship associated with high organic-rich intervals like the ones found by Perez-Infante (1996).

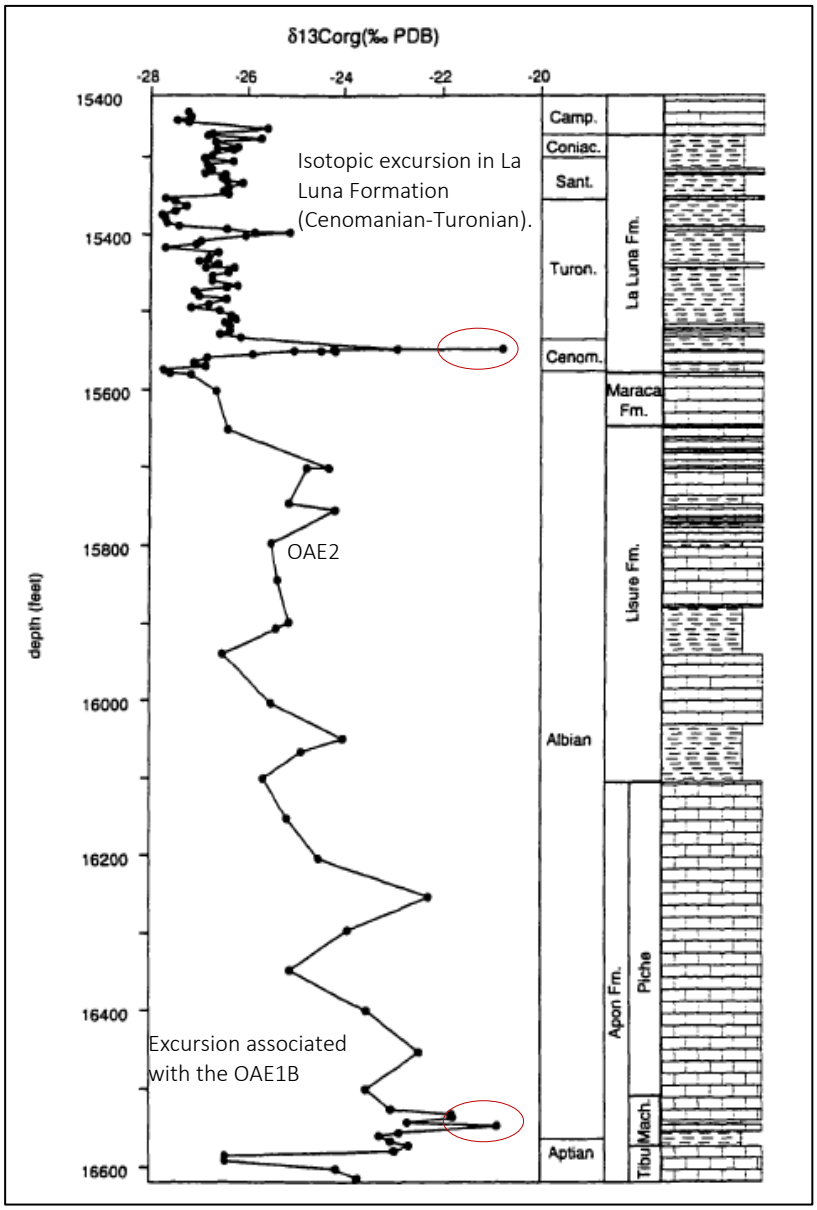

Figure 7. Stable carbon isotopic composition of bulk organic matter and generalized stratigraphy of the ALP-6 core. Davis et al. (1999).

Core analysis in the Northwest Maracaibo Basin (De-Romero et al., 2003) also revealed a marked trend in the isotopic composition of the Cenomanian-Turonian boundary excursion with a positive $\delta\ ^{13}C$ shift of 6.23‰ values relative to the VPDB (Totumo-3 core). This result also correlates with results in Figure 6 developed by the previous work of Davis et al. (1999) in which the values show a similar positive excursion at the Cenomanian- Turonian boundary in the nearby ALPUF-6 Well core.

The correlation of the carbon isotopic curves above the Cenomanian-Turonian boundary with the analyzed sections of Pratt & Threlkeld (1984) can be subjective, especially in the Totumo-3 Well where abundant high-amplitude fluctuations occur. A tentative correlation was provided between the two positive excursions (excursions 2 and 3) that occur in the Coniacian to lowermost Santonian part of the section. Although few data points define these excursions, the proposed correlation made by the author is consistent with the biostratigraphy.

De-Romero et al. (2003) make another interesting conclusion, where the excursion peak in one of the cores located in the northwest Maracaibo basin (Totumo-3) is observed in an interval 5.5m higher than in the ALPUF-6 core concerning the underlying Maraca Formation. This increment can also be related with the contact between Maraca and La Luna Formation that can be interpreted as an uneven, karstic surface similar to Woodford-Hunton (Infante-Paez et al., 2016) previously supported in La Luna by Truskowski et al. (1995).

Thus, carbon isotope stratigraphy can be useful to provide a means of correlation between the Cenomanian-Turonian boundary interval in the La Luna Formation and perhaps of levels within the Coniacian. The application of the combined biostratigraphy, complemented by carbon isotope

stratigraphy, has enabled the establishment of rates and patterns of sedimentation of the La Luna Formation throughout the Maracaibo Basin.

1.2 Objectives

The primary objective of this work was to apply a petroleum source rock evaluation and a high-resolution sequence-stratigraphic characterization of the La Luna Formation in the western Maracaibo Basin. This study attempts to evaluate and recognize patterns or cycles in organic matter input, and how they relate to each other, as well as to develop a predictive model assessing the efficiency of unconventional plays using geological and geochemical data. Goals include:

- Characterization of the stratigraphy, sedimentology, and mineralogy of the La Luna Formation for determining its prospects as an unconventional reservoir.
- Determination of the organic richness, type of organic matter, evaluation of the source rock generation, thermal maturity and variations in the organic-matter input and depositional environment conditions.
- Propose a relationship between sequence stratigraphy, organic input, and anoxic events, to evaluate the efficacy of unconventional plays using biomarkers.

CHAPTER II

2. METHODOLOGY

Three main stages were conducted to achieve the objectives of this work: Fieldwork and core sampling, reservoir characterization, and source rock characterization.

2.1 Study area and sample location

This study was conducted in northern South America, northwest Venezuela. A total of 153 samples were taken from outcrop and core towards northwest Maracaibo (Figures 8 and 9). The Zulia State is located to the south of the Gulf of Venezuela and the Caribbean Sea; it is northwest of Mérida, Táchira and Trujillo states; to the west of Falcón and Lara states and to the east of the Republic of Colombia (Figure 7).

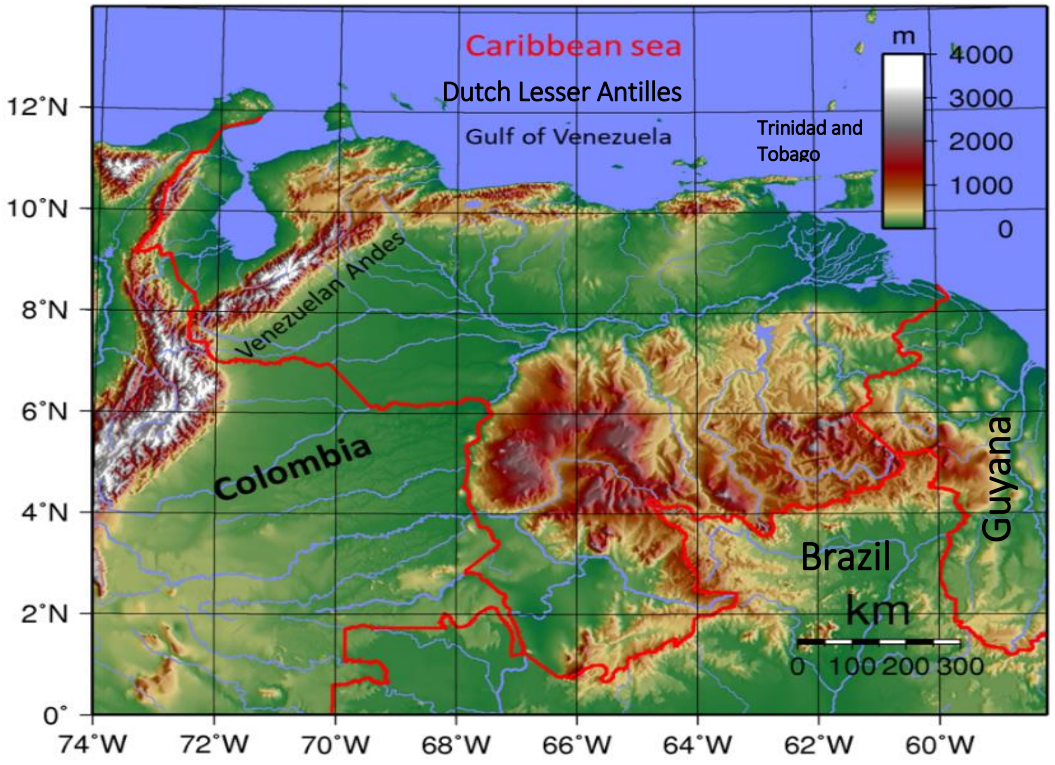

Figure 8. Map of Venezuela bordered by Colombia on the west, Brazil on the south, Guyana on the east, the Dutch Lesser Antilles to the north and Trinidad and Tobago to the north-east. From Acuna et al., 1007.

To characterize the La Luna Formation in the Maracaibo Basin, a fieldwork study was conducted in the La Luna stratotype (Figure 8) and four cores located along the different positions of the basin were also described: La Luna IX (LLIX); La Luna IE (LLIE); La Luna IA (LLIA) and, La Luna IS (LLIS). Cores were provided by the Venezuelan national oil company, Petróleos de Venezuela S.A (PDVSA) in Zulia state, Venezuela (Figure 9).

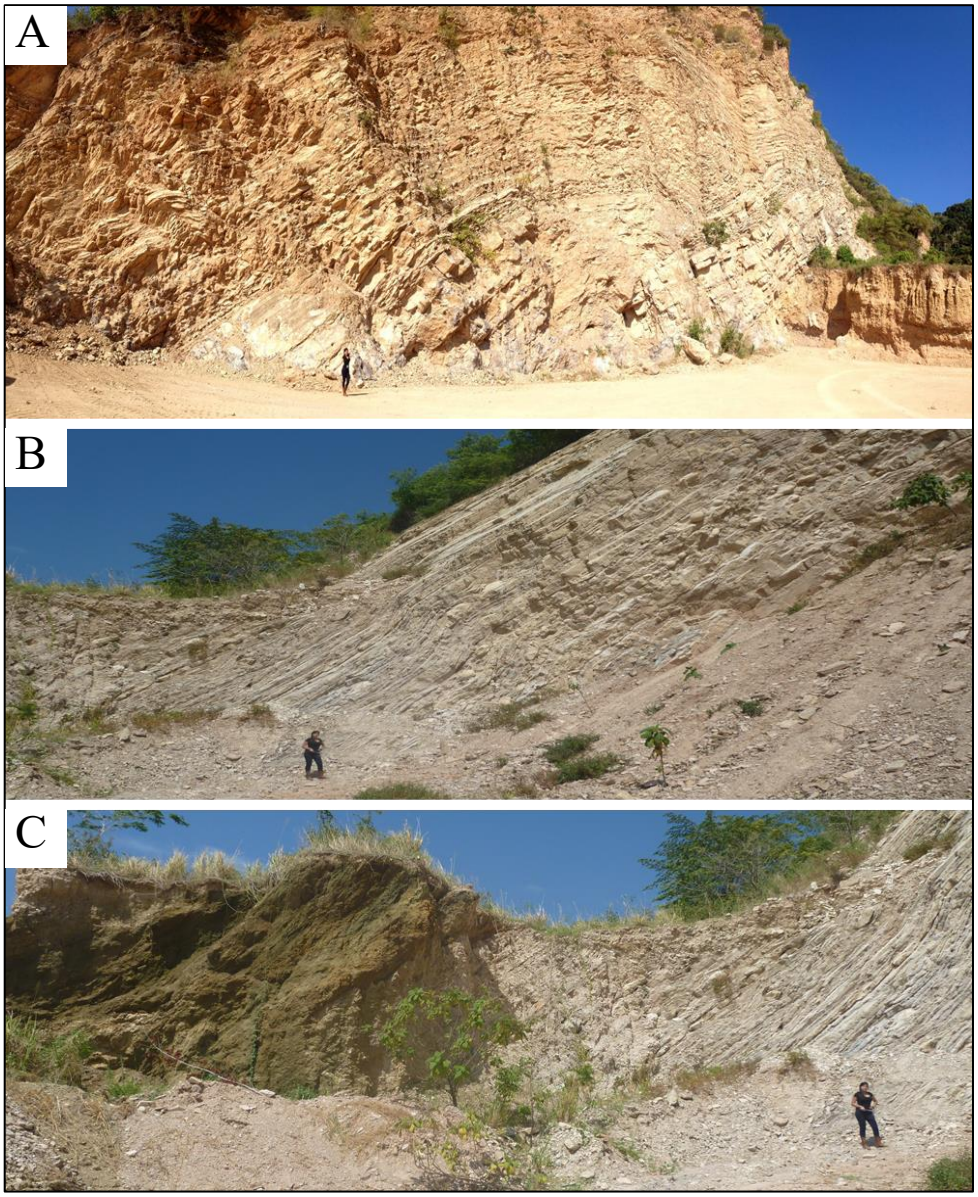

Figure 9. La Luna stratotype outcrop displaying the Lower (A), Middle (B) and Upper (C) La Luna in Flanco Perijanero, Maracaibo-Venezuela.

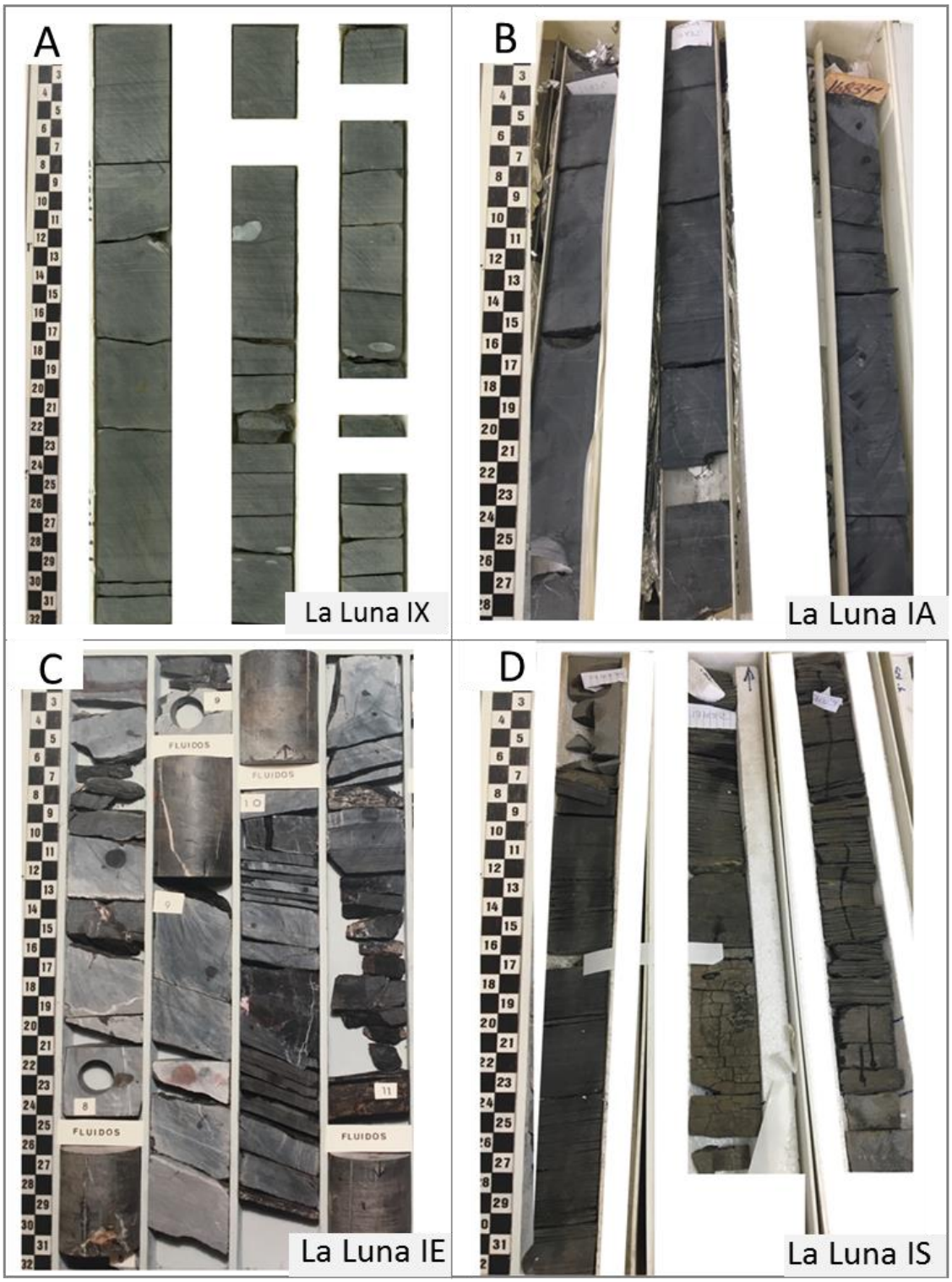

Figure 10. Cores used for the study of unconventional reservoirs in La Luna Formation, Venezuela located along northwest, Venezuela. (A) La Luna IX, (B) La Luna IA; (C) La Luna IE and (D) La Luna IS.

The primary objective of the La Luna IX core analysis was the sedimentological and petrophysical characterization to get a detailed understanding of the lithology, mineralogy, age, porosity, permeability, facies and sedimentary environment of deposition. The methodology proposed by Slatt et al. (2012) and Miceli-Romero & Philp (2012) was applied to the geologic characterization of La Luna Formation samples (Figure 10).

2.1.1 Fieldwork and core samples:

This stage was accomplished by six weeks of fieldwork and core description in the La Concepcion headquarter in July 2014 and December 2017 in northwest Maracaibo. The outcrop was described as follows:

A proposed nomenclature was used for easy sampling identification according to the Universidad de Los Andes fieldwork procedures: name of the location, age, and name of the formation, initials of the researcher, and the number of the sample. The code was the following: PE (Perija); KL (Cretaceous La Luna); AL (Andreina Liborius); 001 (Sample 001).

Collected samples were taken from bottom to top; they were oriented along the magnetic north, to indicate the same position at the time of the removal from the outcrop. Jacob's staff was used for section measurement and scale, 10% HCl for carbonate lithological screening and, outcrop Gamma Ray (GR) to obtain natural occurring radioactivity intensities.

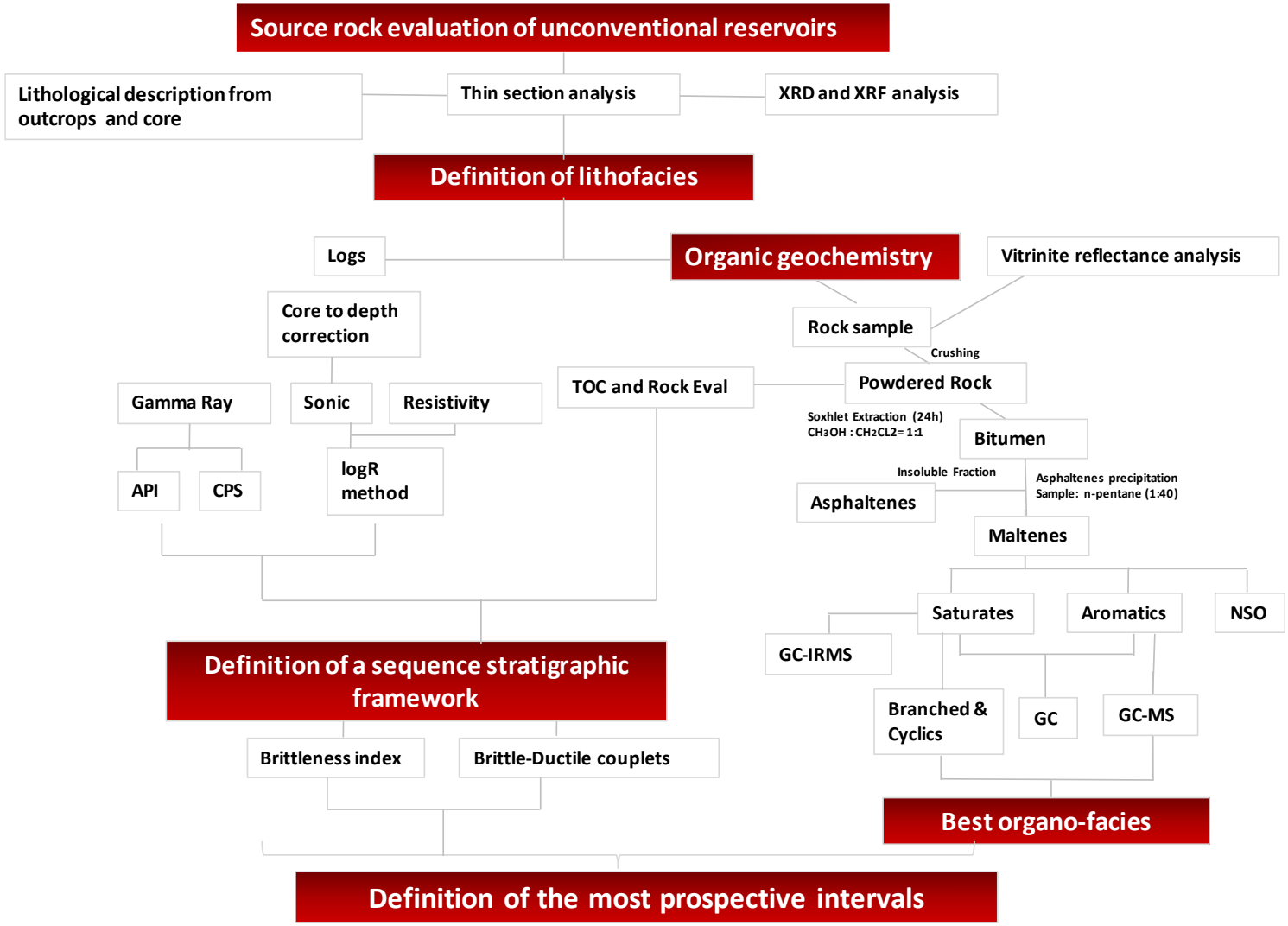

Figure 11. Flowchart for source rock evaluation of unconventional gas shales (Modified from Slatt et al., 2012 and Miceli-Romero & Philp, 2014).

Core description and sample collection were done in four cores located in the northeast and southwestern part of the Maracaibo Basin (Figure 11). Most of the core samples were taken every 5 feet, and high-resolution of lithological description and pictures with scale and a lithological profile (every foot) were done for every core.

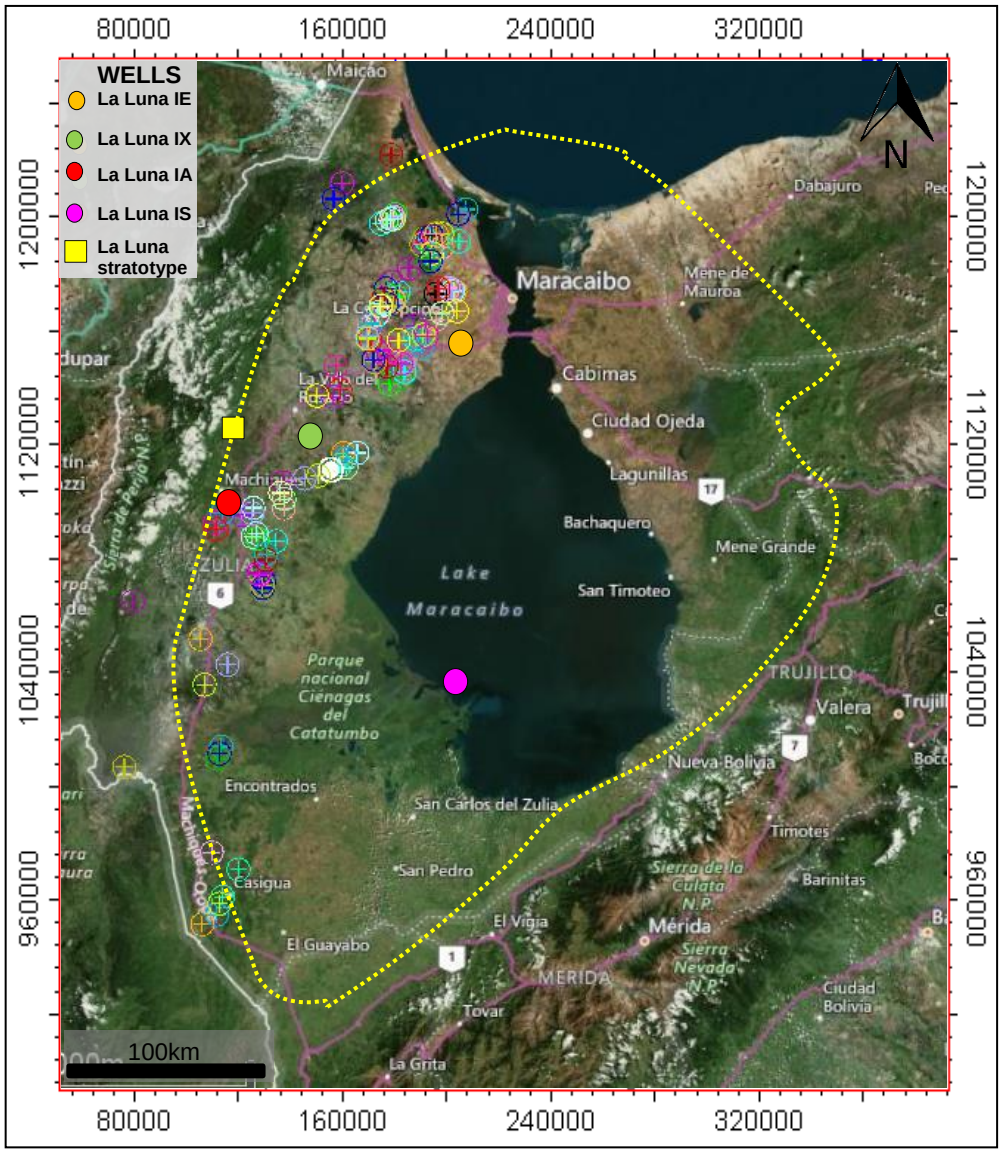

Figure 12 Map showing the core and outcrop location of La Luna Formation in Northwestern Venezuela. The dash yellow line represents the Maracaibo Basin The La Luna IE core represents the dark yellow circle; the pale green circle represents the La Luna IX core, red circle by the La Luna IA and pink circle represents La Luna IS. The yellow square represents the location of the La Luna stratotype.

Cores were described under the following geological criteria: color, lithological changes, significant textural changes, contacts, geometry, observable diagenetic processes, fossils and degree of bioturbation (ichnofossils) and degree of alteration of the core. The nomenclature used was also represented by the same outcrop criteria: name of the core, age and name of the formation, initials of the researcher and number of the sample. The code was the following: La Luna IX (llIX); KL (Cretaceous La Luna); AL (Andreina Liborius); 001 (Sample 001).

Samples collected are summarized in Table 1 and are shown according to the name of the core/outcrop, and the type of analysis done for each sample. It is worth mentioning that only certain samples were subjected to petrographic and biomarker analyses since macroscopic descriptions were similar.

Table 1. Summary of samples used for geochemical and petrographic analysis.

Lithology	**Location**	**Name**	**Samples**	**Geochemistry**		**X-Ray Diffraction and X-Ray Fluorescence**
				Rock-Eval	Biomarkers	
Marlstone	Northwestern Maracaibo Basin	La Luna IX	46	46	37	46
Marlstone	Northwestern Maracaibo Basin	La Luna IE	30	29	0	30
Marlstone	Northwestern Maracaibo Basin	La Luna stratotype	10	10	8	10
Marlstone	Northwestern Maracaibo Basin	La Luna IS	20	19	14	20
Marlstone	Northwestern Maracaibo Basin	La Luna IA	47	47	17	47

2.2 Reservoir Characterization

Across the study area (northwestern- southeastern Maracaibo Basin), 153 samples were collected and TOC, Rock-Eval, X-Ray diffraction (XRD), X-Ray Fluorescence (XRF) analyses were performed. Based on lithological and distinctive facies, representative samples were chosen for petrographic and biomarkers analyses (based on TOC content). In total 76 samples were selected for biomarkers and 35 samples were selected for petrographic analyses.

2.2.1 X-Ray Fluorescence

X-Ray Fluorescence (XRF) is a quick and versatile method to determine the elemental compositions of rock samples. The principle of the X-ray fluorescence (non- destructive technique) is mostly based on the excitement of the sample that is generated by X-rays to ionize atoms and molecules. The spectrum of wavelengths from the energy release as well as their intensities is recorded by an XRF spectrometer that detects and counts proportions of some major and trace elements present in the sample (Turner et al., 2015; Galvis-Portilla, 2017).

A hand-held XRF tracer model IV-SDTM from Bruker Co. was used for the XRF analyses. The analyses were made for all the samples on a smooth surface of the fresh rock. The scanning process was divided into two segments, one for majors elements and one for trace elements. The major elements were monitored for each sample for 90 seconds under vacuum conditions of 15kV and 35 mA. The trace elements were analyzed for a length of 60 seconds with a Ti-Al filter of 40kV and 17.1 mA. Analyses were recorded in parts per million (ppm). The elements and proxies monitored in this research are summarized in Table 2 (Tribovillard et al., 2006 and Turner et al., 2015).

2.2.2 X-Ray Diffraction

Since rocks are mostly composed of minerals, analytical techniques are necessary to characterize these minerals. X-ray diffraction (XRD) is a non-quantitative data that complements other methods used for mineral identification (e.g. electron microprobe and scanning electron microscopy).

Table 2. Summary of key chemostratigraphic elements and proxies as indicators of the depositional environment. Modified from Turner et al., 2015.

Element		Proxy
Titanium and Zirconium	Ti and Zr	Continental Source
Thorium	Th	Clay contents and feldspar
Calcium and strontium	Ca and Sr	Typically carbonate material, but can be associated with clay minerals, feldspars, phosphates, or sulfates
Phosphorous	P	Phosphate accumulation
Magnesium and Manganese	Mg and Mn	Carbonates, dolomitization
Potassium and Aluminum	K and Al	In mudrocks, usually clay minerals, but can also found in feldspars
Molybdenum and Vanadium	Mo and V	The degree of anoxia present within a basin
Silicon/Aluminum or Silicon/Titanium	Si/Al or Si/Ti	How much quartz is present within the sediment (biogenic or detrital)
Sulfur	S	Pyrite, reducing conditions, euxinia
Uranium	U	Organic matter richness
Thorium/ Uranium	Th/U	Amount of clastic input versus organic input
Titanium and Niobium	Ti/Nb	Composition of clastic material, continental source.
Copper, Nickel, Zn	Cu, Ni, Zn	Are known to form pyrite and, consequently, they are often used as 'key' indicators of anoxia
Terrigenous input= Titanium+ Aluminum + Potassium Sodium	Terr. In = Ti + Al + K + Na	Terrigenous Input

XRD is based on the principle of Bragg's Law ($n\lambda=2d\sin\theta$) where the integer n is the order of the diffracted beam, λ is the wavelength of the incident X-ray beam, d is the distance between adjacent planes of atoms (the d-spacings), and θ is the angle of incidence of the x-ray beam. Since lambda is known, theta can be measured to calculate the d-spacing. Moreover, since each mineral has a unique set of d-spacing, XRD allows precise identification of the minerals (Moore & Reynolds, 1997).

The software provided by Paladin Geological Services is based on powder X-ray diffraction patterns that generate a quantitative analysis of samples supported by three methods based on calibration curves (internal standard method, external standard method, and standard addition method). The XRD analyses were done using 3g of powdered rock per sample placed on a steel holder. Each sample was analyzed in 18 min where the matching peaks and the ID phase identification was completed with an integrated X-ray powder diffraction software PDXL 2.2 from Rigaku. One hundred and fifty-three (153) randomly oriented samples were prepared for XRD analyses in which the crystalline phase identification was performed by the Rietveld analysis, which generally refines structure parameters to calculate the diffraction pattern and obtain the mineral percentage of the rock.

XRD values are always obtained after the phase identification. The identification of mineral phases was based on the position (2-θ) and d-spacing (Å) of individual peaks according to Moore & Reynolds (1997) and their values based on the intensities of peaks.

2.2.3 Petrographic thin sections

Petrographic thin sections are considered an essential tool for the unique physical characteristics that every facies can represent within a specific interval. Petrographic thin sections are made of rock samples that are analyzed under a polarizing petrographic microscope. A thin

section of rock is cut from the sample with a diamond saw and ground optically flat. It is then mounted on a glass slide of only 30μm thick on average. When placed between two polarizing filters set at right angles to each other, the optical properties of the minerals in the thin section alter the color and intensity of the light as seen by the viewer. As different minerals have different optical properties, most rock-forming minerals can be easily identified (Tarbuck et al., 2016). Texture, composition, and porosity are considered the three most fundamental properties to evaluate and compare to other mineralogical analyses such as XRF, XRD, SEM, and TOC since it can provide a tangible indication of the organic and inorganic content.

Forty-four (42) thin sections were taken for petrographic analysis representing the most distinctive lithofacies of the studied cores towards the NE-SW Maracaibo Basin. The analysis was assessed using a Zeiss Axio Imager Z1 polarizing microscope with varying degrees of magnification (10–100x).

2.3 Source Rock Characterization

A comprehensive geochemical work-flow was developed for source rock characterization, including Rock-Eval pyrolysis, total organic carbon (TOC), and vitrinite reflectance (%Ro). Moreover, rock extracts were subjected to gas chromatography (GC) and gas chromatography-mass spectrometry (GCMS) for biomarker analyses. Rock-Eval pyrolysis and TOC determination were performed at GEOMARK^{TM} Research in Humble, Texas. Biomarker analyses were conducted at the University of Oklahoma Organic Geochemistry Laboratories.

2.3.1 Preliminary sample treatment

Rock samples were cleaned and dipped in a solution of 1:1 CH_2Cl_2 (dichloromethane) and methanol (CH_3OH) with sterilized metal tongs to minimize experimental bias from handling, plastics, drilling mud and other potential contaminants (microorganisms, groundwater, loose

sediment). Samples were dried for 24 hours in a hood to ensure complete solvent evaporation before being crushed to < US Standard Mesh No. 40 (0.425mm) in a cleaned porcelain mortar and pestle. Samples were crushed until adequate powder was acquired for extraction/fractionation procedures.

2.3.2 Rock-Eval pyrolysis and Total Organic Carbon

In the laboratory total organic carbon is a critical source rock screening tool to determine which samples will be subjected to further analysis. TOC values are obtained through oxidation of the organic material, then through measuring the CO_2 that is produced. Today, most TOC determinations are part of the Rock-Eval analyses (Philp, R.; personal communication. 2014). A hundred and fifty-three (153) crushed rock samples were sent to GEOMARK^{TM} Research, Ltd. in Humble, Texas for Total Organic Carbon (TOC) determination and Rock-Eval pyrolysis. Approximately 2g of each sample was needed to perform these analyses. Results were used as a screening process for the selection of samples used for Soxhlet extraction and further fractionation.

The S1 peak represents the free oil hydrocarbons remaining in the rock and volatilize at 300°C (mg HC/g rock). The S2 peak represents the remaining potential to generate hydrocarbons by kerogen degradation using programmed pyrolysis from 300-600°C, usually at 25°C/min (mg HC/g rock) and maximizes of temperatures depending upon the structure of the kerogen along with the maturity of the source rock. The S3 peak is the organic carbon dioxide evolved between 300-390°C (mg CO_2/g rock), generated during the decomposition of the kerogen. The S4 peak is the residual carbon from the oxidation of dead carbon remaining after pyrolysis. These peaks are represented by a pyrogram that is obtained from the volatilization and pyrolysis products of the source rock.

The organic matter distribution is divided into live carbon and dead carbon. The former is composed of gas/oil and organic matter (Kerogen) and is related to the S1 and S2 peaks of a pyrogram plot. The latter is related to the S4 peak.

Furthermore, other parameters are linked to the S1, S2, S3, and S4 peaks. The Tmax parameter is the temperature of maximum evolution of the S2 hydrocarbons and an indication of thermal maturity. Also, using these three parameters (S1, S2, and S3) together with the TOC content of the sample, two critical parameters can be developed (Tissot & Welte, 1984). The former is the hydrogen index, (HI) which is the S2 peak normalized to the TOC and gives a measure of the amount of kerogen in the rock and indirectly the hydrogen content. The latter is the oxygen index, (OI) which is the S3 peak normalized to the TOC and shows a measure of the organic oxygen content of the kerogen. Lastly, the production index (PI) is the ratio of S1 to S1+S2. S1 and PI increase with maturation and most reservoirs have very high PI values.

2.3.3 Vitrinite Reflectance

GEOMARK^{TM} Research generated the calculated vitrinite reflectance measurements. The calculated values were obtained from Rock-Eval Tmax data according to the equation proposed by Jarvie et al. (2007):

$$\text{Calculated \%VRo} = 0.0180 \times \text{Tmax} - 7.16$$

Measured vitrinite reflectance values were obtained from pellets prepared at the Oklahoma Geological Survey Organic Petrography Laboratories in Norman, Oklahoma under the supervision of Brian Cardott. A least 10 grams of whole rock samples were needed for the preparation of organic pellets. A mixture of epoxy resin and hardener (5:1) was centrifuged for 3 minutes to remove air bubbles from it and then transferred into the ring forms until half full.

Each crushed rock sample was sprinkled into its designated ring form and mixed with the epoxy until all the grains were covered with the epoxy mixture and evenly spread across the bottom of the ring form. Additional bubble-free epoxy was poured into the ring forms up to the rim. The pellets were left to harden at room temperature for about 12 hours. Dispersed organic pellets were polished using a Buehler Ecomet III Griding and Polishing Apparatus to remove any scratches and obtain a relief-free surface for visual analysis. Pellets were polished with 320, 400, and 600 grit paper for 3 minutes using tap water as a lubricant. Each sample was subsequently rinsed off using distilled water and placed in an ultrasonic bath with distilled water and a few drops of Kodak Photo-Flo 200 solution for 1 to 2 minutes.

Sample pellets were further polished using a Buehler Texmet polishing cloth with Wendt Dunnington 0.3μm alumina slurry and distilled water as a lubricant for 4 minutes. Pellets were then washed with distilled water and placed in the ultrasonic bath for 2 minutes. After this step, the pellets were rinsed with distilled water and blow-dried using filtered air. Finally, the pellets were polished with Wendt Dunnington 0.05μm alumina slurry following the same workflow indicated above and placed in a desiccator to dry. Vitrinite reflectance measurements were performed using a Leitz Ortholux 2 Microscope under oil immersion and reflected white light following the methodology from ASTM Standard D2797(2011).

2.3.4 Extraction of soluble organic matter

Before sample extraction, Soxhlet extraction system (Soxhlet apparatus, thimble, and glass wool) was pre-extracted for 24 hours using a 1:1 mixture of dichloromethane (CH_2Cl_2) and methanol (CH_3OH) to remove pre-existent contaminants in the Soxhlet extraction system. Powdered samples were introduced to the thimble by carefully pouring crushed rock from an aluminum foil funnel to avoid powder adherence to the wall of the thimble. After the sample

introduction, glass wool was inserted to assist in repressing sample overflow during peak levels of solvent while cycling. Activated copper (treated with concentrated HCl) and boiling chips were placed in each 500mL round-bottom flask after approximately 400mL of solvent was added.

Samples were subjected to 24 hours of cycling with mild heat applied to avoid unintentional alteration of extracted organic matter. A 500 mL round-bottom flask was then placed on a rotary evaporator to evaporate the solvent. The bitumen extracted was filtered through a pipette packed with glass wool using dichloromethane (CH_2Cl_2) to remove any debris left over from the extraction process. Extracts were then transferred to their respective 40 mL centrifuge tubes; an excess of n-pentane (C_5H_{12}) was later added, and the samples were placed in the freezer (~-2^oC) overnight to precipitate the asphaltenes.

Later, samples were centrifuged in a Daman IEC Model K centrifuge for 10 minutes to ensure asphaltenes and other polar components remained in the pellet while maltenes were decanted off using a pipette. After another stage of rotary evaporation, the samples were transferred into 4mL vials using dichloromethane (CH_2Cl_2).

2.3.5 Maltene Fractionation

In a 4 mL vial, 17.5 mg of the maltene fraction was weighed out and diluted with 200 microliters of hexane. In a glass pipette, a centimeter of glass wool was packed into the bottom, and 3.8 grams of powdered alumina was measured on aluminum foil and poured into the pipette. The pipettes were tapped until the powder was settled and leveled with additional assistance from compressed air. Approximately 40 mL of hexane was pushed through the column. By doing this, while avoiding the column drying out, the alumina forms a continuous substrate on which the various compound classes could be fractionated. The maltene/hexane solution (200 μl) was

introduced to the column for fractionation where saturates, aromatics and NSO products were collected in 100mL round bottom flasks.

The aliphatic (saturate) fraction was collected using 8.5 mL of hexane (C_6H_{14}) followed by the aromatic fraction using 25 mL of a 3:7 mix of dichloromethane (CH_2Cl_2) and methanol (CH_3OH); the remaining polar (NSO) fraction was collected using 25mL of 100% dichloromethane (CH_2Cl_2). The products collected were dried via rotary evaporation. The dried fractions were diluted with approximately 1 mL of their respective solvents and transferred to pre-weighed 4 mL vials. The final weight of each fraction was recorded.

2.3.6 Gas Chromatography (GC)

Agilent Technologies 6890 gas chromatograph was used to analyze the aliphatic and aromatic fractions that were diluted in a 3:1 ratio with hexane (C_6H_{14}). 1 µl of each sample was injected using the splitless capillary injection mode on to a 60 m J&W Scientific DB-1 122-0162 fused silica column using helium as the carrier gas at a flow rate of 1.4 mL/min. The oven was programmed such that each run began with a 1.5-minute hold at 40°C, followed by a 4 °C per minute ramp, until it reached 310 °C, where the oven was held isothermally for 24 minutes. The injector and flame ionization detector (FID) temperatures were set at 300ºC respectively.

2.3.7 Gas Chromatography-Mass Spectrometry (GC-MS)

GCMS is a technique that allows the identification of biomarkers that are related to each ion using the respective retention times. Selected ions were chosen to analyze aliphatic and aromatic fractions using single ion monitoring (SIM) or multiple ion detection (MID) mode. The GCMS analyses were performed using an Agilent Technologies 7890A gas chromatograph with a splitless capillary injector coupled to an Agilent Technologies 5975 XL Mass Selective Detector. The mass spectrometer ion source operated in electron impact mode with an energy of 70 eV. The

GC used a 60m x40 0.32mm (i.d.) J&D Scientific DB-5 fused silica capillary column coated with a 0.25μm liquid film.

The temperature program for the analyses started at 40ºC with 1.5 minutes hold time and was later increased to 300ºC at a rate of 4ºC per minute and held isothermal for 34 minutes for a total run time of 100.5 minutes. The fractions were analyzed by both single ion monitoring (SIM) and multiple ion detection (MID) modes depending on the target compound.

2.3.8 Quantitative Biomarker Analysis

In addition to the relative abundance of selected biomarkers, absolute concentrations of geochemical families can provide significant information. To quantify biomarkers, internal standards must be added to the samples as reference concentrations.

In this analysis, approximately 10**μ**L of 108ppm (w/v) 5α-cholestane-2,2,3,3,4,4-d6 dissolved in hexane was added to both the branched and cyclic aliphatic and aromatic fractions after fractionation of the rock extract prior to GCMS analysis. To calculate the concentration of a standard in a sample standard concentration, the standard volume was calculated (Equation 1 and 2) using the volume of the standard divided by the mass of the sample (From Symcox, C.; personal communication, 2019).

$$[C_{ISTD}] = \frac{[C_{STD}] \times V_{STD}}{M_{Sample}} \quad [1]$$

Where,

C_{ISTD} = Concentration of internal standard in the sample in ppm W/W

C_{STD} = Concentration of internal standard solution in ppm W/V

V_{STD} = Total volume of internal standard solution added to the B&C or aromatics solution

M_{sample}= Mass of sample

The concentration of a biomarker is calculated from the relative peak height of the known internal standard area and concentration.

$$[C_{bio}] = [C_{ISTD}] \times \left[\frac{A_{BIO}}{A_{ISTD}}\right] \times RF \quad [2]$$

Where,

C_{BIO} = Concentration of biomarker in the solution prepared in ppm W/W

C_{ISTD} = Concentration of internal standard in the sample in ppm W/W

A_{BIO} = Peak area of the biomarker in GCMS analysis

A_{ISTD} =Peak area of the standard in GCMS analysis

RF= Relative response factor between internal standard and analyte biomarker as a ratio of the area of the standard to the area of the analyte at the same concentration.

The relative response factor between 5α-cholestane-2,2,3,3,4,4-d6 and most saturate biomarkers (including sterane and terpanes) is assumed to be very close to 1.0. Aromatic response factors were not calculated for this study but are expected to be very similar across polycyclic aromatic hydrocarbons of different ring count. Although this does not provide an absolute concentration, it allows for relative comparison of concentration between samples.

CHAPTER III

RESERVOIR CHARACTERIZATION

3.1. Lithofacies Characterization

To characterize the La Luna Fm. in the Lago de Maracaibo basin, four cores: La Luna IX, La Luna IA, La Luna IS, and La Luna IE and one outcrop were analyzed along the southwest-northeast trend of the Basin. Liborius and Slatt in 2016 published a description and interpretation of the La Luna IX core. Since this core represents the most characteristic, complete and well-preserved section, La Luna IX would be considered the "standard core" to evaluate differences or similarities of the other cores used for this work.

Eight facies were identified in La Luna IX showing a good relationship with what was observed and analyzed in the field. These facies were defined from bottom to top as the following: (I) dark gray laminated mudstone; (II) fossiliferous wackestone facies;(III) volcanic ash;(IV) laminated mudstone with limestone concretions and packstone;(V) siliceous- calcareous laminated mudstone interbedded with black chert filled with calcite veins;(VI) siliceous-calcareous mudstone interbedded with wackestone facies;(VII) slightly siliceous-calcareous laminated black mudstone interbedded with calcareous fossiliferous wackestone; (VIII) siliceous green mudstone with authigenic glauconite and Pyrite.

To understand the variability in the depositional conditions along the basin, a core description was done for the three new cores located towards the northwest (La Luna IE, La Luna IA) and towards the southwest (La Luna IS). Interestingly, these cores display essential variations from the stratotype and the La Luna IX.

The variations in the core description along geochemical and geophysical parameters contributed to building a proposed model for deposition of the La Luna Formation in Maracaibo

Basin. The parameters that were used for the core description were based on lithology, sedimentological analysis, and core to well calibration.

Lithology was determined based on the color, grain size, mineral composition, organic content, and type of cement. Sedimentological analyses were based on trace fossils, macrofossils, stratification, and contacts to define geologic facies and trends. Organic geochemical, X-Ray Fluorescence and X-Ray Diffraction analyses were conducted to characterize the La Luna core into different facies, which were based on changes in TOC, trace and major elements.

From the description previously generated by Liborius (2015), it is noticeable how the La Luna IX core displays a well-preserved deposition that is characterized by a high organic matter content and an abundance of large foraminifera with uniserial morphology and a micro-granular compound structure in the sample. Moldic dissolution and inter-particle porosity with a small amount of recrystallized aragonite are also present (Figure 12). The diagenetic phases of La Luna Formation are mainly composed of framboidal pyrite, recrystallization of carbonates/silica in fossils and presence of apatite. According to Reimers et al. (1996) and Lev et al. (1998), these diagenetic phases are generally associated with sulfate reduction during relatively early diagenesis.

La Luna IX core is characterized by an alternation of discontinuous planal-parallel mudstones and wackestone-packstones containing uniserial foraminifera, and shell fragments (Figure 12A, B) related to facies I, II and IV. Facies III is represented by small bentonite content in a clay-rich matrix rich in potassium, calcium, and aluminum (Figure 12C).

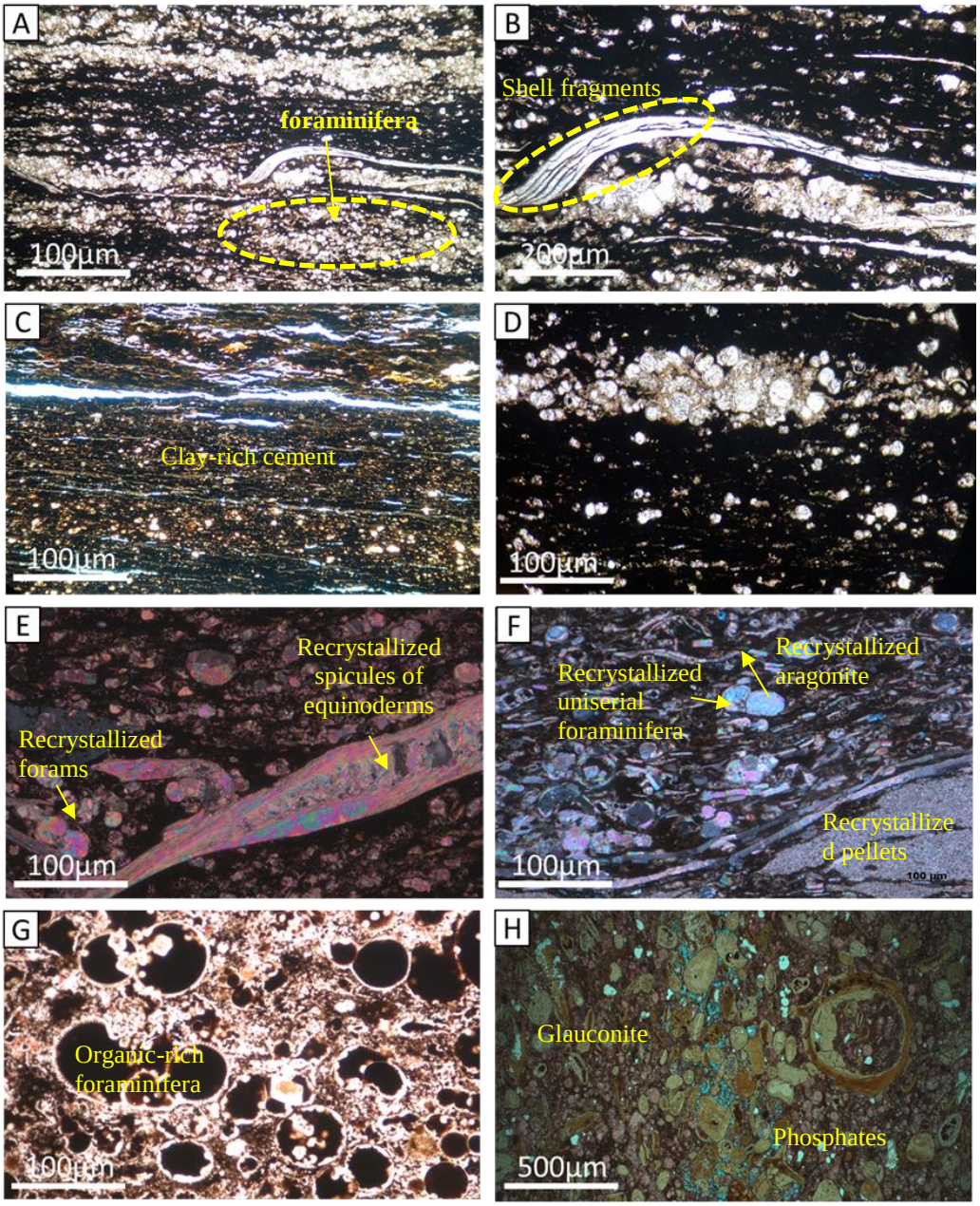

Figure 13. Photographs of La Luna IX core and its most characteristic facies. (A and B) represents facies I (Dark Laminated mudstone) by an alternation of a discontinuous planal-parallel mudstone and wackestone-packstone containing uniserial foraminifera and shell fragments. (C) Presence of bentonites in a clay-rich matrix. (D) Recrystallized foraminifera and small quartz grains in an organic-rich matrix. (E) Recrystallization of forams, spicules of Echinoderms and small quartz grains in an organic matrix. (F) Recrystallization of uniserial foraminifera, pellets, aragonite and small quartz grains in an organic to micrite cement. (G) Diagenetic-altered foraminifera filled with organic matter in a micrite- cement. (H)Packstone- grainstone with high amounts of organic rich-foraminifera and shell fragments in a siderite cement (cross-polarized light) with a high abundance of glauconite and phosphates.

The Upper La Luna contains a more reworked packstone-wackestone with abundant foraminifera filled with organic matter (Figure 12G) and a high amount of drusy porosity in uniserial foraminifera cemented with calcite within an organic matrix. Also, Upper La Luna is characterized by an abundance of glauconite in a packstone- grainstone with high amounts of foraminifera and shell fragments in a siderite cement. Porosity is interparticle and grain-to-grain (Figure 12H).

3.1.1 La Luna IE core

The La Luna IE core is located towards the northwestern part of the Maracaibo Basin. It has a core recovery of 75% and contains the Albian Maraca Formation, the Cenomanian-Santonian La Luna Formation, and the lowermost portion of the Campanian-Maastrichtian Colón Formation. This core represents most of the lithofacies previously described for the La Luna IX core (LLIX) and is also deposited at almost over at the same depth range.

This core depicts major diagenetic processes, forming micritization, dissolution, cementation, compaction, dolomitization and the replacement of carbonate grains and matrix by non-carbonate mineralogy (chertification). According to the established facies mentioned previously for the La Luna IX, several facies can also be found for the La Luna IE core and are the following:

I. Dark gray massive mudstone

From bottom to top this core displays the lower section of the La Luna in the 1E core that starts at the upper contact of the Maraca and La Luna Formations (Figure 13A). A dark gray, massive mudstone is present in this interval (15600’-15680’) massive calcite-filled veins (Figure 13B). This interval (15550’-15602’) changes gradually from calcareous to a more organic-richer

interval (Figure 14). There is also an occurrence of erosion surfaces and lag deposits (15583'-15585').

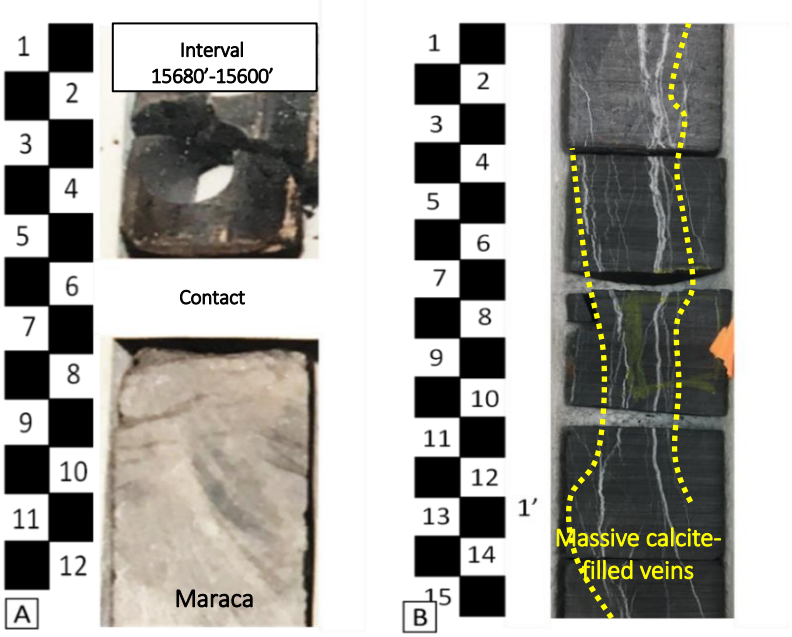

Figure 14. Facies I (Dark gray, massive mudstone). (A) Sharp contact of Maraca and La Luna Formation showing the Early Albian-Cenomanian unconformity. (B) Massive calcite-filled veins (shown almost perpendicular through the interval).



Figure 15. LLIE core interval displaying gradually lithological changes (calcareous to organic-rich mudstone). There is also a presence of erosion surfaces and lag deposits.

II. Fossiliferous wackestone facies

The fossiliferous wackestone facies are present as a light gray marlstone in Figure 15. Foraminifera is present in a micrite matrix, and the upper part of this interval contains organic matter-filled fractures containing dead oil (15560'-15562').

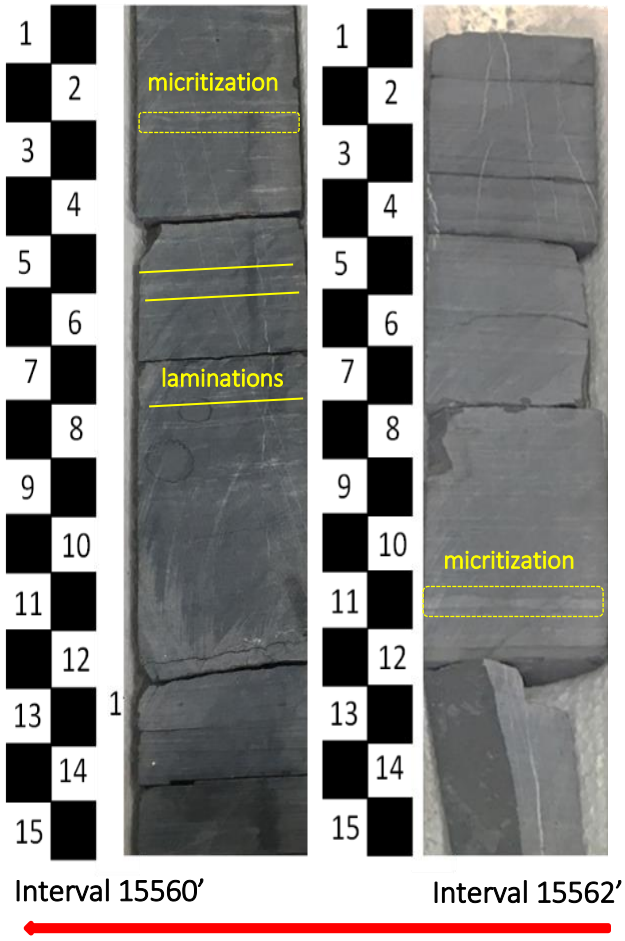

Figure 16. Fossiliferous wackestone facies in LLIE core. Light gray laminated shale with a presence of foraminifera in a micrite matrix.

III. Volcanic Ash

Towards the top of the interval 15546'-15549' (Figure 16) euhedral albite crystals are visible in thin sections and could be related to pulses of bentonites since GR spectral data, XRD

and XRF data illustrate a high kick of potassium, magnesium, and sulfur that could also be related to the pulses of volcanic ash.

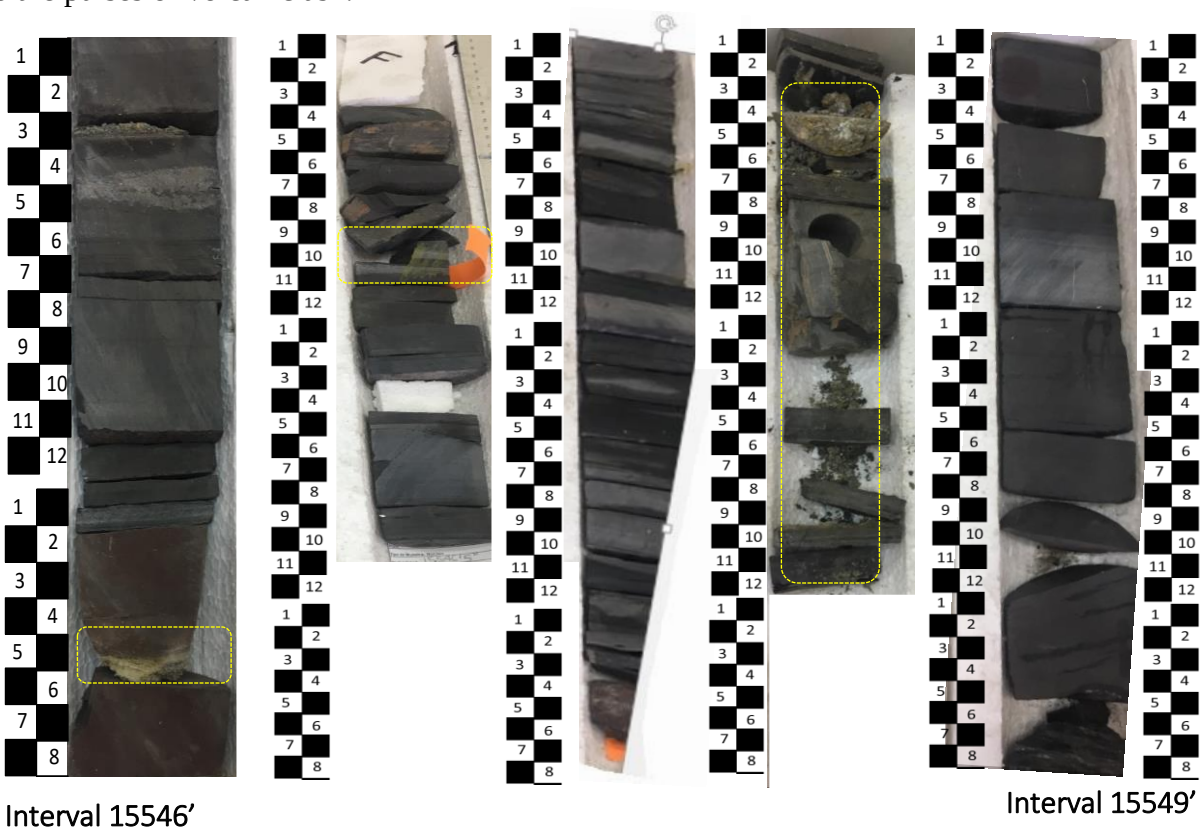

Figure 17. Volcanic ash pulses in the LLIE core (dashed- yellow lines). Presence of euhedral crystals that are locally called "coffee grains."

IV. Massive mudstone with limestone concretions and packstone

The amount of organic matter in this interval (15553'-15559') is higher than in the lower intervals; in fact, it increases dramatically when compared with the whole core (Figure 17). This interval has a very bituminous rock that is displayed as very shiny and massive with a coal appearance. When this interval is compared with the gamma-ray profile, it appears to show the presence of the maximum flooding surface at the interval (15553'-15559'). GR profile was also correlated with the high concentrations of molybdenum and vanadium from the XRF elemental interpretation.

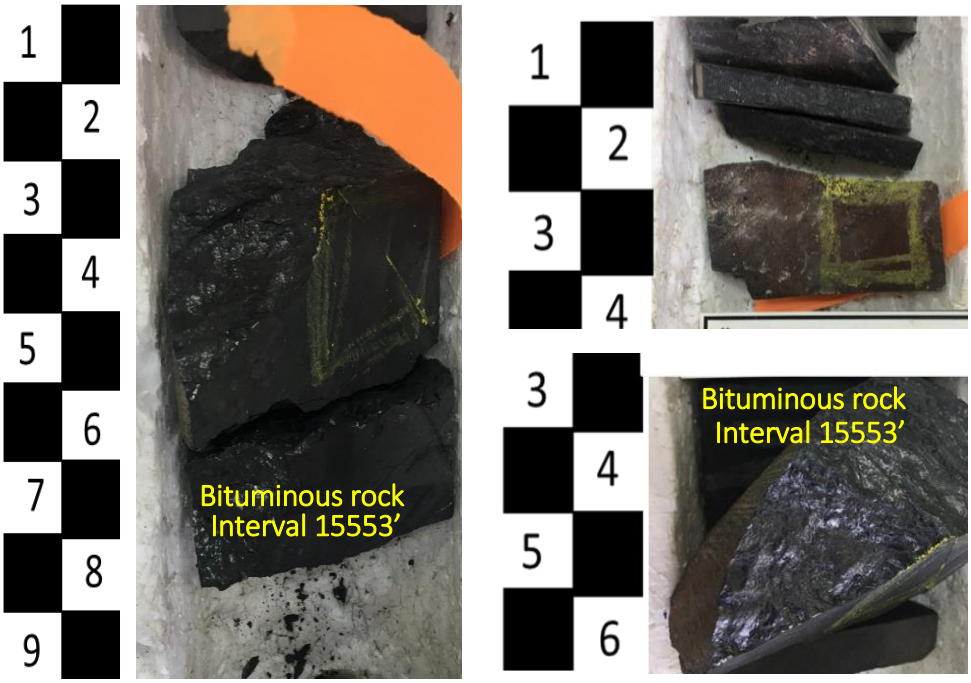

Figure 18. Facies IV (Massive mudstone with limestone concretions and packstone). The LLIE core is displaying a bituminous rock that is displayed as a very shiny and massive looking rock almost like coal.

V. Siliceous- calcareous laminated mudstone interbedded with black chert filled

with calcite veins

Towards these intervals (15344'-15346'; 15450'-15454'), the productivity increases showing a high cyclic concentration of foraminifera and calcite nodules. The intervals represent a variation in lithology since there is a presence of black cherts filled with calcite veins and dolomitization layers (Figures 18 and 19). The fractures are bound within brittle rock concretions compared with surrounding calcareous rock.

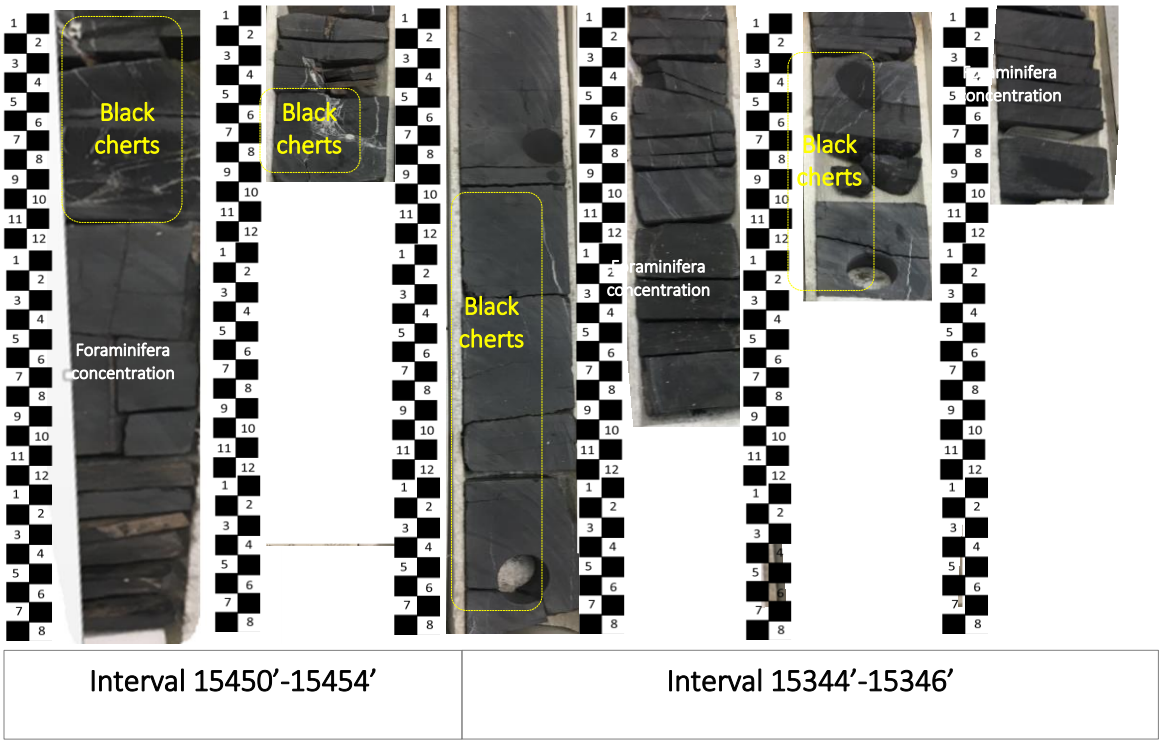

Figure 19. Facies V (Siliceous- calcareous laminated mudstone interbedded with black chert filled with calcite veins).

VI. Slightly siliceous- calcareous laminated black mudstone interbedded with calcareous fossiliferous wackestone.

The sedimentation trend becomes more laminar in this interval than the previous facies. There is a presence of dark gray, finely laminated, benthonic foraminifera with occasional fish fragments towards the base. Interbedded nodules disturb the shale bedding. Presence of occasional packstone with abundant foraminifera as dolomitization of minor layers is also present.

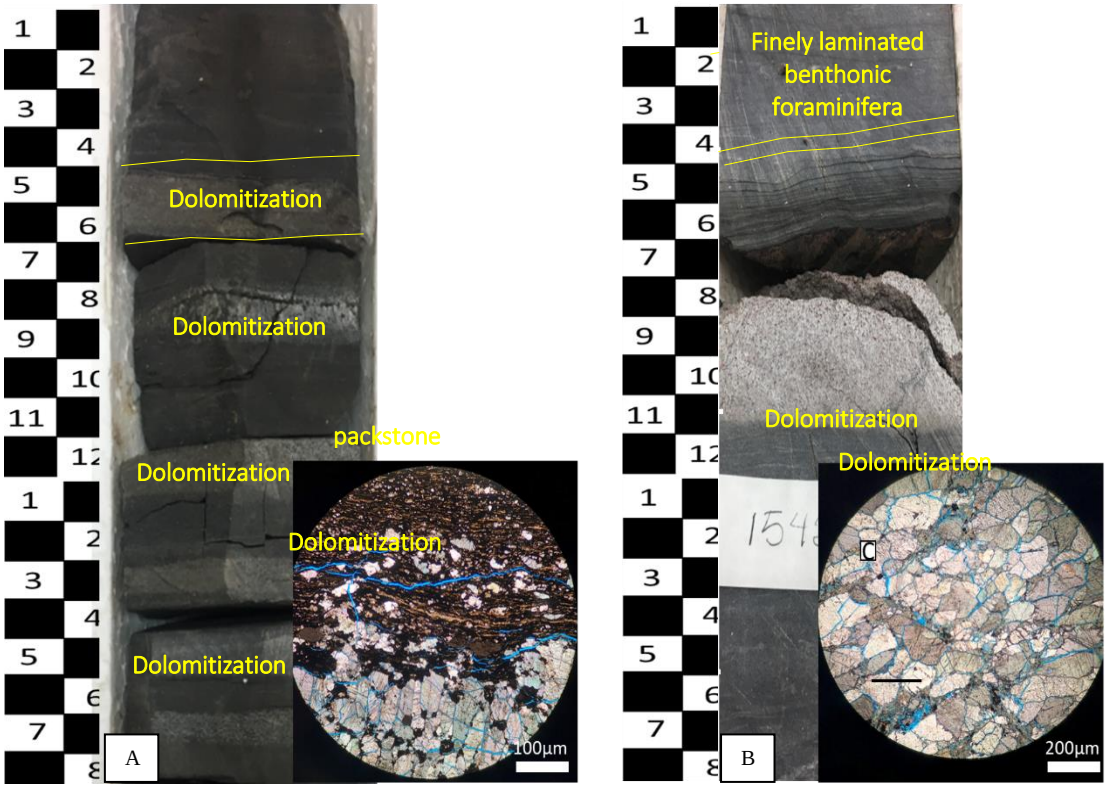

Figure 20. (A and B) Representation of the LLIE core and thin section microphotography depicting dolomitization in interbedded layers of facies V.

In the thin section analyses, the presence of the compacted syn-depositional intraclasts is noticeable. They are shown almost perpendicular through the thin-section interval in an organic-rich matrix as is also displayed in the base of LLIX (Figures 20A, B). Dolomite content is also present (Figure 20C).

Furthermore, a diagenetic process is also displayed by the recrystallization of *tasmanites* (Figure 20D); they are also visible in the interval (15416'-15437'). Small interbedded layers of recrystallized dolomite and feldspars abundant in bentonites are also present, and they are embedded in a clay-rich matrix (Figures 20E, G, and H).

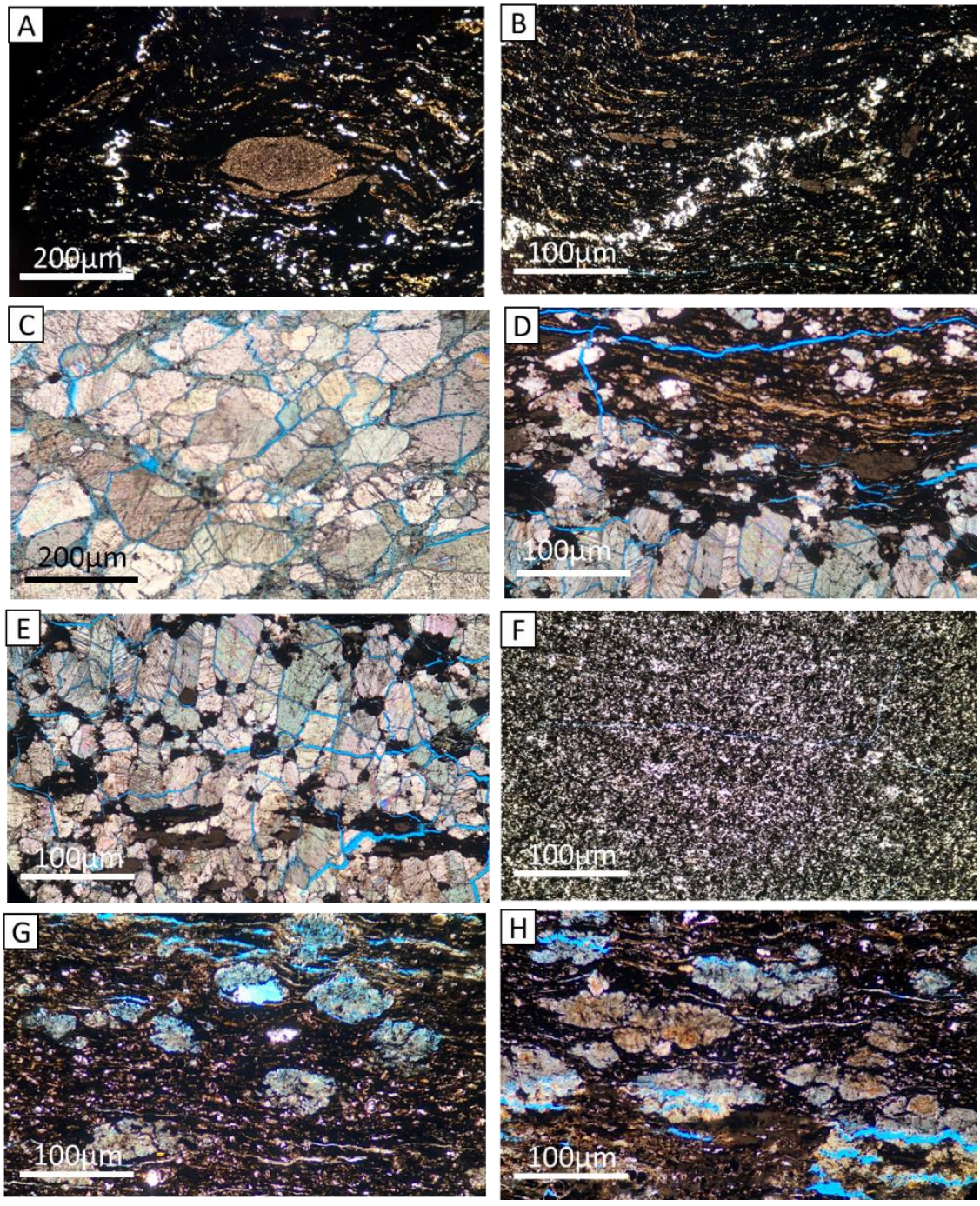

Figure 21. Photographs of La Luna IE core and its most characteristic facies. (A and B) Representation of large calcite-filled veins and compacted syn-depositional intraclasts, also shown almost perpendicular through an organic-rich matrix. (C, D, and E) Dolomitization found in some intervals of the core. (F) Recrystallized cherts filled with calcite veins. (G and H) Interbedded layers of recrystallized dolomite and feldspars abundant in bentonites embedded in a clay-rich matrix.

3.1.2 La Luna IA core

This core is also located towards the northwestern Maracaibo basin. In a comparison with the previous two cores, LLIA represents a different depositional history since not all the lithofacies identified above are present in the same order. This core displays a very monotonous pattern showing most of the facies I, previously characterized from the LLIX core and stratotype (I. Dark gray laminar mudstone) in most of the half of the whole core interval (140 feet, interval 16820'-16960'). From the core description, it could be observed how the paleo-topography of the Maraca Formation possibly controlled the depositional settings as is the case with the Woodford Shale in the United States (Infante-Paez et al., 2017; Milad, 2017 and Torres-Parada et al., 2018), a new facies "Calcareous-marlstone with the presence of pyrite layers" was found for the proposed for La Luna formation lithofacies in this core. The following lithofacies are the ones interpreted for the La Luna IA in the Maracaibo Basin.

I. Dark gray laminar mudstone

The base of La Luna starts at the upper contact of the Maraca Formation in the interval 16960'-16961' with a series of shelly bivalves (Figure 21A). Along with this interval, visible small calcite nodules continue along the 16951'-16953' (Figure 21B) interval are still displaying a very dark coloration rich in organic matter. The whole intervals remain massive and organic-rich showing calcite-filled vertical fractures in the interval 16936'-16939' (Figure 21C). Detailed examinations of the laminae show that dark laminae consist of a brown matrix of clay minerals and organic matter. The rhythmic nature of the carbonate-shale laminations may suggest hemipelagic sedimentation (Reineck & Singh, 1980).

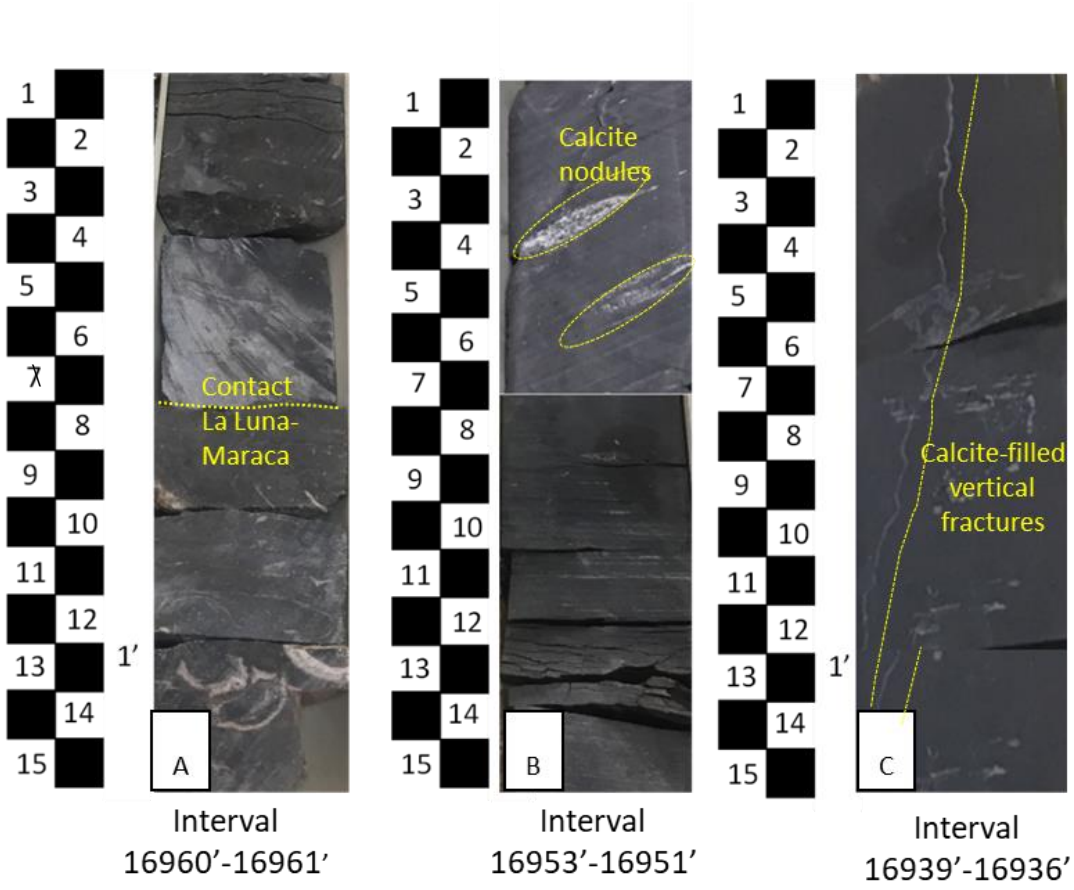

Figure 22. Representation of Facies I (Dark gray laminar mudstone) in LLIA core. (A) Interval is showing the unconformity of Maraca Formation (Cogollo Group) with La Luna Formation displaying a series of conchiferous bivalves. (B) Presence of small calcite nodules recrystallized with anhydrite. (C) Organic-rich interval is showing calcite-filled vertical fractures.

II. Calcareous-marlstone with the presence of pyrite layers

In the interval 16915'-16921' very thin pyrite layers are visible (0.2-0.3cm) and the organic matter content and coloration decrease towards the top showing a light- grey marlstone (Figure 22). This pattern is also displayed in the 16893'-16895' interval. This interval looks like the one found in the Middle Magdalena Basin by Gomez (2014) for the Salada Member of the Luna Formation, Colombia. Continuous non-curved wackestone-packstone deformed bed conformed of

uniserial foraminifera filled with micrite in an organic-matter rich cement. This interval contains some dolomite recrystallization in veins perpendicular to bedding.

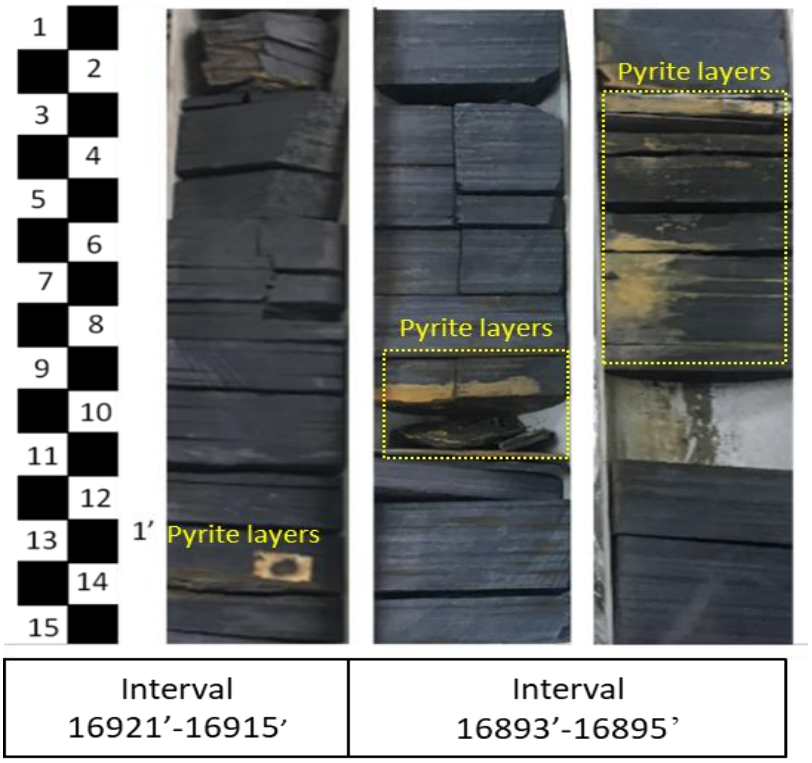

Figure 23. Representation of Facies II (Calcareous-marlstone with the presence of pyrite layers) in LLIA core. (Sulphur layers (0.2-0.3cm) present in an organic matter interval decreasing in coloration towards the top showing a light- grey marlstone.

III. Volcanic Ash

From the core description, there is clear evidence of the volcanic ash pulses found in the lower LLIA core. Towards the top, in the intervals, 16774'-16776';16844'-16846' and 16756'-16758, volcanic ash beds are laminar and friable (Figure 23). Light-green intervals go from 5 to 10 centimeters, and they are embedded in a clay matrix (Figure 24).

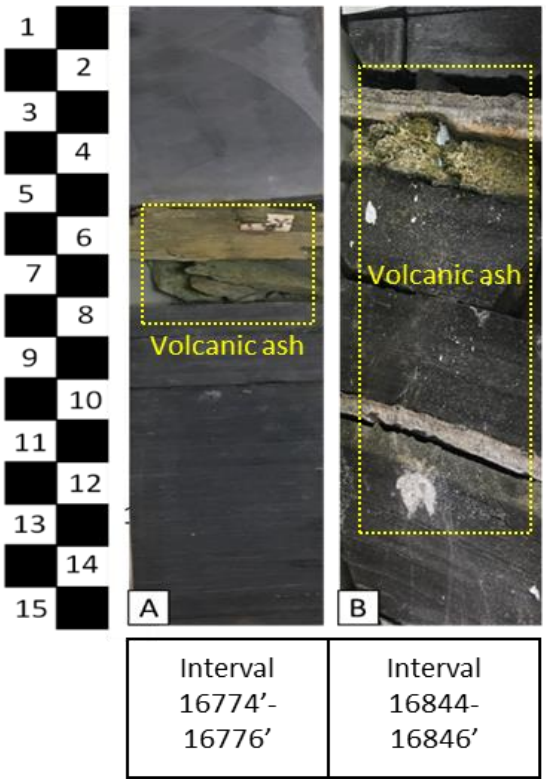

Figure 24. Representation of Facies III (Volcanic Ash facies) in LLIA core displaying a fissile yellowish color with coarse particles of volcanic ash.

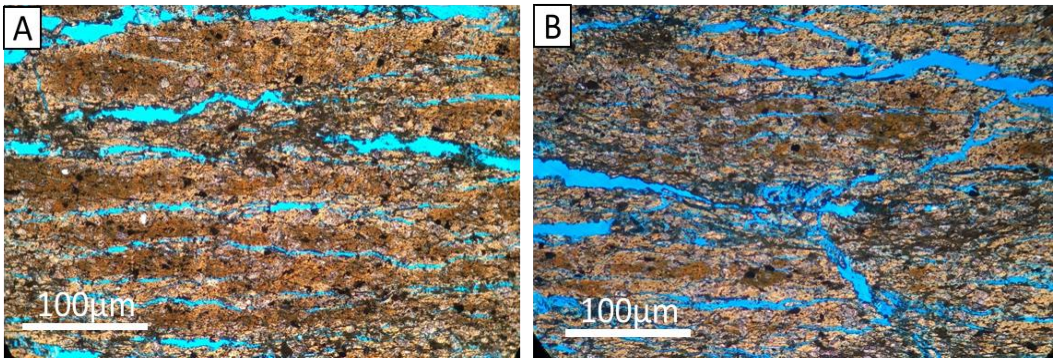

Figure 25. Photographs of La Luna IA core and its most characteristic facies. Fissile bentonites embedded in a clay matrix.

IV. Laminated mudstone with limestone concretions and packstone

These facies consist of a dark to light gray mudstone with an organic-rich character (Figure 25) increments notably showing the possible maximum flooding surface of this well (16900'-16930'). Soft sediment deformation of calcite nodules has deformed the lamination.

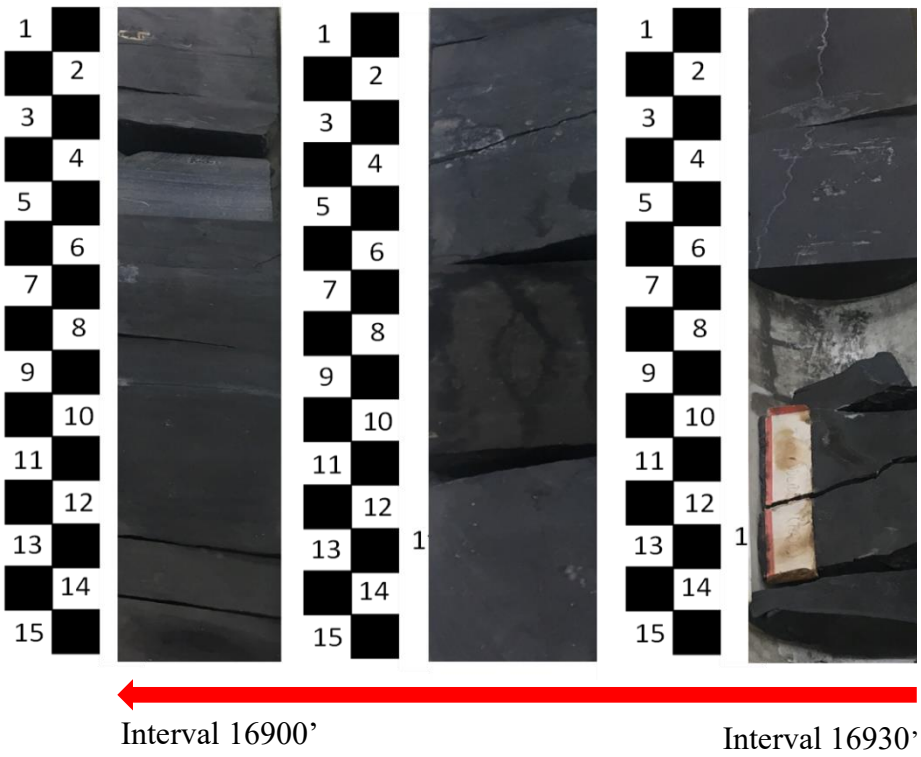

Figure 26. Representation of Facies IV (Laminated mudstone with limestone concretions and packstone) in LLIA core representing the MFS and the most organic-rich lithofacies.

V. Siliceous- calcareous laminated mudstone interbedded with black chert filled with calcite veins

These facies are in the interval 16889'-16893' and 16877'-16879' where there is a presence of small ripples-like structures represented by white-dashed lines in Figure 26 and cross-laminated surfaces in the intercalation of chert and calcareous rocks that are showing a period of higher energy. In this sense, cross-laminations can be the result of storm-transported sediments, where current velocity has decreased rapidly during high-density turbid flows probably related to a lowstand system tract towards the top of this interval. In the interval 16848'-16850' the deposition angle changes direction to almost 45 degrees perpendicular to the underlying sediments (Figure 27). At 16832' smaller vertical fractures are related to calcite.

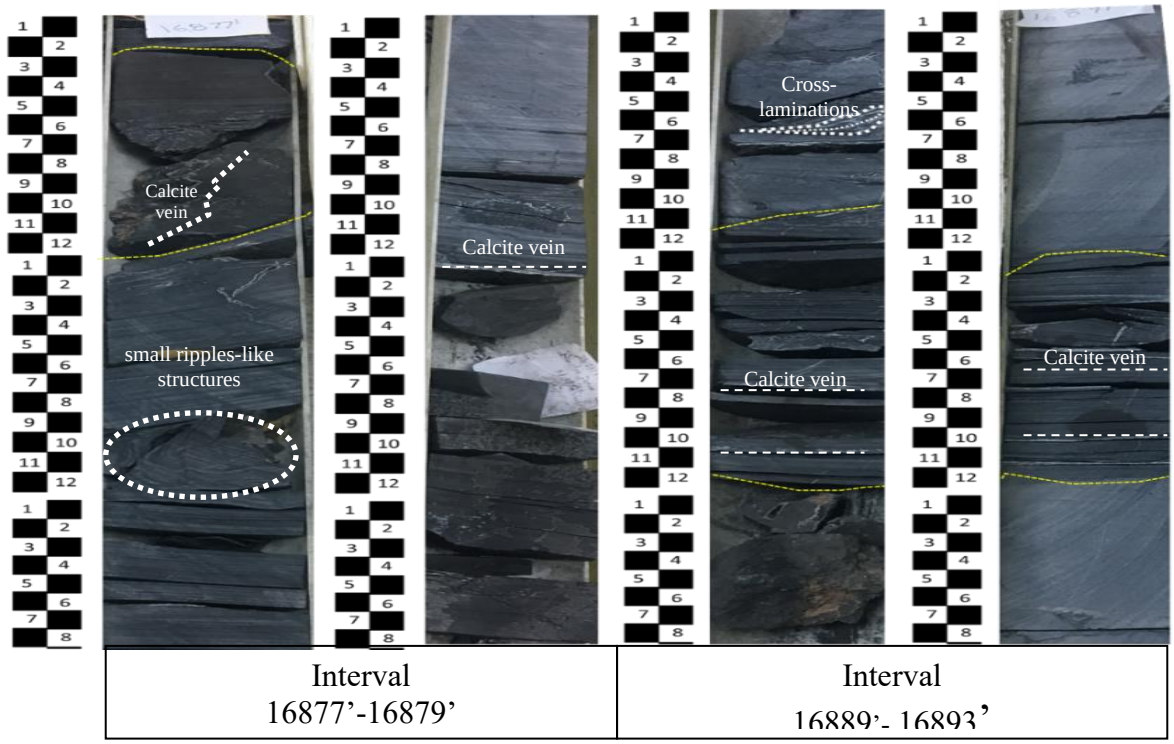

Figure 27. Representation of Facies V (Siliceous- calcareous laminated mudstone interbedded with black chert filled with calcite veins). The yellow dashed lines represent the black chert concretions, and small ripples-like structures and cross-laminated surfaces are represented by, and white dashed lines.

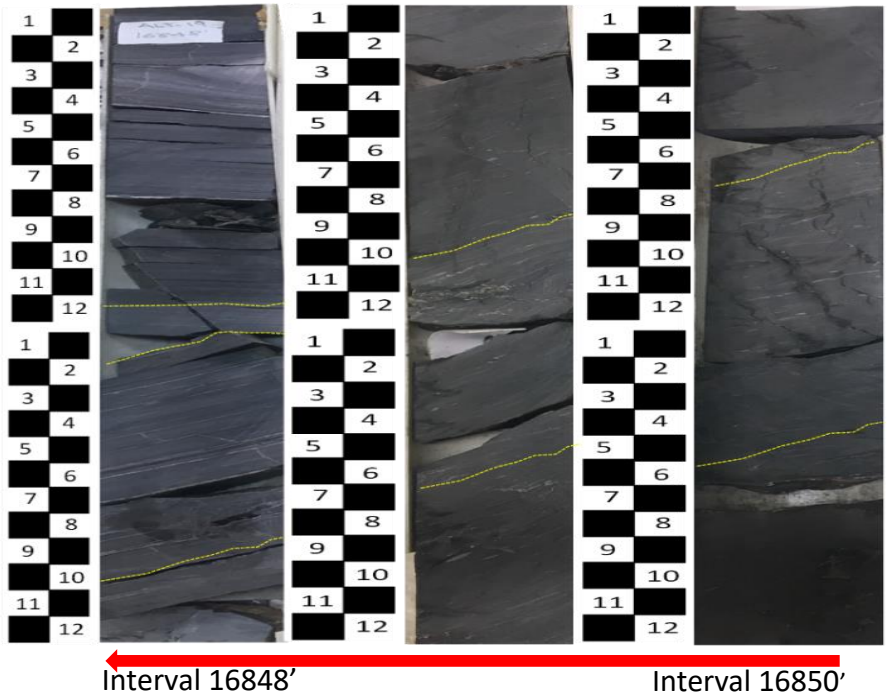

Figure 28. Perpendicular deposition angle of almost 45 degrees perpendicular to the underlying and overlaying massive sediments.

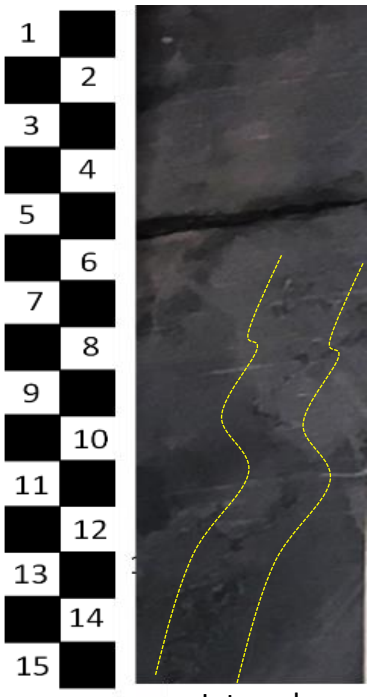

Figure 29. Representation of Facies V (Siliceous- calcareous laminated mudstone interbedded with black chert filled with calcite veins). Yellow-dashed lines represent the position of the bitumen fractures.

The fractures in the concretion are bound within this brittle rock compared with surrounding marlstone. In the interval 16828'-16830' there are some bitumen fractures present (Figure 28), and in thin section, the presence of a finely calcareous- laminated mudstone-wackestone (Figure 29A), formed by uniserial foraminifera and perpendicular fractures dolomite-filled (Figures 29B, C, D and E), representing either direct precipitation from seawater or reworking of carbonate muds from shelf areas into the basin is perceptible (Figure 29F).

Small partially flattened burrows can be recognized in many instances by the textural contrast between the burrow fill and the surrounding sediment. This contrast mostly happens when organisms backfill their burrows with sediment. Lenticular- shaped burrows are characteristic in muddy carbonate units that did not undergo shallow marine or subaerial lithification (Figure 29F).

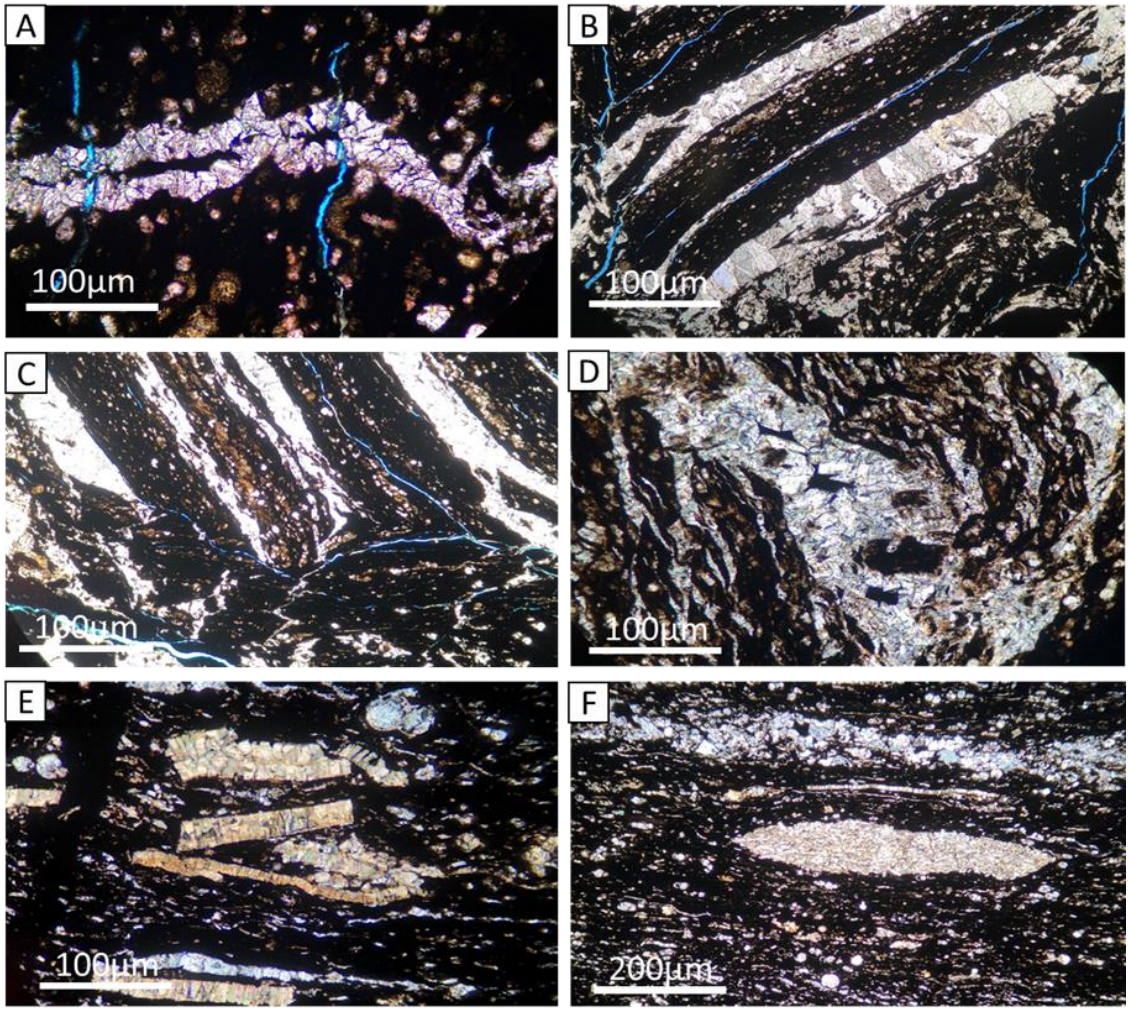

Figure 30. Photographs of La Luna IA core and its most characteristic facies. (A) Discontinuous wavy non-parallel wackestone formed by uniserial foraminifera and perpendicular fractures dolomite-filled. (B and C) Cone in cone structure or beef structure? Continuous parallel mudstone-wackestone is containing an organic-rich matrix and micritized foraminifera. Dissolution of dolomite into organic matter. Cross-lamination. (D) Continuous non-curved wackestone-packstone deformed bed conformed of uniserial foraminifera filled with micrite in an organic-matter rich cement. This interval contains some dolomite recrystallization in veins perpendicular to the bedding plane. (E) Discontinuous planar-parallel packstone-boundstone high organic rich (high intervals of productivity). (F) Finely laminated shaly carbonate was representing either direct precipitation from seawater and a reworking of carbonate muds from shelf areas into the basin. Small partially flattened burrows (recognized in many instances because the textural contrast between the burrow fill and the surrounding sediment) it mostly happens when organisms backfill their burrows with sediment. Also, lenticular- shaped burrows are common in muddy carbonate units that did not undergo early marine or subaerial lithification.

VI. Siliceous- Calcareous mudstone interbedded with wackestone facies

This core contains a significant increment of organic matter and strong petroleum odor. The interval 16810'-16811' contains a high hydrocarbon impregnation (Figure 30). Very characteristic bioturbation and cyclicity of small intervals of dolomitization almost parallel with a cross-lamination-like structure (Figure 31) display the end of the La Luna Formation (interval 16752'-16756'). The dolomitization intervals are characterized by the presence of baroque dolomite, and its occurrence can be associated with a possibly hydrothermal fluids source. Nonetheless, further analysis needs to be done to support this theory.

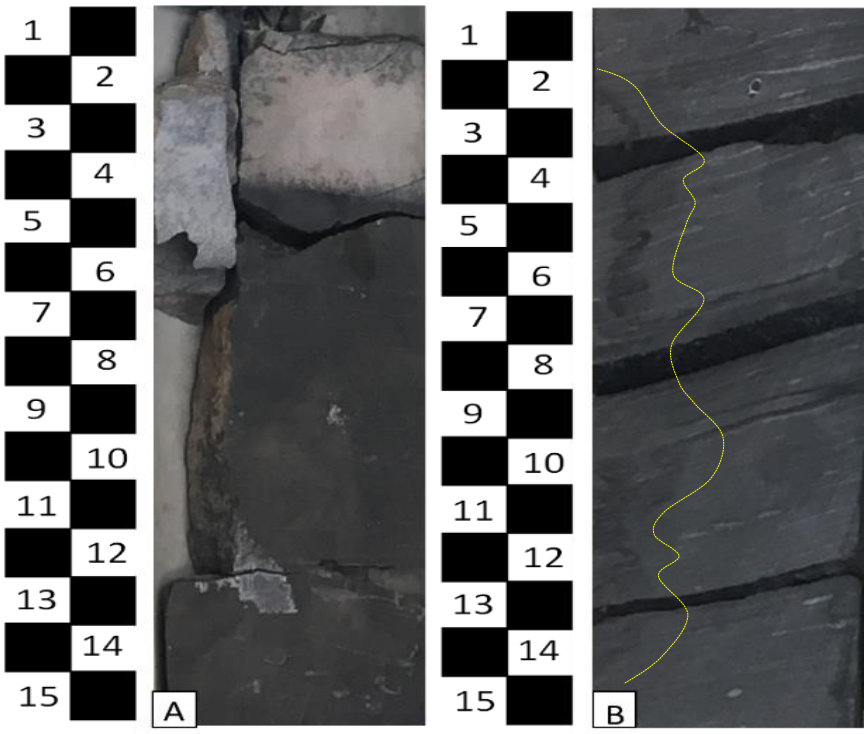

Figure 31. (A) Presence of an organic-rich matrix along small micritized foraminifera (B) vertical stylolite (16798'-16796') possibly related to the bedding at right angles.

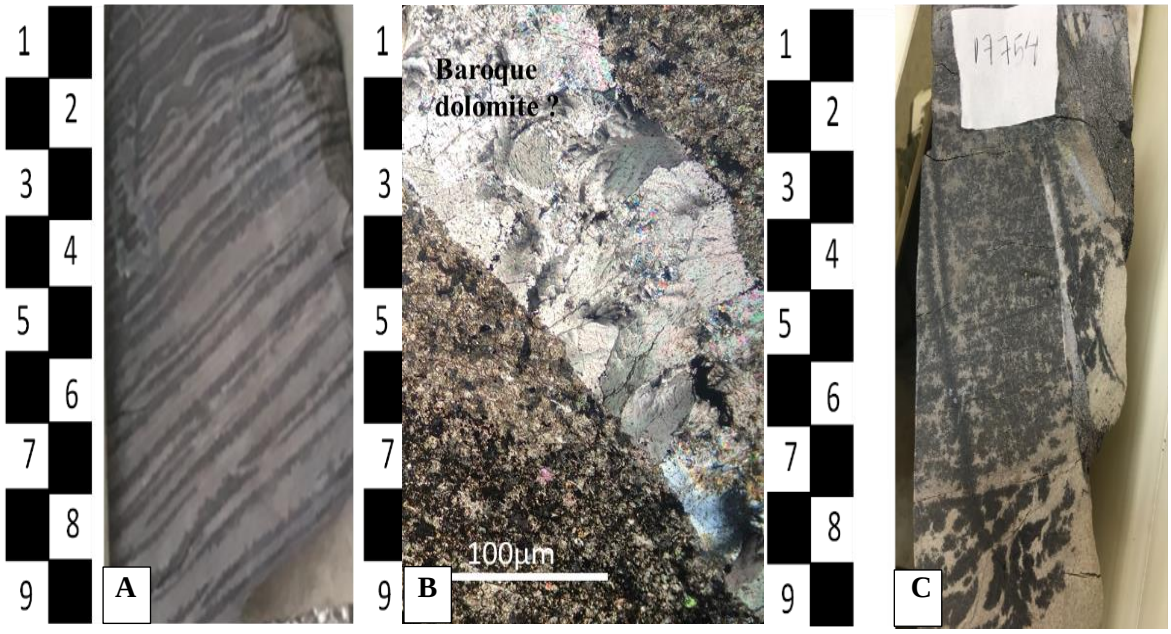

Figure 32. Bioturbation and cyclicity of small intervals of dolomitization almost parallel and with a cross lamination like structure at the end of the La Luna Formation IA core.

In thin section, it is apparent the presence of elongated algae, small micritized foraminifera, and presence of some rip-up clasts transported in the organic-rich matrix (Figures 32A and B). Unlike the previous cores, these facies do not show an unusual amount of chert content but instead a variety of calcite nodules that goes from 5 to 10 centimeters of diameter, also in the interval 16778'-16780'. Presence of dolomitization (Figures 32C and D) vertical stylolite (16796'-16798') possibly related to the bedding at right angles. It may or may not be associated with the tectonic activity since pressure acting perpendicularly to the bedding can cause it.

The end of the LLIA core can be observed from the thin section as a discontinuous non-parallel packstone-boundstone embedded in a micritic matrix presenting some interbedded euhedral dolomitization processes and dispersed ferroan cementation (Figure 32D). Occasional packstone with abundant foraminifera is also present.

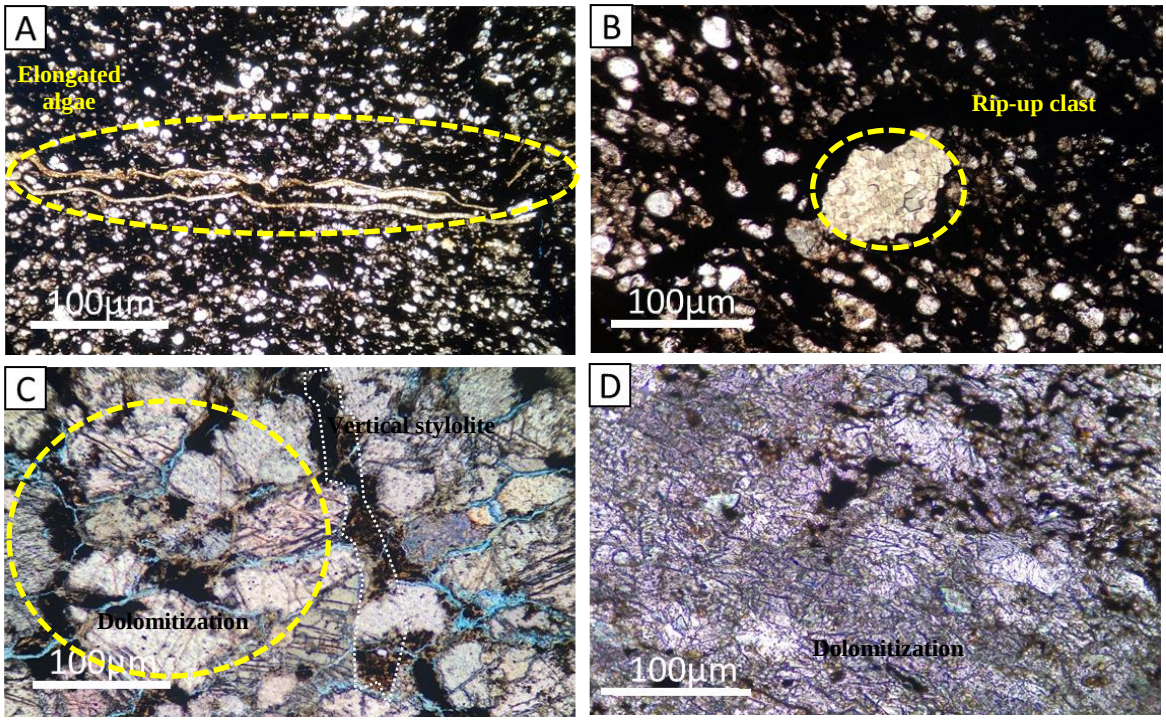

Figure 33. Photographs of La Luna IE core and its most characteristic facies. (A and B). Discontinuous wavy non-parallel recrystallized foraminifera in an organic-rich packstone. (C) Crystalline dolomite in a ferruginous cement with intergranular porosity. (D) Discontinuous non-parallel packstone-boundstone embedded in a micritic matrix presenting some interbedded euhedral dolomitization and micritization processes in a disperse ferruginous cement.

3.1.3 La Luna IS core

This core is the only one located towards the southwestern part of the basin, and it also represents a different sedimentation pattern in comparison with the previous ones. First, in terms of length, this core represents the shortest interval. Second, in terms of lithofacies, this core represents a cyclicity that does not display the typical pattern of deposition of La Luna in the Maracaibo Basin (Figure 33). This core is represented by two main facies (Facies I "Dark gray laminar mudstone" and facies II "Calcareous-marlstone with the presence of pyrite layers") that can be easily identified by the layering, coloration, and mineralogy and brittleness character.

I. “Dark gray laminar mudstone.”

(Interval 17187’-17202’) The boundary from Maraca and La Luna Formations is represented in Figure 34 by a sharp surface that shows the unconformity of Maraca-La Luna as it was seen in the previous cores (Figures 13 and 21).

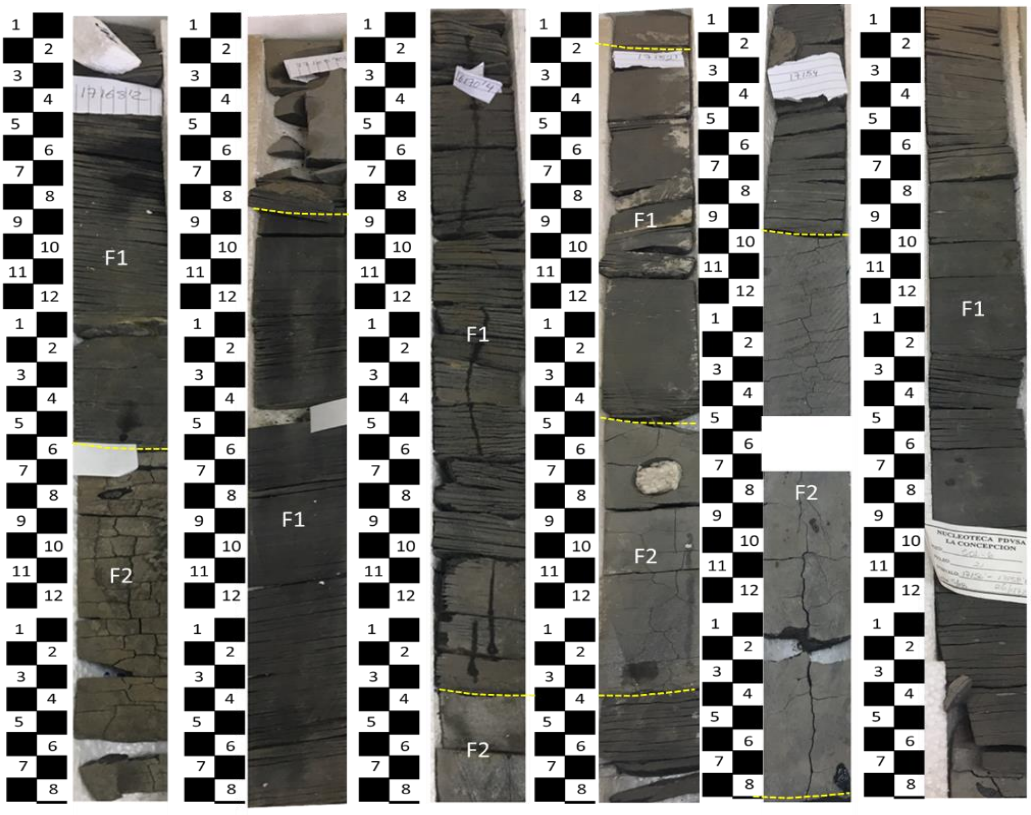

Figure 34. Core interval displaying the significant cyclicity represented for two main facies in La Luna IS core. Facies I (F1) is represented by “Dark gray laminar mudstone,” and facies II (F2) is represented by “Calcareous-marlstone with the presence of pyrite layers.”

Along with this interval, there is a presence of small calcite nodules (less than 0.5cm) that continue along the interval still displaying a medium-to-dark coloration with a fissile character (Figure 34B). The dark intervals are organic matter rich intervals embedded with uniserial foraminifera filled with organic matter. (Figures 35A, B).

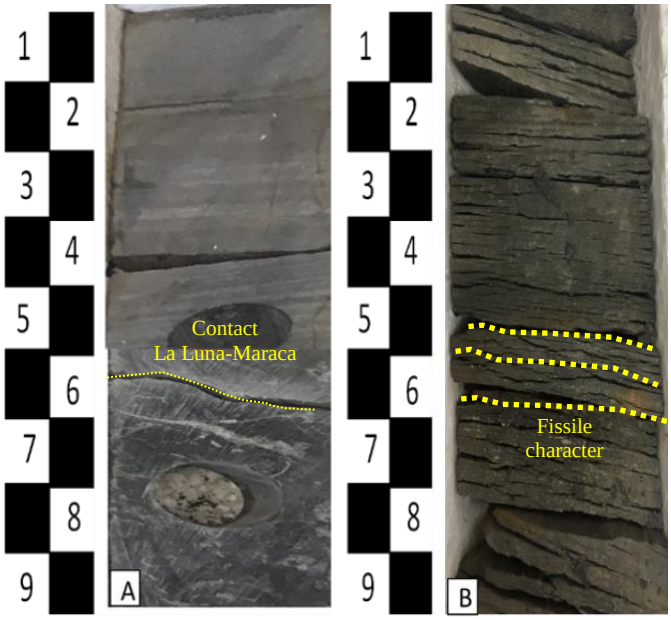

Figure 35. Representation of Facies I (Dark gray laminar mudstone). (A) Sharp erosional contact from Maraca Formation (Cogollo Group) and La Luna Formation (B) Fissile character along with these facies.

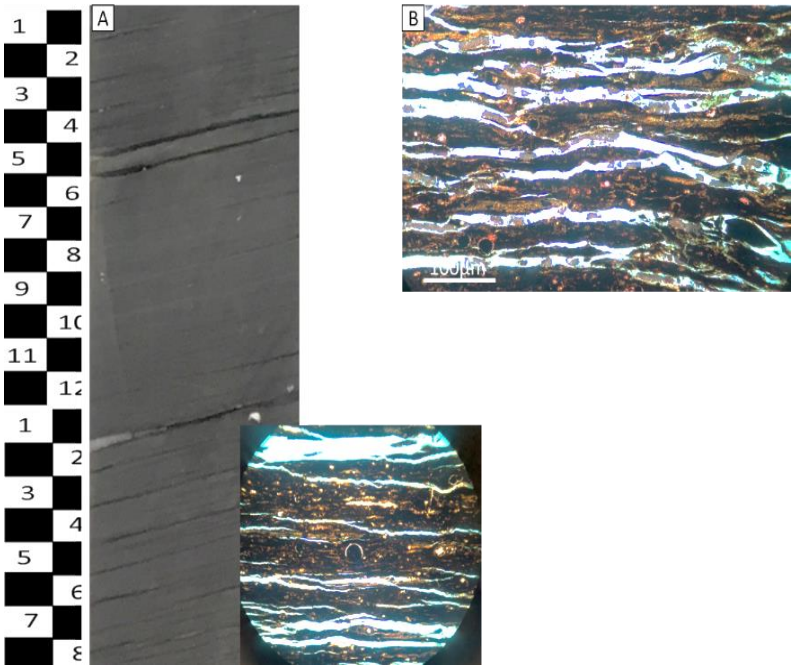

Figure 36. (A) Representation of the LLIE core and thin section microphotography displaying the fissile character in an organic-rich matrix. (B) The separation of the layers presented in thin sections is due to the high fissile character of the rock, the presence of organic-rich filled foraminifera and glossifungites.

The LLIE core and thin section (Figures 35A, B, and 36) depicts the separation of the layers due to the fissile character of the rock. HCl shows a lower effervescence to calcium carbonate than in the previous cores and the clay core increases in high amounts when compared with the XRD and XRF proxies, approximately 30% of clay.

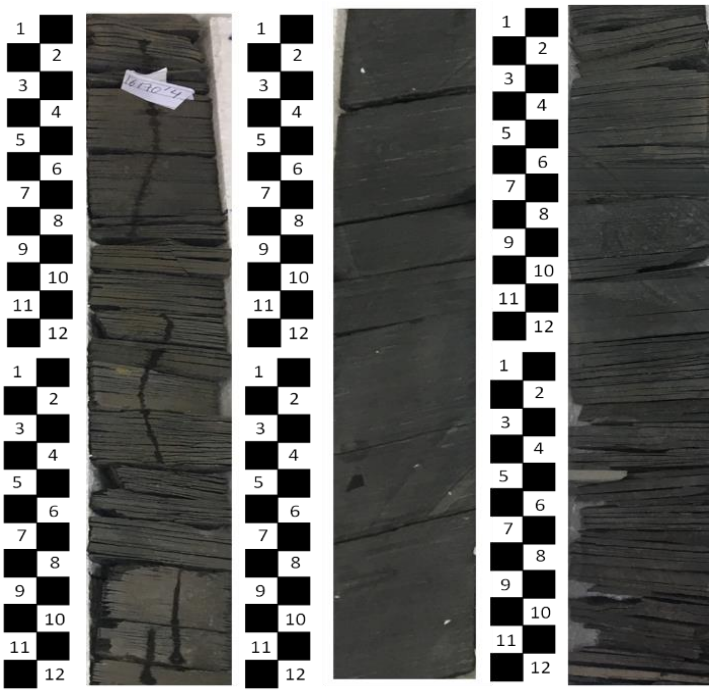

Figure 37. Representation of Facies I (Dark gray laminar mudstone).

II. Calcareous-marlstone with the presence of pyrite layers

These facies are represented by a massive and light-grey calcareous-marlstone (Figure 37), the organic richness and the coloration is less compared with facies I. Thin section analyses displays a micritization cement rich in uniserial and multiserial foraminifera recrystallized to calcite (Figure 38). The unique and atypical characteristic of these facies can be observed by the fractures (joint-system like, Figure 37); a possible reason is that this fracture could be generated by the type of clay that forms this character making it break easily in indistinct directions forming the present fracture pattern.

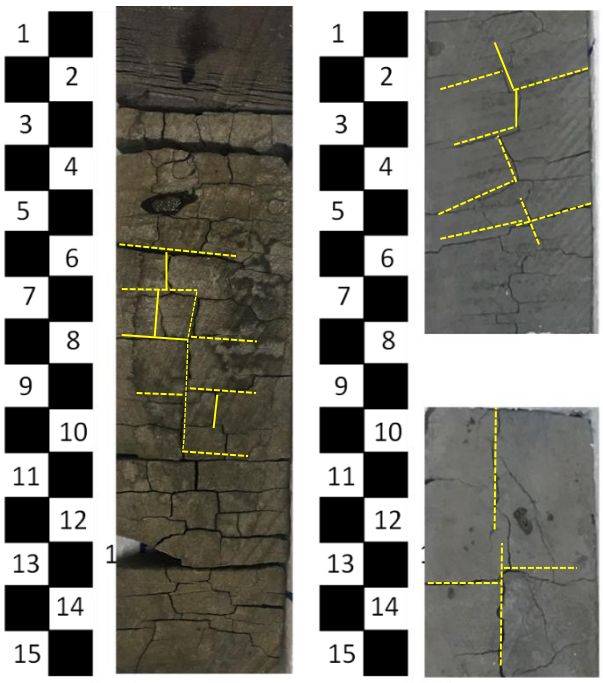

Figure 38. Representation of Facies II (Calcareous-marlstone with the presence of pyrite layers).

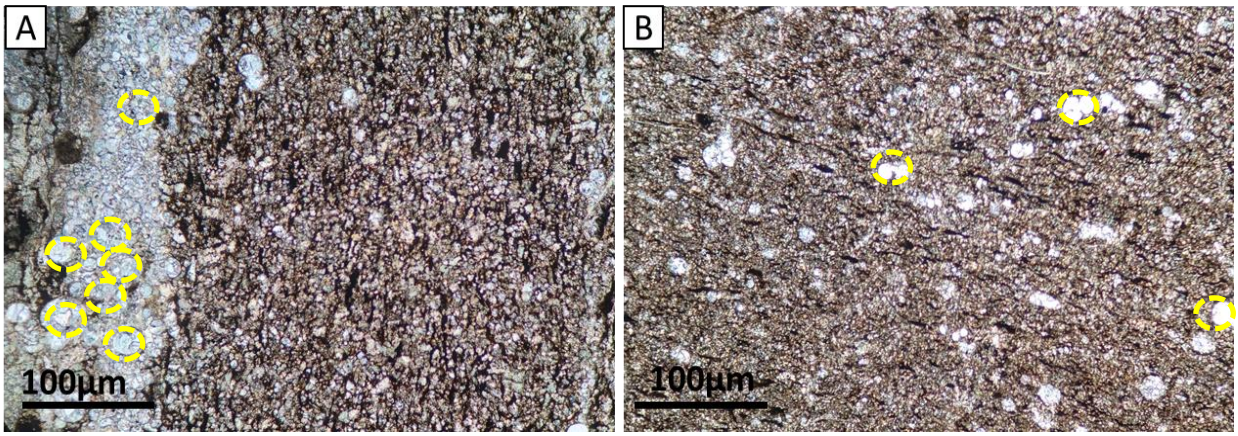

Figure 39. Representation of facies II (Calcareous-marlstone with the presence of pyrite layers) displaying of a micritization cement rich in uniserial and multiserial foraminifera recrystallized to calcite (yellow-dashed lines).

III. Volcanic Ash

There is not a physical property that shows the presence of volcanic ash (Figure 39). However, the interval 17184’17185’ is highly friable, and in fact, the interval 17180’-17184’ is not present in the core possibly due to the friable character of the volcanic ashes.

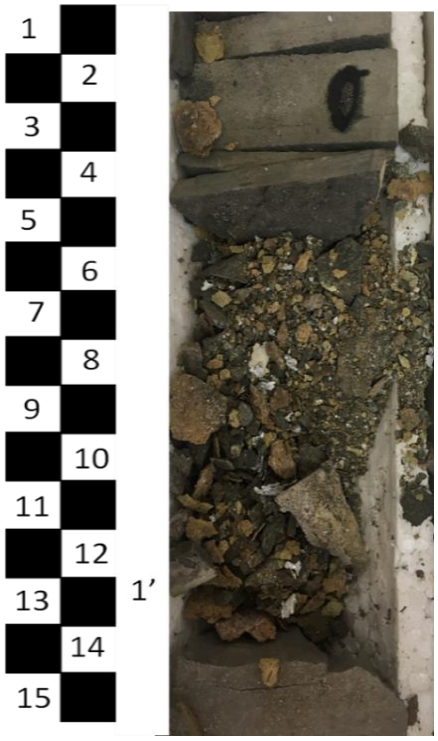

Interval
17185’-17184’

Figure 40. Representation of Facies III (Volcanic Ash facies) in LLIS core displaying a fissile yellowish color with coarse particles of volcanic ash.

This core does not display the Tres Esquinas member; there is no evidence of calcite and chert concretions. It can be even inferred that upwelling currents did not produce any influence in this area. With all these different features, it can be thought that this section could not be part of the La Luna Formation, but biostratigraphic and palynological analysis of these core in the 1900s (PDVSA Exploration, 1990) showed the presence of planktonic foraminifera zones representative

of the Cenomanian- Santonian *(D. brotzeni; H. Helvetica; D. primitiva, D. concavata, D. asymmetric* among others).

In general, it can be noticed that the paragenesis of La Luna formation in the cores studied above, has been primarily established by the generation of calcite and chert concretions, pyritization and development of a micritic cement, calcite-filled veins, and compacted syn-depositional intraclasts. Presence of authigenic calcite, crystallization, and cementation of calcite and silica and secondary porosity formed by dissolution and reprecipitation of dolomite, calcite and fossil replacement. Phosphatization (mostly present in Upper La Luna) can represent the last episode of diagenetic events of La Luna Formation deposition.

3.2 Mineralogical and elemental description of La Luna Formation, NW and SW Maracaibo Basin

According to previous analyses (Gonzalez et al., 1980), La Luna has been characterized as a marlstone and argillaceous limestone with an abundance of laminated and finely dispersed and thinly stratified organic matter. Typically, the mineral composition of La Luna in Northwestern Maracaibo Basin is primarily calcareous (approximately 85-90%) fluctuating in areas where the clay content increases towards the lower and Upper La Luna appearing as an alternating massive and finely laminated limestone.

Alternatively, quartz content can be linked to diagenetic chert which regularly increases towards the Middle and Upper La Luna as a representative siliceous- calcareous, laminated mudstone interbedded with black chert filled with calcite veins. X-ray diffraction (XRD) measurements were conducted on a subset of the four-core collection. Minerals were determined

on a weight percent (wt%) with the most representative minerals being calcite, quartz, dolomite, feldspar, clay, fluorapatite, pyrite and some trace percentages of rutile/marcasite/anatase.

This mineralogical identification was adequate for the lithofacies classification and to define the brittleness of the rock. To understand the mineralogical changes of the formation in the studied area, this image (Figure 40) represents the estimated core location along the basin. The light-yellow square and the rounded light green and dark yellow circles represent the Luna stratotype cores, LLIX, LLE, located towards the southwestern-northeastern trend of the Maracaibo Basin. The rounded red and pink circles represent the cores LLIA and LLIS located towards the northwestern- southeastern trend of the basin (Figure 40).

3.2.1 Southwestern-northeastern trend in the Maracaibo Basin:

These interpretations are related to the La Luna IX (LLIX), La Luna IE (LLIE) and the La Luna stratotype located towards the southwestern-northeastern trend of the study area. Since the outcrop was very steep and high our most significant limitation was the sampling density; thus, few samples were taken representing the most characteristic intervals of Lower, Middle, and Upper La Luna.

As can be noticed in Figure 41, the mineralogy displays calcite-rich predominant mineralogy along with the most representative members. The increment in quartz content is related to the biogenic silica associated with cherts, and the increment of clay content could be linked to the phosphatic and glauconitic intervals characteristic of Upper La Luna. This interpretation was supported by the "*in-situ"* field observations and sample description.

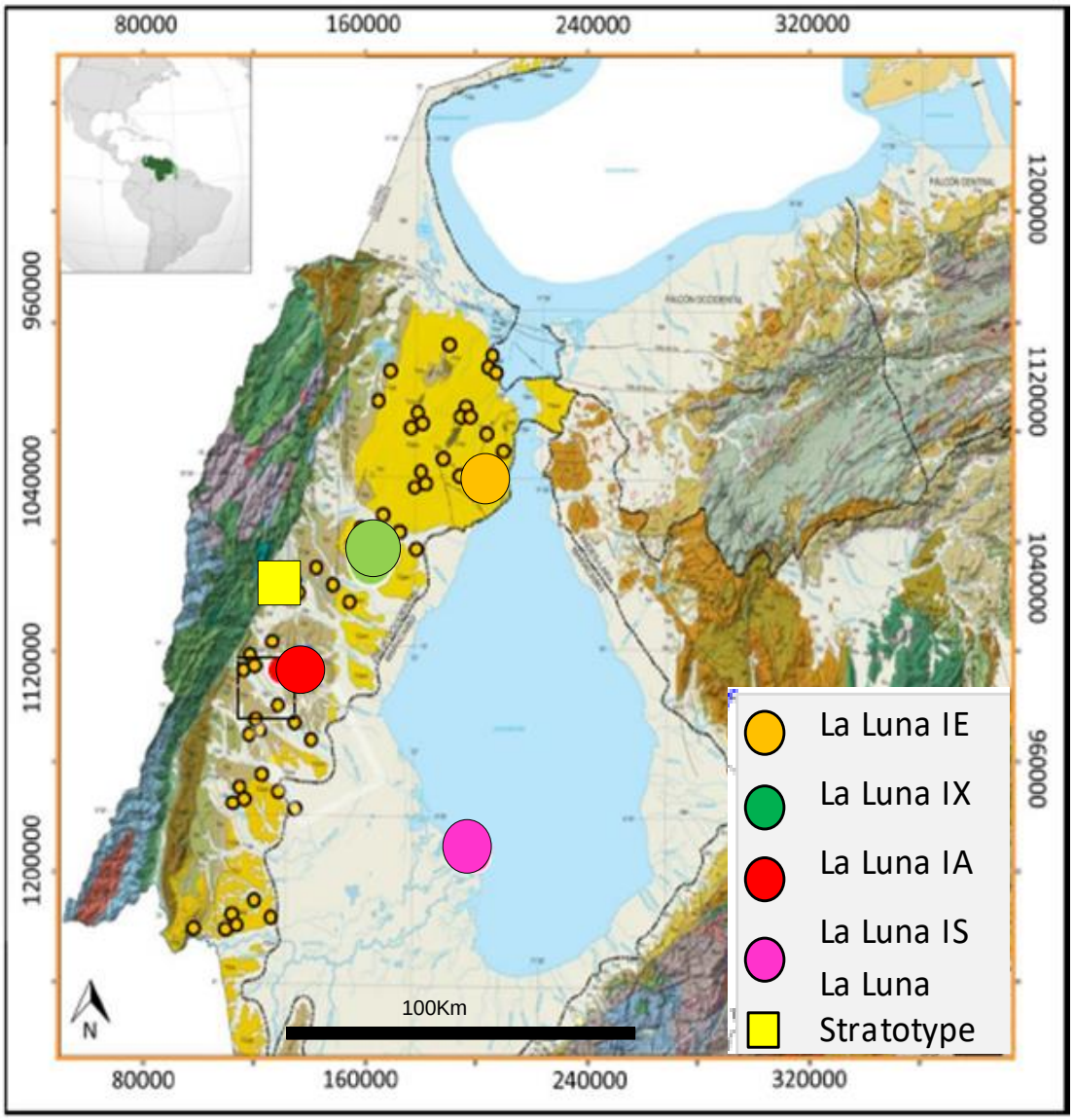

Figure 41. Estimated location and representation of the evaluated cores and stratotype in the study area. The light-yellow square and the rounded dark green and dark-yellow circles represent the cores (LLIE, LLIX, La Luna stratotype) located towards the southwestern-northeastern trend of the Maracaibo Basin. On the contrary, the rounded red and pink circles represent the cores (LLIA, LLIS) located towards the northwestern- southeastern trend of the basin.

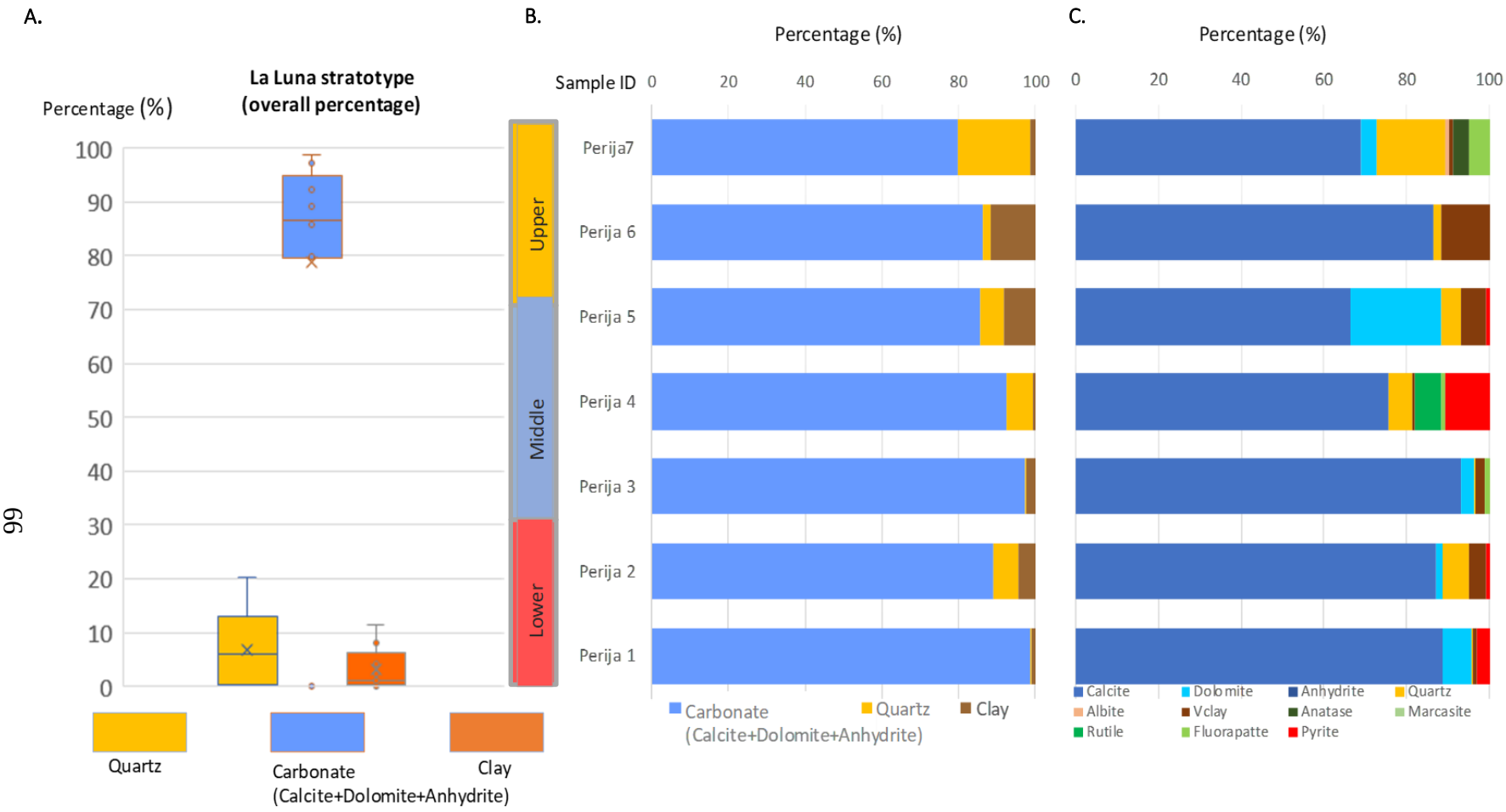

Figure 42. A. Whisker distribution of the principal mineralogical components (quartz, carbonate and clay); B. XRD-derived depth profile depicting the normalized percentage of quartz, carbonate and clay. C. XRD-derived depth profile depicting the relative mineralogy of the Lower, Middle and Upper La Luna Formation in La Luna stratotype.

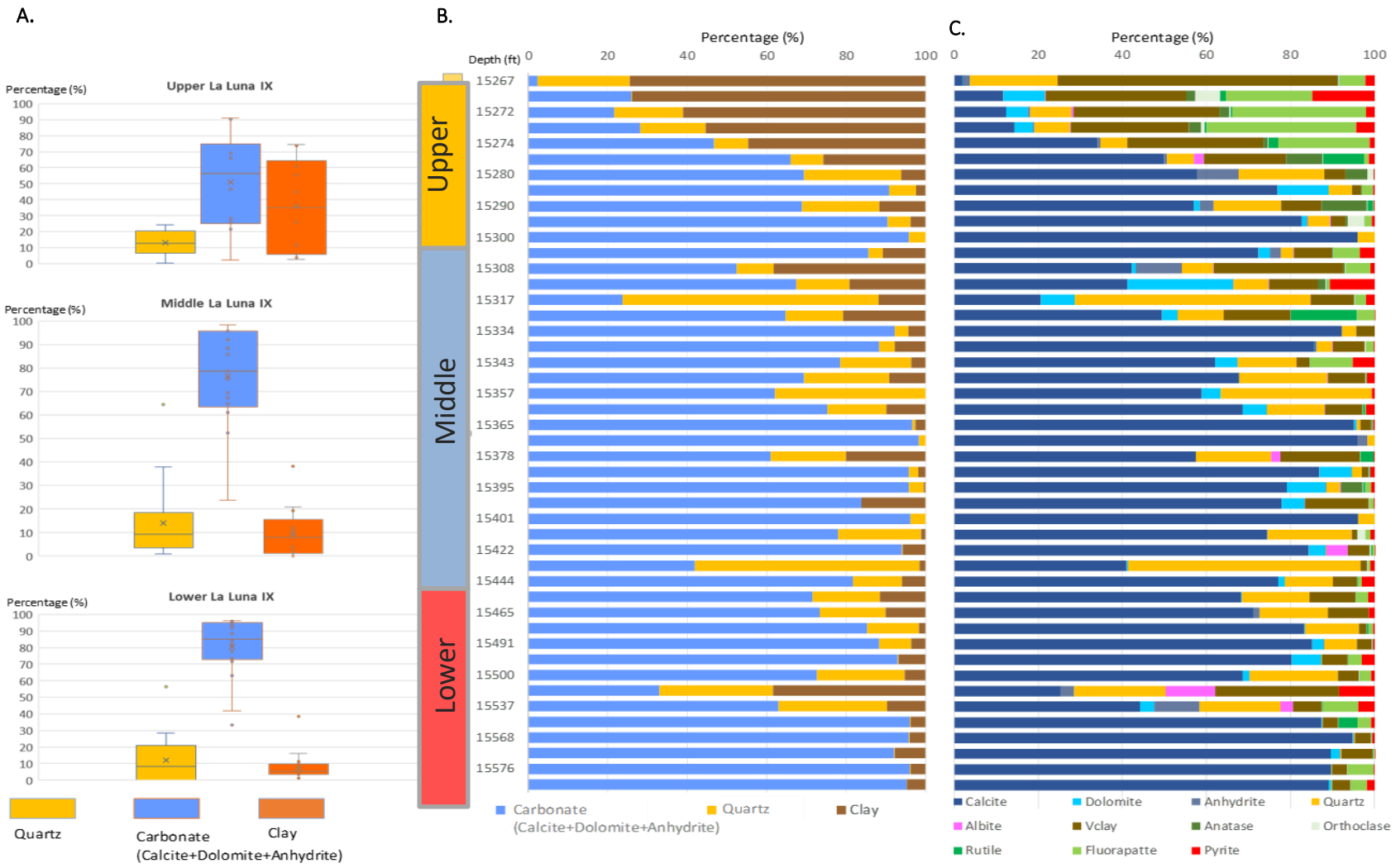

Figure 43. Whisker distribution of the principal mineralogical components (quartz, carbonate and clay); B. XRD-derived depth profile depicting the normalized percentage of quartz, carbonate and clay. C. XRD-derived depth profile depicting the relative mineralogy of the Lower, Middle and Upper La Luna Formation in core La Luna IX.

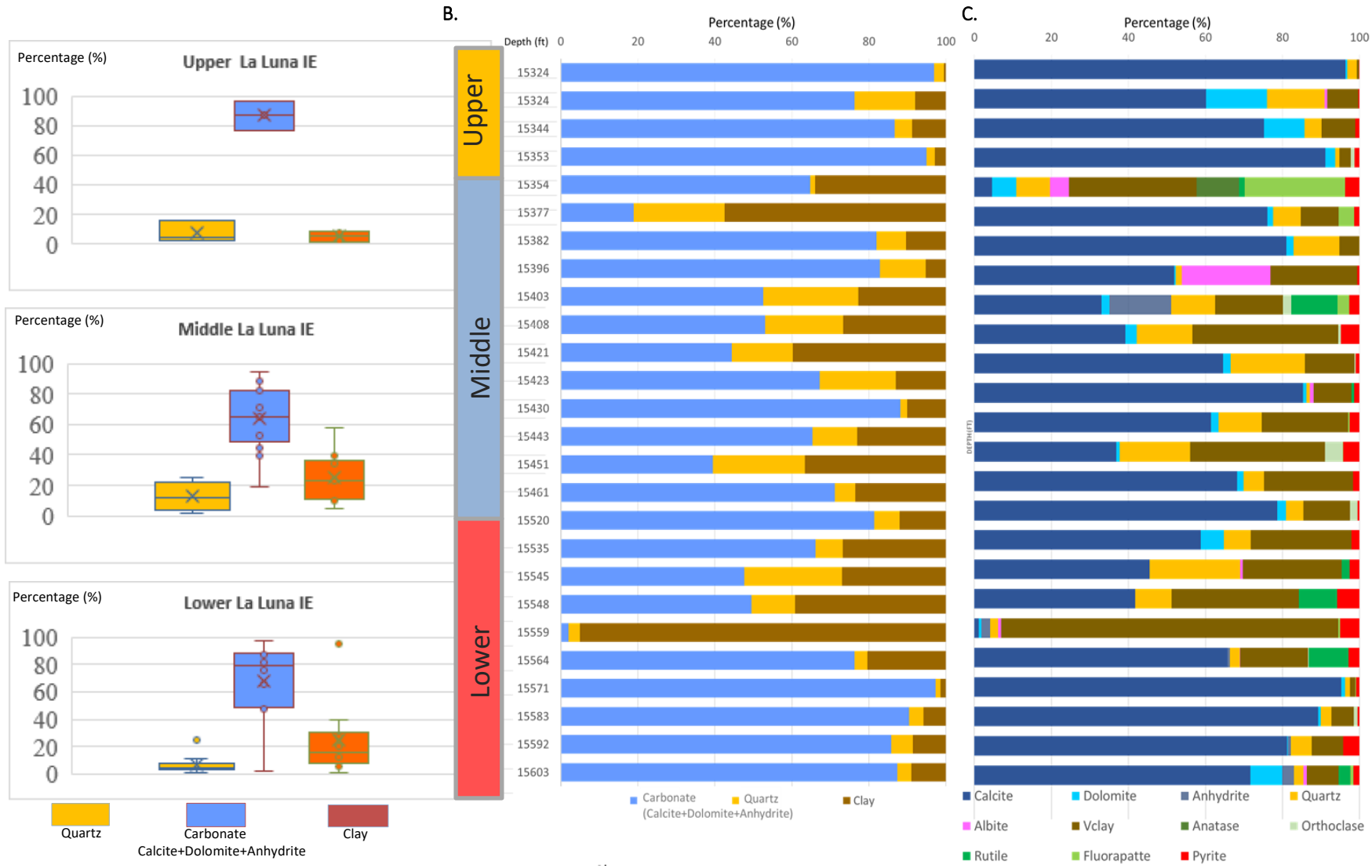

Figure 44. Whisker distribution of the principal mineralogical components (quartz, carbonate and clay); B. XRD-derived depth profile depicting the normalized percentage of quartz, carbonate and clay. C. XRD-derived depth profile depicting the relative mineralogy of the Lower, Middle and Upper La Luna Formation in core La Luna IE.

The high density of samples obtained from cores LLIX and LLIE depicts at a very similar calcite distribution. However, if we look at the different members plotted in the box and whisker distribution, it can be noticed that the calcite and clay content are inversely proportional between the two wells (Figures 42 and 43). In LLIX core the calcite content decreases upwards when the clay content increases. This trend is related to Upper La Luna, due to the presence of the Tres Esquinas Member in this core in which a high phyllosilicate concentration is displayed due to the presence of the glauconite content (Figure 42). On the other hand, core LLIE (Figure 43) presents an inverse trend for Upper La Luna, where the calcite content increases upwards while the clay content decreases. Quartz content distribution does not vary drastically, and its content on average remains between 5 and 20% on average.

Even when most of the cores display a considerable variability, the mineralogy is rich in calcite with a brown matrix of clay minerals and organic matter. Main clay types within the La Luna samples such as illite-smectite, kaolinite and chlorite, a small alkali feldspars (orthoclase) content (6% on average) and albite (8% on average) can be attributed to the volcanic ash pulses during the deposition in Lower La Luna formation, especially in cores LLIX and LLIE (Figure 16).

Figures 42 and 43 display for the La Luna mineralogy some small traces of fluorapatite. This occurrence is possibly related to the diagenetic processes in phosphate-bearing limestones and mudstones that are a very common characteristic in the Epeiric sea within marine shelf environments (Schwennicke et al., 2000). The small amount of dolomite (5-10%) can be a diagenetic product of the calcite related to the dolomitization processes (see thin section analyses of LLIE core in Figure 19A and B and Figure 20C, D and E).

The Upper La Luna in the northwestern Maracaibo Basin is categorized as an interval with a high proportion of biogenic quartz and calcite. The productivity resulting from upwelling currents at the end of the Cretaceous in the La Luna Formation generated a high amount of chert concretions as determined by the XRD analyses.

The phosphate and the glauconite contents reflected in the clay portion of La Luna IX is related to the Tres Esquinas Member and has been used as a key marker for their characteristic texture and coloration. This member marks the end of La Luna deposition and is not present in all the areas of the basin and absent in the LLIE core.

3.2.2 Northwestern-southeastern trend Maracaibo Basin

The mineralogy of the two cores located in NW-SE Maracaibo Basin (La Luna IA (LLIA) and La Luna IS (LLIS) show significant differences compared with the typical documented mineral composition of La Luna Formation in Maracaibo Basin.

LLIA displays a very monotonous pattern showing a higher increment in clay content that is not typical of the La Luna mineralogy in Maracaibo Basin. LLIA core represents the deposition that was controlled by the paleo-topography of the underlying Maraca Formation. Most of the dark gray laminar mudstone (facies I) is present in almost half of the section. In this core, as can be seen in the box and whisker distribution (Figures 44 and 45), the calcite content increases upward while the clay and quartz content decreases.

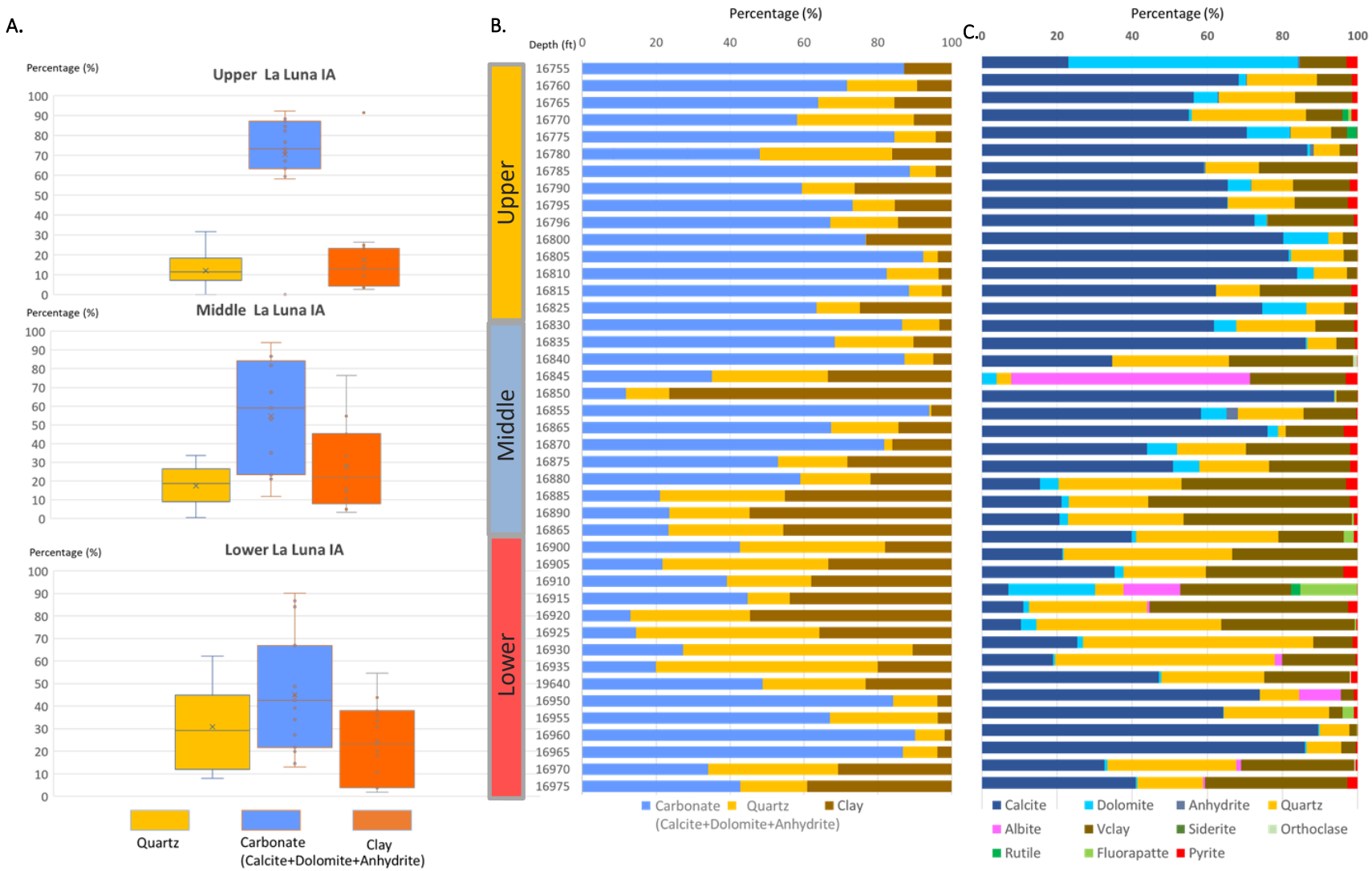

Figure 45. Whisker distribution of the principal mineralogical components (quartz, carbonate and clay); B. XRD-derived depth profile depicting the normalized percentage of quartz, carbonate and clay. C. XRD-derived depth profile depicting the relative mineralogy of the Lower, Middle and Upper La Luna Formation in core La Luna IA

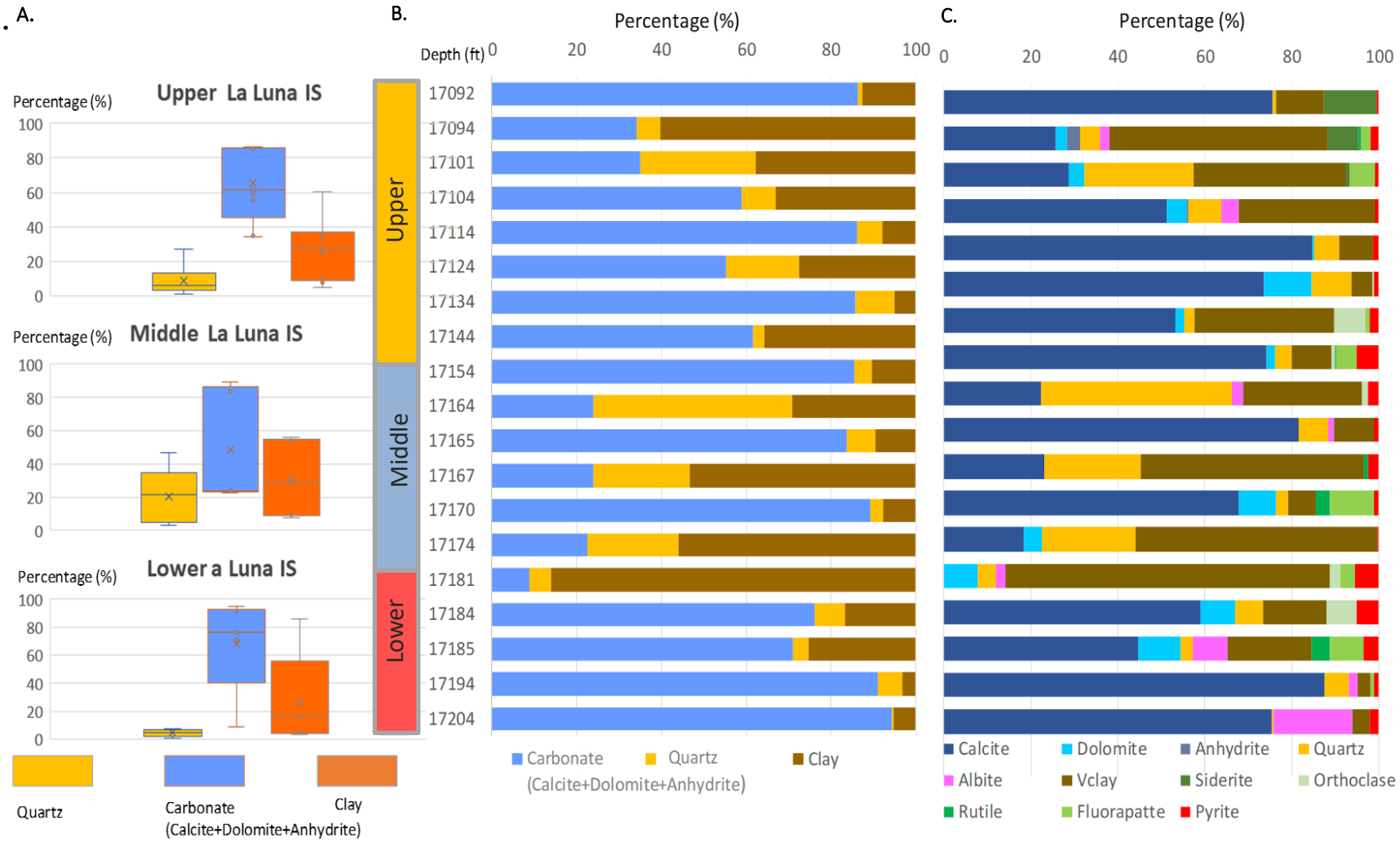

Figure 46. Whisker distribution of the principal mineralogical components (quartz, carbonate and clay); B. XRD-derived depth profile depicting the normalized percentage of quartz, carbonate and clay. C. XRD-derived depth profile depicting the relative mineralogy of the Lower, Middle and Upper La Luna Formation in core La Luna IS.

Dolomite slightly increases from the bottom to top (5-15% on average) and is found in a small fraction of core. It is a diagenetic product of the calcite subjected to the dolomitization processes as seen in thin sections of the LLIE core in Figure 32 (C and D).

The Upper La Luna in LLIA is characterized by a high amount of calcite which has been dolomitized at the very top of La Luna core. There is not glauconitic or phosphatic interval. Alternatively, LLIS core present a lithology pattern that does not correspond with the typical characteristics of the Lower, Middle and Upper La Luna in Maracaibo Basin.

Typically, La Luna is characterized by a high calcite content along the formation, calcite concretions towards Middle La Luna, and an increment of silica concretions towards the Middle-Upper La Luna. This core is represented by cyclicity of two distinctive lithofacies: facies I "Dark gray laminar mudstone" and facies II "Calcareous-marlstone with pyrite layers". They are represented by a similar increment from bottom to top in calcite and clay content. The more fissile areas are characterized by an increase in the clay (55-64% on average) and feldspar content (8-18% on average), particularly in the Lower section) that is also associated with volcanic ash pulses. The brittle character is characterized by high calcite (75-85% on average) and dolomite content (6-10% on average) along the whole interval. Even though the quartz content is not observed in the LLIS core, quartz content fluctuates along the whole section going from 5 to 25% on average increasing towards the Middle La Luna. Since the core and mineralogical results do not show a particular trend for Lower, Middle, and Upper La Luna, the section was divided in the XRD profile by considering the Gamma Ray log and its relationships with the sequence stratigraphic para-sequences sets.

The overall mineralogy of the Maracaibo Basin can be established using the designed ternary plot from Gamero-Diaz et al. (2012) displayed in figure 46. The plot is based on the

lithological description and the analysis of approximately three hundred (300) X-Ray Diffraction samples and forty-two thin sections. Samples were taken in the different cores located towards NW-SE Maracaibo basin for this work. The plot depicts how the mineralogical composition of La Luna is mostly plotted as a mixed carbonate mudstone dominated lithotype (Figure 46).

The frequency of "mixed siliceous mudstone" is given by the high productivity generated by the upwelling currents displayed by the chert nodules that are mainly composed of biogenic silica. The mixed argillaceous mudstone is mostly characterized by the typical glauconitic and phosphatic top of La Luna formation conformed by the Tres Esquinas member and the two most visible pulses of volcanic ash found at the lower and Upper La Luna. These intervals are very valuable since they can be an important correlation parameter.

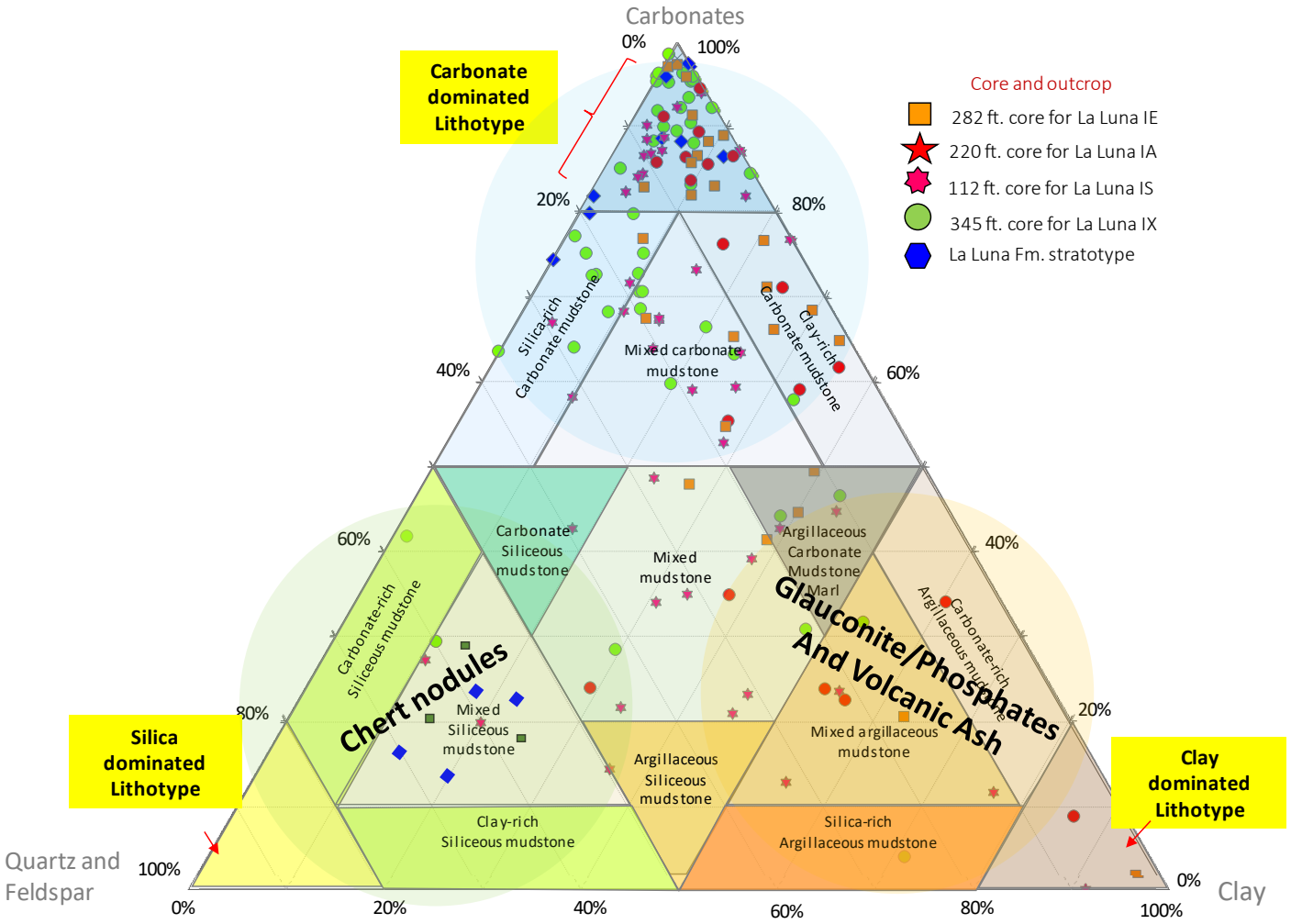

Figure 47. Overall mineralogical composition of La Luna Formation in the trend NE-SW Maracaibo Basin using the ternary plot classification from Gamero-Diaz et al., 2012. The mineralogical composition of La Luna is mainly a carbonate, and a mixed carbonate mudstone dominated lithotype. The frequency of 3 "mixed siliceous mudstone is given by the high productivity generated by the upwelling currents displayed by the chert nodules that are mainly composed of biogenic silica associated with diatom production. The mixed argillaceous mudstone is mostly characterized by the typical glauconitic and phosphatic top of La Luna formation conformed by the Tres Esquinas member and the two most visible pulses of volcanic ash found at the lower and Upper La Luna. These intervals are very valuable since they constitute an important correlation parame

3.3 Elemental Chemostratigraphy

Chemostratigraphy is a technique that can be applied either to field outcrop, core or cuttings samples with an equivalent degree of achievement. Chemostratigraphy brings an important correlation parameter for unconventional reservoirs since it allows the recognition of detrital, carbonate and paleo-redox/paleoenvironmental indicators using inorganic geochemical proxies also called “chemozones” (Ratcliffe et al., 2006). In addition, a comparison of geochemical, petrographic, X-ray diffraction and TOC data permits mineralogical relationships that can be recognized with a high degree of confidence.

Based on the element association by Craigie (2018), the elements used for these interpretations were classified into three main types: (1) elements associated with detrital input and clay content zirconium (Zr), titanium (Ti), silicon (Si), cobalt (Co), lead (Pb), niobium (Nb), aluminum (Al), potassium (K), thorium (Th), phosphorus (P); (2) elements associated with carbonate input strontium (Sr), calcium (Ca), magnesium (Mg), manganese (Mn); and (3) elements associated to paleo-redox/anoxic input: nickel (Ni), copper (Cu), zinc (Zn), uranium (U), molybdenum (Mo), vanadium (V) and sulfur (S).

Plotting concentrations of these elements as a function of depth in a measured section generates a chemostratigraphic profile (Figures 47- 50). These profiles can be used to develop stratigraphic frameworks to correlate units across sedimentary basins. The correlation of chemozones was done for four cores and a stratotype for the study area (northwest Maracaibo Basin).

3.3.1 Elements associated with detrital input and clay content

In marine shales, Zr and Ti are typically present in lower concentrations; their abundance can be associated with continentally-derived sediments (Sageman et al., 2003). Aluminum (Al), silicon (Si) and thorium (Th) are very stable under diagenetic processes since diagenetic or weathering conditions do not modify their distribution. Consequently, these elements are usually used individually and as a ratio with other elements, since they are mostly associated with fine-grained detrital influx (Tribovillard et al., 2006).

According to Sageman et al. (2004), silicon is one of the elements that can be associated with different sources (detrital quartz, authigenic quartz, clay minerals, and feldspars). Silicon can be present as "extrabasinal" in the form of derived detrital fluvial or eolian quartz grains and "interbasinal" in the form of primary biogenic- opaline quartz. This element is commonly used for the estimation of a detrital/biogenetic input present in most of the source rocks (Blood et al., 2013).

A high concentration of the detrital quartz phases can be detected in the continental sedimentation proxies (Turner et al., 2015). These proxies can be associated with a low silica/aluminum ratio (Pearce et al., 1999). Nevertheless, in zones in where the Ti, Zr or K remain constant and the Si/Al ratio increases, the association could be related to biogenic quartz. Turner (2016) described these zones as either hiatal surfaces of non-deposition or episodic algal blooms.

Aluminum and potassium are associated with clay minerals and alkali feldspars (Pearce et al., 1999; Tribovillard et al., 2006). Alkali feldspar grains will perform hydrodynamically like other sand and silt size grains, whereas clay minerals can be carried long distances along the basin and related to an increment in the concentration of K and Al and a diminishment of concentration in Zr. These trends can be associated with an environment of deposition in the distal areas of the basin concerning the source of sedimentation. Nevertheless, if these elemental proxies are

increasing and decreasing at the same rate, it is probable that Al and K can be associated with a feldspar phase.

The distribution of the elements used for the chemo-stratigraphic profile can be associated to the sediment source coming from the Epeiric seas where this formation was deposited in a shallow- water platform (during the Late-Cretaceous time). Most of the initial La Luna deposition could be controlled either by a nearby sediment input, the position of the basin, the paleo-topography developed by the underlying formation (Maraca Fm. Cogollo Group) and sea level fluctuations.

In cores LLIX and LLIE (Figure 47 and 48), the silica contribution fluctuates in concentration along the formation. However, when the titanium, aluminum, and potassium are associated, the detrital input mostly increments in Lower La Luna. This increment has been seen in the argillaceous carbonate mudstone facies, core description, and XRD analysis.

Aluminum and potassium present a similar trend with the uranium proxy. This proxy is also associated with clay and feldspar content. These trends can also be correlated with the dark gray laminar mudstone facies, petrographic and XRD analyses for the LLIX and LLIE.

Furthermore, diagenetic quartz is mostly associated with the Middle and Upper La Luna. This type of quartz can be related to the calcified radiolarians in the mixed siliceous-mudstone facies.

Core LLIA, displayed in Figure 49, represents the highest abundance of detrital proxies (high Al, K, Si) along the four analyzed cores. The exciting part is that this interval also represents a higher concentration of elements associated with paleo-redox/anoxic input (such as uranium, molybdenum, vanadium, and sulfur). The increment can be associated to the marlstone- mudstone facies.

This type of relationship has been seen in the Woodford Shale in Kingfisher Oklahoma, in where its facies are associated to a paleo-topographic control of the Hunton Group (Liborius & Sneddon, 2017).

Thus, these relationships can be compared and related to the ones seen in La Luna. Even when they have deposited in a different age, they can be interpreted as a paleo-topographic control of the shallow- water platform Maraca Formation.

Core LLIS is represented by a cyclical abundance of proxies (high Al, K, Si) not exposing a specific trend. Their increment in the elements associated with detrital input is also related to Dark gray laminar mudstone facies.

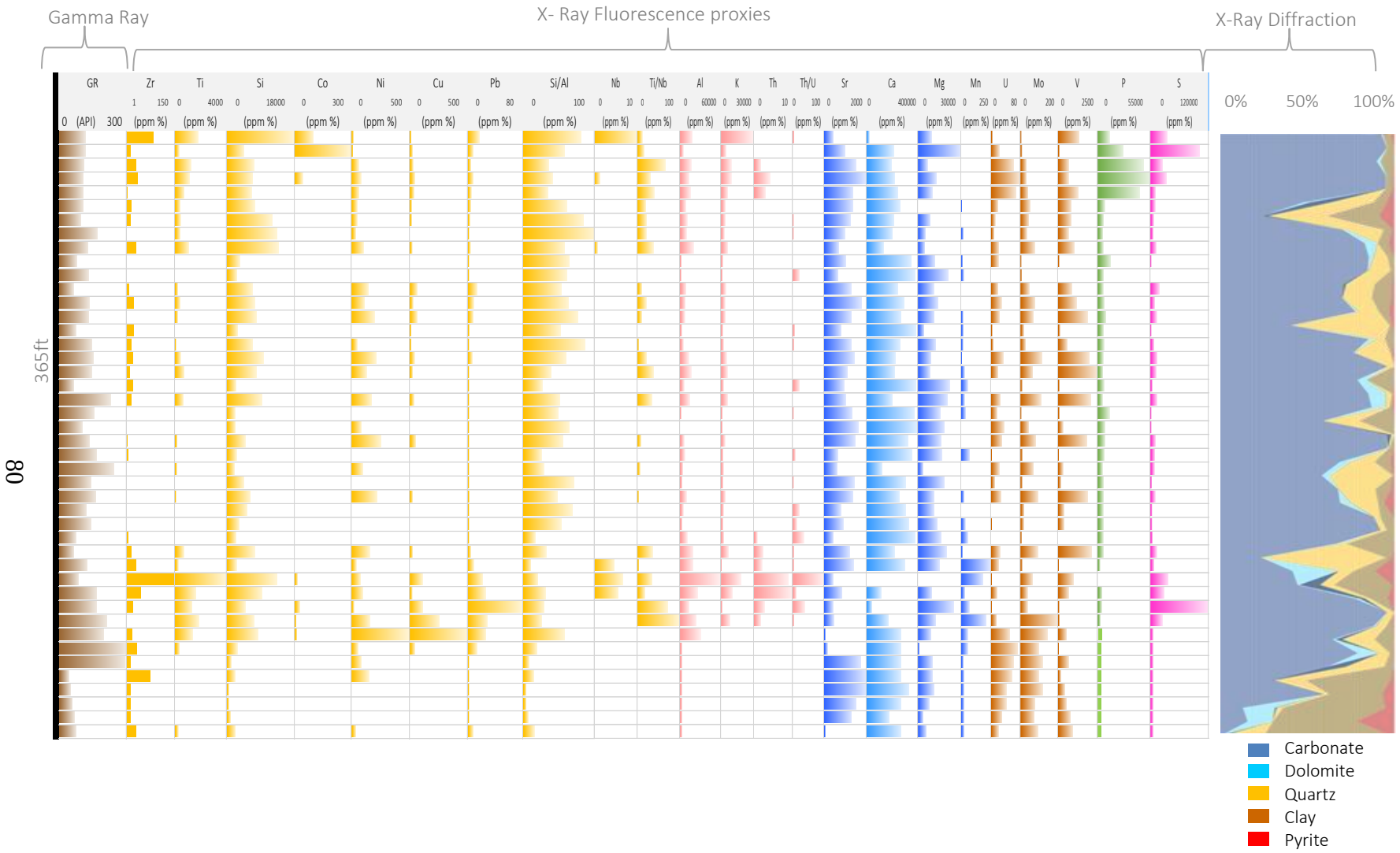

Figure 48. Gamma Ray, XRD and chemostratigraphic profile of the Lower, Middle and Upper La Luna Formation in core La Luna IX showing the overall elements of this study in parts per million (ppm). Elements associated with detrital input are highlighted in yellow, potassium in green and clay content in light pink. Elements associated with carbonate input are shown in blue and elements associated with paleo-redox/anoxic input are highlighted in brown and magenta for sulfur.

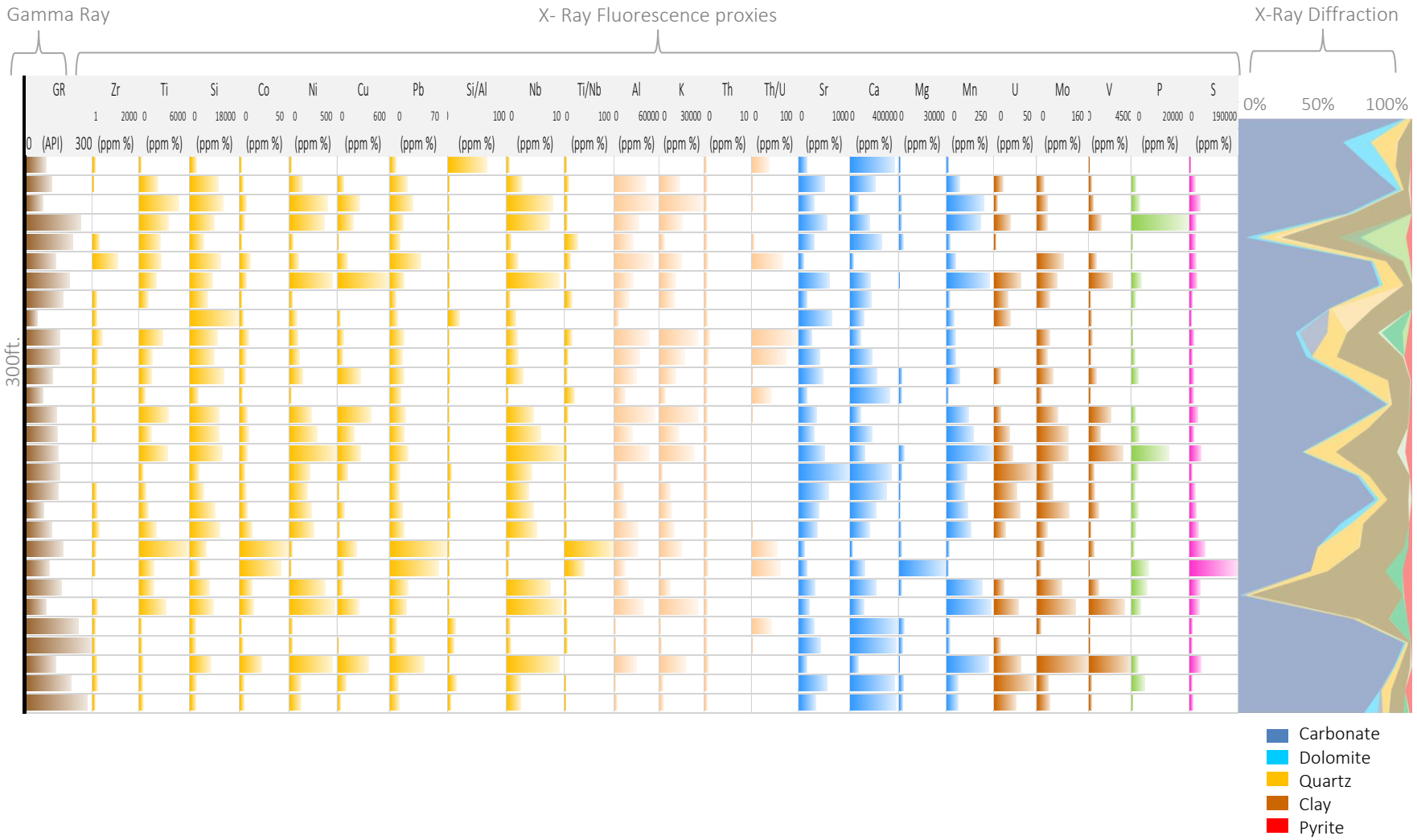

Figure 49. Gamma Ray, XRD and chemostratigraphic profile of the Lower, Middle and Upper La Luna Formation in core La Luna IE showing the overall elements of this study in parts per million (ppm). Elements associated with detrital input are highlighted in yellow, potassium in green and clay content in light pink. Elements associated with carbonate input are shown in blue and elements associated with paleo-redox/anoxic input are highlighted in brown and magenta for sulfur.

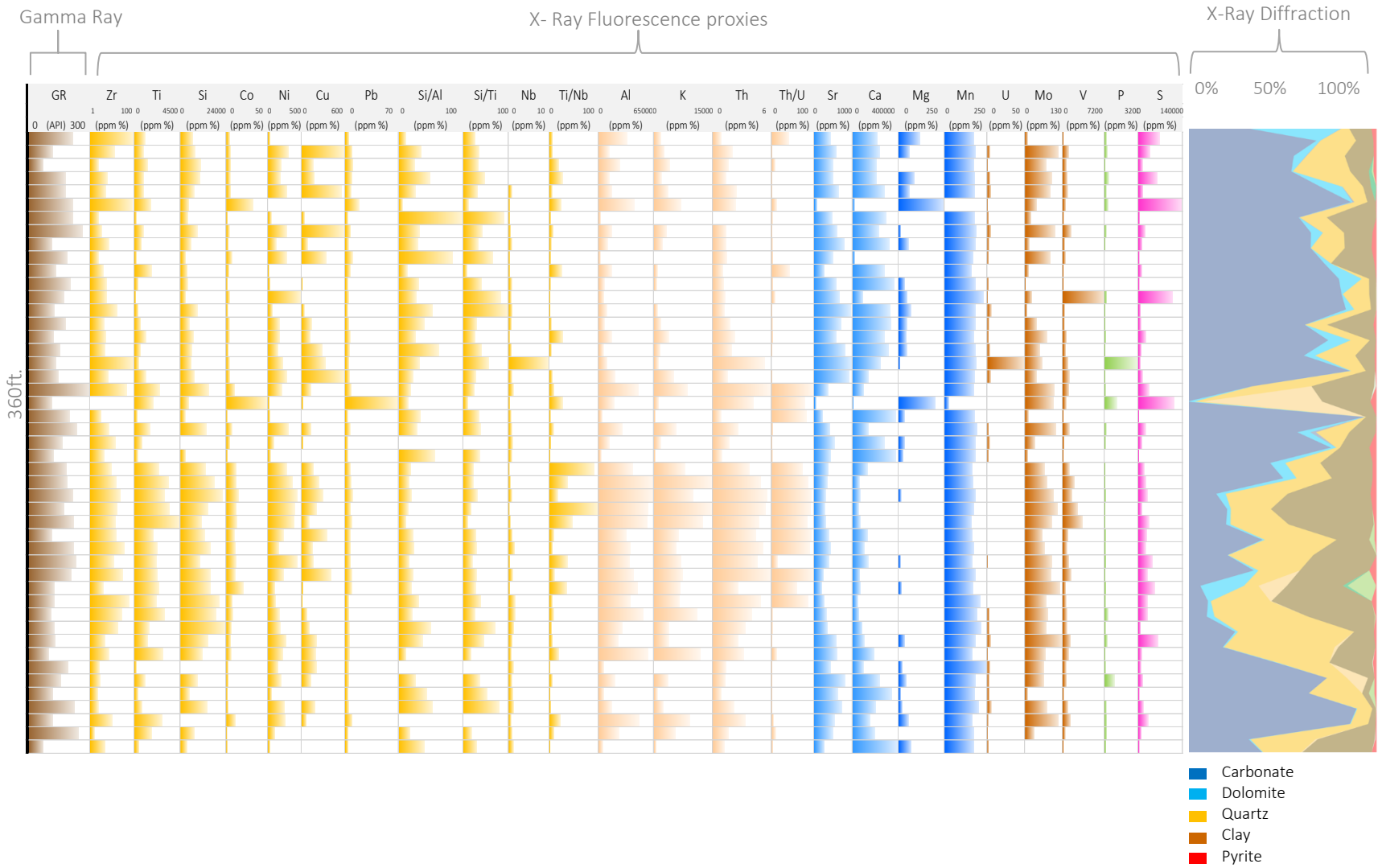

Figure 50. Gamma Ray, XRD and chemostratigraphic profile of the Lower, Middle and Upper La Luna Formation in core La Luna IA showing the overall elements of this study in parts per million (ppm). Elements associated with detrital input are highlighted in yellow, potassium in green and clay content in light pink. Elements associated with carbonate input are shown in blue and elements associated with paleo-redox/anoxic input are highlighted in brown and magenta for sulfur.

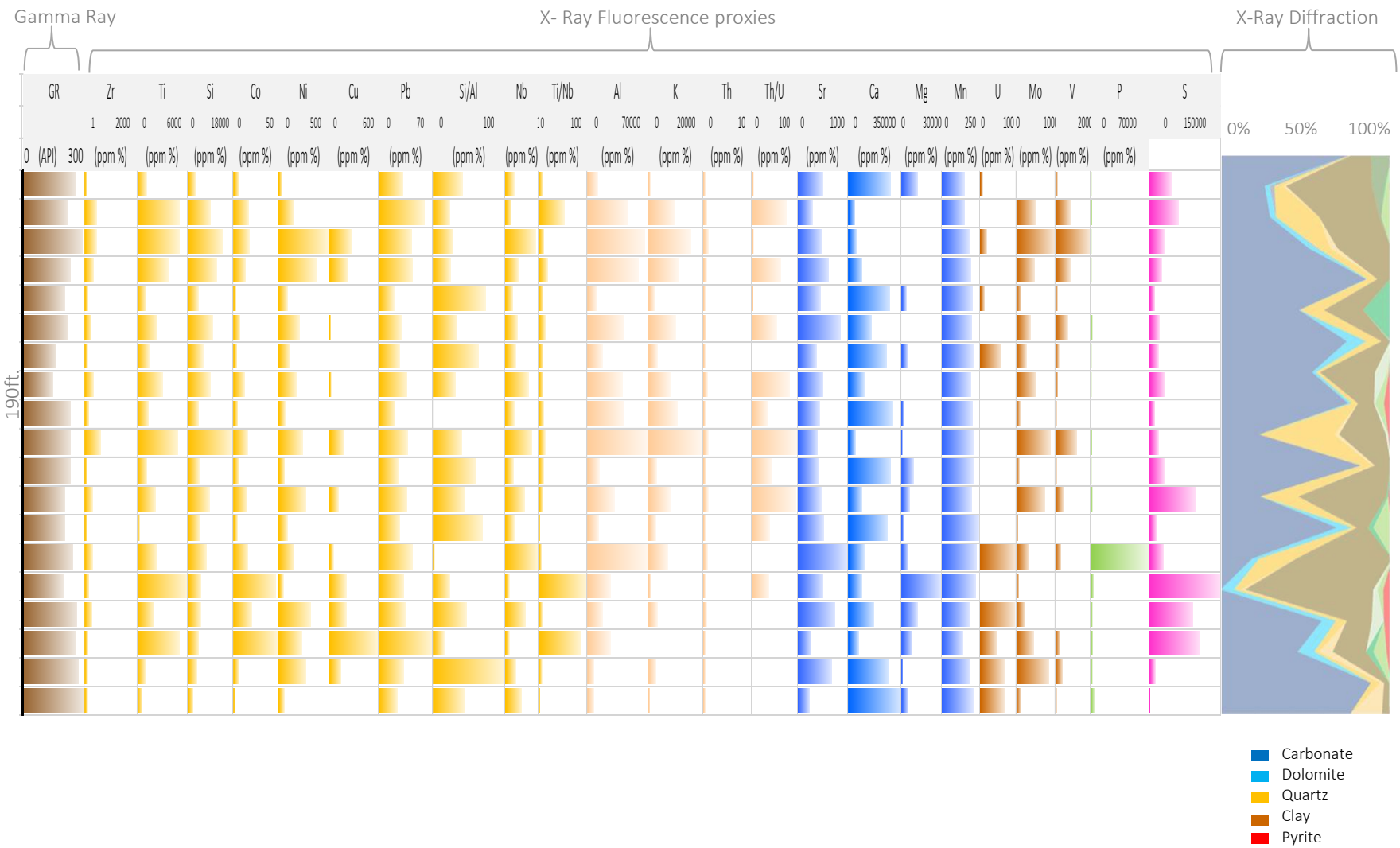

Figure 51. Gamma Ray, XRD and chemostratigraphic profile of the Lower, Middle and Upper La Luna Formation in core La Luna IS showing the overall elements of this study in parts per million (ppm). Elements associated with detrital input are highlighted in yellow, potassium in green and clay content in light pink. Elements associated with carbonate input are shown in blue and elements associated with paleo-redox/anoxic input are highlighted in brown and magenta for sulfur.

3.3.2 Elements associated with carbonate input

Calcium and Sr are associated with carbonates (Banner, 1995; Tribovillard et al., 2006). Calcium is incorporated into calcite, aragonite, and dolomite, while Sr can substitute into the aragonite crystal structure. However, as these elements may migrate during diagenesis, it is useful to use a multi-proxy approach with these elements (Tribovillard et al., 2006). Additionally, Ca and Sr are also present within some feldspars, phosphates, and sulfates. For cores LLIX and LLIE (Figures 47 and 48), the elements associated with carbonate input (calcite, strontium, and magnesium) remain high along the interval as XRD and core description. Thus, La Luna is considered a carbonate-dominated lithotype.

Magnesium spikes can be associated to the dolomitization seen along the core for LLIE, LLIX, and LLIA, especially towards the Upper La Luna Formation. LLIX contains a high increment of S, P, and Sr that can be related to the Tres Esquinas Member and also suggest anoxic bottom water euxinia conditions. In core LLIA (Figure 49), the calcite content in the Lower La Luna is low due to the paleo-topography control of La Luna formation. The deposition of LLIA forms an embayment-type, in which carbonate content increases progressively towards the Middle and Upper La Luna displaying the typical and descriptive La Luna facies with a higher concentration of S, Mg, Al, K, Pb and Zr possibly related to the volcanic ash pulses associated with Upper La Luna.

The increment in strontium and sulfur suggest a possible sulfate and phosphatization increment as it was observed in core description. Furthermore, LLIS (Figure 50) is characterized by a cyclicity of detrital and carbonate proxies. Presence of high sulfur possibly represents the sulfurization/ pyritization developed during deposition and Ca; Sr increases inversely proportional to Ti and Si along the interval in a cyclical way.

3.3.3 Elements associated with paleo-redox/anoxic input

Tribovillard et al. (2006) indicate that elements like Cu, Ni, and Zn are absorbed onto Fe-Mn-oxyhydroxides that are later released upon reductive dissolution of these oxyhydroxides at or below the water-sediment interface forming new minerals like pyrite in reducing environments and, therefore, these proxies are often used as 'key' indicators of anoxia.

Nickel in oxic marine conditions acts as a micronutrient but is present as a soluble Ni carbonate ($NiCO_3$) or within humic or fulvic acids (Calvert and Pedersen., 1993; Algeo & Maynard., 2004; Tribovillard et al., 2006). The association of Cu with organic matter is typical since it absorbs the Fe-Mn oxyhydroxides accelerating the sediment enrichment. Bacterial sulfate, in reducing environments changes and is reduced from $Cu^{2}+$ to $Cu^{1}+$. It can be incorporated in solid solution as pyrite (Tribovillard et al. 2006).

Molybdenum (Mo) is characterized as a critical element for determining the degree of anoxia within paleoceanographic basins (Algeo & Lyons, 2006; Algeo & Rowe, 2012). Molybdenum is a highly mobile element under oxidizing conditions and precipitates under anoxic conditions (Tribovillard et al., 2006). Under oxidizing conditions, Mo is in solution as the molybdate anion.

Vanadium (V) is another key element in determining the anoxia of sedimentary basins. Like Mo, V is highly mobile under oxidizing conditions. Unlike Mo, V does not require sulfur to precipitate under anoxic conditions (Tribovillard et al., 2006). Molybdenum and vanadium concentrations can be used in conjunction with basin morphology to qualitatively assess water depth or bottom-water circulation (Algeo & Lyons, 2006; Algeo & Rowe, 2012).

Based on this information, it is possible to construct high-resolution sequence stratigraphic correlations and potentially identify localized autocyclic variations within the basin-wide

allocyclic signals. Towards the NE, cores LLIX and LLIE (Figure 47 and 48) contain very high concentrations of the elements associated with paleo-redox/anoxic input. Even when uranium is associated with the clay content, its abundance can be associated with organic matter richness along the La Luna Formation. Although the bottom water euxinia and sensitive redox elements (molybdenum and vanadium) are mostly higher in concentration along the core, Lower La Luna displays the highest values of molybdenum and vanadium for LLIX. Its increment is also associated to the euxinic conditions during the Late Cretaceous and the worldwide transgression that formed the best quality organic-rich source rocks in the epicontinental seas.

Core LLIA (Figure 49) contains not only a high detrital input but also very-high bottom water euxinic proxies' concentrations not only high in Mo and V but also S and Cu. High detrital input can be associated with a local source associated with possible paleo-highs described by (Erlich et al., 1996). In his work, he stated that these paleo-highs might act as paleo-bathymetric barriers enhancing the preservation of the organic matter.

Furthermore, core LLIS (Figure 50) also displays a similar depositional control since detrital and paleo-redox proxies concentrations are prominent. This can be interpreted as an anoxic-euxinic environment that is possibly located in the vicinity of the inner shelf-platform in which the lithologic control is linked to sea level changes.

CHAPTER IV

SOURCE ROCK CHARACTERIZATION

4.1 Total Organic Carbon (TOC) and Rock-Eval Pyrolysis

For the preliminary geochemical screening, samples from outcrop and subsurface were analyzed using total organic carbon (TOC) and Rock-Eval Pyrolysis. Results were interpreted according to guidelines in Tissot & Welte (1984), Peters & Cassa (1994), Jarvie et al. (2007) and Philp (2014). Measured and calculated vitrinite reflectance data and Tmax values were used to establish thermal maturity values for the La Luna samples.

4.1.1 Organic Richness

In the laboratory total organic carbon (TOC) is a significant source rock-screening tool. TOC values reflect the amount of organic carbon, including kerogen and bitumen in a source rock (Peters & Cassa, 1994). TOC values are obtained through oxidation of the organic material and the measurement of the CO_2 that is produced.

According to Peters & Cassa (1994) and Jarvie et al. (2007), the parameters and terminology derived from Rock-Eval pyrolysis are the following: the S1 peak contains the free oil content in the rock vaporized at 300°C (mg HC/g); the S2 peak contains the remaining potential to generate hydrocarbons by cracking kerogen using programmed pyrolysis from 300-600ºC, usually at 25°C/min (mg HC/g) and maximizes depending upon the structure of the kerogen along with the maturity of the source rock; the S3 peak is the organic carbon dioxide evolved between 300-390°C (mg CO_2/g), generated during the decomposition of the kerogen; the S4 peak is the residual carbon from the oxidation of dead carbon remaining after pyrolysis. These peaks are represented by a pyrogram that is obtained from the pyrolysis products of material (Figure 51). The organic matter distribution is divided into live carbon and dead carbon. The former is

composed of gas/oil and organic matter (kerogen) and is related to the S1 and S2 peaks of a pyrogram plot and the latter is related to the S4 peak.

Using these three parameters (S1, S2, and S3) along with the TOC content of the sample, two critical parameters have been developed (Tissot & Welte, 1984). The former is the hydrogen index; (HI) which is the S2 peak normalized to the TOC gives a measure of the amount of kerogen in the rock and indirectly the hydrogen content. The latter is the oxygen index, (OI) which is the S3 peak normalized to the TOC that shows a measure of the organic oxygen content of the kerogen. The production index (PI) is the ratio of S1 to S1+S2. The Tmax parameter is the temperature of maximum evolution of the S2 hydrocarbons and an indication of thermal maturity (^{o}C). S_1 and PI increases with maturation and most reservoirs have very high PI values.

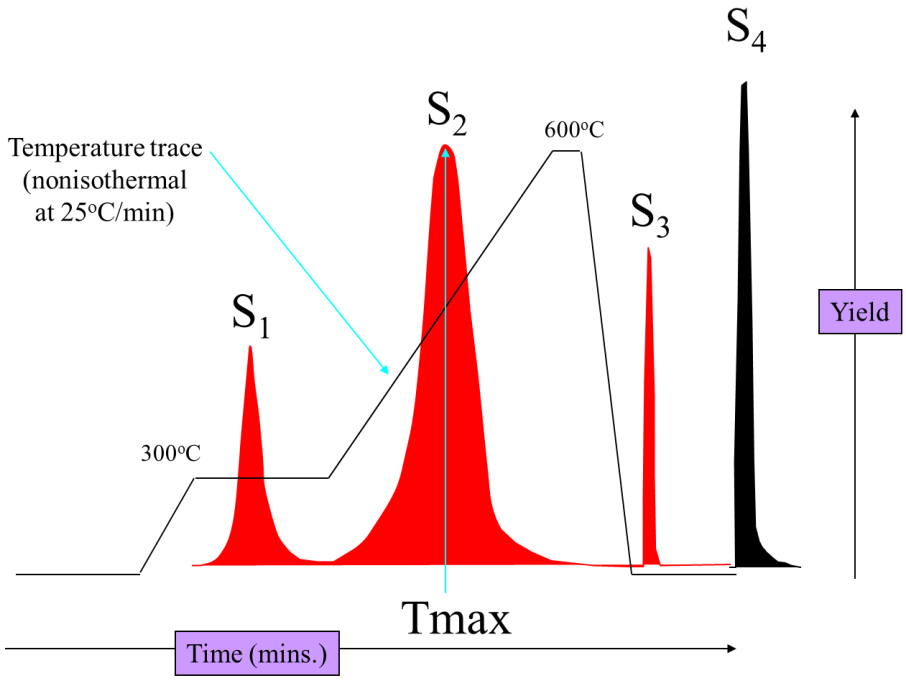

Figure 52. Pyrogram that represents the distribution of Organic Matter in Rock. From Philp, 2014.

As shown by the core description and elemental, mineralogical and organic analyses of the most studied source rocks in the United States: Woodford shale, Eagle Ford, Barnett shale, Albany

shale among others, are not homogeneous (Slatt & Rodriguez, 2012., Miceli-Romero, 2014). This statement is also valid for La Luna Formation since their lithofacies and mineralogy changes as much as their organo-facies. Significant variations of TOC can be found in La Luna Formation and are by some means linked to the variations in lithofacies and depositional environment.

Histogram plots (Figures 52, 55 and 58) were constructed to illustrate the TOC, HI and Ro variations for the subsurface and outcrop sections. According to the geochemical parameters used for the evaluation of a source rock potential in carbonates and conventional shales from Philp (2014), the organic richness histogram determined by TOC content displays a higher frequency towards a very good to excellent source rock for the outcrop and subsurface samples located in the Maracaibo Basin. Values vary from 0.09 to 12.8 wt.% TOC with an average of 3.62 wt.%. The histogram plot shown in Figure 52, displays a higher frequency distribution of the total organic carbon values ranging from 3.5 and 6.5 wt.%, approximately, from all the subsurface and outcrop samples. The lower values observed in the histogram are linked to facies V (siliceous-calcareous laminated mudstone interbedded with black chert filled with calcite veins). The high TOC values can be related to facies I (dark gray, massive mudstone), facies IV (laminated mudstone with limestone concretions and packstone), facies V (siliceous- calcareous mudstone interbedded with wackestone) and in LLIX facies VIII (siliceous green mudstone with authigenic glauconite and Pyrite).

The increase of TOC values of lithofacies associated with the LLIA and LLIS can be attributed to changes in depositional settings as previously explained in the mineralogical and elemental interpretation. Values of the total organic carbon (TOC) and Rock-Eval (RE) parameters for La Luna Formation samples are given in Appendix 7.1.

4.1.2 Organic matter type

Organic matter quality and kerogen type were determined through Rock-Eval pyrolysis parameters which provide useful information for assessing the hydrocarbon generative potential for the La Luna Formation. Hydrogen Index (HI) and Oxygen Index (OI) are the parameters derived from S_2 and S_3 peaks when plotted in a pseudo-Van-Krevelen diagram can be used to determine kerogen type (Tissot & Welte, 1984).

A plot of HI versus OI for the subsurface and outcrop samples is shown in Figure 53. The plot reveals that most samples, with exception to LLIE, have high HI values (200 to 800 mg HC/g TOC) and low OI (<20 mg CO_2/g TOC). Samples fall between Type I to II kerogen (oil prone) range with a predominance of Type II kerogen, which is mainly of marine origin. Samples plotted between the range of Type II and III are related to LLIE containing low HI (<100 mg HC/g TOC) and some of them exhibited higher OI than the previous samples (>40 mgCO_2/g TOC.In this case, their low HI values may be a result of organic matter alteration and not due to a terrigenous source.

As was the case for the Eagle Ford (Miceli-Romero, 2014) in the EFFA samples, low HI values from La Luna in the LLIE core may be the result of its high thermal maturity. Maturity influences the amounts and composition of kerogen and bitumen in the source rock, which in turn affects the HI and OI values. Kerogen maturation involves the loss of hydrogen and oxygen; hydrogen is lost primarily as methane and other light hydrocarbon gases, water, and hydrogen gas; oxygen is lost primarily as water and carbon oxides (Brooks, 1981; Brooks and Welte, 1984). This is possibly the case for the LLIE core since the calculated vitrinite reflectance from Rock-Eval, presents the highest maturity in the Northern part of the study area (1.3-2.3 calculated Ro%).

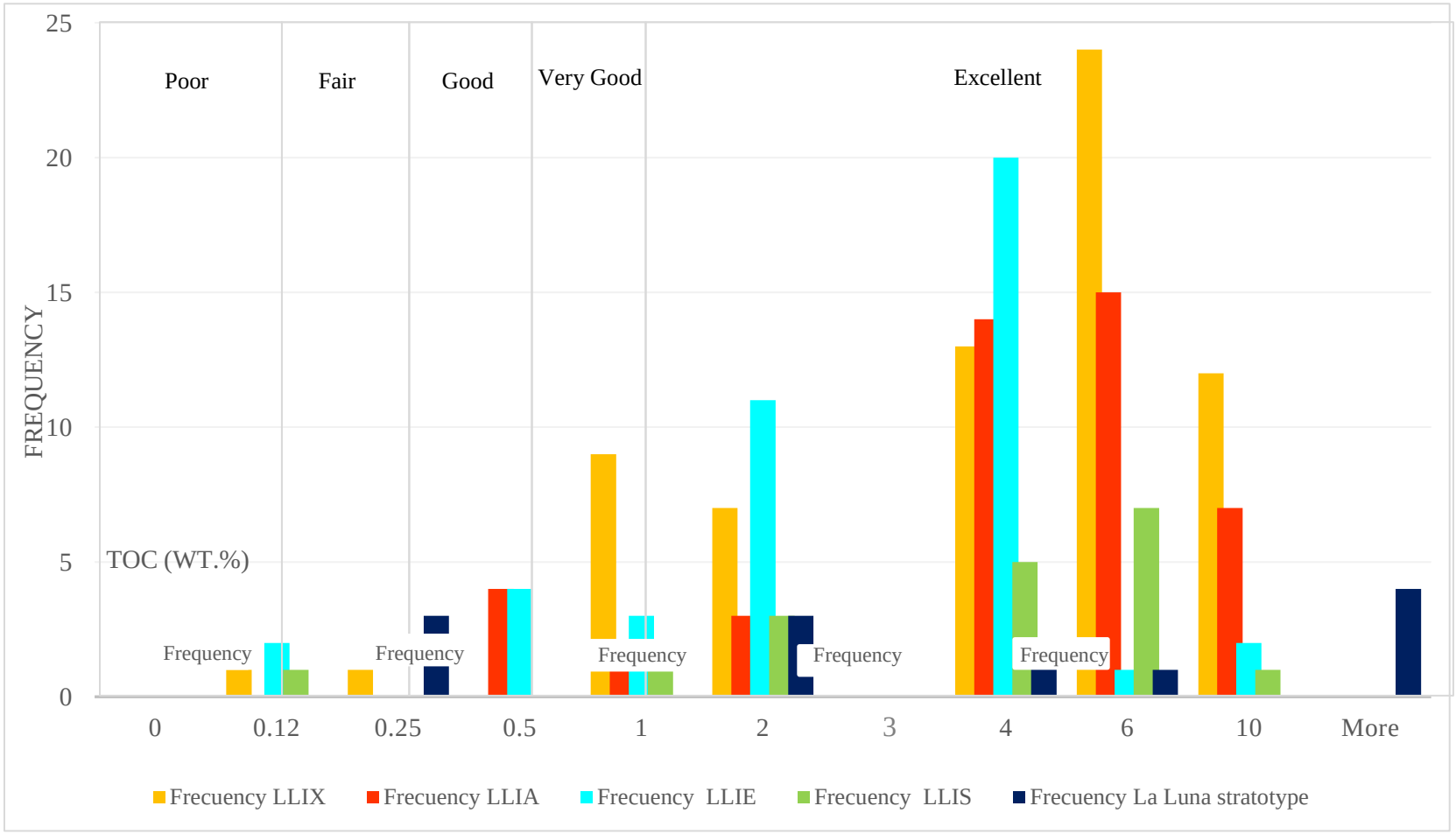

Figure 53. Organic richness histogram determined by TOC content in the outcrop and subsurface samples located in the Maracaibo Basin. It can be noticed how the frequency increases notably towards the very-good to excellent range. The yellow color is represented by La Luna IX (LLIX), red by La Luna IA (LLIA), Light blue by La Luna IE (LLIE), green by La Luna IS (LLIS) and dark blue by La Luna Stratotype.

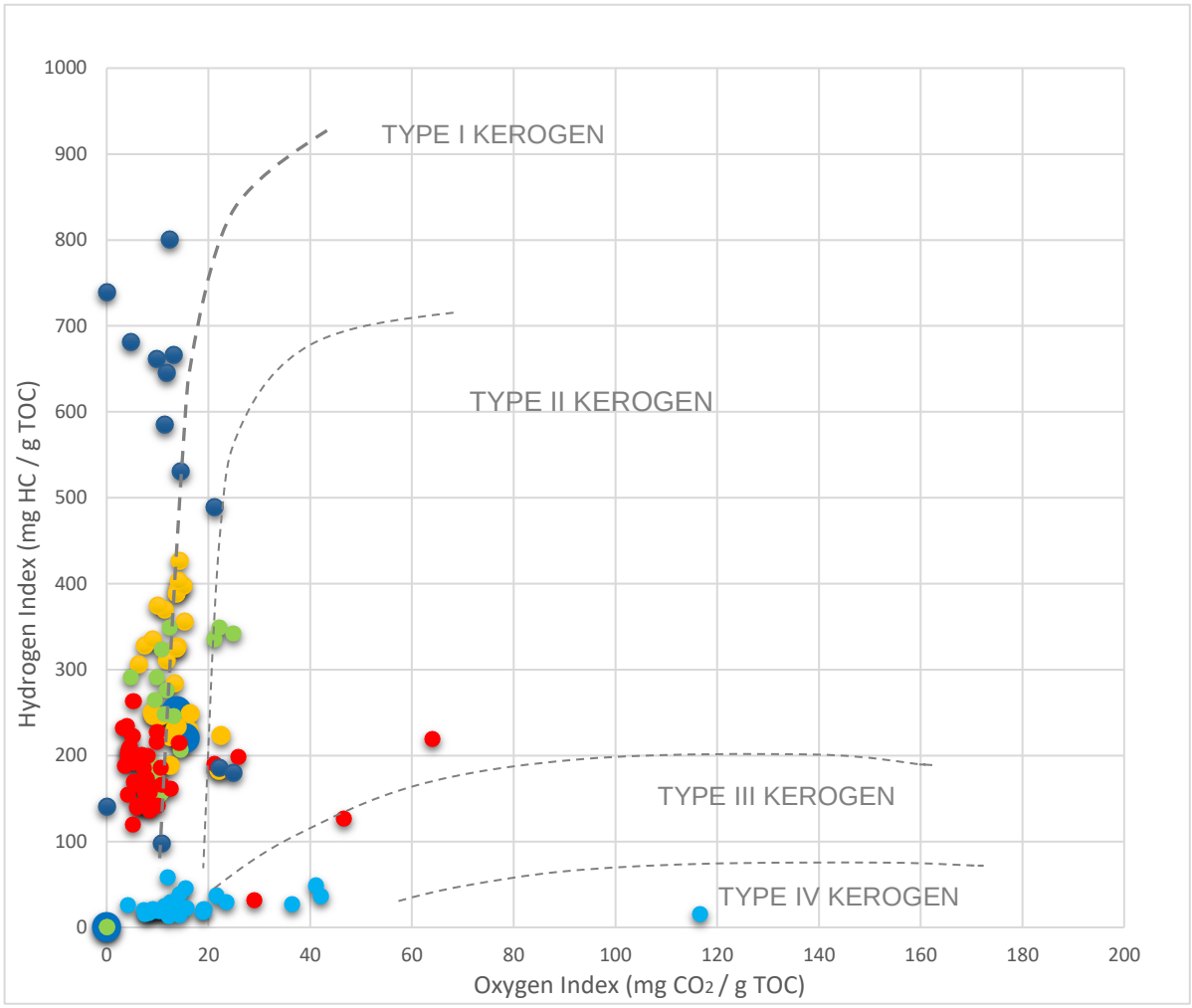

Figure 54. Modified Van-Krevelen diagram for the La Luna Formation samples. The yellow color is represented by La Luna IX (LLIX), red by La Luna IA (LLIA), Light blue by La Luna IE (LLIE), green by La Luna IS (LLIS) and dark blue by La Luna Stratotype.

Since the HI vs. OI results may vary, Langford & Blanc-Valleron (1990) and Cornford (1998) proposed a plot that relates S2 versus TOC to assess the kerogen quality in potential source rock samples with a high index in carbonate content (Figure 54). This plot shows a corresponding predominance of a Type II (marine origin, oil-prone) and mixed type II/III kerogen (marine with terrestrial input, oil/ gas prone) for LLIX, LLIA and, LLIS and a low remaining hydrocarbon potential for LLIE as a result of their high thermal maturity. Also, a Hydrogen Index histogram was determined by S2/TOC content in the outcrop and subsurface samples located in the Maracaibo Basin (Figure 55). The frequency increases for gas and mixed HC towards the NW are represented in the gas-mixed HC category while the wells located towards SW are represented by a mixed-oil (Type II) category. Hunt (1995) describes the migration index (S1/TOC) and its utility to distinguish between migrated hydrocarbons/contaminants and indigenous hydrocarbons. According to Hunt (1995), when S1 is high, and the TOC is low, migrated hydrocarbons are indicated. Most of the samples shown in this plot (Figure 56) are in the oil expulsion area with exception to the LLIE that is plotted in the indigenous plot field indicating that none of the generated oils migrated out of the La Luna Formation.

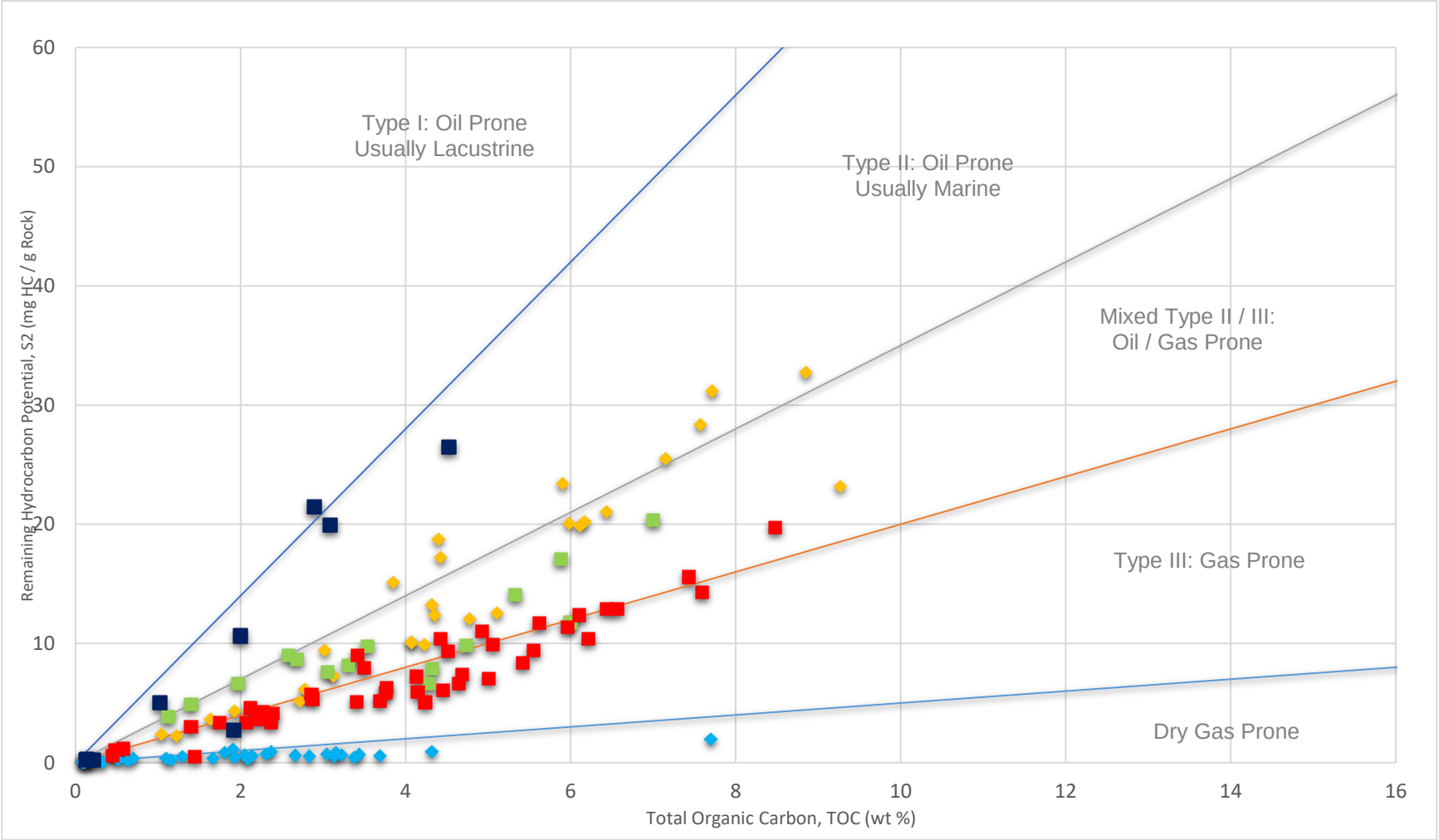

Figure 55. Rock-Eval Remaining Hydrocarbon Potential (S2) vs. TOC plot for determination of kerogen type and maturity of La Luna samples (plot template modified from GeoMark Research Ltd.) The yellow color is represented by La Luna IX (LLIX), red by La Luna IA (LLIA), Light blue by La Luna IE (LLIE), green by La Luna IS (LLIS) and dark blue by La Luna Stratotype.

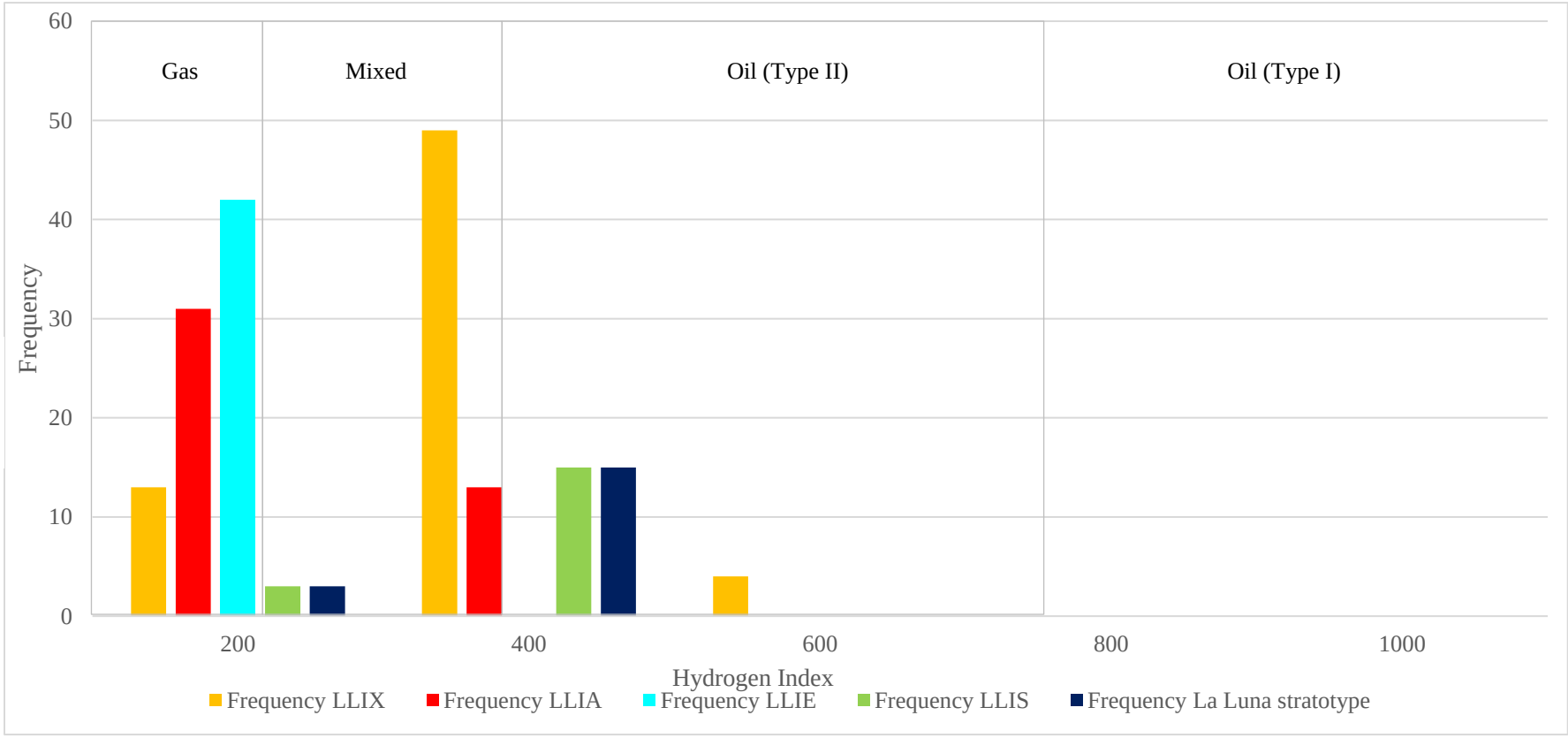

Figure 56. Hydrogen index histogram determined by S_2/TOC content in the outcrop and subsurface samples located in the Maracaibo Basin. It can be noticed how the frequency increases towards gas and mixed HC. It is noticeable how wells located towards the NW are represented in the gas-mixed HC category while the wells located towards SW are represented by a mixed-oil (type II) category. The yellow color is represented by La Luna IX (LLIX), red by La Luna IA (LLIA), Light blue by La Luna IE (LLIE), green by La Luna IS (LLIS) and dark blue by La Luna Stratotype.

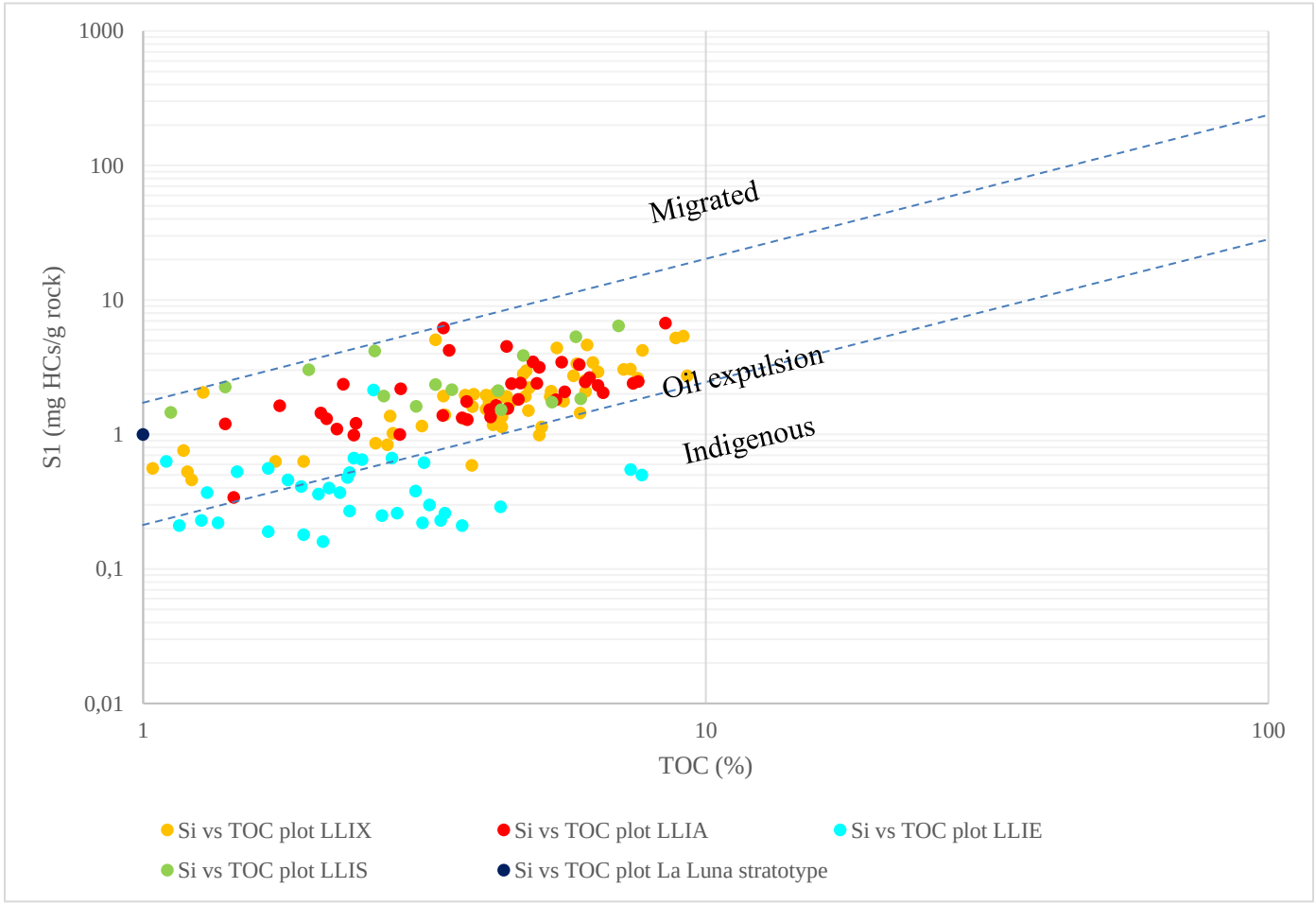

Figure 57. S1 vs. TOC plot (Hunt 1995) indicating migrated versus indigenous hydrocarbons of La Luna subsurface and outcrop samples. La Luna IX is represented by the yellow color (LLIX), red by La Luna IA (LLIA), Light blue by La Luna IE (LLIE), green by La Luna IS (LLIS) and dark blue by La Luna Stratotype.

4.1.3 Thermal Maturity

In this study, thermal maturity was initially determined using parameters derived from Rock-Eval Pyrolysis. A cross plot of Tmax versus HI (Figure 57) indicates that the La Luna Formation is within the oil window, with exception of the La Luna stratotype, which is marginally in the immature-mature range and for the LLIE core, which is over-mature and already in the gas-generation range. A Tmax-based %Rc histogram (Figure 58) was created using the formula [%Rc=(0.0180xTmax)–7.16] (Jarvie et al., 2001). The histogram shows a denser distribution toward the oil-generation window, most of the wells located toward the western (LLIX, La Luna stratotype) and southeastern (LLIA, LLIS) part of the study area are in the oil-generation range. Wells located toward the northwestern part of the study area (LLIE) contain a higher frequency of values that fall in the gas-generation category. The variability in the calculated Rc (from the oil window in the south and southwest to the deep dry gas window in the north-northwest) may be associated with the subsidence that occurred in the Paleogene in central and northeastern Maracaibo Basin (Zambrano et al., 1971). Subsidence created a depocenter along the basin's northeastern margin. It is located parallel to the Burro-Negro fault zone (Talukdar and Marcano, 1994; Escalona and Mann, 2003, 2006), affecting oil generation in these areas.

The core that is located toward the northern section of the study area (LLIE) has the same present depth (15200'–15500') as the core that is located toward the northwestern section (LLIX, 15200'–15550'), but a different maturity level. LLIE is in the dry gas window, with average Rc values of 1.79–2.05, and LLIX is in the oil window, with average Rc values of 1.06–1.17.

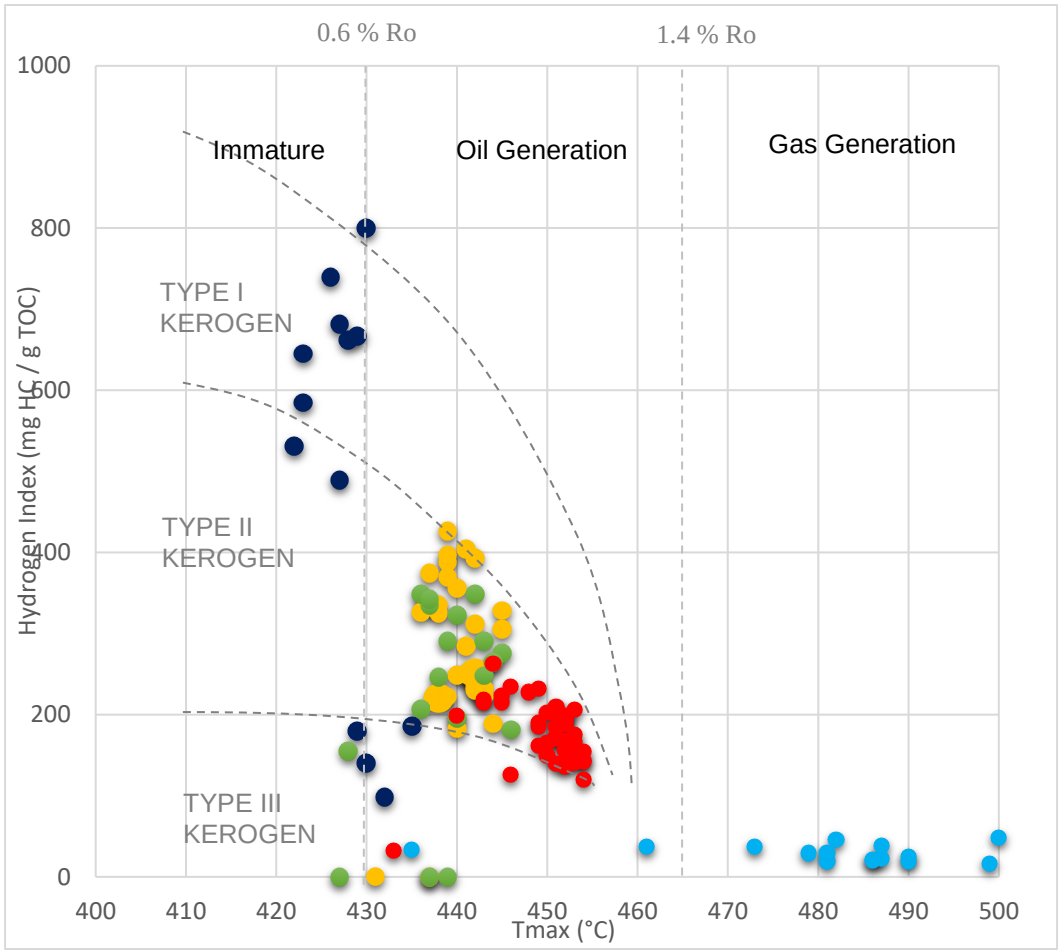

Figure 58. Kerogen type and maturity assessment via integration of HI and Tmax data. The yellow color is represented by La Luna IX (LLIX), red by La Luna IA (LLIA), Light blue by La Luna IE (LLIE), green by La Luna IS (LLIS) and dark blue by La Luna Stratotype.

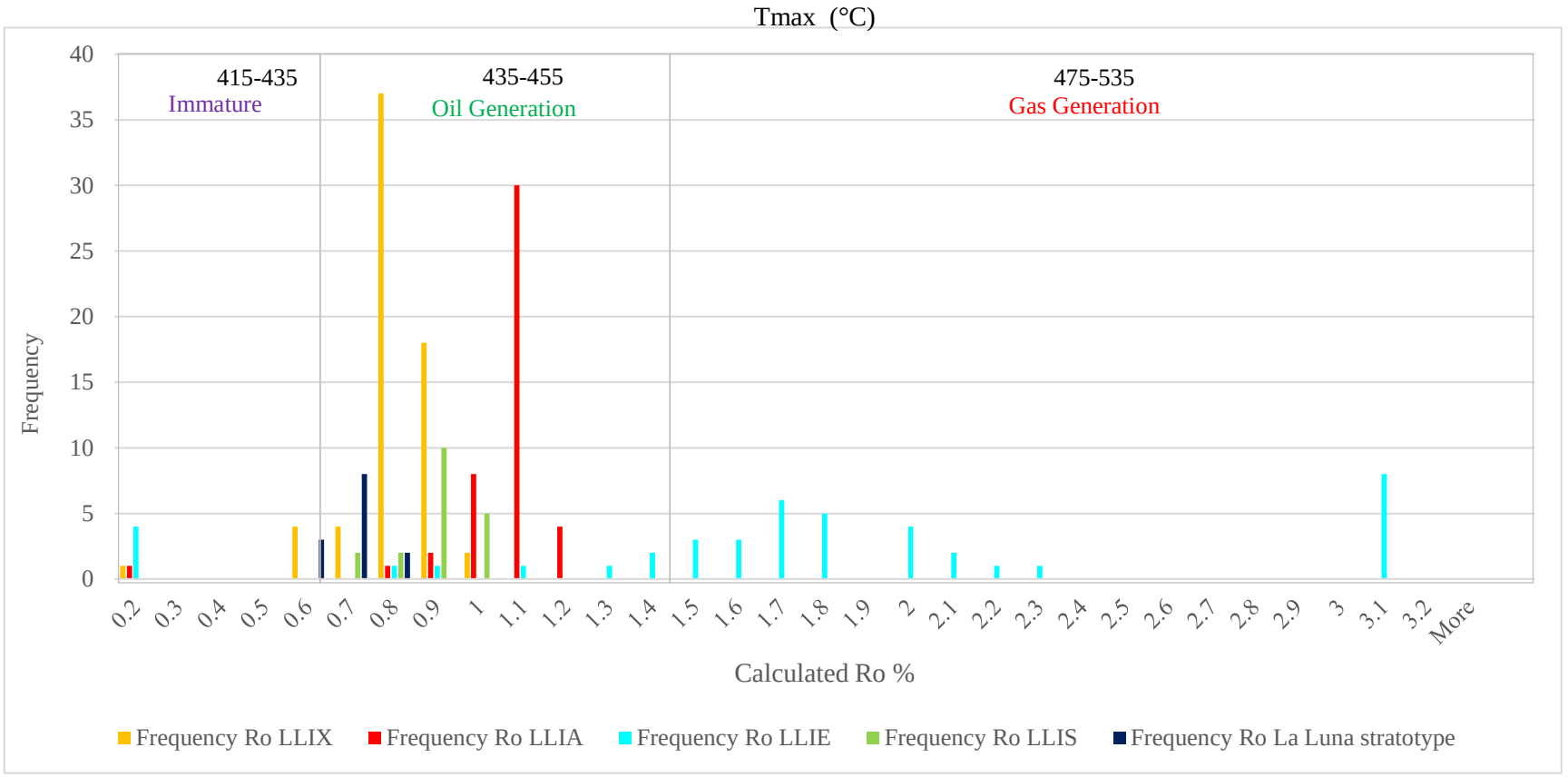

Figure 59. Ro histogram determined by the following formula (0.018*Tmax)-7.16 by Jarvie et al., 2001. Outcrop and subsurface samples located in the Maracaibo Basin. It can be noticed how the frequency increases towards oil generation. Most of the wells located towards the western (LLIX, La Luna stratotype) and southeastern (LLIA, LLIS) part of the study area are cataloged into the higher frequency in the oil generation category while the well located towards the northwestern part of the study area contains a higher frequency of values that fall between the gas generation category. The yellow color is represented by La Luna IX (LLIX), red by La Luna IA (LLIA), Light blue by La Luna IE (LLIE), green by La Luna IS (LLIS) and dark blue by La Luna Stratotype.

Tectonic activity could be one reason for the maturity differences, because the reactivation of Jurassic normal faults during the Cenomanian and Turonian generated differential subsidence in the central and southern Maracaibo Basin, and this could influence maturity levels (Vergara, 1997).

Direct petrographic measurements of VRo% (provided by Cardott, 2018, written communication) were attempted on four La Luna samples from four different locations (LLIX, LLIA, LLIS, and LLIE; Figure 59). Microphotographs of the other subsurface samples are included in Appendix 7.2.

Overall, within these samples, vitrinite identification was challenging, because the vitrinite content was low in the samples selected for Ro analysis. The vitrinite maceral is derived from mainly land-plant material, and the La Luna Formation is mostly deposited in a marine environment, so the low level of vitrinite reflectance equivalent ($VR_{eq.BR}$) was calculated from solid bitumen reflectance. Solid bitumen is not a kerogen component but rather a product generated by kerogen that, along with mineral grains, flowed into pore spaces (Jacob, 1989). Calculating vitrinite reflectance equivalence from solid bitumen reflectance is a suitable approach in this situation, because solid bitumen is the dominant organic matter type in most shales at late and post-mature stages (Hackley & Cardott, 2016). Although several authors have proposed various equations for the vitrinite reflectance equivalent, the two most recognized formulas, shown in equation 3 and 4, were applied for the measurement of the vitrinite reflectance equivalent: Landis and Castano (1995) and Schoenherr et al. (2007). The differences between the two formulas are due to experimental differences observed in source rocks versus reservoir rocks. The measured vitrinite reflectance equivalent values from bitumen are presented in Table 3. Values obtained for

the two formulas indicate that most of the core samples are within the oil window, with the exception of LLE (1.80–2.05 $VR_{eq.BR}$ on average), which, according to the Rock-Eval analysis, was already overmature.

$$VR_{eq.BR}\, BR = \frac{(BR + 0.41)}{1.09} \quad [3]$$

Landis and Castano (1995)

$$VR_{eq.BR}\, BR = \frac{(BR + 0.2443)}{1.0495} [4]$$

Schoenherr et al. (2007).

Where:

$VR_{eq.BR}$= Solid bitumen reflectance conversion to equivalent vitrinite reflectance

BR=Solid bitumen reflectance

Table 3. Vitrinite reflectance equivalent values (on average) of La Luna Formation samples.

VRE values (on average)

	Sample	Bro (a)	Landis and Castano (1995)	Schoenherr et al. (2007).
Average	LLIX	0.86	1.17	1.06
Average	LLIA	0.74	1.05	0.93
Average	LLIS	0.72	1.03	0.92
Average	LLIE	1.82	2.05	1.93

(a) *Bro*= Bitumen reflectance

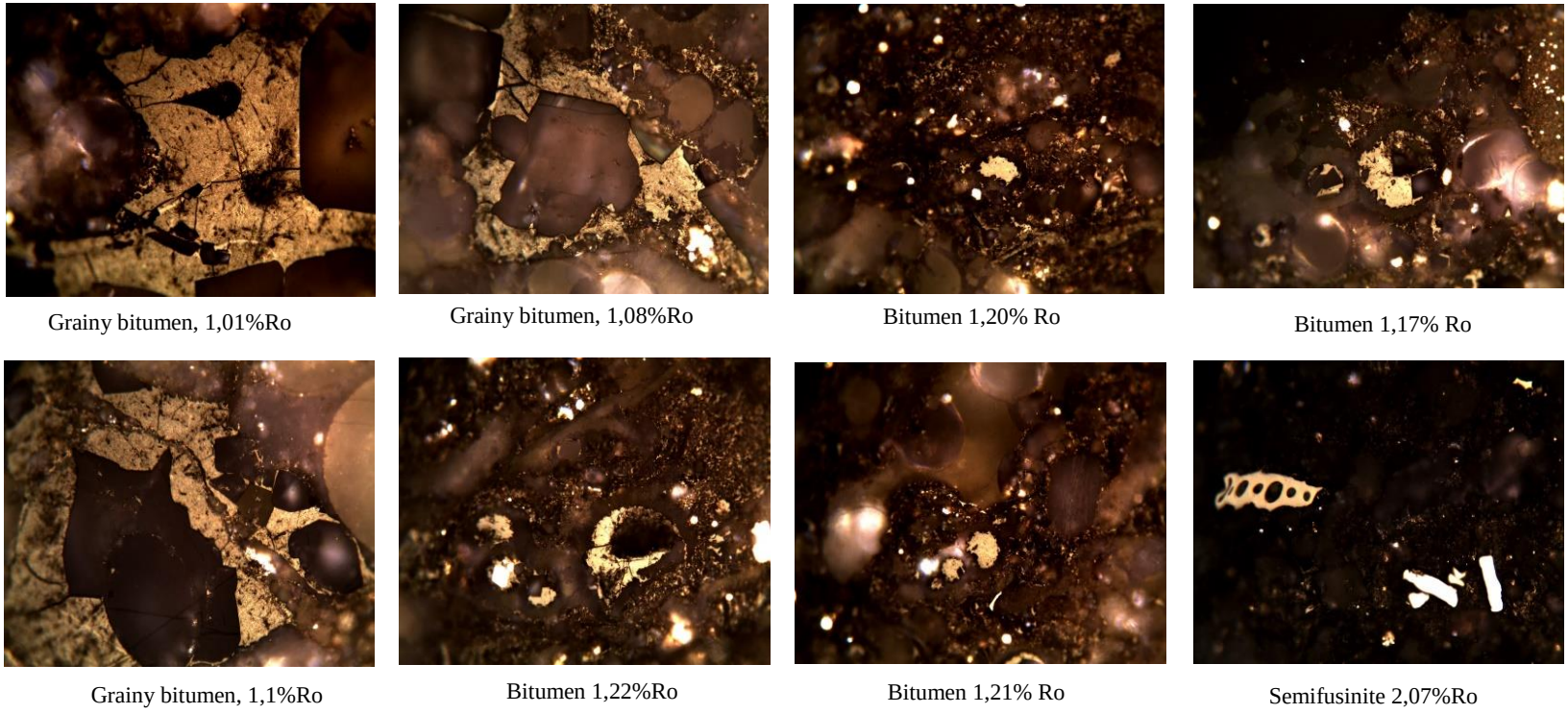

Figure 60. Photomicrographs from the La Luna Formation IX and bitumen vitrinite reflectance values before the conversion to vitrinite reflectance equivalent. (Photomicrographs courtesy of Brian Cardott, 2018).

4.2 Gas Chromatography (GC)

4.2.1 *n*-Alkane distributions

The *n*-alkanes represent the fraction of saturated hydrocarbons from bitumen and oil samples that are determined by gas chromatography (GC), as shown in Figures 60 and 61. These distributions play an essential role in the geochemical screening process, serving as a correlation tool and organic matter source indicator (Peters et al., 2005; Lopez, 2013a). The origin of the *n*-alkanes is primarily lipids in living organisms such as phytoplankton, zooplankton, higher order plants (Eglinton & Hamilton, 1967), or algae (Lopez, 2013a).

The type of organic matter can be indicated by the n-alkane distribution. A predominance of *n*-alkanes <*n*-C_{25} is correlated with marine or lacustrine organic matter (Jacobson et al., 1988; Wang & Philp, 1997), whereas a predominance of n-alkanes >*n*-C_{25} is associated with terrestrial organic matter (Tissot & Welte, 1984). Gas chromatography fingerprints for the saturated hydrocarbon fractions of the La Luna Formation extracts indicate primarily unimodal distribution and, in some instances, bimodal distribution, with the low-carbon-number (<*n*-C_{25}) predominating over those with high molecular weight (>*n*-C_{25}). Appendices 7.3 and 7.4 present detailed results of the n-alkanes analyses, including formulas, chromatograms, and ratios calculated. Bimodal distributions are associated mainly with areas related to the Highstand System Tract (HST), where the detrital input also increases. This can be linked to areas that are controlled by the paleo-topography, as is the case in the LLIA core. This detrital input can also be observed in the XRF proxies.

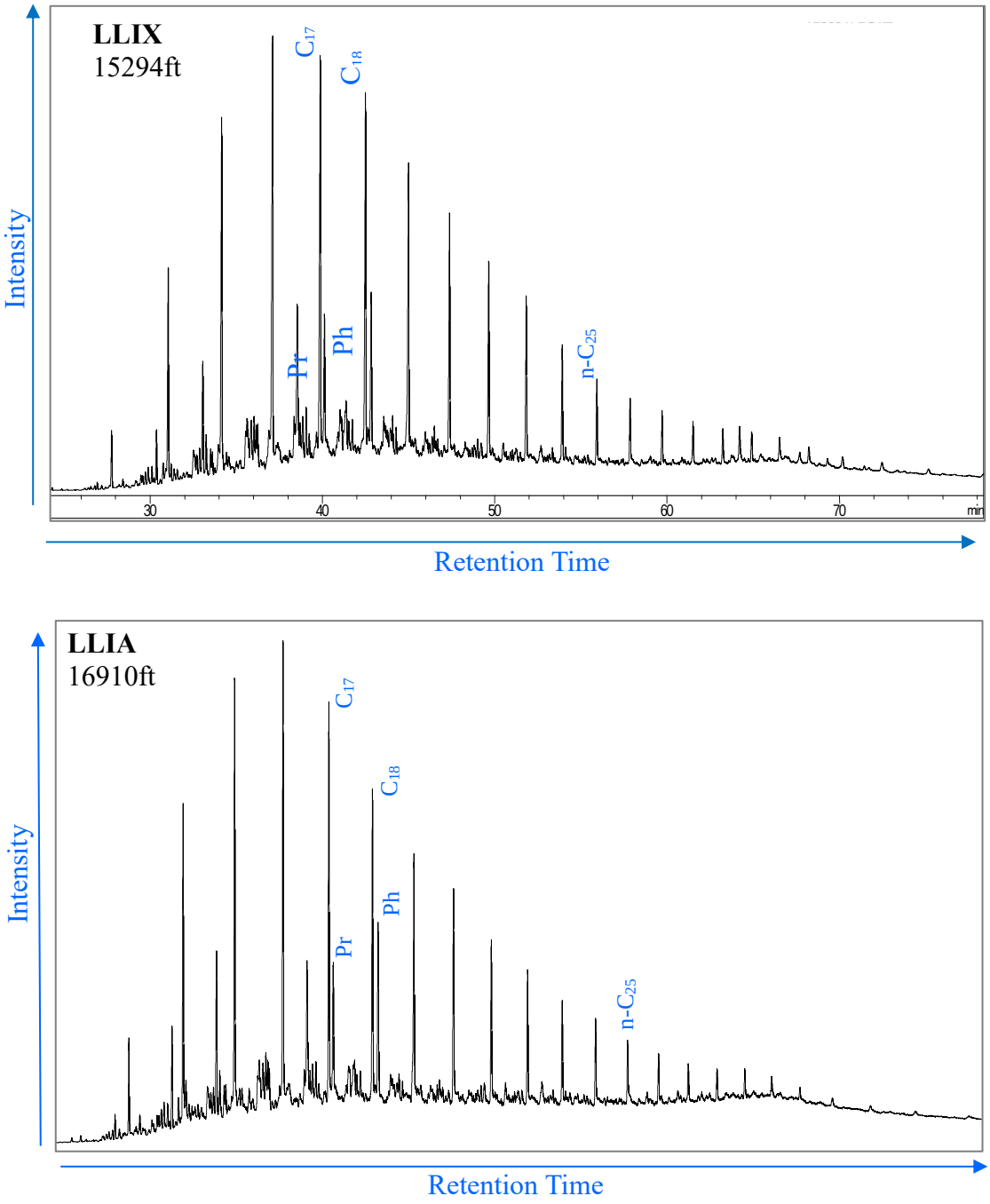

Figure 61. Gas chromatograms of the saturated hydrocarbon fractions from bitumen extracts of the LLIX and LLIA core (Pr = pristane; Ph = phytane, *n*-C_{25} = C_{25} normal alkane).

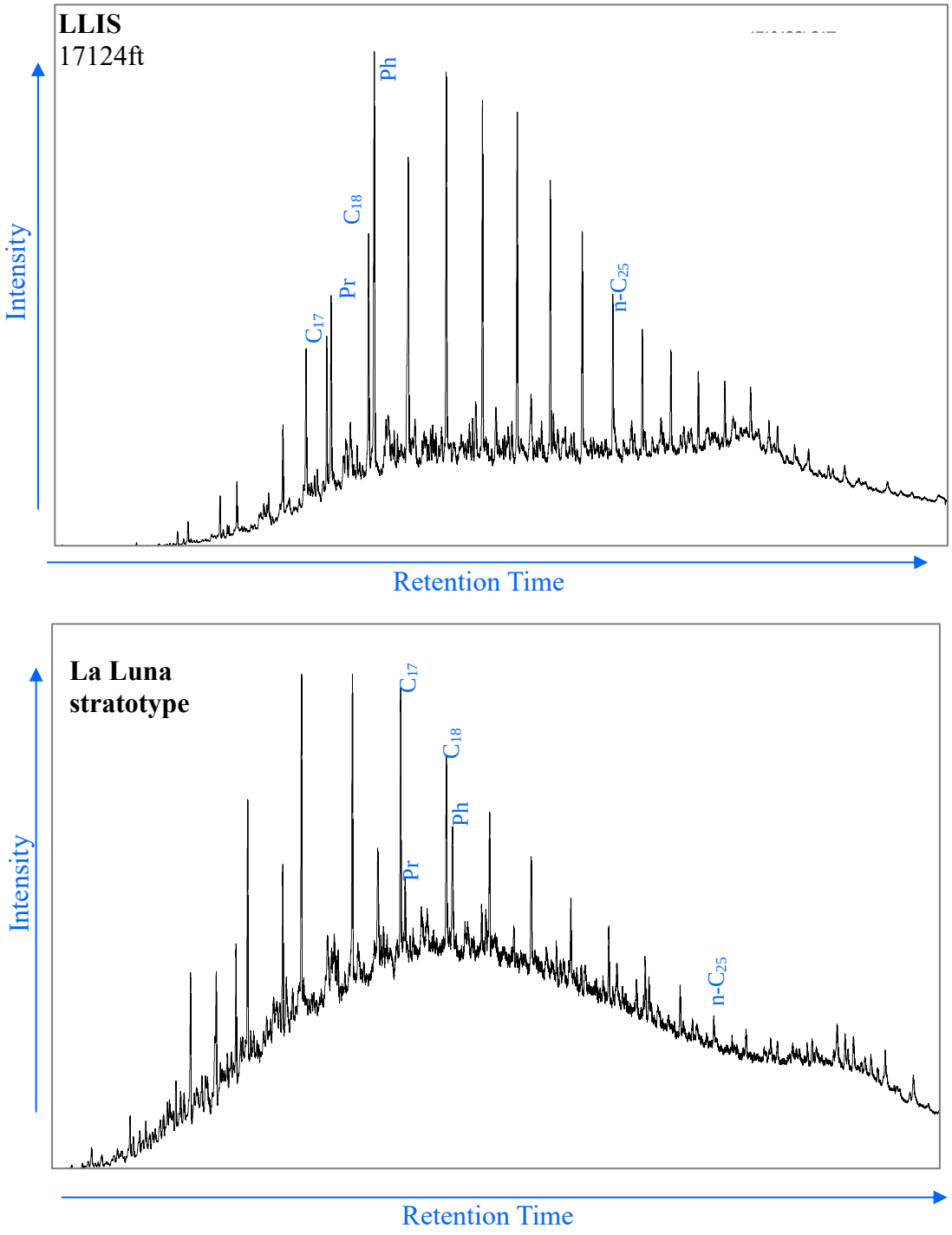

Figure 62. Gas chromatograms of the saturated hydrocarbon fractions from bitumen extracts of the LLIS and La Luna stratotype core (Pr = pristane; Ph = phytane, *n*-C_{25} = C_{25} normal alkane).

The even-over-odd *n*-alkanes predominance can be used to evaluate the origin of the organic matter. A slight predominance of even over odd *n*-alkanes suggests the presence of carbonate source rocks formed in a highly reducing environment (Moldowan et al., 1985; Wang & Philp, 1997). Most samples of the La Luna Formation from the LLIX and the La Luna stratotype display a prevalence of even carbon number *n*-alkanes, suggesting an origin in marine organic matter deposited in a reducing environment. Nevertheless, some cores (LLIA and LLIS) display slight differences in the even/odd *n*-alkane distribution. For most of the samples from the lower and middle La Luna Formation, the LLIA core manifests an odd/even trend from bottom to top for most of the samples of the Lower and Middle La Luna Formation C_{23}~C_{33} *n*-alkanes with a predominance of an odd number of carbons usually indicate terrestrial higher plant input (Sohn, 1986). Thus, the LLIA core's odd/even trend was somewhat expected, because it reinforces the results of mineralogical and elemental analyses that indicate terrestrial reworking in the paleo-lows that were formed by the paleo-topographic control.

The chromatograms shown in Appendix 7.5 displays a bimodal distribution that may be associated with a mixture of organic matter sources. Core LLIS exhibits the even-odd trend for areas associated with facies II (calcareous-marlstone with the presence of pyrite layers) and the odd-even trend for areas associated with facies I (dark gray laminar mudstone).The relative abundance of n-alkanes of low and high molecular weight may indicate organic matter input from aquatic (marine, lacustrine) and terrigenous environments, based on a ratio known as the terrigenous/aquatic ratio (TAR). This ratio indicates the relative proportion of the terrigenous (n-C_{27}, n-C_{29} and n-C_{31}) versus

aquatic (n-C_{15}, n-C_{17} and n-C_{19}) organic matter input in a depositional environment (Bourbonniere & Meyers, 1996). High TAR values indicate high odd-carbon-number n-alkanes, indicating

terrigenous organic matter, and low values indicate low odd-carbon-number n-alkanes, indicating marine organic matter (Peters et al., 2005).

Another calculation of the odd numbers over even numbered alkanes distribution can be done using the carbon preference index (CPI) (Bray & Evans, 1961). This index can be obtained from the distribution of n-alkanes by dividing the sum of the odd carbon-number alkanes (n-C_{25}-n-C_{33}) by the sum of the even-carbon-number alkanes (n-C_{26}-n-C_{34}). The CPI can be obtained by calculating the peak areas of the n-alkanes (n-C_{24}-n-C_{34}) in a gas chromatogram. Hypersaline and carbonate source rocks with low maturity frequently show low (below 1) CPI values due to a predominance of even-carbon-number n-alkanes. Furthermore, oils and rock extracts with CPI values significantly above 1.0 (odd predominance) indicate low thermal maturity (Peters et al., 2005). In general, both TAR and CPI values are influenced by source and thermal maturity, and additional geochemical parameters are needed to compare with these ratios when oils and source rocks are characterized. Several geochemical parameters calculated from the n-alkane chromatograms of rock extracts are summarized in Table 5.TAR and CPI values are low for the La Luna outcrop and subsurface samples located toward the north and northwestern part of the study area (LLIE, LLIX, La Luna stratotype). Higher values are found for the samples located toward the southwest and southern part of the study area, suggesting a higher input of terrestrial organic matter. This higher input toward the south likely is related to the terrigenous organic matter and detrital reworking identified by the inorganic mineralogy (XRD, XRF). The input can be linked either to the organic matter deposited in the paleo-topographic control of the underlying Maraca formation or to a near-shore transitional (mixed-type) depositional environment periodically subjected to terrigenous input.

4.2.2 Pristane and Phytane

Pristane (Pr) and phytane (Ph) are the most abundant isoprenoids found in bitumen and oils. These acyclic isoprenoids are derived mainly from the phytol chain of chlorophyll-a in phototrophic organisms and bacteriochlorophyll in purple sulfur bacteria (Brooks et al., 1969; Powell & McKirdy, 1973). The pristane/phytane (Pr/Ph) ratio is one of the most commonly used correlation parameters reflecting redox conditions in the depositional environments (Didyk et al., 1978; Tissot & Welte, 1984). Low Eh (oxidizing) conditions are favorable for the occurrence of pristane, whereas a high Eh (reducing) depositional environment favors the occurrence of phytane (Powell & McKirdy, 1973). Table 4 shows the different environment associations according to the Pr/Ph ratios, and Table 5 shows a summary of n-alkane analyses from the saturated hydrocarbon fraction of La Luna Formation.

Table 4 shows Pr/Ph ratios for different environments. Pr/Ph<1 indicates anoxic depositional conditions when reinforced by other geochemical data, such as high porphyrin and sulfur content (Peters et al., 2005). Pr/Ph values between 1 and 3 indicate a suboxic environment that was periodically influenced by different redox conditions, and Pr/Ph>3 indicates oxic depositional conditions with terrigenous organic matter influx (ten Haven et al., 1987; Peters et al., 2005). Overall, most of the rock extracts from La Luna Formation show low Pr/Ph ratios, ranging from 0.20– 0.8 on average, indicating the presence of reducing conditions (anoxia) during source rock deposition (see Appendix 7.3).

Table 4. Pristane/Phytane ratios and their relationship with other indicators of redox conditions and the environment of sedimentation (Lewan & Maynar, 1982, Lewan, 1984; ten Haven et al., 1987; Lopez, 2013; Peters et al., 2015).

Ph/Ph < 0.8	Anoxic, hypersaline or carbonate depositional environments
Ph/Ph < 1	Source rocks developed under anoxic conditions High sulfur concentrations High V/Ni ratio Carbonate source rocks
Ph/Ph >1	Oxic-suboxic conditions Low sulfur concentrations Low V/Ni ratio Siliciclastic source rocks
Ph/Ph >3	Terrigenous organic matter input under oxic conditions

The relationship between Pr/C_{17}, and Ph/C_{18} is another tool for evaluating variations in redox conditions, organic matter source, maturity, and alteration in source rock extracts and oils (Shanmugam, 1985). Figure 62 shows a cross plot of Pr/n-C_{17} versus Ph/n-C_{18} for the La Luna rock extracts analyzed in this study. This plot shows that most of the samples contain values of Pr/n-C_{17} and Ph/n-C_{18} lower than 1, representing the marine-algal reducing environment. Even when some of the samples from the LLIA and LLIS present a bimodal, odd-over-even n-alkane distribution and high values of TAR and CPI for the n-alkane parameters, the cross-plot relationship with the isoprenoids suggests that these samples are composed mainly of marine organic matter deposited in a reducing environment.

Table 5. Summary table of *n*-alkanes analyses from the saturated fraction of La Luna Formation bitumens.

Samples	Formation	*n*-alkane	n-alkane distribution	*n*-alkane maximum	Pr/Ph		TAR		CPI	
		range			range		range		range	
					Max	Min	Max	Min	Max	Min
LLIX	La Luna Formation	*n*-C_{12}-*n*-C_{36}	unimodal	*n*-C_{17}	0.84	0.22	1.50	0.06	2.58	1.61
LLIA	La Luna Formation	*n*-C_{11}-*n*-C_{35}	bimodal	*n*-C_{15} and *n*-C_{16}	1.09	0.51	1.18	0.02	2.11	1.38
LLIS	La Luna Formation	*n*-C_{14}-*n*-C_{35}	bimodal	*n*-C_{16} and *n*-C_{18}	0.85	0.23	1.08	0.15	2.11	1.62
La Luna outcrop	La Luna Formation	*n*-C_{13}-*n*-C_{32}	unimodal	*n*-C_{17}	0.73	0.46	0.68	ND	3.05	ND

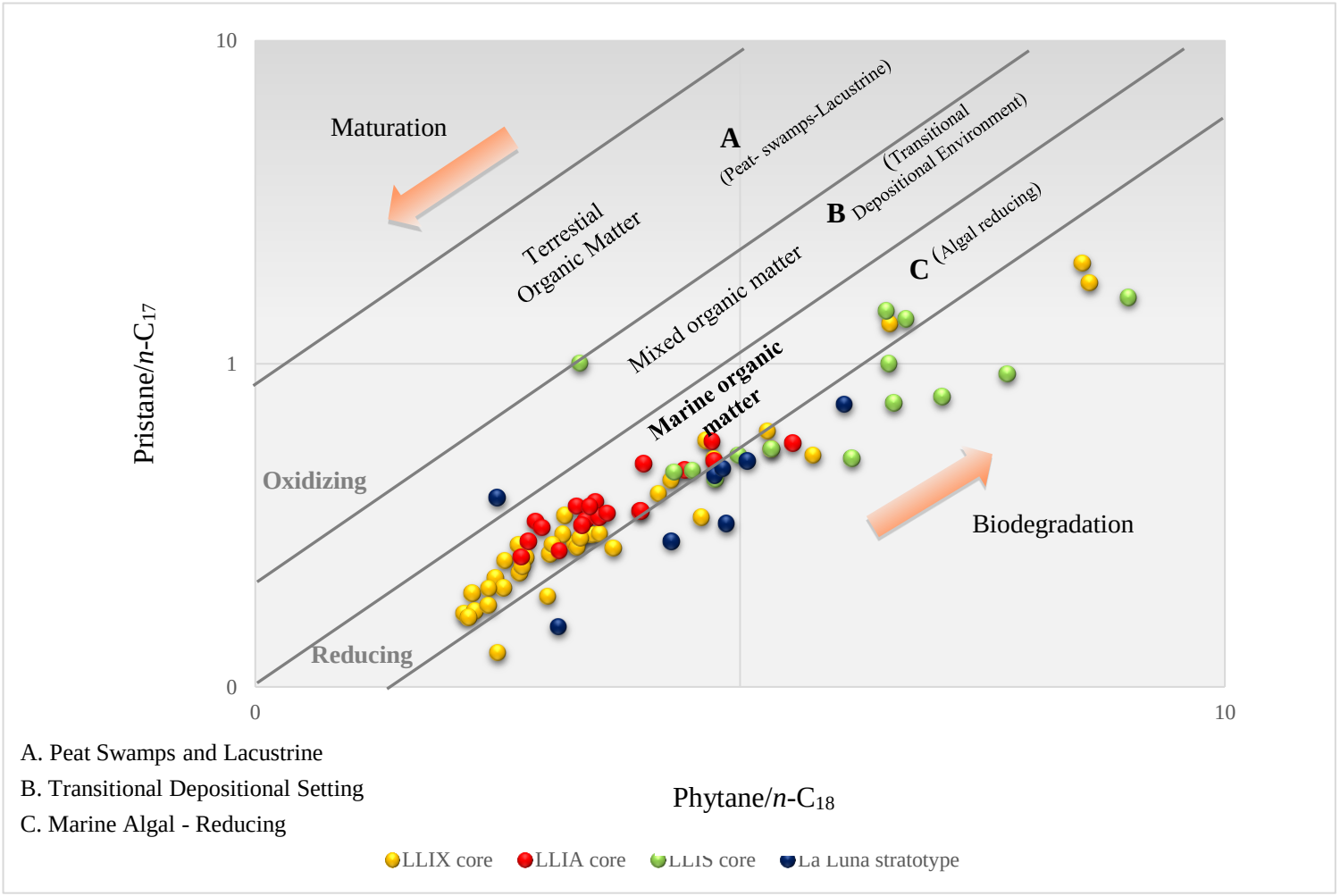

Figure 63. Plot of pristane/*n*-C$_{17}$ versus phytane/*n*-C$_{18}$ showing redox conditions, maturity, and depositional environments for samples of the La Luna Formation (*n*-C$_{17}$ = C$_{17}$ normal alkane; *n*-C$_{18}$ = C$_{18}$ normal alkane).

4.3 Biomarker Analysis and Evaluation of Organic Matter Source and Depositional Environments

The properties of each shelf environment reflect the source of its organic material, which may be terrigenous, marine, or a mixture of both (Galloway & Hobday, 1983). Further examination of hydrocarbons using gas chromatography and mass spectrometry measures the relative proportions of biomarkers. Biomarkers act as fossils, which can be linked back to a parent species from which they are derived (Eglinton et al., 1964). Biomarkers provide information on source; maturity; depositional environments; biodegradation; migration; age dating; and oil/oil and oil/source rock correlations (Wang et al., 2004). Biomarker analysis was completed using GC and GC-MS performed on the saturated and branched and cyclic (B&C) hydrocarbon fractions of the source rock extracts from La Luna Formation.

4.3.1 Steranes Steranes are one of the most commonly used biomarker classes in the application of organic geochemistry to petroleum exploration. Steranes originate from sterols, which are compounds found in eukaryotic organisms, mainly algae and higher plants (Tissot & Welte, 1984). This study performed identification of steranes, diasteranes, pregnanes, and homopregnanes on the B&C hydrocarbon fractions of rock extracts by single ion monitoring (SIM) and gas chromatography mass spectrometry GC-MS monitoring the m/z 217.3 ion. Figures 63–65 and Table 6 present sterane distributions and identifications. Appendix 7.5 shows the formulas for the calculation of geochemical ratios, and Appendix 7.6 shows numerical values of the geochemical ratios calculated. Appendices 7.10–7.14 present the biomarker quantification results.

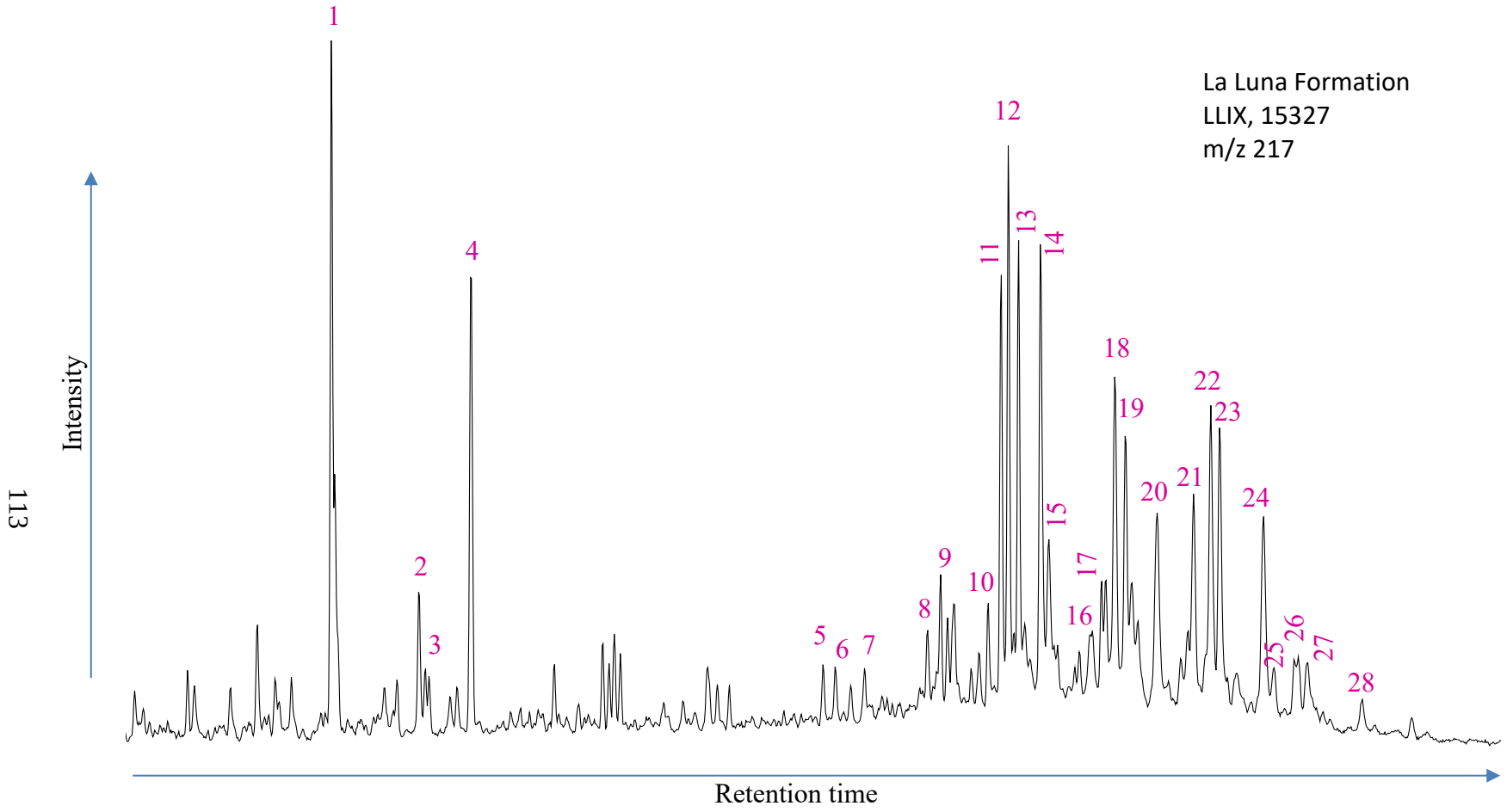

Figure 64. Partial fragmentograms of the m/z 217 ion showing steranes distribution in the branched and cyclic hydrocarbon fractions of the La Luna Formation in LLIX core. Peak identification is presented in Table 6.

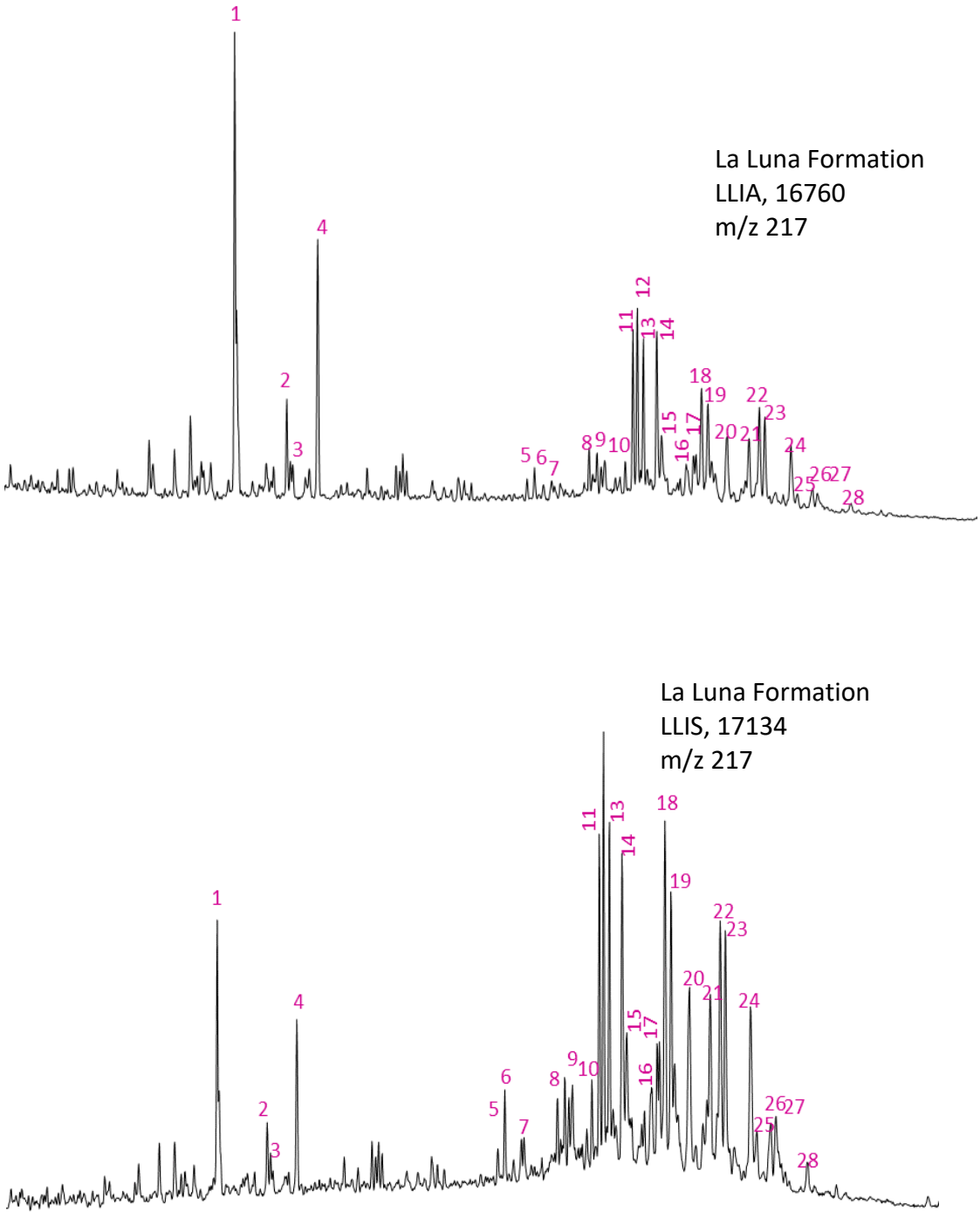

Figure 65. Partial fragmentograms of the m/z 217.3 ion showing distribution of steranes in the branched and cyclic hydrocarbon fractions of the LLIA and LLIS samples. Peak identification is presented in Table 6.

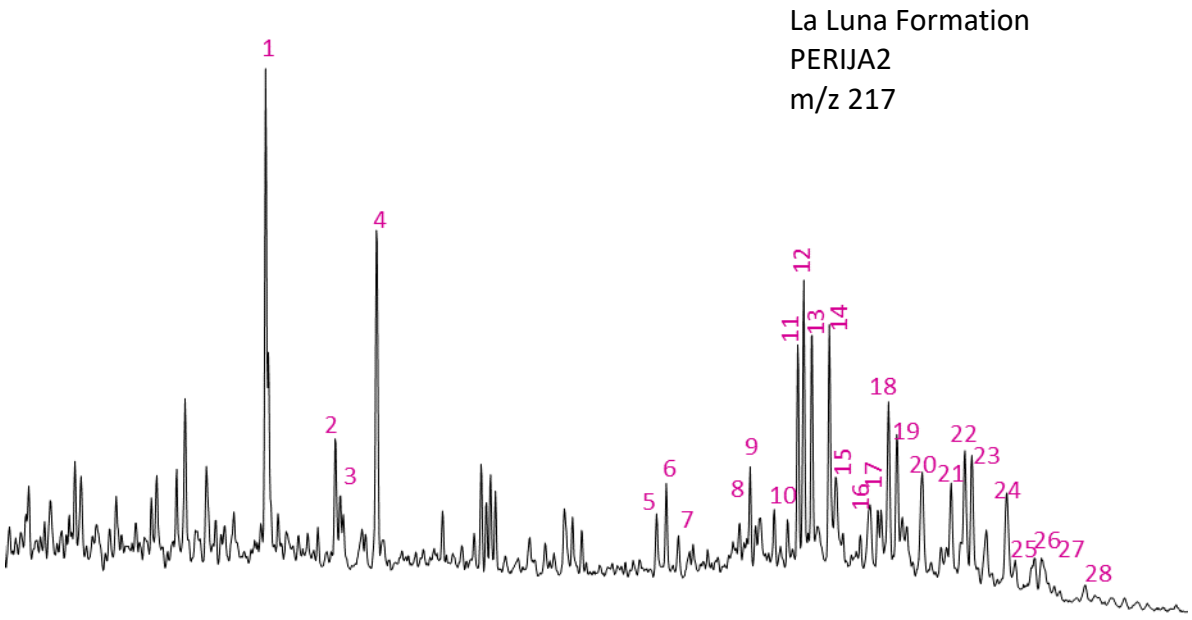

Figure 66. Partial fragmentograms of the m/z 217.3 ion showing distribution of steranes in the branched and cyclic hydrocarbon fractions of the Perija samples. Peak identification is presented in Table 6.

4.3.1.1 Regular steranes

There are four main families of sterols containing 27, 28, 29, or 30 carbon atoms that are converted into regular steranes during diagenesis (Waples & Machihara, 1991). The distribution of C_{27}, C_{28}, and C_{29} steranes from different organisms is very useful in differentiating source input and depositional environments. This relationship can be easily displayed on a ternary plot that distinguishes different source rock input (Peters et al., 2005). C_{27} steranes (cholestane) are derived primarily from precursors found in plankton and marine invertebrates. C_{28} steranes (ergostane) also originate from similar precursors, although they can be generated from terrestrial organisms as well (Huang and Meinschein, 1979; Moldowan et al., 1985).

Table 6. Identification of steranes in the partial m/z 217.3 fragmentogram of the B&C hydrocarbon fractions.

Peak number	Compounds
	(ISTD)
1	**αα** Diapregnane
2	**ββ** 14β(H),17β(H)-Pregnane
3	**αα** Diahomopregnane
4	**ββ** 14β(H),17β(H)-Homopregnane
5	13β(H),17α(H)-Diacholestane (20S)
6	13β(H),17α(H)-Diacholestane (20R)
7	13α(H),17β(H)-Diacholestane (20S)
8	13α(H),17β(H)-Diacholestane (20R)
9	24-Methyl-13β(H),17α(H)-Diacholestane (20S)
10	24-Methyl-13β(H),17α(H)-Diacholestane (20R)
11	24-Methyl-13α(H),17β(H)-Diacholestane (20S) + 14α(H),17α(H)-Cholestane (20S)
12	24-Ethyl-13β(H),17α(H)-Diacholestane (20S) + 14β(H),17β(H)-Cholestane (20R)
13	14β(H),17β(H)-Cholestane (20S) + 24-Methyl-13α(H),17β(H)-Diacholestane (20R)
14	14α(H),17α(H)-Cholestane (20R)
15	24-Ethyl-13β(H),17α(H)-Diacholestane (20R)
16	24-Ethyl-13α(H),17β(H)-Diacholestane (20S)
17	24-Methyl-14α(H),17α(H)-Cholestane (20S)
18	24-Methyl-14β(H),17β(H)-Cholestane (20R) + 24-Ethyl-13α(H),17β(H)-Diacholestane (20R)
19	24-Methyl-14β(H),17β(H)-Cholestane (20S)
20	24-Methyl-14α(H),17α(H)-Cholestane (20R)
21	24-Ethyl-14α(H),17α(H)-Cholestane (20S)
22	24-Ethyl-14β(H),17β(H)-Cholestane (20R)
23	24-Ethyl-14β(H),17β(H)-Cholestane (20S)
24	24-Ethyl-14α(H),17α(H)-Cholestane (20R)
25	24-Propyl-14α(H),17α(H) -Cholestane (20S)
26	24-Propyl-14β(H),17β(H) -Cholestane (20R)
27	24-Propyl-14β(H),17β(H) -Cholestane (20S)
28	24-Propyl-14α(H),17α(H) -Cholestane (20R)

Similarly, C_{29} steranes (stigmastane) are derived from terrigenous organic matter sources and marine algae (Volkman, 1986). Table 7 displays the different relationships of the C_{27}, C_{28}, and C_{29} steranes with the various environments of deposition. Samples in La Luna Formation contain higher proportions of C_{27} than the the C_{28} and C_{29} homologs. This trend reflects an increase of marine organic matter source for La Luna Formation in northwestern Maracaibo Basin in a marine environment that was restricted enough to allow water-density stratification and hypersaline conditions to develop. According to the regular steranes ternary plot presented by Huang & Meinschein (1979), La Luna Formation (Figure 66) displays the sterane homologs in the "open marine" and "marine shale/carbonate" cluster, indicating a common genetic relationship.

The 24-*n*-propylcholestanes, or C_{30} steranes, are another group of steranes used in identifying marine organic matter source. These C_{30} steranes originated from 24-*n*-propylcholesterols. They are biosynthesized in a marine algae (chrysophyte) of the order *Sarcinochrysidales* that is usually found in marine invertebrates (Moldowan et al., 1990). Thus, the presence of C_{30} steranes in source rock and oils are the best means to recognize the input of marine organic matter to the source rock (Moldovan et al., 1985). C_{30} steranes were detected in all the La Luna rock samples.

The C_{30} sterane index, which combines the proportions of the C_{30} sterane versus the C_{27} to C_{30} steranes, generally increase with greater marine versus terrigenous organic matter input to the source rock. Moldowan et al. (1992) found that many oils derived from source rocks deposited under restricted saline to hypersaline lagoonal conditions show lower $C_{30}/(C_{27}\text{-}C_{30})$ steranes than those from open marine systems. Geochemical logs of C_{30} sterane index for the La Luna Formation (Figures 67-70) show small variations in source input, indicating a marine input for the LLIX, LLIA, and LLIS cores and the La Luna stratotype.

Table 7. Sterane homologs and their association with the different depositional environments. (Huang & Meinschein, 1979; Moldowan et al., 1985; Volkman, 1989).

Sterol homologs	Associated depositional environments
C_{27} steranes (cholestane)	Marine phytoplankton and marine invertebrates. Indicators of red algae.
C_{28} steranes (ergostane)	Dominant in lacustrine green algae but they can be derived from similar precursors of the C_{27} and terrigenous organisms.
C_{29} steranes (stigmastane)	Terrestrial higher plants and brown and green algae.

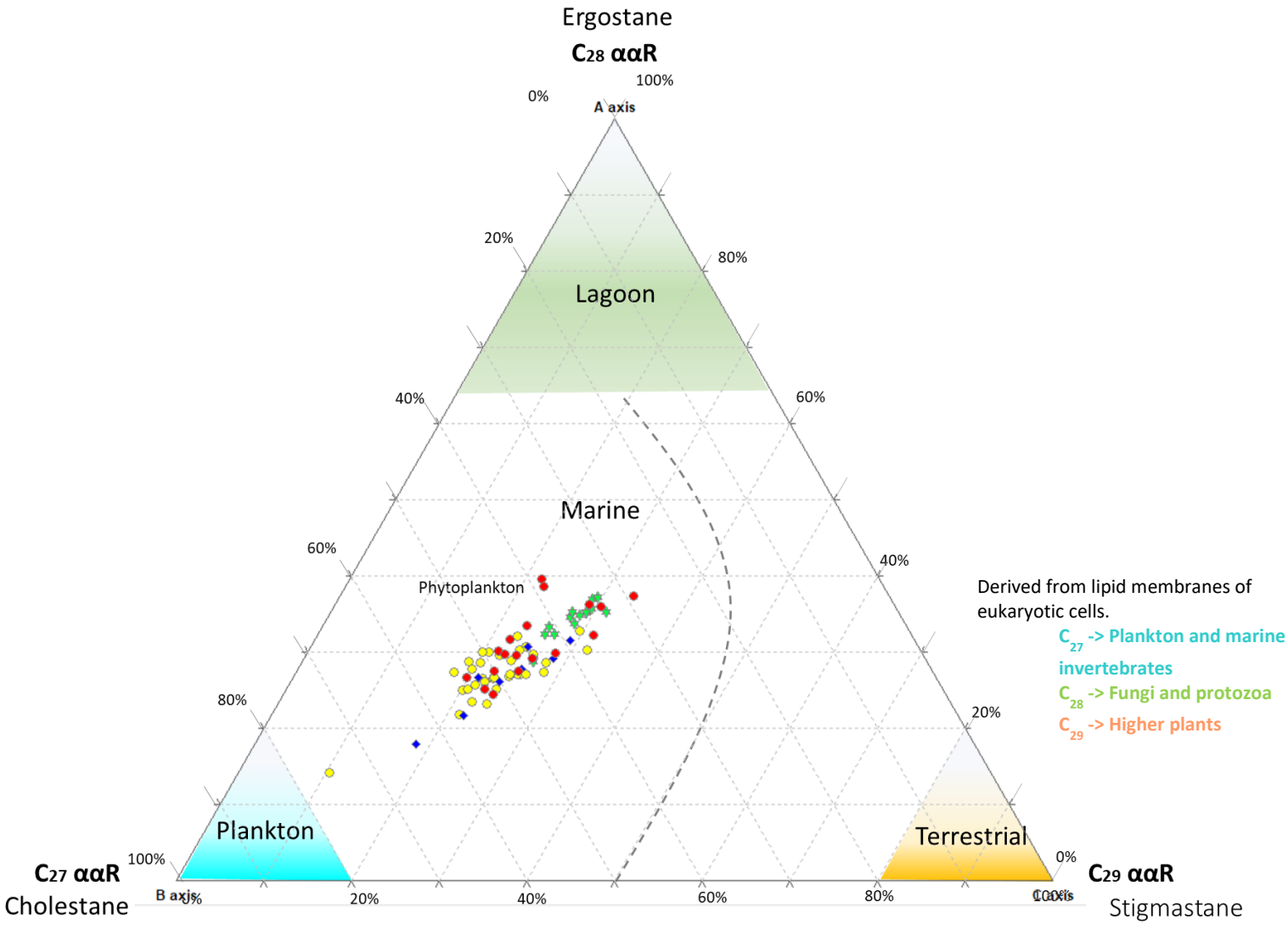

Figure 67. Ternary diagram of C_{27}, C_{28}, and C_{29} regular steranes for the La Luna samples in the Maracaibo Basin.

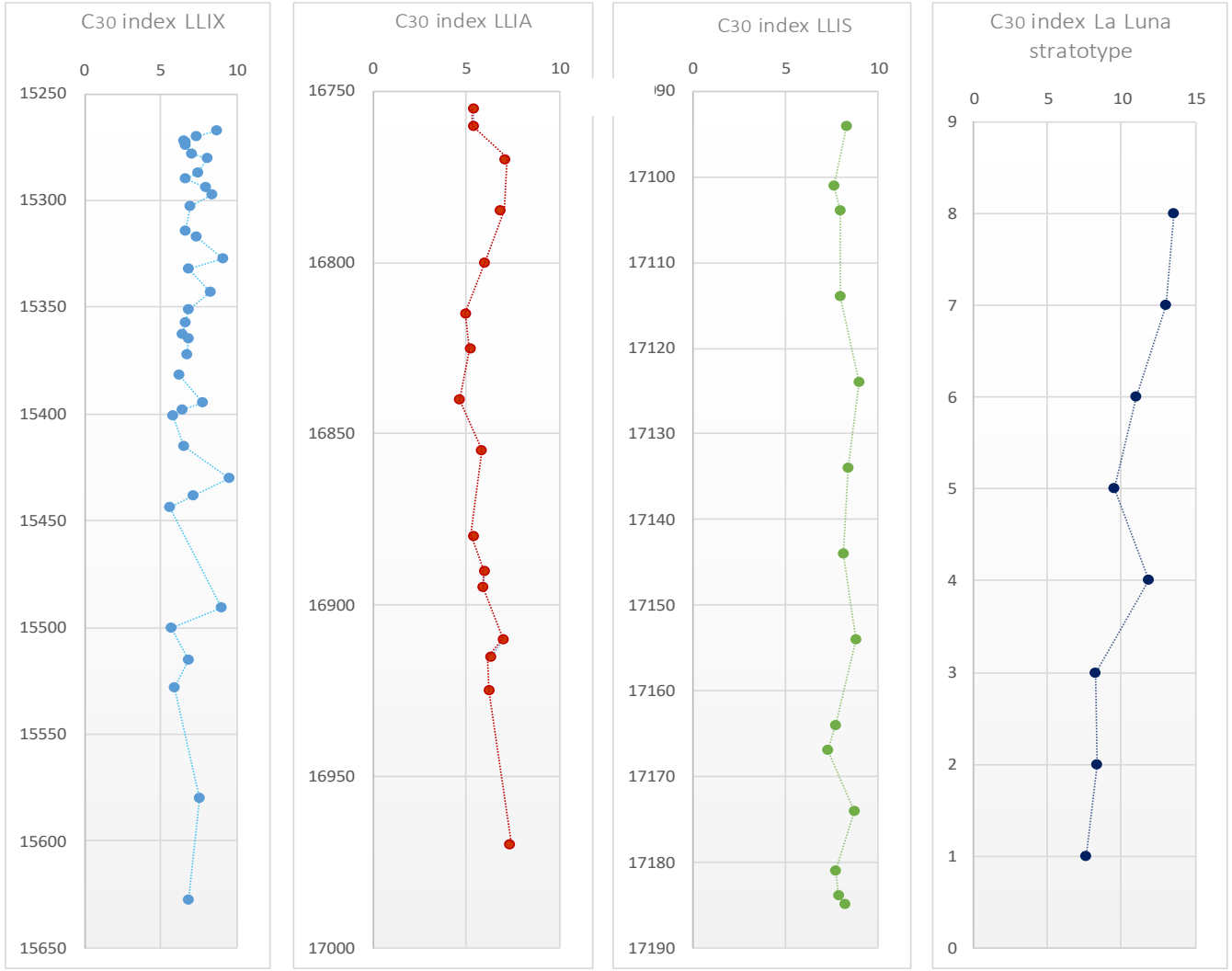

Figure 68. Geochemical logs of the C_{30} index for the LLIX, LLIA, LLIS and La Luna stratotype samples. Formulas for calculation of ratios are in Appendix 7. 5.

4.3.1.2 Diasteranes or “rearranged steranes.”

Diasteranes play an essential role in the assessment of the lithology, redox conditions and the thermal maturity of source rocks (Kirk & Shaw, 1975; Moldowan et al. 1991). The diasteranes structures differ from the regular steranes since they have a methyl group attached to C-5 and C-14 and hydrogens attached to C-10 and C-13 (Waples & Machihara, 1991). The rearrangement of steranes to diasteranes occurs in the presence of clay via acid catalysis (Rubinstein et al., 1975). Lithology of a source rock can be discerned to include clay minerals such as montmorillonite or illite when diasteranes are found in oils and rock extracts. Diasteranes are most readily present in clastic sediments, and the acidic clays in them play the essential role in the conversion of the diasteranes from the regular steranes. Therefore, they are also useful for distinguishing carbonate source rocks from clastic source rocks (Rubinstein et al., 1975; Wang et al., 2015).

Diasteranes also have been identified in high quantities in carbonate source rocks under low pH and high Eh conditions. This suggests that their presence may be associated with redox conditions (Moldowan et al., 1991). Higher concentrations of C_{27} diasteranes have been associated with higher values of Ph/(Pr+Ph). Moldowan et al. (1994) demonstrated that the oxicity and the clay content in the depositional environments are the two main factors that control this association. Thus, oxic/suboxic shale strata tend to have higher C_{27} diasterane/(C_{27} diasteranes+C_{27} steranes) and Pr/(Pr+Ph) values than the anoxic carbonates.

The diasterane/sterane index is the ratio of C_{27} diasterane to (C_{27} diasteranes+C_{27} steranes). This can be used to approximate the conditions in which this conversion is favorable, as increased diasterane concentration requires greater clay content to catalyze the reaction. A lower value of this ratio is linked with more anoxic, clay-poor conditions (Jones, 2017). The diasterane index increases with thermal maturity and is affected by biodegradation. Although diasteranes are more

resistant to thermal and biological degradation, changes in the diasterane ratio (C_{27} diasterane/C_{27} steranes) can also be associated with an oxic/suboxic clay-rich source rock.

In general, the overall values of the C_{27} diasteranes/C_{27} steranes ratios for La Luna Formation are characterized by low concentrations of diasteranes (Figures 67–70). The values are 0.03–0.11 on average for LLIX, 0.07–0.23 on average for LLIA, 0.08–0.06 on average for LLIS, and 0.24–0.03 for La Luna stratotype. For LLIX and LLIA, a decreasing upward trend of the C_{27} diasterane/C_{27} sterane ratio is observed, even when the C_{27} diasterane values remain low, the LLIS present a cyclical trend in the diasterane content toward the whole interval. Furthermore, a slightly higher concentration can be observed in the LLIA and the La Luna stratotype. Relatively higher values of this ratio in the La Luna stratotype are associated with the presence of clay content in the outcrop. C_{27}diasteranes/C_{27} sterane values for LLIA are somehow related to the XRF results that also depicted a higher clay concentration towards Lower La Luna.

4.3.1.3 Pregnane and homopregnane

The C_{20} and C_{21} steranes (pregnane and homopregnane compounds) have been detected in bitumen extracted from source rocks and have been associated with the deposition of hypersaline environments (ten-Haven et al., 1985). Wang et al. (2015) proposed that the occurrence of pregnane and homopregnane and their relationship with regular steranes and diasteranes can be associated with changes in redox conditions, facies, and mineral content of the source rock.

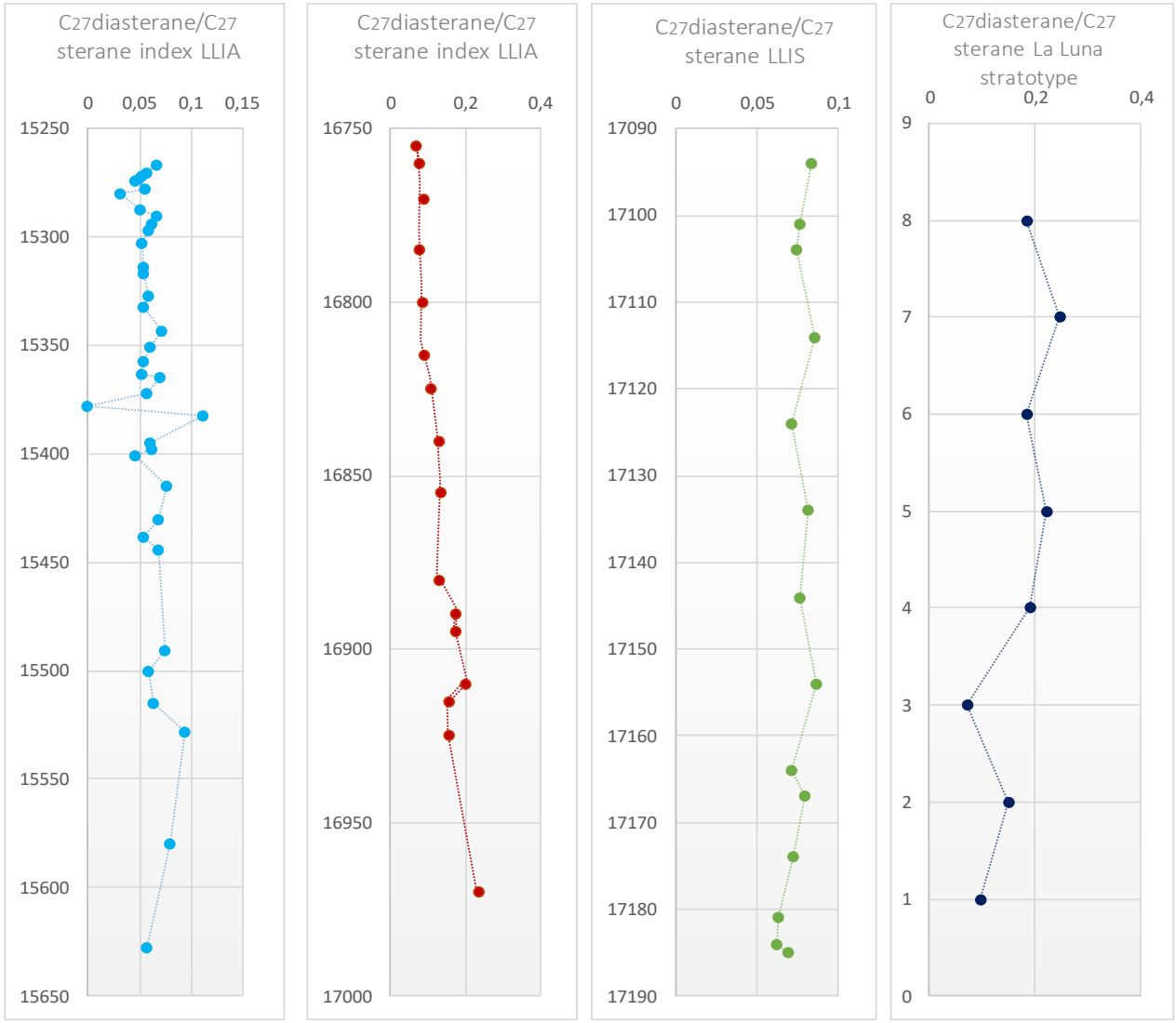

Figure 69 Geochemical logs of the C_{27} diasterane/ C_{27} sterane index for the LLIX, LLIA, LLIS and La Luna stratotype samples. Formulas for calculation of ratios are in Appendix 7. 5.

A higher concentration of diasteranes and lower concentration of pregnanes can be associated with oxic conditions, terrigenous input, high clay content, and organic-lean carbonate rocks. Conversely, low diasterane and high pregnane concentrations are related to hypersaline environments and clastic-starved, non-terrigenous, sulfur-rich source rocks (ten-Haven et al., 1985). Overall, the concentration of the pregnane/sterane ratios is high for the samples of LLIX (1.5–4 on average), LLIA (4–5 on average), and La Luna stratotype (Figures 67, 68, and 70), which suggests a reduced-hypersaline environment containing a sulfur-rich source rock. LLIS, on the other hand, displays lower values, indicating a shallower/suboxic/anoxic environment with an increased terrigenous input (Figure 69).

The plot from Wang et al. (2015) in Figure 70 displays the relationship of the $\Sigma C_{21\text{-}22}/\Sigma C_{27\text{-}29}$ Steranes vs. Σ C_{27} diasteranes/ Σ regular C_{27} Steranes for La Luna Formation extracts. This plot shows that most of the samples are located between the carbonate and carbonate-rich mixed-type source rocks range that occurred under the restricted water boundary. As mentioned before, samples of LLIA and La Luna stratotype contain a higher proportion of clay content, so their values are consistent with this interpretation. Geochemical ratios of steranes for the branched and cyclic hydrocarbon fractions (B&C) of the La Luna formation are found in Appendix 7.6.

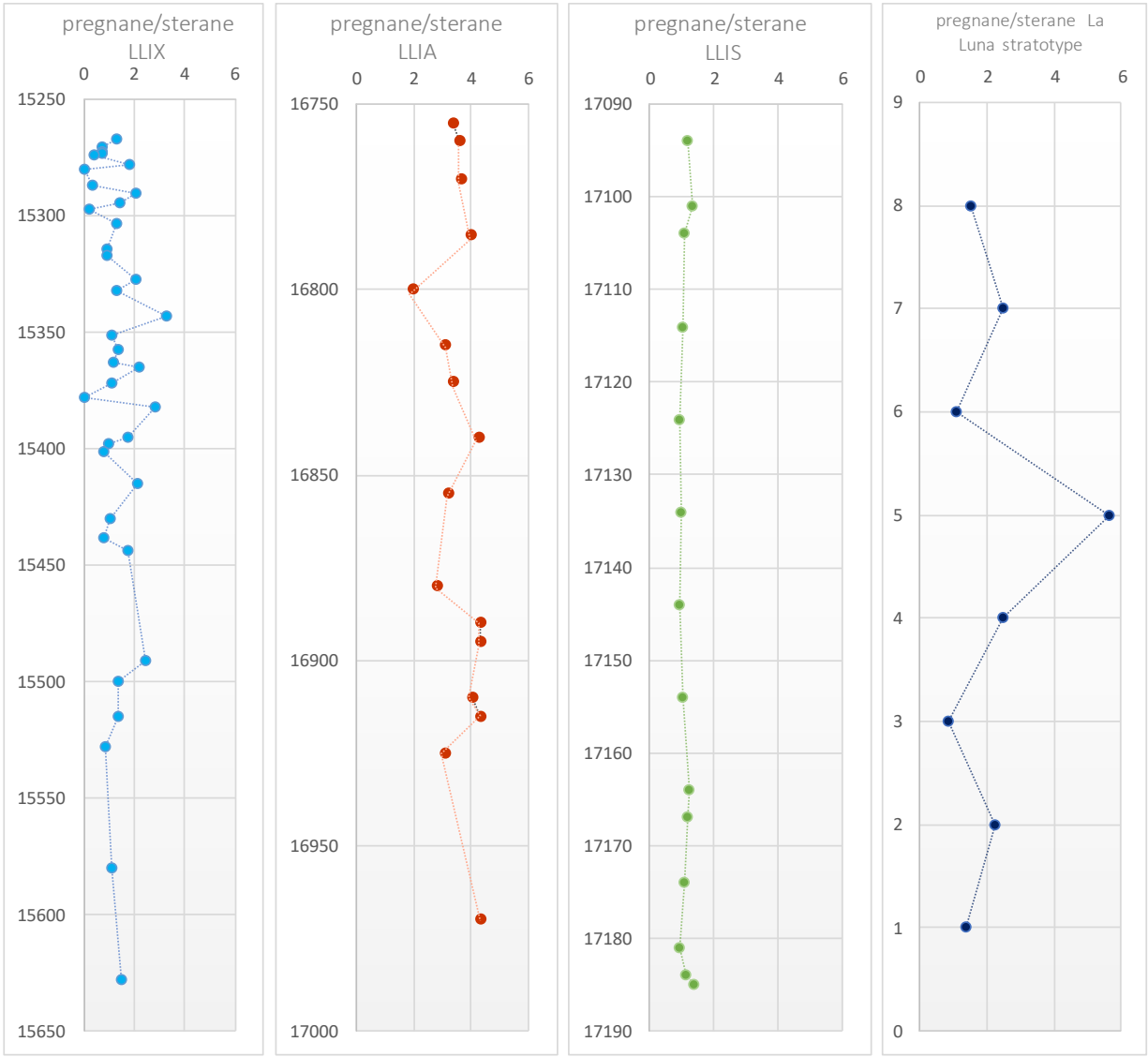

Figure 70 Geochemical logs of the pregnane/sterane ratio for the LLIX, LLIA, LLIS and La Luna stratotype samples. Formulas for calculation of ratios are in Appendix 7. 5

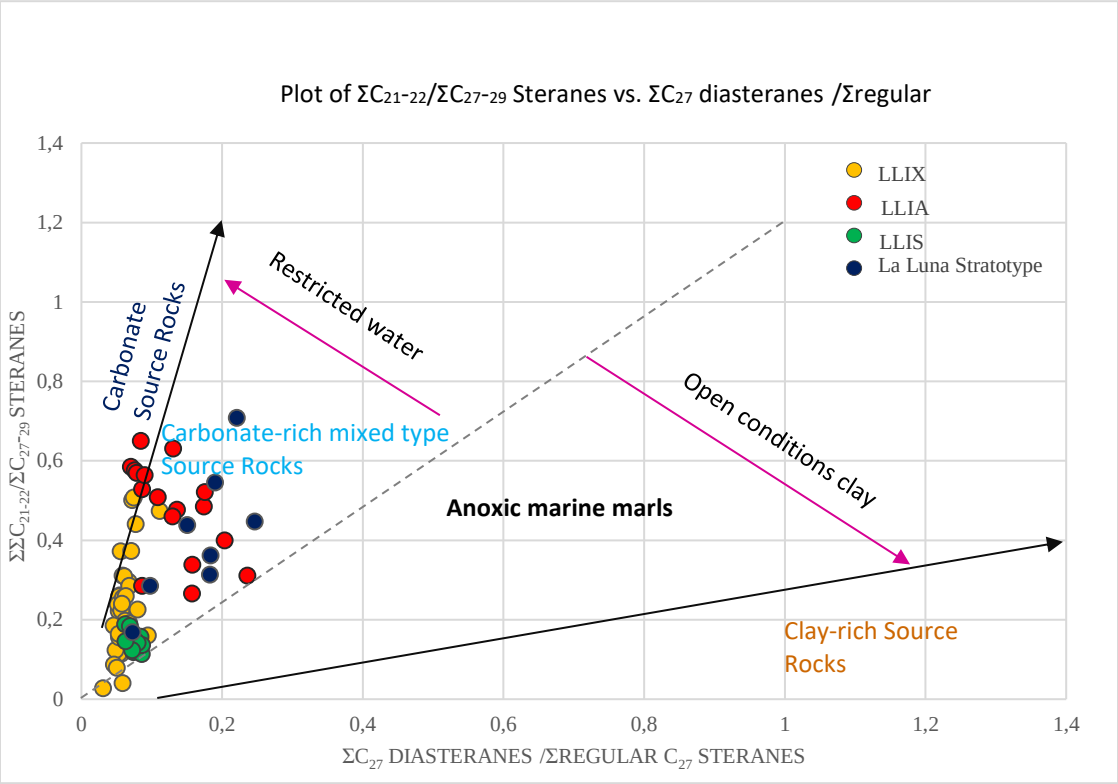

Figure 71 Plot of ΣC21-22/ΣC27-29 Steranes vs. ΣC27 diasteranes /Σregular C27 Steranes (Modified after Wang et al., 2015).

4.3.2 Terpanes

Like the steranes, the terpanes are one of the most common biomarker groups found in the saturated fractions of source rocks and oils. Terpanes constitute several homologous series of compounds originating mainly from prokaryotic organisms (eubacteria and blue-green algae) and membrane lipids (Ourisson et al., 1982; Alexander et al., 1983 and Tissot & Welte, 1984). Because bacteria are widespread in sediments, oils and extracts should show a terpane fingerprint (Peters et al., 2005). For this reason, terpanes are biomarkers used extensively to determine organic matter type and depositional environment. Terpanes are formed by acyclic, bicyclic, tricyclic, tetracyclic, and pentacyclic homologous series. Tri-, tetra-, and pentacyclic terpanes were identified in the La

Luna Formation bitumens by analyzing their B&C hydrocarbon fractions through SIM/GC-MS of the m/z 191.3 ion. Figures 72–74 show fragmentograms of these compounds, and Table 8 gives peak identifications. Appendix 7.7 presents formulas for the calculation of geochemical ratios. Geochemical ratios of terpanes (Figures 75–78) and their relationships with other biomarker groups helped to assess variations in organic matter source, depositional environment, redox conditions, and thermal maturity for the La Luna rock extracts.

The steranes/17α-Hopanes (Figures 67–70) ratio is advantageous to assess the eukaryote (plankton and benthic algae) versus the prokaryote (bacteria) organic matter input. A higher concentration suggests a marine depositional environment, whereas low values (close to zero) are associated with terrigenous and reworked organic matter (Peters et al., 2005). In general, high steranes/17α-Hopanes ratios are identified throughout the La Luna Formation, indicating greater marine organic matter input during deposition of these units. Middle and upper LLIX both reveal some values close to zero that can be attributed mostly to the lithofacies rather than the organic input content.

4.3.2.1 The tricyclic terpanes

This group of homologous series are helpful in correlating oils and source rock extracts, predicting source-rock characteristics, and evaluating the extent of thermal maturity and biodegradation (Seifert & Moldowan, 1979; Seifert et al., 1980; Zumberge, 1984; Peters & Moldowan, 1993). The origin of the tricyclic terpanes has been debated for decades. Some authors have proposed that the precursors of the tricyclic terpanes (for $<C_{30}$) are C_{30} isoprenoids and, therefore, are derived from lipids in prokaryotic membranes.

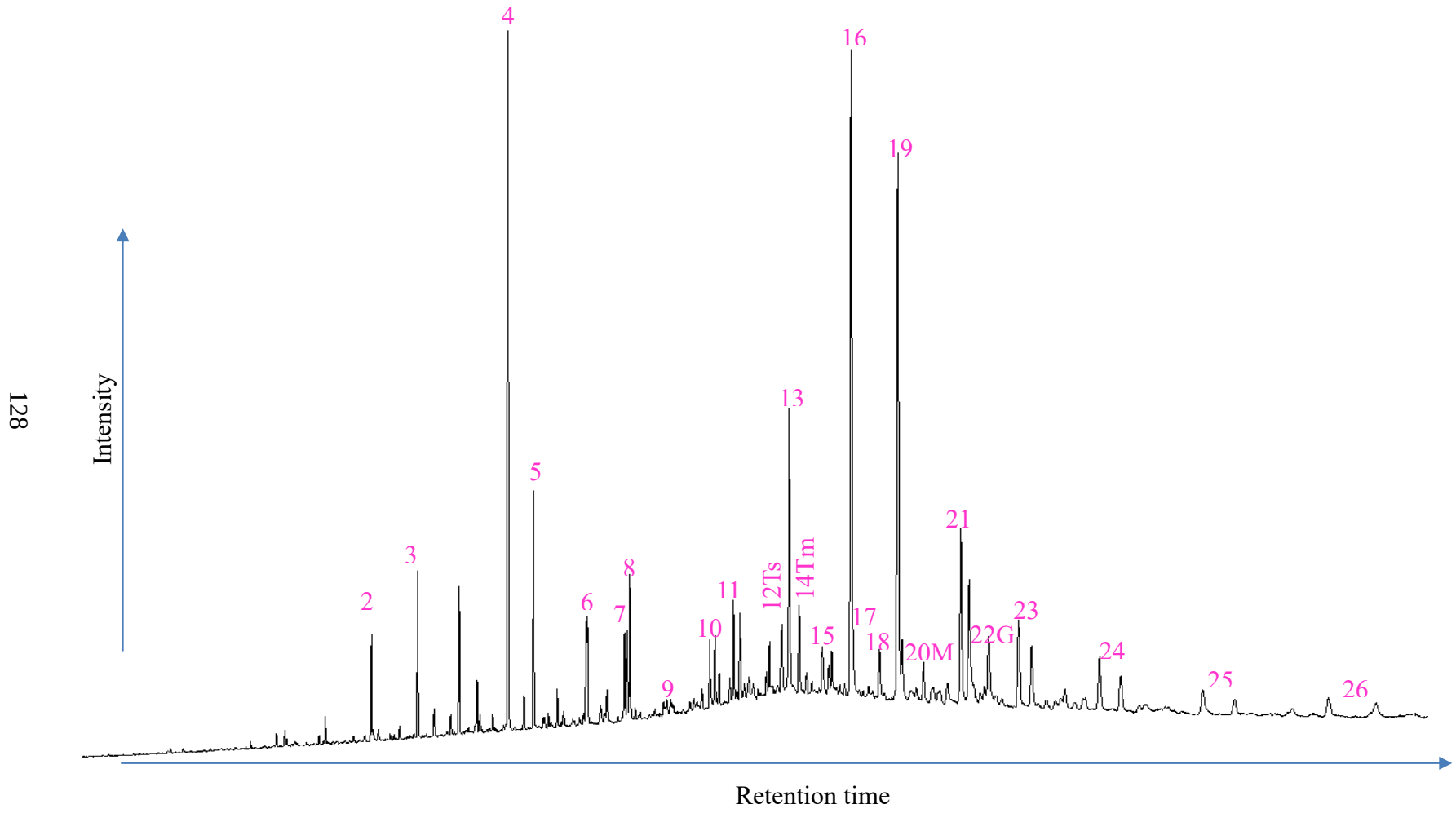

Figure 72. Partial fragmentograms of the m/z 191.3 ion showing distribution of terpanes in the branched and cyclic hydrocarbon fractions of the LLIX samples. Peak identification is presented in Table 8.

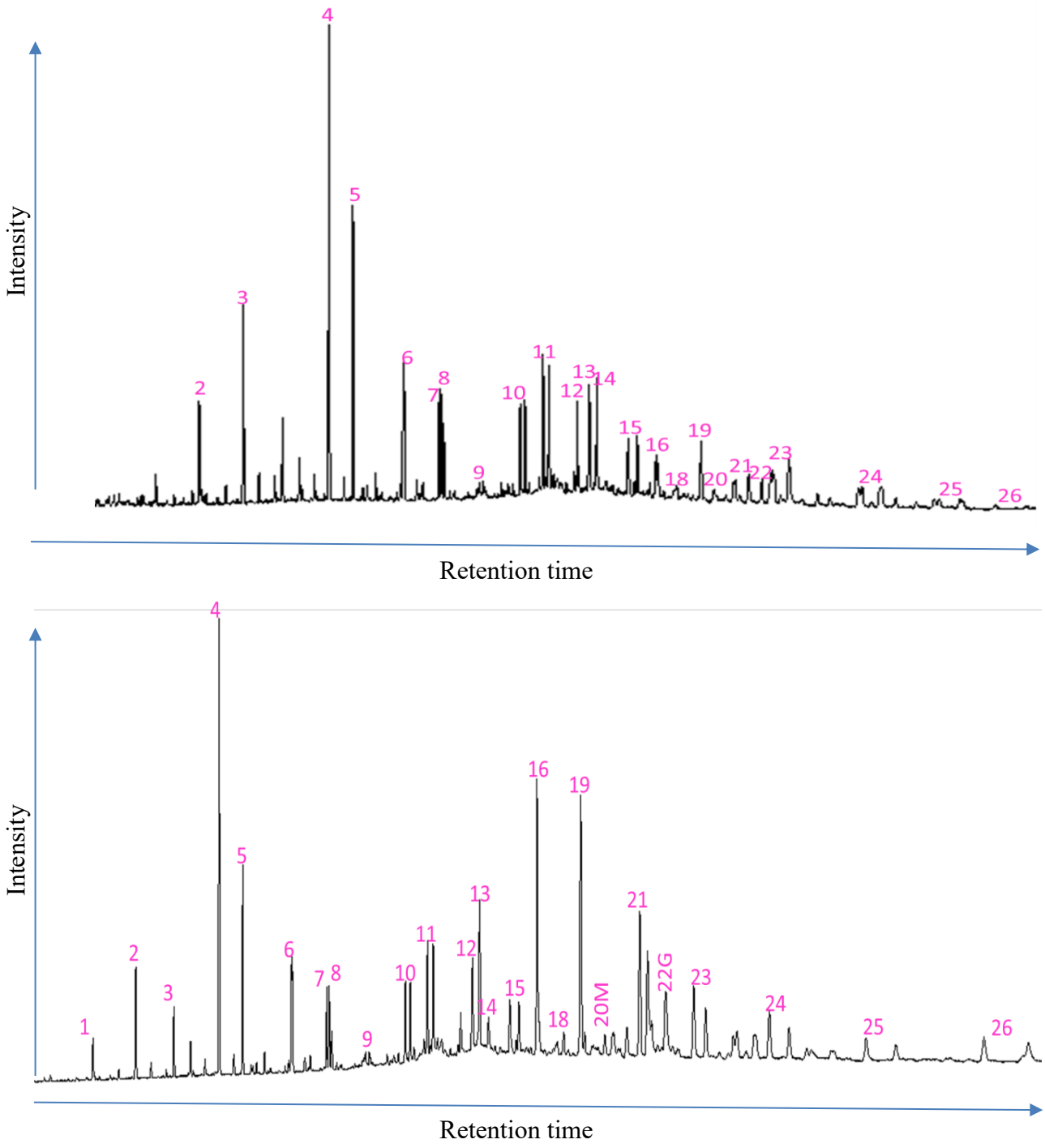

Figure 73. Partial fragmentograms of the m/z 191.3 ion showing distribution of terpanes in the branched and cyclic hydrocarbon fractions of the of the LLIA and LLIS samples. Peak identification is presented in Table 8.

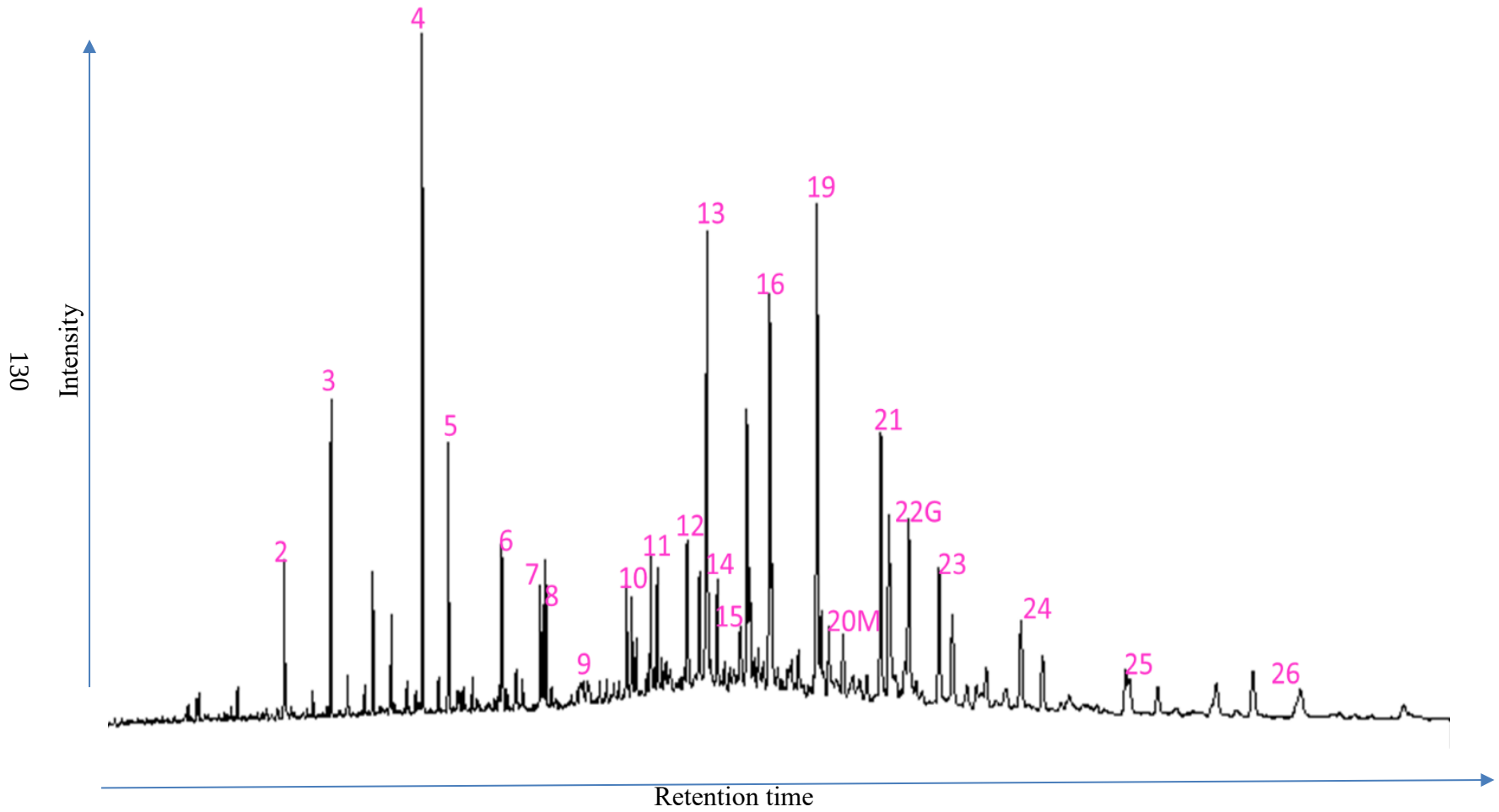

Figure 74. Partial fragmentograms of the m/z 191.3 ion showing distribution of terpanes in the branched and cyclic hydrocarbon fractions of the La Luna stratotype samples. Peak identification is presented in Table 8.

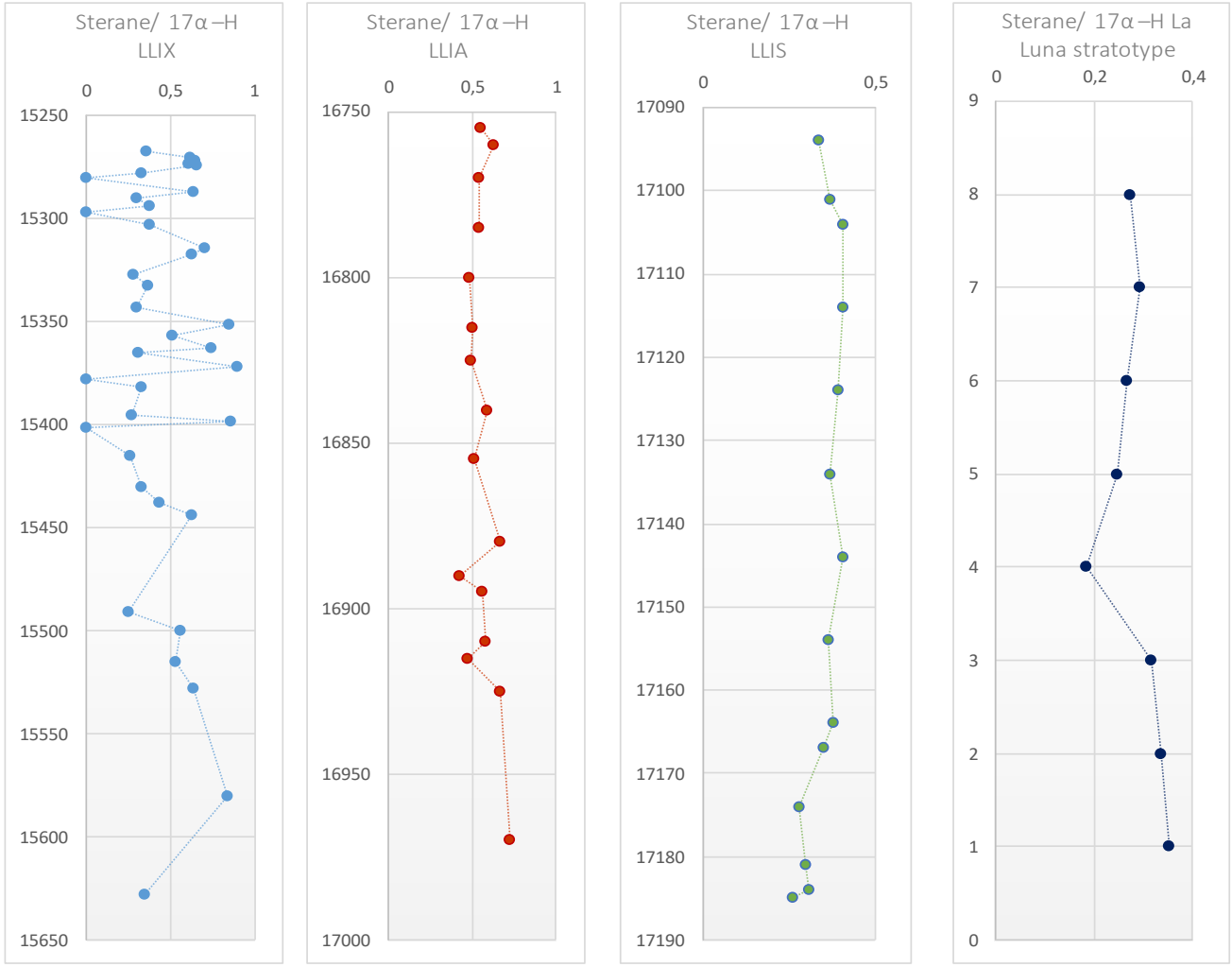

Figure 75 Geochemical logs of the sterane/ 17 α-H ratio for the LLIX, LLIA, LLIS and La Luna stratotype samples. Formulas for calculation of ratios are in Appendix 7. 5.

However, high concentrations of tricyclic terpanes have been found in source rocks containing Tasmanites, proposing that the Tasmanites are the main constituent of the tricyclic terpanes (Volkman et al., 1989; Acevedo et al., 1992; Simoneit et al., 1993). Also, high amounts of C_{19} and C_{20} tricyclic terpanes have been reported to be associated with lacustrine saline and marine carbonate environments (Mello et al., 1988).

Philp & Gilbert (1986) identified significant amounts of tricyclic terpanes in marine oils. Nevertheless, Philp et al. (1992) point out that tricyclic terpanes also have been reported in saline lacustrine oils from China, which suggests a salinity-controlled occurrence of these compounds.

The tricyclic terpanes ratios are also advantageous in assessing the depositional environment, rock lithology, organic matter input, and water salinity variations, because C_{19} and C_{20} are associated with vascular plants (Barnes & Barnes, 1983; Noble et al., 1986) and C_{23} is associated with marine algal input (Chester, 1990). The C_{19}/C_{23} and C_{20}/C_{23} ratios are useful in evaluting the terrigenous versus marine organic matter contribution to the depositional environment (Hanson et al., 2000), and the C_{26}/C_{25} ratio enables identification of the marine and lacustrine organic matter. Bitumens and oils of lacustrine origin present a higher concentration of C_{26} than C_{25} (Peters et al., 2005). A C_{26}/C_{25} ratio value of >1 indicates a possible lacustrine source rock or hypersalinity, whereas values of <1 can be interpreted as possible marine source rocks with moderate or low paleosalinity (Schiefelbein et al., 1999; Volk et al., 2005). C_{19}/C_{23} and C_{20}/C_{23} values for the La Luna samples (LLIX, LLIA, LLIS, La Luna stratotype, Figures 79–82) present values that oscillate from 0.2 to 0.6 for both ratios. Furthermore, the C_{23}/C_{30} values are >1.0 for most of the samples, indicating that the marine depositional environment prevailed during deposition of La Luna Formation. Last, the C_{26}/C_{25} ratio is <1 in all the La Luna samples, indicating marine source rocks with moderate or low paleosalinity of the depositional environment.

For rock lithology, the C_{22}/C_{21} and C_{24}/C_{23} tricyclic terpane ratios are useful in identifying rock extracts and oils generated from carbonate source rocks (Figure 83). The relationship between the C_{24}/C_{23} and the C_{22}/C_{21} ratios can be used to distinguish rock extracts and oils in source rocks with different lithologies (carbonates, marls, shale, evaporites, coals). Oils and extracts generated by carbonates and marls present high C_{22}/C_{21} (>0.4) and low C_{24}/C_{23} values (<0.6). Oils and rock extracts generated by marine marlstones and evaporites have values of 0.2–0.4 for C_{22}/C_{21} and values of 0.6–1 for C_{24}/C_{23}. Last, oils of lacustrine origin range from 0.3 to 0.4 for C_{22}/C_{21} and are >1 for C_{24}/C_{23} (Clark & Philp, 1989; Liu et al., 2017). These plots indicate that most of the La Luna Formation samples are carbonates, with the exception of some of the samples from the LLIA. For these exceptions, marine shales show a good correlation with the inorganic analysis from mineralogy and elemental proxies from XRD and XRF.

Table 8 Identification of terpanes in the partial m/z 191.3 fragmentograms of the branched and cyclic fractions of La Luna Formation samples.

Peak number	Compound
1	C_{20} Tricyclic terpane
2	C_{21} Tricyclic terpane
3	C_{22} Tricyclic terpane
4	C_{23} Tricyclic terpane
5	C_{24} Tricyclic terpane
6	C_{25} Tricyclic terpane
7	C_{24} Tetracyclic terpane
8	C_{26} Tricyclic terpane (22S + 22R)
9	C_{27} Tricyclic terpane (22S + 22R)
10	C_{28} Tricyclic terpane (22S + 22R)
11	C_{29} Tricyclic terpane (22S + 22R)
12ts	17α Trisnorneohopane (C_{27} Ts)
13	Norhopane
14Tm	18α Trisnorneohopane (C_{27} Tm)
15	Tricyclic terpane
16	18α(H),21β(H)- Norhopane
17	18α Neonorhopane (C_{29} Ts)
18	17β (H),21α(H)- Normoretane
19	17α(H),21β(H)-Hopane
20M	17β (H),21α(H)- Moretane
21	17α(H),21β(H)-Homohopanes (22S & 22R)
22G	Gammacerane
23	17α(H),21β(H)-Bishomohopane (22S & 22R)
24	17α(H),21β(H)-Trishomohopane (22S & 22R)
25	17α(H),21β(H)-Tetrakishomohopane (22S & 22R)
26	17α(H),21β(H)-Pentakishomohopane (22S & 22R)

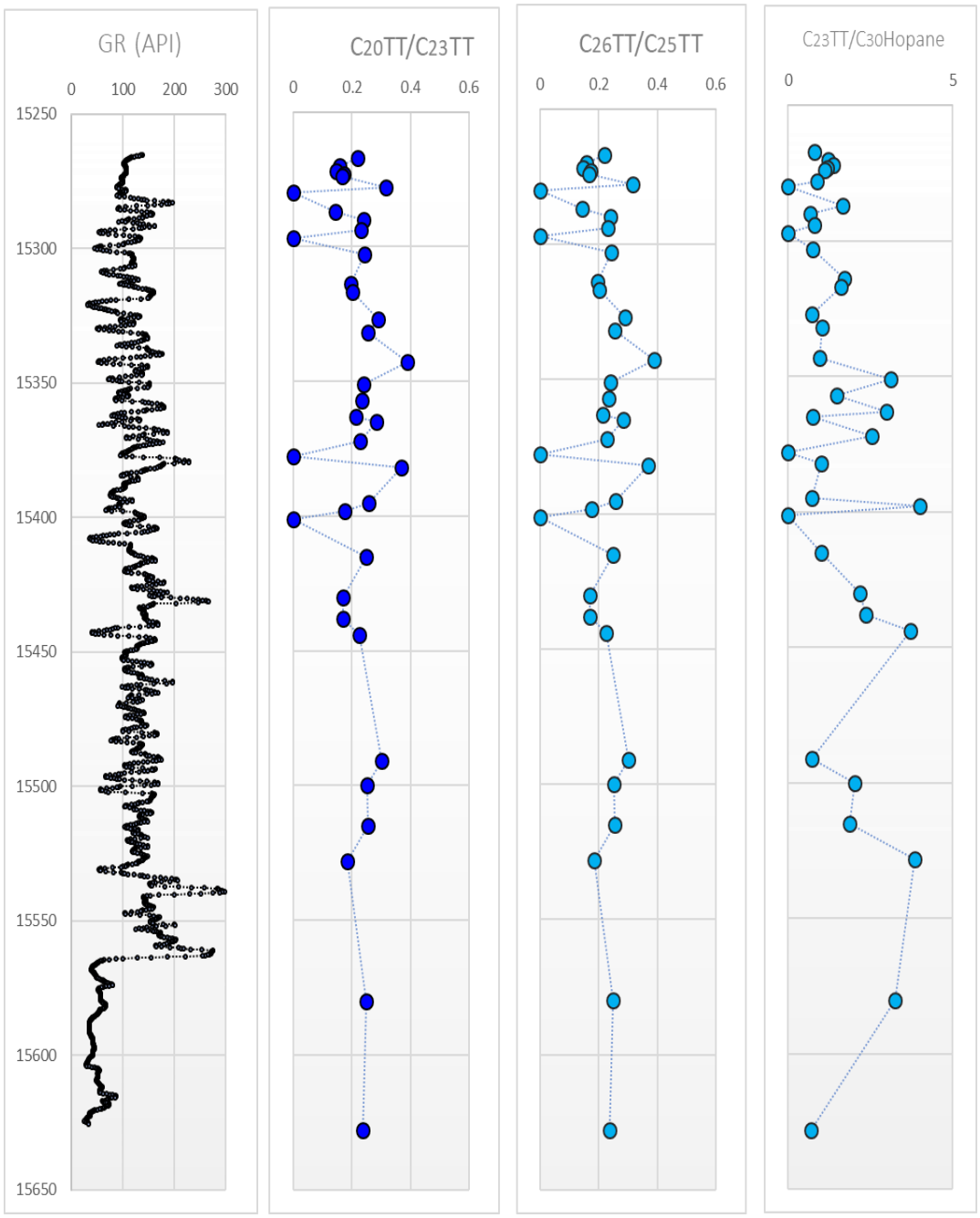

Figure 76. Gamma ray and geochemical logs of the $C_{20}TT/C_{23}TT$; $C_{26}TT/C_{25}TT$ and C_{23}/C_{30}Hopane ratios for LLIX.

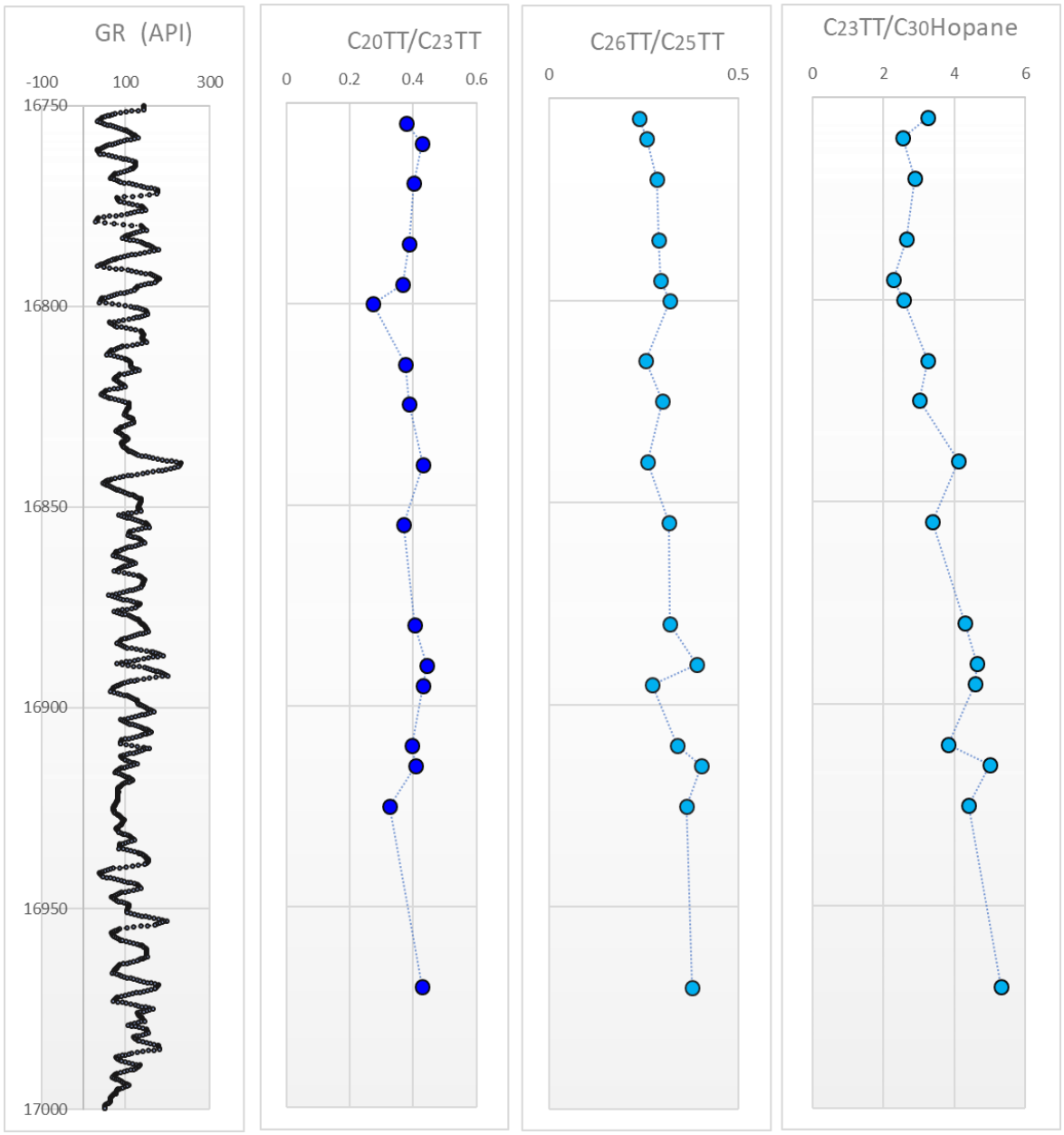

Figure 77. Gamma ray and geochemical logs of the $C_{20}TT/C_{23}TT$; $C_{26}TT/C_{25}TT$ and C_{23}/C_{30}Hopane ratios for LLIA.

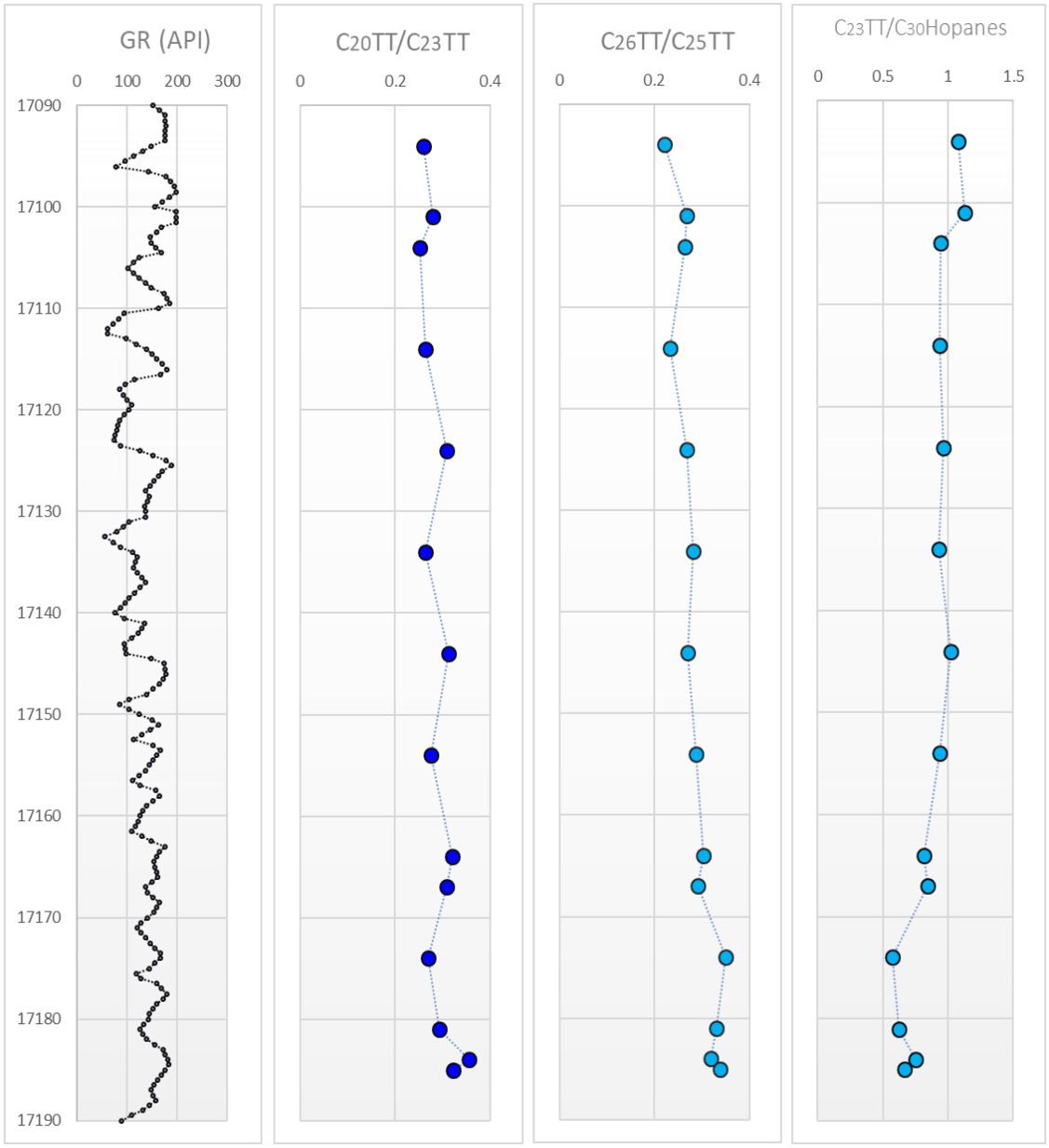

Figure 78. Gamma ray and geochemical logs of the $C_{20}TT/C_{23}TT$; $C_{26}TT/C_{25}TT$ and C_{23}/C_{30}Hopane ratios for LLIS.

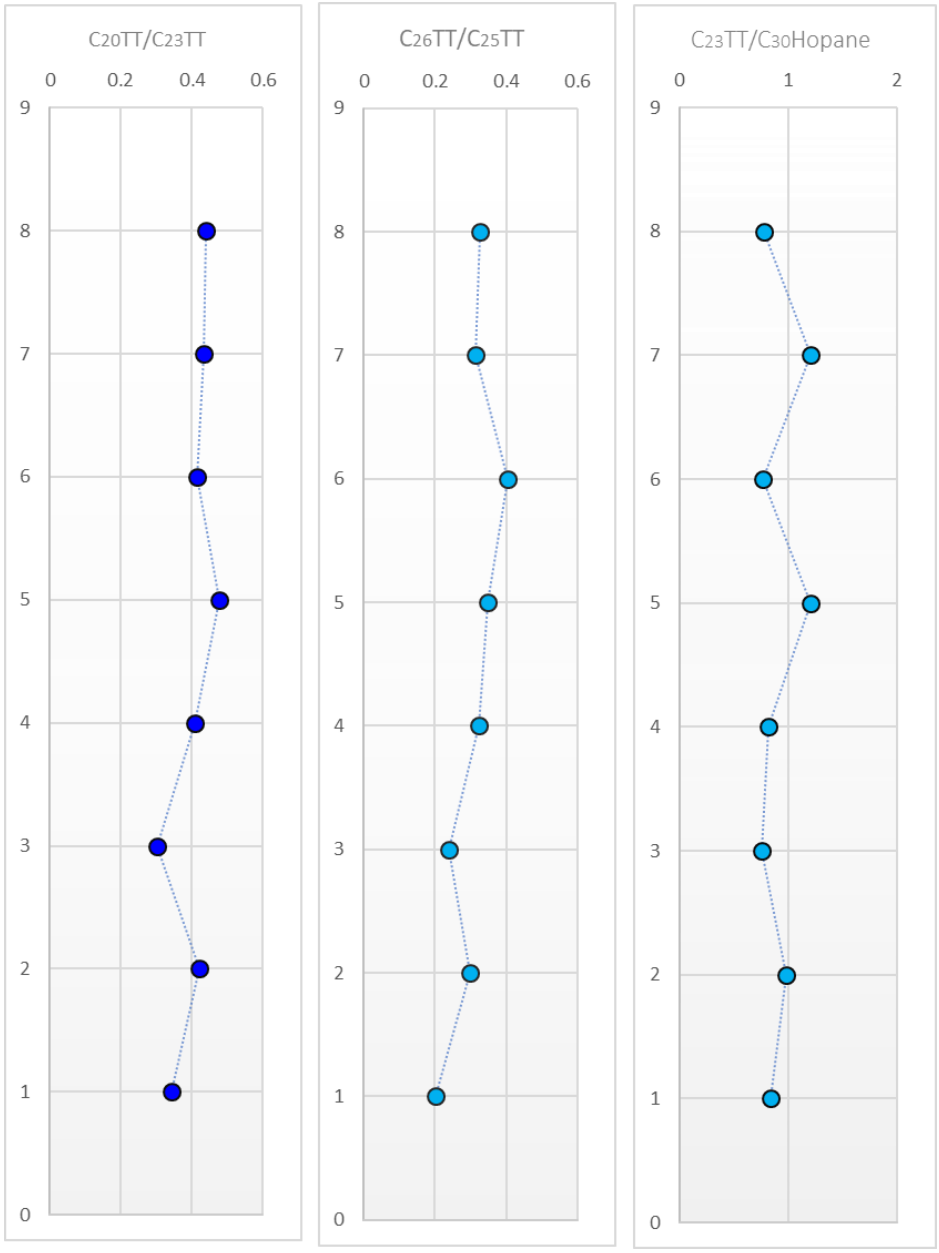

Figure 79. Geochemical logs of the C_{20}TT/C_{23}TT; C_{26}TT/C_{25}TT and C_{23}/C_{30}Hopane ratios for La Luna stratotype.

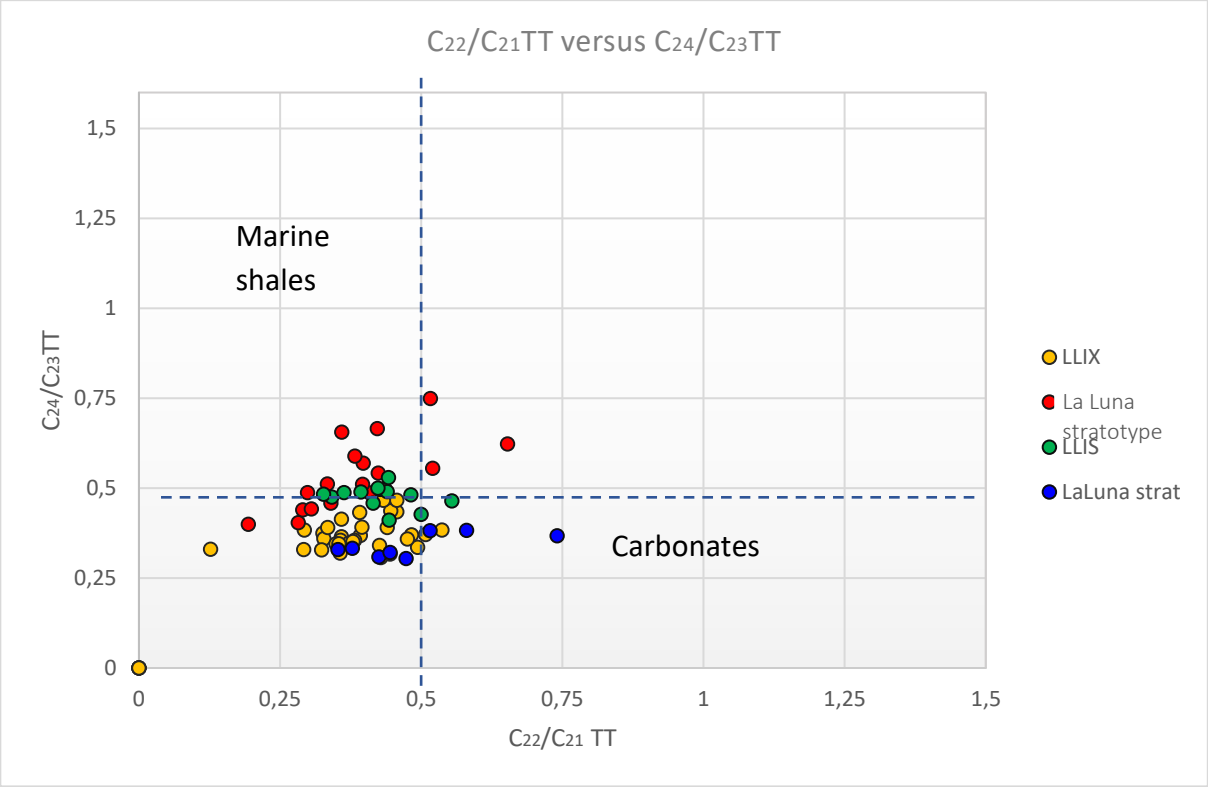

Figure 80. The plot of C_{22}/C_{21} versus C_{24}/C_{23} tricyclic terpanes showing the source rock depositional environments for the La Luna Formation bitumens. Plot modified by Peters et al., 2005).

4.3.2.2 The tetracyclic terpanes

Although it has been accepted that tetracyclic terpanes derive from hopanes or precursor hopanoids, the biological origin of tetracyclic terpanes has been controversial through time. A study performed on the CSIA (compound specific isotope analysis) on C_{24} tetracyclic terpanes by Grice et al. (2001) demonstrated that the stable carbon isotopic composition of the C_{24} tetracyclic terpane is consistent among torbanites from boghead coals. This may suggest an origin from hopanoids or terrigenous precursors. Furthermore, many studies have shown that these compounds are more resistant to thermal maturity and biodegradation compared to hopanes and can be used for correlation of biodegraded oils (Palacas et al., 1984; Connan et al., 1986; Clark and Philp, 1989; Grice et al., 2001). Tetracyclic terpanes range from C_{24} to C_{27} with tentative evidence for

homologs up to C_{35}, with the C_{24} homolog generally being the most abundant (Aquino Neto et al., 1983). Abundant C_{24} tetracyclic terpanes were believed to be indicative of carbonate and evaporite depositional environments (Palacas et al., 1984; Clark & Philp, 1989). The C_{24} tetracyclic terpane was identified in all the analyzed bitumens of La Luna Formation and the C_{24} tetracyclic terpane/C_{30} hopane ratio does not show significant variations within the different La Luna Formation members (Figure 80).

4.3.2.3 The Pentacyclic Terpanes

The pentacyclic terpanes are originated from hopanoids precursors present in prokaryotes organisms (bacteria and cyanobacteria) and higher plants (Ourisson et al., 1987). The C_{29} 17α(H)-norhopane (30-Norhopane) and the C_{30} 17α(H)-hopane (30H) appear in the m/z 191 ion chromatogram, along with the tricyclic and tetracyclic terpanes, and are usually the major peaks. They are important since these biomarkers can be used as environmental indicators (Waples & Machihara, 1991). The 30-NorH/30H hopane ratio increases with increasing thermal maturity due to the higher stability of the C_{29} hopane compared to the C_{30} homolog (Peters et al., 2005). Values of the 30-NorH/30H hopane ratio greater than 1.0 are associated with anoxic carbonates, evaporites or marl source rocks (Connan et al., 1986; Riva et al.,1989). Most of the La Luna samples analyzed have 30-NorH/30H values that range from 0.9 to 1.0. Lower concentrations of 30-Norhopane were observed in LLIS and LLIA, probably due to changes in lithology and increment of biogenic silica (for LLIX) and clay (for LLIA) in this interval (Figure 81).

The C_{35} homohopane index is an indicator of redox potential in marine sediments during diagenesis (Peters & Moldowan, 1991). High values indicate anoxia, but also affected thermal maturity; the index is also expressed as C_{35}/C_{34} hopanes. The C_{35}/C_{34} hopane ratio uses the 22S epimer rather than the 22S and 22R to avoid interference.

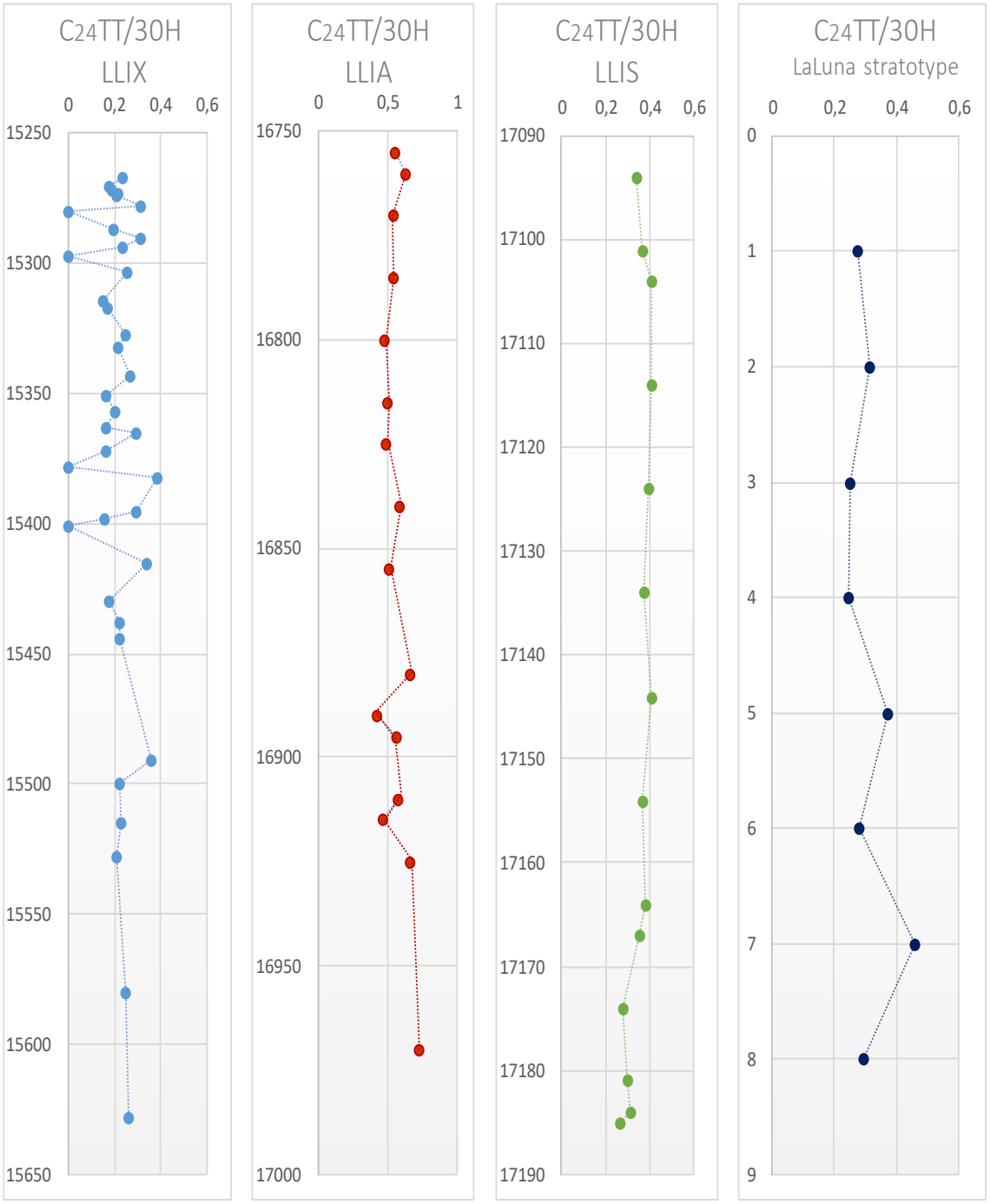

Figure 81. Geochemical logs of the C24TT/30H for La Luna stratotype.

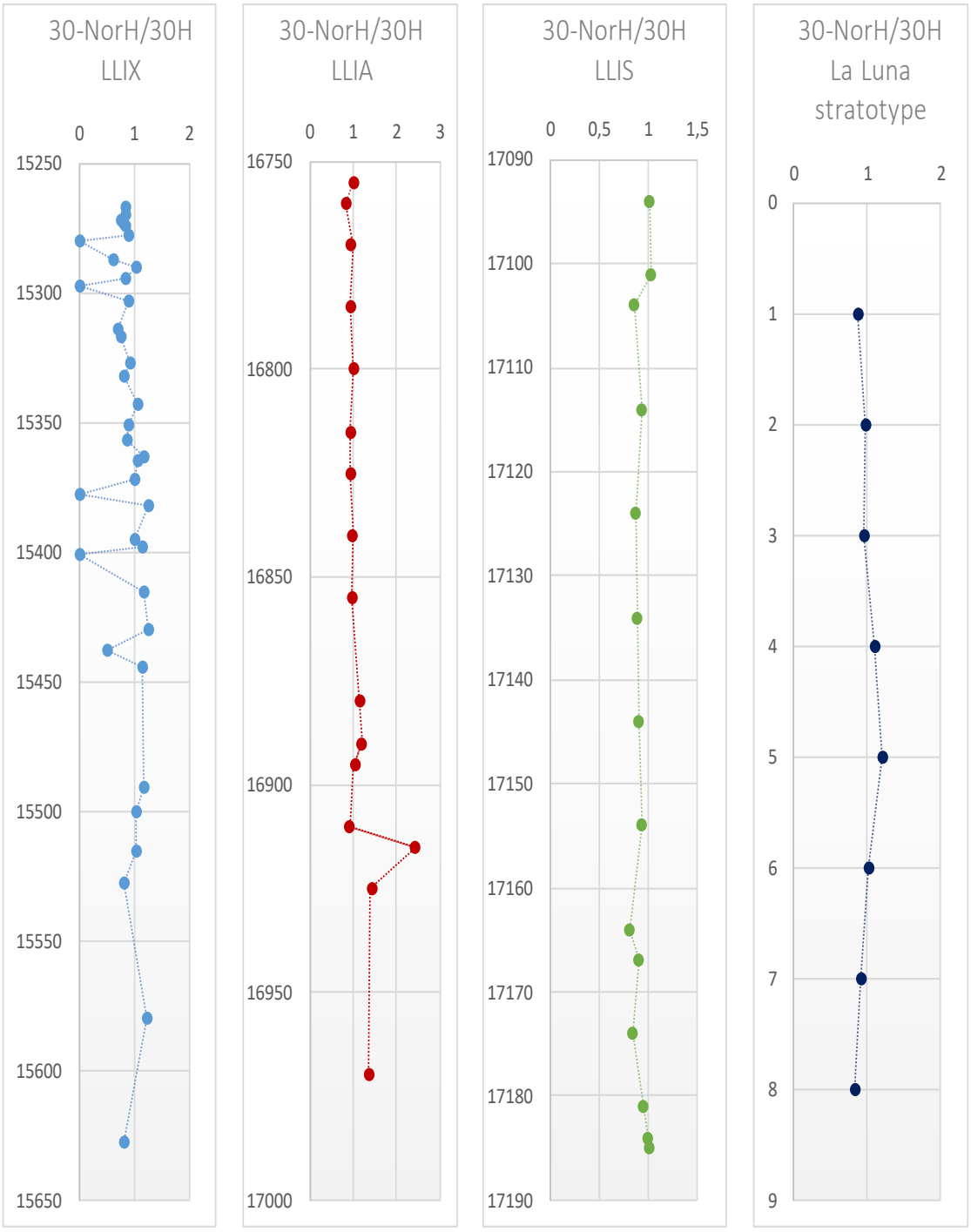

Figure 82. Geochemical logs of the 30-NorH/30H for La Luna stratotype.

The C_{35}/C_{34} hopane ratio in this plot uses the 22S epimer rather than both 22S and 22R to avoid interference. When this ratio is compared with the 30-NorH/30H, is possible to identify the source facies of oils and extracts (Figure 82). This relationship is observed in most of the La Luna Formation extracts confirming the presence of marine carbonates and marl facies.

The C_{31} 22R/C_{30} hopane ratio (31R/30H) is a useful parameter to access the identification of marine and lacustrine source-rock depositional environments. Unlike crude oils or extracts from lacustrine source rocks, shale, carbonates and marl source rocks usually display high C_{31}22R homohopane/C_{30}hopane ratio values higher than 0.25. Geochemical logs of this ratio (Figure 83) for the La Luna sample extracts (except LLIX) do not present a significant variation between the different members. Most samples have values of 31R/30H higher than 0.25, indicative of a marine origin. When this ratio is correlated with the C_{26}/C_{25} tricyclic terpane ratio, it can work as an environmental indicator allowing to distinguish marine from lacustrine source rocks (Schiefelbein et al., 1999). A C_{26}/C_{25} ratio greater than 1.0 may indicate possible lacustrine source rocks and/or hypersalinity, while lower values can be interpreted as possible marine source rocks with moderate or low paleosalinity of the depositional environment (Schiefelbein et al., 1999; Volk et al., 2005). The plot of C_{26}/C_{25} tricyclic terpane versus C_{31}R/C_{30} hopane confirms that all samples are marine carbonates and marls (Figure 84).

The relative distribution of the homohopanes has been used to assess redox potential during marine source rock deposition. According to Peters and Moldowan (1993), low ratios of C_{35} to C_{34} homohopanes (0.38–0.65) suggest prevailing oxic to sub-oxic (high Eh) conditions during deposition, and hence low organic matter with low hydrogen index (Dahl et al., 1994). Conversely, values of this ratio greater than 0.8 are frequently related to marine carbonate source rocks (Peters et al., 2005). Also, a higher proportion of the C_{35} homohopane concerning its C_{34} homolog is

associated with anoxic marine depositional environments due to preferential preservation of the C_{35} homolog (Moldowan et al., 1992; Peters et al., 2005). Plots of homohopane distributions for the analyzed the La Luna Formation samples indicate that, in general, these source rocks were deposited under anoxic conditions, which promoted the preservation of the C_{35} homohopane (Figure 85). Although samples from the La Luna stratotype do not show the predominance of the C_{35} homohopane, most of the geochemical plots suggest the presence of anoxic conditions for this unit. It is possible that these results are not reliable since these samples from outcrop and weathering conditions may have altered the organic composition of the rocks.

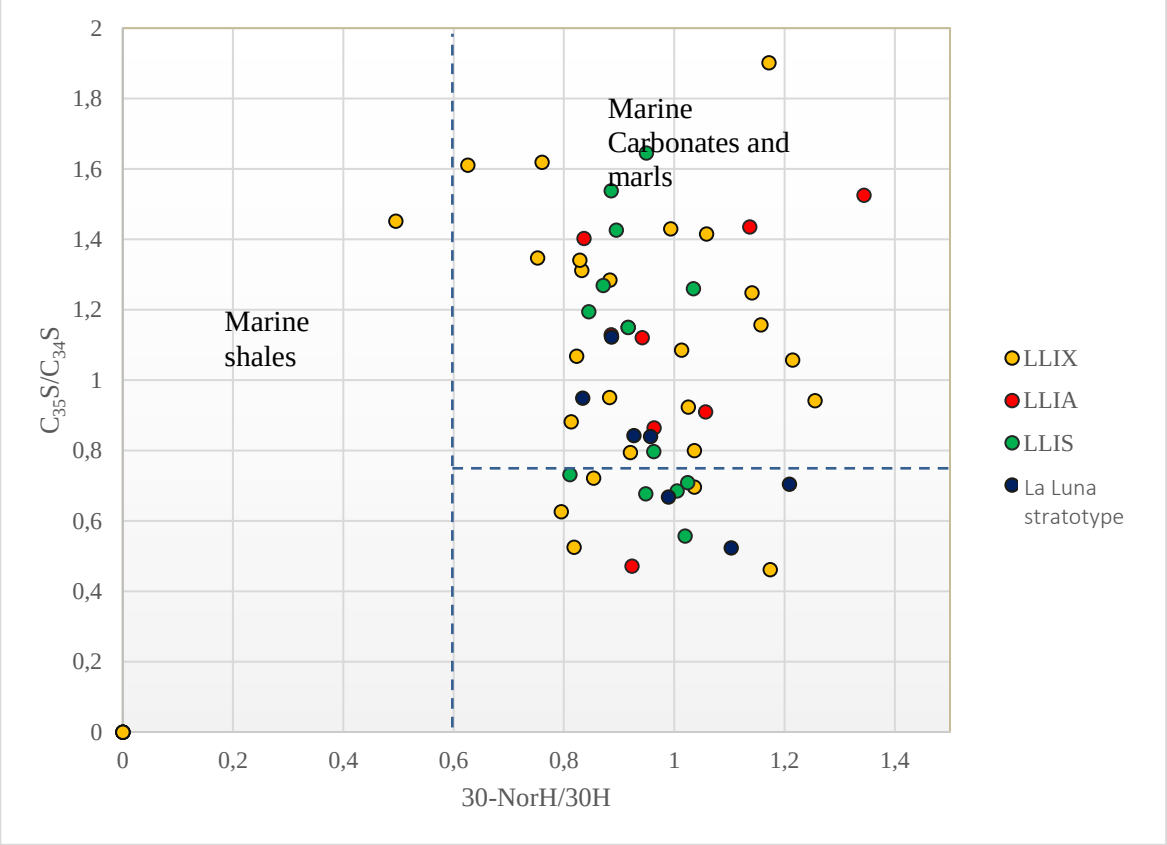

Figure 83. Plot of 30-Nor/C_{30} hopane versus $C_{35}S/C_{34}S$ homohopanes indicating that most of the La Luna samples are in the marine carbonates and marls range. (Plot modified by Peters et al., 2005).

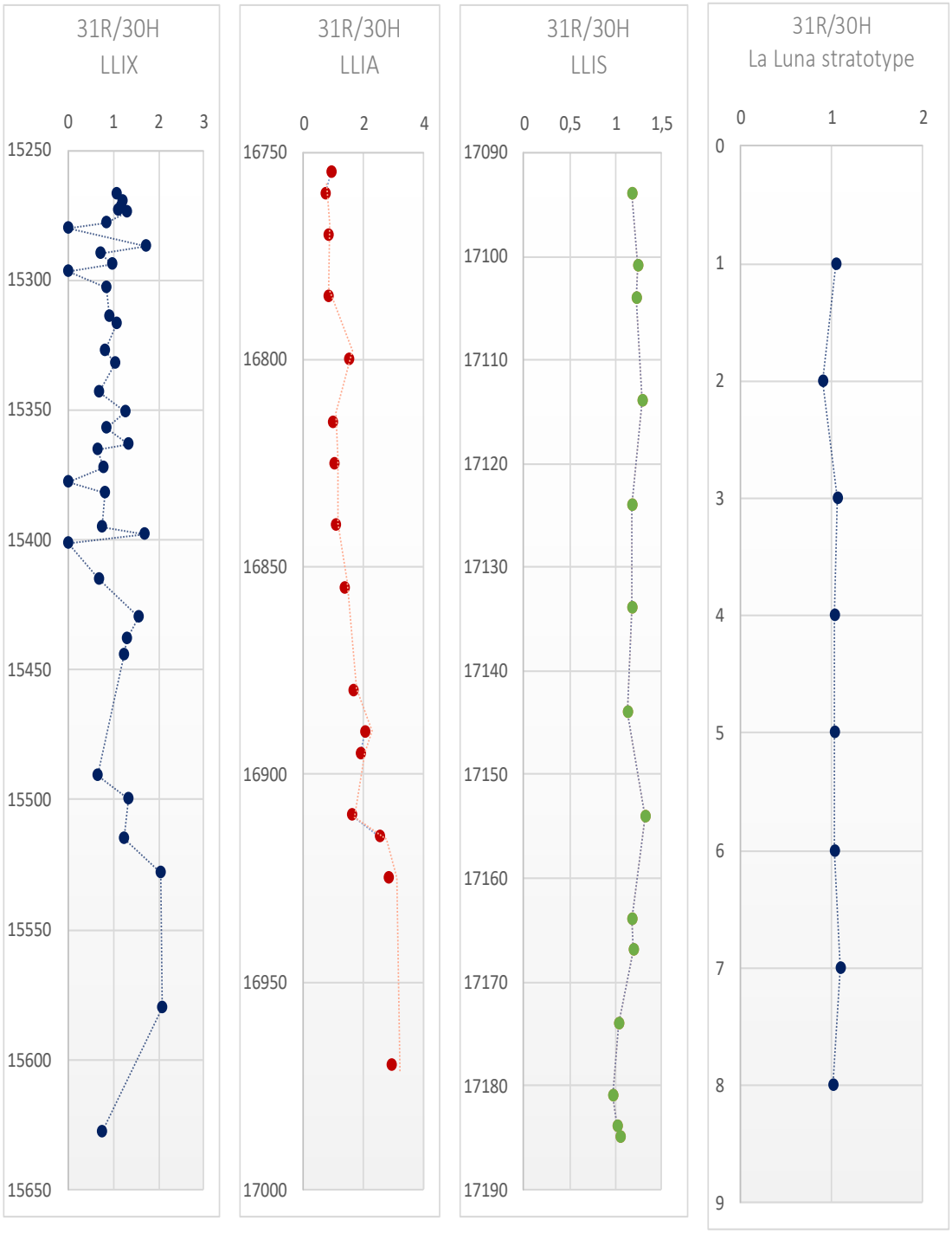

Figure 84. Geochemical logs of the 31R/30H for La Luna stratotype.

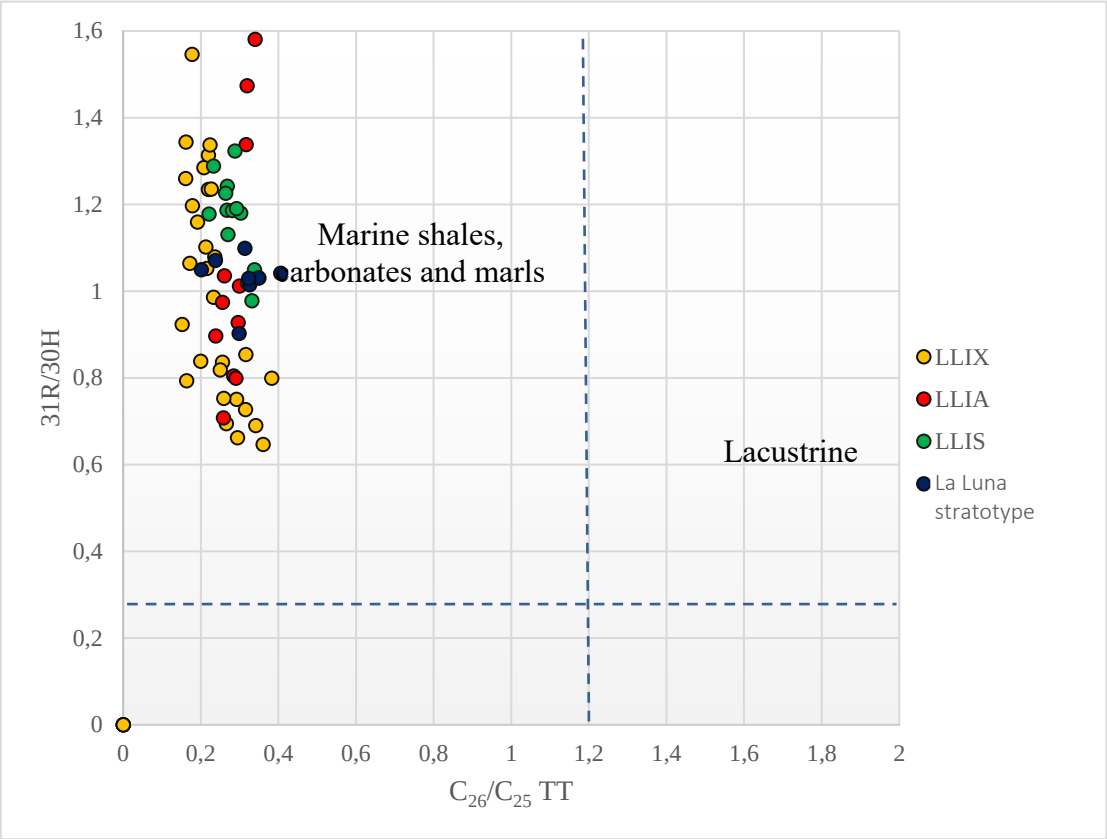

Figure 85. Plot of C_{26}/C_{25} versus $C_{31}R/C_{30}$ hopane displaying the marine origin of the La Luna samples. (Plot modified by Peters et al., 2005).

Gammacerane is a C_{30} triterpane derived from the diagenesis of tetrahymanol (a compound biologically related to the freshwater ciliated protozoan *Tetrahymena*). Gammacerane is important because it is an excellent indicator of water-column stratification during sedimentation in marine and non-marine environments. It is usually associated with high salinity conditions, especially in alkaline lakes and carbonate-evaporite environments; but, it is not necessarily restricted to this type of setting (Damsté et al., 1995). Gammacerane was tentatively recognized in all the analyzed samples; its presence indicates the existence of a stratified water column. The geochemical log for the gammacerane index illustrated in Figure 86 shows a higher proportion of gammacerane in the base of the Lower La Luna for LLIX and LLIA cores. As Torres (2013) interpreted the data for La

Luna Formation in Colombia (Pujamada and Galembo member), the results suggest that water stratification and salinity play an important role when the transgressive sequences start to be deposited. This observation positively correlates with the low Pr/Ph ratios and the predominance of the ββ steranes over the αα steranes, both parameters also related to hypersalinity (ten-Haven et al., 1988). To accurately analyze variations in the concentration of gammacerane, its presence should be confirmed by full- scan GCMS or GC MSMS analysis for the La Luna formation samples.

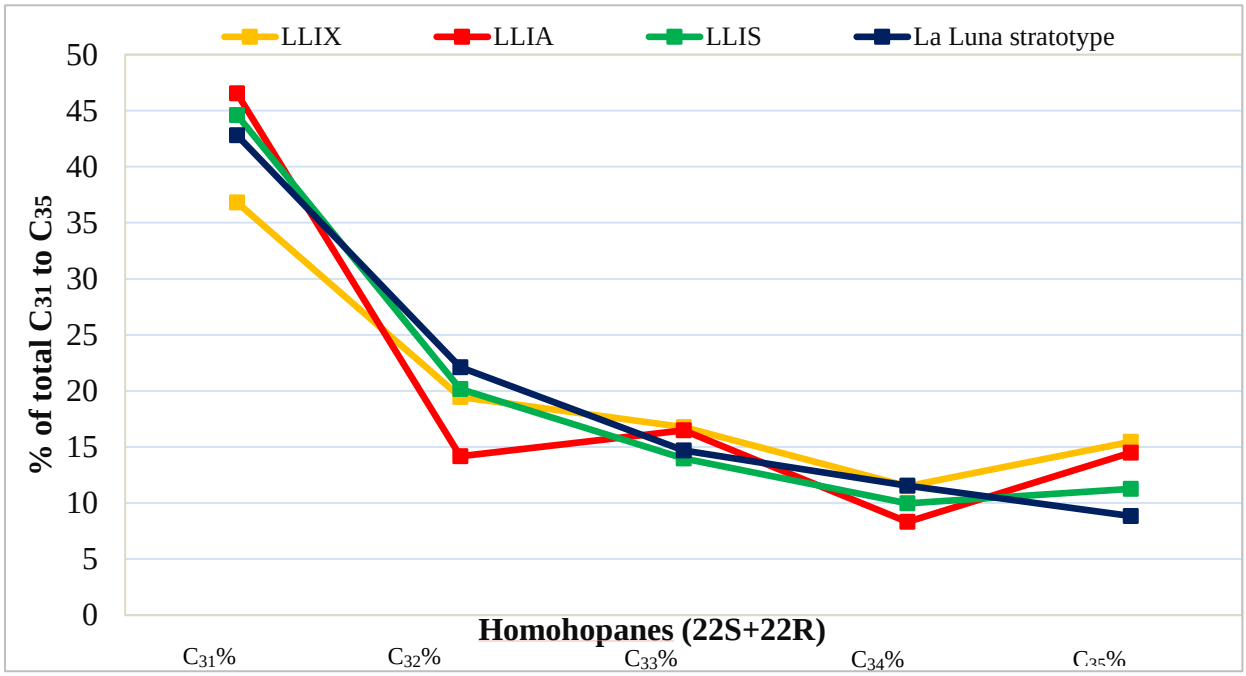

Figure 86. Homohopanes distribution for bitumens from the La Luna Formation.

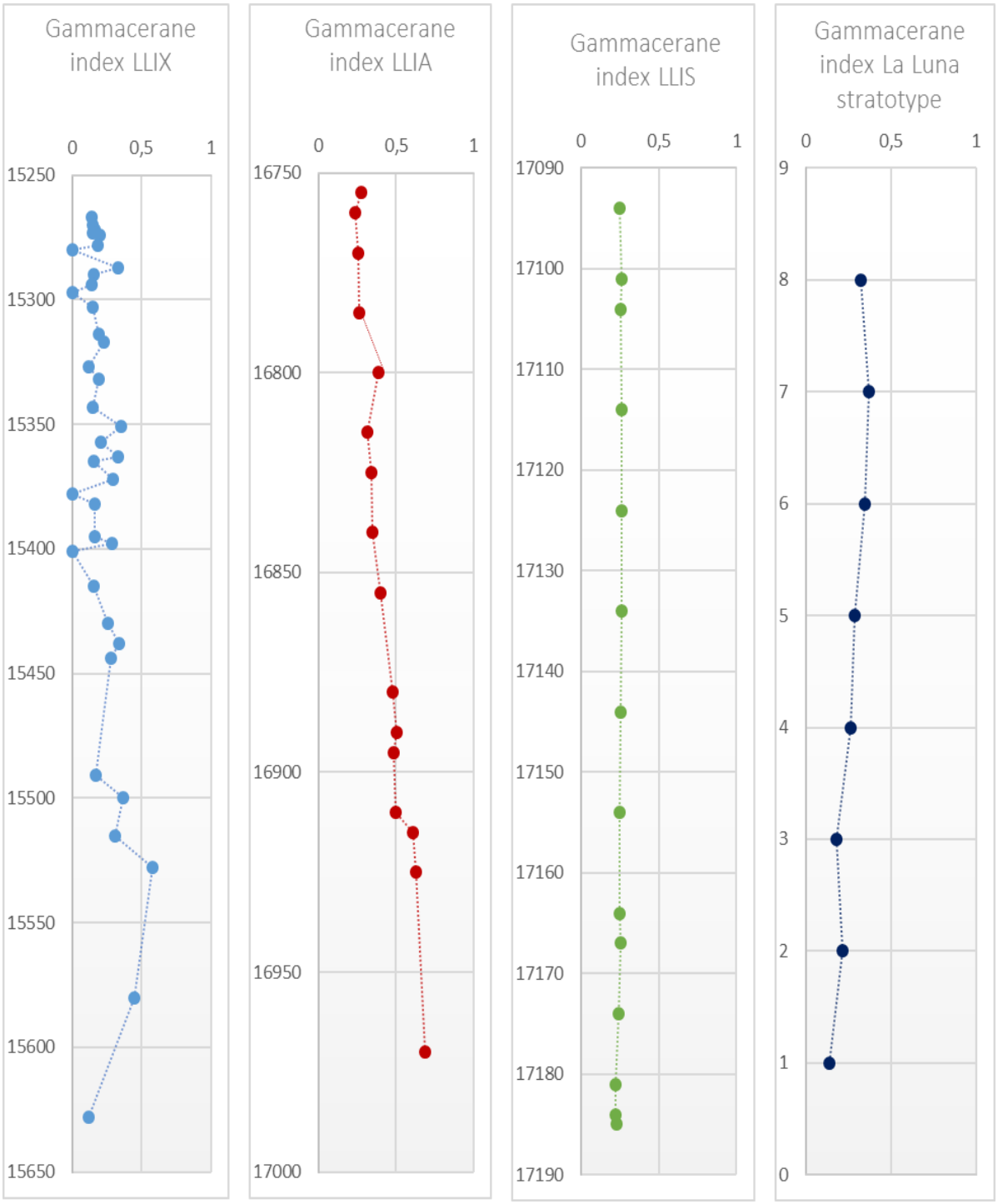

Figure 87. Geochemical logs of the 31R/30H for La Luna stratotype.

4.3.3 Aryl Isoprenoids

Aryl isoprenoids play an important role in the organo-facies of the source rocks since they can be considered the biological markers for the green sulfur bacteria *(Chlorobiaceae*). These compounds are derived from isorenieratene, a C_{40} diaromatic carotenoid pigment formed by *Chlorobiaceae* (Brown & Kenig, 2004; Schwark & Frimmel, 2004). *Chlorobiaceae* are photosynthetic bacteria that contain a pigment called bacteriochlorophyll, which absorbs the light of long, low-energy wavelengths. These organisms require an electron donor other than water and do not release oxygen; the green bacteria use elemental sulfur, sulfide, thiosulfate, or hydrogen gas as an electron donor. Thus, this type of bacteria requires anaerobic conditions for the development of photosynthetic activity. Compounds derived from these bacteria can act as specific indicators of photic zone anoxia and can be used as a geochemical parameter for paleoenvironmental studies (Schwark & Frimmel, 2004). Furthermore, the aryl isoprenoids have an aromatic ring in their structure and contain a long acyclic side chain. They tend to elute into the saturated hydrocarbon fraction, which is a common occurrence for typical oil fractionations (Brown & Kenig, 2004)..

Analysis of aryl isoprenoids was performed on the branched and cyclic hydrocarbon fractions of the extracts by SIM/GC-MS using the m/z 133.1 and 134.1 ions. Results from quantification of the aryl isoprenoids are given in Appendix 7.8. Identification of these compounds was achieved by comparison with reference mass chromatograms published by Schwark & Frimmel (2004); Miceli-Romero & Philp (2012); Miceli-Romero (2014) and Jones (2017). The compounds identified from the rock extracts in the current study included a series of C_{13}-C_{31} aryl isoprenoids. The 1-alkyl-2,3,6-trimethyl substituted aryl isoprenoids, as monitored by the m/z 133 ion, were the most abundant in all of the samples. In addition, low concentrations of the 1-alkyl-

3,4,5 trimethyl substituted isoprenoids were determined by the m/z 134 ion (Figure 87). The aryl isoprenoids generally present a series of C_{13}-C_{22} homologs, with homologs above C_{24} being present in lower concentrations .

The aryl-isoprenoid ratio (AIR, (2,3,6/3,4,5-trimethyl-substituted isoprenoids) is considered an important parameter to assess and understand the changes of the photic zone anoxia (PZA) in the La Luna Formation through the relative amounts of aryl-isoprenoids derived from *Chlorobiaceae*. Schwark & Frimmel (2004) introduced this ratio which mainly uses the proportions of the short-chain (C_{13}-C_{17}) and intermediate-chain (C_{18}-C_{22}) aryl-isoprenoids. High ratios (values equal to or higher than 3.0) can be linked to relatively oxic conditions and episodic PZA (Miceli-Romero & Philp, 2012), leading to the alteration of the long- and intermediate-chain aryl isoprenoids. On the other hand, lower ratios (values of approximately 0.5) are related to more anoxic conditions reflecting a persistent PZA (Miceli-Romero, 2010), conserving the long-chain aryl isoprenoids (Schwark & Frimmel, 2004).

Most of the samples (LLIX, LLIS, and La Luna stratotype) show AIR values of 0.3-0.6 on average suggesting more anoxic conditions. Furthermore, the LLIA present values are higher than 1 indicating more episodic periods of PZA, where shifts of the chemocline occurred periodically. Results of these values are given in Appendix 7.9. A plot of the AIR versus the Pr/Ph ratio (Figure 88) is useful to evaluate the redox conditions and PZA during sediment deposition (Schwark & Frimmel, 2004). From this diagram, it can also be seen that most of the samples (LLIX, LLIS, and La Luna stratotype) were probably deposited under more anoxic-suboxic settings and persistent photic zone anoxia. Samples from LLIA had higher AIR and Pr/Ph ratios suggesting episodic photic zone anoxia. An important observation made by Wang (2016) on the Woodford shale displayed a positive correlation between the Pr/Ph and a negative correlation between relative sea

level changes and the aryl-isoprenoid ratio. Wang (2016) also indicates that when sea level increases a transgression event occurs, the Pr/Ph ratio and AIR decreases. Thus, transgression events can be related to a persistent PZA, and highstand events can be related to a high Pr/Ph and AIR ratio indicating episodic PZA as is the case of LLIA core (Figure 89).

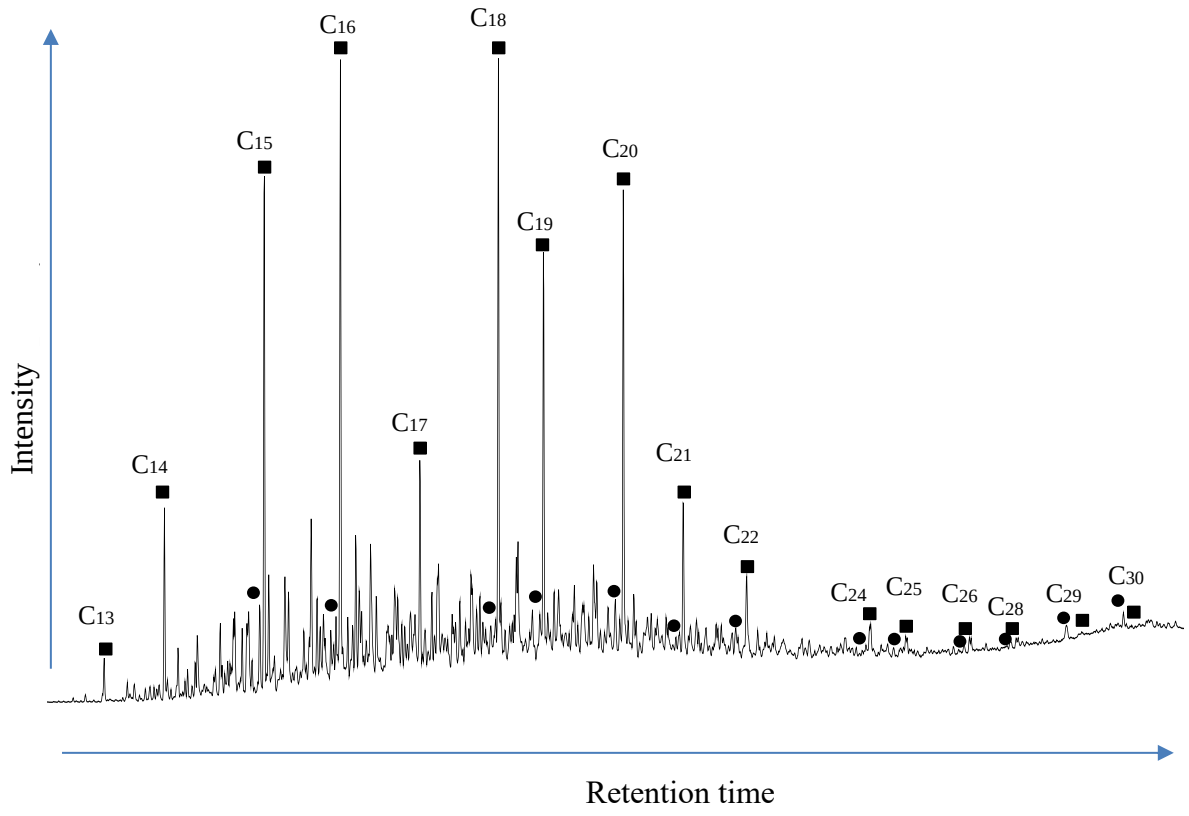

Figure 88. Summed mass chromatograms of m/z 133, 134 of the B&C fractions showing the aryl isoprenoids distributions of the La Luna samples. (filled squares = 2,3,6-trimethyl substituted aryl isoprenoids, filled circles = 3,4,5- trimethyl substituted aryl isoprenoids. Number of carbon atoms is indicated above each peak)

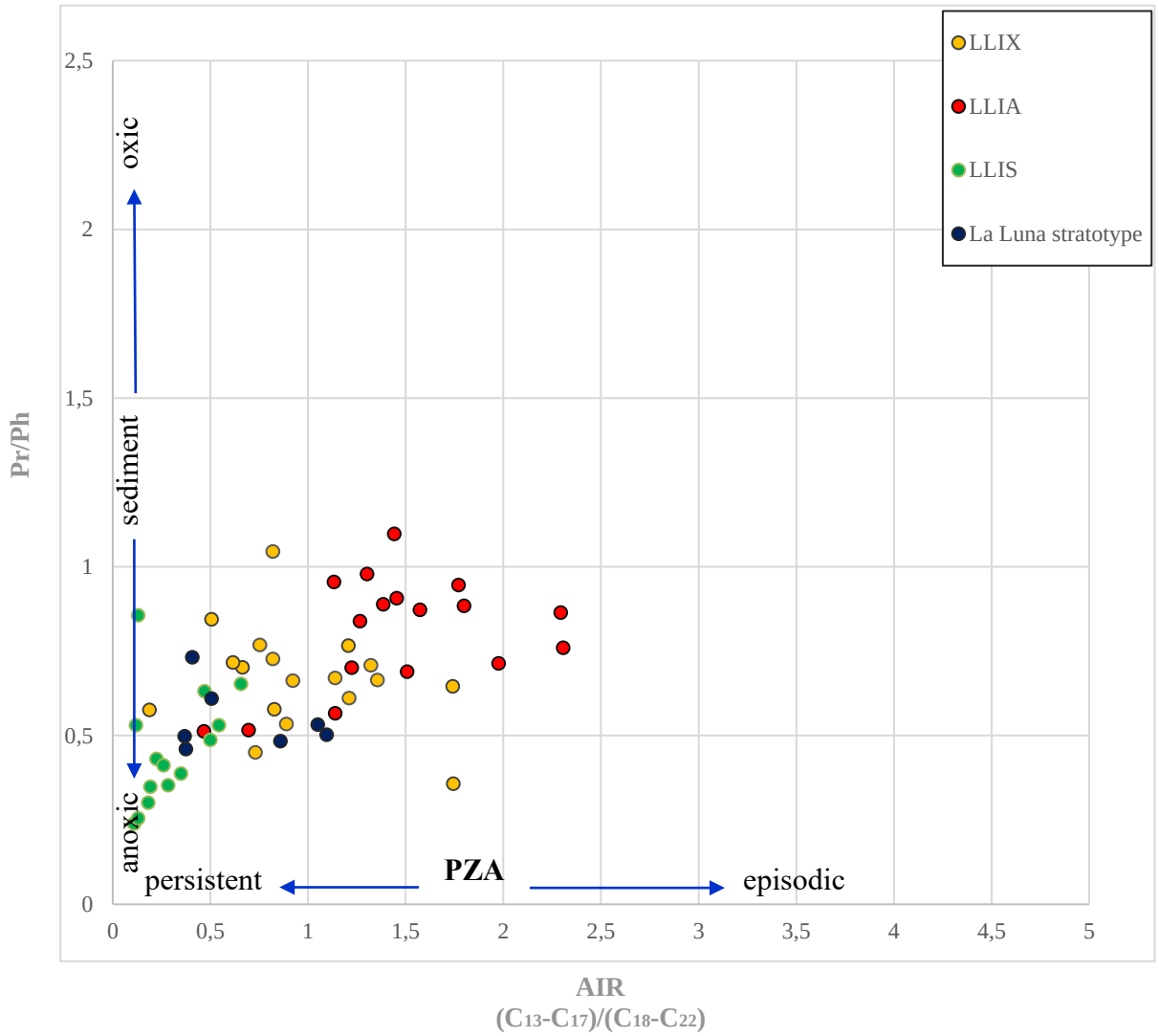

Figure 89. AIR versus Pr/Ph plot for the La Luna samples. Plot template from Schwark and Frimmel, 2004).

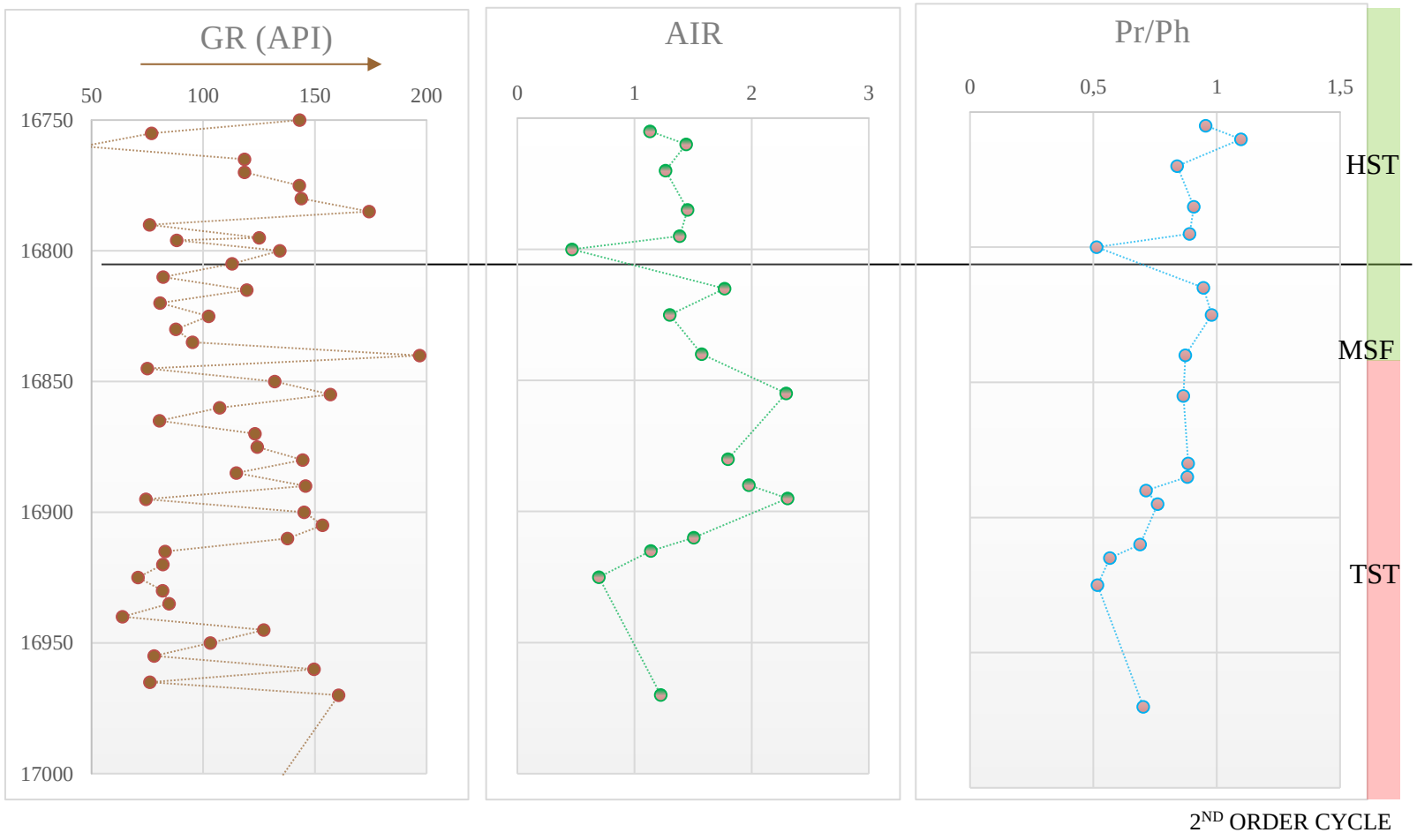

Figure 90. Gamma ray log and geochemical logs of the Pr/Ph aryl-isoprenoids ratio for the LLIA.

4.3.4 Monoaromatic Steroid Hydrocarbons

The occurrence of aromatic steroid hydrocarbons was first mentioned by Tissot et al. (1972) who documented their potential as a geochemical parameter (Tissot et al., 1974; Riolo et al., 1986). Monoaromatic steroid hydrocarbons (MAS) are derived from sterols containing a side-chain double bond during diagenesis (Riolo et al., 1986). Monoaromatic steroid hydrocarbons were identified in the branched and cyclic hydrocarbon fraction of the La Luna Formation rock extracts through SIM/GC-MS by the analysis of the m/z 253.3 ion (Figure 90). Variations in the depositional environments are reflected in the relationship of the C_{27}, C_{28}, and C_{29} monoaromatic steranes ternary plot (Figure 91).

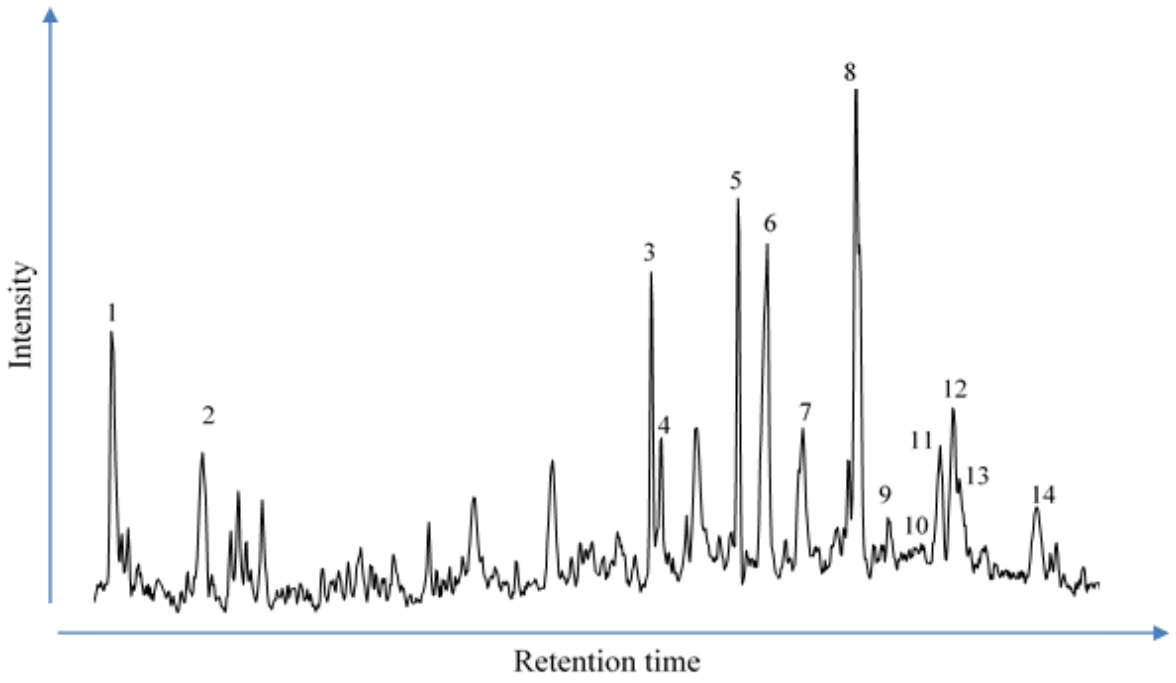

Figure 91. Partial fragmentograms of the m/z 253.3 ion showing distribution of the monoaromatic steroids (MAS) in the B&C fractions of the LLIS samples. Peak identification is presented in Table 9.

Monoaromatic steroid ternary plot commonly distinguishes oil and bitumen samples derived from non-marine versus marine shale source rocks. Oils and bitumens derived from marine organic matter contain greater amounts of C_{28} MAS than those of non-marine origin. Alternatively, oils derived from marine carbonate source rocks contain higher amounts of C_{29} MAS than oils derived from marine shales (Moldowan et al., 1985). Furthermore, non-marine oils are associated with high amounts of the C_{27} homologs and these oils generally are related to source rocks deposited under algal-dominated lacustrine settings, with small amounts of plant input. Therefore, these ternary plots are mainly used to differentiate marine and non-marine source rocks.

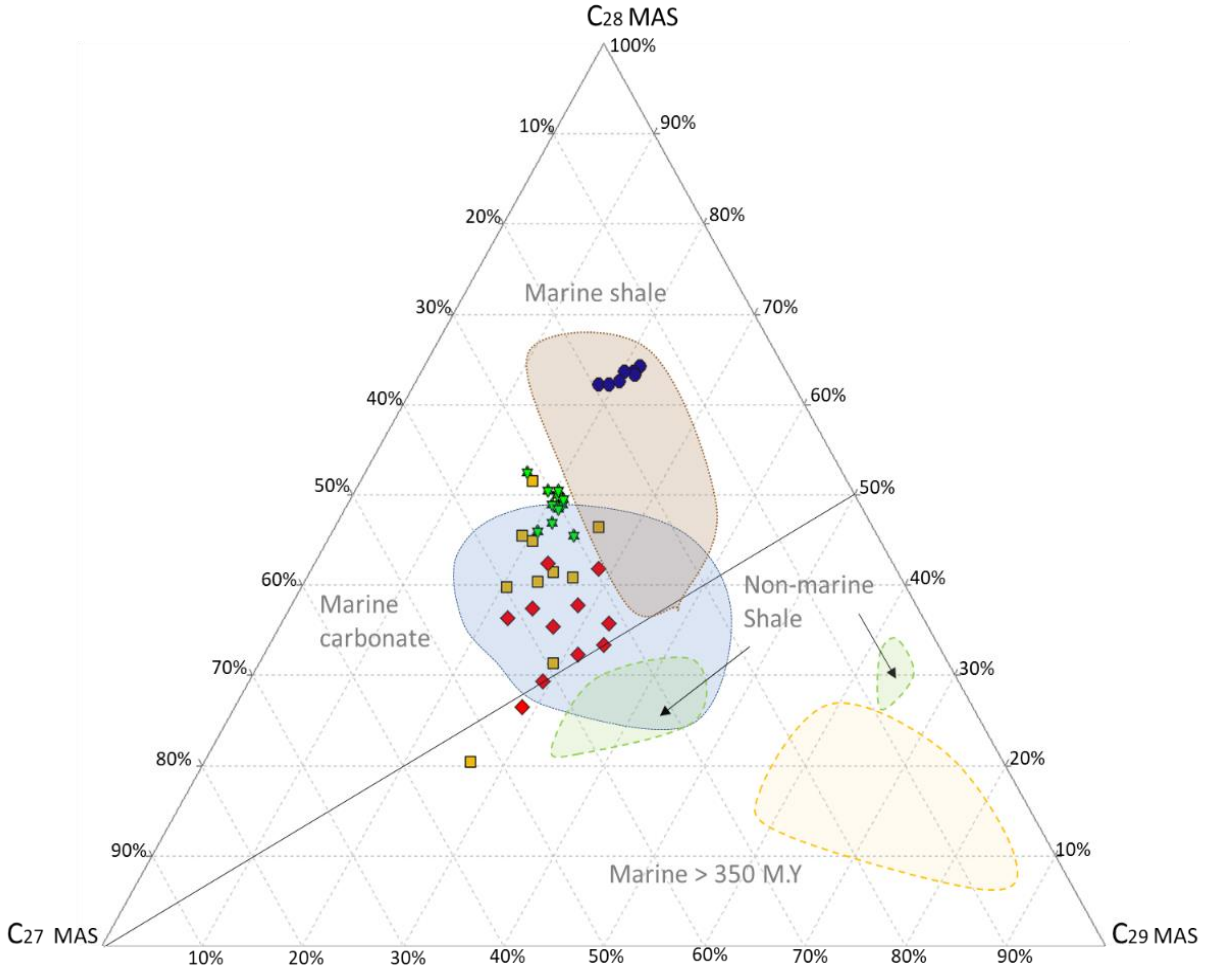

Figure 92. Ternary diagram of C_{27}, C_{28}, and C_{29} monoaromatic steroids for La Luna samples (Plot modified from Moldowan et al., 1985).

The ternary plot reflects a higher proportion of C_{28} and C_{29} MAS for most of the samples, and according to the Moldowan et al. (1985) classification, most of the samples (LLIX, LLIA, LLIS) with exception to the La Luna stratotype are marine carbonates. According to the MAS plot, the La Luna stratotype is classified as a marine shale, but possibly these values reflect the weathering and clay content that is present in the outcrop samples since according to the XRD analysis, the La Luna stratotype mineralogy is predominately a marine carbonate. Overall, their distribution is similar to the one displayed by the regular steranes (Figure 66), indicating a marine source for all the samples.

Table 9. Identification of monoaromatic steroids (MAS) in the partial m/z 253.3 fragmentograms of the branched and cyclic fractions.

Peak number	Compounds name
1	Pregnane
2	20-Methylpregnane
3	5β-Cholestane 20S
4	Diacholestane 20S
5	Monoaromatic steroid
6	5β-Ergostane 20S + C_{28} Diaergostane 20S
7	5α-Cholestane 20R
8	5α-Ergostane 20S
9	5β-Ergostane 20R + C_{28} Diaergostane 20R
10	5β-Stigmastane 20S + C_{29} Diastigmastane 20S
11	5α-Stigmastane 20S
12	5α-Ergostane 20R
13	5β-Stigmastane 20R + C_{29} Diastigmastane 20R
14	5α-Stigmastane 20R

4.3.4 Dibenzothiophene, phenanthrene and pristane, phytane as indicators of the depositional environment

Dibenzothiophenes and phenanthrenes are found in oils and rock extracts and are predominant in sulfur-rich environments.The ratio of dibenzothiophene/phenanthrene along with pristane/phytane ratios have been known since the 1990s to evaluate the availability of reduced sulfur for incorporation into organic matter and to characterize paleo-depositional environments (Hughes et al., 1995). Hughes et al. (1995) proposed the relationship of the dibenzothiophene/phenanthrene and pristane/phytane ratios which provide a powerful way to infer crude oil source rock depositional environments and lithologies since they can characterize the different Eh-pH regimes which are a consequence of the microbiological and chemical processes that occur during the deposition and early diagenesis of sediments. A plot of the DBT/P and Pr/Ph ratios (Figure 92) shows that all the samples from La Luna Formation fell on the Marine carbonate-marine marl, lacustrine sulfate-rich and anoxic marine deposits.

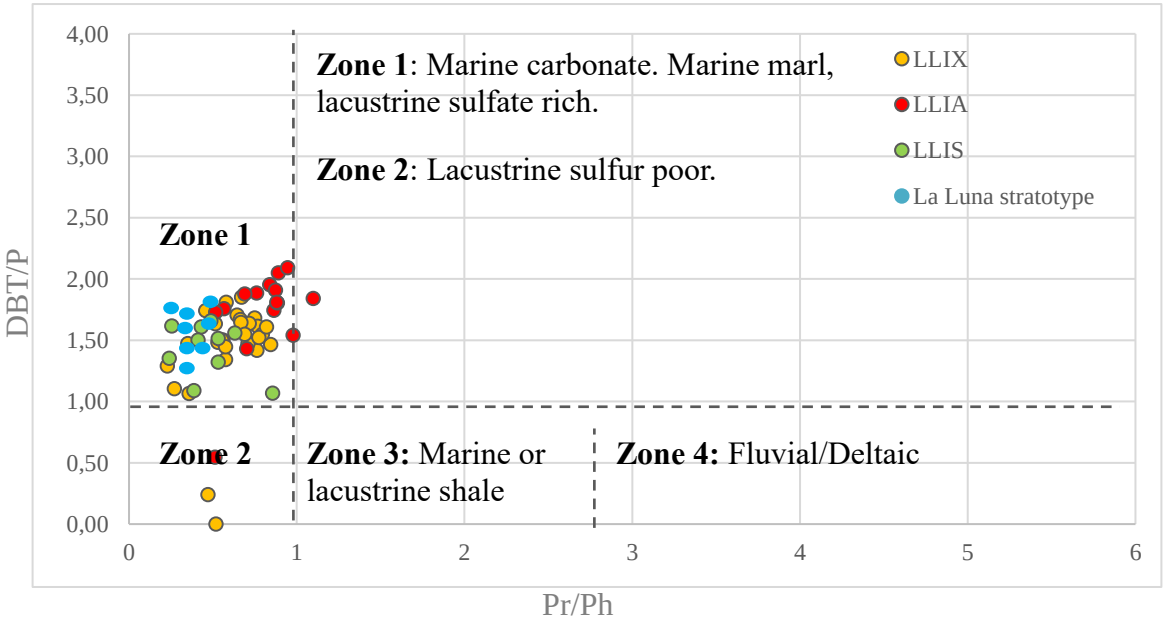

Figure 93. Ratio **of dibenzothiophene to phenanthrene (DBT/P) plotted against the ratios of pristane to phytane (Pr/Ph) to determine shale depositional environments in La Luna Formation.**

4.4 Evaluation of thermal maturity based on biomarker distribution

4.4.1 Steranes (m/z 217)

Biomarkers rarely retain their original chemical structure because of diagenetic alterations in the water column and shallow sediments as the effects of temperature with deeper burial (Lillis, 1992). Subsequently, it is often difficult to correlate a biomarker found in the geosphere with a specific source organism. However, in some cases, the biomarker reaction pathway from the biological form found through several diagenetic steps to the most stable form has been studied in detail (De Leeuw & Bass, 1986).

The R configuration progressively changes with increasing maturation and is converted to a mixture of R (biological) and S (thermal) isomers (Peters et al., 2005). Certain biomarker ratios have been related to thermal maturation of organic matter, vitrinite reflectance, and the generation of petroleum (Mackenzie et al., 1980; Radke et al., 1980) and consequently have been utilized as thermal maturity indicators for petroleum and source rocks in sedimentary basins.

Waples & Machihara (1991) indicate that 20R and 20S epimers of steranes provide a very important maturity assessment along with other biomarkers. They proposed that the ααα form of the 20-R configuration is the biologically derived form of the steranes and with increasing maturity, 20R configuration decomposes with increasing 20S concentration. The C_{29} (ααα20S)/(ααα20S + ααα20R) steranes ratio in Figure 93, ranges from 0 to 0.5, with increasing thermal maturity, reaching equilibrium at 0.52-0.55 (Seifert & Moldowan, 1986).

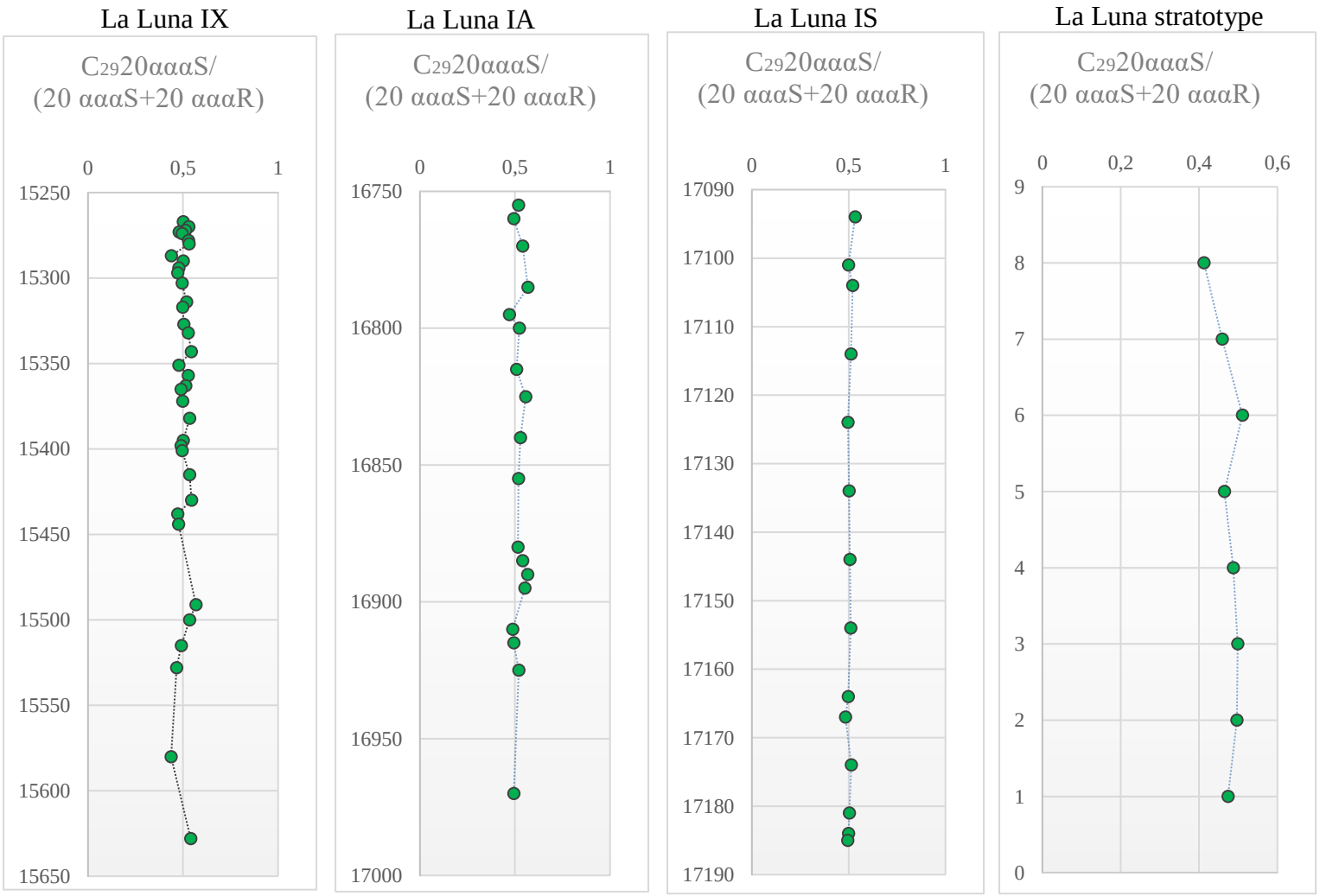

Figure 94. C_{29}(ααα20S/ ααα20S + ααα20R) vs. depth showing the maturity variation through the La Luna subsurface wells.

The plots presented for the La Luna Formation samples do not display any significant changes with depth in any core, with values ranging from 0.5-0.6 for all cores. Calculations of these maturity ratios for the La Luna Formation samples shows that all samples are thermally mature along all cores (Figure 94).

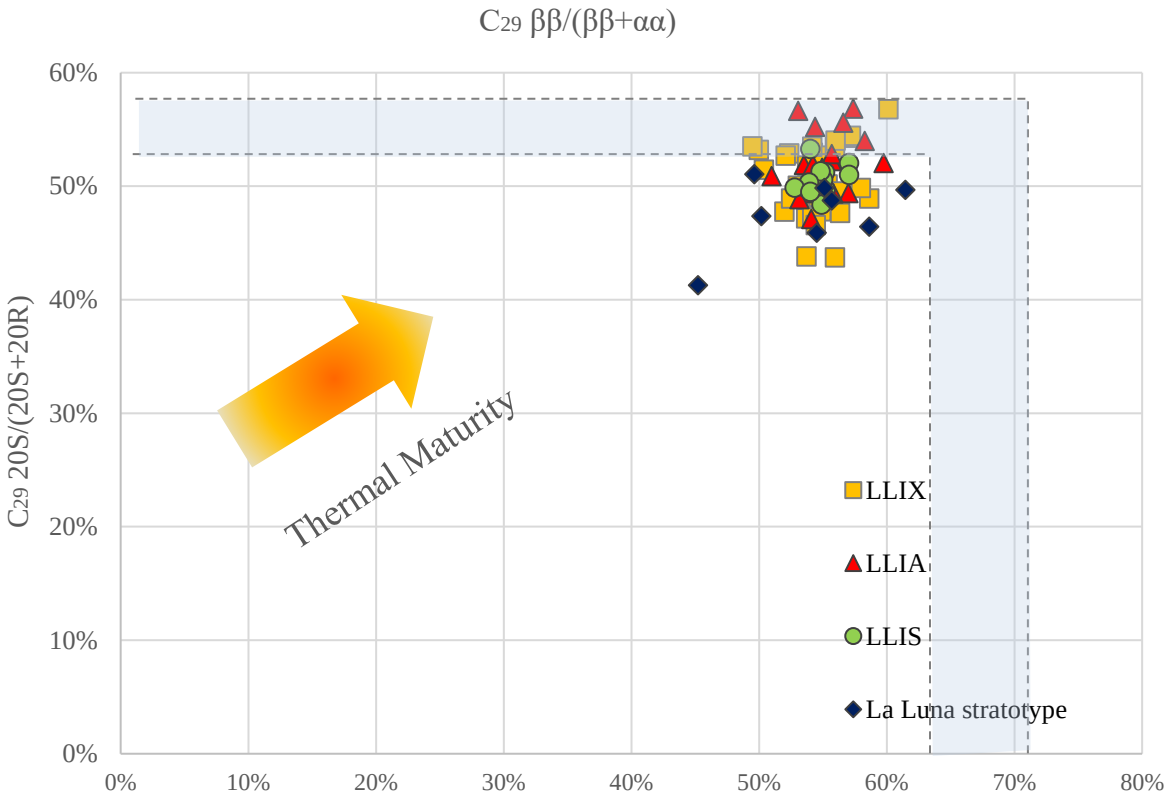

Figure 95. Plot of C_{29} ββ/(ββ+αα) steranes vs. C_{29} 20S/(20S+20R) steranes displaying variations of thermal maturity for the La Luna samples (Light blue area is represented by endpoints of isomerization reactions (Plot modified from Peters et al., 2005).

4.4.2 Terpanes (m/z 191)

4.4.2.1 Hopanes

In the terpanes, the 22R and 22S configurations of the homohopanes are useful for maturity assessment by the use of the 17α-homohopanes in the C_{31} 22S/(22S+22R) ratio (Figure 95). The

22R epimer is biologically derived and converted into 22S with increasing maturity (from 0 to 0.6 reaching equilibrium at ratios of 0.57 to 0.62). This conversion occurs during the early stages of organic matter maturation. The isomerization at the C-22 position gradually converts the homohopanes to a mixture of 22R and 22S configurations. The early oil window is represented by values that range from 0.50 to 0.54. Furthermore, late oil window values range between 0.57 and 0.62 (Peters et al., 2005). Ratios of C_{31} 22S/(22S+22R) calculated for the La Luna samples have average 22S/(22S+22R) ratios greater than 0.50, indicating that these samples have reached the main stage of oil generation.

4.4.2.2 Moretanes

Another critical parameter for thermal maturity assessment is the moretane/hopane ratio (Figure 96). The 17β(H),21α(H)-moretanes are thermally less stable than the 17α(H)21β(H)-hopanes, and the C_{29} and C_{30} abundances decrease relative to the hopane when maturity increases. The ratio typically ranges from 0.8 when it is immature with values less than 0.15-0.05 when it is mature (Peters et al., 2005). Hopanoids in organisms have a 17β(H),21(β)H-configuration (ββ), which becomes unstable during organic matter burial and easily converts to βα-moretanes and αβ-hopanes.

Most of the C_{30} moretane/hopane ratios calculated for the La Luna samples range from 0.08 to 0.09 indicating that all samples except a few ones located in the LLIA are thermally mature. However, the samples found in the LLIA well are not necessarily a product of maturity but in this case, changes in the deposition environment and lithology. Rullkötter& Marzi (1988) describe high values of the moretane/hopane ratios associated with hypersaline source rocks. Furthermore, high values can also be related to transgressive or highstand systems tracts containing a high input of terrigenous organic matter (Isaken & Bohacs, 1995).

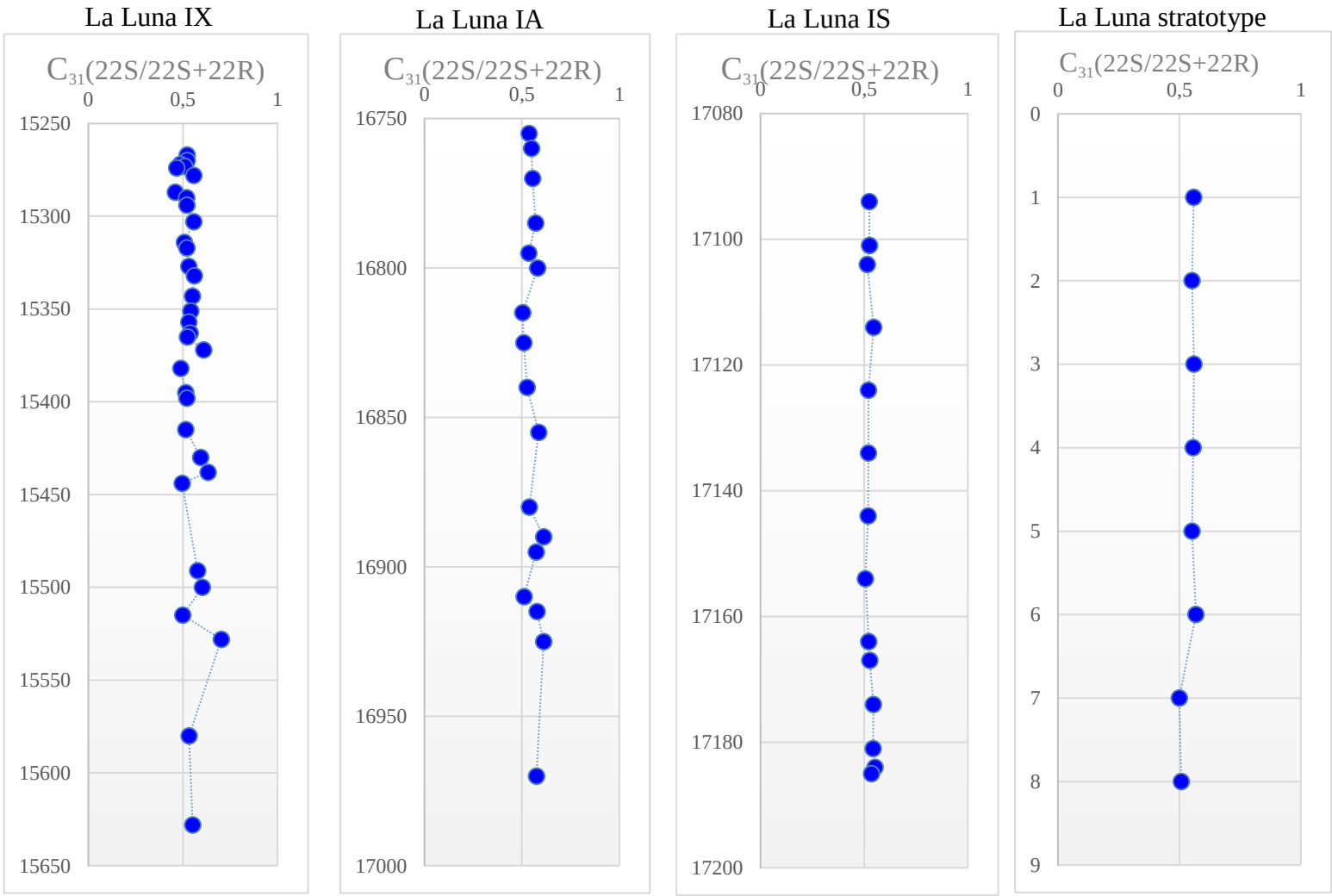

Figure 96. C_{31} 22S/(22S+22R) logs vs. depth in the subsurface and outcrop La Luna samples.

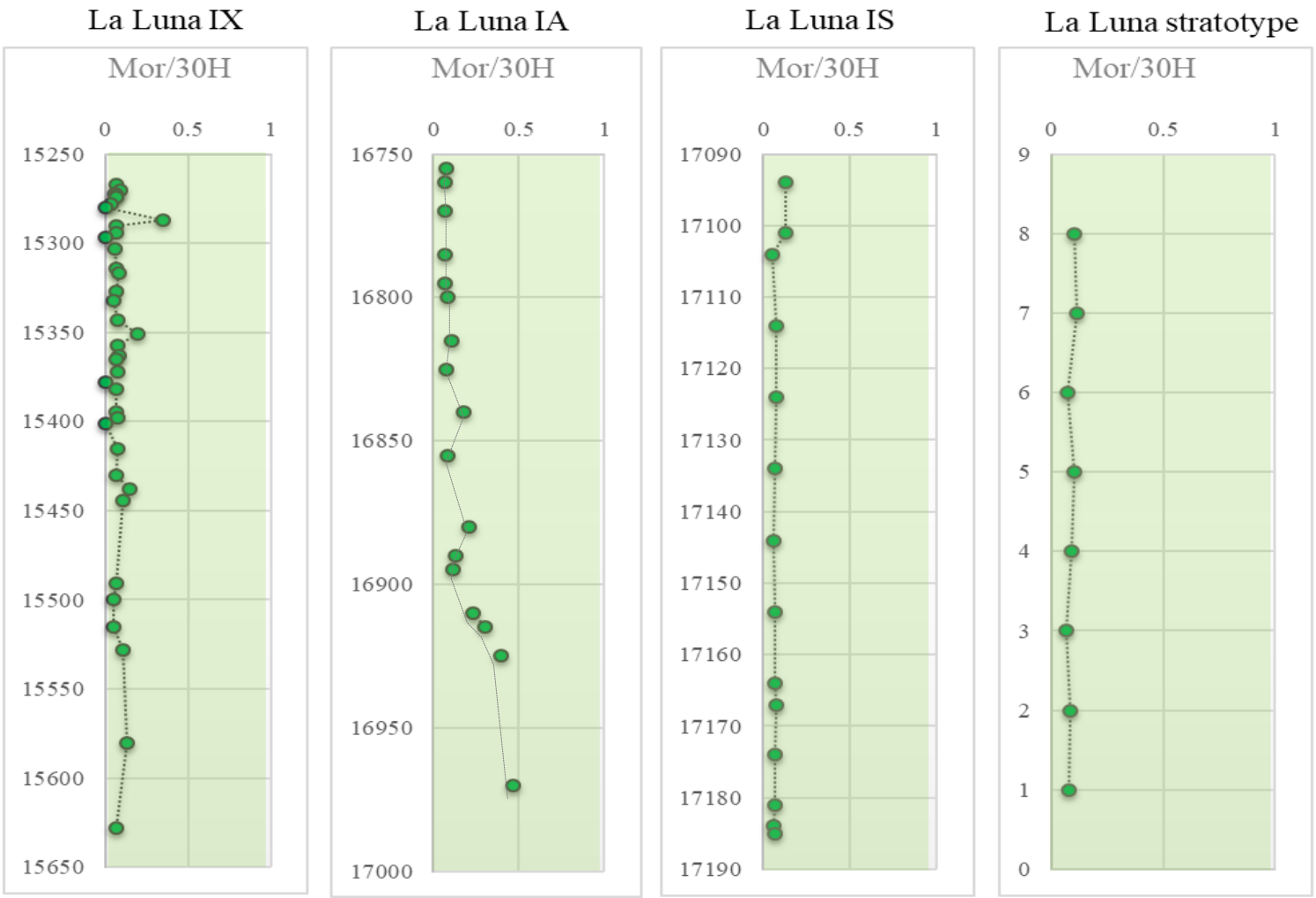

Figure 97. C_{30} moretanes/hopanes logs vs. depth are showing the maturity variation the subsurface and outcrop La Luna samples.

This statement indicates that these high moretanes/hopane values are possibly associated with the increase of clay content in that embayment type that has also been observed in the diasteranes and the inorganic analysis.

4.4.2.3 Ts and Tm

The 18(α)-trisnorhopane (Ts) and the 17(α)-trisnorhopane(Tm) ratio (Ts/Ts+Tm) is another useful parameter for maturity assessment purposes in the immature to the postmature range (Figure 97). Since Ts is more stable than Tm, the ratio is expected to increase with increasing maturity. However, variations in this ratio are not only caused by maturity but by changes in organo-facies (Waples & Machihara, 1991).

The Ts/Tm ratio can be correlated with the diasteranes/diasteranes+regular C_{27} steranes to assess thermal maturity and characterize depositional environments in the La Luna data (Figure 98). The relationship between these two parameters reveals three different groups. The first group of samples are from LLIX, LLIS and some from LLIA and LLIS suggesting bitumens derived from low maturity carbonate source rocks deposited under anoxic conditions. The second group is composed of most of the La Luna stratotype samples indicating bitumens derived from low maturity, in carbonate-clay rich source rocks deposited under anoxic conditions. Lastly, the third group encompasses the LLIA samples that are located in the embayment with diasteranes/(diasteranes+regular) C_{27} sterane ratios and the Ts/Ts+Tm ratios are slightly higher than the other groups.

The differences suggest that the rocks that sourced these bitumens were at a higher level of maturity and are more clay-rich than the other samples. The geochemical ratios based on terpanes in the branched and cyclic hydrocarbon fractions of the La Luna are given in Appendix 7.7.

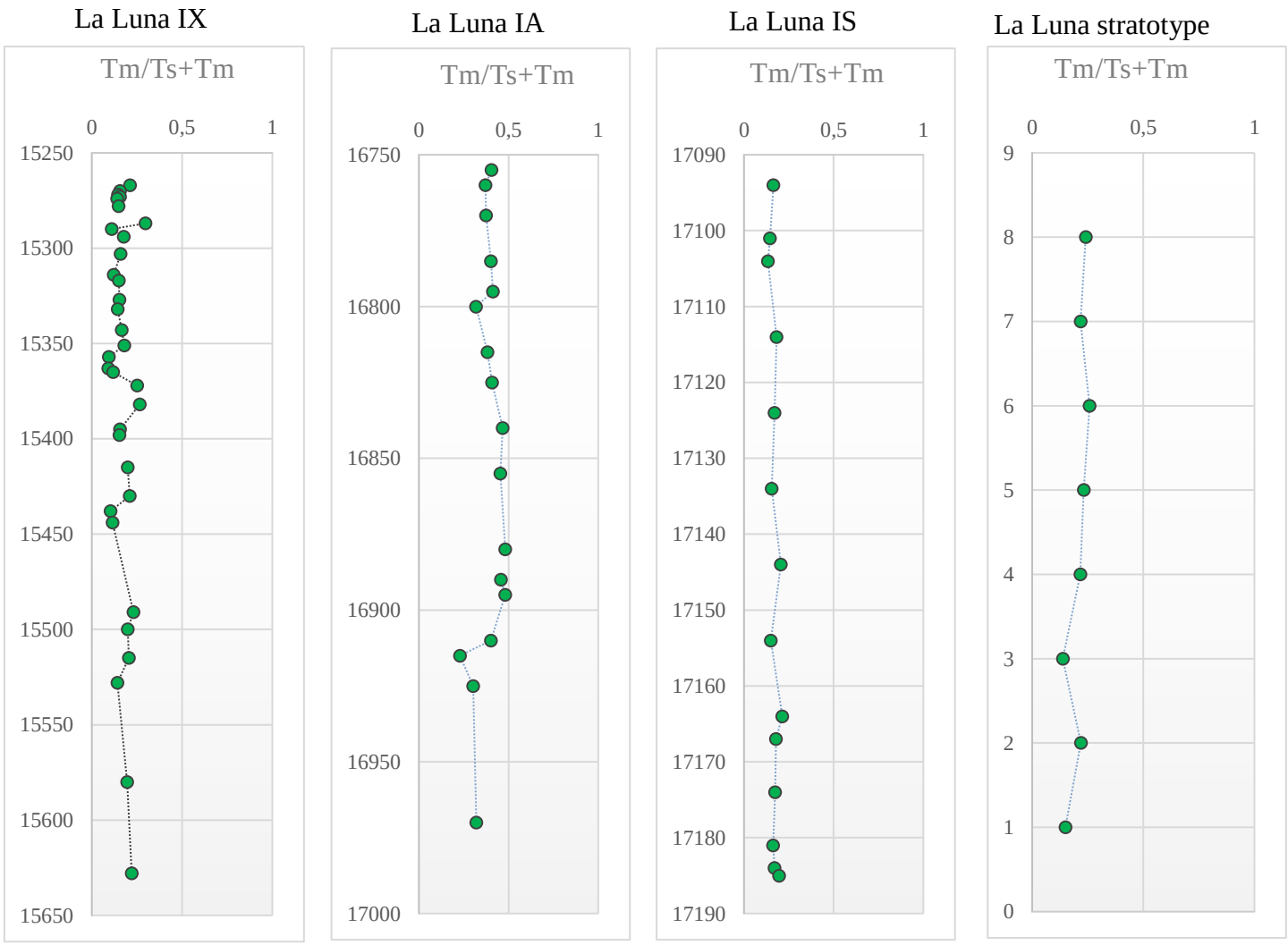

Figure 98. T_s/T_s+T_m logs vs. depth showing the maturity variation the subsurface and outcrop La Luna samples.

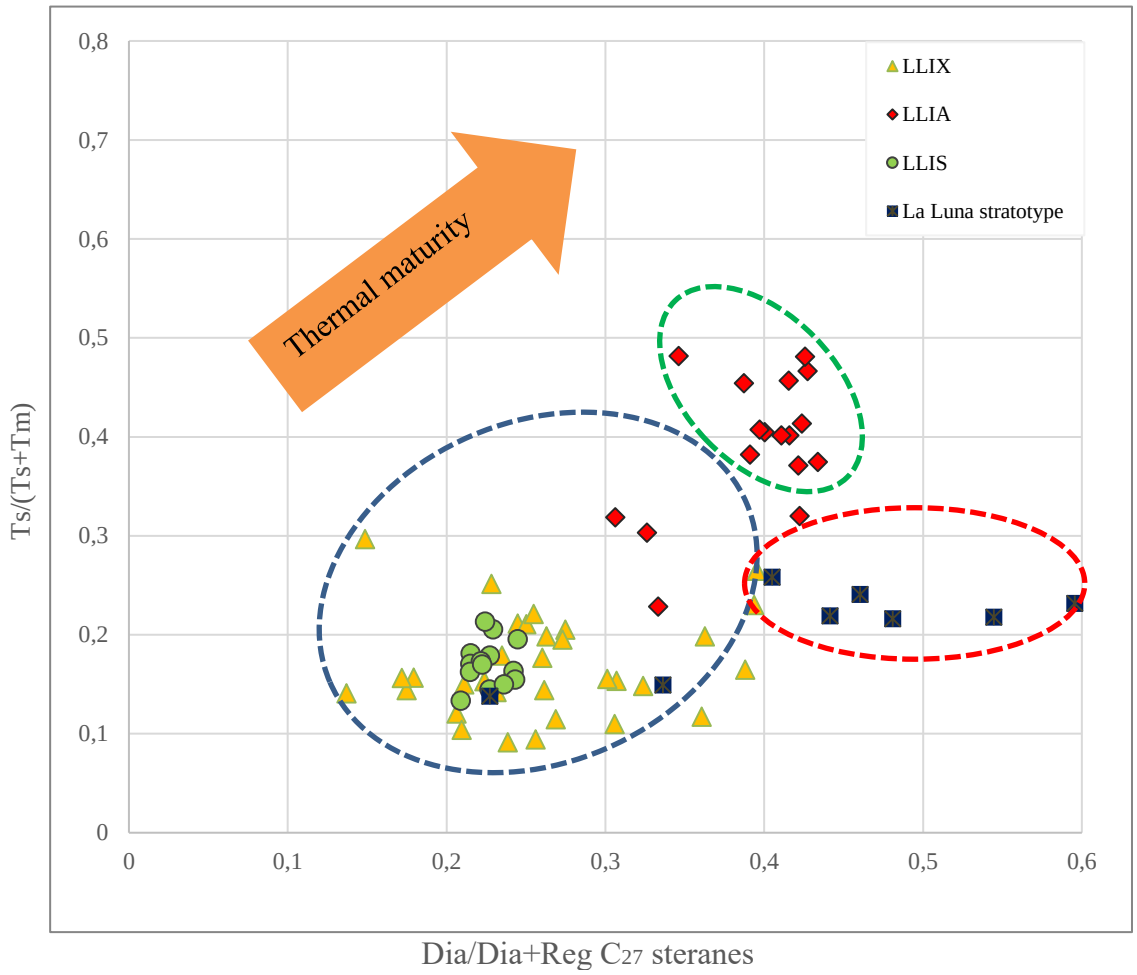

Figure 99. Plot of diasteranes/(diasteranes+regular) C_{27} Steranes versus Ts/(Ts+Tm) ratios displaying a variation in thermal maturity, source, and redox potential for the La Luna samples (Plot modified from Moldowan et al., 1994).

4.4.2.4 Monoaromatic and Triaromatic Steroids

Triaromatic steroids hydrocarbons (TA) are derived from the A-ring monoaromatic (MA) steroids with increasing maturity and aromatization of B and C rings and loss of methyl group at the A/B junction and the stereocenter at C-5 (Mackenzie, 1984; Miceli-Romero, 2014). Monoaromatic and triaromatic steroids hydrocarbon distribution were determined for all the B&C and aromatic fractions of the La Luna Formation rock extracts (Figure 90 and 99). Peak

identification was developed by the analysis of m/z 231.3 chromatograms obtained by GC-MS (Figure 99). Selected fragmentograms of MAS and TAS are presented in Figures 90 and 99 and peak identifications are in Table 10. Geochemical ratios for aromatic biomarkers of the La Luna formation of all samples are in Appendix 7.19. Identification of these compounds was achieved by comparison with reference mass chromatograms published by Miceli-Romero (2014) for the Eagle Ford shale (age equivalent formation).

Thermal maturity evaluation for immature to early oil window rock extracts (Ro~0.8%; Peters et al., 2005) can be assessed by the TA28/(MA29+TA28) ratio which increases with maturity and ranges from 0 to 100%. Furthermore, thermal maturity evaluation for immature to late oil generation for rock extracts and oils can be assessed by the MA(I)/MA(I+II) and TA(I)/TA(I+II) ratios (Ro~1.4%; Peters et al., 2005). These ratios (TA28/(MA29+TA28) range from 0 to 100% when maturity increases. Because, the triaromatic steroids are formed by the monoaromatic steroids, the TA(I)/TA(I+II) ratio is more reliable than the MAS ratio, since it is more sensitive to high levels of thermal maturity (Peters et al., 2005). MAS and TAS ratios (Appendix 7.9) obtained for the La Luna Formation samples indicate that all the samples are marginally mature as suggested by the other maturity parameters previously described.

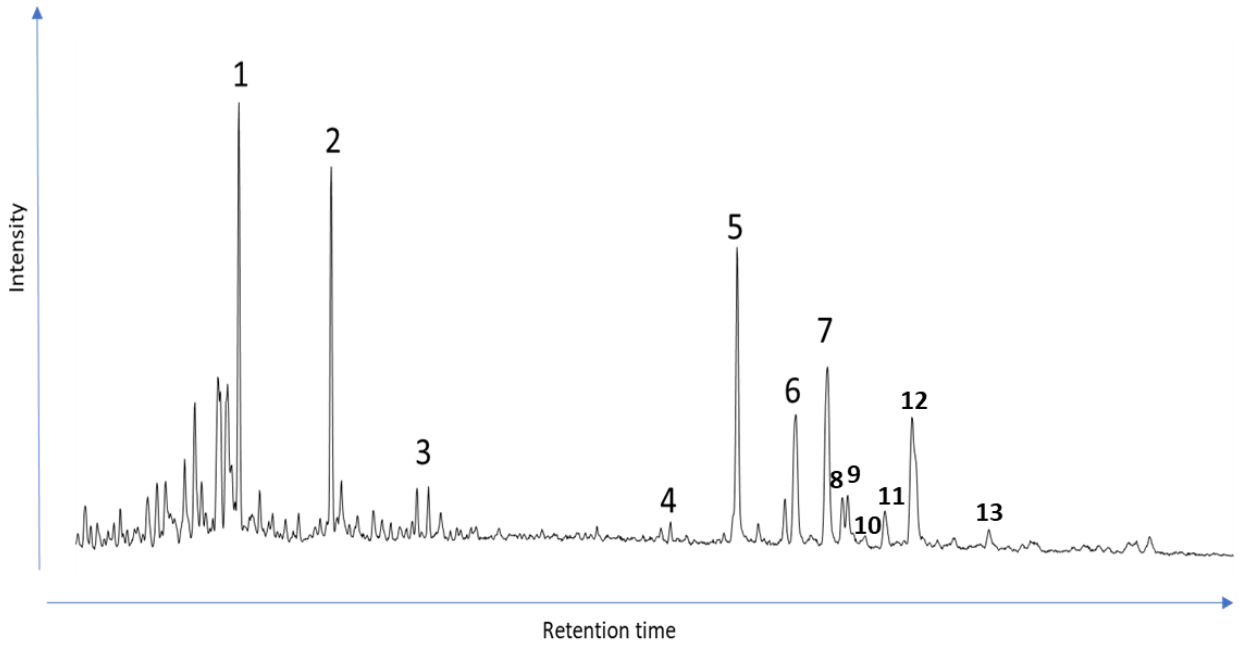

Figure 100. Partial fragmentograms of the m/z 231.3 ion showing the distribution of the triaromatic steroids (TAS) in the aromatic fractions of sample LLIS. Peak identification is presented in Table 10.

4.4.2.5 Phenanthrenes

Due to the higher thermal stability of aromatic hydrocarbons, some useful maturity parameters are based on the isomerization or alkylation–dealkylation processes of substituted phenanthrenes (Stojanović et al., 2001) Phenanthrenes, methylphenanthrenes, and dimethylphenanthrenes play an essential tool for the maturity assessment of the source rocks (Figure 100). (Radke and Welte, 1981; Radke et al., 1984; 1986). The Methylphenanthrene Indices (MPI-1 and MPI-2) are the classical aromatic hydrocarbon maturity parameters that can be used to calculate vitrinite reflectance equivalent (Rc) values for the extracts samples. Phenanthrenes and methylphenanthrenes were determined in the aromatic fraction by SIM/GC-MS monitoring the ions m/z 106.3, 192.3, and 206.3 (Figure 99, Table 11).

Table 10. Identification of triaromatic steroids (TAS) in the partial m/z 231.3 fragmentogram of the aromatic fractions.

Peak number	Compound
1	Pregnane
2	20-Methylpregnane
3	20-Ethylpregnanes (a and b are epimeric at C_{20})
4	Cholestane (20S)
5	Cholestane (20R) + C_{27} Ergostane (20S)
6	Stigmastane (20S) (24-Ethylcholestane 20S)
7	Ergostane (20R) (24-Methylcholestane 20R)
8	Triaromatic 23,24-dimethylcholestane
9	Triaromatic 23,24-dimethylcholestane Triaromatic 24-n-propylcholestane (20S)
10	Triaromatic 24-n-propylcholestane (20S)
11	Triaromatic 23,24-dimethylcholestane
12	Triaromatic 23,24-dimethylcholestane Triaromatic (24-Ethylcholestane 20S)
13	Triaromatic 24-n-propylcholestane (20R)

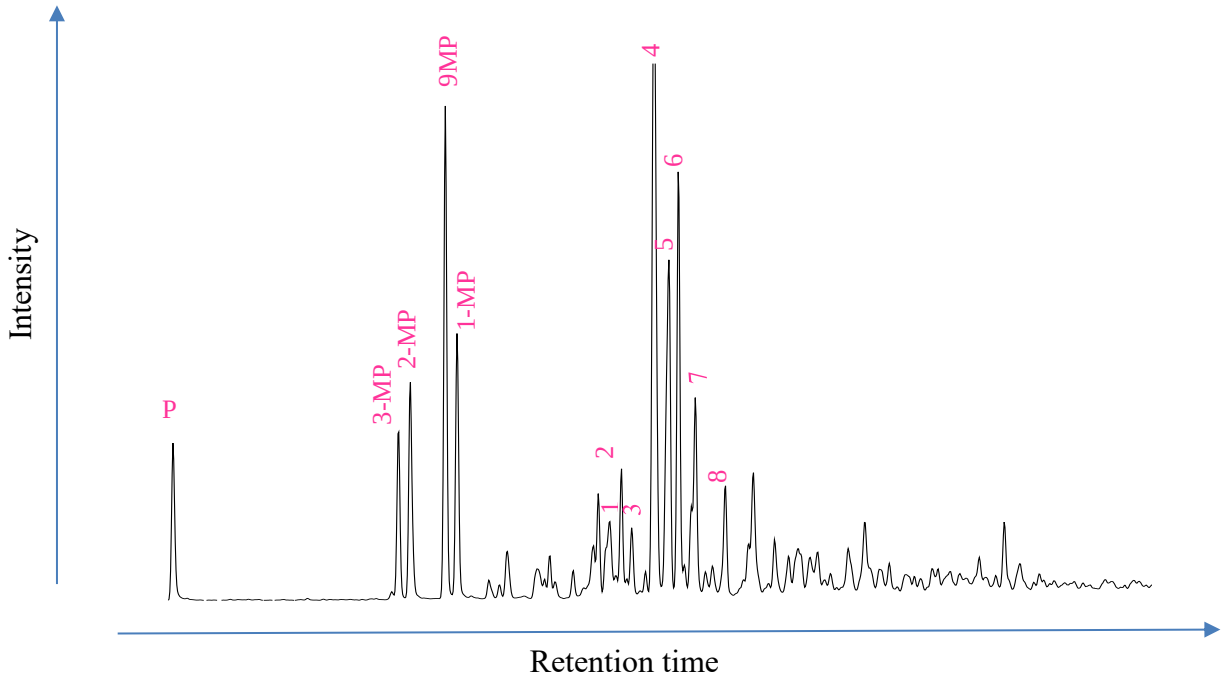

Figure 101. Summed mass chromatograms of m/z 178.3, 192.3, 206.3 ions showing the distribution of phenanthrenes compounds in the aromatic fractions of LLIS sample. Peak identification is presented in Table 11.

It's important to point out that some aromatic hydrocarbons maturity parameters only can be applied in a certain maturity range. For instance, methyl phenanthrene index MPI-1 and MPI-2 show a reversal at higher thermal maturity (Radke et al., 1982). Thus, the equation 5 from Radke & Welte (1981), corresponding to low maturity levels, was used to calculate vitrinite reflectance (Rc) values for the oil samples.

Values of MPI-1 ratios were obtained for the La Luna samples (Appendix 7.9) and, vitrinite reflectance equivalent values were calculated and from the MPI-1 parameter (Table 12). Results indicate that most of the samples are within the oil window (Rc ~0.98-1.10 on average)., showing an agreement with the maturity parameters previously described.

Table 11. Identification of phenanthrenes in the partial mass chromatograms of m/z 178.3, 192.3, 206.3 of the aromatic fractions.

Peak number	Compound name
P	P Phenanthrene
3-MP	3-Methylphenanthrene
2-MP	2-Methylphenanthrene
9-MP	9-Methylphenanthrene
1-MP	1-Methylphenanthrene
1	Dimethylphenanthrene
2	Dimethylphenanthrene
3	Dimethylphenanthrene
4	1,3 + 2,10 + 3,9 + 3,10-Dimethylphenanthrene
5	1,6 +2,9 + 2,5-Dimethylphenanthrene
6	1, 7-Dimethylphenanthrene
7	2,3-Dimethylphenanthrene
8	1,9+ 4,9 +4,10-Dimethylphenanthrene

Table 12. Average of the calculated vitrinite reflectance (Rc) for La Luna Formation samples from MPI-1 values.

Core	MPI-1 (on average)	Rc % Low (on average)
LLIX	1.03	1.02
LLIA	1.18	1.11
LLIS	1.17	1.10
La Luna stratotype	1.02	1.03

4.4.2.6 Maturity assessment based on dibenzothiophene and its methyl-homologs

Dibenzothiophenes are important in maturity determination. DBT is detected by the m/z=184.3 ion and its methyl- homologs (1-MDBT; 2-MDBT;3-MDBT and 4-MDBT are detected in the 198.3 ions. The changes are based on the higher thermal stability of the 4-Methyldibenzothiophene (4-MDBT) with respect to the 1-methyldibenzothiophene (1-MDBT) (Schou & Myhr, 1988). With increasing maturity, a decrease in the amount of the less stable α-substituted isomer (l-MDBT) is observed compared with the amount of more stable β-substituted isomer (4-MDBT) (Radke et al., 1986; Radke, 1988). Standard indices developed by Radke et al. (1988) are somewhat resistant to biodegradation.

The maturity parameter is calculated according to the following equation.

$$MDR = \frac{4 - MDBT}{1 - MDBT} [5]$$

Where:

4-MDBT= 4-Methyldibenzothiophene

1-MDBT= 1-Methyldibenzothiophene

The ratio can be used to calculate equivalent vitrinite reflectance (%Rm) for bitumen extracts using the equation ($Rm=0.40+0.30(MDR)-0.094(MDR)^2+0.011(MDR)^3$.The distribution of the dibenzothiophenes in the representative extracts are shown in Figure 101. Methyldibenzothiophene (1-MDBT), 2 + 3 Methyldibenzothiophene (2 +3-MDBT) and 4-Methyldibenzothiophene (4-MDBT) were identified in all the extracts. This distribution suggests that the bitumen samples are within the oil window. The %Rm averages values for the extracts range from 1.06-1.15 respectively (Table 13).

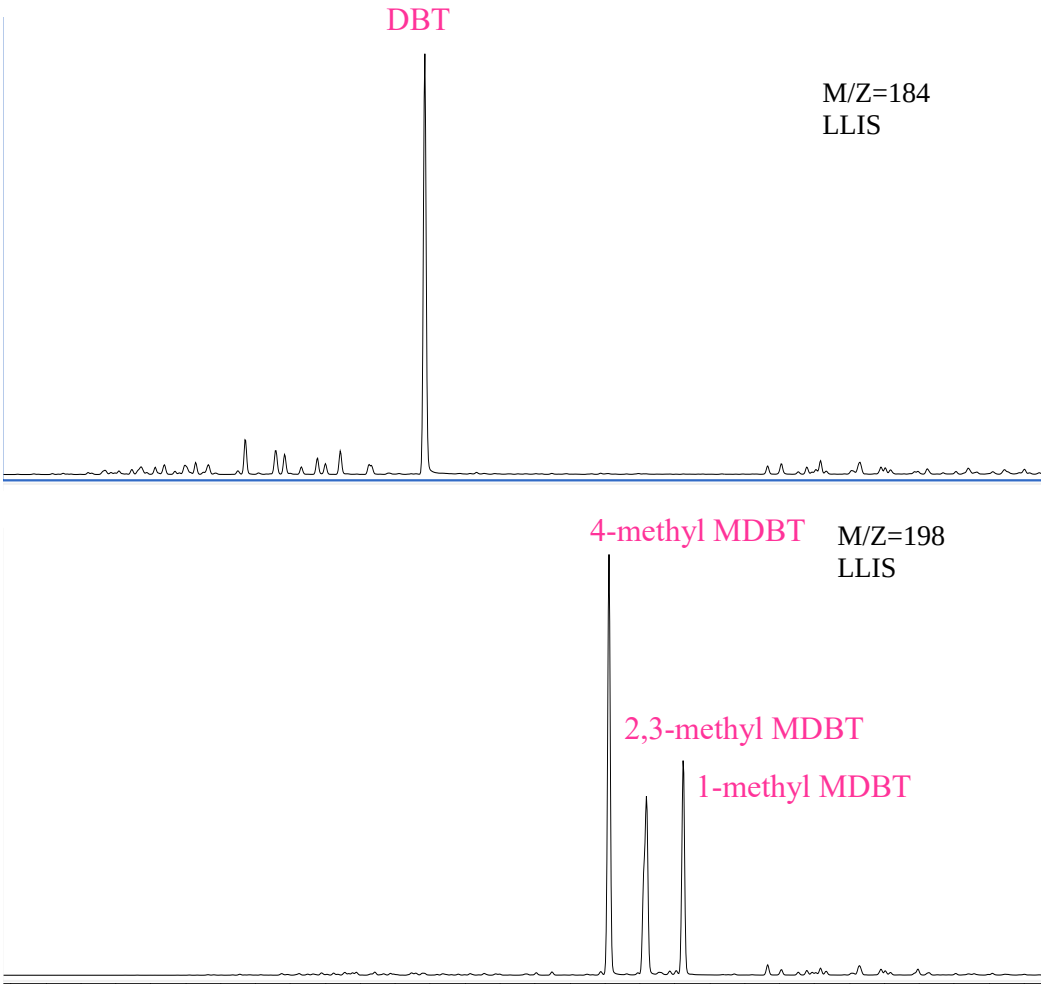

Figure 102. Maturity effect on the distributions of 4-Methyldibenzothiophene (4-MDBT) with respect to the 1-Methyldibenzothiophene (1-MDBT) in La Luna Formation samples.

Table 13. Measured vitrinite reflectance calculated by the 4-Methyldibenzothiophene (4-MDBT) over the 1-Methyldibenzothiophene (1-MDBT) ratio.

Core	%Rm (on average)
LLIX	1.06
LLIA	1.15
LLIS	1.07
La Luna stratotype	1.10

CHAPTER 5

The world's remaining oil and gas resources are becoming more challenging to find and develop. As the industry targets these resources, the need to thoroughly understand and characterize all the components of the prospective petroleum systems becomes very important. In addition, to studying the reservoir, trap, and seal of their prospects, exploration and production companies should also focus on the evaluation of the petroleum generating capacity of the source rock.

In the last years, the multidisciplinary analysis of unconventional resources for source rock evaluation are so linked to organic geochemistry that it is necessary to work and integrate the sequence stratigraphy and some other disciplines (inorganic geochemistry, petrophysics, sedimentology, etc.) for a clearer understanding of these "new reservoirs." Traditional sequence stratigraphic models and analysis (Van Wagoner et al., 1990) have been applied to many of the major unconventional reservoirs. The correct understanding of sequence stratigraphy along with organic geochemistry plays an important role in any project related to exploration of unconventional resources.

5.1 Sequence stratigraphy framework

Shales like the Barnett Shale, Woodford Shale, Marcellus Shale, Haynesville Shale, Eagle Ford Shale, and the La Luna Formation exhibit stratigraphic zonation that indicates at least two superimposed scales of predictable relative sea level cyclicity. Thus, a sequence stratigraphy model is established consisting of a basal erosion surface of underlying strata (sequence boundary, SB) which can be combined with an early transgressive surface of erosion (TSE), generally overlain by an organic-rich transgressive system tract (TST) condensed section (CS) capped by a

maximum flooding surface (MFS), which is overlain by downlapping progradational highstand systems tract (HST) deposits" (Slatt & Rodriguez, 2012).

Currently, the unconventional boom has triggered a different approach in the source rock characterization showing in the last ten years the heterogeneity and the variations of the source rocks that might result from the differences in the depositional environments and anoxic conditions among other factors. This means that the heterogeneity that a source rock presents may generate different parameters that are needed to consider for the analysis of sequence stratigraphy and organic geochemistry in unconventional reservoirs.

5.1.2 Sub-regional sequence stratigraphy and the relative hydrocarbon potential

As is the case with the age-equivalent Eagle Ford Group, La Luna Formation presents a typical gamma-ray log response that diminishes in API progressively upward, indicating a second order sequence that begins with SB/TSE and ends with the HST. It is also represented by a superimposed series of third order sequences of Highstand and Transgressive System Tracts overlying the erosional top of the underlying Maraca Formation, a shallow water carbonate platform with a subaerial exposure surface (Figure 102). The TST of the La Luna Formation sits on this unconformity. According to Slatt et al. (2011), this model is strongly indicative of the shelf upper slope environment of deposition for resource shales. A refined biostratigraphic framework made by Davis et al. (1999) for the same study area allowed the calculation of the third order sequences for the study area for La Luna Formation samples (Liborius, 2015).



Figure 103. La Luna stratotype. Black dashed lines show the erosional contact of the Maraca and overlying La Luna Formation. This image represents the Lower-Middle la Luna formation.

The third order sequences for La Luna have a duration on the order of 1-5 million years that are useful for seismic and well log interpretation at the play and prospect generation levels. (Slatt, 2013).

Biostratigraphy is represented by the presence of *Rotalipora cushmani* and *Whiteinella archaeocretacea* (Late Cenomanian); *Helveroglobotruncan Helvetica- Marginotruncana sigali* (Early-middle Turonian); *Dicarinella primitiva* (late Turonian); *Dicarinella concavata (Conician) and Dicarinella asymmetrical* (Santonian) display that the deposition was generated during the early Cenomanian through Santonian (Figure 103).

The Relative Hydrocarbon Potential (RHP) is an indicator of anoxic and oxic depositional environmental conditions (Fang et al., 1993) and it is used as a paleoenvironmental indicator

assuming that most of the samples are at similar levels of maturity. The relative hydrocarbon potential is calculated using equation 6:

$$RHP = \frac{S1\ mg\ HC/g + S2\ mg\ HC/g}{TOC\ wt.\%} \quad [6]$$

Where:

S1= Free oil content

S2=Potential to generate hydrocarbons

TOC=Total Organic Carbon

It is useful since it also reflects the fluctuations in the oxygen level of the depositional environment and is used instead of the Hydrogen Index because it reduces the influence of organic matter maturation (Gomez, 2014). Any change in S1 and S2 is not caused by maturity changes but reflects changes in the amount of preserved organic matter (kerogen). Therefore, it can be expected that under anoxic conditions in the depositional environment, larger amounts of organic matter (TOC) will be preserved in the sediment and the S2 peak will be higher than under oxic conditions, where less TOC is preserved, and the S2 peak will be smaller. Depths with maximum RHP values (anoxic conditions) correspond with interpreted TST/CS, while minimum RHP values (oxic conditions) correlate with oxidizing conditions due to greater oxygenation of the water column (Slatt and Rodriguez, 2012). The RHP profile of the La Luna Formation is presented in Figures 104,105,106 and 107 describing the main fluctuations of the anoxic/oxic conditions provided by the changes in the S1, S2 and TOC values.

The biostratigraphy and the RHP already generated for this area allowed the calculation of a resolution of 4th order surfaces and seven parasequence sets (Figure 104 to 107). These variations in the RHP curve indicate several cycles of transgression and regression that positively correlate with the proposed transgressive-regressive cycles from the TOC and Gamma ray log. The inorganic-organic geochemical parameters and the GR well log response shown in the previous chapters illustrated that the La Luna Formation is deposited on top of the Maraca Formation (Cogollo Group) unconformity and is overlain by the Colon Formation in the study area.

A gamma ray correlation in the study area allowed the visualization of a "bigger picture" towards a cross-section (Figure 108, 109) demonstrating the paleo-topographic control for some areas of the Maracaibo Basin as was already interpreted in the previous chapters for La Luna Formation in Venezuela and the direction of deposition. The datum was taken where a maximum flooding surface (MFS-2) was interpreted for the end of la Luna Formation based on the work of Liborius (2015). As the author presented it, the general sequence stratigraphic framework of La Luna formation begins (from bottom to top) with an erosional surface that was developed after a relative sea level drop on the Maracaibo platform producing a sequence boundary on the underlying shallow water and karstic platform of the Maraca Formation. Sea level rise in a short period allowed the deposition of marine transgressive and highstand system tract deposits.

The first MFS corresponds to the highest sea level rise during the Turonian (91.5 and 90.3 million years ago; Haq et al., 1987). Another marine regression formed an HST, followed by a set of parasequences developed by the sea level fall and rise. Volcanic ashes seem to be reflected towards the bottom and top of La Luna Formation from all the studied cores. Their origin can be associated with a volcanic arc located on the western margin of northern South America (Parnaud et al., 1995).

The LLIX and the LLIE core is represented by the characteristic glauconite and phosphate deposits from the Tres Esquinas Member but is not present in the LLIA and LLIS. During the Santonian, after the high productivity generated by upwelling currents, low bottom water oxygen content can be found in “the rare molluscan and benthic foraminiferal faunal assemblages which, as stated previously, are known to have been associated with low oxygen levels” possibly forming another maximum flooding surface confirming the final deposition of the La Luna Formation or as named by Elrich et al. (2000) “The end of La Luna sea”. After this period, a regressive trend forms the Colon Formation corresponding to a closure of the Tethys basin and formation of another SB.

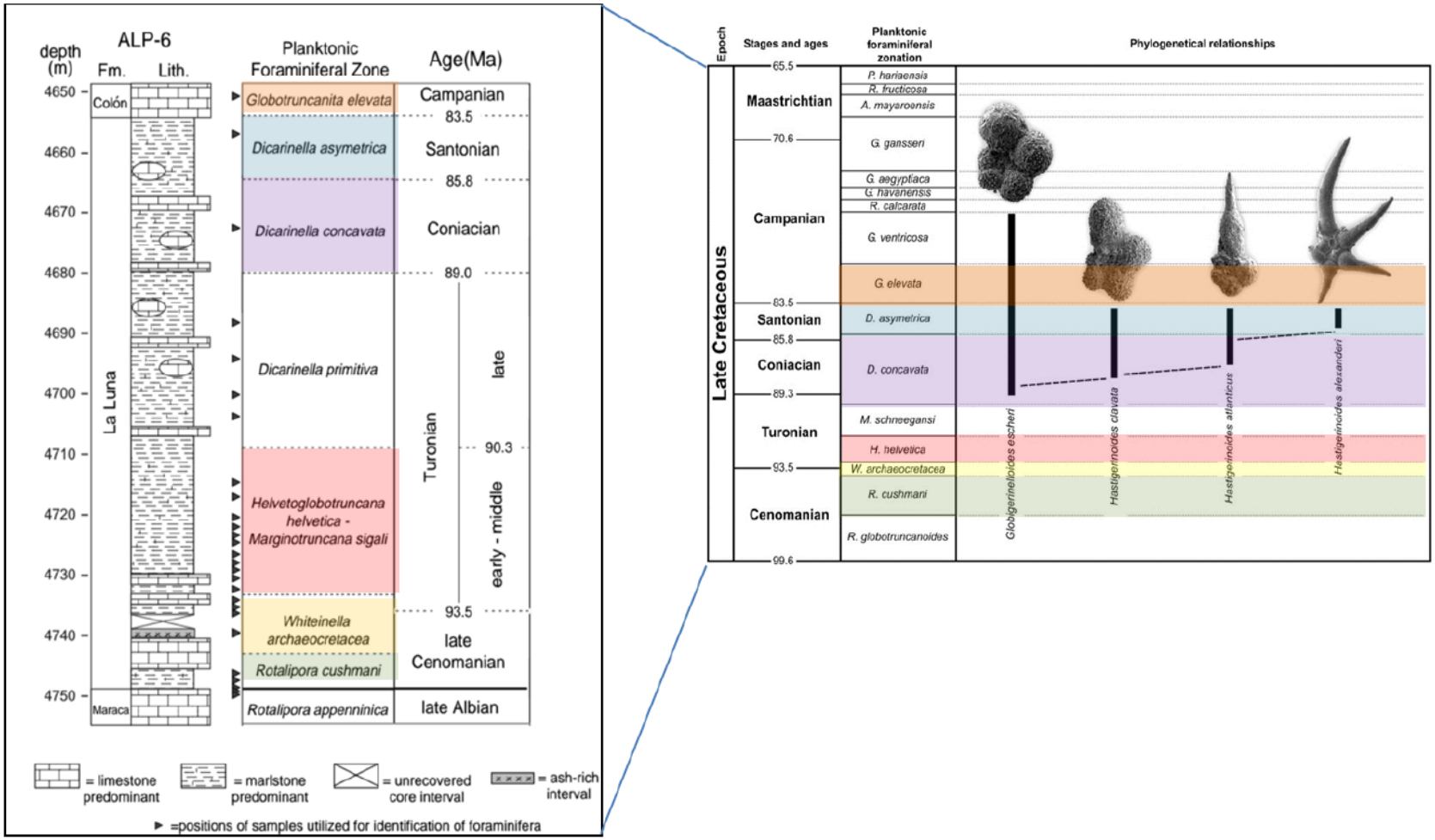

Figure 104. Generalized planktonic foraminiferal biozones, and stage boundaries for the La Luna Formation and surrounding units in La Luna IX. Biostratigraphy is determined after Sliter (1989). B) Age dates for stage boundaries taken from Gradstein et al. (1994), and middle-late Turonian boundary date from Kauffman et al., 1993, Liborius, 2015).

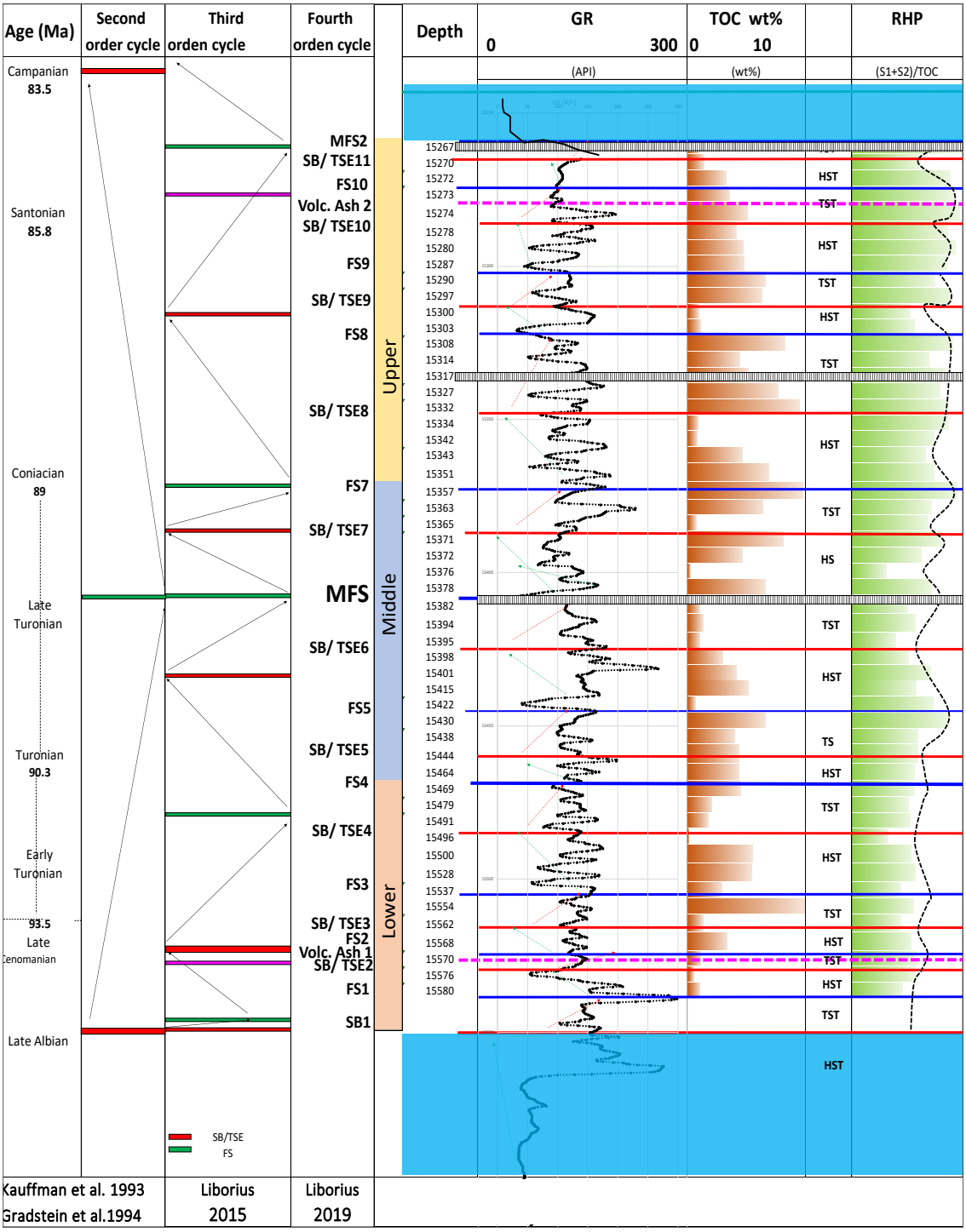

Figure 105. Sequence stratigraphy cycles of the La Luna Formation based on Gamma Ray, TOC and relative hydrocarbon potential (RHP) vs depth for LLIX (HST, highstand systems tract; TST, transgressive systems tract, MFS, maximum flooding surface; FS flooding surface, SB/TSE, Sequence boundary and transgressive surface of erosion).

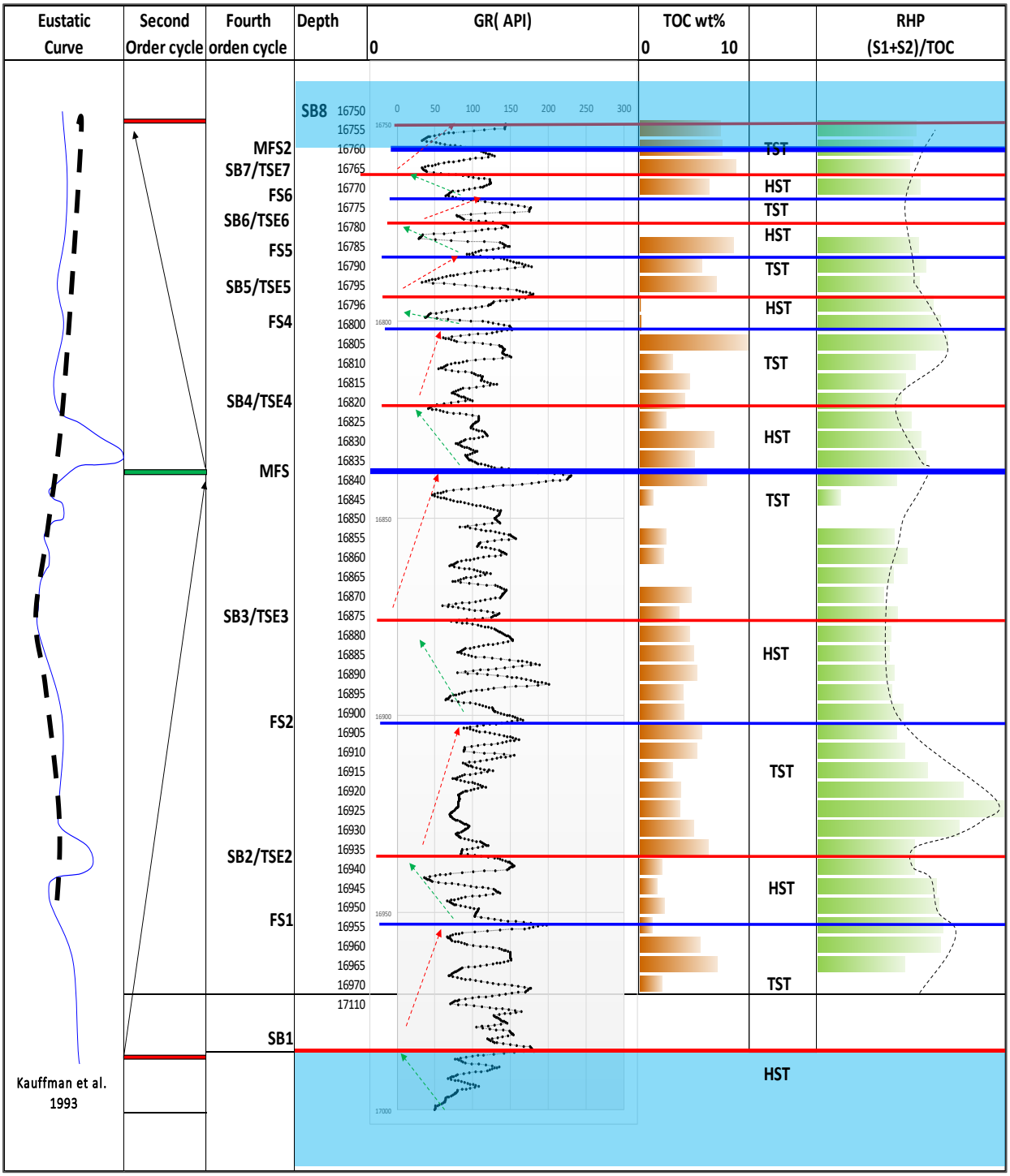

Figure 106. Sequence stratigraphy cycles of the La Luna Formation based on Gamma Ray, TOC and relative hydrocarbon potential (RHP) vs. depth for LLIA (HST, Highstand systems tract; TST, Transgressive systems tract, MFS, maximum flooding surface; SB/TSE, Sequence boundary and the transgressive surface of erosion).

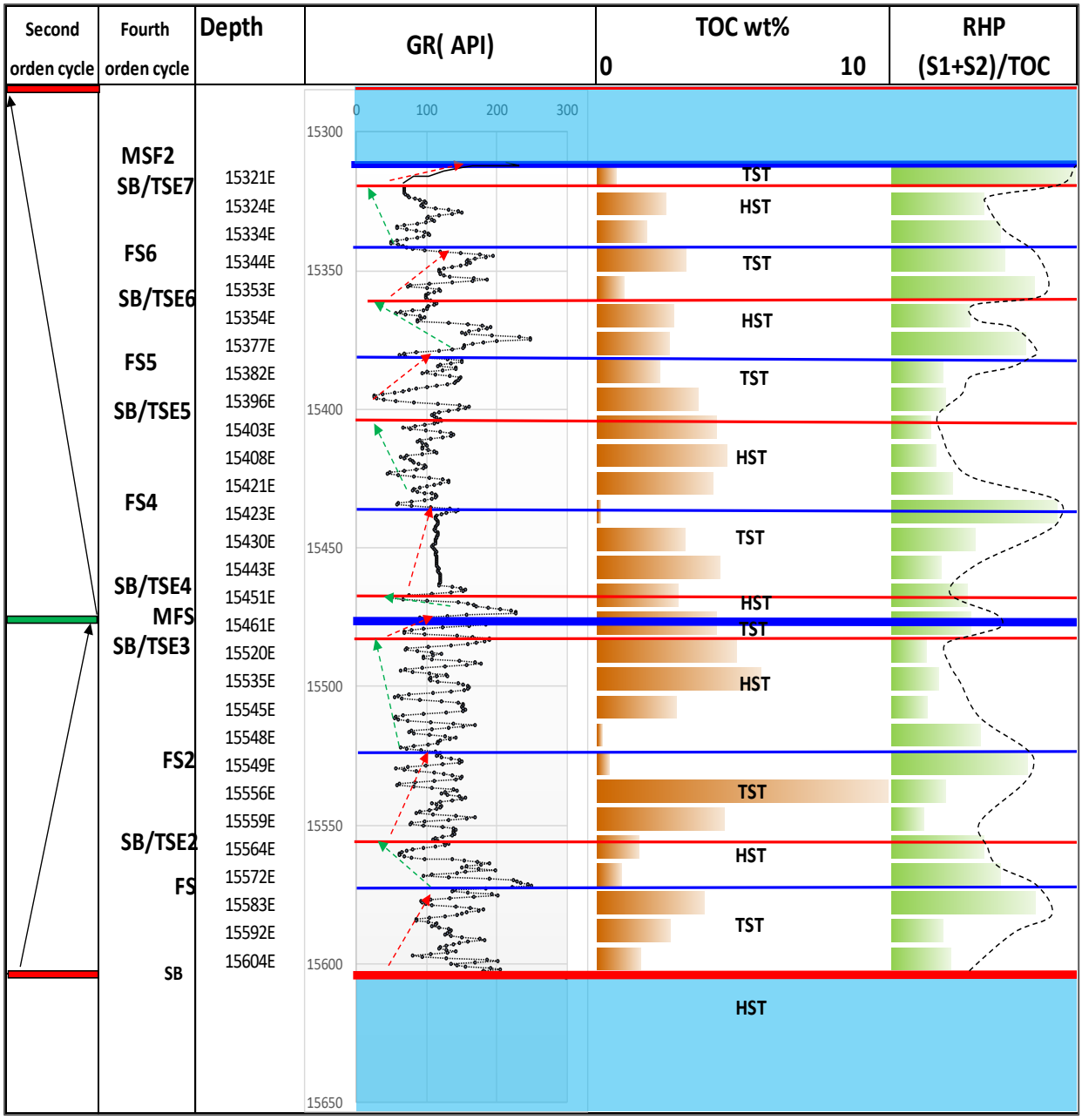

Figure 107. Sequence stratigraphy cycles of the La Luna Formation based on Gamma Ray, TOC and relative hydrocarbon potential (RHP) vs. depth for LLIE (HST, Highstand systems tract; TST, transgressive systems tract, MFS, maximum flooding surface; SB/TSE, Sequence boundary and the transgressive surface of erosion).

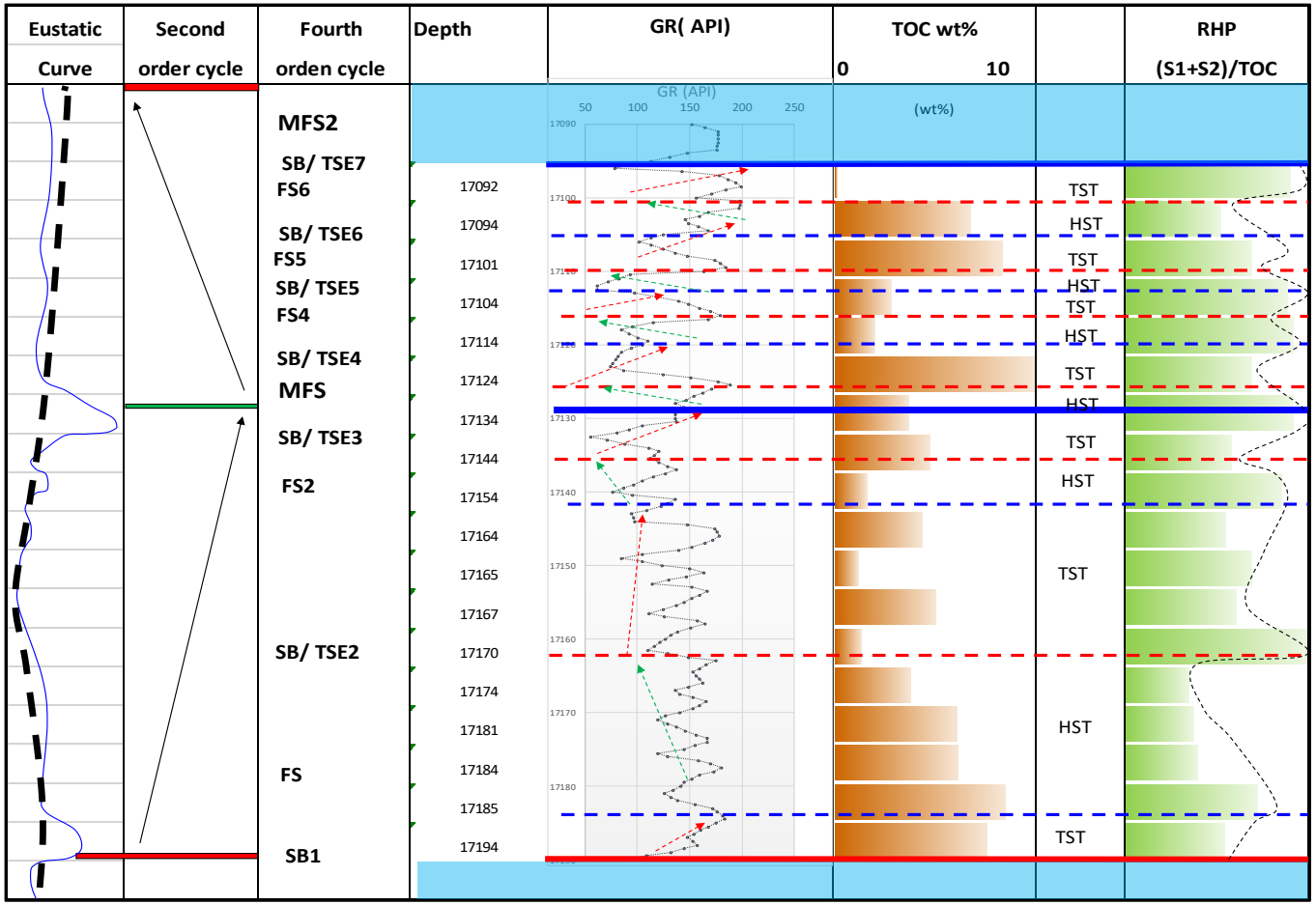

Figure 108. Sequence stratigraphy cycles of the La Luna Formation based on Gamma Ray, TOC and relative hydrocarbon potential (RHP) vs. depth for LLIS (HST, Highstand systems tract; TST, transgressive systems tract, MFS, maximum flooding surface; SB/TSE, Sequence boundary and the transgressive surface of erosion). Dashed lines are the proposed surfaces for this core due to the low sampling density.

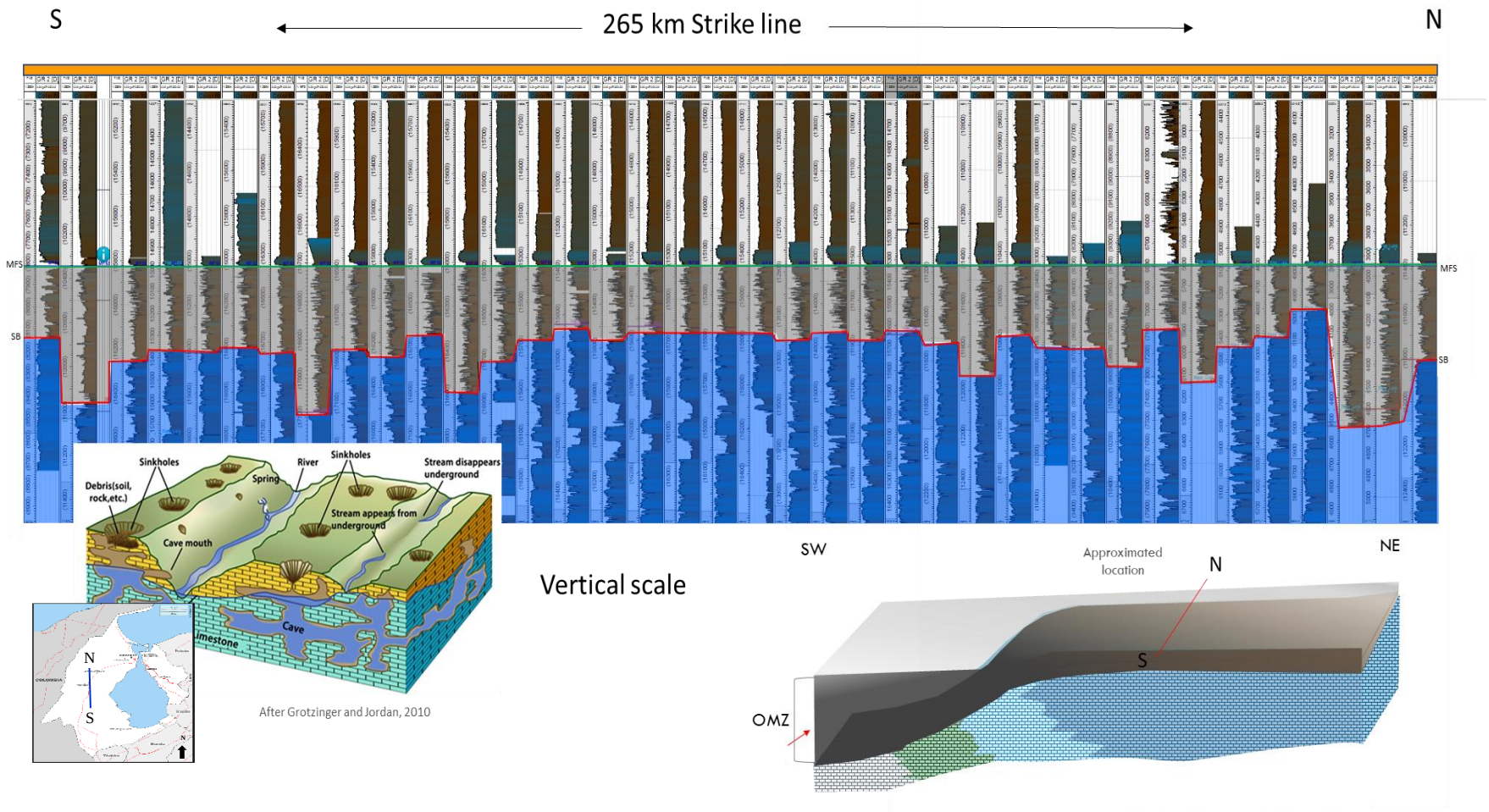

Figure 109. N-S Stratigraphic cross section in La Luna 1X well using the second MFS (green line) as a stratigraphic datum. Red line represents the main unconformity of the Cogollo Group (Maraca Formation) with La Luna Formation. This cross section displays how the paleo-topography of the Cogollo Group controls the deposition of La Luna Formation Venezuela in the NE-SW Trend of the Maracaibo Basin.

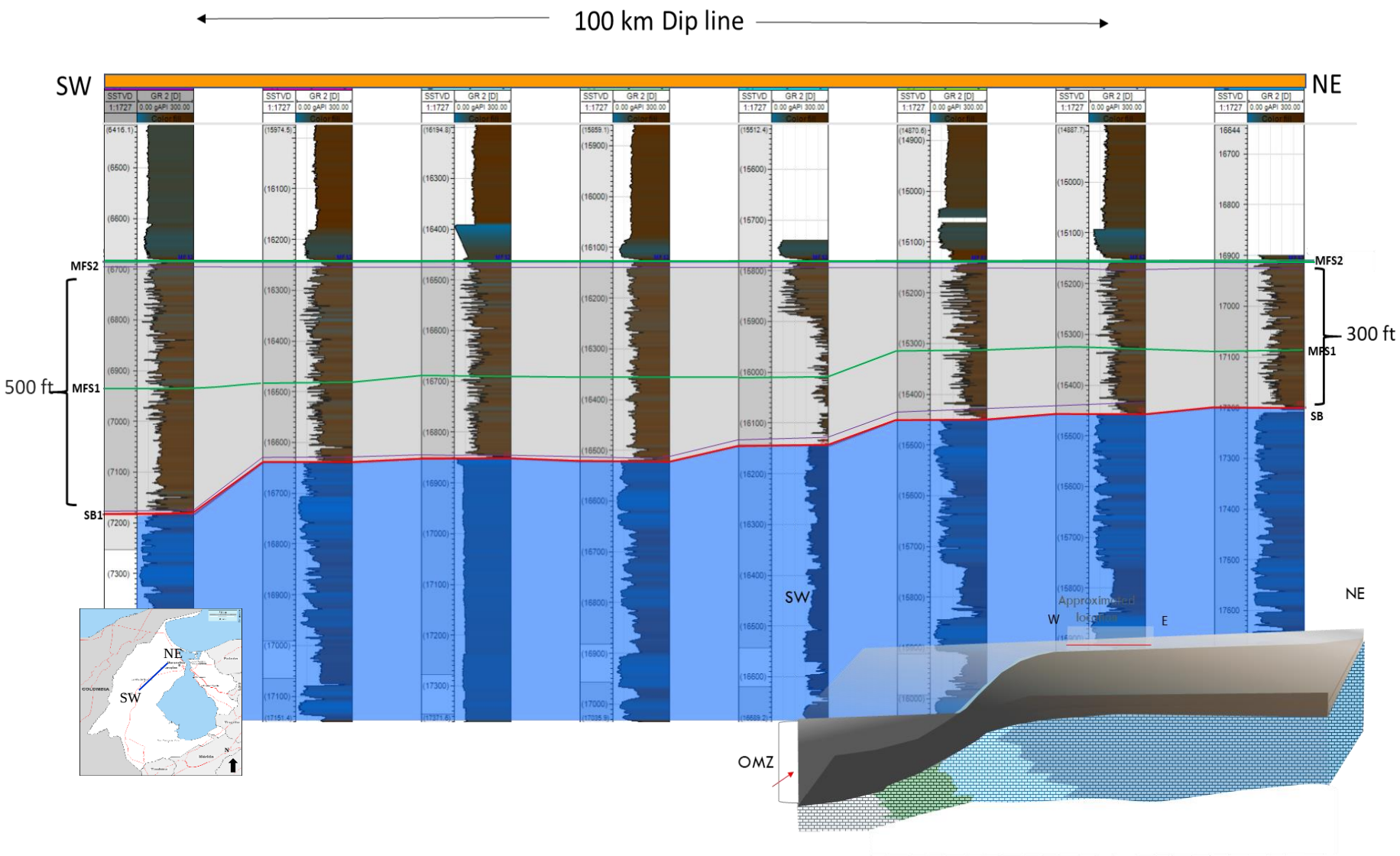

Figure 110. SW-NE Stratigraphic cross section in La Luna 1X well using the second MFS (green lines) as a stratigraphic datum. Red line represents the main unconformity of the Cogollo Group (Maraca Formation) with La Luna Formation. This cross-section is intended to display the dipping of the La Luna Formation towards the SW.

5.1.3 Brittleness index

A rock can be subjected to increased stress through three successive stages of deformation: elastic, plastic, and fracture. Based on these behaviors it is possible to classify the rocks into two end member classes: ductile and brittle. If the rock has a smaller region of elastic behavior and a larger region of plastic behavior, absorbing much energy before failure, it is considered ductile. In contrast, if the material under stress has a larger region of elastic behavior but only a small region of plastic behavior, the rock is considered brittle" (Perez- Altamar & Marfurt, 2014).

The Brittleness Index (BI, Equation 7) is based on the mineral composition of the rock. Since rock brittleness is a response of the abundance of "brittle minerals" compared to "ductile minerals" within the rock, BI estimates the stiffness by the relationship of the most brittle minerals, that constitutes the rock, with the total organic carbon and clay content. Modified from Wang & Gale (2009) and Jing (2014).

$$BI = \frac{Qtz + Dol + Cal}{Qtz + Dol + Lm + Cl + TOC} \quad [7]$$

Where:

Qtz= quartz
Cal= Calcite
Dol= dolomite
Cl= Clay
TOC=Total Organic Carbon

The brittleness of the LLIX core was calculated for fifty-two (52) samples. Based on those calculations, the average values for Lower and Middle La Luna are 0.90. Upper La Luna (before the phosphatic-glauconitic content interval 15278'-15327') contains values of 0.82 which remain high. As was stated before, La Luna in NW Maracaibo basin is about 90% carbonate. Thus its brittleness index would remain high. As it was previously stated, the La Luna Formation varies in

mineralogical content in areas where they are paleo-topographically controlled; this is also perceived in the BI of the LLIA where 45 samples were calculated. Lower La Luna (topographically controlled) contains an average value of 0.70, while Middle and Upper La Luna increase upward in BI content (0.85 on average), these values are lower than LLIX but remain high. In contrast, the values for Lower, Middle, and Upper La Luna in LLIS fluctuates between 0.35-0.45 on average meaning that the stiffness of the core is less than 0.5 which is not presenting a good BI. Calculations of the BI average values for each well are in Table 14.

It is important to point out that the brittleness of the rock should also be evaluated with the rock-hardness since the brittleness index does not necessarily indicate the strength of the rock and other parameters (such as the rock fabric and their internal arrangement) could play a more important role in the geomechanical properties (Becerra-Rondon, 2017).

Table 14. Average constituent minerals in the rock and total organic carbon used for the Brittleness Index equation (modified from Wang & Gale, 2009).

	La Luna core.	*Qtz+Dol+Lm (% from XRD analyses)*	*Qtz+Dol+Lm+Clay (% from XRD analyses)*	*TOC (wt%)*	*BI*
Core LLIX	Upper (phosphatic-glauconitic beds not included)	76,82	87,51	5,31	0,82
	Middle	89,51	95,72	5,60	0,90
	Lower	96,82	94,21	3,40	0,91
Core LLIA	Upper	77,38	93,85	6,44	0,82
	Middle	89,23	99,37	4,13	0.86
	Lower	69,70	93,89	3,61	0,73
Core LLIS	Upper	55,64	87,67	5,31	0,38
	Middle	71,48	92,09	3,46	0,43
	Lower	66,59	90,63	3,16	0,41

5.2 Biomarkers, relationship with sequence stratigraphy and prospective organo-facies

Sequence stratigraphy has provided a generalized framework for constructing depositional models and has thus impacted the interpretation of shelf depositional systems (Miall, 1992). Slight fluctuations during parasequence alternation could have much more prominent effects in a continental shelf system as opposed to deeper settings since most of the studies have focused on organic matter produced from modern continental shelf environments (Shiah et al., 2000; Tselepides et al., 2000). “The ecosystems present in these shallow water environments play an integral role in organic carbon fluctuation and primary productivity” (Fleck et al., 2002). This is one of the other reasons to integrate the sequence stratigraphy with the geochemistry.

As discussed earlier, biomarkers are extremely useful for determining the depositional environment and maturity in source rocks. Rodriguez (2007) stated that these analyses also correlate with the hypothesis of fluctuating sea level during the deposition of source rocks. Thus they can work along with sequence stratigraphic frameworks for the evaluation of the oxic vs. anoxic bottom-water conditions. The depositional environment determines the amount and type of organic matter found in a rock.

In the previous chapter, a series of biomarker ratios were analyzed for the outcrop and subsurface samples in the La Luna Formation. Furthermore, a high-definition sequence stratigraphic framework was generated for the La Luna Formation. The final objective of this work was mainly focus on the integration of these two important disciplines to generate a depositional model and predict the best organo-facies of La Luna Formation in Venezuela as a prospective unconventional reservoir.

The vertical plots displayed for the LLIX, LLIA and LLIS core (Figure 110-112) depicts a relationship between biomarkers, sequence stratigraphy and brittleness index. The LLIX profile

displays how using the Pr/Ph and C_{13}-C_{20} regular isoprenoids provide a level of detail in the oxic and anoxic environments due to sea level fluctuations even more significant than the regular RHP (4th order resolution) in the sequence stratigraphic framework.

Biomarkers in the vertical plots display the depositional history of the variability in the oxic/anoxic environments, hypersalinity, marine vs. terrestrial input, and algae vs bacterial input and photic zone euxinia. These variations create a higher impact on the quality of the organic matter.

A low Pr/Ph ratio (0.5), the gammacerane index (C_{30} triterpane), the C_{23} tricyclic terpane and the pregnane/sterane ratios are parameters associated with hypersaline and highly reduced environments. A hypersaline environment can be defined as a shallow, restricted seaway with low sedimentation, anoxic conditions and highly stratified in marine and non-marine environments. The salinity of the water can be considerable, but the evaporitic conditions are not always the cause. According to Nissenbaum et al. (1972), there is a higher association of hydrocarbons and hypersaline environments since they can be rich in several components of organic matter and the source of the organic matter is mainly the biota in the water body. Sediments deposited under hypersaline conditions, i.e., marine carbonates and evaporites, are increasingly recognized as a potential source for oil. Environments that lie in waters with elevated salinities are sites of very high biological productivity in which organic-rich cyanobacterial carbonates form and accumulate in large quantities (Schreiber et al., 2001).

The La Luna IX does not display a particular trend (Figure 110). However, the Pr/Ph ratio, the gammacerane index, the C_{23} tricyclic terpane, and the pregnane/sterane ratios slightly decreases towards the top of the formation showing a higher concentration of hypersalinity in

Lower La Luna that notably decreases when it passes the Tres Esquinas Member (Phosphatic-Glauconitic interval).

Likewise, the relationship of the eukaryote vs. prokaryote input is given by the steranes/17α-Hopanes. Fluctuations along the core do not show a specific trend, but a slight increase of the plankton towards the oceanic anoxic event (OAE2). This occurred in the late Turonian, characterized by higher productivity that was enhanced, in which the marine input is coming from the increased C_{30}/C_{29}.

The Brittleness Index and the calculated maturity given by the Methyl Phenanthrene Index (MPI) remains constant along the whole formation, but the HI and the S1 and S2 are higher towards the uppermost Middle and Upper La Luna formation displaying the best organic matter quality and the best prospect for the NW Maracaibo basin.

In contrast, La Luna IA exhibits a different trend (Figure 109). As this core represents the deposition of an embayment-type given by the Maraca paleo-topography, the deposition of Lower La Luna shows significant changes in terms of lithofacies (see core description and petrography), detrital input, the increase of clay content (see XRD and XRF and biomarkers interpretation) and hypersalinity. By the use of biomarkers and the integration of the other parameters presented in Figures 110 and 112, a fourth order cyclicity was also generated for the La Luna Formation in the LLIA core.

It is very interesting to see how the RHP (which is reflected by the S1+S2)/TOC) displays the highest anoxia for the lowermost part of La Luna Formation but not necessarily where the MFS is located. This shows the importance of using biomarkers for an accurate understanding of the depositional environment organo-facies and variations about the general sequence stratigraphy.

Conversely, the Pr/Ph ratio, the gammacerane index, the C_{23} tricyclic terpane, and the pregnane/sterane ratios display a notable increase of hypersalinity in the Lower La Luna.

As it was stated in the previous chapters, the C_{27} diasteranes/diasteranes + regular steranes remains higher. This statement, corroborates the different lithofacies already found in the inorganic analysis that are not characteristic in the La Luna Formation, since the clay content increases notably in comparison to the characteristic deposition of La Luna for Lower, Middle, and Upper for the Maracaibo basin, in which most of their mineralogical content ranges between 80-90% carbonate.

There is a higher presence of Photic Zone Euxinia (PZE) in LLIA than LLIX; values are higher than 0.5 suggesting an episodic PZA where the shift of the chemocline occurred periodically. Calculated Ro from MPI remains constant along the well, but the highest hydrogen index values are in the Lower and Upper La Luna. S1 and S2 values are higher in the Upper La Luna followed by the Lower La Luna which seems to have a higher hydrocarbon expulsion displayed by the highest potential to generate given by the S1 vertical plot.

As was expected (according to the mineralogical results), the brittleness index for the whole formation ranges from 0.7-8.0 (increasing upwards) displaying still a considerably good value for prospectivity for the Lower and Upper La Luna. Thus, the best organic matter quality for the NW Maracaibo basin suggests two different prospects for this type of deposition. The first one to be considered is the organo-facies located in the Lower La Luna (given by the highest hypersalinity and higher organic matter preservation) and Upper La Luna since the HI index, S1 and S2 are higher, but the PZA decreases towards the top of the formation).

Furthermore, the La Luna IS core (located towards the southernmost part of the study area) displays a good representation of the lateral changes in lithofacies and depositional environments

when the La Luna was deposited towards the shallower part of the platform (Figure 109). Due to the accommodation space, this interval represents the shortest section. The gammacerane index, the C_{23} tricyclic terpane, and the pregnane/sterane ratio do not change drastically.

The Pr/Ph ratio and the steranes/17α-Hopanes ratio depicts an increase of anoxia and a phytoplankton bloom possibly coming from a benthic alga. Moreover, the presence of sulfur, molybdenum and vanadium content (from the XRF profile) suggests that the environment of deposition could be interpreted as a lagoon-like system that is located towards the shallower platform. In terms of prospectivity, the best organo-facies can be represented by the Upper La Luna.

The only limitation could be the lower brittleness that this section contains (0.3-0.4 on average) Thus, it is recommended to develop a further evaluation of the geomechanical properties to be considered a target zone. Based on all the evidence provided during the last five chapters of this work, the depositional model for La Luna Formation is represented in Figures 113 to 118.

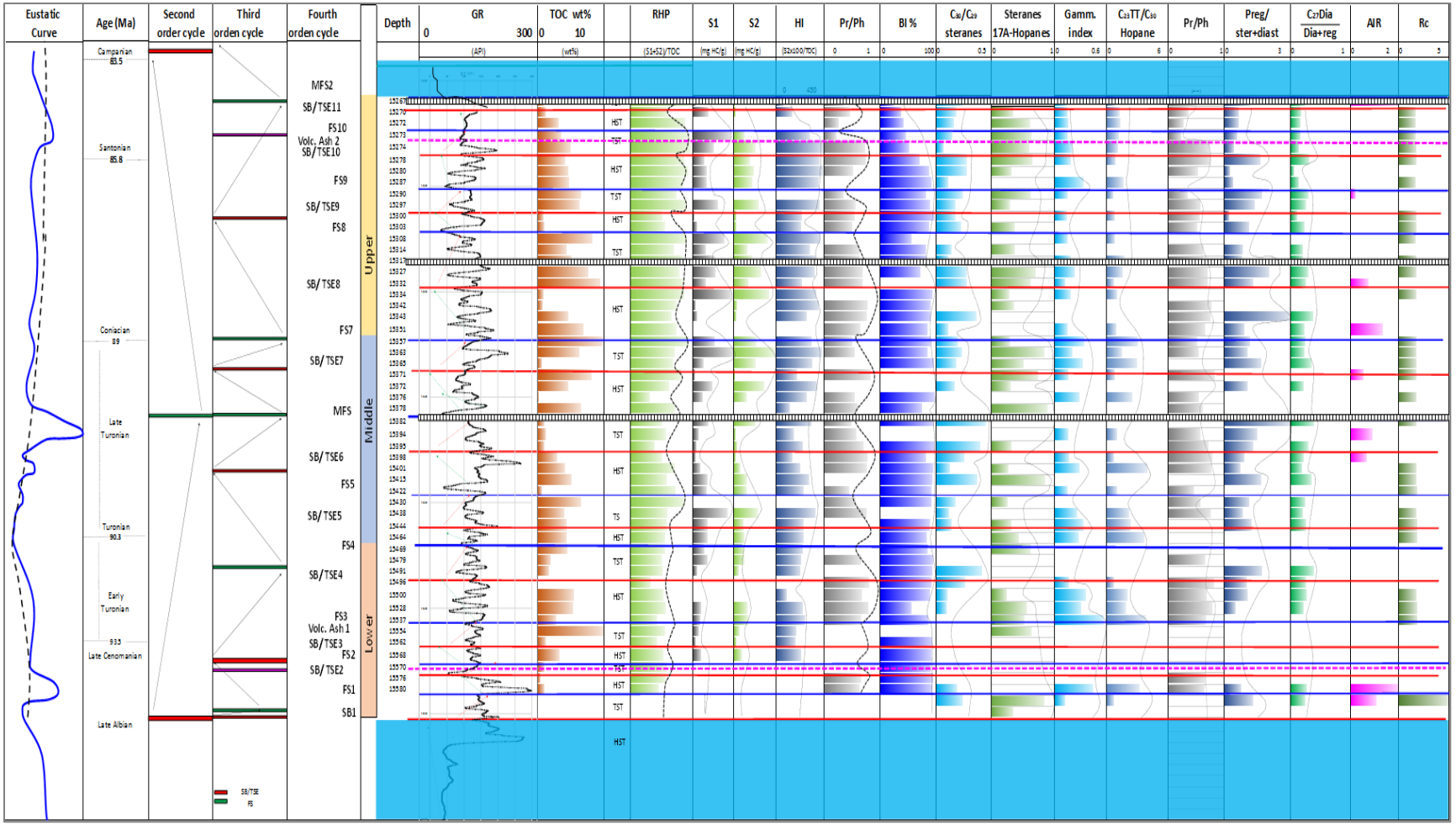

Figure 111. GR, BI, sea level curve, 4th order sequence stratigraphic framework and geochemical logs of La Luna Formation IX in Maracaibo Basin displaying the best organo-facies for prospective unconventional reservoirs. (HST, highstand systems tract; TST, transgressive systems tract, MFS, maximum flooding surface; SB/TSE, Sequence boundary and the transgressive surface of erosion).



Figure 112. GR, BI, sea level curve, 4th order sequence stratigraphic framework and geochemical logs of La Luna Formation IA in Maracaibo Basin displaying the best organo-facies for prospective unconventional reservoirs. (HST, highstand systems tract; TST, transgressive systems tract, MFS, maximum flooding surface; SB/TSE, Sequence boundary and the transgressive surface of erosion).

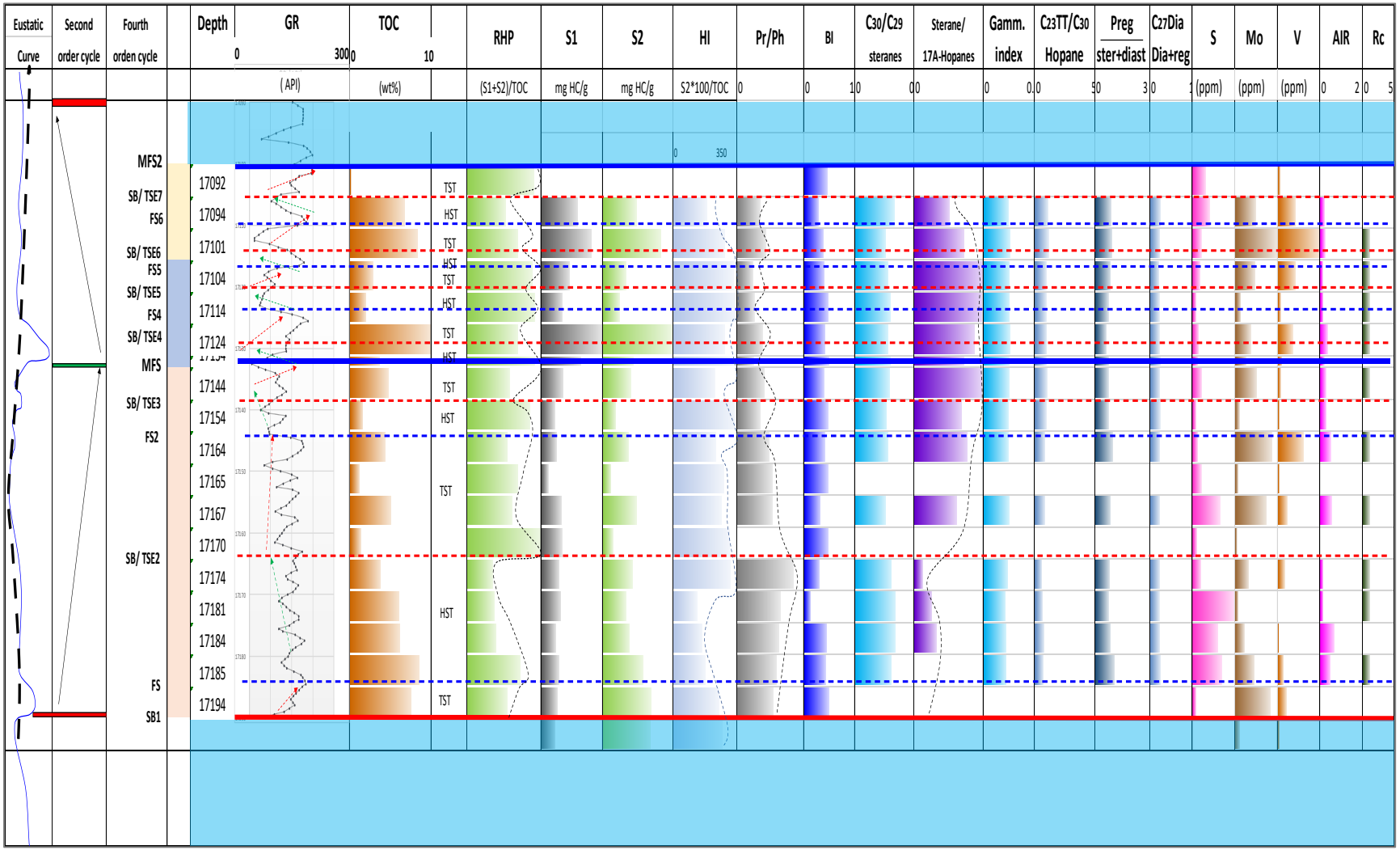

Figure 113. GR, BI, sea level curve, 4th order sequence stratigraphic framework and geochemical logs of La Luna Formation IS in Maracaibo Basin displaying the best organo-facies for prospective unconventional reservoirs. (HST, highstand systems

tract; TST, transgressive systems tract, MFS, maximum flooding surface; SB/TSE, Sequence boundary and the transgressive surface of erosion).

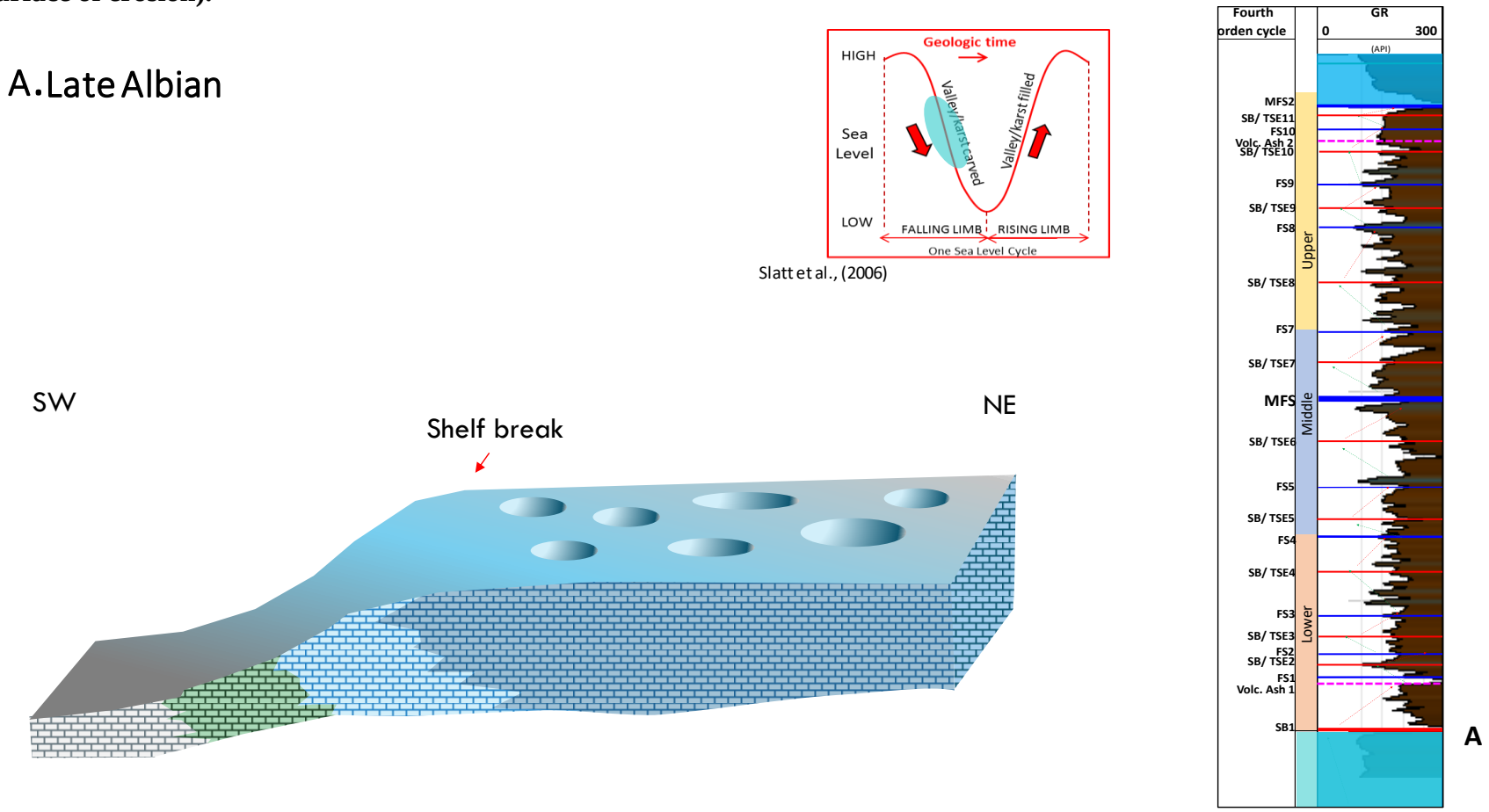

Figure 114. Depositional model through one eustatic sea level cycle represented by the deposition of the shallow-water platform of Maraca Formation (Cogollo Group) suggesting a paleo-karst development and subaerial exposure before deposition of the La Luna (Trukowski et al., 1995).

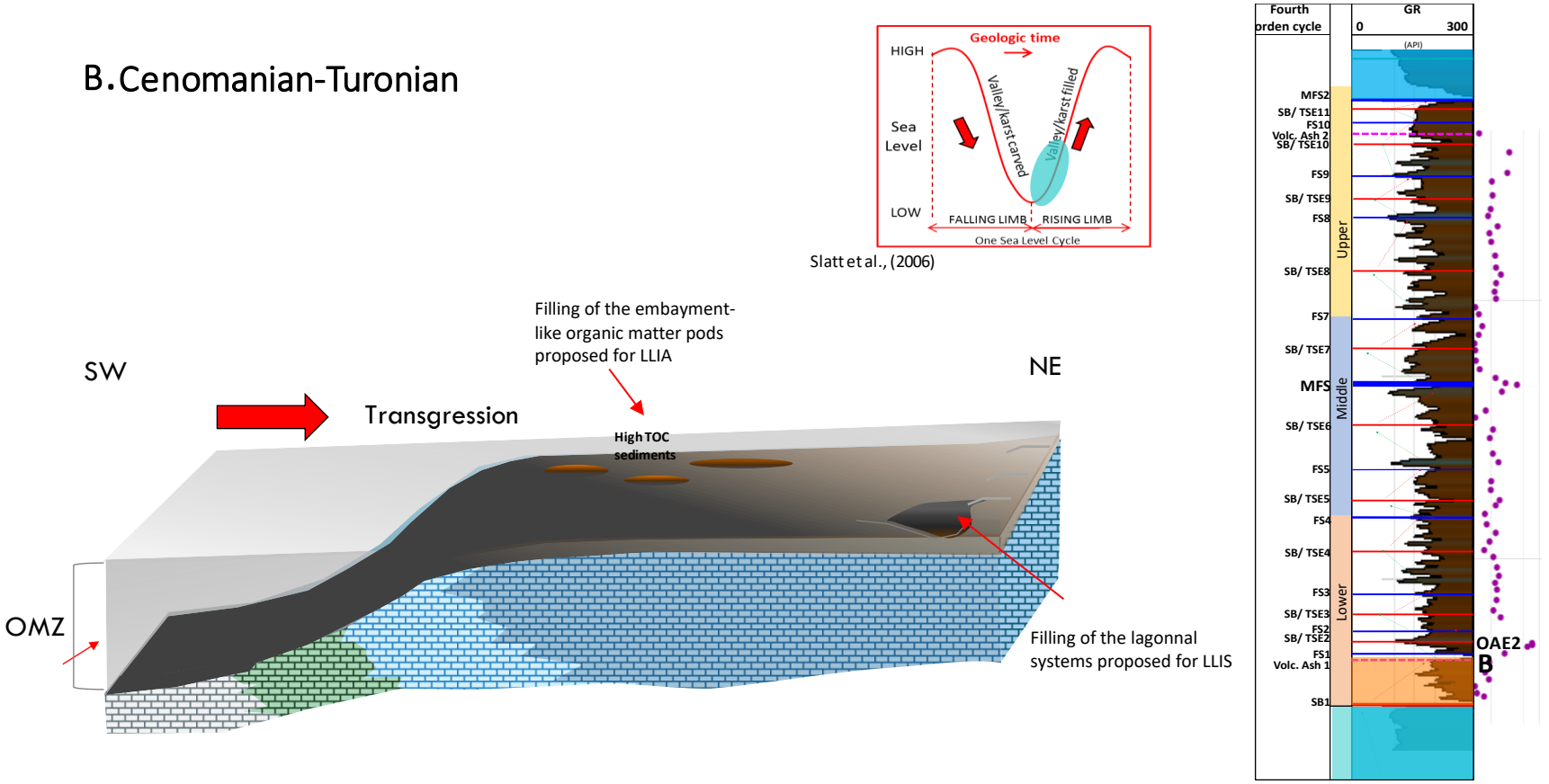

Figure 115. Depositional model of the La Luna Formation through one eustatic sea level cycle represented by the initial worldwide transgression that represents the major time of organic matter accumulation in the La Luna Formation and the OAE-2 in the Cenomanian- Turonian Boundary. Note the development of the "embayment types" and the lagoon-like system proposed for the study area. Results are supported by the isotopic analysis in the La Luna Formation found by Davis et al. (1999) in the Cenomanian- Turonian boundary carbon isotope curve of La Luna Formation ALP-6 core.

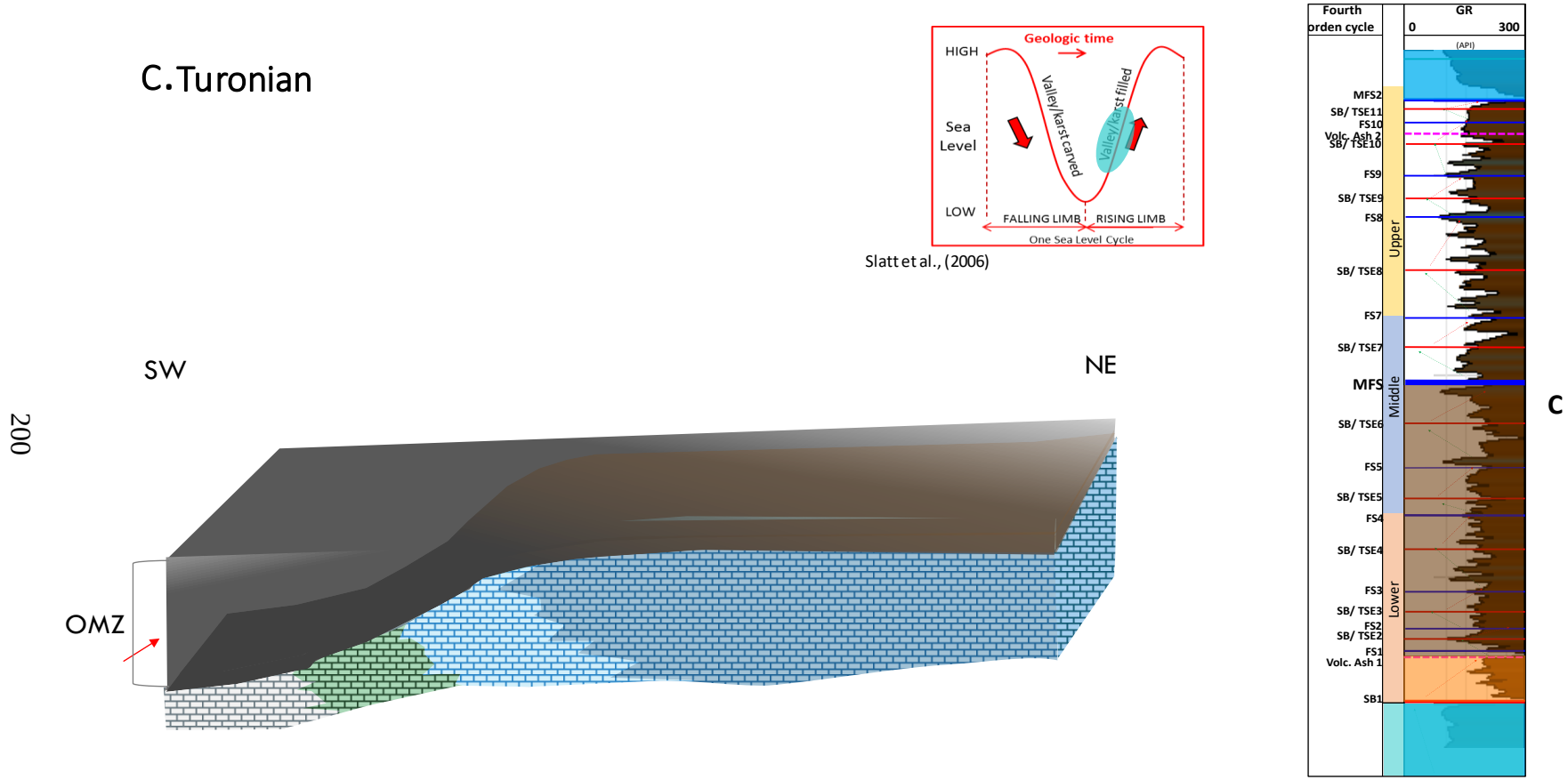

Figure 116. Depositional model of the La Luna Formation through one eustatic sea level cycle representing the highest period of sea level cycle (MFS).

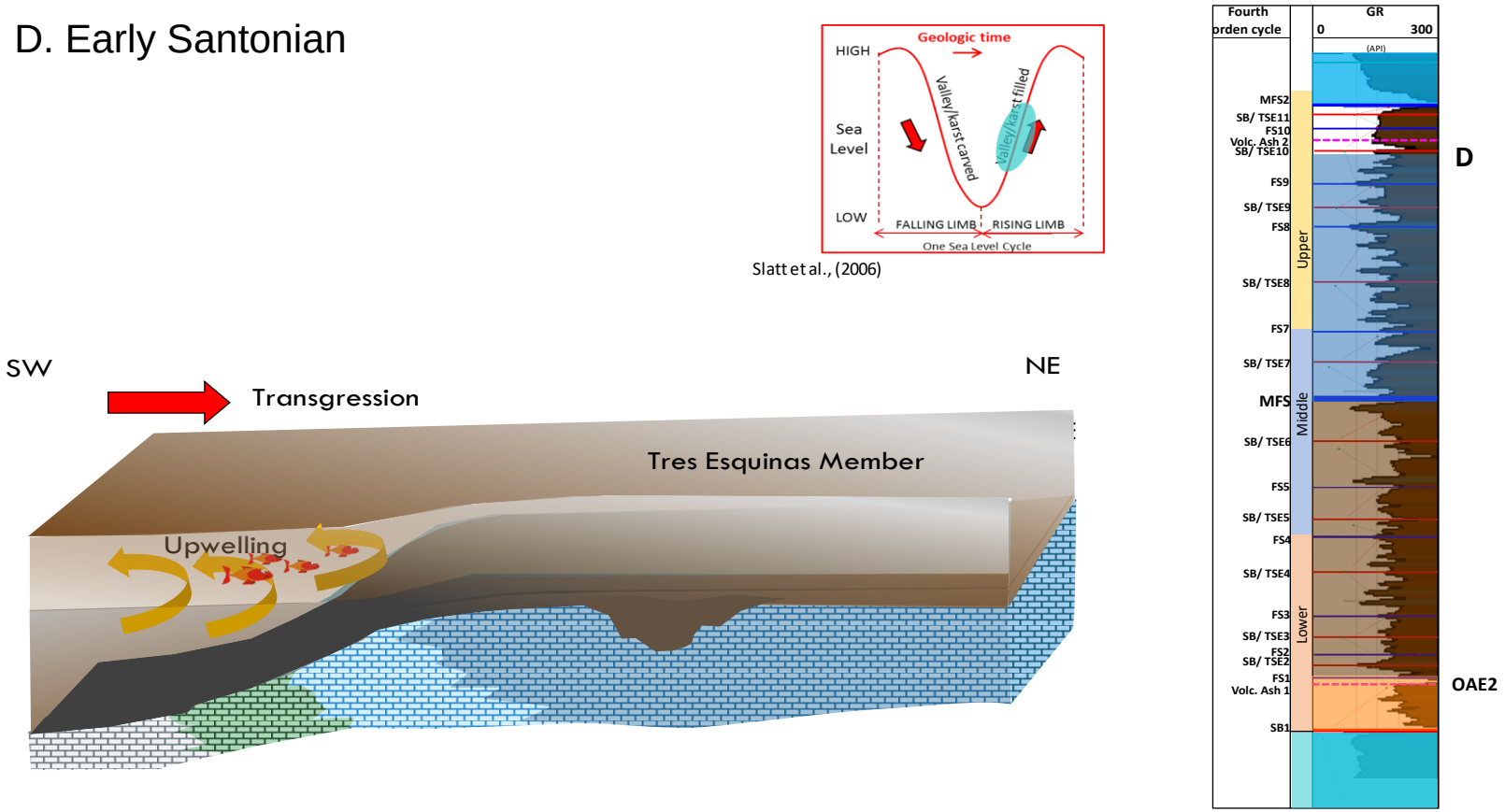

Figure 117. Depositional model of the La Luna Formation through one eustatic sea level cycle represented by the development of the Upwelling currents that brought all these nutrients towards the ocean surface generating higher productivity (plankton blooms) and higher quality of organic matter generated.

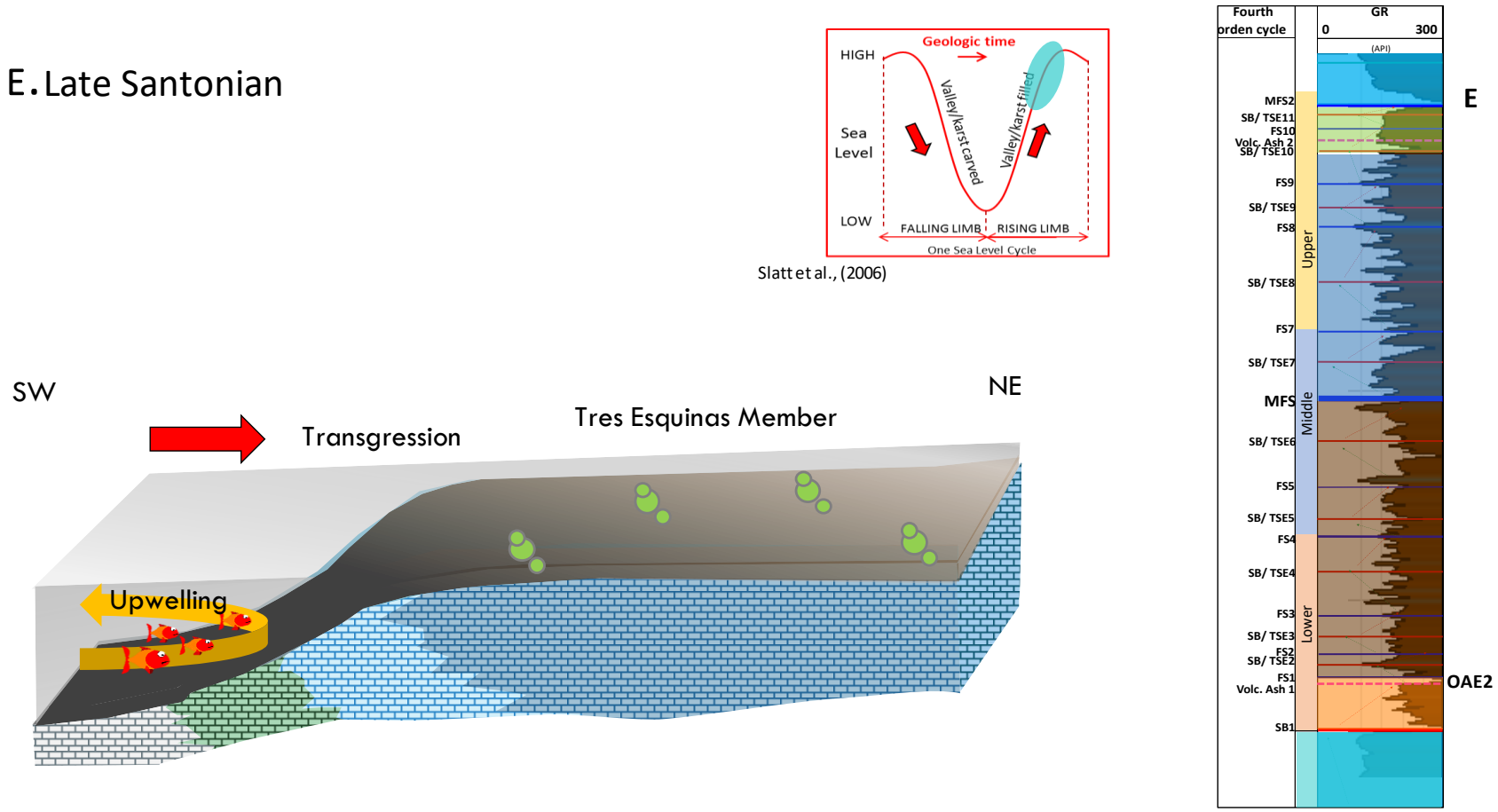

Figure 118. Depositional model of the La Luna Formation through one eustatic sea level cycle represented by the final deposition of the La Luna Formation. The Tres Esquinas Member (composed of highly bioturbated, dark-gray, phosphatic and glauconitic laminated shales).

F. Campanian

Colon Formation

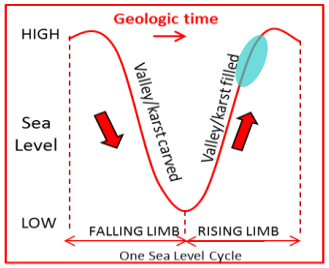

Slatt et al., (2006)

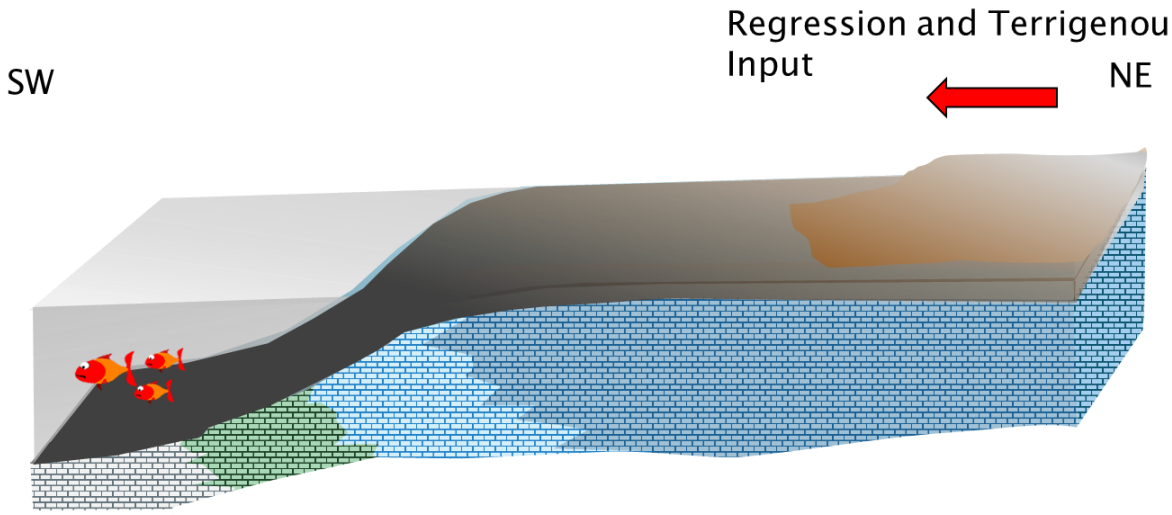

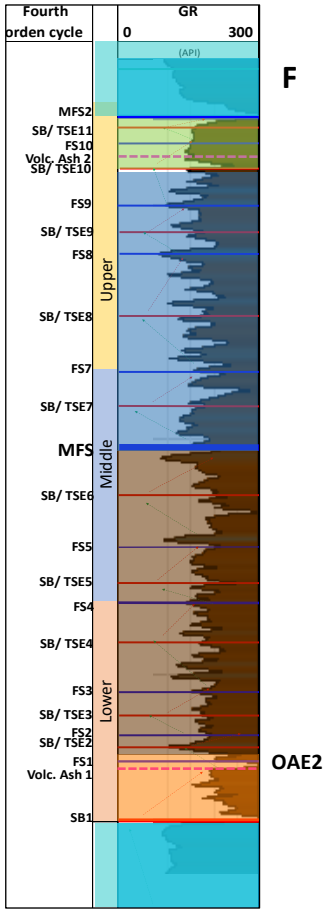

Figure 119. Depositional model of the La Luna Formation through one eustatic sea level cycle represented by a regression that is represented by the shale facies of the overlying Colón and Mito Juan Formations.

6. CONCLUSIONS

Based on organic geochemistry and maturity parameters, the organic-rich marine carbonates of the La Luna Formation have been proven to have excellent source rock potential in the northwestern Maracaibo Basin, Venezuela dominated by Type IIS kerogen, indicating an oil and gas prone marine organic matter.

The reservoir characterization allowed the identification of lithofacies and mineralogical content. The mineralogical composition of La Luna can also be described as a mixed carbonate mudstone dominated lithotype. The frequency of mixed siliceous mudstone is given by the high productivity generated by the upwelling currents displayed by chert nodules that are mainly composed of biogenic silica. The mixed argillaceous mudstone is mostly characterized by the typical glauconitic and phosphatic top of La Luna formation conformed by the Tres Esquinas member and the two most visible pulses of volcanic ash found at the lower and Upper La Luna.

Higher frequency distribution of the total organic carbon (TOC) ranges from 7.5 to 10.5 wt.% approximately from all the subsurface and outcrop samples. The lower values are linked to facies V (Siliceous- calcareous laminated mudstone, interbedded with black chert filled with calcite veins) and the high TOC values can be related to facies I (Dark gray, massive mudstone), facies IV (Laminated mudstone with limestone concretions and packstone), facies V (Siliceous-Calcareous mudstone interbedded with wackestone) and in LLIX facies VIII (Siliceous green mudstone with authigenic glauconite and Pyrite).

The RHP parameter constitutes a valuable parameter for evaluating sea-level changes that can be linked to regressive-transgressive cycles and consequently to temporal variations in depositional environments. However, when this parameter was correlated with the biomarkers the RHP parameter does not entirely relate the sea level fluctuations (Figure 110 and 112). Thus, an

RHP profile can be useful for the overall estimation of the sea- level fluctuations, but it does not show a good correlation with biomarkers. This illustrates how important the use of biomarkers is for the generation of a high-resolution sequence stratigraphic framework.

The level of anoxia evaluated by the Pr/Ph values and the $C_{35}S/C_{34}S$ homohopanes suggest that La Luna was deposited under anoxic conditions. Distributions of the C_{27}, C_{28} and C_{29} regular steranes and monoaromatic steroids (MAS), high ratios of C_{24}/C_{23} tricyclic terpane, high concentration of steranes/17α-Hopanes and C_{23} tricyclic terpane/C_{30} hopane indicate a marine-carbonate depositional environment for the La Luna Formation, as also evidenced by lithologic analyses.

The predominance of even-numbered n-alkanes and ββ steranes, high pregnane/sterane ratios, and the presence of gammacerane suggest higher hypersaline conditions during the La Luna Formation deposition. Since 5α,14β,17β-pregnane and homopregnane, are geological products derived from steroids bound to the kerogen by a sulfurized side chain (Wang et al., 2015).The higher values of pregnanes and homopregnanes can also be related to the sulfur content in the water column (euxinic conditions). The presence of aryl isoprenoids suggests the occurrence of intermittent photic zone anoxia (PZA) for La Luna Formation.

Measured and calculated vitrinite reflectance (Tmax, Ts and Tm ratios, and steranes and hopanes values) indicate that the La Luna formation in the northwest Maracaibo Basin has reached the oil window generation maturity level. Also, subsurface samples from core LLIS prove that the dry gas window is reached towards the northern part of the study area. This suggests that liquid hydrocarbons will occur in the northern and central part of the Maracaibo basin and condensates and dry/wet gases will occur towards the northern part of the study area.

A reservoir and source rock characterization proposed two different sedimentation histories for the LLIA and LLIS cores in comparison to the characteristic deposition of the La Luna Formation as shown by the cores LLIX and LLIE.

The LLIA well in northwest Maracaibo basin and its depositional variation is mainly a consequence of the paleo-topographic control of the underlying Maraca Formation (as is the case with the more siliceous Woodford Shale in the United States, Infante et al., 2016). It is constituted by an increase of detrital input and clay content and higher salinity conditions and water density stratification. In this core, S1 and S2 values are higher in Upper La Luna followed by Lower La Luna which seems to have a higher hydrocarbon expulsion. Brittleness index ranges from 0.7-8.0 considered a prospectivity value for the Lower and Upper La Luna. Thus, the best organic matter quality for the NW Maracaibo basin suggests two different prospects for this type of deposition.

The LLIS well is located towards the southwestern part of the study area. It also represents a different sedimentation pattern in comparison with the previous ones. First, in terms of length, this core represents the shortest interval since the vertical accommodation space is less towards the outer platform. Second, in terms of lithofacies, this core represents a cyclicity that does not display the typical pattern of deposition of La Luna in Maracaibo Basin. Biomarker data along with inorganic proxies proposes a lagoon-like system possibly deposited towards the inner shallower platform.

The Upper La Luna can represent the best organo-facies. The only limitation could be the lower brittleness that this section contains (0.3-0.4 on average). Thus, further evaluation is recommended to better understand the geomechanical properties to determine the target zone. The organic-rich marine carbonates of the La Luna Formation have been proven to have an excellent source rock potential in the northwestern Maracaibo Basin, Venezuela. The La Luna IX core

located towards the northwest of the study area represents the typical deposition of the La Luna Formation. Biostratigraphic and isotopic data provided by Davis et al. (1999) allowed the calculation of a higher frequency of 4th order sequences. This, along with the integration of the organic and inorganic interpretation, generated a depositional model for the La Luna formation in the Maracaibo Basin. LLIX displays very-high concentrations of chemical (XRF) elements associated with paleo-redox/anoxic input. The organic-rich marine carbonates of the La Luna Formation have been proven to have an excellent source rock potential in the northwestern Maracaibo Basin, Venezuela, its abundance can be associated with the organic matter richness along the La Luna Formation. Higher TOC values recognized the Lower La Luna as the most organic-rich unit. However, Rock-Eval Parameters depict that the best quality organo-facies are in the Upper La Luna (with exception to the Tres Esquinas Member) with a TOC value that ranges from 1 to 10 wt.%.

Inorganic and organic proxies, biomarker analysis and reservoir characterization for the La Luna Formation allowed the identification of the best organo-facies and the best prospective areas as unconventional reservoirs. A higher TOC, hydrogen index, water stratification, thickness, and Brittle Index indicate the Upper La Luna as the most prospective followed by Lower La Luna for the LLIX and LLIA cores.

This work represents the first stage of exploration for the La Luna Formation as an unconventional resource shale in Venezuela. It is recommended to perform additional geochemical, geomechanical, petrophysical, 3D seismic interpretation and reservoir properties analysis on a more extensive suite of samples, particularly to core samples, to evaluate all the variations in the depositional environment along the basin, especially towards the northeast part of the Maracaibo Basin.

7. REFERENCES

Acevedo, D., Neto, F. A., Simoneit, B., & Pinto, A. 1992. Novel series of tricyclic aromatic terpanes characterized in Tasmanian tasmanite. *Organic Geochemistry, 18*(1), 9-16.

Acuna, H., Gil, J., Riegstra, J., Taha, J., Barrientos, M., Menier, M., & Singer, J. 1997. *Proceedings from Venezuela WEC 1997: Well Evaluation Conference Venezuela*. Caracas, Venezuela: Schlumberger Surenco, 339p.

Alexander, R., Kagi, R., & Noble, R. 1983. Identification of the bicyclic sesquiterpanes, drimane, and eudesmane in petroleum. *Journal of the Chemical Society, Chemical Communications, 5,* 226-228.

Algeo, T. J., & Lyons, T. W. 2006. Mo–total organic carbon covariation in modern anoxic marine environments: Implications for analysis of paleoredox and paleohydrographic conditions. *Paleoceanography, 21*(1), 1-23.

Algeo, T. J., & Maynard, J. B. 2004. Trace-element behavior and redox facies in core shales of Upper Pennsylvanian Kansas-type cyclothems. *Chemical Geology, 206*(3-4*),* 289-318.

Algeo, T., & Rowe, H. 2012. Paleoceanographic applications of trace-metal concentration data. *Chemical Geology, 324,* p. 6-18.

Aquino-Neto, F. R., Trendel, J. M., Restle, A., Connan, J., & Albrecht, P. A. 1983. Occurrence and formation of tricyclic and tetracyclic terpanes in sediments and petroleums. In M. Bjoroy (Ed.), *Advances in Organic Geochemistry 1981,* p. 659-667.

ASTM Standard D2797, 2011. Standard Practice for Preparing Coal Samples for Microscopical Analysis by Reflected Light. ASTM International, West Conshohocken, PA.

Banner, J. L. 1995. Application of the trace element and isotope geochemistry of strontium to studies of carbonate diagenesis. *Sedimentology, 42*(5), 805-824.

Barnes, M. A., & Barnes, W. C. 1983. Oxic and anoxic diagenesis of diterpenes in lacustrine sediments. In M. Bjoroy (Ed.), *Advances in Organic Geochemistry 1981,* 289-298.

Bartok, P. 1993. Prebreakup geology of the Gulf of Mexico–Caribbean: Its relation to Triassic and Jurassic rift systems of the region. *Tectonics, 12*(2), 441-459.

Becerra Rondon, D. M. 2017. Integrated geological characterization at the bed scale of the Woodford shale at the I-35 outcrop, Southern Oklahoma (Master's thesis). University of Oklahoma, Norman, Oklahoma, 202p.

Blood, R., Lash, G., & Bridges, L. Biogenic silica in the Devonian Shale succession of the Appalachian Basin, USA. American Association of Petroleum Geologists, Search and Discovery Article #50864.

Bourbonniere, R. A., & Meyers, P. A. 1996. Sedimentary geolipid records of historical changes in the watersheds and productivities of Lakes Ontario and Erie. *Limnology and Oceanography, 41*(2), 352-359.

Bray, E. E., & Evans, E. D. 1961. Distribution of n-paraffins as a clue to recognition of source beds. *Geochimica et Cosmochimica Acta, 22*(1), 2-15.

Brooks, J. 1981. Organic maturation of sedimentary organic matter and petroleum exploration: In J. Brooks (Ed.) *Organic Maturation Studies and Fossil Fuel Exploration,* London: Academic Press, 310-311.

Brooks, J. D., Gould, K., & Smith, J. W. 1969. Isoprenoid hydrocarbons in coal and petroleum. *Nature, 222*(5190), 237-259.

Brooks, J., & Welte, D. H. 1984. *Advances in Petroleum Geochemistry.* Cambridge, MA: Academic Press, 344p.

Brown, T. C., & Kenig, F. 2004. Water column structure during deposition of Middle Devonian–Lower Mississippian black and green/gray shales of the Illinois and Michigan Basins: A biomarker approach. *Palaeogeography, Palaeoclimatology, Palaeoecology, 215*(1-2), 59-85.

Calvert, S. E., & Pedersen, T. F. 1993. Geochemistry of recent oxic and anoxic marine sediments: Implications for the geological record. *Marine Geology, 113*(1-2), 67-88.

Chester, R. 1990. *Marine Geochemistry*. London: Chapman & Hall, 698p.

Clark, J. P., & Philp, R. P. 1989. Geochemical characterization of evaporite and carbonate depositional environments and correlation of associated crude oils in the Black Creek Basin, Alberta. *Bulletin of Canadian Petroleum Geology, 37*(4), 401-416.

Connan, J., Bouroullec, J., Dessort, D., & Albrecht, P. 1986. The microbial input in carbonate-anhydrite facies of a sabkha palaeoenvironment from Guatemala: A molecular approach. *Organic Geochemistry, 10*(1-3), 29-50.

Cornford, C. 1998. Source rocks and hydrocarbons of the North Sea. In K. W. Glennie (Ed.), *Petroleum Geology of The North Sea: Basic Concepts and Recent Advances* (pp. 376-462). Oxford, U.K.: Blackwell Science.

Craigie, N. 2018. *Principles of Elemental Chemostratigraphy: A Practical User Guide.* New York, NY: Springer International Publishing, 189p.

Dahl, J. E., Moldowan, J. M., Teerman, S. C., McCaffrey, M. A., Pena, P. S., & Stelting, C. E. 1994. Source rock quality determination from oil biomarkers I: An example from the

Aspen Shale, Scully's Gap, Wyoming. *American Association of Petroleum Geologists Bulletin, 78*(10*),* 1507-1526.

Damsté, J. S., Kenig, F., Koopmans, M. P., Köster, J., Schouten, S., Hayes, J. M., & de Leeuw, J. W. 1995. Evidence for gammacerane as an indicator of water column stratification. *Geochimica et Cosmochimica Acta, 59*(9), 1895-1900.

Davis, C., Pratt, L., & Sliter, W. 1999. Factors influencing organic carbon and trace metal accumulation in the Upper Cretaceous La Luna Formation of the western Maracaibo Basin, Venezuela. *Geological Society of America Special Paper 332*, 203-231.

De Leeuw, J. W., & Bass, M. 1986. Early-stage diagenesis of steroids, *Methods in Geochemistry and Geophysics, 24,* 101-123.

De Romero, L., Truskowski, I., Bralower, T., Bergen, J., Odreman, O., Zachos, J., & Galea-Alvarez, F. 2003. An integrated calcareous microfossil biostratigraphic and carbon-isotope stratigraphic framework for the La Luna Formation, western Venezuela. *Palaios, 18*(4-5), 349-366.

Degarmo, D. C. 2015. Geochemical Characterization of the Woodford Shale (Devonian-Mississippian), McAlister Cemetery Quarry, Criner Hills Uplift, Ardmore Basin, Oklahoma (Master's thesis). University of Oklahoma, Norman, Oklahoma, 198p.

Didyk, B. 1978. Organic geochemical indicators of paleoenvironmental conditions of sedimentation. *Nature, 272*(5650), 216-222.

Dunham, R. J. 1962. Classification of carbonate rocks according to depositional textures. *American Association of Petroleum Geologists Bulletin Memoir,* 108-121.

Eglinton, G., & Hamilton, R. J. 1967. Leaf epicuticular waxes. *Science 156*(3780), 1322-1335.

Eglinton, G., Scott, P., Belsky, T., Burlingame, A., & Calvin, M. 1964. Hydrocarbons of biological origin from a one-billion-year-old sediment. *Science, 145*(3629), 263-264.

Erlich, R. N., Nederbragt, A. J., & Lorente, M. A. 2000. Birth and death of the Late Cretaceous "La Luna Sea," and origin of the Tres Esquinas phosphorites. *Journal of South American Earth Sciences, 13*(1-2), 21-45.

Erlich, R. N., Macsotay, I., Nederbragt, A. J., & Lorente, M. A. 1996. Palaeocenography, palaeoecology, and depositional environments of Upper Cretaceous rocks of western Venezuela. *Palaeogeography, Palaeoclimatology, Palaeoecology, 153*(1-4), 203-238.

Escalona, A. y Mann, P. 2003. Paleogene Depocenter along the Northeast Margin of the Maracaibo Basin: Structure along an Exhumed, Eocene Age Lateral Ramp Fault in the Maracaibo Basin, Western Venezuela. American Association of Petroleum Geologists, Search and Discovery Article #30018.

Escalona, A., & Mann, P. 2006. An overview of the petroleum system of Maracaibo Basin. *American Association of Petroleum Geologists Bulletin, 90*(4), 657-678.

Fang, H., Jianyu, C., Yongchuan, S., & Yaozong, L. 1993. Application of organic facies studies to sedimentary basin analysis: A case study from the Yitong Graben, China. *Organic Geochemistry 20*(1), 27-42.

Fleck, S., Michels, R., Ferry, S., & Malartre, F. E. 2002. Organic geochemistry in a sequence stratigraphic framework: The siliciclastic shelf environment of Cretaceous series, SE France. *Organic Geochemistry, 33*(12), 1533-1557.

Galloway, W., & Hobday, D. 1983. *Terrigenous Clastic Depositional Systems: Applications to Petroleum, Coal, and Uranium Exploration*. New York, NY: Springer, 375p.

Galvis-Portilla, H. A. 2017. Detailed lithostratigraphic characterization and sequence stratigraphy of a complete Woodford Shale outcrop section in Southern Oklahoma (Master's thesis). University of Oklahoma, Norman, Oklahoma, 156p.

Gamero-Diaz, H., Miller, C., & Lewis, R. 2012. A classification scheme for organic mudstones based on bulk mineralogy. Search and Discovery Article #40951.

Gomez, A. 2014. Integrated geological characterization and distribution of the Salada member, La Luna Formation, in the central area of the Middle Magdalena Basin, Colombia (Master's thesis). University of Oklahoma, Norman, Oklahoma, 194p.

González, C., Iturralde, J., & Picard, X. 1980. *Geologia de Venezuela y de sus cuencas petrolíferas.* Caracas, Ediciones Fonives, 131p.

Goossens, H. D., De Leeuw, J. W., Schenck, P. A., & Brassell, S. C. 1984. Goossens, tocopherols as likely precursors of pristane in ancient sediments and crude oils. *Nature, 312*(5993), 440.

Grandstein, F. M., Agterberg, F. P., Ogg, J. G., Hardenbol, J., van Veen, P., Thierry, J., & Huang, Z. 1994. A mesozoic time scale. *Journal of Geophysical Research, 99*(B12), 24051-24074.

Grice, K., Audino, M., Boreham, C. J., Alexander, R., & Kagi, R. I. 2001. Distributions and stable carbon isotopic compositions of biomarkers in torbanites from different palaeogeographical locations. *Organic Geochemistry, 32*(10), 1195-1210.

Grice, K., Schaeffer, P., Schwark, L., & Maxell, J. R. 1997. Changes in paleoenvironmental conditions during deposition of the Permian Kupfeschiefer (Lower Rhine Basin, northwest Germany) inferred from molecular and isotopic compositions of biomarker components. *Organic Geochemistry, 26*(11-12), 677-690.

Hackley, P. C., & Cardott, B. J. 2016. Application of organic petrography in North American shale petroleum systems: A review. *International Journal of Coal Geology, 163,* 8-51.

Hanson, A. D., Zhang, S. C., Moldowan, J. M., Liang, D. G., & Zhang, B. M. 2000. Molecular organic geochemistry of the Tarim Basin, Northwest China. *American Association of Petroleum Geologists Bulletin, 84*(8), 1109-1128.

Haq, B. U., Hardenbol, J. A., & Vail, P. R. 1987. Chronology of fluctuating sea levels since the Triassic. *Science, 235*(4793), 1156-1167.

Huang, W. Y., & Meinschein, W. G. 1979. Sterols as ecological indicators. *Geochemica et Cosmochimica Acta, 43*(5), 739-745.

Hughes, W. B., Holba, A. G., & Dzou, L. I. 1995. The ratios of dibenzothiophene to phenanthrene and pristane to phytane as indicators of depositional environment and lithology of petroleum source rocks. *Geochimica et Cosmochimica Acta, 59*(17), 3581-3598.

Hunt, J. M. 1995. *Petroleum Geochemistry and Geology* (2nd ed.). New York, NY: Freeman, 743p.

Infante-Paez, L., Cardona, L. F., McCullough, B., & Slatt, R. 2016. Seismic analysis of paleotopography and stratigraphic controls on total organic carbon: Rich sweet spot distribution in the Woodford Shale, Oklahoma, USA. *Interpretation, 5*(1), 33-47.

Isaksen, G. H., & Bohacs, K. M. 1995. Geological controls on source rock geochemistry through relative sea level; Triassic, Barents Sea. In B. J. Katz (Ed.), *Petroleum Source Rocks* (pp. 25-50). New York, NY: Springer.

Jacob, H. 1989. Classification, structure, genesis and practical importance of natural solid oil bitumen ("migrabitumen"). *International Journal of Coal Geology, 11*(1), 65-79.

Jacobson, S. R., Hatch, J. R., Teerman, S. C., & Askin, R. A. 1988. Middle Ordovician organic matter assemblages and their effect on Ordovician-derived oils. *American Association of Petroleum Geologists Bulletin, 72*(9), 1090-1100.

Jarvie, D. M., Claxton, B. L., Henk, F., & Breyer, J. T. 2001. Oil and shale gas from the Barnett Shale, Ft. Worth Basin, Texas (abs.). *American Association of Petroleum Geologists, Annual Meeting Program, 10*, 100.

Jarvie, D. M., Hill, R. J., Ruble, T. E., & Pollastro, R. M. 2007. Unconventional shale-gas systems: The Mississippian Barnett Shale of north-central Texas as one model for thermogenic shale-gas assessment. *American Association of Petroleum Geologists Bulletin, 91*(4), 475-499.

Jing, X. 2014. An integrated geomechanics and petrophysics study of hydraulic fracturing in naturally fractured reservoirs (Doctoral dissertation). University of Oklahoma, Norman, Oklahoma, 160p.

Ji-Yang, S., Mackenzie, A. S., Alexander, R., & Eglinton, G. 1982. A biological marker investigation of petroleum and shales from the Shengli oilfield, The People's Republic of China. *Chemical Geology, 35*(1-2), 1-30.

Jones, M. R. 2017, March. Bacterial Photosynthesis. *Photobiological sciences online.* American Society for Photobiology. Retrieved November 08, 2018 from http://www.photobiology.info/Jones.html.

Kauffman, E. G., Sageman, B. B., Kirland, J. I., Elder, W. P., & Harries, P. J. 1993. Molluscan biostratigraphy of the Cretaceous Western Interior Basin, North America. *Geological Association of Canada, Special Paper, 39*, 397-434.

Kirk, D. N., & Shaw, P. M. 1975. Backbone rearrangements of steroidal 5-enes. *Journal of the Chemical Society Perkin Transactions I, 22*, 2284-2294.

Landis, C. R., & Castaño, J. R. 1995. Maturation and bulk chemical properties of a suite of solid hydrocarbons. *Organic Geochemistry, 22*(1), 137-149.

Langford, F. F., & Blanc-Valleron, M. M. 1990.Interpreting rock-eval pyrolysis data using graphs of pyrolizable hydrocarbons vs. total organic carbon. *American Association of Petroleum Geologists Bulletin, 74*(6), 799-804.

Lev, S. M., McLeman, S. M., Meyers, W. J., & Hanson, G. N. 1998. A petrographic approach for evaluating trace element mobility in a black shale. *Journal of Sedimentary Research, 68*(5), 970-980.

Lewan, M. D., & Maynard, J. B. 1982. Factors controlling enrichment of vanadium and nickel in the bitumen of organic sedimentary rocks. *Geochimica et Cosmochimica Acta, 46*(12), 2547-2560.

Liborius, A. 2015. Outcrop-subsurface geological characterization of La Luna Formation as an unconventional resource in the northwest Lago de Maracaibo basin and North-Andean flank, Venezuela. (Master's thesis). University of Oklahoma, Norman, Oklahoma, 213p.

Liborius, A., & Slatt, R. 2016. Geological characterization of La Luna Formation as an unconventional resource in Lago de Maracaibo Basin, Venezuela. *Unconventional Resources Technology Conference, 25*, 3280-3299.

Liborius, A., & Sneddon, A. 2017. Organic-inorganic distribution of the Woodford Shale in Kingfisher County, STACK play, Northern Oklahoma. American Association of Petroleum Geologists, Search and Discovery Article #51444.

Lillis, P. G. 1992. Biomarkers as thermal maturity indicators. In L. B. Magoon (Ed.) *The Petroleum System: Status of Research and Methods* (pp. 49-51). Denver, CO: U.S. Geological Survey Bulletin.

Liu, C., Clift, P. D., Murray, R. W., Blusztajn, J., Ireland, T., Wan, S., & Ding, W. 2017. Geochemical evidence for initiation of the modern Mekong Delta in the southwestern South China Sea after 8Ma. *Chemical Geology, 451*, 38-54.

Lopez, L. 2013a. *Biomarcadores. Aplicaciones en la geoquímica del petróleo.* Caracas, Venezuela: Universidad Central de Venezuela, Ediciones de la Biblioteca, 122p.

Lopez, L. 2013b. *Caracterizacion geoquimica y sedimentologica de la Formacion Colon con fines de prospeccion de lutitas gasiferas en los municipios Moran-Andrez Eloy Blanco, Estado Lara.* (Trabajo especial de grado). Universidad de Los Andes, Merida, Venezuela, 99p.

Lugo, J., & Mann, P. 1995. Jurassic-Eocene tectonic evolution of Maracaibo Basin, Venezuela. In A. Tankard, R. Suarez, & H. Welsink, *Petroleum basins of South America* (pp. 699-725). Tulsa, OK: American Association of Petroleum Geologists.

Macellari, C., & De Vries, T. 1987. Late Cretaceous upwelling and anoxic sedimentation in northwestern South America. *Palaeogeography, Palaeoclimatology, Palaeoecology,* 59, 279-292.

Mackenzie, A. S. 1984. Application of biological markers in petroleum geochemistry. In J. Brooks and D. H. Welte (Eds.), *Advances in Petroleum Geochemistry* (vol. 1, pp. 115-214). London, U.K.: Academic Press.

Mackenzie, A. S., Hotfmann, C. F., & Maxwell, J. R. 1981. Molecular parameters of maturation in the Toarcian shales, Paris Basin, France. III: Changes in aromatic steroid hydrocarbons. *Geochimica et Cosmochimica Acta, 45*(8), 1345-1355.

Mackenzie, A. S., Patience, R. L., Maxwell, J. R., Vandenbroucke, M., & Durand, B. 1980. Molecular parameters of maturation in the Toarcian shales, Paris Basin: Changes in the configuration of acyclic isoprenoid alkanes, steranes, and triterpanes. *Geochimica et Cosmochimica Acta, 45*(12), 2369-2376.

McKenzie, M. 2019, January. *Petrographic Thin Section Preparation.* Retrieved January 10, 2019 from http://www.kemet.co.uk/blog/petrography/rock-thin-sections.

Martinez R., J., & Hernandez, R. 1992. Evolution and drowning of the Late Cretaceous Venezuelan carbonate platform. *Journal of South American Earth Science, 5*(2), 197-210.

Maze, W. B., & Hargraves, R. B. 1984. Paleomagnetic results from the Jurassic La Quinta Formation in the Perijá Range, Venezuela, and their tectonic significance. In W. E. Bonini, R. B. Hargraves, & R. Shagam, *The Caribbean–South American Plate Boundary and Regional Tectonics* (pp. 287-293). Boulder, CO: Geological Society of America.

Mello, M. R., Telnaes, N., Gaglianone, P. C., Chicarelli, M. I., Brassell, S. C., Maxwell, J R. 1988. Organic geochemical characterization of depositional paleoenvironments of source rocks and oils in Brazilian marginal basins. *Organic Geochemistry, 13*, 31-45.

Miall, A. D. 1992. Exxon global cycle chart: An event for every occasion? *Geology, 20*(9), 787-790.

Miceli Romero, A., & Philp, R. P. 2012. Organic geochemistry of the Woodford Shale, southeastern Oklahoma: How variable can shales be? *American Association of Petroleum Geologists Bulletin, 96*(3), 493-517.

Miceli-Romero, A. 2014. Subsurface and outcrop organic geochemistry of the Eagle Ford shale (Cenomanian-Coniacian) in West, Southwest, Central, and East Texas. (Doctoral dissertation). University of Oklahoma, Norman, Oklahoma, 289p.

Milad, B. 2017. The effect of karsting on natural fracture, hardness, and brittleness of the Hunton Limestone and paleo-deposition of the Woodford Shale: A study using 3-D seismic, outcrop, well log, and core data. American Association of Petroleum Geologists, Search and Discovery Article #51417.

Mizukami, T., Kaiho, K., & Oba, M. 2013. Significant changes in land vegetation and oceanic redox across the Cretaceous/Paleogene boundary. *Palaeogeography, Palaeoclimatology, Palaeoecology, 369*, 41-47.

Moldowan, J. M., Carlson, F. J., & R, M. K. 1991. Rearranged hopanes in sediments and petroleum. *Geochimica et Cosmochimica Acta, 55*(11), 3333-3353.

Moldowan, J. M., Fago, F. J., Lee, C. Y., Jacobson, S. R., Watt, D. S., Slougui, N. E., & Young, D. C. 1990. Sedimentary 24-n-propylcholestanes, Molecular Fossils Diagnostic of Marine Algae. *Science, 247*(4940), 309-312.

Moldowan, J. M., Lee, C. Y., Sundararaman, P., Salvatori, T., Alajbeg, A., Gjukić, B., Watt, D. 1992. Source correlation and maturity assessment of selected oils and rocks from the Central Adriatic Basin (Italy and Yugoslavia): In J. M. Moldowan, P. Albrecht, & R. P. Philp (Eds.), *Biological Markers in Sediments and Petroleum* (pp. 370-401). Englewood Cliffs, NJ: Prentice Hall.

Moldowan, J. M., Lee, C. Y., Watt, D. S., Jeganathan, A., Slougui, N., & Gallegos, E. J. 1991. Analysis and occurrence of C_{26}-steranes in petroleum and source rocks. *Geochimica et Cosmochimica Acta, 55*(4), 1065-1081.

Moldowan, J. M., Peters, K. E., Carlson, R. M., Schoell, M., & Abu-Ali, M. A. 1994. Diverse applications of petroleum biomarker maturity parameters. *The Arabian Journal for Science and Engineering, 19*(2B), 273-298.

Moldowan, J. M., Seifert, W. K., & Gallegos, E. J. 1985. Relationship between petroleum composition and depositional environment of petroleum source rocks. *American Association of Petroleum Geologists Bulletin, 69*(8), 1255-1268.

Monsalve, J. 2014. Areas prospectivas de lutitas gasiferas en la Formacion Colon, Municipio Torres y Moran, Estado Lara. *Terra Nueva, 30*(48), 117-142.

Moore, D., & Reynolds, R. 1997. *X-Ray diffraction and the identification and analysis of clay minerals.* New York, NY: Oxford University Press, 373p.

Mouawad, J. 2009, June 17. Estimate places natural gas reserves 35% higher. *The New York Times*, p. B1.

Nissenbaum, A., Baedecker, M. J., & Kaplan, I. R. 1972. Organic geochemistry of Dead Sea sediments. *Geochimica et Cosmochimica Acta, 36*(7), 709-727.

Noble, R. A., Alexander, R., Kagi, R. I., & Nox, J. K. 1986. Identification of some diterpenoid hydrocarbons in petroleum. *Organic Geochemistry, 10*(4-6), 825- 829.

Ourisson, G., Albrecht, P., & Rohmer, M. 1982. Predictive microbial biochemistry: From molecular fossils to prokaryotic membranes. *Trends in Biochemical Sciences, 7*(7), 236-239.

Ourisson, G., Rohmer, M., & Porolla, K. 1987. Prokaryotic hopanoids and other polyterpenoid sterol surrogates. *Annual Review of Microbiology, 41*(1), 301-333.

Pachano, M. 2013. *Caracterizacion geoquimica y sedimentologica de la Formacion Colon para la prospeccion de lulitas gasiferas en los Municipios Jimenez y Torres-Estado Lara.*

Merida, Venezuela. (Trabajo especial de grado). Universidad de Los Andes, Merida, Venezuela, 142p.

Palacas, J. G., Anders, D. E., & King, J. D. 1984. South Florida Basin: A prime example of carbonate source rocks in petroleum. In J. G. Palacas (Ed.), *Petroleum Geochemistry and Source Rock Potential of Carbonate Rocks* (pp. 71-96). Tulsa, OK: American Association of Petroleum Geologists.

Parnaud, F., Go, Y., Pascual, J., Truskowski, I., Gallango, O., Passalacqua, H., & Roure, F. 1995. Petroleum geology of the central part of the Eastern Venezuelan Basin. In A. J. Tankard, R. Suarez Soruco, & H. J. Welsink (Eds.), *Petroleum basins of South America* (pp. 741-756). Tulsa, OK: American Association of Petroleum Geologists.

Passalacqua, H., Fernandez, F., Gou, F., & Roure, F. 1995. Crustal architecture and strain partitioning in the Eastern Venezuelan Ranges. In A. J. Tankard, R. Suarez Soruco, & H. J. Welsink (Eds.), *Petroleum Basins of South America* (pp. 667-679). Tulsa, OK: American Association of Petroleum Geologists.

Pearce, T. J., Besly, B. M., Wray, D. S., & Wright, D. K. 1999. Chemostratigraphy: A method to improve interwell correlation in barren sequences. A case study using onshore Duckmantian/Stephanian sequences (West Midlands, U.K.). *Sedimentary Geology, 124*(1-4), 197-220.

Pedersen, T., & Calvert, S. 1990. Anoxia vs. productivity: What controls the formation of organic-carbon-rich sediments and sedimentary rocks? *American Association of Petroleum Geologists Bulletin, 74*(4), 454-466.

Perez Altamar, R., & Marfurt, K. 2014. Mineralogy-based brittleness prediction from surface seismic data: Application to the Barnett Shale. *Interpretation, 2*(4), 255-271.

Perez-Infante, J., Farrimond, P., & Furrer, M. 1996. Global and local controls influencing the deposition of the La Luna Formation (Cenomanian-Carnpanian), western Venezuela. *Chemical Geology, 130*(3-4), 271-288.

Peters, K. E. 1986. Guidelines for evaluating petroleum source rock using programmed pyrolysis. *American Association of Petroleum Geologists Bulletin, 70*(3), 318-329.

Peters, K. E., & Cassa, M. R. 1994. Applied source rock geochemistry. In L. B. Magoon & W. G. Dow (Eds.), *The Petroleum System: From Source to Trap* (pp. 93-120). Tulsa, OK: American Association of Petroleum Geologists.

Peters, K. E., & Moldowan, J. M. 1993. *The Biomarker Guide: Interpreting Molecular Fossils in Petroleum and Ancient Sediments*. Englewood Cliffs, N.J.: Prentice Hall, 1132.

Peters, K. E., & Moldowan, J. M.1997. Effects of source, thermal maturity, and biodegradation on the distribution and isomerization of homohopanes in petroleum. *Organic Geochemistry, 17*(1), 47-61.

Peters, K. E., Snedden, J. W., Sulaeman, A., & Sarg, J. 2000. A new geochemical-sequence stratigraphic model for the Mahakam Delta and Makassar Slope, Kalimantan, Indonesia. *American Association of Petroleum Geologists Bulletin, 84*, 12-44.

Peters, K. E., Walters, C. C., & Moldowan, J. M. 2005. *The Biomarker Guide, Biomarkers and Isotopes in Petroleum Systems and Earth History.* Cambridge, U.K.: Cambridge University Press, 451p.

Petroleos de Venezuela, Sociedad Anonima. 2012. *Proyecto de investigacion en estudio de formaciones lutiticas como reservorio de gas natural en la Cuenca de Lago de Maracaibo, Maracaibo, Venezuela.* Unpublished manuscript.

Philp, R. P. 2014. Formation and geochemistry of oil and gas. *Treatise on Geochemistry* (Second edition, volume 9, pp. 233-265). Oxford, U.K.: Elsevier.

Philp, R. P., & Gilbert, T. D. 1986. Biomarker distributions in Australian oils predominantly derived from terrigenous source material. *Organic Geochemistry, 10*(1-3), *73-84.*

Philp, R. P., Chen, J. H., Galvez-Sinibaldi, A., Wang, H. D., & Allen, J. D. 1992. Effects of weathering and maturity on the geochemical characteristics of the Woodford Shale. In K. S. Johnson & B. J. Cardott (Eds.), *Source Rocks in the Southern Midcontinent* (pp. 106-121). Norman, Oklahoma: Oklahoma Geological Survey.

Powell, T. G., & McKirdy, D. M. 1973. Relationship between ratio of pristane to phytane, crude oil composition and geological environment in Australia. *Nature, 243*(124), 37-39.

Pratt, L., & Threlkeld, C. 1984. Stratigraphic significance of $\delta^{13}C$ /$\delta^{12}C$ ratios in mid- Cretaceous rocks of the western interior, U.S.A. *Memoir, Canadian Society of Petroleum Geologists, 9,* 305-312.

Quero, V., Lopez, L., Salvador, L., Marco, C., Gaston, E., & Escobar, M. 2007. Evaluación de la formación La Luna como roca madre de petróleo en secciones del estado Táchira, Venezuela. *Revista Técnica de la Facultad de Ingeniería Universidad del Zulia, 30,* 326-335.

Radke, M. M., Welte, D. H, & Willsch, H. 1982. Geochemical study on a well in the Western Canada Basin: Relation of the aromatic distribution pattern to maturity of organic matter. *Geochimica et Cosmochimica Acta, 46*(1), 1-10.

Radke, M. 1988. Application of aromatic compounds as maturity indicators in source rocks and crude oils. *Marine and Petroleum Geology, 5*(3), 224-236.

Radke, M., Schaffer, R. G., & Leythauser, D. 1980. Composition of the soluble organic matter in coals and its relation to rank and liptinite fluorescence. *Geochimica et Cosmochimica Acta*, *44*(11), 1787-1799.

Radke, M., & Welte, D. H. 1988. The methylphenanthrene index (MPI): A maturity parameter based on aromatic hydrocarbons. In M. Bjoroy (Ed.), *Advances in Organic Geochemistry 1981,* 504-512.

Radke, M., Leythaeuser, D., & Teichmüller, M. 1984. Relationship between rank and composition of aromatic hydrocarbons for coal of different origins. *Organic Geochemistry, 6,* 423-430.

Radke, M., Welte, D. H., & Willsch, H. 1986. Maturity parameters based on aromatic hydrocarbons: Influence of the organic matter type. *Organic Geochemistry, 10*(1-3), 51-63.

Ratcliffe, K., Martin, J., Pearce, T., Hughes, A., Lawton, D., & Wray, D. 2006. A regional chemostratigraphically-defined correlation framework for the Late Triassic TAG-I formation in blocks 402 and 405a, Algeria. *Petroleum Geoscience*, *12*(1), 3-12.

Readman, J. W., Preston, M. R., & Mantoura, R. F. C. 1986. An integrated technique to quantify sewage, oil and PAH pollution in estuarine and coastal environments. *Marine Pollution Bulletin*, *17*(7), 298-308.

Reimers, C. E., Ruttenberg, K. C., Canfield, D. E., Christiansen, M. B., & Martin, J. B. 1996. Porewater pH and authigenic phases formed in the uppermost sediments of the Santa Barbara Basin. *Geochimica et Cosmochimica Acta*, *60*(21), 4037-4057.

Reineck, H. E., & Singh, I. B. 1980. *Depositional Sedimentary Environments*. New York: Springer-Verlag, 549p.

Riolo, J., Hussler, G., Albrecht, P., & Connan, J. 1986. Distribution of aromatic steroids in geological samples: Their evaluation as geochemical parameters. *Organic Geochemistry*, *10*(4-6), 981-990.

Risatti, J. B., Rowland, S. J., Yon, D. A., & Maxwell, J. R. 1984. Stereochemical studies of acyclic isoprenoids: Lipids of methanogenic bacteria and possible contributions to sediments. *Organic Geochemistry, 6*, 93-104.

Riva, A., Riolo, J., Mycke, B., Ocampo, R., Callot, H. J., Albrecht, P., & Nali, M. 1989. Molecular parameters in Italian carbonate oils: Reconstruction of past depositional environments. In B. Durand & F. Behar (Eds.), *Advances in Geochemistry 1989* (pp. 18-22). Oxford, U.K.: Pergamon.

Rodriguez, N. 2007. Geochemical characterization of gases from the Barnett shale, Fort Worth Basin, Texas (Master's thesis). University of Oklahoma, Norman, Oklahoma, 123p.

Rubenstein, I., Sieskind, O., & Albrecht, P. 1975. Rearranged sterenes in a shale: occurrence and simulated formation. *Journal of the Chemical Society Perkin Transactions 1, 19*, 1833-1836.

Rullkötter, J., & Marzi, R. 1988. Natural and artificial maturation of biological markers in a Toarcian shale from northern Germany. *Organic Geochemistry, 13*(4-6), 639-645.

Sageman, B. B., & Lyons, T. W. 2003. Geochemistry of fine-grained sediments and sedimentary rocks: volume 7. In F. Mackenzie (Ed.), *Treatise on Geochemistry*: volume 7 (pp. 115-158). New York, Elsvier Publishing.

Schiefelbein, C. F., Zumberge, J. E., Cameron, N. R., & Brown, S. W. 1999. Petroleum systems in the South Atlantic margins. In V. S. Clure, N. R. Cameron, & R. H. Bate, *The Oil and*

Gas Habitats of the South Atlantic (pp. 169-179). London, U.K.: Geological Society of London.

Schoenherr, J., Littke, R., Urai, J. L., Kukla, P. A., & Rawahi, Z. 2007. Polyphase thermal evolution in the Infra-Cambrian Ara Group (South Oman Salt Basin) as deduced by maturity of solid reservoir bitumen. *Organic Geochemistry, 38(8),* 1293-1318.

Scholle, P., & Arthur, M. 1980. Carbon isotope fluctuations in Cretaceous pelagic limestones. *American Association of Petroleum Geologists Bulletin, 64*(1), 67-87.

Schou, L., & Myhr, M. B. 1988. Sulfur aromatic compounds as maturity parameters. In L. Mattavelli & L. Novelli (Eds.), *Organic Geochemistry in Petroleum Exploration,* (pp. 61-66). Oxford, U.K.: Pergamon.

Schreiber, B. C., Philp, R. P., Benali, S., Helman, M. L., De la Peña, J. A., Marfil, R., & Kendall, C. S. 2001. Characterization of organic matter formed in hypersaline carbonate/evaporite environments: Hydrocarbon potential and biomarkers obtained through artificial maturation studies. *Journal of Petroleum Geology, 24*(3), 309-338.

Schwark, L., & Frimmel, A. 2004. Chemostratigraphy of the Posidonia Black Shale, SW-Germany: II. Assessment of extent and persistence of photic-zone anoxia using aryl isoprenoid distributions. *Chemical Geology, 206*(3-4), 231-248.

Schwennicke, T., Siegmund, H., & Jehl, C. 2000. Marine phosphogenesis in shallow-water environments: Cambrian, Tertiary, and recent examples. In: C. R. Glenn & L. Prévôt-Lucas & J. Lucas, *Marine Authigenesis: From Global to Microbial* (pp. 481-498). Tulsa, OK: Society for Sedimentary Geology.

Seifert, W. K., & Moldowan, J. M. 1979. The effect of biodegradation on steranes and terpanes in crude oils. *Geochimica et Cosmochimica Acta, 43*(1) , 111-126.

Seifert, W. K., & Moldowan, J. M. 1986. Use of biological markers in petroleum exploration. In R. B. Johns (Ed.), *Methods in Geochemistry and Geophysics, 24*, 261-290.

Seifert, W. K., Moldowan., J. M., & Jones, R. W. 1980. Application of biological marker chemistry to petroleum exploration. *Proceedings of the Tenth World Petroleum Congress*, 425-440.

Shagam, R. 1984. Tectonic implications of Cretaceous-Pliocene fission-track ages from rocks of the circum-Maracaibo Basin region of western Venezuela and Eastern Colombia. *Geological Society of America Memoirs, 162*, 385-412.

Shanmugam, G. 1985. Significance of coniferous rain forests and related organic matter in generating commercial quantities of oil, Gippsland Basin, Australia. *American Association of Petroleum Geologists Bulletin, 69*(8), 1241-1254.

Shiah, F. K., Chung, S. W., Kao, S. J., Gong, G. C., & Liu, K. K. 2000. Biological and hydrographical responses to tropical cyclones (typhoons) in the continental shelf of the Taiwan Strait. *Continental Shelf Research, 20*(15), 2029-2044.

Simoneit, B. R., Schoell, M., Dias, F. R., & Aquino, N. 1993. Unusual carbon isotope compositions of biomarker hydrocarbons in a Permian tasmanite. *Geochimica et Cosmochimica Acta, 57*(17), 4205-4211.

Slatt, R. M. 2013. Sequence stratigraphy of the Woodford Shale and application to drilling and production. American Association of Petroleum Geologists, Search and Discover Article #50792.

Slatt, R. M., P. R. Philp, Y. Abousleiman, P. Singh, R. Perez, R. Portas, K. J. Marfurt, S. Madrid-Arroyo, N. O'Brien, E. V. Eslinger, and E. T. Baruch. 2012. Pore-to-regional-

scale Integrated Characterization Workflow for Unconventional Gas Shales. *American Association of Petroleum Geologists Memoir, 97,* 127-150.

Slatt, R. M., & Rodriguez, N. D. 2012. Comparative sequence stratigraphy and organic geochemistry of gas shales: Commonality or coincidence? *Journal of Natural Gas Science and Engineering, 8*, 68-84.

Slatt, R. M., Philp, R. P., Abousleiman, Y., Singh, P., Perez, R, R., & Portas, R. 2011. Pore-to-regional-scale integrated characterization workflow for unconventional gas shales. In A. Breyer (Ed.), *Shale reservoirs: Giant resources for the 21st century* (pp. 127-150). Tulsa, OK: *American Association of Petroleum Geologists.*

Sliter, W. V. 1989. Biostratigraphic zonation for Cretaceous planktonic foraminifers examined in thin section. *Journal of Foraminiferal Research, 19*(1), 1-19.

Sohn, M. L. 1986. *Organic marine geochemistry.* American Chemical Society, Washington, DC: ACS Symposium Series, 270p.

Stojanovic, K., Jovancicevic, B., Pevneva, G. S., Golovko, J., Golovko, A. K., & Pfendt, P. 2001. Maturity assessment of oils from the Sakhalin oil fields in Russia: phenanthrene content as a tool. *Organic Geochemistry 32*(5), 721-731.

Summons, R. E., & Powell, T. G. 1987. Identification of aryl isoprenoids in a source rock and crude oils: Biological markers for the green sulfur bacteria. *Geochimica et Cosmochimica Acta, 51*(3), 557-566.

Talukdar, S., & Marcano, F. 1994. Petroleum systems in the Maracaibo Basin, Venezuela. The petroleum system: From source to trap. *American Association of Petroleum Geologists Memoirs, 60*, 463-481.

Talukdar, S., Gallango, O., & Chin-A-Lien, M. 1986. Generation and migration of hydrocarbons in the Maracaibo Basin, Venezuela: An integrated basin study. *Organic Geochemistry, 10*(1-3), 261-279.

Tarbuck, E. J., Lutgens, F.K & Tasa, D.G. 2016. *Earth: an introduction to physical geology*. Harlow, United Kingdom: Pearson/Prentice Hall, 605p.

ten Haven, De Leeuw, Rullkotter, & Damste, 1987. Restricted utility of the pristane/phytane ratio as a palaeoenvironmental indicator. *Nature, 330*(6149), 641-643.

ten Haven, H. L., De Leeuw, J. W., & Schenck, P. A. 1985. Organic geochemical studies of a Messinian evaporitic basin, northern Apennines (Italy) I: Hydrocarbon biological markers for a hypersaline environment. *Geochimica et Cosmochimica Acta, 49*(10), 2181-2191.

Tissot, B. P., & Welte, D. H. 1984. *Petroleum Formation and Occurrence*. Berlin, Germany: Springer, 702p.

Tissot, B. P., Durand, B., Espitalie, J., & Combaz, A. 1974. Influence of nature and diagenesis of organic matter in the formation of petroleum. *American Association of Petroleum Geologists Bulletin, 58*(3), 499-506.

Torres, E. 2013. Unconventional gas shale assessment of La Luna Formation in the Middle Magdalena Basin. (Master's thesis.) University of Oklahoma, Norman, Oklahoma, 210p.

Torres-Parada, E. J., Liborius-Parada, A., Infante-Paez, L. E., Zhang, J., Slatt, R., Marfurt, K., & Sneddon, A. 2018. Geological controls of the organic-inorganic distributions within the Woodford Shale in Northern Oklahoma USA: Integrating for finding the unconventional sweet spots. American Association of Petroleum Geologists, Search and Discovery Article #51444.

Tribovillard, N., Algeo, T. J., Lyons, T., & Riboulleau, A. 2006. Trace metals as paleoredox and paleoproductivity proxies: An update. *Chemical Geology*, *232*(1-2), 12-32.

Truskowski, I., Galea-Alvarez, F., & Sliter, W. 1995. Cenomanian hiatus in Venezuela. *Geological Society of America, Abstracts with Programs, 27*, A-303.

Tselepides, A., Polychronaki, T., Marrale, D., Akoumianaki, I., Dell'Anno, A., Pusceddu, A., & Danovaro, R. 2000. Organic matter composition of the continental shelf and bathyal sediments of the Cretan Sea (NE Mediterranean). *Progress in Oceanography, 46*(2-4), 311-344.

Turner, B. W. 2016. Utilization of chemostratigraphic proxies for generating and refining sequence stratigraphic frameworks in mudrocks and shales (Doctoral dissertation). University of Oklahoma, Norman, Oklahoma, 135p.

Turner, B. W., Molinares-Blanco, C. E., & Slatt, R. M. 2015. Chemostratigraphic, palynostratigraphic, and sequence stratigraphic analysis of the Woodford Shale, Wyche Farm Quarry, Pontotoc County, Oklahoma. *Interpretation, 3*(1), 1-9.

U.S-Energy-Information-Administration. 2015. *Technically recoverable shale oil and shale gas resources: Northern South America.* Washington, DC: U.S. Energy Information Administration, IV-22p.

Van Wagoner, J. C., Mitchum, R. M., Campion, K. M., & Rahmanian, V. D. 1990. *Siliciclastic sequence stratigraphy in well logs, cores, and outcrops: concepts for high-resolution correlation of time and facies.* Methods in Exploration Series, 7. Tulsa, Oklahoma: American Association of Petroleum Geologists.

Vergara, L. S. 1997. Cretaceous black shales in the Upper Magdalena Valley, Colombia. New organic geochemical results (Part II). *Journal of South American Earth Sciences, 10*(2), 133-145.

Villamil, T. 2002, May. *Formacion La Luna-La cuna del petroleo.* Retrieved July 07, 2014 from http://www.palacio.org.

Volk, H., George, S. C., Dutkiewicz, A., & Ridley, J. 2005. Characterization of fluid inclusion oil in a mid-Proterozoic sandstone and dolerite (Roper Superbasin, Australia). *Chemical Geology, 223*(1-3*)*, 109–135.

Volkman, J. K. 1986. A review of sterol markers for marine and terrigenous organic matter. *Organic Geochemistry, 9*(2), 83-99.

Volkman, J. K., Banks, M. R., Denwer, K., & Aquino, N. 1989. Biomarker composition and depositional setting of tasmanite oil shale from northern Tasmania, Australia. 14th International Meeting on Organic Geochemistry, Paris, 18–22 September, Abstract #168.

Wang, F. P., & Gale, J. F. 2009. Screening criteria for shale-gas systems. *Transactions of the Gulf Coast Association of Geological Societies, 59,* 779-794.

Wang, G., Chang, X., Wang, T. G., & Simoneit, B. R. 2015. Pregnanes as molecular indicators for depositional environments of sediments and petroleum source rocks. *Organic Geochemistry, 78*, 110-120.

Wang, H. D., & Philp, R. P. 1997. Geochemical study of potential source rocks and crude oils in the Anadarko Basin, Oklahoma. *American Association of Petroleum* Geologists *Bulletin, 81*(2), 249-275.

Wang, T., 2016, An Organic Geochemical Study of Woodford Shale and Woodford Mississippian Tight Oil from Central Oklahoma. (Doctoral dissertation). University of Oklahoma, Norman, Oklahoma, 299p.

Wang, Z., Fingas, C., & Hollebone, B. 2004. Biomarker fingerprinting: Application and limitation for correlation and source identification of oils and petroleum products. *Journal of the American Chemical Society Division of Fuel Chemistry 49*(1), 332.

Waples, D. W., & Machihara, T. 1991. *Biomarkers for geologists: A practical guide to the application of steranes and triterpanes in petroleum geology.* American Association of Petroleum Geologist Methods in Exploration Series No. 9. Tulsa, OK: American Association of Petroleum Geologists, 91p.

Yang, C., Wang, Z., Liu, Y., Yang, Z., Li, Y., Shah, K., & Lambert, P. 2013. Aromatic steroids in crude oils and petroleum products and their applications in forensic oil spill identification. *Environmental Forensics, 14*(4), 278-293.

Zambrano, E. E. 1971. Sıntesis paleogeografica y petrolera del occidente de Venezuela. *Memorias Cuarto Congreso Geologico*, 483-552.

Zumberge, J. 1984. Source rocks of the La Luna Formation (Upper Cretaceous) in the Middle Magdalena Valley, Colombia. *American Association of Petroleum Geologists, Studies in Geology, 18*, 127-133.

8. APPENDIX

7.1. Total Organic Carbon (TOC) and Rock-Eval (RE) parameters for La Luna Formation samples

7.1.1. La Luna IX *core (cont.)*

Sample	Depth(ft)	TOC (wt%)	S1	S2	S3	S1/TOC	S1+S2	S2/S3	T_{max}	Ro	HI	OI	PI
LLIX1	15267	0.98	0.42	0.72	0.37	42.94	1.14	1.95	437.00	0.71	73.62	37.83	0.37
LLIX2	15270	1.28	2.06	1.90	0.79	160.94	3.96	2.41	430.00	0.58	148.44	61.72	0.52
LLIX3	15273	3.31	5.08	10.15	1.08	153.47	15.23	9.40	431.00	0.60	306.65	32.63	0.33
LLIX4	15274	4.74	2.82	20.37	0.62	59.49	23.19	32.85	441.00	0.78	429.75	13.08	0.12
LLIX5	15275	5.44	4.40	20.47	0.13	80.88	24.87	157.46	442.00	0.80	376.29	2.39	0.18
LLIX6	15277	4.84	1.51	15.50	0.25	31.20	17.01	62.00	443.00	0.81	320.25	5.17	0.09
LLIX7	15278	3.85	1.61	15.13	0.54	41.82	16.74	28.02	442.00	0.80	392.99	14.03	0.10
LLIX8	15280	4.40	1.90	18.76	0.63	43.18	20.66	29.78	439.00	0.74	426.36	14.32	0.09
LLIX9	15287	4.43	1.92	17.18	0.61	43.34	19.10	28.16	439.00	0.74	387.81	13.77	0.10
LLIX10	15297	5.90	3.36	23.42	0.90	56.95	26.78	26.02	439.00	0.74	396.95	15.25	0.13
LLIX11	15300	0.88	0.22	2.10	0.25	25.03	2.32	8.40	436.00	0.69	238.91	28.44	0.09
LLIX12	15303	1.04	0.56	2.39	0.17	53.85	2.95	14.06	442.00	0.80	229.81	16.35	0.19
LLIX13	15308	7.72	4.23	31.17	1.09	54.79	35.40	28.60	441.00	0.78	403.76	14.12	0.12
LLIX14	15313	5.82	2.73	17.40	0.15	46.91	20.13	116.00	443.00	0.81	298.97	2.58	0.14
LLIX15	15314	4.12	1.75	12.70	0.55	42.48	14.45	23.09	439.00	0.74	308.25	13.35	0.12
LLIX16	15317	4.80	2.98	17.26	0.76	62.08	20.24	22.71	437.00	0.71	359.58	15.83	0.15
LLIX17	15327	7.15	3.05	25.46	1.10	42.66	28.51	23.15	440.00	0.76	356.08	15.38	0.11
LLIX18	15330	5.59	1.77	13.28	0.03	31.66	15.05	442.67	444.00	0.83	237.57	0.54	0.12
LLIX19	15332	8.85	5.22	32.73	1.02	58.98	37.95	32.09	439.00	0.74	369.83	11.53	0.14
LLIX20	15334	0.84	0.41	3.28	0.47	48.58	3.69	6.98	439.00	0.74	388.63	55.69	0.11

La Luna IX core (cont.)

Sample	Depth(ft)	TOC (wt%)	S1	S2	S3	S1/TOC	S1+S2	S2/S3	T_{max}	Ro	HI	OI	PI
LLIX21	15335	6.30	3.44	22.60	0.02	54.60	26.04	1130.00	444.00	0.83	358.73	0.32	0.13
LLIX22	15342	0.75	0.67	2.13	0.54	89.33	2.80	3.94	433.00	0.63	284.00	72.00	0.24
LLIX23	15349	7.35	3.07	21.92	0.01	41.77	24.99	2192.00	443.00	0.81	298.23	0.14	0.12
LLIX24	15351	6.44	2.93	21.04	0.90	45.50	23.97	23.38	436.00	0.69	326.71	13.98	0.12
LLIX25	15357	9.13	5.40	38.26	1.06	59.15	43.66	36.09	440.00	0.76	419.06	11.61	0.12
LLIX26	15361	6.11	2.53	21.14	0.01	41.41	23.67	2114.00	445.00	0.85	345.99	0.16	0.11
LLIX27	15363	5.98	1.45	20.05	0.54	24.25	21.50	37.13	438.00	0.72	335.28	9.03	0.07
LLIX28	15365	0.56	0.30	1.08	0.24	53.19	1.38	4.50	439.00	0.74	191.49	42.55	0.22
LLIX29	15370	5.29	1.91	16.53	0.01	36.11	18.44	1653.00	443.00	0.81	312.48	0.19	0.10
LLIX30	15371	7.57	2.63	28.31	0.76	34.74	30.94	37.25	437.00	0.71	373.98	10.04	0.09
LLIX31	15372	4.35	1.36	12.36	0.58	31.26	13.72	21.31	441.00	0.78	284.14	13.33	0.10
LLIX32	15376	0.22	0.07	0.28	0.15	31.39	0.35	1.87	443.00	0.81	125.56	67.26	0.20
LLIX33	15377	4.86	2.23	15.02	0.01	45.88	17.25	1502.00	443.00	0.81	309.05	0.21	0.13
LLIX34	15378	6.12	2.09	19.88	0.84	34.15	21.97	23.67	438.00	0.72	324.84	13.73	0.10
LLIX35	15382	0.96	0.83	1.61	0.69	86.10	2.44	2.33	431.00	0.60	167.01	71.58	0.34
LLIX36	15393	2.59	0.86	6.50	0.04	33.20	7.36	162.50	441.00	0.78	250.97	1.54	0.12
LLIX37	15394	1.20	0.53	2.93	0.26	44.17	3.46	11.27	436.00	0.69	244.17	21.67	0.15
LLIX38	15395	0.96	0.45	1.44	0.40	46.73	1.89	3.60	440.00	0.76	149.53	41.54	0.24
LLIX39	15398	2.78	1.02	6.13	0.43	36.69	7.15	14.26	438.00	0.72	220.50	15.47	0.14
LLIX40	15401	3.87	1.99	11.84	0.63	51.42	13.83	18.79	441.00	0.78	305.94	16.28	0.14

La Luna IX core (cont.)

Sample	Depth(ft)	TOC (wt%)	S1	S2	S3	S1/TOC	S1+S2	S2/S3	T_{max}	Ro	HI	OI	PI
LLIX41	15410	0.69	0.54	0.76	0.11	78.26	1.30	6.91	426.00	0.51	110.14	15.94	0.42
LLIX42	15415	4.78	1.92	12.02	0.66	40.17	13.94	18.21	442.00	0.80	251.49	13.81	0.14
LLIX43	15418	5.31	2.10	13.24	0.02	39.55	15.34	662.00	445.00	0.85	249.34	0.38	0.14
LLIX44	15430	6.16	4.64	22.38	0.93	75.32	27.02	24.06	439.00	0.74	363.31	15.10	0.17
LLIX45	15431	3.42	1.93	6.69	0.01	56.43	8.62	669.00	443.00	0.81	195.61	0.29	0.22
LLIX46	15438	3.74	1.96	9.28	0.70	52.41	11.24	13.26	442.00	0.80	248.13	18.72	0.17
LLIX47	15444	1.18	0.76	2.35	0.41	64.41	3.11	5.73	440.00	0.76	199.15	34.75	0.24
LLIX48	15444	4.07	1.96	10.11	0.67	48.16	12.07	15.09	440.00	0.76	248.40	16.46	0.16
LLIX49	15450	1.72	0.63	3.68	0.01	36.63	4.31	368.00	441.00	0.78	213.95	0.58	0.15
LLIX50	15460	3.44	1.40	8.07	0.03	40.70	9.47	269.00	446.00	0.87	234.59	0.87	0.15
LLIX51	15464	4.07	1.55	10.02	0.37	38.08	11.57	27.08	442.00	0.80	246.19	9.09	0.13
LLIX52	15469	4.23	2.03	9.90	0.59	47.99	11.93	16.78	442.00	0.80	234.04	13.95	0.17
LLIX53	15476	3.73	1.31	9.20	0.01	35.12	10.51	920.00	442.00	0.80	246.65	0.27	0.12
LLIX54	15479	1.93	0.63	4.29	0.24	32.64	4.92	17.88	439.00	0.74	222.28	12.44	0.13
LLIX55	15495	2.75	1.37	5.79	0.01	49.82	7.16	579.00	443.00	0.81	210.55	0.36	0.19
LLIX56	15496	0.10	0.06	0.10	0.01	61.04	0.16	10.00	0.00	-7.16	101.73	10.17	0.38
LLIX57	1500	5.11	1.14	12.57	0.55	22.31	13.71	22.85	442.00	0.80	245.99	10.76	0.08
LLIX58	15515	4.34	1.14	9.03	0.01	26.27	10.17	903.00	449.00	0.92	208.06	0.23	0.11
LLIX59	15527	4.19	1.18	8.63	0.01	28.16	9.81	863.00	445.00	0.85	205.97	0.24	0.12
LLIX60	15528	5.06	0.99	13.50	0.50	19.57	14.49	27.00	438.00	0.72	266.80	9.88	0.07

La Luna IX core (cont.)

Sample	Depth(ft)	TOC (wt%)	S1	S2	S3	S1/TOC	S1+S2	S2/S3	T_{max}	Ro	HI	OI	PI
LLIX61	15534	3.84	0.59	7.69	0.01	15.36	8.28	769.00	449.00	0.92	200.26	0.26	0.07
LLIX62	15537	2.72	0.84	5.14	0.34	30.88	5.98	15.12	444.00	0.83	188.97	12.50	0.14
LLIX63	15551	4.50	1.73	8.02	0.01	38.44	9.75	802.00	445.00	0.85	178.22	0.22	0.18
LLIX64	15554	9.27	2.73	23.16	0.83	29.45	25.89	27.90	441.00	0.78	249.84	8.95	0.11
LLIX65	15560	0.97	0.43	1.82	0.01	44.33	2.25	182.00	443.00	0.81	187.63	1.03	0.19
LLIX66	15562	1.22	0.46	2.23	0.27	37.70	2.69	8.26	440.00	0.76	182.79	22.13	0.17
LLIX67	15568	3.13	1.16	7.26	0.42	37.06	8.42	17.29	443.00	0.81	231.95	13.42	0.14

7.1.2. La Luna IE core

Sample	Depth(ft)	TOC (wt%)	S1	S2	S3	S1/TOC	S1+S2	S2/S3	T_{max}	Ro	HI	OI	PI
LLIE1	15321	0.52	0.38	0.19	0.22	72.94	0.57	0.86	461.00	1.14	36.47	42.23	0.67
LLIE2	15324	1.81	0.46	0.83	0.28	25.41	1.29	2.96	482.00	1.52	45.86	15.47	0.36
LLIE3	15334	1.30	0.37	0.48	0.28	28.46	0.85	1.71	473.00	1.35	36.92	21.54	0.44
LLIE4	15339	2.45	0.65	1.39	0.40	26.53	2.04	3.48	468.00	1.26	56.73	16.33	0.32
LLIE5	15343	0.36	0.74	0.31	0.46	205.56	1.05	0.67	449.00	0.92	86.11	127.78	0.70
LLIE6	15351	1.47	0.53	0.92	0.21	36.05	1.45	4.38	487.00	1.61	62.59	14.29	0.37
LLIE7	15353	0.71	0.26	0.34	0.29	36.88	0.60	1.17	500.00	1.84	48.23	41.13	0.43
LLIE8	15354	2.05	0.36	0.60	0.26	17.56	0.96	2.31	479.00	1.46	29.27	12.68	0.38
LLIE9	15360	2.77	0.67	1.22	0.33	24.19	1.89	3.70	470.00	1.30	44.04	11.91	0.35
LLIE10	15367	0.49	0.64	0.30	0.33	130.61	0.94	0.91	474.00	1.37	61.22	67.35	0.68
LLIE11	15377	1.91	0.41	1.12	0.23	21.47	1.53	4.87	502.00	1.88	58.64	12.04	0.27
LLIE12	15382	1.67	0.19	0.32	0.18	11.38	0.51	1.78	481.00	1.50	19.16	10.78	0.37
LLIE13	15391	2.57	2.14	1.50	0.46	83.27	3.64	3.26	473. 00	1.35	58.37	17.90	0.59

La Luna IE core (cont.)

Sample	Depth(ft)	TOC (wt%)	S1	S2	S3	S1/TOC	S1+S2	S2/S3	T_{max}	Ro	HI	OI	PI
LLIE14	15396	2.66	0.25	0.60	0.42	9.40	0.85	1.43	487.00	1.61	22.56	15.79	0.29
LLIE15	15401	0.41	0.32	0.11	0.23	78.05	0.43	0.48	438.00	0.72	26.83	56.10	0.74
LLIE16	15403	3.14	0.22	0.52	0.26	7.01	0.74	2.00	499.00	1.82	16.56	8.28	0.30
LLIE17	15408	3.44	0.26	0.66	0.31	7.56	0.92	2.13	490.00	1.66	19.19	9.01	0.28
LLIE18	15412	2.24	0.37	0.59	0.15	16.52	0.96	3.93	483.00	1.53	26.34	6.70	0.39
LLIE19	15421	3.05	0.38	0.74	0.35	12.46	1.12	2.11	490.00	1.66	24.26	11.48	0.34
LLIE20	15423	0.09	0.06	0.03	0.36	65.93	0.09	0.08	435.00	0.67	32.97	395.60	0.67
LLIE21	15425	2.33	0.52	0.75	0.26	22.32	1.27	2.88	483.00	1.53	32.19	11.16	0.41
LLIE22	15430	2.31	0.48	0.68	0.31	20.78	1.16	2.19	481.00	1.50	29.44	13.42	0.41
LLIE23	15443	3.23	0.30	0.64	0.24	9.29	0.94	2.67	486.00	1.59	19.81	7.43	0.32
LLIE24	15445	2.33	0.27	0.71	0.28	11.59	0.98	2.54	483.00	1.53	30.47	12.02	0.28
LLIE25	15451	2.14	0.40	0.56	0.26	18.69	0.96	2.15	562.00	2.96	26.17	12.15	0.42
LLIE26	15461	3.16	0.62	0.87	0.43	19.62	1.49	2.02	562.00	2.96	27.53	13.61	0.42
LLIE27	15465	1.67	0.56	0.49	0.34	33.53	1.05	1.44	507.00	1.97	29.34	20.36	0.53
LLIE28	15520	3.69	0.21	0.55	0.28	5.69	0.76	1.96	560.00	2.92	14.91	7.59	0.28
LLIE29	15535	4.32	0.29	0.93	0.39	6.71	1.22	2.38	486.00	1.59	21.53	9.03	0.24
LLIE30	15544	1.36	0.22	0.32	0.26	16.18	0.54	1.23	502.00	1.88	23.53	19.12	0.41
LLIE31	15545	2.09	0.16	0.29	0.30	7.66	0.45	0.97	562.00	2.96	13.88	14.35	0.36
LLIE32	15548	0.11	0.04	0.02	0.32	35.40	0.06	0.06	349.00	0.88	17.70	283.19	0.67
LLIE33	15548'9	0.33	0.22	0.05	0.39	65.87	0.27	0.13	345.00	0.95	14.97	116.77	0.81
LLIE34	15556	7.70	0.50	1.97	0.33	6.49	2.47	5.97	505.00	1.93	25.58	4.29	0.20

La Luna IE core (cont.)

Sample	Depth(ft)	TOC (wt%)	S1	S2	S3	S1/TOC	S1+S2	S2/S3	T_{max}	Ro	HI	OI	PI
LLIE35	15559	3.38	0.23	0.43	0.41	6.80	0.66	1.05	562	2.96	12.72	12.13	0.35
LLIE36	15561	7.36	0.55	2.70	0.47	7.47	3.25	5.74	509	2.00	36.68	6.39	0.17
LLIE37	15564	1.10	0.63	0.32	0.26	57.27	0.95	1.23	375	0.41	29.09	23.64	0.66
LLIE38	15571'6	0.63	0.24	0.17	0.23	38.03	0.41	0.74	372	0.46	26.94	36.45	0.59
LLIE39	15583	2.83	0.26	0.53	0.29	9.19	0.79	1.83	562	2.96	18.73	10.25	0.33
LLIE40	15589	1.27	0.23	0.33	0.25	18.11	0.56	1.32	519	2.18	25.98	19.69	0.41
LLIE41	15592	1.93	0.18	0.42	0.37	9.33	0.60	1.14	562	2.96	21.76	19.17	0.30
LLIE42	15603'8	1.16	0.21	0.20	0.22	18.10	0.41	0.91	560	2.92	17.24	18.97	0.51
LLIE43	15344	2.37	0.67	0.92	0.34	28.27	1.59	2.71	487	1.61	38.82	14.35	0.42

7.1.3. La Luna stratotype

Depth(ft)	TOC (wt%)	S_1	S_2	S_3	S_1/TOC	S_1+S_2	S_2/S_3	T_{max}	Ro	HI	OI	PI
La Luna stratotype 1	2.9	1.76	21.44	0.58	60.69	23.20	36.97	426	0.51	739.31	20.00	0.08
La Luna stratotype 2	7.24	1.2	48.45	1.12	16.57	49.65	43.26	427	0.53	669.20	15.47	0.02
La Luna stratotype 3	0.14	0.04	0.26	0.11	28.57	0.30	2.36	435	0.67	185.71	78.57	0.13
La Luna stratotype 4	12.8	3.29	102.44	1.03	25.70	105.73	99.46	430	0.58	800.31	8.05	0.03
La Luna stratotype 5	10.3	2.14	78.17	0.91	20.78	80.31	85.90	430	0.58	758.93	8.83	0.03
La Luna stratotype 7	1.92	0.26	2.69	1.01	13.54	2.95	2.66	430	0.58	140.10	52.60	0.09
La Luna stratotype 8	2.9	1.76	21.44	0.58	60.69	23.20	36.97	426	0.51	739.31	20.00	0.08

7.1.4. La Luna IA core

Sample	Depth(ft)	TOC (wt%)	S1	S2	S3	T_{max}	Ro	HI	OI	S2/S3	S1/TOC	PI	S1+S2
LLIA1	15755	6.44	2.32	12.89	0.45	451.00	0.96	200.16	6.99	28.64	36.02	0.15	15.21
LLIA2	15760	6.57	2.05	12.90	0.28	452.00	0.98	196.35	4.26	46.07	31.20	0.14	14.95
LLIA3	15765	7.59	2.48	14.25	0.27	452.00	0.98	187.75	3.56	52.78	32.67	0.15	16.73
LLIA4	15770	5.62	2.08	11.69	0.25	451.00	0.96	208.01	4.45	46.76	37.01	0.15	13.77
LLIA5	15775	0.34	0.10	0.09	0.21	378.00	-0.36	26.24	61.22	0.43	29.15	0.53	0.19
LLIA6	15780	0.91	1.00	2.26	0.25	437.00	0.71	247.54	27.38	9.04	109.53	0.31	3.26
LLIA7	15785	7.43	2.40	15.58	0.34	451.00	0.96	209.69	4.58	45.82	32.30	0.13	17.98
LLIA8	15790	5.06	3.16	9.90	0.28	452.00	0.98	195.65	5.53	35.36	62.45	0.24	13.06
LLIA9	15795	6.11	2.47	12.37	0.26	450.00	0.94	202.45	4.26	47.58	40.43	0.17	14.84
LLIA10	15796	0.48	0.27	1.06	0.31	443.00	0.81	219.01	64.05	3.42	55.79	0.20	1.33
LLIA11	15800	0.58	0.55	1.15	0.15	440.00	0.76	198.62	25.91	7.67	94.99	0.32	1.70
LLIA12	15805	8.48	6.74	19.70	0.27	449.00	0.92	232.31	3.18	72.96	79.48	0.25	26.44
LLIA13	15810	2.86	1.00	5.70	0.23	452.00	0.98	199.30	8.04	24.78	34.97	0.15	6.70
LLIA14	15815	4.13	1.53	7.22	0.31	453.00	0.99	174.82	7.51	23.29	37.05	0.17	8.75
LLIA15	15820	3.77	1.29	6.26	0.22	453.00	0.99	166.05	5.84	28.45	34.22	0.17	7.55
LLIA16	15825	2.39	1.21	4.13	0.19	451.00	0.96	172.80	7.95	21.74	50.63	0.23	5.34
LLIA17	15830	5.96	3.32	11.38	0.32	452.00	0.98	190.94	5.37	35.56	55.70	0.23	14.70
LLIA18	15835	4.52	2.39	9.30	0.20	453.00	0.99	205.75	4.42	46.50	52.88	0.20	11.69
LLIA19	15840	5.42	1.82	8.36	0.23	454.00	1.01	154.24	4.24	36.35	33.58	0.18	10.18
LLIA20	15845	1.45	0.34	0.46	0.42	433.00	0.63	31.72	28.97	1.10	23.45	0.43	0.80

La Luna IA core (cont.)

Sample	Depth(ft)	TOC (wt%)	S1	S2	S3	T_{max}	Ro	HI	OI	S2/S3	S1/TOC	PI	S1+S2
LLIA21	15850	0.29	0.19	0.33	0.23	447.00	0.89	112.24	78.23	1.43	64.63	0.37	0.52
LLIA22	15855	2.37	0.99	3.36	0.24	452.00	0.98	141.77	10.13	14.00	41.77	0.23	4.35
LLIA23	15860	2.21	1.10	3.66	0.24	450.00	0.94	165.61	10.86	15.25	49.77	0.23	4.76
LLIA24	15865	0.45	0.25	0.57	0.21	446.00	0.87	126.39	46.56	2.71	55.43	0.30	0.82
LLIA25	15870	4.24	1.65	5.06	0.22	454.00	1.01	119.34	5.19	23.00	38.92	0.25	6.71
LLIA26	15875	3.41	1.39	5.10	0.27	450.00	0.94	149.56	7.92	18.89	40.76	0.21	6.49
LLIA27	15880	4.15	1.35	5.90	0.27	454.00	1.01	142.17	6.51	21.85	32.53	0.19	7.25
LLIA28	15885	4.45	1.56	6.06	0.38	452.00	0.98	136.18	8.54	15.95	35.06	0.20	7.62
LLIA29	15890	4.65	1.83	6.64	0.32	454.00	1.01	142.80	6.88	20.75	39.35	0.22	8.47
LLIA30	15895	3.69	1.33	5.19	0.31	453.00	0.99	140.65	8.40	16.74	36.04	0.20	6.52
LLIA31	15900	3.76	1.76	5.87	0.28	452.00	0.98	156.12	7.45	20.96	46.81	0.23	7.63
LLIA32	15905	5.01	2.40	7.01	0.30	451.00	0.96	139.92	5.99	23.37	47.90	0.26	9.41
LLIA33	15910	4.69	2.41	7.38	0.40	453.00	0.99	157.36	8.53	18.45	51.39	0.25	9.79
LLIA34	15915	2.87	2.19	5.31	0.21	451.00	0.96	185.02	7.32	25.29	76.31	0.29	7.50
LLIA35	15920	3.50	4.22	7.97	0.35	448.00	0.90	227.71	10.00	22.77	120.57	0.35	12.19
LLIA36	15925	3.42	6.21	9.00	0.18	444.00	0.83	263.16	5.26	50.00	181.58	0.41	15.21
LLIA37	15930	4.43	4.52	10.40	0.18	446.00	0.87	234.76	4.06	57.78	102.03	0.30	14.92
LLIA38	15935	5.55	3.45	9.43	0.30	451.00	0.96	169.91	5.41	31.43	62.16	0.27	12.88
LLIA39	15940	2.07	1.45	3.35	0.26	449.00	0.92	161.84	12.56	12.88	70.05	0.30	4.80
LLIA40	15945	1.75	1.64	3.33	0.37	449.00	0.92	190.29	21.14	9.00	93.71	0.33	4.97

La Luna IA core (cont.)

Sample	Depth(ft)	TOC (wt%)	S_1	S2	S3	T_{max}	Ro	HI	OI	S_2/S_3	S_1/TOC	PI	S_1+S_2
LLIA41	15950	2.27	2.37	4.22	0.24	449.00	0.92	185.90	10.57	17.58	104.41	0.36	6.59
LLIA42	15955	1.40	1.20	3.00	0.20	443.00	0.81	214.29	14.29	15.00	85.71	0.29	4.20
LLIA43	15960	4.93	3.48	10.99	0.25	445.00	0.85	222.92	5.07	43.96	70.59	0.24	14.47
LLIA44	15965	6.22	2.65	10.40	0.39	452.00	0.98	167.20	6.27	26.67	42.60	0.20	13.05
LLIA45	15970	2.12	1.31	4.57	0.21	445.00	0.85	215.57	9.91	21.76	61.79	0.22	5.88

7.1.5. La Luna IS core

Sample	Depth(ft)	TOC (wt%)	S_1	S2	S3	S_1/TOC	S_1+S_2	S_2/S_3	T_{max}	Ro	HI	OI	PI
LLIS1	17092	0.0772	0.03	0.03	0.3	38.86	0.06	0.10	439	0.74	38.86	388.60	0.50
LLIS2	17094	4.74	3.88	9.8	0.69	81.86	13.68	14.20	436	0.69	206.75	14.56	0.28
LLIS3	17101	5.88	5.35	17.09	0.58	90.99	22.44	29.47	439	0.74	290.65	9.86	0.24
LLIS4	17104	1.97	3.04	6.61	0.42	154.31	9.65	15.74	437	0.71	335.53	21.32	0.32
LLIS5	17114	1.4	2.26	4.88	0.31	161.43	7.14	15.74	436	0.69	348.57	22.14	0.32
LLIS6	17124	7	6.44	20.35	0.34	92.00	26.79	59.85	443	0.81	290.71	4.86	0.24
LLIS7	17134	2.58	4.18	8.99	0.32	162.02	13.17	28.09	442	0.80	348.45	12.40	0.32
LLIS8	17143	4.67	3.9	17.79	0.69	83.51	21.69	25.78	437	0.71	380.94	14.78	0.18
LLIS9	17144	3.31	2.36	8.14	0.44	71.30	10.50	18.50	438	0.72	245.92	13.29	0.22
LLIS10	17154	1.12	1.46	3.83	0.28	130.36	5.29	13.68	437	0.71	341.96	25.00	0.28
LLIS11	17164	3.06	1.62	7.59	0.35	52.94	9.21	21.69	443	0.81	248.04	11.44	0.18
LLIS12	17165	0.801	0.75	2.32	0.18	93.63	3.07	12.89	437	0.71	289.64	22.47	0.24

La Luna IS core (cont.)

Sample	Depth(ft)	TOC (wt%)	S1	S2	S3	S1/TOC	S1+S2	S2/S3	T_{max}	Ro	HI	OI	PI
LLIS13	17167	3.54	2.16	9.76	0.42	61.02	11.92	23.24	445	0.85	275.71	11.86	0.18
LLIS14	17170	0.936	2.19	2.96	0.32	233.97	5.15	9.25	427	0.53	316.24	34.19	0.43
LLIS15	17174	2.68	1.93	8.65	0.29	72.01	10.58	29.83	440	0.76	322.76	10.82	0.18
LLIS16	17181	4.28	2.12	6.63	0.46	49.53	8.75	14.41	428	0.54	154.91	10.75	0.24
LLIS17	17184	4.33	1.53	7.86	0.43	35.33	9.39	18.28	446	0.87	181.52	9.93	0.16
LLIS18	17185	6	1.85	11.74	0.5	30.83	13.59	23.48	440	0.76	195.67	8.33	0.14
LLIS19	17194	5.33	1.74	14.09	0.5	32.65	15.83	28.18	444	0.83	264.35	9.38	0.11
LLIS20	17200	5	1.5	14	0.5	30.00	15.50	28.00	443	0.81	280.00	10.00	0.10

7.2. Photomicrographs of La Luna Formation bitumen for measured vitrinite equivalent values.

7.2.1. Photomicrographs from the La Luna Formation IA and bitumen vitrinite reflectance values before the conversion to vitrinite reflectance equivalent. (Photomicrographs courtesy of Brian Cardott, 2018).

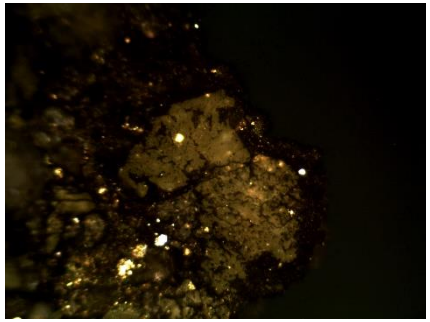

Bitumen % 0.60 Ro

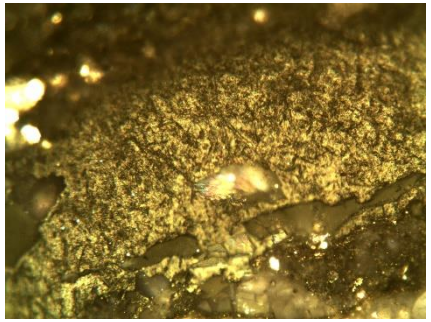

Bitumen %0.75 Ro

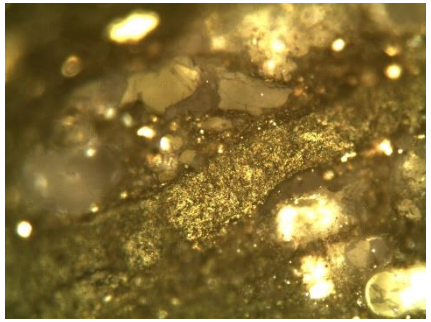

Bitumen %0.70 Ro

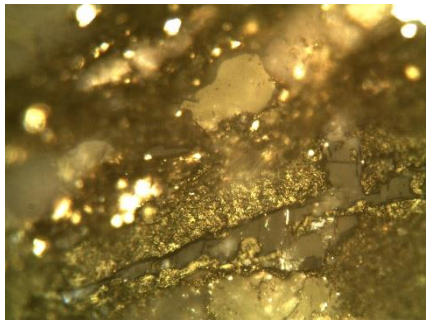

Bitumen %0.70 Ro

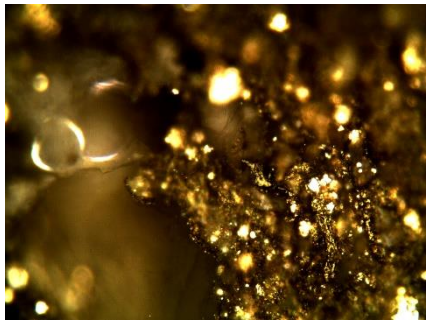

Pitted bitumen %0.46 Ro

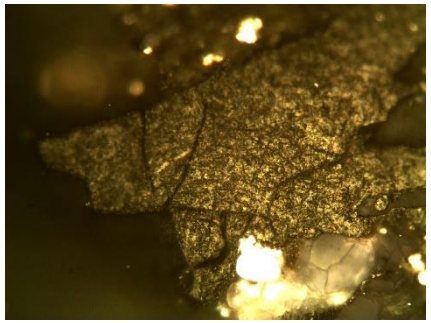

Pitted bitumen %0.60 Ro

7.2.2. Photomicrographs from the La Luna Formation IS and bitumen vitrinite reflectance values before the conversion to vitrinite reflectance equivalent. (Photomicrographs are courtesy of Brian Cardott, 2018).

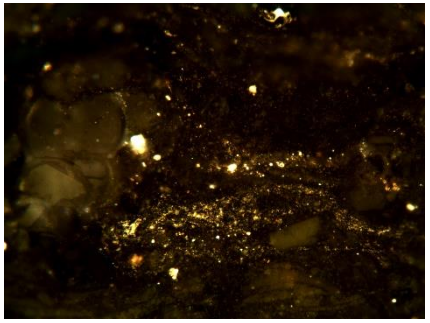

Pitted bitumen % 0.56 Ro

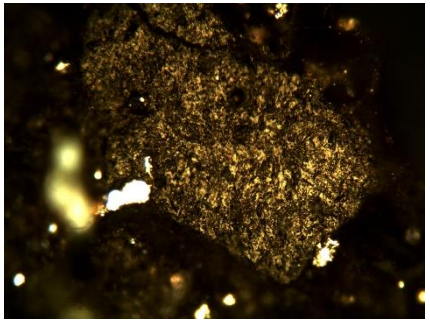

Bitumen % 0.60 Ro

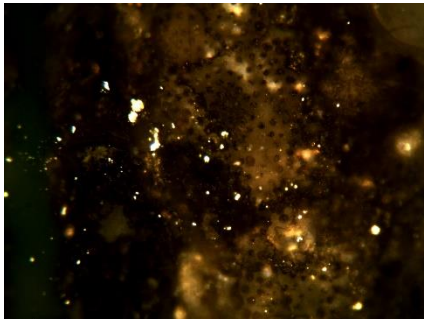

Bryozoan within the sample

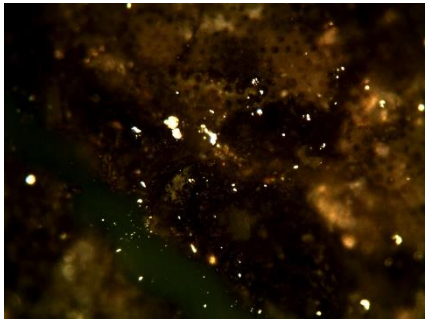

Bitumen % 0.72 Ro

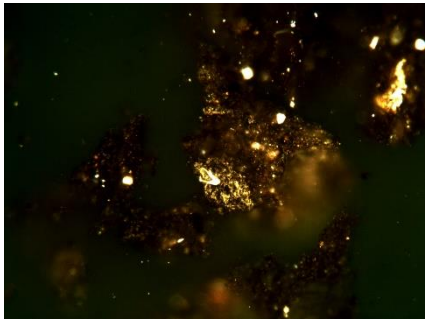

Bitumen % 0.50 Ro

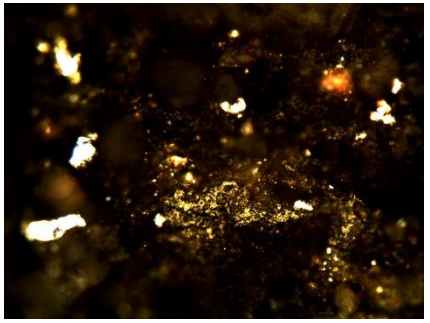

Bitumen % 0.52 Ro

7.2.3. Photomicrographs from the La Luna Formation IS and bitumen vitrinite reflectance values before the conversion to vitrinite reflectance equivalent. (Photomicrographs are courtesy of Brian Cardott, 2018).

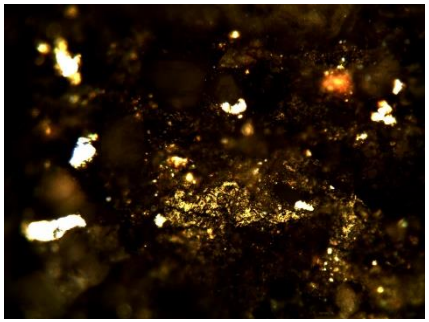

Bitumen % 1.1Ro

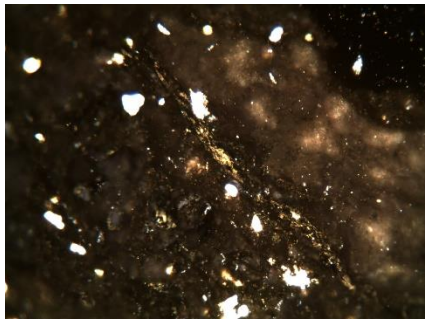

Bitumen % 1.2Ro

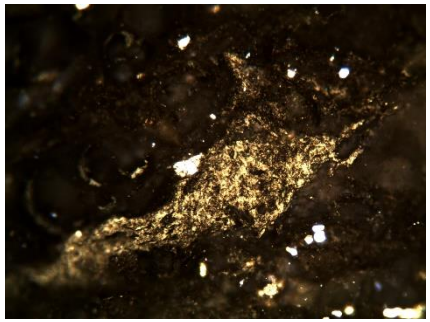

Pitted bitumen %. 1.74 Ro

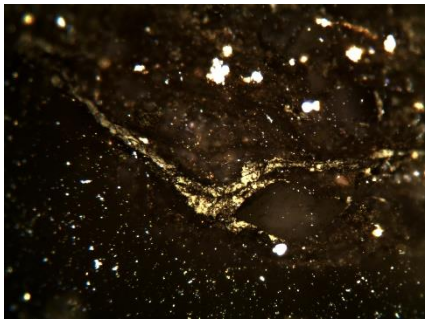

Bitumen with dolomite% 1.47 Ro

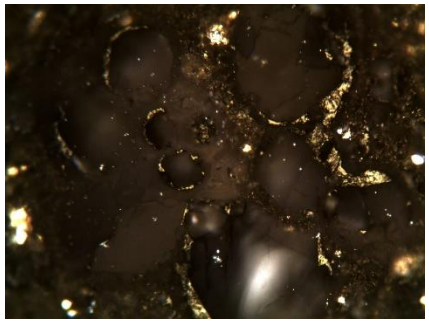

Bitumen % 1.5 Ro

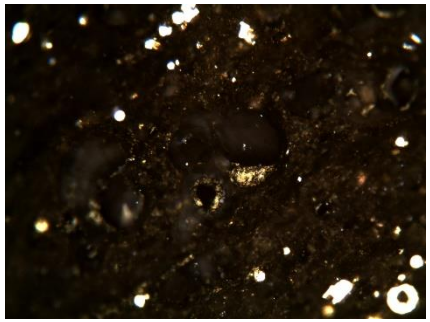

Bitumen % 1.3 Ro

7.2.4. Photomicrographs from the La Luna Formation IS and bitumen vitrinite reflectance values before the conversion to vitrinite reflectance equivalent. (Photomicrographs are courtesy of Brian Cardott, 2018).

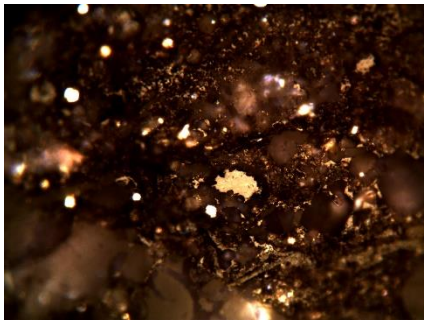

Bitumen % 0.90 Ro

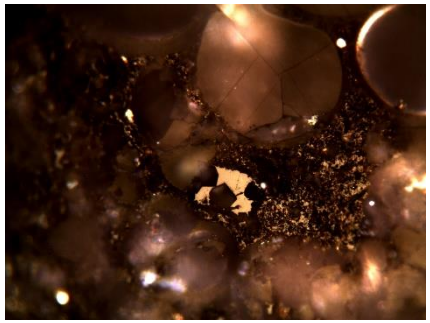

Bitumen % 0.92 Ro

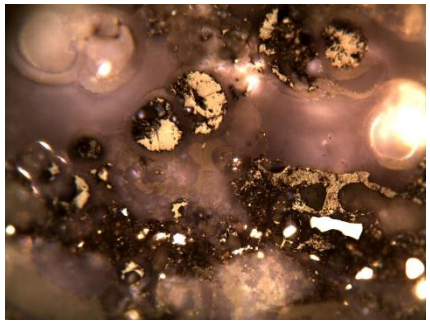

Bitumen % 0.99 Ro

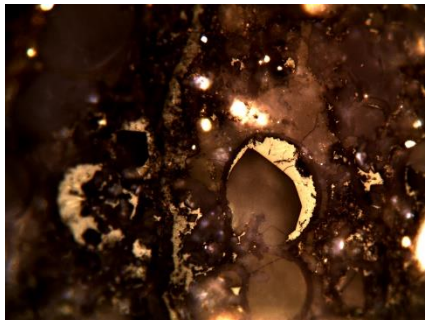

Bitumen % 1.1Ro



Speckled post oil solid Bitumen % 1.1 Ro

7.3. Geochemical ratios of *n*-alkanes and isoprenoids for the saturate fractions of the La Luna Formation bitumen samples (ND = not determined)

7.3.1. La Luna IX core

Well	Depth (ft)	Pr/Ph	Pr/ n-C_{17}	Ph/ n-C_{18}	Pr/ (Pr+Ph)	TAR	CPI	long/short chain n-alkanes	Observation
LLIX	15267glau	0.47	0.57	0.851634	0.32	0.54	1.78	1.16	
LLIX	15270	0.35	0.52	1.41732	0.26	0.28	1.85	0.63	Highly biodegraded
LLIX	15272	0.27	2.05	5.095359	0.21	1.02	2.32	1.27	Highly biodegraded
LLIX	15273	0.22	1.77	5.270978	0.18	0.81	2.58	1.32	Highly biodegraded
LLIX	15274	0.74	0.96	0.575994	0.42	0.38	2.10	0.85	
LLIX	15278	0.76	0.21	0.31371	0.43	0.16	2.03	0.46	
LLIX	15280	0.53	0.50	0.885247	0.34	0.07	2.51	0.43	
LLIX	15287	0.50	0.55	0.88	0.30	0.16	1.90	0.45	
LLIX	15290	0.35	0.61	1.142523	0.26	0.15	1.88	0.49	
LLIX	15294	0.57	0.33	0.833762	0.36	0.11	1.95	0.51	
LLIX	15297	0.56	0.43	0.721536	0.35	0.18	1.79	ND	
LLIX	15303	0.51	0.26	0.549159	0.34	0.15	1.74	0.54	
LLIX	15314	0.6438	0.27	0.457204	0.39	0.36	1.61	0.80	
LLIX	15317	0.64	0.27	0.462563	0.39	0.17	1.73	0.56	
LLIX	15327	0.70	0.29	0.482424	0.41	0.12	1.85	0.40	
LLIX	15332	0.70	0.29	0.497288	0.41	0.09	1.95	0.35	
LLIX	15343	0.78	0.28	0.469495	0.44	0.06	1.83	0.33	
LLIX	15351	0.76	0.27	0.350393	0.43	0.12	1.62	0.45	
LLIX	15357	0.66	0.22	0.351708	0.39	0.17	1.78	0.57	
LLIX	15363	0.51	0.12	0.317099	0.34	0.12	1.76	0.43	

Well	Depth (ft)	Pr/Ph	Pr/ n-C17	Ph/ n-C18	Pr/ (Pr+Ph)	TAR	CPI	long/short chain n-alkanes	Observation
LLIX	15365	0.55	0.34	0.44	0.36	0.37	2.24	1.07	
LLIX	15372	0.85	0.25	0.33	0.46	0.09	1.61	0.41	
LLIX	15378	0.56	0.40	0.68	0.36	0.20	1.65	0.77	
LLIX	15382	0.61	0.17	0.27	0.38	0.16	1.73	0.51	
LLIX	15395	0.58	0.26	0.41	0.37	0.59	1.70	1.19	
LLIX	15398	0.72	0.17	0.28	0.42	0.11	1.84	0.43	
LLIX	15401	0.79	0.25	0.36	0.44	0.05	2.12	0.33	
LLIX	15415	0.77	0.24	0.36	0.44	0.10	1.85	0.40	
LLIX	15430	0.46	1.33	2.04	0.31	0.94	2.20	1.67	
LLIX	15438	0.58	0.19	0.40	0.37	0.17	1.80	0.52	
LLIX	15444	0.77	0.30	0.43	0.43	0.07	1.74	0.32	
LLIX	15491	0.67	0.20	0.33	0.40	0.12	2.17	0.47	
LLIX	15500	0.82	0.19	0.28	0.45	0.11	1.64	0.41	
LLIX	15515	0.69	0.20	0.30	0.41	0.11	1.64	0.55	
LLIX	15528	0.80	0.28	0.41	0.44	0.09	1.81	0.36	
LLIX	15554	0.67	0.16	0.28	0.40	0.09	1.98	0.37	
LLIX	15580	0.67	0.30	0.51	0.40	0.10	1.88	0.43	
LLIX	15628	0.65	0.18	0.30	0.39	0.15	1.79	0.51	

7.3.2. La Luna IA core

Well	Depth (ft)	Pr/Ph	Pr/ n-C17	Ph/ n-C18	Pr/ (Pr+Ph)	TAR	CPI	long/short chain n-alkanes	Observation
LLIA	16755	0.96	0.49	0.63	0.49	0.02	1.39	0.16	
LLIA	16760	1.10	0.32	0.38	0.52	0.06	1.94	0.25	
LLIA	16770	0.84	0.26	0.43	0.46	0.04	1.81	0.23	
LLIA	16785	0.91	0.25	0.36	0.48	0.05	1.60	0.24	
LLIA	16795	0.89	0.28	0.37	0.47	0.09	1.88	0.29	
LLIA	16800	0.51	0.57	1.29	0.34	1.18	1.56	2.00	
LLIA	16815	0.95	0.36	0.46	0.49	0.05	1.67	0.27	
LLIA	16825	0.98	0.37	0.51	0.49	0.13	1.79	0.34	
LLIA	16840	0.87	0.33	0.48	0.47	0.08	1.94	0.29	
LLIA	16855	0.86	0.33	0.51	0.46	0.26	1.89	0.59	
LLIA	16870	0.88	0.36	0.49	0.47	0.11	1.84	0.33	
LLIA	16880	0.88	0.34	0.53	0.46	0.06	1.54	0.30	
LLIA	16885	0.88	0.31	0.39	0.47	0.18	1.97	0.44	
LLIA	16890	0.71	0.35	0.62	0.42	0.07	2.01	0.30	
LLIA	16895	0.76	0.32	0.47	0.43	0.34	1.89	0.60	
LLIA	16910	0.69	0.35	0.63	0.41	0.08	1.79	0.34	
LLIA	16915	0.57	0.50	0.89	0.36	0.14	2.11	0.51	
LLIA	16925	0.52	0.58	0.88	0.34	0.22	1.84	0.77	
LLIA	16940	0.70	0.47	0.77	0.41	0.07	1.85	0.36	

7.3.3. La Luna IS core

Well	Depth (ft)	Pr/Ph	Pr/ n-C17	Ph/ n-C18	Pr/ (Pr+Ph)	TAR	CPI	long/short chain n-alkanes	Observation
LLIS	17094	0.35	1.00	2.03	0.26	0.56	1.90	1.39	
LLIS	17101	0.43	1.37	2.20	0.30	0.46	1.99	1.23	
LLIS	17104	0.24	0.93	3.57	0.19	0.93	1.97	1.84	
LLIS	17114	0.26	0.79	2.62	0.20	1.09	2.11	1.92	
LLIS	17124	0.39	1.46	2.01	0.28	0.34	1.62	1.01	
LLIS	17134	0.30	1.60	6.33	0.23	1.01	1.64	2.10	
LLIS	17144	0.41	10.06	1.74	0.29	0.75	1.82	1.53	
LLIS	17154	0.35	0.76	2.08	0.26	1.03	1.67	1.74	
LLIS	17164	0.49	0.51	1.71	0.33	0.23	1.97	0.81	
LLIS	17167	0.53	0.47	0.80	0.35	0.22	1.79	0.68	
LLIS	17165	0.53	0.47	0.80	0.35	0.22	1.79	0.68	
LLIS	17181	0.86	0.44	0.89	0.46	0.63	1.99	0.90	
LLIS	17184	0.65	0.52	1.00	0.40	0.16	1.74	0.53	
LLIS	17185	0.63	0.46	0.73	0.39	0.17	1.85	0.47	

7.3.4. La Luna stratotype

Well	Pr/Ph	Pr/ n-C17	Ph/ n-C18	Pr/ (Pr+Ph)	TAR	CPI	long/short chain n-alkanes	Observation
La Luna stratotype	0.48	0.50	1.04	0.33	0.29	2.90	0.59	
La Luna stratotype	0.53	0.75	1.64	0.35	0.23	3.05	0.49	
La Luna stratotype	0.46	0.32	0.94	0.32	0.44	1.79	0.67	
La Luna stratotype	0.61	0.45	0.89	0.38	0.25	1.61	0.49	
La Luna stratotype	0.50	0.28	0.72	0.33	0.18	2.23	0.38	
La Luna stratotype	0.67	0.47	0.92	0.40	0.69	2.51	1.34	
La Luna stratotype	0.73	0.38	0.32	0.42	0.00	ND	0.00	Highly biodegradeted
La Luna stratotype	0.50	0.15	0.42	0.33	0.00	ND	0.00	Highly biodegradeted

7.4. Gas chromatograms of the saturate fractions for the La Luna Formation samples analyzed in this study (Pr = pristane; Ph = phytane, n-$C_{25=}C_{25}$ normal alkane)

7.4.1. La Luna IX core.

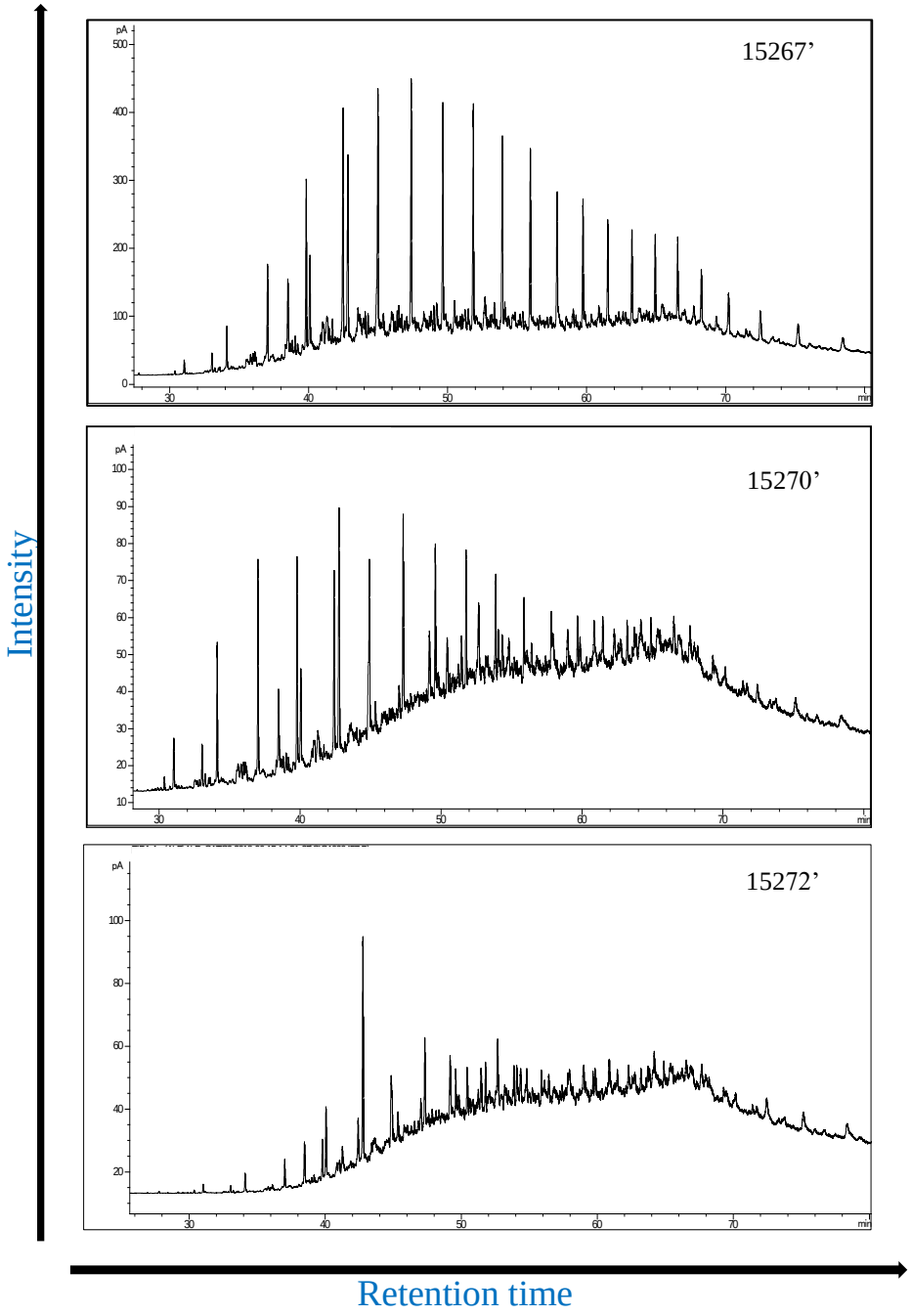

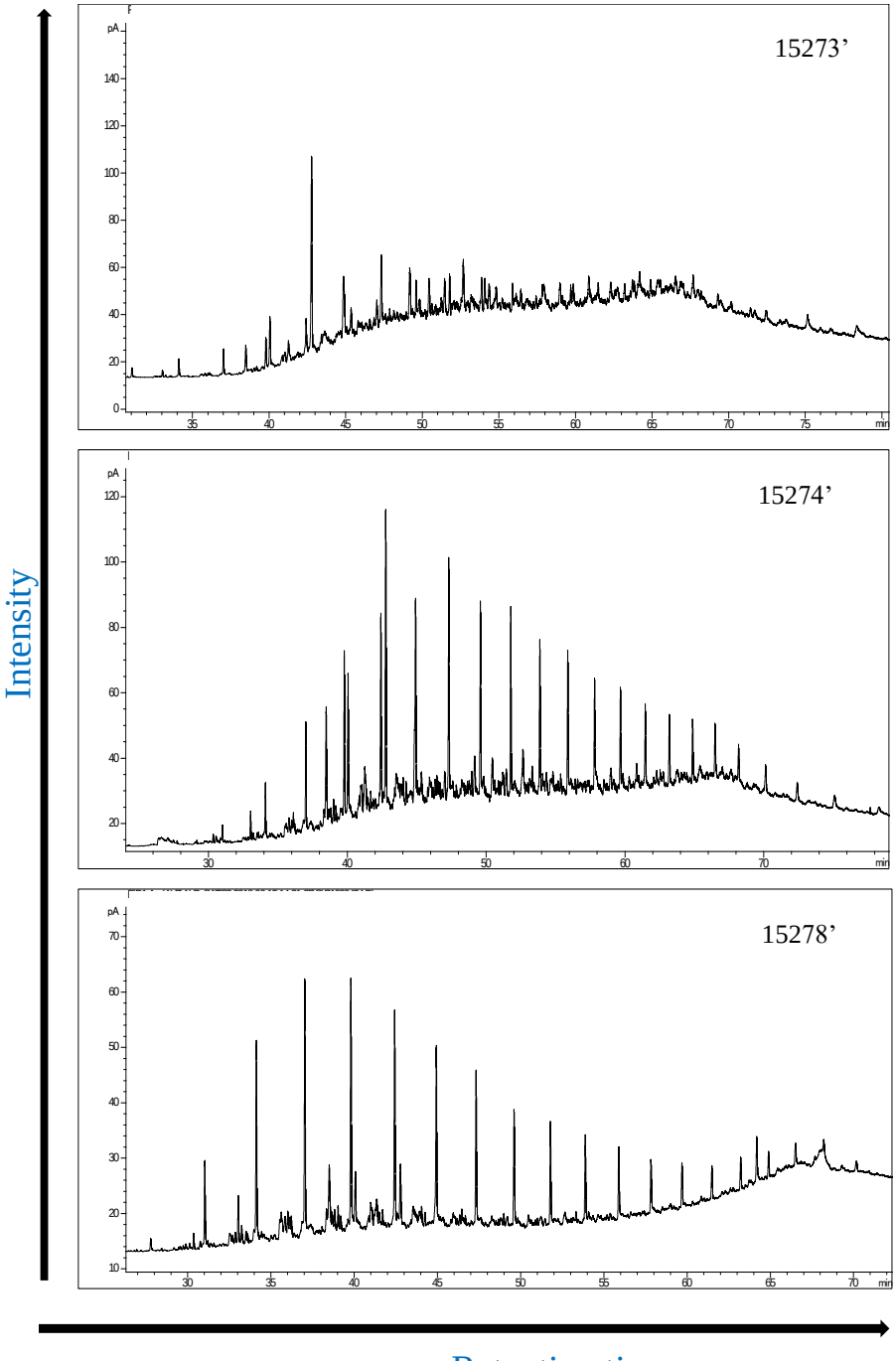
15273’
15274’
15278’
pA
min
Intensity
Retention time

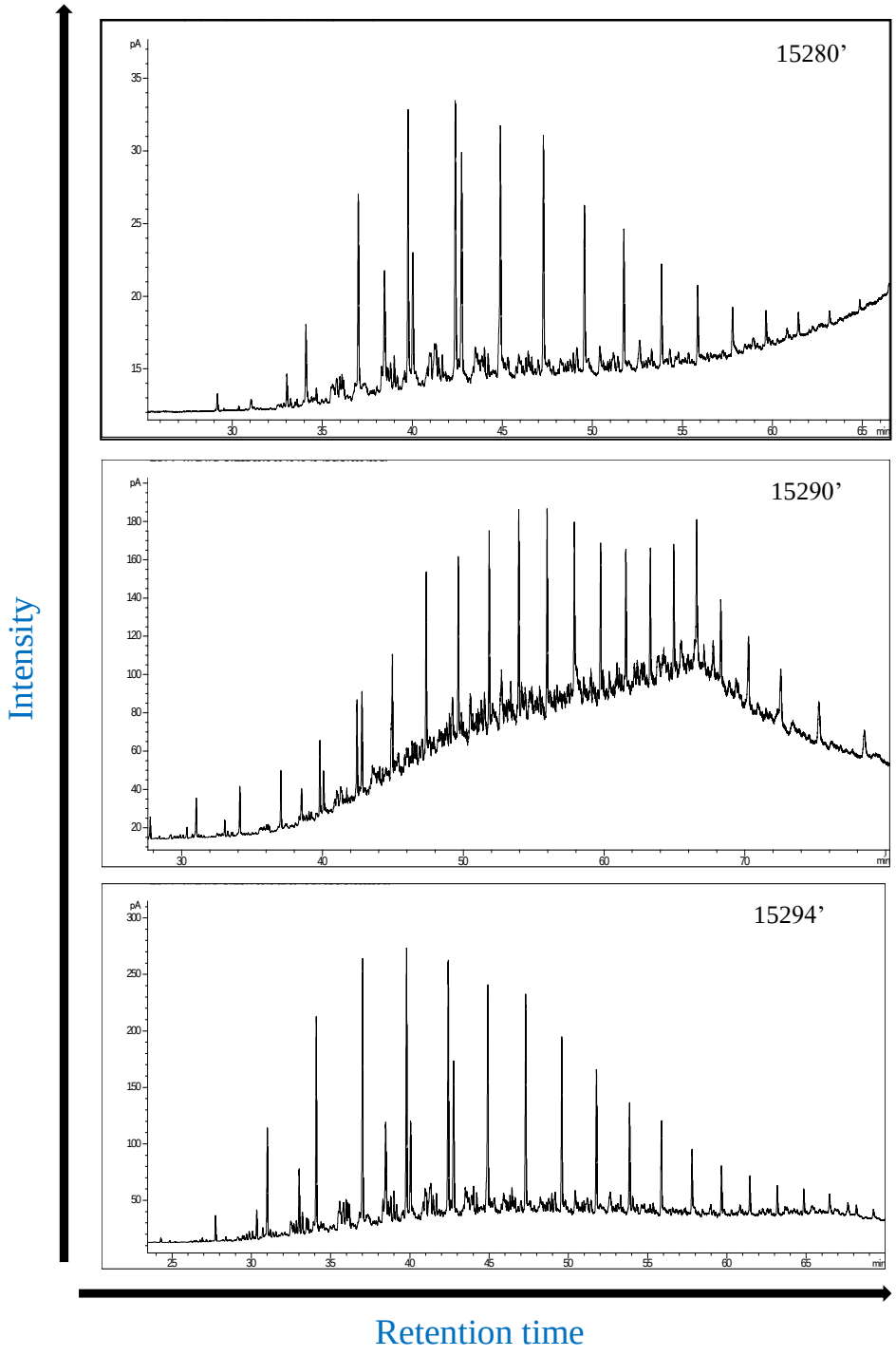
15280’
15290’
15294’
pA
min
Intensity
Retention time

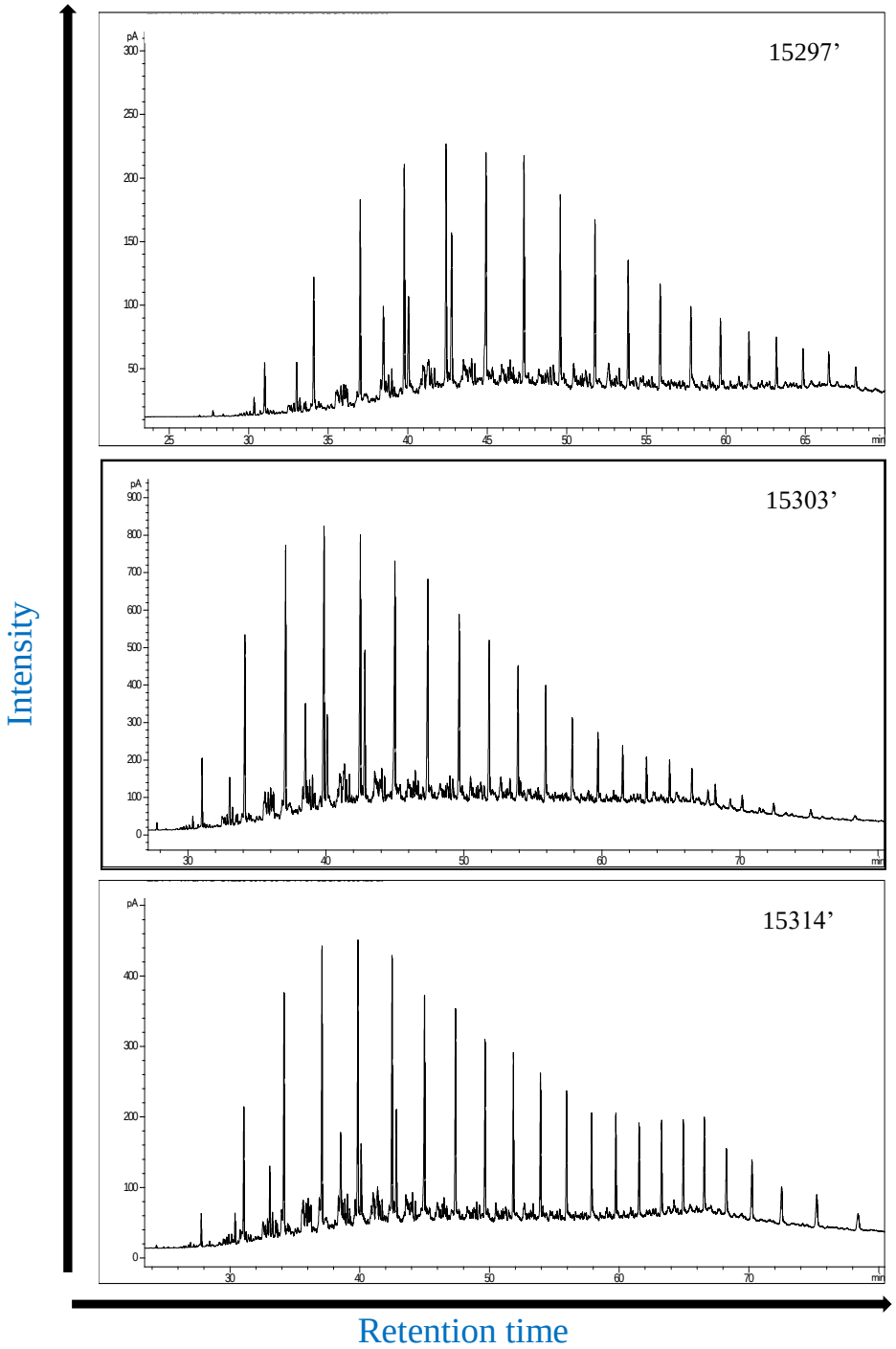
15297’
15303’
15314’
Intensity
Retention time

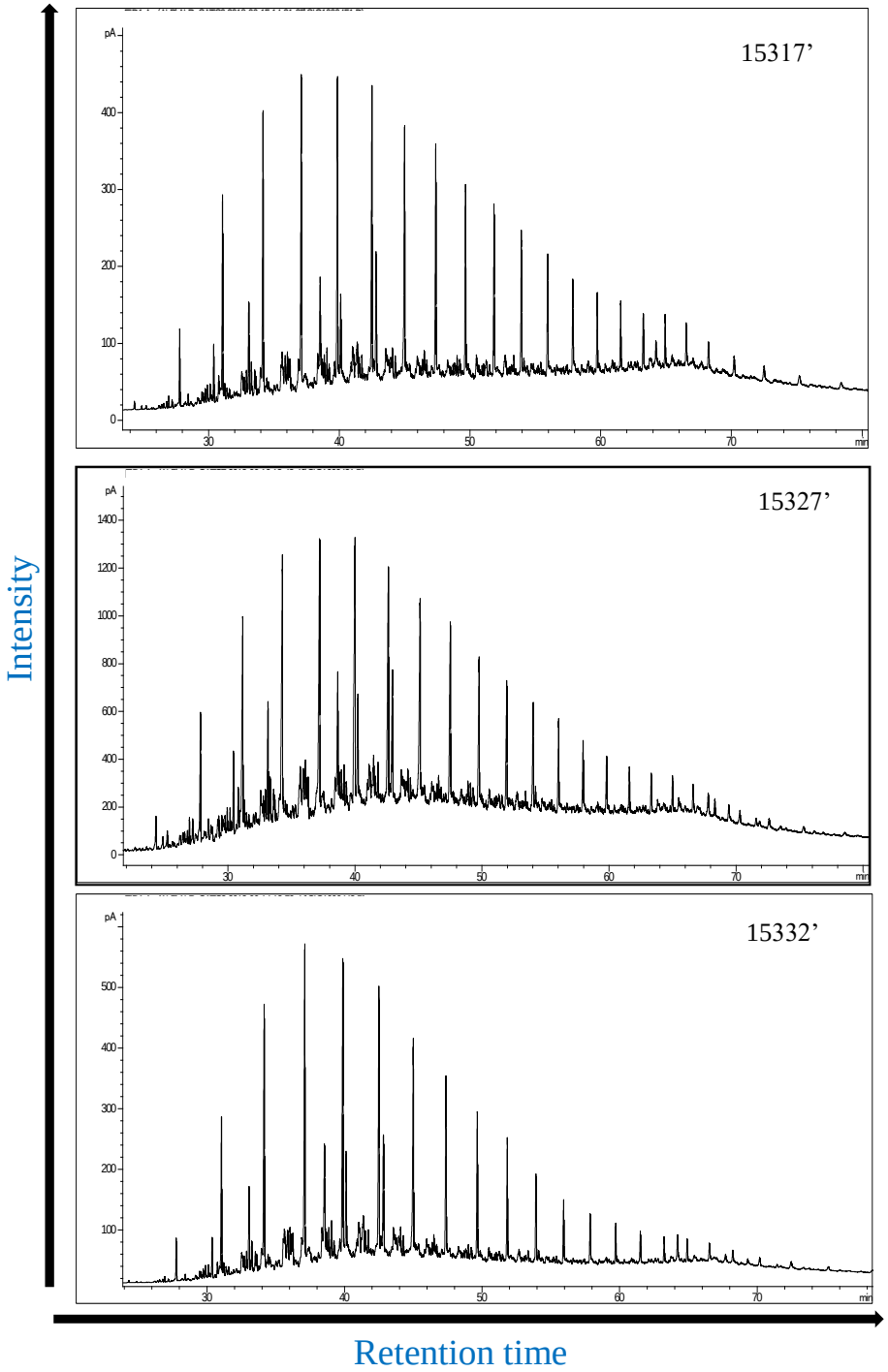
15317’
15327’
15332’
pA
min
Intensity
Retention time

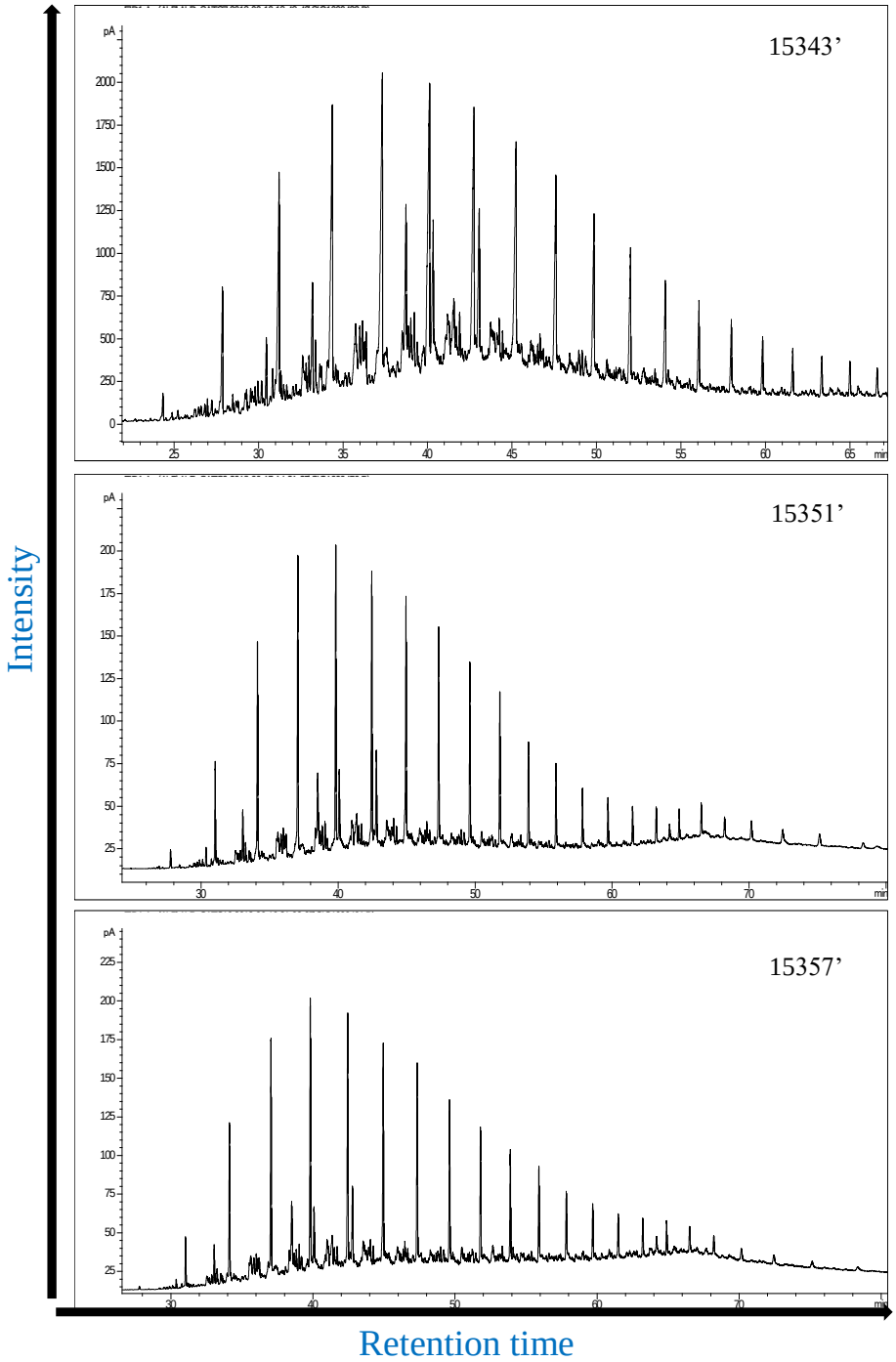
15343’
15351’
15357’
pA
min
Intensity
Retention time

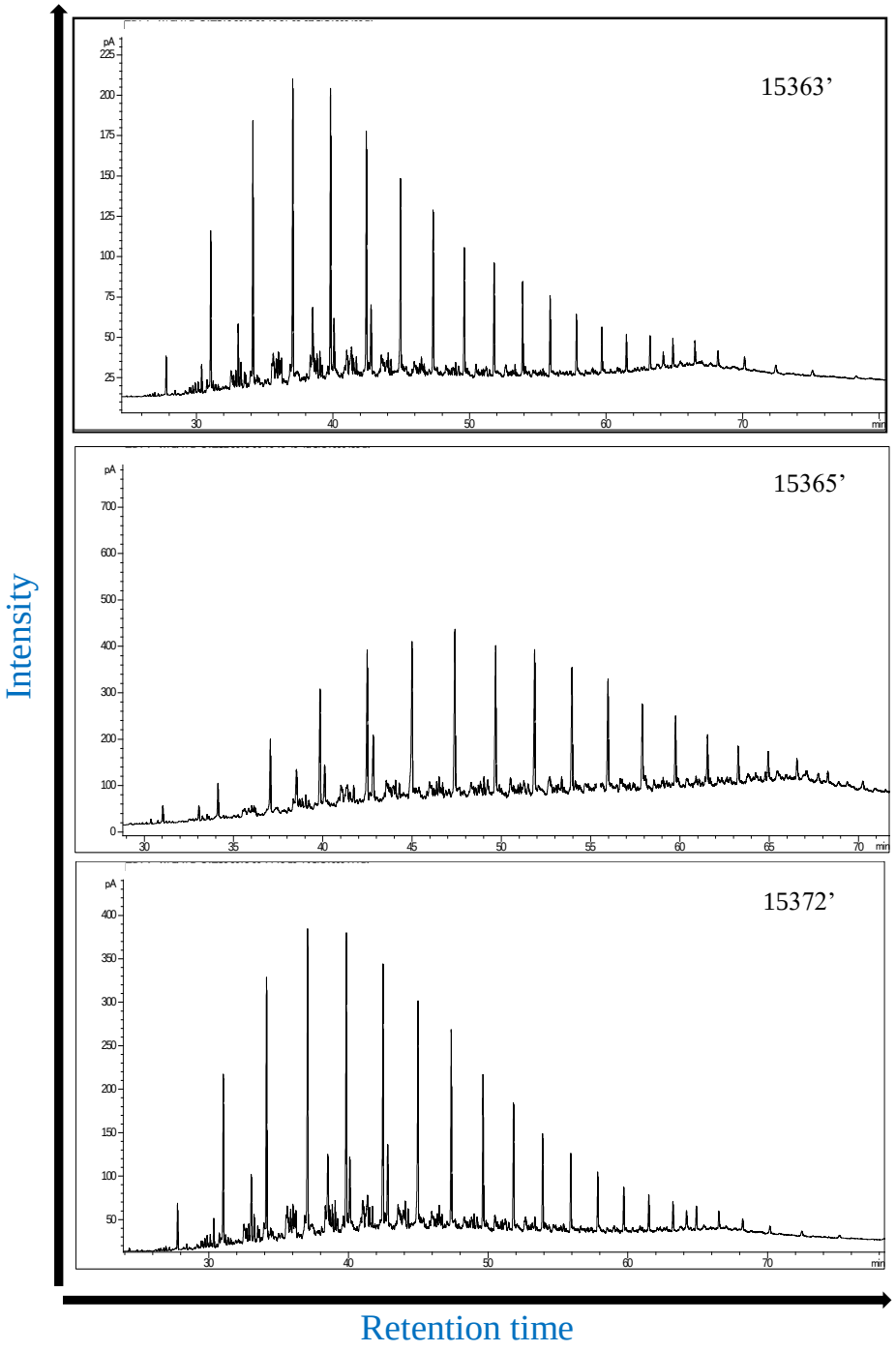
15363’
15365’
15372’
Intensity
Retention time

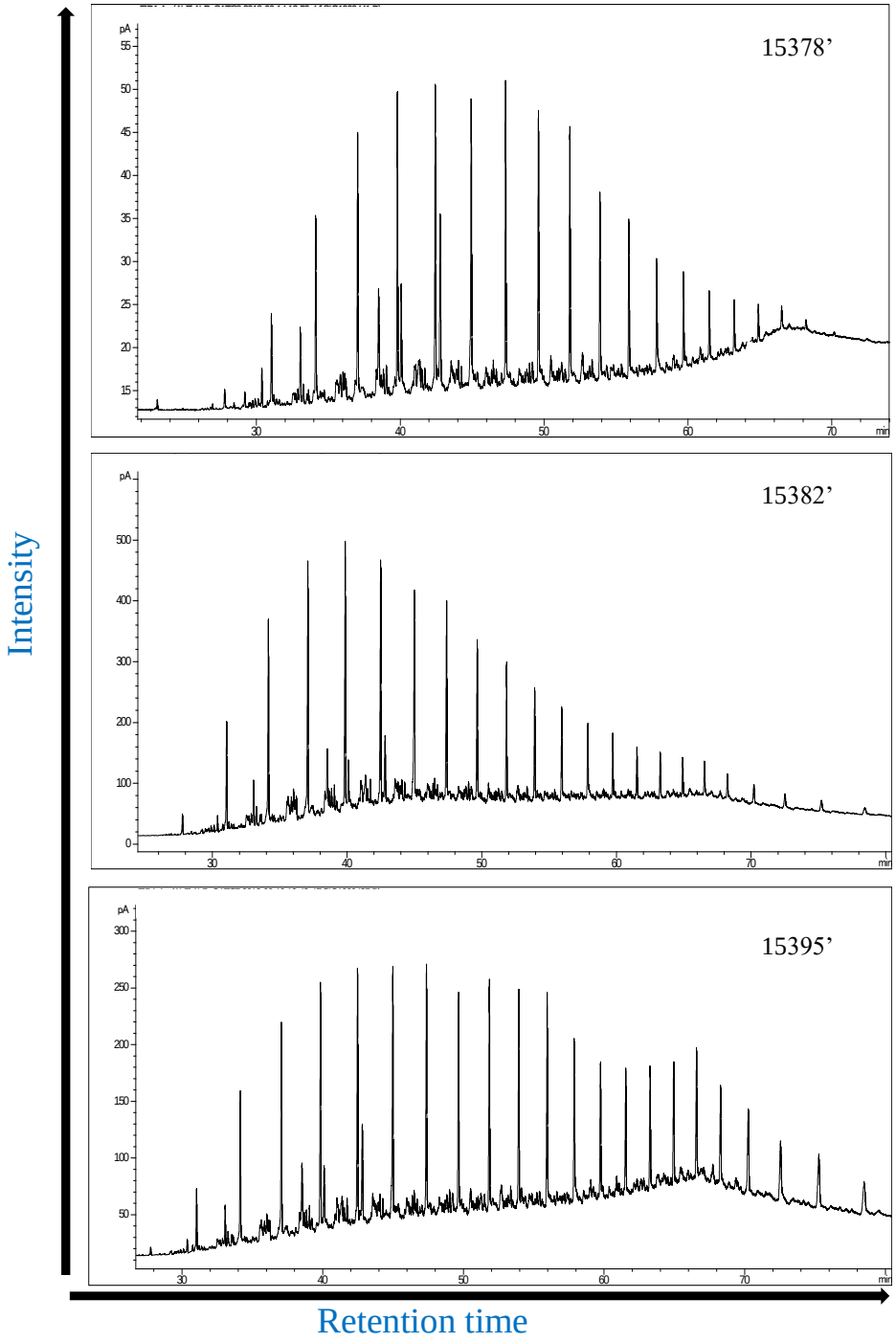
15378’
15382’
15395’
pA
min
Intensity
Retention time

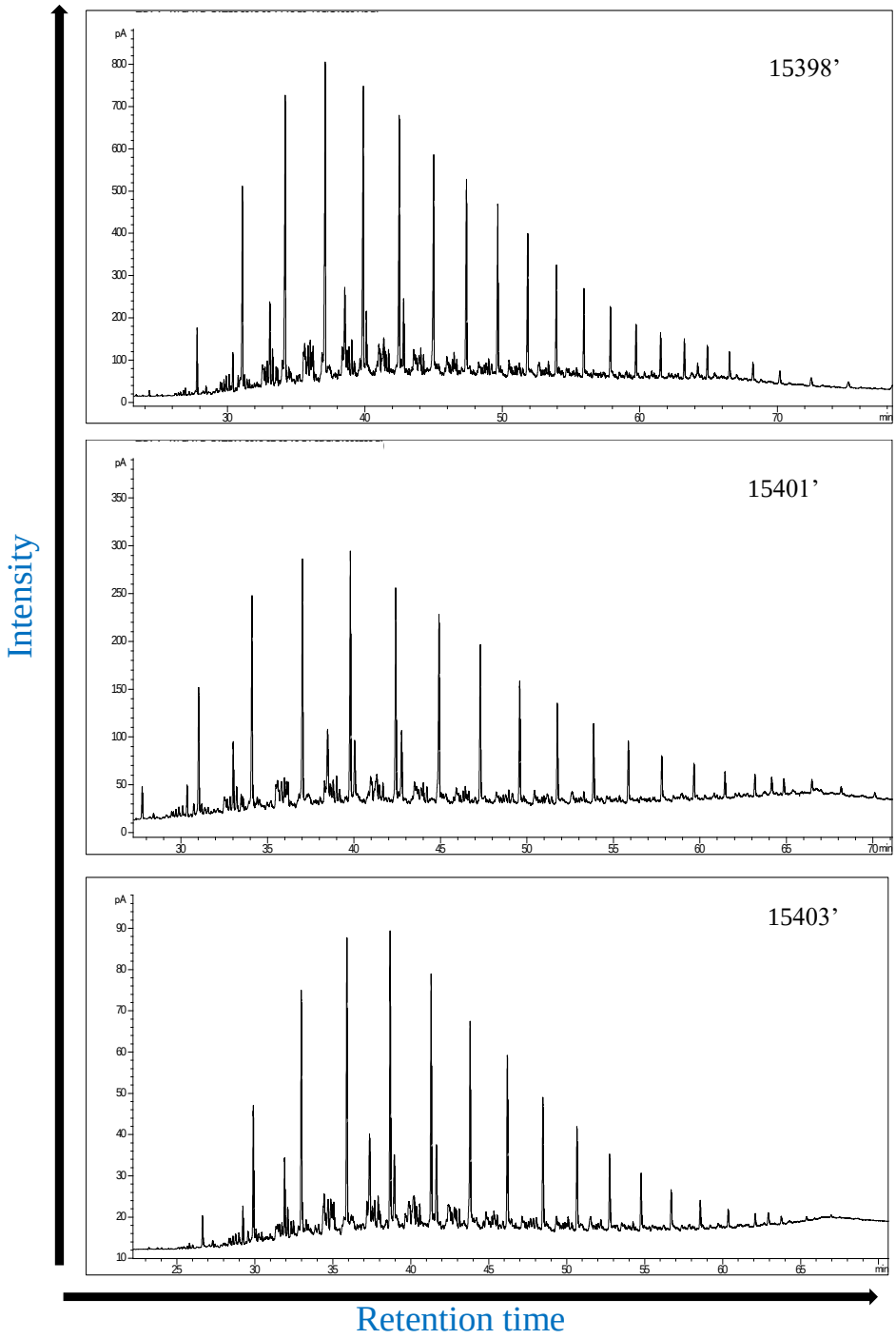
15398’
15401’
15403’
Intensity
Retention time

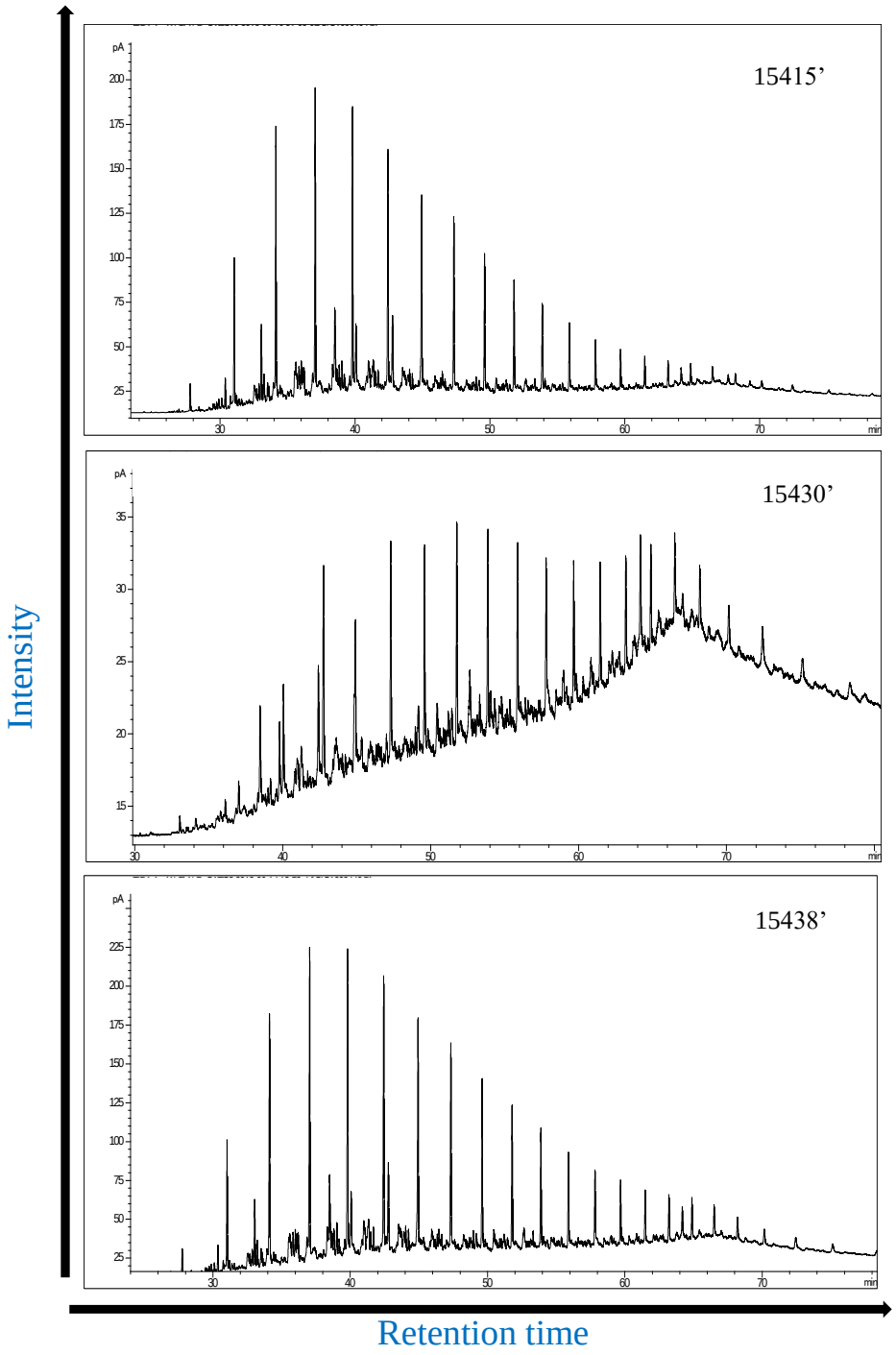
15415’
15430’
15438’
pA
min
Intensity
Retention time

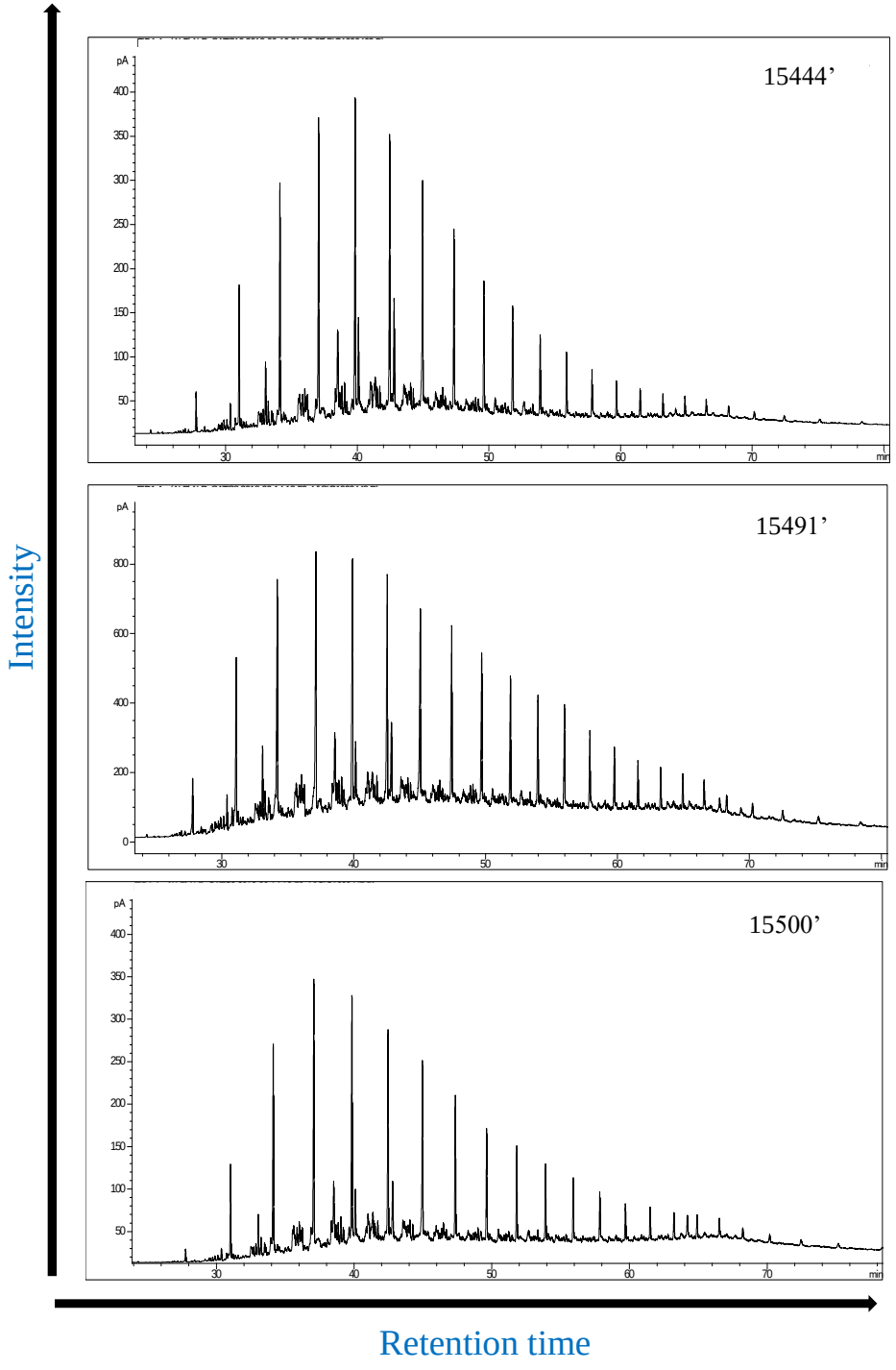
15444’
15491’
15500’
pA
min
Intensity
Retention time

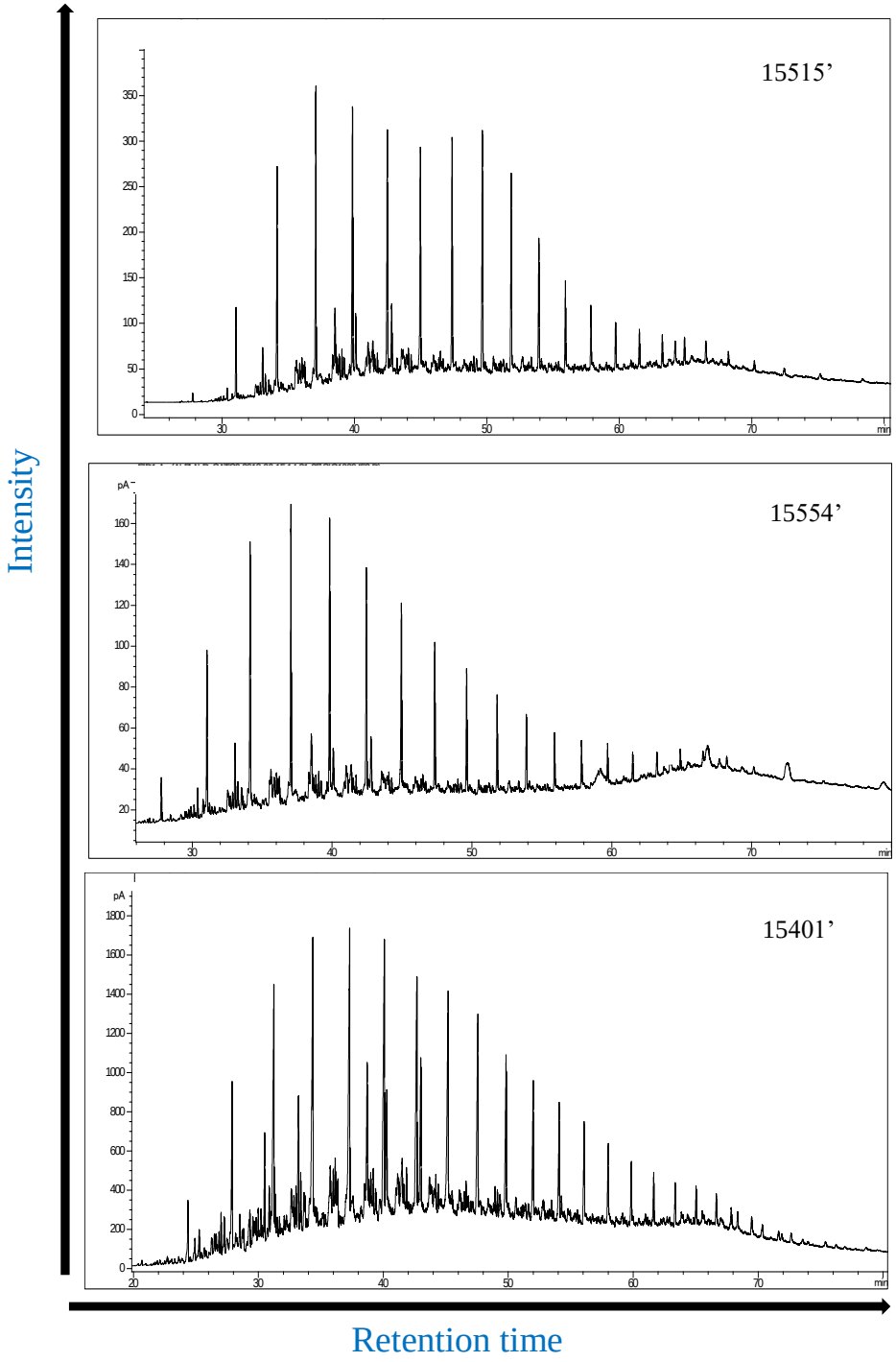
15515’
15554’
15401’
Intensity
Retention time

7.4.2. La Luna IA core

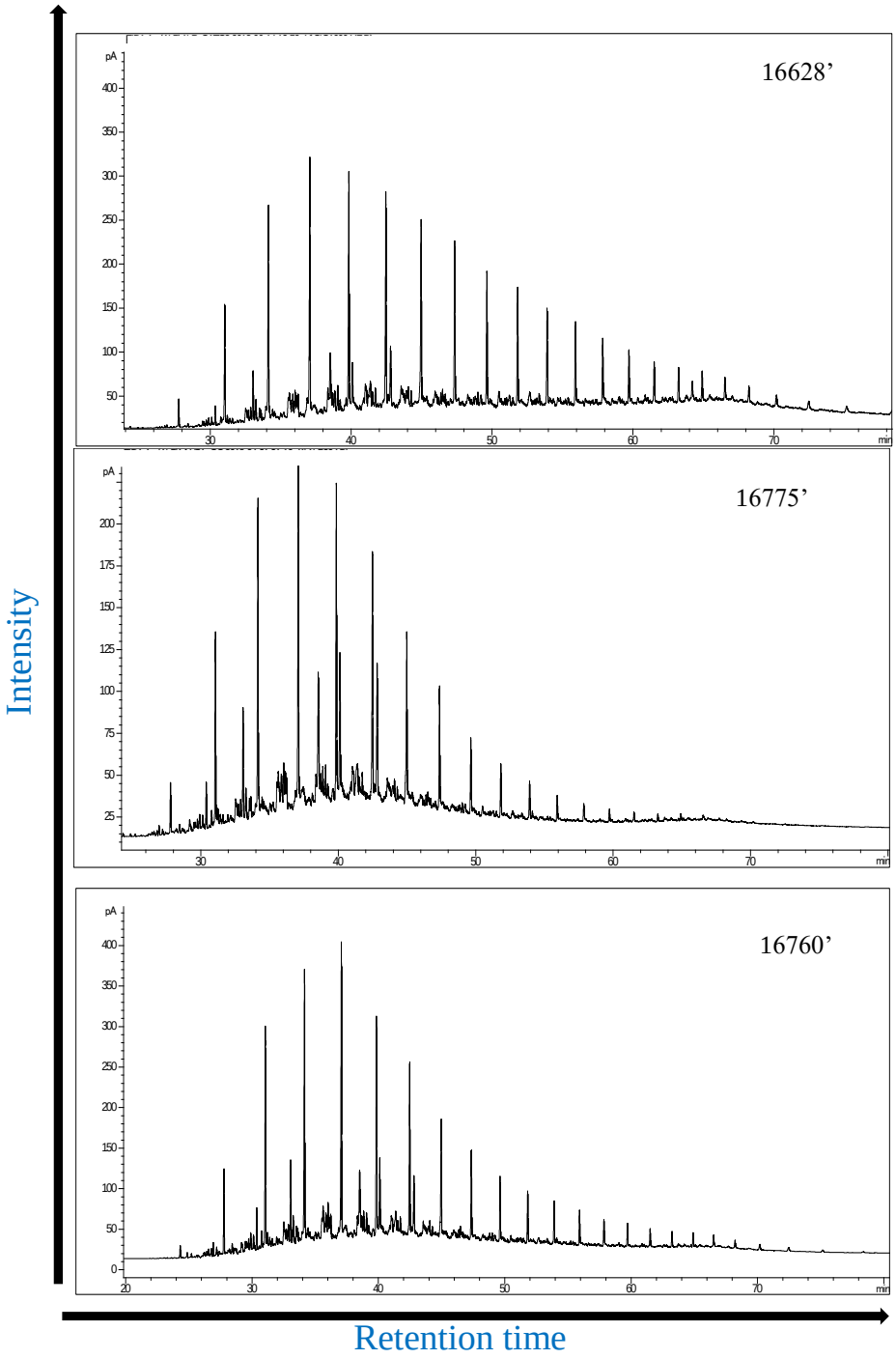

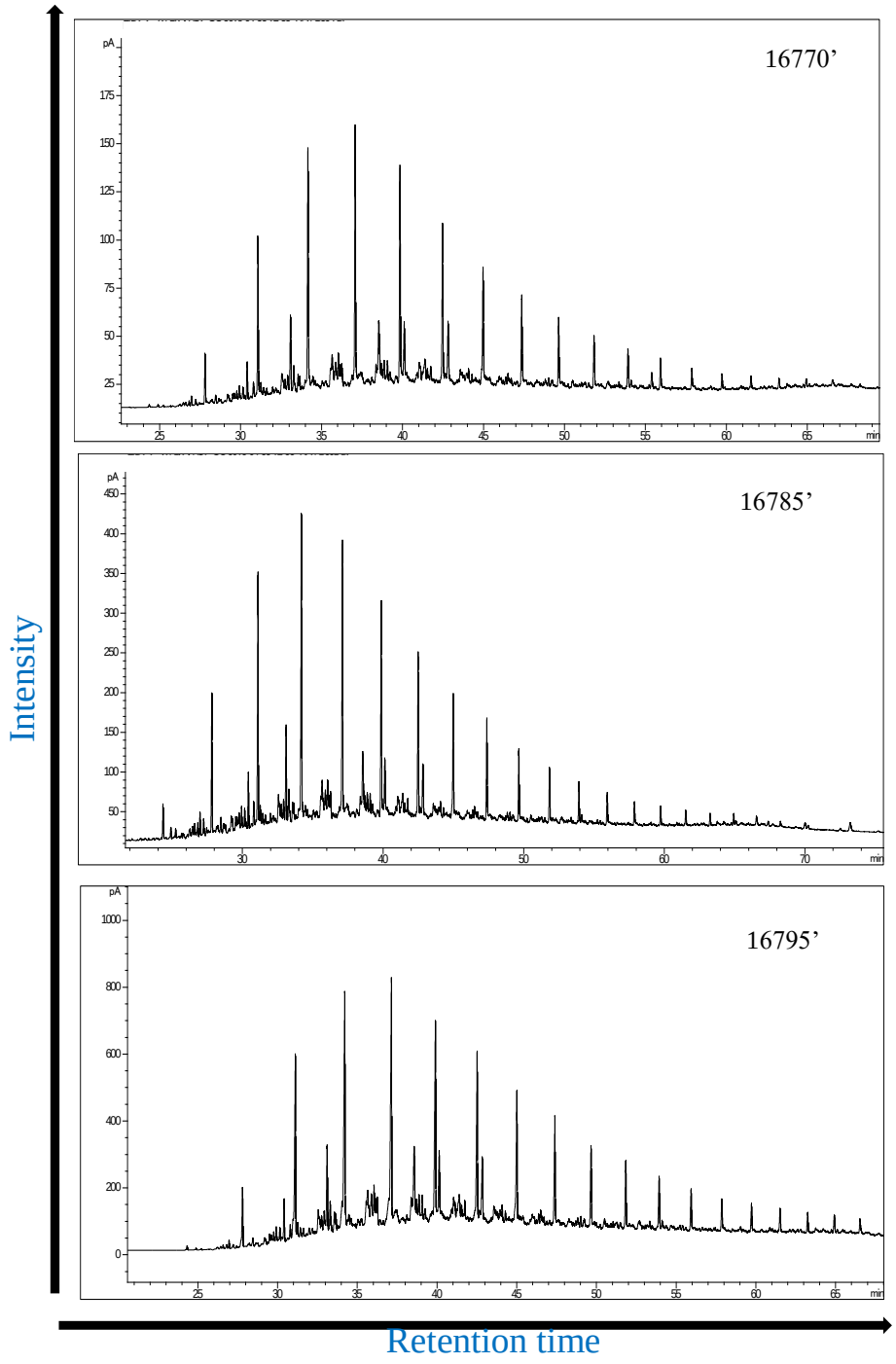
16770’
16785’
16795’
Intensity
Retention time

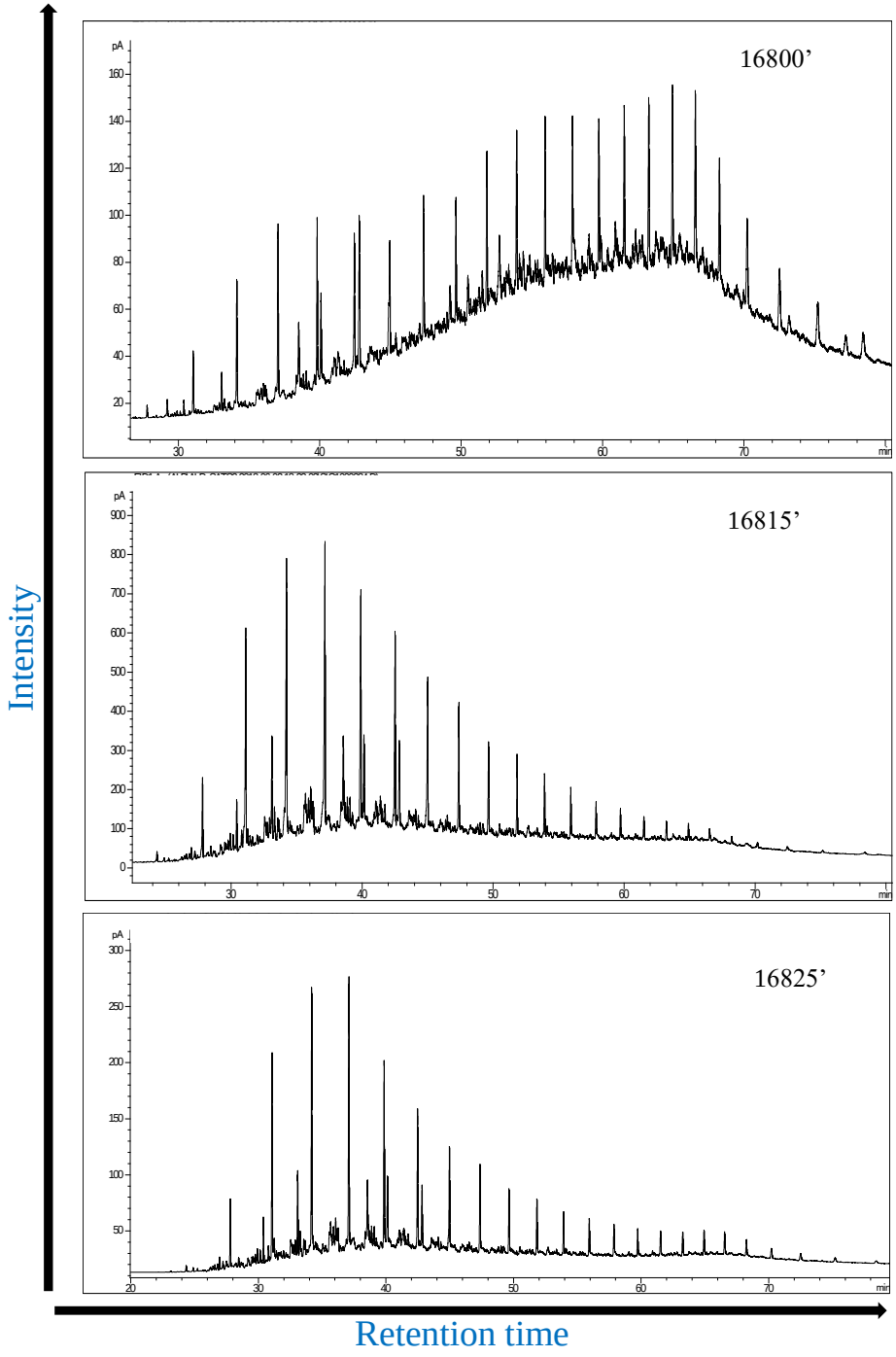
16800’
16815’
16825’
Intensity
Retention time

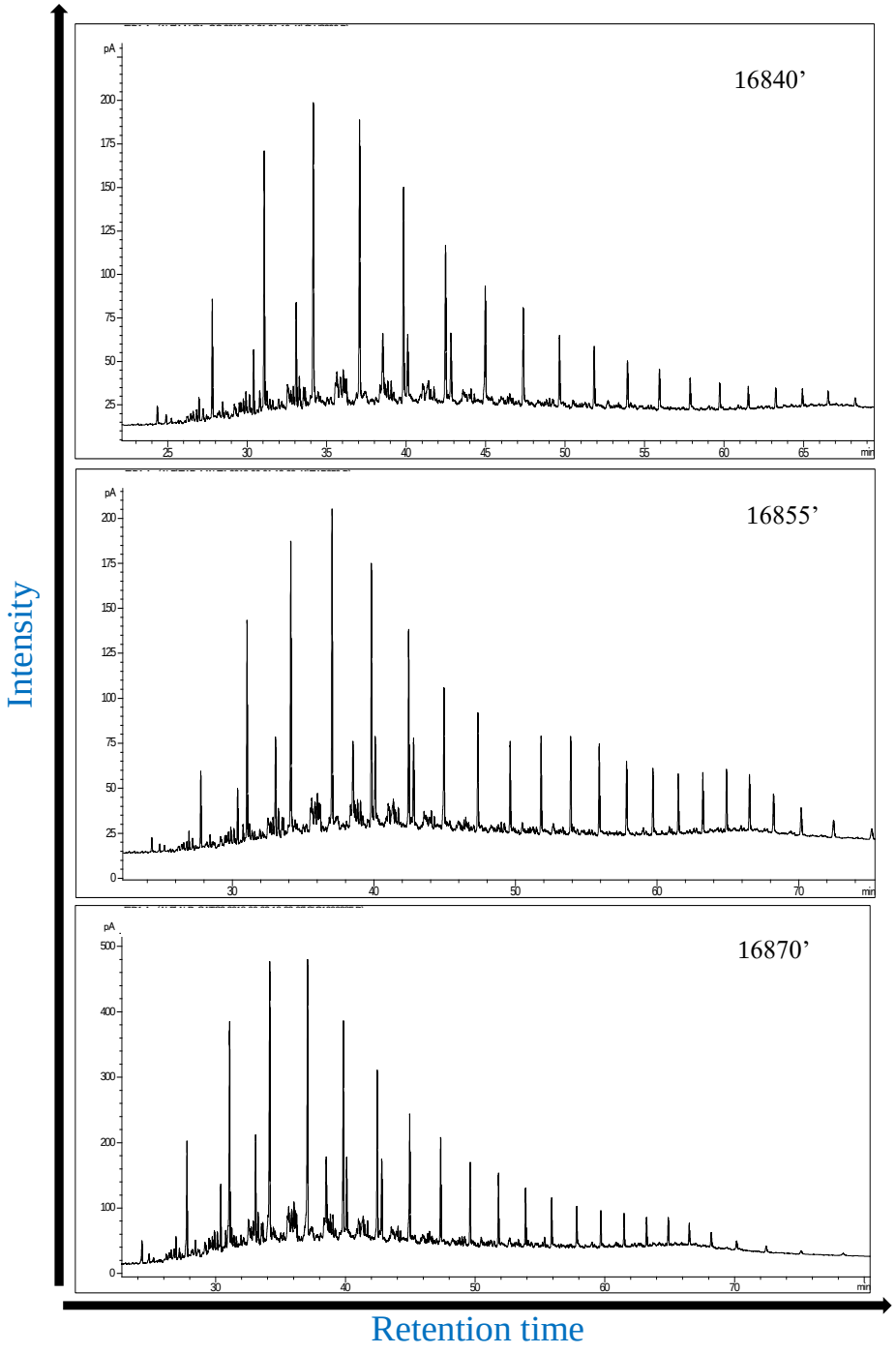
16840’
16855’
16870’
pA
min
Intensity
Retention time

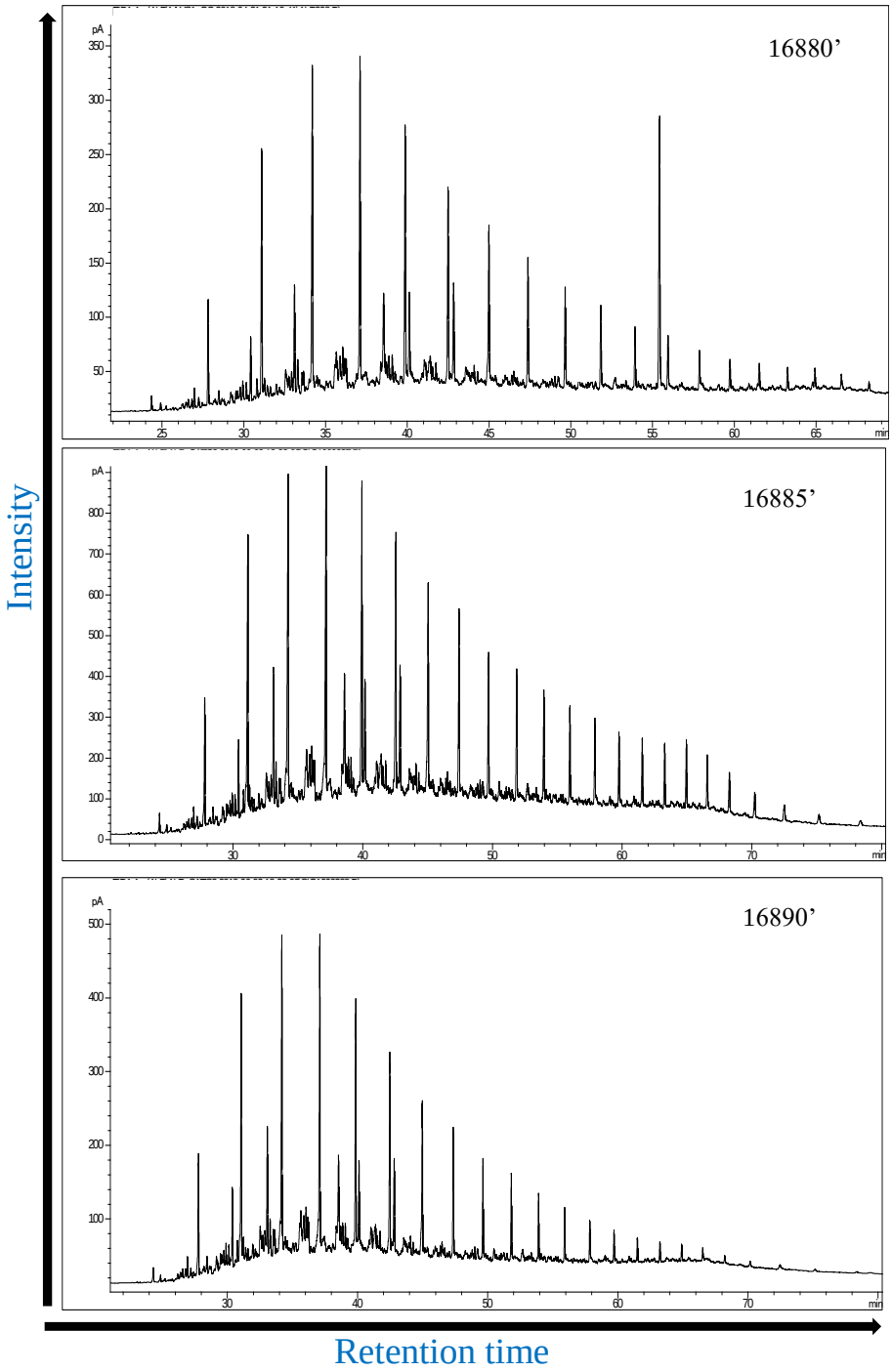
16880’
16885’
16890’
Intensity
Retention time

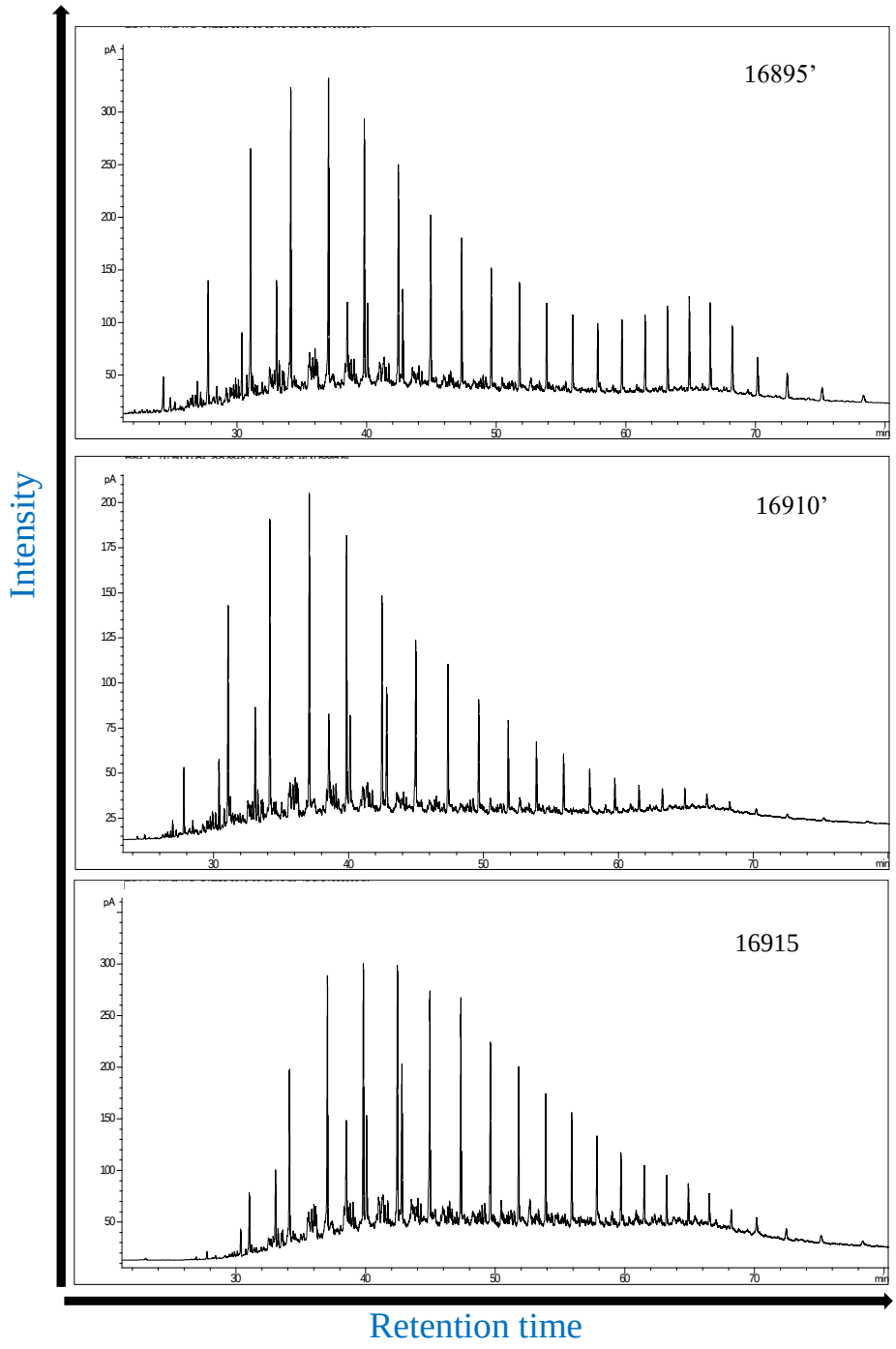
16895’
16910’
16915
pA
min
Intensity
Retention time

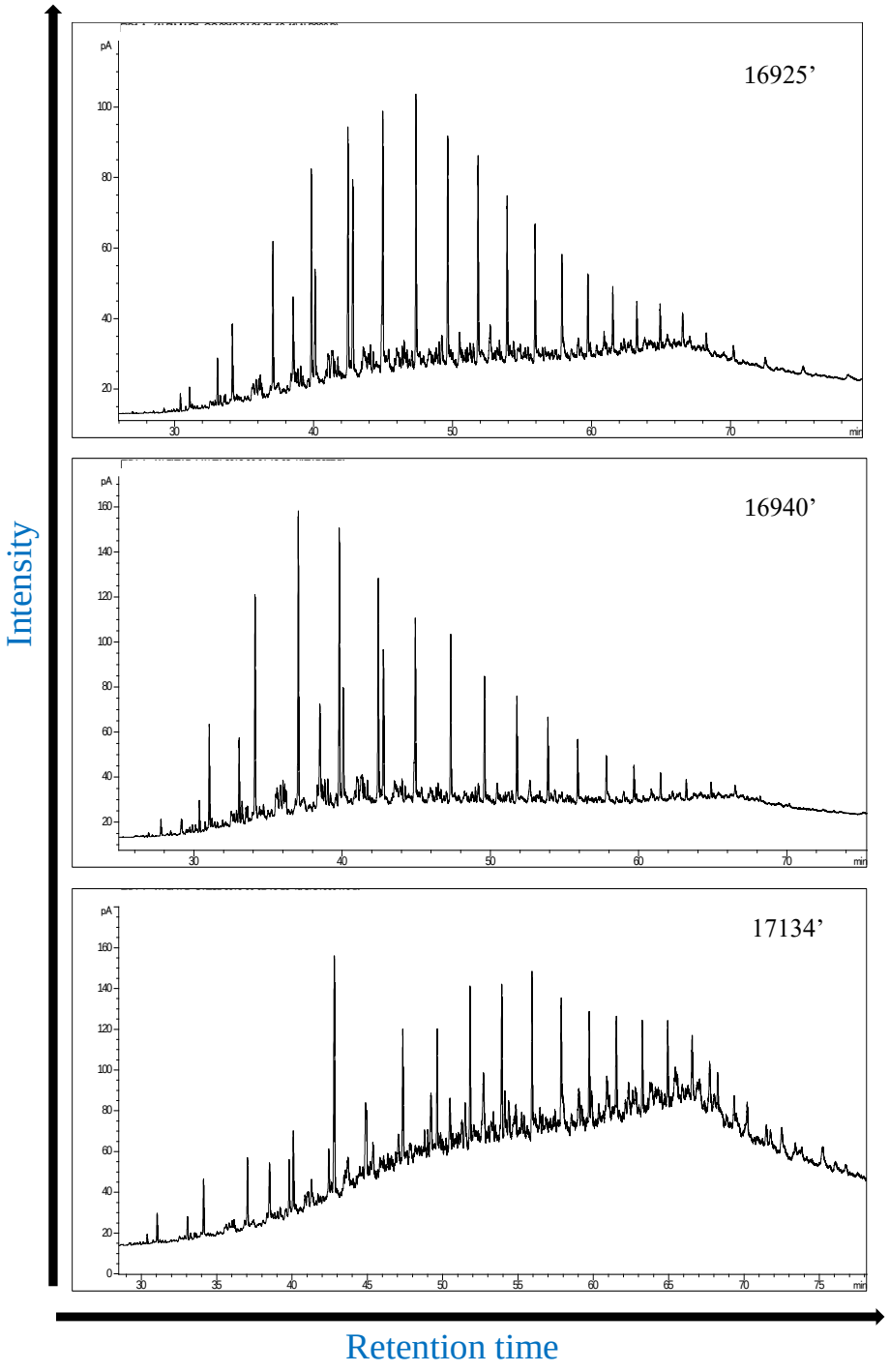
16925’
16940’
17134’
Intensity
Retention time

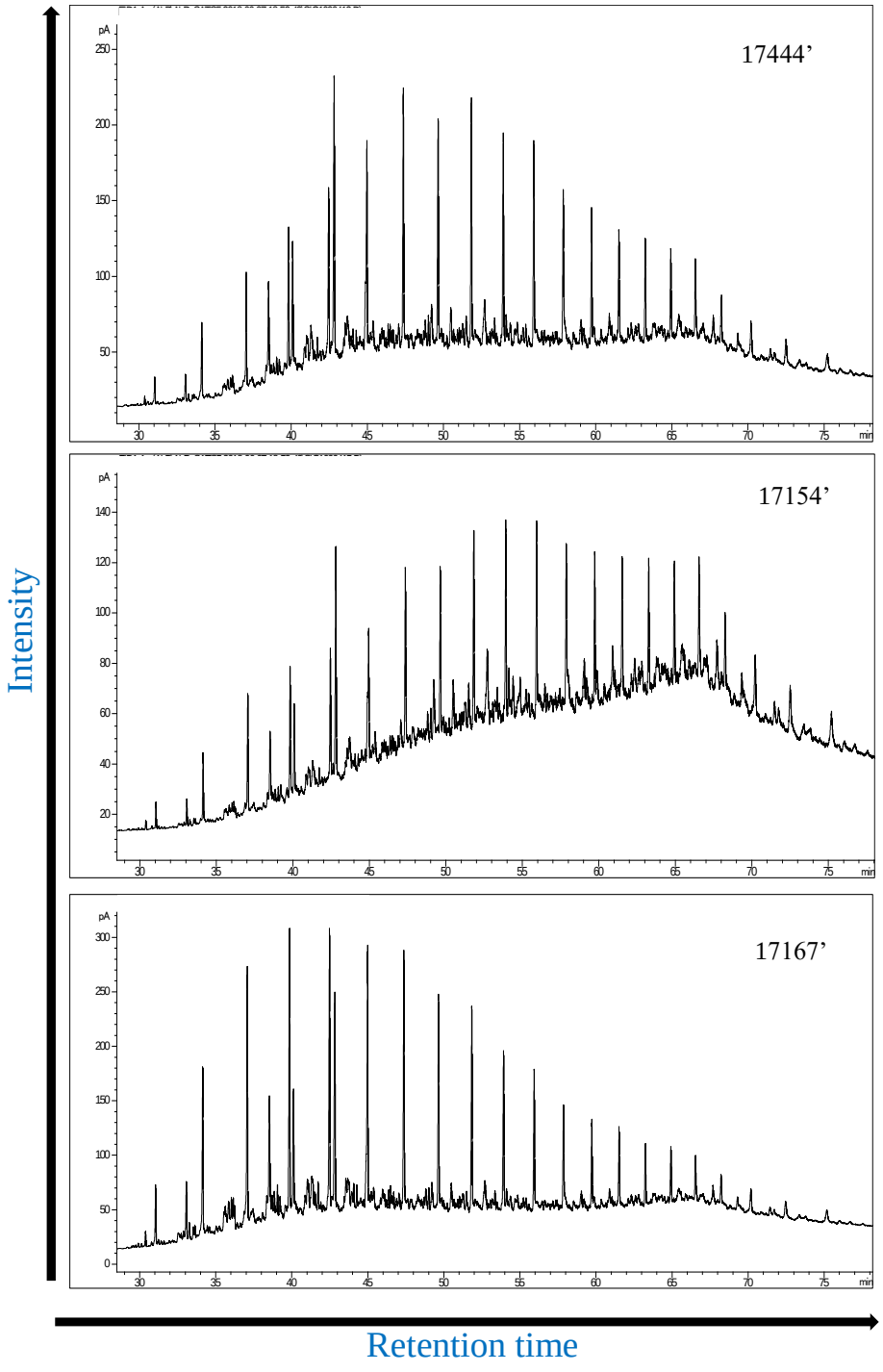
17444’
17154’
17167’
Intensity
Retention time

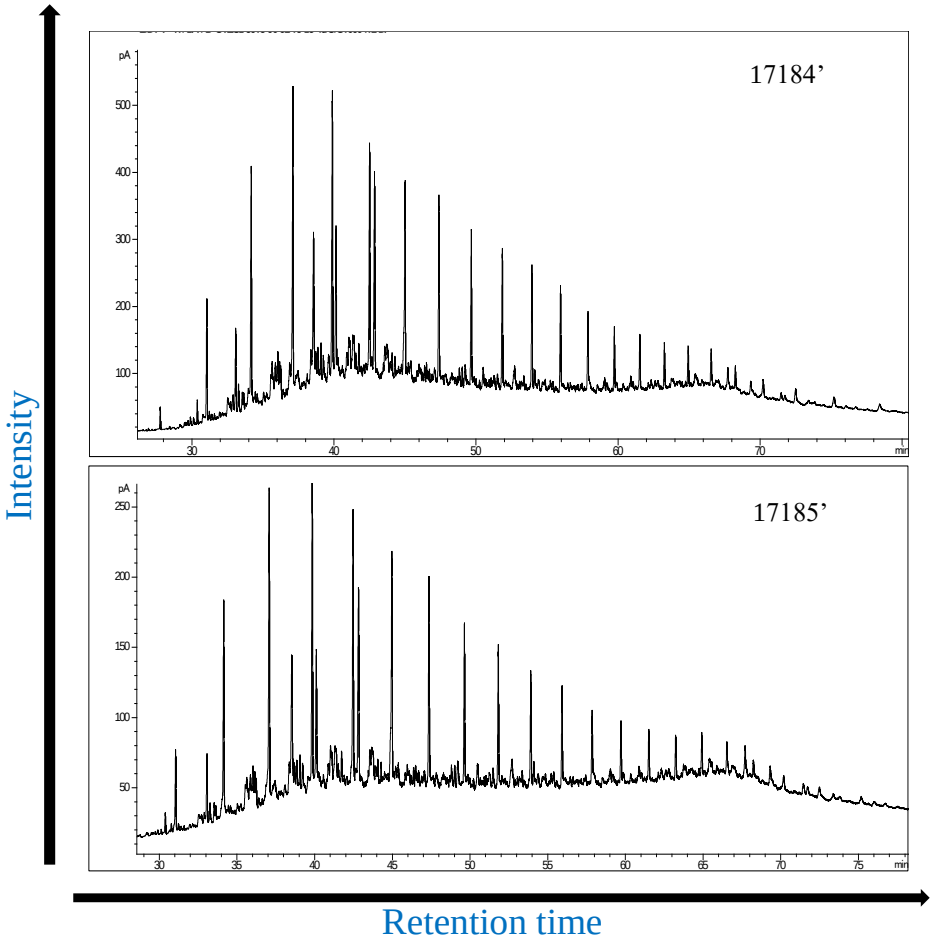

7.4.3. La Luna IS core

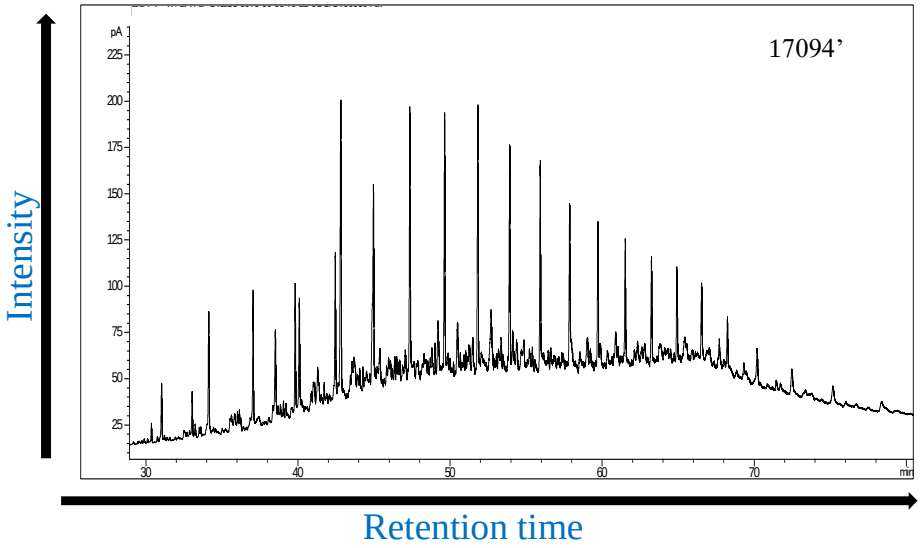

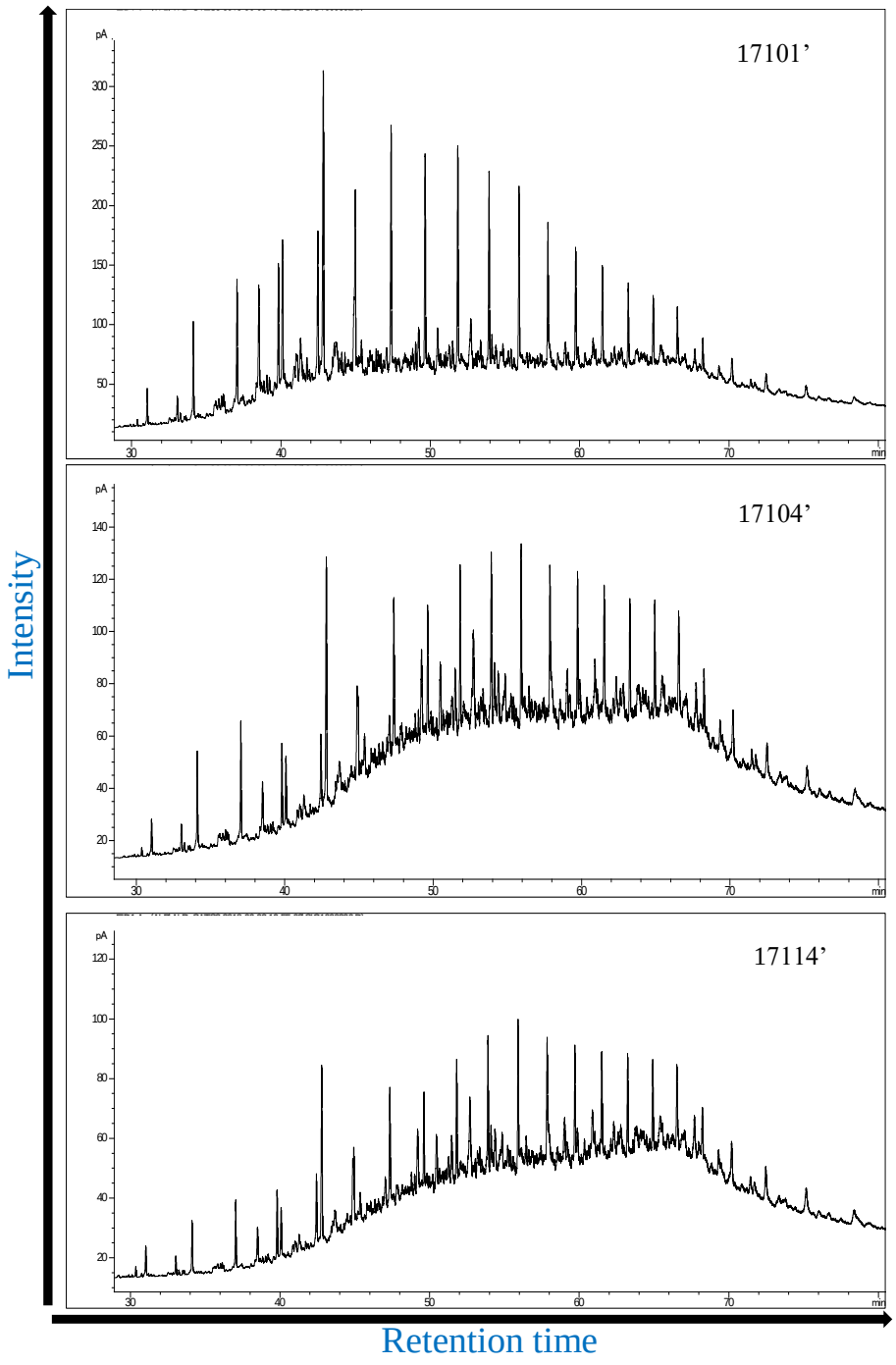
17101’
17104’
17114’
pA
min
Intensity
Retention time

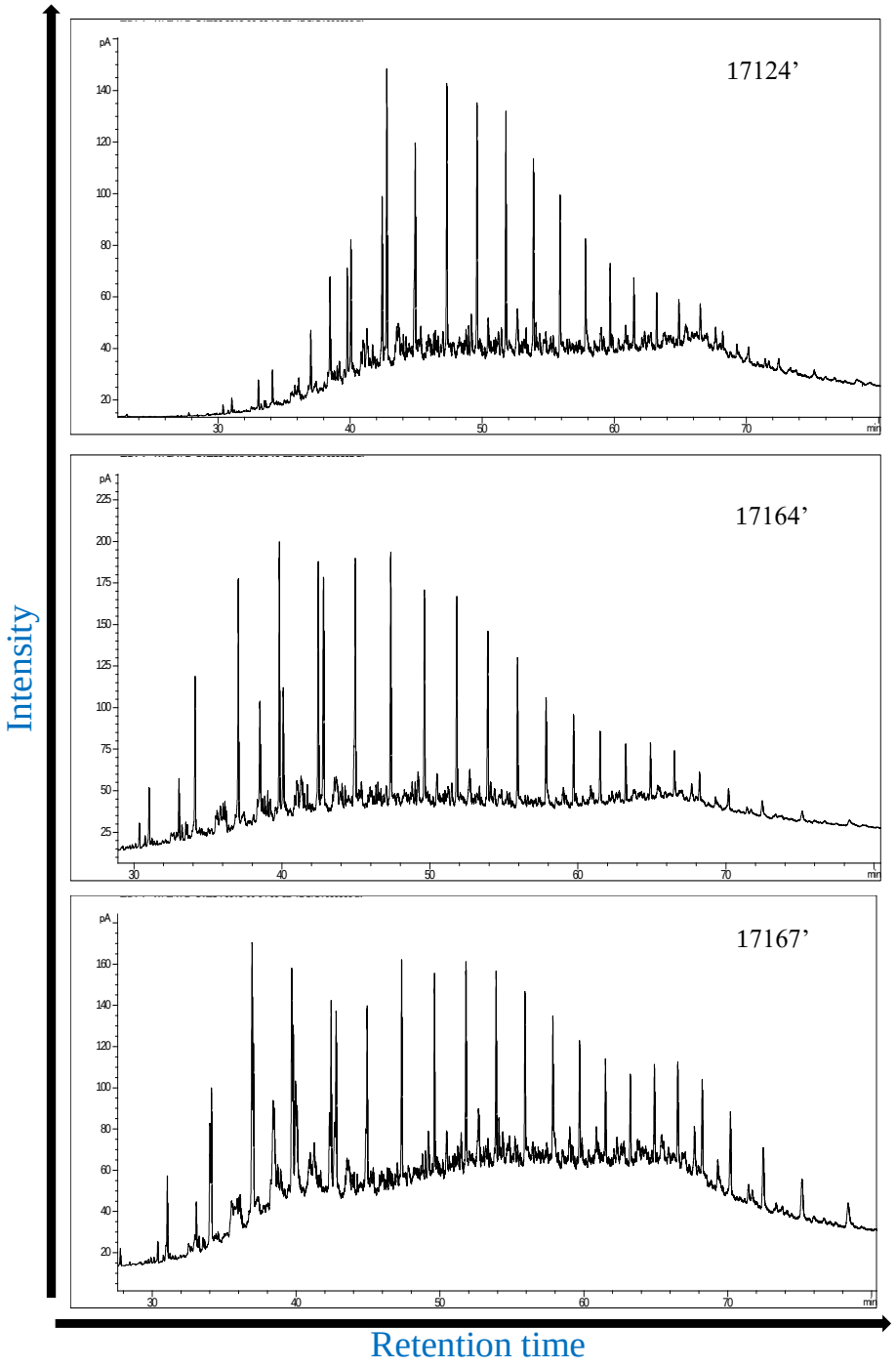
17124’
17164’
17167’
pA
min
Intensity
Retention time

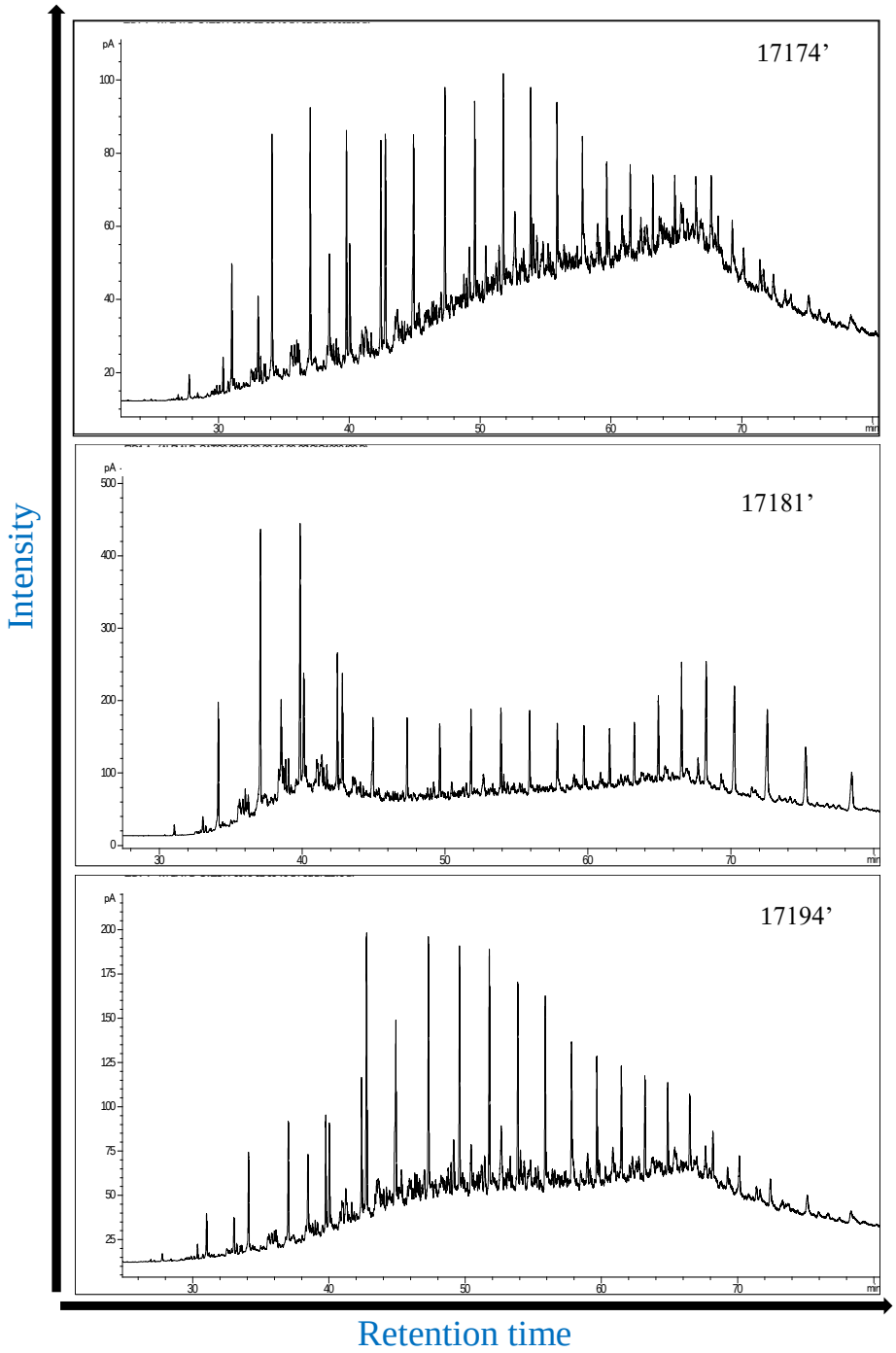
17174’
17181’
17194’
pA
Intensity
Retention time
min

7.4.4. La Luna stratotype

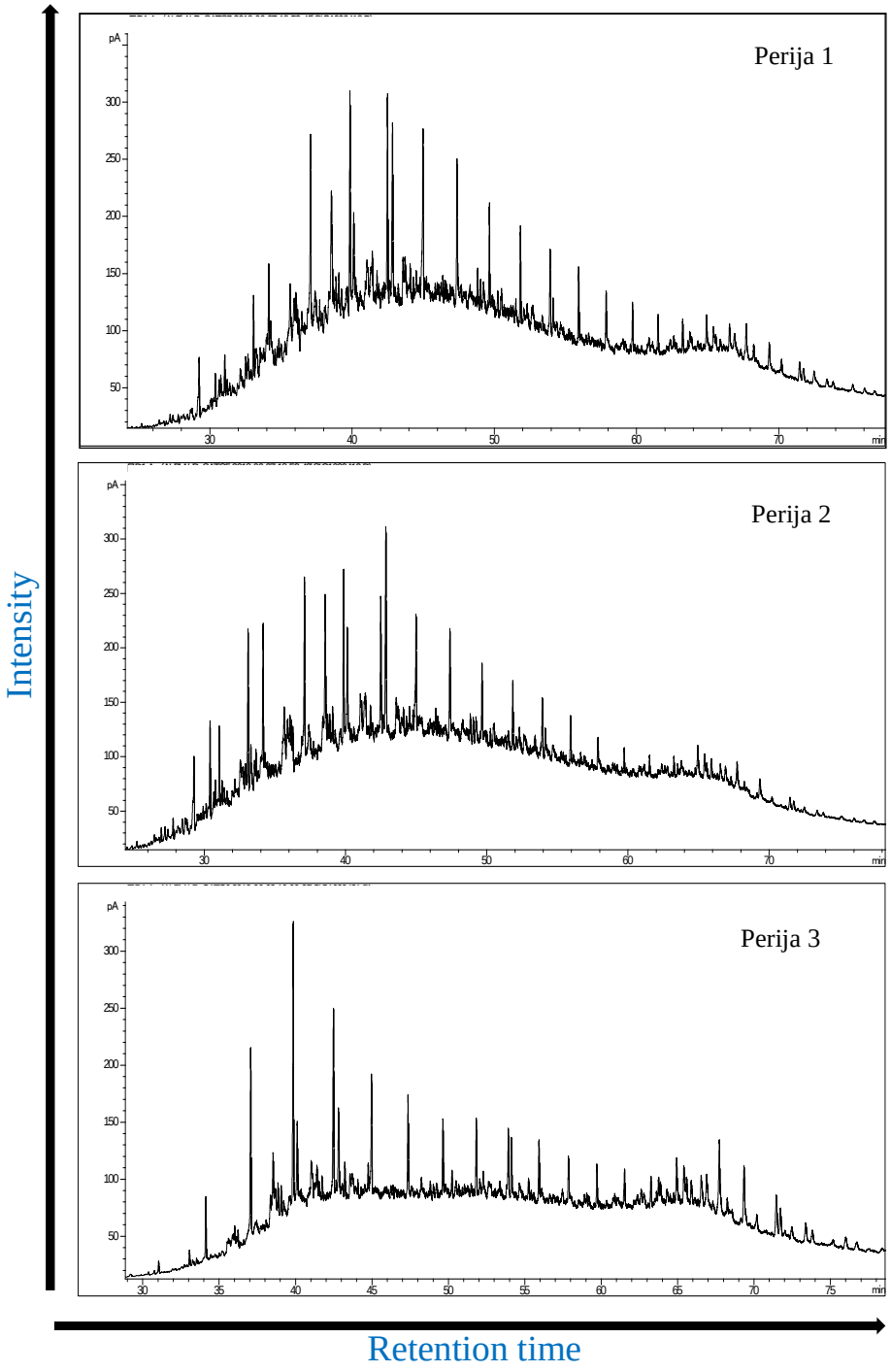

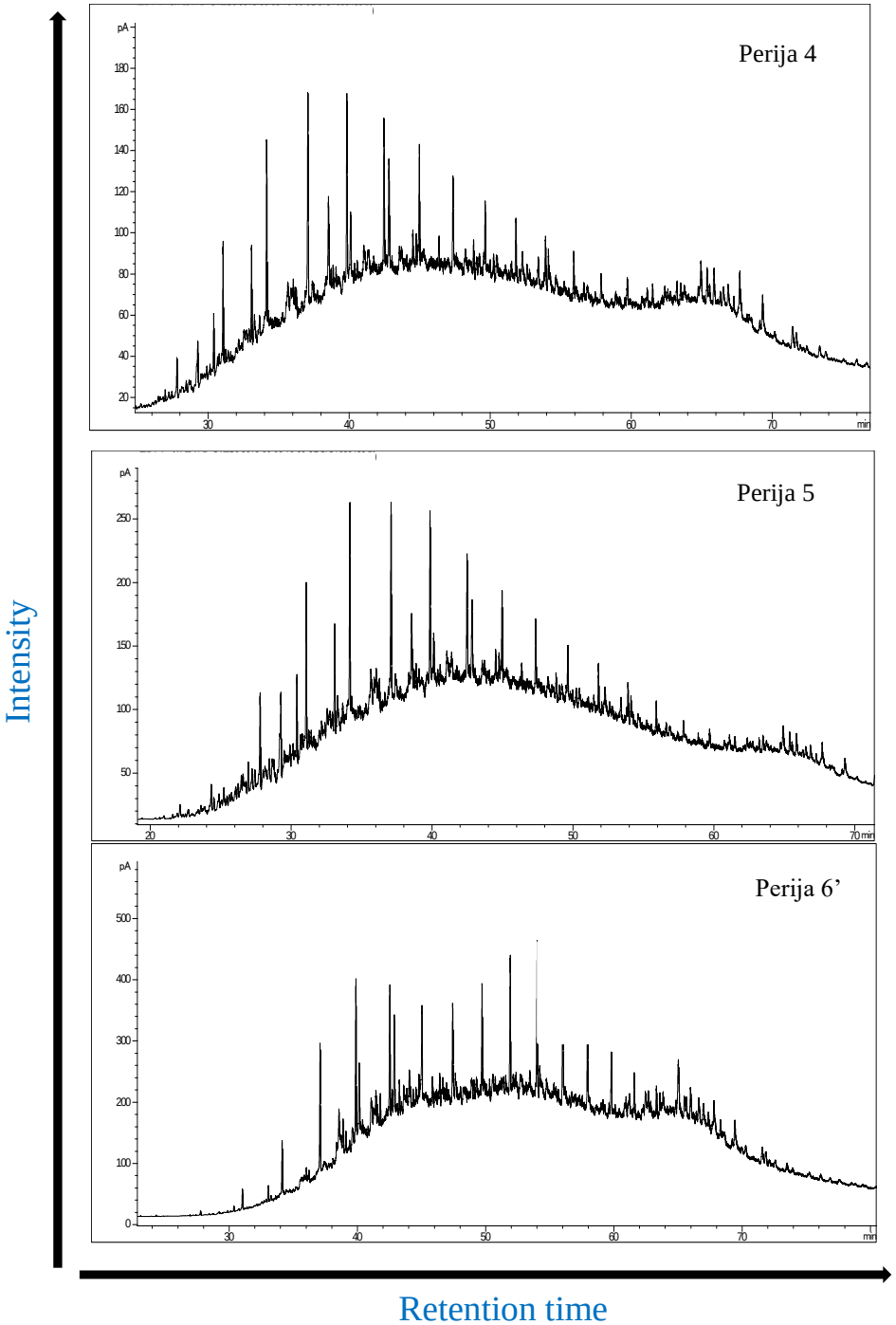
Perija 4
Perija 5
Perija 6’
Intensity
Retention time

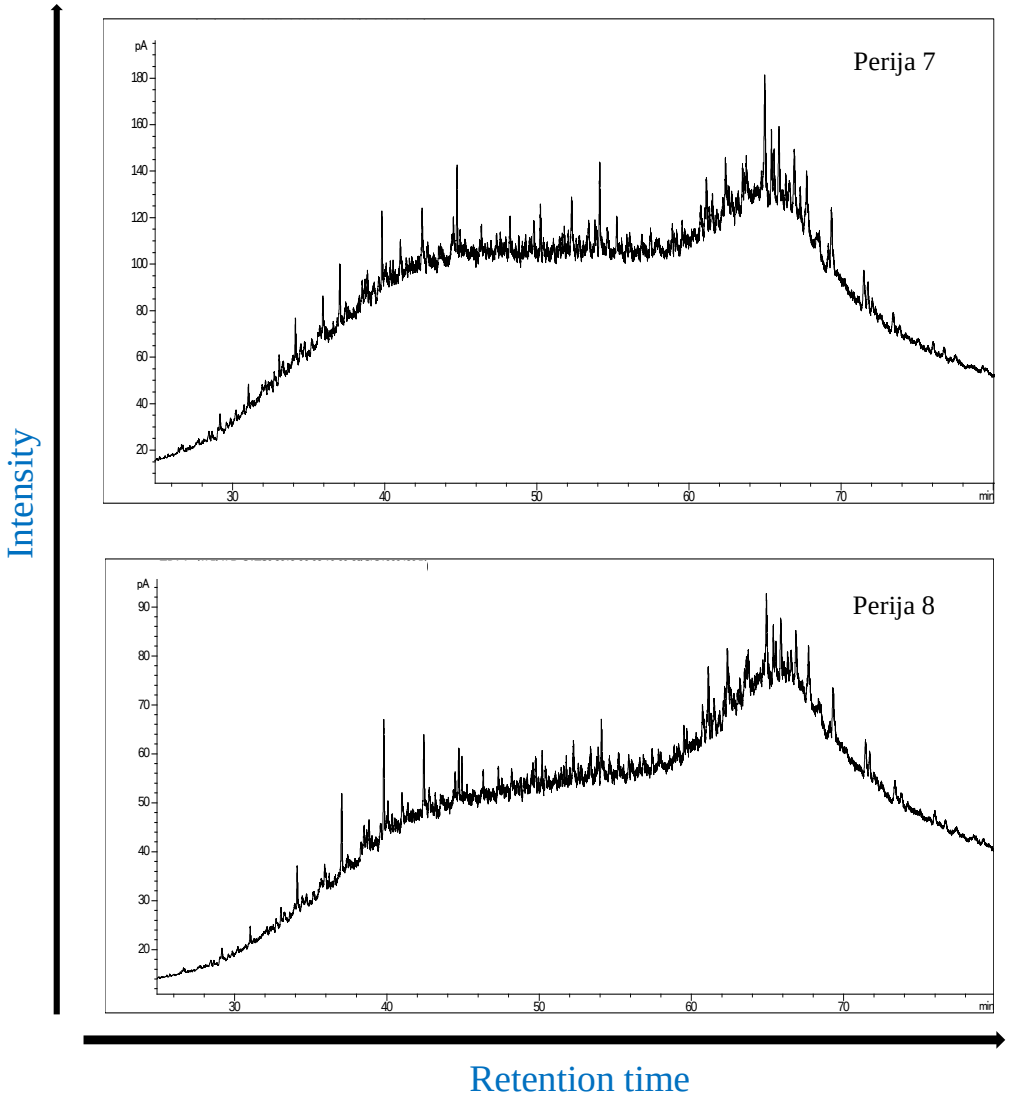
Perija 7
Perija 8
pA
min
Intensity
Retention time

7.5.Abbreviations and formulas used for calculation of geochemical biomarker ratios

7.5.1. *n*-alkanes

Carbon Preference Index (CPI)

$$CPI = \frac{1}{2}\left[\frac{C_{25}+C_{27}+C_{29}+C_{31}+C_{33}}{C_{26}+C_{28}+C_{30}+C_{32}+C_{34}} + \frac{C_{25}+C_{27}+C_{29}+C_{31}+C_{33}}{C_{24}+C_{26}+C_{28}+C_{30}+C_{32}}\right]$$

Terrigenous/Aquatic Ratio (TAR):

$$TAR = \left[\frac{C_{27}+C_{29}+C_{31}}{C_{15}+C_{17}+C_{19}}\right]$$

Long- versus Short-chain *n*-alkanes:

$$\text{long-/short-chain n-alkanes} = \frac{\sum(C_{21}-C_{31})}{\sum(C_{15}-C_{21})}$$

7.5.2. Steranes

C_{27}%, C_{28}%, C_{29}% = C_{27}, C_{28}, C_{29} [14α(H),17α(H)- + 14β (H),17β (H)-Cholestane (20S+ 20R)]

C_{29} 20S/ (20S + 20R) = C_{29} [14α(H),17α(H)-Cholestane (20S)]/[14α(H),17α(H)-Cholestane (20S+20R)]

C_{29} ββ/(ββ + αα) = C_{29} [14β(H),17β(H)-Cholestane (20S+20R)]/[14β(H),17β(H)- + 14α(H),17α(H)-Cholestane (20S+20R)]

Preg/Ster = C_{21} 14β(H),17β(H)-Pregnane/C_{27} 14α(H),17α(H)-Cholestane (20R)

C_{27} Dia/C_{27} Sterane = [C_{27} 13β(H),17α(H)-Diacholestane (20S+20R)]/[C_{27} 14α(H),17α(H)- + 14β(H),17β(H)-Cholestane (20S+20R)]

C_{27} Dia/(Dia+Reg) = [C_{27} 13β(H),17α(H)- + 13α(H),17β(H)-Diacholestane (20S+20R)]/ [C_{27} 13β(H),17α(H)- + 13α(H),17β(H)-Diacholestane (20S+20R) + C_{27} 14α(H),17α(H)- + 14β(H),17β(H)-Cholestane (20S+20R)]

Sterane Index = $C_{30}/(C_{27}-C_{30})$ = [C_{30} 14α(H),17α(H)- + 14β(H),17β(H)-Cholestane (20S+20R)]/ C_{27}, C_{28}, C_{29}, C_{30} [14α(H),17α(H)- + 14β(H),17β(H)-Cholestane (20S+20R)]

7.5.3. Hopanes

Sterane/17α-Hopanes = [C_{27}, C_{28}, C_{29}, C_{30} 14α(H),17α(H)- + 14β(H),17β(H)-Cholestane (20S+20R)]/[C_{29} 17α(H),21β(H)-30-Norhopane + C_{30} 17α(H),21β(H)-Hopane + C_{31}+C_{32}+C_{33} 17α(H),21β(H)-Homohopanes (22S+22R)]

TR/17α-H = C_{28} + C_{29} Tricyclic terpanes (20S+20R)/17α-Hopanes

C_{22}/C_{21}TR = C_{22}/C_{21} Tricyclic terpanes

C_{24}/C_{23}TR = C_{24}/C_{23} Tricyclic terpanes

C_{26}/C_{25}TR = C_{26}/C_{25} Tricyclic terpanes

C_{23}TR/30H = C_{23} Tricyclic terpanes/C_{30} 17α(H),21β(H)-Hopane

C_{24}TT/30H = C_{24} Tetracyclic terpane/C_{30} 17α(H),21β(H)-Hopane

30-NorH/30H = C_{29} 17α(H),21β(H)-30-Norhopane/C_{30} 17α(H),21β(H)-Hopane

Mor/30H = C_{30} 17β(H),21α(H)-Moretane/C_{30} 17α(H),21β(H)-Hopane

31R/30H = C_{31} 17α(H),21β(H)-Homohopane (22R)/C_{30} 17α(H),21β(H)-Hopane
35S/34S = C_{35} 17α(H),21β(H)-Pentakishomohopane (22S)/C_{34} 17α(H),21β(H)-Tetrakishomohopane (22S)

HH Index = $C_{35}/(C_{31} – C_{35})$ = C_{35} 17α(H),21β(H)-Pentakishomohopane

(22S+22R)/[C_{31}+C_{32}+C_{33}+C_{34}+C_{35} 17α(H),21β(H)-Homohopanes (22S+22R)]

C_{31} 22S/22S+22R = C_{31} [17α(H),21β(H)-Homohopanes (22S)/17α(H),21β(H)-Homohopanes (22S+22R)]

7.5.4. Aryl Isoprenoids

Aryl Isoprenoid ratio (AIR):

AIR = (C_{13}-C_{17})/(C_{18}-C_{22}) 2,3,6-trimethyl substituted aryl isoprenoids

7.5.5. Aromatics

MPI-1:

$$MPI\ 1 = 1.5\ \times \frac{[2 - MP + 3 - MP]}{[P + 1 - MP + 9 - MP]}$$

Calculated vitrinite reflectance:

For 0.65 to 1.35% R_o: R_c = 0.60 MPI-1 + 0.40

For 1.35 to 2.00% R_o: R_c = -0.60 MPI-1 + 2.30

MPI-2:

$$MPI\ 2 = 3 \times \frac{[2 - MP]}{P + 1 - MP + 9 - MP}$$

MA(I):

$$MA(I) = \sum C_{27} - C_{29}\ MAS$$

MA(II):

$$MA\ (II) = \sum C_{21} - C_{22}\ MAS$$

TA(I):

$$TA(I) = \sum C_{26} - C_{28}\ (20S + 20R)\ TAS$$

TA(II):

$$TA(II) = \sum C_{20} - C_{21}\ TAS$$

C_{26}TA 20S/20S+20R = C_{26} Cholestane 20S/20S+20R (Triaromatic steroids)

TA_{28} = C_{28} Stigmastane (20S+20R) (Triaromatic steroids)

MA_{29} = C_{29} [5α- + 5β-Stigmastane (20S+20R)]

C_{27}R/C_{28}R TAS = C_{27} Ergostane (20R)/C_{28} Stigmastane (20R)

C_{26}S/C_{28}S TAS = C_{26} Cholestane (20S)/C_{28} Stigmastane (20S)

%C_{27}, %C_{28}, %C_{29} MAS = ΣC_{27}, ΣC_{28}, ΣC_{29} MAS

7.6. Geochemical ratios of steranes for the branched and cyclic fractions (B&C) of the La Luna Formation bitumen

7.6.1. La Luna IX core

SAMPLE	*C_{27}%*	*C_{28}%*	*C_{29}%*	*C_{30}/C_{29} steranes*	*C_{29} 20S/ (20S+20R)*	*$C_{29}ββ/ (ββ+αα)$*	*Pregnanes/ Steranes*	*Sterane/ 17A-Hopanes*	*C_{27}Dia/ C_{27} Sterane*	*C_{27}Dia/ Dia+reg*	*Sterane Index*
LLIX1	37.650	32.762	29.589	0.297	0.50	0.55	1.289	0.35	0.067	0.24	0.087
LLIX2	44.596	30.748	24.656	0.248	0.53	0.54	0.701	0.61	0.057	0.18	0.073
LLIX3	44.706	30.732	24.562	0.229	0.51	0.55	0.692	0.64	0.053	0.17	0.065
LLIX4	44.613	29.257	26.129	0.220	0.48	0.55	0.745	0.60	0.049	0.17	0.066
LLIX5	50.531	26.533	22.936	0.154	0.50	0.54	0.413	0.66	0.046	0.14	0.066
LLIX6	54.775	25.032	20.193	0.323	0.53	0.52	1.790	0.33	0.056	0.32	0.070
LLIX7	75.390	14.162	10.448	0.324	0.53	0.50	0.048	ND	0.031	0.06	0.081
LLIX8	53.051	23.144	23.805	0.188	0.44	0.54	0.331	0.63	0.050	0.15	0.074
LLIX9	44.465	29.742	25.793	0.294	0.50	0.55	2.044	0.30	0.067	0.31	0.066
LLIX10	38.010	30.266	31.724	0.245	0.48	0.52	1.443	0.37	0.062	0.26	0.080
LLIX11	44.416	27.423	28.161	0.243	0.47	0.54	0.240	ND	0.058	0.11	0.083
LLIX12	47.299	27.331	25.371	0.283	0.50	0.56	1.313	0.37	0.053	0.24	0.069
LLIX13	48.691	26.831	24.478	0.217	0.52	0.54	0.887	0.71	0.054	0.21	0.066
LLIX14	47.172	27.054	25.774	0.190	0.50	0.55	0.901	0.63	0.053	0.21	0.073
LLIX15	43.581	28.576	27.843	0.324	0.50	0.54	2.078	0.28	0.059	0.31	0.091
LLIX16	49.364	30.028	20.608	0.322	0.53	0.55	1.329	0.36	0.054	0.26	0.068
LLIX17	48.341	29.526	22.133	0.392	0.54	0.57	3.309	0.29	0.072	0.39	0.083
LLIX18	51.842	26.517	21.641	0.192	0.48	0.55	1.087	0.85	0.061	0.23	0.068
LLIX19	50.450	26.625	22.925	0.263	0.53	0.52	1.363	0.51	0.054	0.26	0.066
LLIX20	53.017	25.700	21.282	0.287	0.51	0.50	1.151	0.74	0.052	0.24	0.064

SAMPLE	C_{27}%	C_{28}%	C_{29}%	C_{30}/C_{29} steranes	C_{29} 20S/ (20S+20R)	$C_{29}\beta\beta/(\beta\beta+\alpha\alpha)$	Pregnanes/ Steranes	Sterane/ 17A-Hopanes	C_{27}Dia/ C_{27} Sterane	C_{27}Dia/ Dia+reg	Sterane Index
LLIX21	46.59	27.11	26.30	0.25	0.49	0.59	2.22	0.90	0.07	0.36	0.07
LLIX22	52.27	28.70	19.04	0.24	0.50	0.58	1.10	ND	0.06	0.23	0.07
LLIX23	51.2	28.5	20.3	0.35	0.50	0.52	1.5	0.32	0.7	0.20	0.6
LLIX24	50.12	29.95	19.93	0.47	0.53	0.49	2.81	0.27	0.11	0.40	0.06
LLIX25	47.52	27.08	25.40	0.42	0.50	0.53	1.75	0.85	0.06	0.30	0.08
LLIX26	54.51	23.51	21.98	0.31	0.49	0.53	0.97	ND	0.06	0.22	0.06
LLIX27	56.80	21.80	21.40	0.20	0.49	0.54	0.81	0.26	0.05	0.19	0.06
LLIX28	54.14	25.11	20.75	0.40	0.53	0.54	2.12	0.32	0.08	0.36	0.07
LLIX29	50.98	28.62	20.40	0.24	0.54	0.57	1.01	0.44	0.07	0.25	0.10
LLIX30	51.79	26.08	22.13	0.19	0.47	0.54	0.78	0.63	0.05	0.21	0.07
LLIX31	45.06	32.09	22.85	0.22	0.48	0.56	1.73	0.25	0.07	0.27	0.06
LLIX32	54.69	27.33	17.98	0.44	0.57	0.60	2.45	0.56	0.07	0.39	0.09
LLIX33	52.38	27.78	19.84	0.31	0.53	0.56	1.35	0.53	0.06	0.26	0.06
LLIX34	47.40	28.82	23.78	0.18	0.49	0.55	1.38	0.63	0.06	0.27	0.07
LLIX35	48.40	27.09	24.51	0.18	0.47	0.54	0.87	0.84	0.09	0.23	0.06
LLIX36	50.87	25.14	23.99	0.26	0.44	0.56	1.12	0.35	0.08	0.27	0.08
LLIX37	45.72	30.21	24.07	0.30	0.54	0.56	1.49	ND	0.06	0.25	0.07

7.6.2. La Luna IA core

SAMPLE	C_{27}%	C_{28}%	C_{29}%	C_{30}/C_{29} steranes	C_{29} 20S/ (20S+20R)	$C_{29}\beta\beta$/ ($\beta\beta+\alpha\alpha$)	Pregnanes/ Steranes	Sterane/ 17A-Hopanes	C_{27}Dia/ C_{27} Sterane	C_{27}Dia/ Dia+reg	Sterane Index
LLIA1	50.00	27.50	22.49	0.27	0.51	0.54	3.34	0.55	0.07	0.40	0.05
LLIA2	46.40	29.64	23.94	0.24	0.49	0.54	3.58	0.63	0.07	0.42	0.05
LLIA3	53.52	26.69	19.77	0.17	0.53	0.58	3.65	0.54	0.08	0.43	0.07
LLIA4	46.06	31.65	22.28	0.20	0.56	0.57	3.99	0.54	0.07	0.42	0.06
LLIA5	41.80	29.88	28.31	0.28	0.47	0.54	3.79	0.43	0.08	0.42	0.06
LLIA6	44.76	29.17	26.05	0.23	0.52	0.56	1.97	0.48	0.08	0.31	0.06
LLIA7	52.20	25.17	22.61	0.26	0.50	0.51	3.11	0.50	0.09	0.39	0.05
LLIA8	48.15	30.13	21.71	0.24	0.55	0.57	3.39	0.49	0.10	0.40	0.05
LLIA9	47.70	29.68	22.61	0.19	0.52	0.56	4.25	0.59	0.13	0.43	0.05
LLIA10	47.29	27.44	25.25	0.20	0.51	0.54	3.21	0.51	0.13	0.39	0.05

SAMPLE	*C_{27}%*	*C_{28}%*	*C_{29}%*	*C_{30}/C_{29} steranes*	*C_{29} 20S/ (20S+20R)*	*$C_{29}\beta\beta$/ ($\beta\beta$+$\alpha\alpha$)*	*anes/ Steranes*	*Sterane/ 17A-Hopanes*	*C_{27}Dia/ C_{27} Sterane*	*C_{27}Dia/ Dia+reg*	*Sterane Index*
LLIA11	51.57	24.47	23.96	0.23	0.52	0.55	2.81	0.66	0.13	0.35	0,05
LLIA12	43.21	33.47	23.32	1.25	0.54	0.60	5.65	ND	0.15	0.39	0,14
LLIA13	38.45	39.64	21.91	0.29	0.57	0.53	4.32	0.42	0.17	0.42	0,06
LLIA14	38.80	38.55	22.66	0.27	0.55	0.54	4.35	0.56	0.18	0.43	0,06
LLIA15	36.34	32.23	31.43	0.24	0.49	0.53	4.03	0.58	0.20	0.41	0,07
LLIA16	33.57	36.01	30.42	0.29	0.49	0.57	4.30	0.47	0.16	0.33	0,06
LLIA17	34.83	36.23	28.94	0.19	0.52	0.60	3.06	0.66	0.16	0.33	0,06
LLIA18	29.21	37.31	33.48	0.22	0.49	0.56	4.33	0.73	0.24	0.42	0,07

7.6.3. La Luna IS core

SAMPLE	C_{27}%	C_{28}%	C_{29}%	C_{30}/C_{29} Steranes	C_{29} 20s/ (20S+20R)	$C_{29}\beta\beta$/ (Bβ+Aα)	Pregnanes/ Steranes	Sterane/ 17a-Hopanes	C_{27}dia/ C_{27} Sterane	C_{27}dia/ Dia+Reg	Sterane Index
LLIS1	37.76	34.61	27.62	0.34	0.53	0.54	1.19	0.34	0.08	0.24	0.08
LLIS2	33.29	35.34	31.37	0.26	0.50	0.54	1.31	0.37	0.08	0.23	0.08
LLIS3	35.67	35.17	29.17	0.28	0.52	0.57	1.07	0.41	0.07	0.21	0.08
LLIS4	34.01	36.93	29.06	0.30	0.51	0.55	1.02	0.41	0.09	0.22	0.08
LLIS5	40.70	32.34	26.96	0.28	0.50	0.55	0.93	0.39	0.07	0.21	0.09
LLIS6	37.69	33.82	28.49	0.31	0.50	0.54	0.97	0.37	0.08	0.24	0.08
LLIS7	40.79	33.29	25.92	0.30	0.51	0.55	0.96	0.41	0.08	0.23	0.08
LLIS8	37.22	35.25	27.53	0.27	0.51	0.57	1.02	0.36	0.09	0.24	0.09
LLIS9	34.75	35.72	29.53	0.28	0.50	0.55	1.25	0.38	0.07	0.22	0.08
LLIS10	35.68	35.22	29.09	0.26	0.48	0.55	1.18	0.35	0.08	0.23	0.07
LLIS11	33.40	37.16	29.43	0.31	0.51	0.55	1.10	0.28	0.07	0.22	0.09
LLIS12	41.70	32.43	25.87	0.35	0.50	0.54	0.95	0.30	0.06	0.21	0.08
LLIS13	44.83	28.79	26.38	0.34	0.50	0.53	1.12	0.31	0.06	0.22	0.08
LLIS14	36.59	34.88	28.53	0.31	0.49	0.54	1.40	0.26	0.07	0.24	0.08

7.6.4. La Luna stratotype

Sample	*C_{27}%*	*C_{28}%*	*C_{29}%*	*C_{30}/C_{29} Steranes*	*C_{29} 20S/ (20S+20R)*	*$C_{29}\beta\beta/$ (Bβ+Aα)*	*Pregnanes/ Steranes*	*Sterane/ 17a-Hopanes*	*C_{27}dia/ C_{27} Sterane*	*C_{27}dia/ Dia+Reg*	*Sterane Index*
PERIJA 1	46.71	27.78	25.51	0.31	0.41	0.45	1.40	0.27	0.10	0.46	0.08
PERIJA 2	52.21	26.62	21.17	0.31	0.46	0.55	2.26	0.29	0.15	0.54	0.08
PERIJA 3	49.99	26.18	23.83	0.33	0.51	0.50	0.86	0.27	0.07	0.41	0.08
PERIJA 4	56.37	21.67	21.95	0.48	0.46	0.59	2.46	0.25	0.19	0.60	0.12
PERIJA 5	42.39	29.16	28.45	0.41	0.49	0.56	5.66	0.18	0.22	0.48	0.09
PERIJA 6	63.63	17.94	18.42	0.25	0.50	0.55	1.12	0.31	0.18	0.23	0.11
PERIJA 7	44.60	30.63	24.77	0.27	0.50	0.61	2.47	0.33	0.25	0.44	0.13
PERIJA 8	39.22	31.59	29.19	0.34	0.47	0.50	1.53	0.35	0.18	0.34	0.14

7.7. Geochemical ratios of terpanes for the branched and cyclic fractions (B&C) of the La Luna bitumen (ND) not determined)

7.7.1. La Luna IX core

Sample	*TR/17A-H*	*C_{22}/ C_{21} TT*	*C_{24}/ C_{23}TT*	*C_{26}/ C_{25}TT*	*C_{23}TT /C_{30}H*	*C_{24}TT/ 30H*	*30-NORH/ 30H*	*MOR/ 30H*	*31R/ 30H*	*35S/ 34S*	*HH INDEX*	*TS/ TS+TM*	*G.I*
LLIX1	*0.12*	*0.49*	*0.34*	*0.24*	*0.81*	*0.27*	*0.83*	*0.06*	*1.08*	*1.31*	*0.11*	*0.21*	*0.14*
LLIX2	*0.21*	*0.48*	*0.37*	*0.18*	*1.22*	*0.45*	*0.83*	*0.09*	*1.20*	*1.34*	*0.09*	*0.16*	*0.15*
LLIX3	*0.23*	*0.36*	*0.36*	*0.19*	*1.38*	*0.50*	*0.76*	*0.05*	*1.16*	*1.62*	*0.13*	*0.14*	*0.16*
LLIX4	*0.20*	*0.48*	*0.36*	*0.21*	*1.20*	*0.43*	*0.80*	*0.06*	*1.10*	*0.63*	*0.06*	*0.16*	*0.15*
LLIX5	*0.22*	*0.51*	*0.37*	*0.21*	*1.12*	*0.42*	*0.83*	*0.07*	*1.28*	*2.45*	*0.21*	*0.14*	*0.20*
LLIX6	*0.10*	*0.29*	*0.38*	*0.32*	*0.87*	*0.33*	*0.88*	*0.04*	*0.85*	*1.28*	*0.20*	*0.15*	*0.19*
LLIX7	*ND*	*ND*	*ND*	*ND*	*ND*	*ND*	*ND*	*ND*	*ND*	*ND*	*ND*	*ND*	*ND*
LLIX8	*0.26*	*0.54*	*0.38*	*0.19*	*1.65*	*0.63*	*0.63*	*0.34*	*1.72*	*1.61*	*0.25*	*0.30*	*0.33*
LLIX9	*0.10*	*0.36*	*0.36*	*0.32*	*0.66*	*0.23*	*1.03*	*0.06*	*0.73*	*0.92*	*0.07*	*0.11*	*0.15*
LLIX10	*0.12*	*0.39*	*0.37*	*0.23*	*0.81*	*0.30*	*0.82*	*0.07*	*0.99*	*1.07*	*0.09*	*0.18*	*0.14*
LLIX11	*ND*	*ND*	*ND*	*ND*	*ND*	*ND*	*ND*	*ND*	*ND*	*ND*	*ND*	*ND*	*ND*
LLIX12	*0.13*	*0.36*	*0.34*	*0.26*	*0.75*	*0.26*	*0.88*	*0.06*	*0.84*	*0.95*	*0.08*	*0.16*	*0.15*
LLIX13	*0.31*	*0.33*	*0.37*	*0.15*	*1.72*	*0.64*	*0.69*	*0.06*	*0.92*	*2.06*	*0.14*	*0.12*	*0.19*
LLIX14	*0.23*	*0.44*	*0.39*	*0.17*	*1.61*	*0.63*	*0.75*	*0.08*	*1.06*	*1.35*	*0.16*	*0.15*	*0.23*
LLIX15	*0.09*	*0.38*	*0.36*	*0.25*	*0.72*	*0.25*	*0.92*	*0.06*	*0.82*	*0.79*	*0.08*	*0.15*	*0.12*
LLIX16	*0.13*	*0.43*	*0.34*	*0.22*	*1.04*	*0.36*	*0.82*	*0.05*	*1.05*	*2.65*	*0.25*	*0.14*	*0.19*
LLIX17	*0.09*	*0.37*	*0.35*	*0.27*	*0.95*	*0.33*	*1.05*	*0.07*	*0.69*	*4.80*	*0.20*	*0.16*	*0.15*
LLIX18	*0.33*	*0.36*	*0.41*	*0.16*	*3.10*	*1.28*	*0.89*	*0.19*	*1.26*	*3.61*	*0.25*	*0.18*	*0.35*
LLIX19	*0.21*	*0.33*	*0.36*	*0.20*	*1.48*	*0.53*	*0.85*	*0.07*	*0.84*	*0.72*	*0.08*	*0.09*	*0.20*
LLIX20	*0.29*	*0.35*	*0.35*	*0.16*	*2.98*	*1.03*	*1.16*	*0.08*	*1.34*	*1.16*	*0.14*	*0.09*	*0.33*

Sample	TR/ 17A-H	C_{22}/ C_{21} TT	C_{24}/ C_{23}TT	C_{26}/ C_{25}TT	C_{23}TT/ C_{30}H	C_{24}TT/ 30H	30-NORH/ 30H	MOR/ 30H	31R/ 30H	35S/34S	HH INDEX	TS/ TS+TM	G.I
LLIX21	0.11	0.29	0.33	0.29	0.76	0.25	1.06	0.07	0.66	1.42	0.08	0.12	0.16
LLIX22	0.35	0.33	0.39	0.16	2.53	0.99	0.99	0.08	0.79	1.43	0.27	0.25	0.29
LLIX23	0.18	0.40	0.40	0.25	1.52	0.62	1.01	0.06	0.78				
LLIX24	0.16	0.46	0.43	0.38	1.01	0.44	1.26	0.06	0.80	0.94	0.10	0.26	0.16
LLIX25	0.10	0.32	0.33	0.29	0.72	0.24	1.01	0.06	0.75	1.09	0.12	0.16	0.16
LLIX26	0.39	0.13	0.33	0.16	4.00	1.32	1.14	0.07	1.67	1.25	0.20	0.15	0.29
LLIX28	0.11	0.43	0.31	0.34	1.02	0.31	1.17	0.07	0.69	0.46	0.05	0.20	0.15
LLIX29	0.23	0.45	0.32	0.18	2.18	0.69	1.26	0.06	1.55	3.46	0.29	0.21	0.26
LLIX30	0.40	0.36	0.32	0.22	2.36	0.75	0.49	0.15	1.31	1.45	0.27	0.10	0.33
LLIX31	0.39	0.38	0.35	0.22	3.70	1.30	1.16	0.11	1.23	3.08	0.27	0.11	0.28
LLIX32	0.09	0.40	0.39	0.36	0.71	0.28	1.17	0.06	0.65	1.90	0.13	0.23	0.17
LLIX33	0.39	0.45	0.44	0.22	2.01	0.88	1.04	0.05	1.34	0.80	0.16	0.20	0.37
LLIX34	0.25	0.39	0.43	0.23	1.86	0.80	1.04	0.05	1.24	0.70	0.22	0.21	0.31
LLIX35	0.54	0.46	0.47	0.21	3.84	1.79	0.82	0.11	2.06	0.53	0.11	0.14	0.58
LLIX36	0.47	0.43	0.47	0.24	3.24	1.51	1.21	0.13	2.06	1.06	0.22	0.20	0.45
LLIX37	0.10	0.35	0.35	0.26	0.69	0.24	0.81	0.07	0.75	0.88	0.09	0.22	0.12

7.7.2. La Luna IA core

Sample	*TR/ 17A-H*	*C_{22}/ C_{21} TT*	*C_{24}/ C_{23}TT*	*C_{26}/ C_{25}TT*	*C_{23}TT/ C30H*	*C_{24}TT/ 30H*	*30-NORH/ 30H*	*MOR/ 30H*	*31R/ 30H*	*35S/34S*	*HH INDEX*	*TS/ TS+TM*	*G.I*
LLIA1	0.43	0.28	0.40	0.24	3.25	1.31	0.99	0.07	0.90	2.44	0.12	0.40	0.27
LLIA2	0.38	0.34	0.46	0.26	2.54	1.17	0.84	0.07	0.71	1.40	0.10	0.37	0.24
LLIA3	0.40	0.19	0.40	0.28	2.87	1.15	0.92	0.07	0.80	0.47	0.07	0.37	0.25
LLIA4	0.42	0.29	0.44	0.29	2.65	1.17	0.94	0.06	0.80	2.25	0.11	0.40	0.26
LLIA5	0.41	0.31	0.44	0.30	2.27	1.00	0.77	0.07	0.93	4.23	0.19	0.41	0.29
LLIA6	0.60	0.30	0.49	0.32	2.57	1.26	1.01	0.08	1.47	3.63	0.17	0.32	0.39
LLIA7	0.53	0.41	0.49	0.26	3.24	1.57	0.94	0.11	0.97	1.12	0.13	0.38	0.31
LLIA8	0.54	0.33	0.51	0.30	3.00	1.54	0.92	0.07	1.01	1.15	0.08	0.41	0.34
LLIA9	0.66	0.40	0.51	0.26	4.10	2.09	0.96	0.17	1.04	2.45	0.17	0.47	0.35
LLIA10	0.62	0.42	0.54	0.32	3.37	1.83	0.96	0.08	1.34	0.86	0.11	0.45	0.40
LLIA11	0.82	0.52	0.56	0.32	4.30	2.38	1.14	0.21	1.65	1.44	0.17	0.48	0.48
LLIA12	ND	ND	ND	ND	ND	ND	ND	ND	ND	ND	ND	ND	ND
LLIA13	0.56	0.40	0.57	0.39	4.63	2.64	1.17	0.13	2.04	5.27	0.16	0.46	0.50
LLIA14	0.73	0.38	0.59	0.27	4.59	2.70	1.06	0.11	1.87	0.91	0.13	0.48	0.48
LLIA15	0.82	0.65	0.62	0.34	3.83	2.38	0.89	0.23	1.58	1.13	0.17	0.40	0.50
LLIA16	0.81	0.36	0.66	0.40	4.99	3.27	2.41	1.09	2.52	5.09	0.20	0.23	0.61
LLIA17	0.90	0.42	0.67	0.36	4.39	2.92	1.42	0.39	2.83	9.52	0.19	0.30	0.63
LLIA18	1.11	0.52	0.75	0.38	5.31	3.98	1.34	0.47	2.89	1.53	0.17	0.32	0.69

7.7.3. La Luna IS core

Sample	*TR/ 17A-H*	*C_{22}/ C_{21}TT*	*C_{24}/ C_{23}TT*	*C_{26}/ C_{25}TT*	*C_{23}TT/ C_{30}H*	*C_{24}TT/*	*30-NORH/ 30H*	*MOR/ 30H*	*31R/ 30H*	*35S/ 34S*	*HH INDEX*	*TS/ TS+TM*	*G.I*
LLIS1	*0.21*	*0.50*	*0.43*	*0.22*	*1.08*		*1.02*	*0.13*	*1.18*	*0.56*	*0.06*	*0.16*	*0.25*
LLIS2	*0.21*	*0.44*	*0.41*	*0.27*	*1.13*	*0.46*	*1.03*	*0.13*	*1.24*	*1.26*	*0.11*	*0.14*	*0.26*
LLIS3	*0.21*	*0.55*	*0.46*	*0.26*	*0.94*	*0.44*	*0.87*	*0.05*	*1.23*	*1.27*	*0.11*	*0.13*	*0.26*
LLIS4	*0.21*	*0.48*	*0.48*	*0.23*	*0.94*	*0.45*	*0.95*	*0.08*	*1.29*	*0.68*	*0.12*	*0.18*	*0.26*
LLIS5	*0.20*	*0.34*	*0.48*	*0.27*	*0.97*	*0.46*	*0.89*	*0.07*	*1.19*	*1.54*	*0.17*	*0.17*	*0.26*
LLIS6	*0.21*	*0.36*	*0.49*	*0.28*	*0.93*	*0.45*	*0.89*	*0.07*	*1.19*	*1.43*	*0.13*	*0.15*	*0.26*
LLIS7	*0.21*	*0.41*	*0.46*	*0.27*	*1.02*	*0.47*	*0.92*	*0.06*	*1.13*	*1.15*	*0.11*	*0.21*	*0.25*
LLIS8	*0.20*	*0.43*	*0.50*	*0.29*	*0.94*	*0.47*	*0.95*	*0.07*	*1.32*	*1.65*	*0.15*	*0.15*	*0.25*
LLIS9	*0.23*	*0.44*	*0.50*	*0.30*	*0.81*	*0.40*	*0.81*	*0.07*	*1.18*	*0.73*	*0.08*	*0.21*	*0.25*
LLIS10	*0.19*	*0.44*	*0.49*	*0.29*	*0.84*	*0.41*	*0.91*	*0.07*	*1.19*	*2.42*	*0.18*	*0.18*	*0.25*
LLIS11	*0.18*	*0.44*	*0.53*	*0.35*	*0.57*	*0.30*	*0.84*	*0.07*	*1.03*	*1.19*	*0.11*	*0.17*	*0.24*
LLIS12	*0.13*	*0.42*	*0.50*	*0.33*	*0.62*	*0.31*	*0.96*	*0.06*	*0.98*	*0.80*	*0.06*	*0.16*	*0.22*
LLIS13	*0.16*	*0.33*	*0.48*	*0.32*	*0.75*	*0.36*	*1.01*	*0.06*	*1.02*	*0.69*	*0.06*	*0.17*	*0.22*
LLIS14	*0.14*	*0.39*	*0.49*	*0.34*	*0.67*	*0.33*	*1.02*	*0.07*	*1.05*	*0.71*	*0.06*	*0.20*	*0.23*

7.7.4. La Luna stratotype

Sample	*TR/ 17A-H*	*C_{22}/ C_{21}TT*	*C_{24}/ C_{23}TT*	*C_{26}/ C_{25}TT*	*C_{23}TT/ C30H*	*C_{24}TT/ 30H*	*30-NORH/ 30H*	*MOR/ 30H*	*31R/ 30H*	*35S/ 34S*	*HH INDEX*	*TS/ TS+TM*	*G.I*
PERIJA 1	*0.14*	*0.52*	*0.38*	*0.33*	*0.78*	*0.30*	*0.83*	*0.10*	*1.01*	*0.95*	*0.12*	*0.24*	*0.32*
PERIJA 2	*0.18*	*0.58*	*0.38*	*0.31*	*1.21*	*0.46*	*0.93*	*0.11*	*1.10*	*0.84*	*0.10*	*0.22*	*0.37*
PERIJA 3	*0.11*	*0.74*	*0.37*	*0.41*	*0.77*	*0.28*	*1.02*	*0.07*	*1.04*	*2.95*	*0.22*	*0.26*	*0.34*
PERIJA 4	*0.09*	*0.43*	*0.31*	*0.35*	*1.20*	*0.37*	*1.21*	*0.10*	*1.03*	*0.70*	*0.09*	*0.23*	*0.29*
PERIJA 5	*0.07*	*0.47*	*0.30*	*0.32*	*0.82*	*0.25*	*1.10*	*0.09*	*1.03*	*0.52*	*0.06*	*0.22*	*0.27*
PERIJA 6	*0.09*	*0.38*	*0.33*	*0.24*	*0.76*	*0.25*	*0.96*	*0.07*	*1.07*	*0.84*	*0.07*	*0.14*	*0.18*
PERIJA 7	*0.10*	*0.44*	*0.32*	*0.30*	*0.98*	*0.31*	*0.99*	*0.08*	*0.90*	*0.67*	*0.09*	*0.22*	*0.21*
PERIJA 8	*0.08*	*0.35*	*0.33*	*0.20*	*0.84*	*0.28*	*0.89*	*0.08*	*1.05*	*1.12*	*0.14*	*0.15*	*0.14*

7.8 Aryl isoprenoids ratio (AIR) for the branched and cyclic fractions (B&C) of the La Luna bitumen (ND = not determined).

7.8.1. La Luna IX core

Sample	*AIR*
LLIX1	1.74
LLIX2	1.80
LLIX3	1.78
LLIX4	1.72
LLIX5	1.72
LLIX6	2.40
LLIX7	2.59
LLIX8	0.43
LLIX9	0.19
LLIX10	0.32
LLIX11	0.54
LLIX12	0.45
LLIX13	0.62
LLIX14	0.60
LLIX15	0.66
LLIX16	0.52
LLIX17	1.21
LLIX18	0.45
LLIX19	0.45
LLIX20	0.44
LLIX21	0.51
LLIX22	0.55
LLIX23	0.61
LLIX24	0.83
LLIX25	0.62
LLIX26	0.60
LLIX27	0.54
LLIX28	0.52
LLIX29	0.60
LLIX30	0.60
LLIX31	0.56
LLIX32	0.49
LLIX33	0.48
LLIX34	1.02
LLIX35	1.50
LLIX36	1.74

7.8.2. La Luna IA core

Sample	*AIR*
LLIA1	1.13
LLIA2	1.44
LLIA3	1.27
LLIA4	1.45
LLIA5	1.39
LLIA6	0.47
LLIA7	1.77
LLIA8	1.30
LLIA9	1.57
LLIA10	2.29
LLIA11	1.80
LLIA12	1.78
LLIA13	1.98
LLIA14	2.31
LLIA15	1.51
LLIA16	1.14
LLIA17	0.70
LLIA18	1.22

7.8.3. La Luna IS core

Sample	*AIR*
LSIS1	0.19
LSIS2	0.22
LSIS3	0.11
LSIS4	0.13
LSIS5	0.35
LSIS6	0.18
LSIS7	0.26
LSIS8	0.28
LSIS9	0.50
LSIS10	0.54
LSIS11	0.12
LSIS12	0.13
LSIS13	0.66
LSIS14	0.47

7.8.4 La Luna stratotype

Sample	*AIR*
PERIJA1	0.37
PERIJA2	0.41
PERIJA3	0.42
PERIJA4	1.09
PERIJA5	0.51
PERIJA6	0.37
PERIJA7	1.05
PERIJA8	0.86

7.9. Geochemical ratios for aromatic biomarkers of the La Luna Formation bitumen (ND= not determined)

7.9.1. La Luna IX core

Sample	*MPI1*	*MA(I)/MA(I+II)*	*TA(I)/TA(I+TAII)*	*C_{26}TA (20S/20S+20R)*	*%C_{27}MAS*	*%C_{28}MAS*	*%C_{29}MAS*
LLIX1	1.10	0.44	0.40	0.16	27.05	46.51	26.44
LLIX2	1.09	0.36	0.40	0.17	30.05	42.12	27.83
LLIX3	1.20	0.37	0.39	0.12	52.81	20.67	26.52
LLIX4	1.15	0.39	0.39	0.10	52.69	22.89	24.41
LLIX5	1.01	0.34	0.39	0.10	55.41	24.46	20.11
LLIX6	0.98	0.39	0.17	0.31	45.97	30.90	23.12
LLIX7	0.97	0.38	0.34	0.12	43.32	34.78	21.9
LLIX8	1.05	0.38	0.37	0.13	36.78	37.85	25.37
LLIX9	1.03	0.40	0.16	0.24	32.58	40.45	26.97
LLIX10	1.02	0.38	0.36	0.11	48.20	24.40	27.39
LLIX11	1.02	0.37	0.33	0.14	58.70	17.23	24.05
LLIX12	1.00	0.35	0.34	0.15	52.36	22.53	25.11
LLIX13	1.00	0.37	0.27	0.20	52.48	25.95	21.56
LLIX14	0.98	0.36	0.28	0.18	60.72	17.32	21.94
LLIX15	0.98	0.41	0.16	0.29	35.80	45.13	19.07
LLIX16	0.99	0.37	0.26	0.21	34.53	43.23	2.24
LLIX17	0.99	0.39	0.21	0.29	34.68	44.96	20.36
LLIX18	1.00	0.37	0.33	0.18	47.16	29.61	23.22
LLIX19	1.00	0.34	0.22	0.27	46.02	30.25	23.73
LLIX20	0.97	0.39	0.20	0.36	43.81	31.94	24.23

Sample	*MPI1*	*MA(I)/MA(I+II)*	*TA(I)/TA(I+TAII)*	*C_{26}TA (20S/20S+20R)*	*%C_{27}MAS*	*%C_{28}MAS*	*%C_{29}MAS*
LLIX21	0.96	0.41	0.17	0.35	39.61	39.43	20.96
LLIX22	0.96	0.42	0.18	0.32	37.89	38.96	23.15
LLIX23	0.97	0.35	0.35	0.11	39.98	38.56	21.46
LLIX24	0.99	0.41	0.17	0.32	38.63	39.63	21.74
LLIX25	0.97	0.41	0.17	0.32	36.60	40.32	23.08
LLIX26	1.01	0.39	0.17	0.35	35.69	38.96	25.35
LLIX27	1.04	0.41	0.16	0.35	39.63	39.56	20.81
LLIX28	1.03	0.40	0.17	0.46	38.69	42.03	19.28
LLIX29	1.13	0.39	0.19	0.33	37.58	40.36	22.06
LLIX30	1.08	0.41	0.16	0.30	39.56	41.36	19.08
LLIX31	1.06	0.41	0.16	0.37	36.52	39.56	23.92
LLIX32	1.05	0.38	0.17	0.40	34.06	41.46	24.47
LLIX33	1.05	0.38	0.14	0.42	36.05	38.69	25.26
LLIX34	1.06	0.39	0.16	0.40	35.89	36.96	27.15
LLIX35	1.06	0.41	0.18	0.31	36.58	39.89	23.53
LLIX36	1.06	0.39	0.18	0.33	33.36	45.63	21.01
LLIX37	1.09	0.43	0.15	0.35	31.29	51.32	17.39

7.9.2. La Luna IA core

Sample	*MPI1*	*MA(I)/MA(I+II)*	*TA(I)/TA(I+TAII)*	*C_{26}TA (20S/20S+20R)*	*%C_{27}MAS*	*%C_{28}MAS*	*%C_{29}MAS*
LLIA1	1.10	0.38	0.18	0.41	32.52	40.23	27.25
LLIA2	0.99	0.38	0.15	0.45	34.72	42.07	23.20
LLIA3	2.57	0.40	0.16	0.45	29.46	41.67	28.86
LLIA4	1.39	0.37	0.16	0.38	41.03	36.32	22.65
LLIA5	1.00	0.38	0.16	0.35	42.36	32.36	25.28
LLIA6	1.14	0.42	0.17	0.38	44.57	26.44	28.99
LLIA7	1.08	0.40	0.16	0.40	40.53	36.53	22.94
LLIA8	1.05	0.38	0.16	0.45	33.78	37.84	28.38
LLIA9	1.04	0.41	0.16	0.43	35.63	35.45	28.92
LLIA10	1.08	0.41	0.18	0.35	36.25	36.52	27.23
LLIA11	1.09	0.42	0.19	0.34	37.14	35.22	27.64
LLIA12	1.10	0.42	0.19	0.26	37.63	36.63	25.74
LLIA13	1.04	0.41	0.18	0.29	38.27	37.70	24.02
LLIA14	1.09	0.40	0.18	0.31	40.23	32.32	27.45
LLIA15	1.11	0.38	0.22	0.30	41.07	29.89	29.04
LLIA16	1.13	0.39	0.22	0.31	31.85	35.47	32.69
LLIA17	1.12	0.41	0.24	0.31	33.73	33.19	33.08
LLIA18	1.09	0.41	0.26	0.29	36.54	32.44	31.02

7.9.3. La Luna IS core

Sample	*MPI1*	*MA(I)/MA(I+II)*	*TA(I)/TA(I+TAII)*	*C26TA (20S/20S+20R)*	*%C_{27}MAS*	*%C_{28}MAS*	*%C_{29}MAS*
LLIS1	1.16	0.46	0.36	0.13	29.96	49.33	20.71
LLIS2	1.16	0.46	0.37	0.15	29.50	49.06	21.44
LLIS3	1.24	0.46	0.36	0.16	29.58	49.78	20.64
LLIS4	1.19	0.46	0.37	0.14	30.58	48.88	20.53
LLIS5	1.15	0.45	0.32	0.34	30.26	50.26	19.49
LLIS6	1.16	0.45	0.36	0.30	29.30	49.00	21.70
LLIS7	1.18	0.45	0.36	0.13	29.16	49.25	21.59
LLIS8	1.18	0.46	0.34	0.18	29.41	49.09	21.50
LLIS9	1.14	0.45	0.34	0.16	30.21	48.27	21.52
LLIS10	1.12	0.46	0.34	0.17	29.06	50.35	20.59
LLIS11	1.22	0.45	0.35	0.16	31.26	52.36	16.38
LLIS12	1.14	0.44	0.33	0.19	31.98	46.12	21.90
LLIS13	1.10	0.42	0.33	0.20	33.92	45.40	20.68
LLIS14	1.06	0.44	0.31	0.22	30.25	45.53	24.22

7.10. Biomarker quantification results for steranes (Concentrations are expressed as in ppm W/W)

7.10.1. La Luna IX core

Sample	*Diapregnane*	*Pregnane*	*Diahomopregnane*	*Homopregnane*	*$C_{27}\beta\alpha$-Dia (20S)*	*$C_{27}\ \beta\alpha$-Dia(20R)*	*$C_{27}\alpha\beta$ Dia (20S)*	*$C_{27}\ \alpha\beta$-Dia(20R)*	*$C_{28}\ \beta\alpha$-Dia (20S)*	*$C_{28}\ \beta\alpha$-Dia(20R)*	*C28$\alpha\beta$-Dia (20S) +$C_{27}\alpha\alpha$ (20S)*	*$C_{27}\ \beta\beta$ (20R) +$C_{29}\ \beta\alpha$ (20S)*	*C27 $\beta\beta$(20S) +C28 $\alpha\beta$ (20R)*	*$C_{27}\alpha\alpha$ (20R)*	*$C_{29}\beta\alpha$-Dia (20R)*	*$C_{29}\ \alpha\beta$-Dia (20S)*	*$C_{29}\alpha\alpha$ (20S)*	*$C_{28}\beta\beta$ (20R) + $C_{29}\alpha\beta$-Dia (20R)*	*$C_{28}\ \beta\beta$ (20S)*	*$C_{29}\alpha\alpha$ (20R)*	*$C_{29}\ \alpha\alpha$ (20S)*	*$C_{29}\beta\beta$ (20R)*	*$C_{29}\beta\beta$ (20S)*	*$C_{29}\ \alpha\alpha$ (20R)*	*$C_{30}\alpha\alpha$ (20S)*	*$C_{30}\beta\beta$ (20R)*	*$C_{30}\ \beta\beta$ (20S)*	*$C_{30}\ \alpha\alpha$ (20R)*
LLIX1	4	26	14	14	2	3	1	11	11	7	18	25	19	20	6	5	7	21	14	18	16	22	17	16	4	7	7	3
LLIX2	3	25	14	14	3	5	2	15	17	11	27	42	34	35	13	7	8	28	18	24	22	29	20	19	4	7	9	4
LLIX3	2	16	9	9	2	3	1	10	10	8	17	27	22	23	10	4	5	19	12	16	13	18	13	13	18	4	6	2
LLIX4	3	23	13	13	2	4	2	13	14	11	24	39	29	31	15	3	7	25	16	21	17	23	19	18	4	5	7	3
LLIX5	0	23	2	0	3	0	0	0	0	0	0	0	22	23	9	4	5	19	12	16	13	16	13	13	16	4	5	2
LLIX6	3	26	1	0	0	0	0	0	0	0	0	0	0	0	0	0	0	0	0	0	0	0	0	0	0	0	0	0
LLIX7	6	40	2	0	1	0	0	0	0	0	0	0	1	3	2	0	3	1	2	1	1	1	0	0	0	0	0	0
LLIX8	3	1	0	0	0	0	0	1	1	1	2	2	1	3	1	0	0	1	1	1	1	1	1	1	0	0	1	0
LLIX9	2	23	10	0	1	0	0	0	0	0	0	0	22	23	10	4	5	19	12	16	13	18	13	13	18	4	6	2

Sample	*Diapregnane*	*Pregnane*	*Diahomopregnane*	*Homopregnane*	*$C_{27}\beta\alpha$-Dia (20S)*	*$C_{27}\beta\alpha$-Dia(20R)*	*$C_{27}\alpha\beta$ Dia (20S)*	*$C_{27}\ \alpha\beta$-Dia(20R)*	*$C_{28}\ \beta\alpha$-Dia (20S)*	*$C_{28}\ \beta\alpha$-Dia(20R)*	*$C_{28}\alpha\beta$-Dia (20S) +$C_{27}\alpha\alpha$ (20S)*	*$C_{27}\ \beta\beta$ (20R) +$C_{29}\ \beta\alpha$ (20S)*	*$C_{27}\ \beta\beta$(20S) +$C_{28}\ \alpha\beta$ (20R)*	*$C_{27}\alpha\alpha$ (20R)*	*$C_{29}\beta\alpha$-Dia (20R)*	*$C_{29}\ \alpha\beta$-Dia (20S)*	*$C_{28}\alpha\alpha$ (20S)*	*$C_{28}\beta\beta$ (20R) + $C_{29}\alpha\beta$-Dia (20R)*	*$C_{28}\ \beta\beta$ (20S)*	*$C_{28}\alpha\alpha$ (20R)*	*$C_{29}\ \alpha\alpha$ (20S)*	*$C_{29}\beta\beta$ (20R)*	*$C_{29}\ \beta\beta$ (20S)*	*$C_{29}\ \alpha\alpha$ (20R)*	*$C_{30}\alpha\alpha$ (20S)*	*$C_{30}\beta\beta$ (20R)*	*$C_{30}\ \beta\beta$ (20S)*	*$C_{30}\ \alpha\alpha$ (20R)*
LLIX10	5	44	23	23	3	4	2	16	16	13	27	34	22	23	10	4	5	19	12	16	15	23	10	12	16	7	6	1
LLIX11	3	23	0	0	0	0	0	0	0	0	0	0	22	28	9	3	6	18	10	16	13	18	13	13	18	4	6	2
LLIX12	4	346	175	175	23	28	19	116	108	96	183	291	6	5	2	1	1	3	2	3	2	3	3	2	1	1	1	1
LLIX13	24	151	89	89	15	31	12	70	50	44	136	162	161	175	77	32	45	103	70	92	83	105	99	83	19	34	48	17
LLIX14	1	9	5	5	1	1	1	4	4	4	7	11	9	10	4	2	2	7	4	6	6	7	6	6	1	1	3	1
LLIX15	14	69	23	23	2	17	4	29	13	6	27	41	34	22	10	15	17	28	22	23	20	36	22	19	4	7	6	3
LLIX16	1	7	4	4	0	0	0	1	2	2	3	5	4	5	2	1	1	3	2	3	2	3	3	2	1	1	1	0
LLIX17	10	60	32	32	6	18	5	35	36	26	63	86	77	59	19	20	23	98	55	64	53	67	60	50	10	20	26	10
LLIX18	1	325	142	3	0	1	0	2	2	2	3	4	4	5	2	0	1	3	2	3	2	3	2	2	1	1	1	0
LLIX19	1	13	6	6	1	1	1	4	3	3	6	9	7	9	4	1	1	5	4	5	5	5	4	4	1	1	2	1
LLIX20	1	9	5	5	1	1	1	4	2	3	5	7	6	8	3	1	1	4	3	4	3	4	3	3	1	1	1	1

Sample	*Diapregnane*	*Pregnane*	*Diahomopregnane*	*Homopregnane*	*C_{27} βα-Dia(20R)*	*C_{27}αβ Dia (20S)*	*C_{27} αβ-Dia(20R)*	*C_{28} βα-Dia (20S)*	*C_{28} βα-Dia(20R)*	*C_{28}αβ-Dia (20S) +C_{27}αα (20S)*	*C_{27} ββ (20R) +C_{29} βα (20S)*	*C_{27} ββ(20S) +C_{28} αβ (20R)*	*C_{27}αα (20R)*	*C_{29}βα-Dia (20R)*	*C_{29} αβ-Dia (20S)*	*C_{28}αα (20S)*	*C_{28}ββ (20R) + C_{29}αβ-Dia (20R)*	*C_{28} ββ (20S)*	*C_{28}αα (20R)*	*C_{29} αα (20S)*	*C_{29}ββ (20R)*	*C29 ββ (20S)*	*C_{29} αα (20R)*	*C_{30}αα (20S)*	*C_{30}ββ (20R)*	*C_{30} ββ (20S)*	*C_{30} αα (20R)*
LLIX21	7	55	27	27	3	3	13	10	8	18	22	17	25	10	3	6	17	10	14	13	22	16	14	2	6	4	2
LLIX22	1	7	3	3	1	0	3	2	2	3	5	5	6	2	1	1	3	2	3	2	3	3	2	1	1	1	0
LLIX23	1	22	9	13	1	2	6	6	6	8	13	0	0	0	0	0	0	0	0	0	0	0	0	0	0	0	0
LLIX24	6	46	19	19	4	2	11	7	11	11	15	10	16	7	2	5	11	7	10	8	7	7	7	1	3	2	1
LLIX25	6	48	25	25	3	2	13	10	10	18	24	24	28	13	5	6	19	11	16	15	16	17	15	3	7	6	3
LLIX26	1	6	3	3	1	1	3	2	2	4	6	5	7	2	1	1	3	2	3	3	3	3	3	1	1	1	0
LLIX27	0	2	1	1	0	0	1	1	1	2	2	3	7	0	2	1	1	0	0	0	0	1	1	0	1	1	1
LLIX28	2	19	9	9	1	1	4	3	2	5	8	5	9	3	1	2	5	3	4	4	5	4	3	1	2	1	0
LLIX29	0	3	1	1	0	0	2	1	1	2	2	2	3	1	0	1	2	1	2	1	2	2	1	0	0	1	1
LLIX30	0	3	1	1	0	0	2	1	1	2	2	2	3	1	0	1	2	1	2	1	2	1	1	0	0	1	0

Sample	*Diapregnane*	*Pregnane*	*Diahomopregnane*	*Homopregnane*	*C_{27} βα-Dia(20R)*	*C_{27}αβ Dia (20S)*	*C_{27} αβ-Dia(20R)*	*C_{28} βα-Dia (20S)*	*C_{28} βα-Dia(20R)*	*C28αβ-Dia (20S) +C_{29}αα (20S)*	*C_{27} ββ (20R) +C_{29} βα (20S)*	*C_{27} ββ(20S) +C_{28} αβ (20R)*	*C_{27}αα (20R)*	*C_{29}βα-Dia (20R)*	*C_{29} αβ-Dia (20S)*	*C_{28}αα (20S)*	*C_{28}ββ (20R) + C_{29}αβ-Dia (20R)*	*C_{28} ββ (20S)*	*C_{28}αα (20R)*	*C_{29} αα (20S)*	*C_{29}ββ (20R)*	*C_{29} ββ (20S)*	*C_{29} αα (20R)*	*C_{30}αα (20S)*	*C_{30}ββ (20R)*	*C_{30} ββ (20S)*	*C_{30} αα (20R)*
LLIX31	2	14	5	5	1	1	5	3	3	5	8	6	8	2	1	1	5	3	6	4	5	5	4	1	1	1	0
LLIX32	3	24	11	11	1	1	5	3	2	5	8	4	10	4	1	2	6	4	5	4	5	6	3	1	2	3	0
LLIX33	1	6	3	3	0	1	2	1	1	3	4	3	5	2	1	1	3	2	3	2	3	2	2	0	1	0	0
LLIX34	1	10	4	4	1	1	3	2	2	4	5	5	7	3	1	1	4	3	5	4	5	4	4	0	1	1	1
LLIX35	1	4	2	2	1	0	2	1	1	2	4	2	4	2	1	1	3	2	2	2	3	2	2	0	0	1	0
LLIX36	1	5	2	2	1	1	2	1	1	3	3	2	4	2	0	1	2	2	2	2	3	2	2	0	1	1	1
LLIX37	12	88	45	45	7	4	32	21	20	43	68	53	59	21	9	15	45	27	39	37	45	41	31	6	13	11	6

7.10.2. La Luna IA core

Sample	*Diapregnane*	*Pregnane*	*Diahomopregnane*	*Homopregnane*	*C27βα-Dia (20S)*	*C27 βα-Dia(20R)*	*C27αβ Dia (20S)*	*C27 αβ-Dia(20R)*	*C28 βα-Dia (20S)*	*C28 βα-Dia(20R)*	*C28αβ-Dia (20S) +C27αα (20S)*	*C27 ββ (20R) +C29 βα (20S)*	*C27 ββ(20S) +C28 αβ (20R)*	*C27αα (20R)*	*C29βα-Dia (20R)*	*C29 αβ-Dia (20S)*	*C28αα (20S)*	*C28 ββ (20R) + C29αβ-Dia (20R)*	*C28 ββ (20S)*	*C28αα (20R)*	*C29 αα (20S)*	*C29ββ (20R)*	*C29 ββ (20S)*	*C29 αα (20R)*	*C30αα (20S)*	*C30ββ (20R)*	*C30 ββ (20S)*	*C30 αα (20R)*
LLIA1	17	134	54	54	4	5	4	20	14	15	26	36	24	40	17	8	12	24	17	22	19	24	19	18	4	7	3	3
LLIA2	15	111	50	50	4	5	3	18	12	12	26	33	20	31	10	7	10	21	15	20	16	22	15	16	3	5	3	2
LLIA3	12	114	48	48	3	5	4	18	11	10	18	28	19	31	8	6	9	19	12	16	14	21	14	12	2	4	3	7
LLIA4	17	139	57	57	4	6	4	25	16	11	27	42	24	35	18	9	13	27	18	24	22	31	22	17	4	6	10	2
LLIA5	14	109	46	46	3	5	3	18	12	12	26	33	20	31	10	7	10	21	15	20	16	20	15	15	3	4	3	1
LLIA6	9	60	25	25	3	7	3	22	13	10	22	30	25	30	13	11	11	24	17	20	19	27	19	18	3	6	4	3
LLIA7	16	131	52	52	4	8	4	24	13	12	25	40	22	42	19	9	15	24	15	20	19	24	14	18	3	6	3	2
LLIA8	10	68	25	25	2	5	2	14	8	5	14	20	13	20	6	6	8	16	10	13	11	16	11	9	1	4	2	1
LLIA9	11	74	25	25	2	6	2	12	7	3	11	17	11	17	8	6	8	13	8	11	9	12	10	8	1	2	2	1
LLIA10	12	74	25	25	3	8	2	16	9	8	15	23	13	23	11	7	10	18	10	13	13	17	13	12	2	3	4	2

Sample	*Diapregnane*	*Pregnane*	*Diahomopregnane*	*Homopregnane*	*$C_{27}\beta\alpha$-Dia (20S)*	*$C_{27}\ \beta\alpha$-Dia(20R)*	*$C_{27}\alpha\beta$ Dia (20S)*	*$C_{27}\ \alpha\beta$-Dia(20R)*	*$C_{28}\ \beta\alpha$-Dia (20S)*	*$C_{28}\ \beta\alpha$-Dia(20R)*	*$C_{28}\alpha\beta$-Dia (20S) +$C_{27}\alpha\alpha$ (20S)*	*$C_{27}\ \beta\beta$ (20R) +$C_{29}\ \beta\alpha$ (20S)*	*$C_{27}\ \beta\beta$(20S) +C28 $\alpha\beta$ (20R)*	*$C_{27}\alpha\alpha$ (20R)*	*$C_{29}\beta\alpha$-Dia (20R)*	*$C_{29}\ \alpha\beta$-Dia (20S)*	*$C_{28}\alpha\alpha$ (20S)*	*$C_{28}\ \beta\beta$ (20R) + $C_{29}\alpha\beta$-Dia (20R)*	*$C_{28}\ \beta\beta$ (20S)*	*$C_{28}\alpha\alpha$ (20R)*	*$C_{29}\ \alpha\alpha$ (20S)*	*$C_{29}\beta\beta$ (20R)*	*$C_{29}\ \beta\beta$ (20S)*	*$C_{29}\ \alpha\alpha$ (20R)*	*$C_{30}\alpha\alpha$ (20S)*	*$C_{30}\beta\beta$ (20R)*	*$C_{30}\ \beta\beta$ (20S)*	*$C_{30}\ \alpha\alpha$ (20R)*
LLIA11	9	60	25	25	3	7	3	22	13	10	21	30	23	30	13	11	11	24	17	20	19	27	19	18	3	5	4	4
LLIA12	5	29	9	9	1	3	1	6	3	2	5	13	5	5	3	2	4	5	3	4	3	5	4	3	0	6	2	0
LLIA13	16	92	29	29	3	12	4	22	13	6	17	27	20	21	10	8	15	20	14	22	16	18	14	12	2	5	4	3
LLIA14	17	89	28	28	2	11	2	20	10	5	17	19	19	21	7	10	13	17	13	20	15	19	13	12	2	5	4	1
LLIA15	13	70	21	21	2	13	3	19	9	7	16	24	15	17	6	10	12	24	13	15	14	20	13	15	3	5	5	2
LLIA16	10	52	16	16	2	10	2	16	7	6	17	28	20	12	7	9	10	17	11	13	11	18	11	11	2	5	3	2
LLIA17	14	69	23	23	2	17	4	29	13	6	27	41	34	22	10	15	17	28	22	23	20	36	22	19	4	7	6	3
LLIA18	11	56	18	18	1	15	4	23	8	5	16	24	14	13	6	13	13	27	15	17	14	25	12	15	3	6	6	2

7.10.3. La Luna IS core

Sample	*Diapregnane*	*Pregnane*	*Diahomopregnane*	*Homopregnane*	*C_{27}βα-Dia (20S)*	*C_{27} βα-Dia(20R)*	*C_{27}αβ Dia (20S)*	*C_{27} αβ-Dia(20R)*	*C_{28} βα-Dia (20S)*	*C_{28} βα-Dia(20R)*	*C_{28}αβ-Dia (20S) +C_{27}αα (20S)*	*C_{27} ββ (20R) +C_{29} βα (20S)*	*C_{27} ββ(20S) +C28 αβ (20R)*	*C_{27}αα (20R)*	*C_{29}βα-Dia (20R)*	*C_{29} αβ-Dia (20S)*	*C_{28}αα (20S)*	*C_{28} ββ (20R) + C_{29}αβ-Dia (20R)*	*C_{28} ββ (20S)*	*C_{28}αα (20R)*	*C_{29} αα (20S)*	*C_{29}ββ (20R)*	*C_{29} ββ (20S)*	*C_{29} αα (20R)*	*C_{30}ααα (20S)*	*C_{30}ββ (20R)*	*C_{30} ββ (20S)*	*C_{30} αα (20R)*
LLIS 1	10	57	27	27	5	11	4	27	25	17	39	56	44	48	16	13	18	54	35	44	40	44	43	35	8	15	16	7
LLIS 2	8	44	22	22	4	9	3	20	20	12	38	51	44	34	11	11	15	56	28	36	31	40	32	32	6	11	13	6
LLIS 3	16	80	43	43	8	20	7	43	44	27	88	112	111	75	22	30	32	137	64	74	67	89	81	62	13	25	35	12
LLIS 4	10	60	32	32	6	18	5	35	36	26	63	86	77	59	19	20	23	98	55	64	53	67	60	50	10	20	26	10
LLIS 5	15	83	41	41	7	16	6	43	38	35	69	93	76	89	45	26	26	86	55	71	58	78	67	59	13	22	29	19
LLIS 6	17	94	51	51	9	21	9	54	47	42	83	101	83	97	40	31	34	118	68	87	74	95	79	74	15	29	33	13
LLIS 7	21	109	60	60	10	23	9	58	50	40	90	120	109	114	50	33	37	111	70	93	74	93	87	73	19	28	35	13
LLIS 8	16	86	45	45	7	21	6	47	42	26	70	95	79	85	36	28	31	105	59	81	65	89	82	63	14	24	35	13
LLIS 9	15	86	41	41	7	16	7	38	36	34	81	102	77	69	19	25	28	111	59	71	58	76	65	59	9	22	30	11
LLIS 10	11	66	31	31	6	13	4	32	26	26	51	69	58	56	18	19	22	84	46	55	43	58	50	46	9	15	24	2

Sample	*Diapregnane*	*Pregnane*	*Diahomopregnane*	*Homopregnane*	*C_{27}βα-Dia (20S)*	*C_{27} βα-Dia(20R)*	*C_{27}αββ Dia (20S)*	*C_{27} αβ-Dia(20R)*	*C_{28} βα-Dia (20S)*	*C_{28} βα-Dia(20R)*	*C_{28}αβ-Dia (20S) +C_{27}αα (20S)*	*C_{27} ββ (20R) +C_{29} βα (20S)*	*C_{27} ββ(20S) +C28 αβ (20R)*	*C_{27}αα (20R)*	*C_{29}βα-Dia (20R)*	*C_{29} αβ-Dia (20S)*	*C_{28}αα (20S)*	*C_{28} ββ (20R) + C_{29}αβ-Dia (20R)*	*C_{28} ββ (20S)*	*C_{28}αα (20R)*	*C_{29} αα (20S)*	*C_{29}ββ (20R)*	*C_{29} ββ (20S)*	*C_{29} αα (20R)*	*C_{30}αα (20S)*	*C_{30}ββ (20R)*	*C_{30} ββ (20S)*	*C_{30} αα (20R)*
LLIS 11	8	44	22	22	4	9	3	20	20	12	38	51	44	34	11	11	15	56	28	36	31	40	32	32	6	11	13	6
LLIS 12	10	64	33	33	5	11	5	31	28	23	59	71	62	68	29	17	21	62	38	53	43	53	47	42	8	18	18	8
LLIS 13	7	39	19	19	3	5	2	14	11	11	24	35	33	35	15	8	10	27	17	22	20	24	22	20	4	8	9	3
LLIS 14	11	77	38	38	6	10	4	28	23	21	50	69	57	55	20	14	20	59	36	52	42	54	45	43	7	17	19	9

7.10.4. La Luna stratotype

Sample	*Diapregnane*	*Pregnane*	*Diahomopregnane*	*Homopregnane*	*$C_{27}\beta\alpha$-Dia (20S)*	*$C_{27}\beta\alpha$-Dia(20R)*	*$C_{27}\alpha\beta$ Dia (20S)*	*$C_{27}\alpha\beta$-Dia(20R)*	*$C_{28}\beta\alpha$-Dia (20S)*	*$C_{28}\beta\alpha$-Dia(20R)*	*$C_{29}\alpha\beta$-Dia (20S) +$C_{27}\alpha\alpha$ (20S)*	*$C_{27}\beta\beta$ (20R) +$C_{29}\beta\alpha$ (20S)*	*$C_{27}\beta\beta$(20S) +C28 $\alpha\beta$ (20R)*	*$C_{27}\alpha\alpha$ (20R)*	*$C_{29}\beta\alpha$-Dia (20R)*	*$C_{29}\alpha\beta$-Dia (20S)*	*$C_{29}\alpha\alpha$ (20S)*	*$C_{28}\beta\beta$ (20R) + $C_{29}\alpha\beta$-Dia (20R)*	*$C_{28}\beta\beta$ (20S)*	*$C_{28}\alpha\alpha$ (20R)*	*$C_{29}\alpha\alpha$ (20S)*	*$C_{29}\beta\beta$ (20R)*	*$C_{29}\beta\beta$ (20S)*	*$C_{29}\alpha\alpha$ (20R)*	*$C_{30}\alpha\alpha$ (20S)*	*$C_{30}\beta\beta$ (20R)*	*$C_{30}\beta\beta$ (20S)*	*$C_{30}\alpha\alpha$ (20R)*
Perija1	6	40	26	26	4	5	2	11	9	9	21	27	17	29	10	5	6	18	11	17	14	14	16	16	3	4	7	2
Perija2	14	83	48	48	7	9	5	20	13	15	23	29	22	37	13	7	14	21	12	19	15	23	25	15	3	7	10	3
Perija3	24	151	89	89	15	31	12	70	50	44	136	162	161	175	77	32	45	103	70	92	83	105	99	83	19	34	48	17
Perija4	5	20	11	11	2	2	1	5	2	2	5	5	4	8	4	1	3	4	3	3	3	5	3	3	1	2	2	2
Perija5	11	52	31	31	4	5	3	10	5	6	12	12	8	9	7	4	8	7	5	6	5	9	7	6	1	4	4	1
Perija6	0	2	1	1	0	0	0	1	0	0	1	1	0	2	1	0	1	0	0	1	1	1	0	1	0	0	0	0
Perija7	12	65	38	38	6	12	5	19	12	10	21	16	9	26	18	6	17	13	5	18	12	18	14	15	4	5	13	6
Perija8	13	53	31	31	5	11	6	21	12	9	24	17	9	35	19	8	18	19	7	28	18	21	16	26	6	7	16	9

7.11. Biomarker quantification results for for terpanes (Concentrations are expressed as in ppm W/W)

7.11.1. La Luna IX core

Sample	*C_{20} TR*	*C_{21} TR*	*C_{22} TR*	*C_{23} TR*	*C_{24} TR*	*C_{25} TR*	*C_{24} TR*	*C_{26} TR*	*C_{27} TR*	*C_{28} TR*	*C_{29} TR*	*Ts*	*Tm*	*C_{29} αβ Norhopame*	*C_{29} Ts*	*C_{30} D*	*C_{29}βα-30-NorM*	*C_{30} -Hopane*	*C_{30}- Moretane*	*C_{31} HH (22S & 22R)*	*Gammacerane*	*C_{32} HH (22S & 22R)*	*C_{33} HH (22S & 22R)*	*C_{34} HH (22S & 22R)*	*C_{35} HH (22S & 22R)*
LLIX1	31	24	12	142	48	45	16	34	13	35	46	18	69	146	7	44	11	175	11	189	29	90	66	37	48
LLIX2	26	25	12	164	61	55	19	29	13	46	68	8	45	111	6	45	9	134	12	160	24	79	55	24	32
LLIX3	16	17	6	108	40	28	18	21	10	30	47	4	26	60	7	31	5	79	4	92	15	48	50	19	31
LLIX4	25	22	11	145	52	49	28	31	15	35	58	7	39	96	4	39	7	121	8	133	22	72	55	31	19
LLIX5	17	17	6	110	39	28	18	20	10	36	49	4	26	58	6	30	5	79	4	92	15	50	50	16	26
LLIX6	18	22	10	125	36	36	17	26	12	25	39	7	39	98	4	25	7	118	8	140	18	62	37	11	18
LLIX7	1	1	0	7	3	3	1	1	1	2	4	1	2	3	0	2	1	4	1	7	2	4	8	5	8
LLIX8	11	24	10	52	31	20	10	17	7	11	10	11	24	52	6	27	4	62	3	62	12	36	36	25	23
LLIX9	6	14	9	58	19	24	7	6	10	6	7	7	8	42	3	12	2	23	2	52	18	23	23	25	17
LLIX10	18	16	6	110	40	27	12	20	10	30	47	4	25	51	7	30	3	66	4	92	14	48	50	19	21

Sample	*C_{20} TR*	*C_{21} TR*	*C_{22} TR*	*C_{23} TR*	*C_{24} TR*	*C_{25} TR*	*C_{24} TR*	*C_{26} TR*	*C_{27} TR*	*C_{28} TR*	*C_{29} TR*	*Ts*	*Tm*	*C_{29} αβ Norhopame*	*C_{29} Ts*	*C_{30} D*	*C_{29}βα-30-NorM*	*C_{30} -Hopane*	*C_{30}- Moretane*	*C_{31} HH (22S & 22R)*	*Gammacerane*	*C_{32} HH (22S & 22R)*	*C_{33} HH (22S & 22R)*	*C_{34} HH (22S & 22R)*	*C_{35} HH (22S & 22R)*
LLIX11	17	16	7	67	21	18	10	23	8	12	13	7	27	77	11	10	5	66	5	45	12	20	17	11	12
LLIX12	16	15	6	60	23	18	7	17	10	11	14	10	30	80	12	10	6	83	5	50	17	23	16	8	13
LLIX13	11	10	4	53	21	19	7	9	7	14	18	2	9	25	3	11	3	33	3	35	10	27	19	14	19
LLIX14	9	8	4	45	25	25	4	8	7	10	12	2	3	23	2	6	3	20	3	32	9	23	10	11	20
LLIX15	8	6	3	32	11	10	3	7	6	7	8	2	9	25	2	6	1	30	2	32	7	15	9	8	21
LLIX16	22	39	13	177	58	52	18	52	25	40	47	17	93	249	25	30	18	245	16	184	48	96	69	51	55
LLIX17	6	6	2	26	11	8	3	4	4	5	9	1	4	8	0	7	1	8	2	11	5	8	8	3	10
LLIX18	13	12	4	55	20	17	6	11	7	12	17	1	9	32	3	10	2	37	3	31	10	17	19	9	6
LLIX19	9	9	3	43	15	13	5	7	6	9	13	1	7	17	1	11	1	15	1	20	7	14	10	7	8
LLIX20	45	33	10	158	52	45	18	47	24	33	39	11	79	220	29	31	17	208	14	138	38	68	42	17	24

Sample	*C_{20} TR*	*C_{21} TR*	*C_{22} TR*	*C_{23} TR*	*C_{24} TR*	*C_{25} TR*	*C_{24} TR*	*C_{26} TR*	*C_{27} TR*	*C_{28} TR*	*C_{29} TR*	*Ts*	*Tm*	*C_{29} αβ Norhopame*	*C_{29} Ts*	*C_{30} D*	*C_{29}βα-30-NorM*	*C_{30} -Hopane*	*C_{30}- Moretane*	*C_{31} HH (22S & 22R)*	*Gammacerane*	*C_{32} HH (22S & 22R)*	*C_{33} HH (22S & 22R)*	*C_{34} HH (22S & 22R)*	*C_{35} HH (22S & 22R)*
LLIX21	6	5	2	26	10	8	3	4	5	5	11	1	3	10	1	4	1	10	1	8	4	8	9	9	13
LLIX22	38	24	11	103	45	42	17	40	17	25	34	20	55	129	3	16	9	102	6	82	20	35	23	18	17
LLIX23	45	39	13	177	58	52	18	52	25	40	47	17	93	249	25	30	18	245	16	184	48	96	69	51	55
LLIX24	6	7	1	36	12	9	5	6	3	10	10	1	5	10	1	9	1	9	1	15	4	9	8	8	10
LLIX25	19	16	6	78	27	20	5	15	9	17	26	2	12	23	2	11	1	20	2	25	8	15	16	7	22
LLIX26	17	15	7	67	21	18	10	23	8	12	13	7	27	77	11	10	5	66	5	45	12	24	17	11	5
LLIX27	4	5	2	26	8	9	4	5	5	6	9	1	5	15	1	7	4	12	1	18	4	10	12	6	19
LLIX28	4	5	2	25	8	8	3	6	5	9	11	1	5	5	2	9	1	11	2	14	5	8	13	12	17
LLIX29	17	16	6	78	27	21	5	17	9	17	22	2	12	24	2	12	1	21	2	26	8	15	15	8	24
LLIX30	18	15	6	60	23	18	7	21	10	11	14	10	32	98	2	7	6	83	5	54	17	23	16	8	15

Sample	*C_{20} TR*	*C_{21} TR*	*C_{22} TR*	*C_{23} TR*	*C_{24} TR*	*C_{25} TR*	*C_{24} TR*	*C_{26} TR*	*C_{27} TR*	*C_{28} TR*	*C_{29} TR*	*Ts*	*Tm*	*C_{29} αβ Norhopame*	*C_{29} Ts*	*C_{30} D*	*C_{29}βα-30-NorM*	*C_{30} -Hopane*	*C_{30}- Moretane*	*C_{31} HH (22S & 22R)*	*Gammacerane*	*C_{32} HH (22S & 22R)*	*C_{33} HH (22S & 22R)*	*C_{34} HH (22S & 22R)*	*C_{35} HH (22S & 22R)*
LLIX31	6	5	2	24	11	9	3	5	7	8	15	1	4	13	1	7	1	12	1	16	7	8	11	11	9
LLIX32	10	9	4	40	17	14	6	9	7	13	12	2	8	22	1	15	2	22	1	27	10	16	15	41	29
LLIX33	5	4	2	26	12	11	5	5	10	11	16	1	6	6	3	10	1	7	1	14	9	8	15	12	6
LLIX34	45	4	2	20	9	8	4	5	8	7	10	1	4	7	2	8	2	6	1	12	5	5	4	8	9
LLIX35	79	62	22	334	116	101	31	87	38	66	95	45	160	397	53	73	27	488	32	367	65	180	129	86	76

7.11.2. La Luna IA core

Sample	*C_{20} TR*	*C_{21} TR*	*C_{22} TR*	*C_{23} TR*	*C_{24} TR*	*C_{25} TR*	*C_{24} TR*	*C_{26} TR*	*C_{27} TR*	*C_{28} TR*	*C_{29} TR*	*Ts*	*Tm*	*C_{29} αβ Norhopame*	*C_{29} Ts*	*C_{30} D*	*C_{29}βα-30-NorM*	*C_{30} -Hopane*	*C_{30}- Moretane*	*C_{31} HH (22S & 22R)*	*Gammacerane*	*C_{32} HH (22S & 22R)*	*C_{33} HH (22S & 22R)*	*C_{34} HH (22S & 22R)*	*C_{35} HH (22S & 22R)*
LLIA1	188	115	33	497	201	152	45	118	77	99	135	67	99	151	17	87	12	153	11	137	58	59	42	14	34
LLIA2	149	78	26	348	160	108	38	90	54	66	90	41	69	115	14	59	10	137	9	97	43	38	24	14	20
LLIA3	150	88	17	374	149	113	42	106	50	72	94	43	72	120	10	61	10	130	9	105	44	35	27	34	16
LLIA4	189	113	33	489	215	169	57	142	73	109	142	72	107	174	25	108	10	185	12	147	66	57	35	14	32
LLIA5	165	96	29	451	199	157	50	133	66	112	152	72	102	153	19	80	13	198	14	184	80	68	43	17	72
LLIA6	173	95	33	480	267	286	100	150	76	203	267	50	242	515	49	186	41	581	40	690	204	318	220	187	286
LLIA7	150	96	54	616	286	296	98	162	87	237	315	58	375	570	52	180	47	560	35	650	225	300	255	150	191
LLIA8	119	70	34	452	217	225	86	105	70	172	245	47	212	457	43	173	31	482	36	620	168	282	177	156	180
LLIA9	111	67	28	333	188	182	78	124	59	131	122	48	245	580	44	125	39	123	39	588	169	272	187	99	114
LLIA10	111	111	32	220	99	93	56	85	80	89	88	39	261		36	110	37	88	11	169	111	56	25	58	52

Sample	*C_{20} TR*	*C_{21} TR*	*C_{22} TR*	*C_{23} TR*	*C_{24} TR*	*C_{25} TR*	*C_{24} TR*	*C_{26} TR*	*C_{27} TR*	*C_{28} TR*	*C_{29} TR*	*Ts*	*Tm*	*C_{29} αβ Norhopame*	*C_{29} Ts*	*C_{30} D*	*C_{29}βα-30-NorM*	*C_{30} -Hopane*	*C_{30}- Moretane*	*C_{31} HH (22S & 22R)*	*Gammacerane*	*C_{32} HH (22S & 22R)*	*C_{33} HH (22S & 22R)*	*C_{34} HH (22S & 22R)*	*C_{35} HH (22S & 22R)*
LLIA11	111	50	26	274	152	133	52	87	56	98	133	66	71	73	24	80	10	64	13	105	59	23	16	25	36
LLIA12	125	45	29	310	158	166	61	111	59	128	150	64	96	72	27	110	13	80	19	129	79	23	65	47	54
LLIA13	180	79	31	406	231	200	76	158	65	144	191	98	117	102	20	106	9	88	11	179	89	43	191	16	83
LLIA14	125	52	30	236	156	146	63	98	53	137	98	50	96	78	28	110	17	76	7	78	27	43	26	22	12
LLIA15	124	45	29	313	195	166	61	106	59	128	176	64	96	72	27	113	13	82	19	129	80	23	67	47	53
LLIA16	99	44	16	244	160	134	54	98	53	109	215	46	156	117	21	101	4	49	53	123	75	60	54	12	64
LLIA17	115	49	21	352	234	213	89	128	92	181	271	64	147	114	39	206	20	80	32	227	135	40	40	8	72
LLIA18	106	42	22	249	186	156	66	94	54	125	213	45	96	63	27	125	15	47	22	135	103	24	36	31	47

7.11.3. La Luna IS core

Sample	*C_{20} TR*	*C_{21} TR*	*C_{22} TR*	*C_{23} TR*	*C_{24} TR*	*C_{25} TR*	*C_{24} TR*	*C_{26} TR*	*C_{27} TR*	*C_{28} TR*	*C_{29} TR*	*Ts*	*Tm*	*C_{29} αβ Norhopame*	*C_{29} Ts*	*C_{30} D*	*C_{29}βα-30-NorM*	*C_{30} -Hopane*	*C_{30}- Moretane*	*C_{31} HH (22S & 22R)*	*Gammacerane*	*C_{32} HH (22S & 22R)*	*C_{33} HH (22S & 22R)*	*C_{34} HH (22S & 22R)*	*C_{35} HH (22S & 22R)*
LLIS1	107	66	33	411	176	179	54	91	53	137	200	38	196	389	25	133	28	382	50	450	125	200	188	99	55
LLIS2	92	52	23	327	135	139	47	88	43	108	156	27	157	301	24	107	19	290	37	361	102	162	168	76	96
LLIS3	155	96	54	616	286	296	98	162	87	237	315	58	375	570	52	219	47	654	35	802	225	360	255	150	191
LLIS4	119	71	34	452	217	225	86	105	70	172	245	47	212	457	43	173	31	482	36	621	168	282	177	264	179
LLIS5	173	95	33	562	267	286	100	150	76	203	267	50	242	515	49	186	41	581	41	690	204	318	225	187	287
LLIS6	180	110	40	681	332	393	127	191	56	261	344	60	326	654	63	239	47	731	48	867	253	393	286	190	271
LLIS7	231	122	51	741	340	346	130	200	109	252	351	69	266	668	64	238	54	728	45	824	246	374	269	180	207
LLIS8	165	97	42	599	298	301	115	173	99	240	295	51	291	606	64	227	50	639	43	845	207	357	277	176	289
LLIS9	170	94	41	531	263	264	101	161	252	299	260	72	264	528	42	190	40	652	45	769	212	322	195	178	130
LLIS10	127	70	31	411	202	207	81	120	60	168	212	46	210	446	44	142	28	488	36	581	167	261	178	102	247

Sample	C_{20} TR	C_{21} TR	C_{22} TR	C_{23} TR	C_{24} TR	C_{25} TR	C_{24} TR	C_{26} TR	C_{27} TR	C_{28} TR	C_{29} TR	Ts	Tm	C_{29} αβ Norhopame	C_{29} Ts	C_{30} D	C_{29}βα-30-NorM	C_{30} -Hopane	C_{30}- Moretane	C_{31} HH (22S & 22R)	Gammacerane	C_{32} HH (22S & 22R)	C_{33} HH (22S & 22R)	C_{34} HH (22S & 22R)	C_{35} HH (22S & 22R)
LLIS11	112	60	28	380	186	178	77	122	99	108	152	47	245	458	43	128	41	587	41	550	156	245	222	99	85
LLIS12	110	67	28	375	188	182	69	124	59	131	167	48	245	580	44	125	39	602	39	589	169	272	187	99	79
LLIS13	72	38	12	203	98	95	35	65	32	71	87	23	110	271	18	51	17	270	17	275	76	124	76	49	33
LLIS14	131	75	29	407	199	198	74	138	67	129	200	57	235	625	29	109	44	611	43	641	178	308	220	117	83

7.11.4. La Luna stratotype

Sample	*C_{20} TR*	*C_{21} TR*	*C_{22} TR*	*C_{23} TR*	*C_{24} TR*	*C_{25} TR*	*C_{24} TR*	*C_{26} TR*	*C_{27} TR*	*C_{28} TR*	*C_{29} TR*	*Ts*	*Tm*	*C_{29} αβ Norhopame*	*C_{29} Ts*	*C_{30} D*	*C_{29}βα-30-NorM*	*C_{30} -Hopane*	*C_{30}- Moretane*	*C_{31} HH (22S & 22R)*	*Gammacerane*	*C_{32} HH (22S & 22R)*	*C_{33} HH (22S & 22R)*	*C_{34} HH (22S & 22R)*	*C_{35} HH (22S & 22R)*
Perija1	47	29	10	138	45	41	13	28	17	26	25	13	74	145	4	46	10	163	13	171	26	84	67	55	61
Perija2	92	47	21	218	70	104	23	65	38	41	38	44	157	221	9	130	17	223	18	201	61	108	68	62	41
Perija3	258	175	66	856	285	276	91	204	109	182	241	81	507	1080	142	312	65	1129	74	1209	246	671	454	213	179
Perija4	25	13	6	62	19	21	7	20	13	11	12	15	54	83	2	40	5	76	7	78	27	43	26	22	12
Perija5	61	30	13	128	40	44	13	45	30	17	21	32	105	129	14	90	8	106	11	110	43	49	31	29	21
Perija6	3	1	1	7	2	3	1	3	1	2	2	2	6	9	1	5	1	9	1	9	5	5	3	2	5
Perija7	95	45	26	220	84	83	33	69	52	58	75	52	185	169	26	169	14	182	21	200	109	101	75	57	48
Perija8	85	40	21	193	74	75	33	63	48	64	73	53	167	207	29	190	16	248	25	251	118	143	148	91	86

7.12. Quantitative biomarker analysis results for aryl isoprenoids (Concentrations are expressed as in ppm W/W)

7.12.1. La Luna IX core

Aryl Isoprenoids

Sample	**C_{13}**	**C_{14}**	**C_{15}**	**C_{16}**	**C_{17}**	**C_{18}**	**C_{19}**	**C_{20}**	**C_{21}**	**C_{22}**	**C_{24}**	**C_{25}**	**C_{26}**	**C_{27}**	**C_{29}**	**C_{30}**	**C_{31}**
LLIX1	448	33	270	330	127	43	188	170	55	171	62	61	33	55	18	38	51
LLIX2	255	229	1892	2310	892	301	184	236	387	208	433	426	234	388	125	269	360
LLIX3	51	104	856	39	404	136	83	107	175	94	196	193	106	176	57	122	163
LLIX4	40	93	770	35	363	122	75	96	158	85	176	173	95	158	51	109	147
LLIX5	364	91	753	34	355	120	73	94	154	83	172	169	93	154	50	107	143
LLIX6	49	3	22	1	11	4	2	3	5	2	5	5	3	5	1	3	4
LLIX7	191	107	881	40	415	140	86	110	180	97	202	198	109	181	58	125	168
LLIX8	328	183	22	68	712	240	147	188	309	166	346	340	187	310	100	215	288
LLIX9	191	107	13	40	26	140	86	110	60	97	116	42	37	34	66	125	40
LLIX10	187	104	13	39	26	137	84	107	58	95	114	42	36	33	64	122	39

Aryl Isoprenoids

Sample	**C_{13}**	**C_{14}**	**C_{15}**	**C_{16}**	**C_{17}**	**C_{18}**	**C_{19}**	**C_{20}**	**C_{21}**	**C_{22}**	**C_{24}**	**C_{25}**	**C_{26}**	**C_{27}**	**C_{29}**	**C_{30}**	**C_{31}**
LLIX11	159	89	11	33	22	117	72	92	50	81	97	35	31	28	55	105	33
LLIX12	165	92	11	34	23	121	74	95	51	83	100	37	32	29	57	108	35
LLIX13	177	99	12	37	24	130	80	102	55	90	108	39	35	31	61	116	37
LLIX14	301	168	20	62	42	220	135	173	94	152	183	67	59	53	103	197	63
LLIX15	3	13	46	85	36	72	65	70	29	39	32	13	11	9	4	8	6
LLIX16	238	32	113	207	87	175	157	14	71	96	78	32	27	21	10	18	16
LLIX17	694	1297	777	350	603	1204	74	1173	557	661	344	180	165	145	62	87	67
LLIX18	247	195	117	214	91	181	163	176	84	99	67	27	25	22	9	13	10
LLIX19	170	134	80	147	62	125	112	121	58	68	46	19	17	15	6	9	7
LLIX20	258	204	122	223	95	189	170	184	87	104	70	28	26	23	10	14	11

Aryl Isoprenoids

Sample	**C_{13}**	**C_{14}**	**C_{15}**	**C_{16}**	**C_{17}**	**C_{18}**	**C_{19}**	**C_{20}**	**C_{21}**	**C_{22}**	**C_{24}**	**C_{25}**	**C_{26}**	**C_{27}**	**C_{29}**	**C_{30}**	**C_{31}**
LLIX21	6	13	46	92	42	86	128	105	47	63	53	24	20	19	13	13	13
LLIX22	295	19	70	140	63	130	195	159	71	96	80	36	31	29	20	20	19
LLIX23	127	8	30	61	27	56	84	69	31	42	35	16	13	12	9	8	8
LLIX24	102	56	127	186	22	136	117	161	60	72	46	21	23	17	13	15	11
LLIX25	184	16	47	82	40	67	61	80	33	59	38	21	21	17	15	16	16
LLIX26	247	22	63	110	53	90	82	107	44	79	51	28	29	22	20	22	21
LLIX27	245	22	62	109	53	89	81	106	44	78	50	28	29	22	20	22	21
LLIX28	230	21	59	102	49	84	76	100	41	74	47	26	27	21	19	21	20
LLIX29	345	31	88	153	74	126	115	150	62	110	71	132	40	31	28	31	30
LLIX30	341	31	87	152	73	124	113	148	61	109	70	131	40	31	28	30	30

Aryl Isoprenoids

Sample	**C_{13}**	**C_{14}**	**C_{15}**	**C_{16}**	**C_{17}**	**C_{18}**	**C_{19}**	**C_{20}**	**C_{21}**	**C_{22}**	**C_{24}**	**C_{25}**	**C_{26}**	**C_{27}**	**C_{29}**	**C_{30}**	**C_{31}**
LLIX31	206	18	53	92	44	75	69	90	37	66	42	79	24	19	17	18	18
LLIX32	166	1	10	36	19	42	44	51	19	29	11	64	6	6	6	4	2
LLIX33	310	724	19	67	36	79	82	95	35	55	20	119	11	11	12	7	4
LLIX34	183	427	11	40	21	47	48	56	21	32	12	70	6	6	7	4	2
LLIX35	276	644	17	60	32	71	73	85	31	49	18	106	9	10	11	6	3
LLIX36	676	496	373	421	198	473	56	65	24	169	73	81	54	71	27	44	68
LLIX37	48	111	178	228	83	169	158	195	70	82	39	24	25	18	14	15	14

7.12.2. La Luna IA core

Aryl Isoprenoids

Sample	**C_{13}**	**C_{14}**	**C_{15}**	**C_{16}**	**C_{17}**	**C_{18}**	**C_{19}**	**C_{20}**	**C_{21}**	**C_{22}**	**C_{24}**	**C_{25}**	**C_{26}**	**C_{27}**	**C_{29}**	**C_{30}**	**C_{31}**
LLIA1	82	83	89	297	119	116	56	191	112	116	27	26	24	20	14	14	6
LLIA2	152	161	166	260	99	113	131	134	110	94	47	26	21	19	9	16	9
LLIA3	71	103	141	227	93	102	106	126	89	77	8	16	18	10	5	5	10
LLIA4	153	177	177	289	111	117	136	160	117	95	57	30	31	30	11	19	10
LLIA5	116	146	159	280	113	104	123	170	113	79	46	29	30	23	7	7	9
LLIA6	26	31	36	76	39	57	88	120	92	90	77	50	53	48	22	61	41
LLIA7	329	307	288	489	137	181	200	227	154	114	64	40	53	33	17	40	20
LLIA8	286	366	463	802	271	335	420	430	286	210	116	67	75	55	32	91	51
LLIA9	222	270	306	507	167	198	240	227	165	106	73	39	37	29	46	42	16
LLIA10	712	528	379	618	191	200	249	283	181	145	88	55	62	47	39	82	39

Aryl Isoprenoids

Sample	**C_{13}**	**C_{14}**	**C_{15}**	**C_{16}**	**C_{17}**	**C_{18}**	**C_{19}**	**C_{20}**	**C_{21}**	**C_{22}**	**C_{24}**	**C_{25}**	**C_{26}**	**C_{27}**	**C_{29}**	**C_{30}**	**C_{31}**
LLIA11	219	218	212	365	109	120	153	155	116	81	32	29	30	25	17	39	20
LLIA12	25	28	26	35	10	12	24	13	9	6	4	2	3	2	2	3	2
LLIA13	384	386	369	490	141	170	335	174	131	85	52	34	44	28	23	48	22
LLIA14	368	311	264	397	118	141	151	143	119	78	51	28	38	26	19	43	24
LLIA15	148	165	193	337	100	136	163	123	120	84	55	34	40	33	17	63	32
LLIA16	45	74	120	251	80	106	126	99	98	74	48	43	30	32	15	49	39
LLIA17	31	51	83	182	67	105	149	118	126	98	67	52	55	45	36	96	65
LLIA18	72	88	115	238	71	84	127	100	93	73	47	26	29	26	11	52	27

7.12.3. La Luna IS core

Aryl Isoprenoids

Sample	**C_{13}**	**C_{14}**	**C_{15}**	**C_{16}**	**C_{17}**	**C_{18}**	**C_{19}**	**C_{20}**	**C_{21}**	**C_{22}**	**C_{24}**	**C_{25}**	**C_{26}**	**C_{27}**	**C_{29}**	**C_{30}**	**C_{31}**
LLIS1	25	17	60	153	93	367	354	509	232	207	162	86	105	73	47	69	69
LLIS2	27	6	39	152	83	294	280	364	166	142	131	68	70	54	34	50	48
LLIS3	9	3	43	131	81	404	447	748	362	361	309	145	177	127	96	124	125
LLIS4	13	7	40	105	55	264	319	501	261	250	205	105	128	96	60	89	90
LLIS5	13	51	245	496	219	700	668	862	378	324	254	137	154	110	75	113	113
LLIS6	17	44	120	240	123	586	615	978	463	366	324	176	196	140	75	131	124
LLIS7	20	45	202	525	268	973	954	1190	543	411	374	192	213	163	96	152	138
LLIS8	42	88	208	362	139	603	637	900	446	376	314	176	197	148	94	150	152
LLIS9	20	109	435	699	241	746	679	871	391	323	244	114	151	106	79	127	114
LLIS10	39	116	340	564	171	564	478	655	298	266	207	106	112	83	58	87	79

Aryl Isoprenoids

Sample	**C_{13}**	**C_{14}**	**C_{15}**	**C_{16}**	**C_{17}**	**C_{18}**	**C_{19}**	**C_{20}**	**C_{21}**	**C_{22}**	**C_{24}**	**C_{25}**	**C_{26}**	**C_{27}**	**C_{29}**	**C_{30}**	**C_{31}**
LLIS11	770	2202	133	387	215	1026	1226	1933	1028	939	736	401	542	395	246	581	404
LLIS12	13	4	27	94	62	305	340	403	204	185	148	71	103	74	47	88	80
LLIS13	37	114	289	427	133	414	372	417	184	133	104	55	66	42	28	52	43
LLIS14	16	93	380	601	202	677	644	766	374	285	217	91	137	92	55	127	104

7.12.1. La Luna stratotype

Aryl Isoprenoids

Sample	**C_{13}**	**C_{14}**	**C_{15}**	**C_{16}**	**C_{17}**	**C_{18}**	**C_{19}**	**C_{20}**	**C_{21}**	**C_{22}**	**C_{24}**	**C_{25}**	**C_{26}**	**C_{27}**	**C_{29}**	**C_{30}**	**C_{31}**
Perija1	18	71	221	272	92	244	180	221	78	61	36	16	15	9	12	13	10
Perija2	72	170	282	289	96	262	192	247	83	83	56	26	23	15	11	27	15
Perija3	3	17	56	98	46	137	140	174	64	74	54	30	34	18	14	47	20
Perija4	1	4	21	35	13	45	33	40	15	17	8	3	3	2	2	5	4
Perija5	52	91	121	130	45	121	94	106	36	43	25	9	8	8	6	10	6
Perija6	1	3	6	34	6	11	53	16	11	16	5	6	3	5	4	6	0
Perija7	1	3	10	33	7	29	26	34	20	24	16	4	8	3	11	12	4
Perija8	1	1	6	27	3	14	18	24	17	30	18	5	10	7	7	17	11

7.13. Quantitative biomarker analysis results for monoaromatic steroids (Concentrations are expressed as in ppm W/W)

7.13.1. La Luna IX core

Sample	*Pregnane*	*20-Mpreg*	*C_{27} 5β-Chol (20S)*	*C_{27} Diachol (20S)*	*C_{27} MAS*	*C_{28} 5β-Ergost (20S) + C_{28} Diaergost (20S)*	*C_{27} 5α-Chol (20R)*	*C_{28} 5α-Ergost 20S*	*C_{28} 5β-Ergost 20R + C_{28} Diaergost 20R*	*C_{29} 5β-Stigmast 20S + C_{29} Diastig 20R*	*C_{29} 5α-Stigmast 20S*	*C_{28} 5α-Ergost20R + C_{29} 5β-Stigmast 20R*	*C_{29} 5α-Stigmastane 20R*
LLIX1	3	6	1	0	3	5	4	9	1	1	2	4	4
LLIX2	6	7	3	1	3	1	3	1	0	1	1	1	2
LLIX3	7	7	5	1	1	1	4	2	1	0	1	1	3
LLIX4	1	2	1	0	1	0	1	0	0	0	0	0	0
LLIX5	3	4	1	2	1	2	2	1	0	0	1	1	1
LLIX6	0	0	0	0	0	0	0	0	0	0	0	0	0
LLIX7	0	0	0	0	0	0	0	0	0	0	0	0	0
LLIX8	3	5	2	2	1	10	12	11	2	1	4	5	8
LLIX9	13	19	4	2	1	10	12	11	2	1	4	5	8
LLIX10	2	2	1	0	0	0	1	0	0	0	0	1	0

Sample	*Pregnane*	*20-Mpreg*	*C_{27} 5β-Chol (20S)*	*C_{27} Diachol (20S)*	*C_{27} MAS*	*C_{28} 5β-Ergost (20S) + C_{28} Diaergost (20S)*	*C_{27} 5α-Chol (20R)*	*C_{28} 5α-Ergost 20S*	*C_{28} 5β-Ergost 20R + C_{28} Diaergost 20R*	*C_{29} 5β-Stigmast 20S + C_{29} Diastig 20R*	*C_{29} 5α-Stigmast 20S*	*C_{28} 5α-Ergost20R + C_{29} 5β-Stigmast 20R*	*C_{29} 5α-Stigmastane 20R*
LLIX11	1	1	0	0	0	0	1	0	0	0	0	0	0
LLIX12	1	1	0	0	0	0	0	0	0	0	0	0	0
LLIX13	1	1	0	0	1	0	1	0	0	0	0	0	0
LLIX14	2	3	1	0	1	0	2	0	0	0	0	0	1
LLIX15	15	15	4	5	6	9	9	14	4	1	3	4	4
LLIX16	12	13	3	4	5	7	5	10	2	1	2	3	4
LLIX17	13	13	3	4	5	7	5	10	2	1	2	3	4
LLIX18	8	10	4	2	5	2	5	4	1	1	2	3	1
LLIX19	6	7	2	1	2	1	2	2	0	1	1	1	1
LLIX20	5	6	3	1	2	2	3	3	1	1	2	1	1

Sample	*Pregnane*	*20-Mpreg*	*C_{27} 5β-Chol (20S)*	*C_{27} Diachol (20S)*	*C_{27} MAS*	*C_{28} 5β-Ergost (20S) + C_{28} Diaergost (20S)*	*C_{27} 5α-Chol (20R)*	*C_{28} 5α-Ergost 20S*	*C_{28} 5β-Ergost 20R + C_{28} Diaergost 20R*	*C_{29} 5β-Stigmast 20S + C_{29} Diastig 20R*	*C_{29} 5α-Stigmast 20S*	*C_{28} 5α-Ergost20R + C_{29} 5β-Stigmast 20R*	*C_{29} 5α-Stigmastane 20R*
LLIX22	36	35	24	7	29	3	22	7	2	5	6	6	12
LLIX23	5	7	3	1	4	2	5	6	1	1	2	2	2
LLIX24	4	6	2	1	2	3	4	5	1	0	1	2	2
LLIX25	9	9	3	3	4	6	7	8	1	1	2	3	4
LLIX26	12	12	4	4	1	2	2	3	0	0	1	1	1
LLIX27	12	13	4	4	2	2	2	3	1	0	1	1	1
LLIX28	11	11	3	4	1	2	2	3	0	0	1	1	1
LLIX29	16	16	5	6	2	3	3	4	1	1	1	2	2
LLIX30	16	16	5	6	2	3	3	4	1	1	1	1	2

Sample	*Pregnane*	*20-Mpreg*	*C_{27} 5β-Chol (20S)*	*C_{27} Diachol (20S)*	*C_{27} MAS*	*C_{28} 5β-Ergost (20S) + C_{28} Diaergost (20S)*	*C_{27} 5α-Chol (20R)*	*C_{28} 5α-Ergost 20S*	*C_{28} 5β-Ergost 20R + C_{28} Diaergost 20R*	*C_{29} 5β-Stigmast 20S + C_{29} Diastig 20R*	*C_{29} 5α-Stigmast 20S*	*C_{28} 5α-Ergost20R + C_{29} 5β-Stigmast 20R*	*C_{29} 5α-Stigmastane 20R*
LLIX31	10	10	3	3	1	2	2	2	0	0	1	1	1
LLIX32	4	2	1	0	1	1	1	2	0	0	1	1	1
LLIX33	7	5	2	1	7	13	7	20	4	1	3	7	3
LLIX34	4	3	1	0	4	7	4	12	2	1	2	4	2
LLIX35	6	4	2	1	6	11	6	17	3	1	3	6	3
LLIX36	5	3	1	0	5	9	5	13	3	1	2	5	2
LLIX37	9	9	3	6	5	9	5	14	3	1	2	5	2

7.13.2. La Luna IA core

Sample	*Pregnane*	*20-Mpreg*	*C_{27} 5β-Chol (20S)*	*C_{27} Diachol (20S)*	*C_{27} MAS*	*C_{28} 5β-Ergost (20S) + C_{28} Diaergost (20S)*	*C_{27} 5α-Chol (20R)*	*C_{28} 5α-Ergost 20S*	*C_{28} 5β-Ergost 20R + C_{28} Diaergost 20R*	*C_{29} 5β-Stigmast 20S + C_{29} Diastig 20R*	*C_{29} 5α-Stigmast 20S*	*C_{28} 5α-Ergost20R + C_{29} 5β-Stigmast 20R*	*C_{29} 5α-Stigmastane 20R*
LLIA1	7	6	1	1	2	3	3	4	1	0	2	1	2
LLIA2	5	4	1	0	2	3	2	3	1	1	2	1	2
LLIA3	8	11	2	3	2	3	5	5	1	0	2	2	2
LLIA4	31	94	56	23	26	58	33	3	3	10	26	15	36
LLIA5	7	16	13	4	6	14	8	1	1	2	6	4	8
LLIA6	14	17	2	4	5	7	9	8	1	1	4	3	6
LLIA7	6	8	1	0	2	3	4	3	0	0	2	1	3
LLIA8	3	10	1	1	2	3	4	3	1	1	2	2	2
LLIA9	3	9	1	1	2	2	3	2	1	0	1	1	2

Sample	*Pregnane*	*20-Mpreg*	*C_{27} 5β-Chol (20S)*	*C_{27} Diachol (20S)*	*C_{27} MAS*	*C_{28} 5β-Ergost (20S) + C_{28} Diaergost (20S)*	*C_{27} 5α-Chol (20R)*	*C_{28} 5α-Ergost 20S*	*C_{28} 5β-Ergost 20R + C_{28} Diaergost 20R*	*C_{29} 5β-Stigmast 20S + C_{29} Diastig 20R*	*C_{29} 5α-Stigmast 20S*	*C_{28} 5α-Ergost20R + C_{29} 5β-Stigmast 20R*	*C_{29} 5α-Stigmastane 20R*
LLIA10	4	7	1	2	3	3	5	4	1	1	2	2	3
LLIA11	0	1	0	0	0	0	0	0	0	0	0	0	0
LLIA12	7	10	2	2	4	5	7	5	2	0	2	3	4
LLIA13	25	11	13	2	6	8	16	11	2	2	7	6	11
LLIA14	15	17	8	1	4	5	10	7	1	1	4	4	7
LLIA15	15	13	2	2	5	5	8	6	2	1	3	8	7
LLIA16	10	26	4	6	7	7	16	8	5	3	6	11	12
LLIA17	7	15	2	4	5	5	10	6	3	2	4	4	8

7.13.3. La Luna IS core

Sample	*Pregnane*	*20-Mpreg*	*C_{27} 5β-Chol (20S)*	*C_{27} Diachol (20S)*	*C_{27} MAS*	*C_{28} 5β-Ergost (20S) + C_{28} Diaergost (20S)*	*C_{27} 5α-Chol (20R)*	*C_{28} 5α-Ergost 20S*	*C_{28} 5β-Ergost 20R + C_{28} Diaergost 20R*	*C_{29} 5β-Stigmast 20S + C_{29} Diastig 20R*	*C_{29} 5α-Stigmast 20S*	*C_{28} 5α-Ergost20R + C_{29} 5β-Stigmast 20R*	*C_{29} 5α-Stigmastane 20R*
LLIS1	14	11	10	6	14	20	12	32	5	1	6	13	8
LLIS2	10	9	7	6	11	16	9	24	4	1	5	11	7
LLIS3	24	24	17	15	27	41	22	61	9	2	13	24	16
LLIS4	19	13	15	10	22	31	19	48	7	3	10	18	12
LLIS5	23	20	13	12	20	32	19	50	10	2	11	16	13
LLIS6	29	23	18	14	27	41	23	61	11	4	15	24	18
LLIS7	26	24	16	12	24	36	22	57	9	4	12	23	15
LLIS8	27	19	20	17	28	43	23	67	9	4	14	27	19
LLIS9	22	18	14	12	19	31	18	47	6	5	10	18	13
LLIS10	16	14	11	8	16	29	17	38	7	2	9	15	10

Sample	*Pregnane*	*20-Mpreg*	*C_{27} 5β-Chol (20S)*	*C_{27} Diachol (20S)*	*C_{27} MAS*	*C_{28} 5β-Ergost (20S) + C_{28} Diaergost (20S)*	*C_{27} 5α-Chol (20R)*	*C_{28} 5α-Ergost 20S*	*C_{28} 5β-Ergost 20R + C_{28} Diaergost 20R*	*C_{29} 5β-Stigmast 20S + C_{29} Diastig 20R*	*C_{29} 5α-Stigmast 20S*	*C_{28} 5α-Ergost20R + C_{29} 5β-Stigmast 20R*	*C_{29} 5α-Stigmastane 20R*
LLIS11	4	4	3	3	4	6	4	11	2	1	2	4	37
LLIS12	15	15	7	6	11	17	14	25	4	2	6	10	8
LLIS13	8	8	3	3	5	7	6	10	1	1	2	4	3
LLIS14	15	13	7	5	11	16	12	22	3	2	7	10	9

7.13.4. La Luna stratotype

Sample	*Pregnane*	*20-Mpreg*	*C_{27} 5β-Chol (20S)*	*C_{27} Diachol (20S)*	*C_{27} MAS*	*C_{28} 5β-Ergost (20S) + C_{28} Diaergost (20S)*	*C_{27} 5α-Chol (20R)*	*C_{28} 5α-Ergost 20S*	*C_{28} 5β-Ergost 20R + C_{28} Diaergost 20R*	*C_{29} 5β-Stigmast 20S + C_{29} Diastig 20R*	*C_{29} 5α-Stigmast 20S*	*C_{28} 5α-Ergost20R + C_{29} 5β-Stigmast 20R*	*C_{29} 5α-Stigmastane 20R*
Perija 1	48	15	72	15	62	190	17	289	12	12	44	101	34
Perija2	149	38	136	49	148	380	32	590	35	18	90	212	64
Perija 3	66	23	147	42	150	449	31	689	33	20	110	258	69
Perija 4	52	14	47	16	53	132	14	199	13	6	28	65	21
Perija 5	132	33	99	37	108	285	25	414	29	13	66	153	46
Perija 6	4	1	9	2	9	28	2	46	3	1	8	17	6
Perija 7	62	22	206	50	204	647	58	1058	58	35	180	391	135
Perija 8	127	38	381	92	382	1263	86	2028	79	57	341	761	258

7.14. Quantitative biomarker analysis results for phenanthrenes and triaromatic steroids (Concentrations are expressed as in ppm W/W)

7.14.1. La Luna IX core

Sample	*P*	*3-MP*	*2-MP*	*9+4-MP*	*1-MP*	*C_{20} Pregnane*	*C_{21} 20-Mpreg*	*C_{26} Chol (20S)*	*C_{26} Chol (20R) + C_{27} Ergost (20S)*	*C_{28} Stig (20S)*	*C_{27} Ergost*	*C_{28} Stig (20R)*
LLIX1	62	42	61	107	63	14	12	4	20	12	18	15
LLIX2	58	39	58	101	60	13	12	4	19	12	17	14
LLIX3	23	24	35	67	38	10	9	2	14	9	13	11
LLIX4	26	27	35	71	42	10	9	2	15	7	12	10
LLIX5	228	131	178	322	192	21	19	3	28	16	24	19
LLIX6	125	66	90	142	89	7	4	0	1	1	1	1
LLIX7	243	117	171	306	189	12	10	1	9	5	7	6
LLIX8	95	62	84	164	96	13	12	2	13	9	12	10
LLIX9	57	37	50	165	97	10	8	1	8	6	7	6
LLIX10	114	67	90	158	93	9	8	1	8	5	7	6

Sample	*P*	*3-MP*	*2-MP*	*9+4-MP*	*1-MP*	*C_{20} Pregnane*	*C_{21} 20-Mpreg*	*C_{26} Chol (20S)*	*C_{26} Chol (20R) + C_{27} Ergost (20S)*	*C_{28} Stig (20S)*	*C_{27} Ergost*	*C_{28} Stig (20R)*
LLIX11	119	70	96	166	102	8	7	1	6	4	5	4
LLIX12	151	84	119	208	133	12	10	1	8	6	7	6
LLIX13	288	148	220	342	216	16	12	1	5	4	5	5
LLIX14	391	191	289	481	311	24	18	2	10	7	8	8
LLIX15	356	174	263	677	429	28	19	2	8	7	8	7
LLIX16	573	284	430	619	393	25	18	2	7	6	7	6
LLIX17	682	338	513	243	149	10	6	1	2	1	2	1
LLIX18	111	57	82	123	76	7	5	1	2	1	1	1
LLIX19	100	52	75	123	74	7	5	1	1	1	1	1
LLIX20	233	114	114	260	159	15	10	1	2	2	2	2

Sample	*P*	3-*MP*	2-*MP*	9+4-*MP*	1-*MP*	C_{20} *Pregnane*	C_{21} *20-Mpreg*	C_{26} *Chol (20S)*	C_{26} *Chol (20R)* + C_{27} *Ergost (20S)*	C_{28} *Stig (20S)*	C_{27} *Ergost*	C_{28} *Stig (20R)*
LLIX21	365	178	178	265	169	12	8	1	1	4	1	1
LLIX22	222	110	154	230	146	10	7	1	1	1	1	1
LLIX23	147	77	105	183	114	9	8	1	8	4	7	5
LLIX24	118	62	241	387	238	22	13	1	2	4	2	2
LLIX25	155	81	316	507	313	29	18	2	3	5	3	2
LLIX26	373	76	295	475	293	27	16	2	3	3	3	2
LLIX27	198	115	167	249	151	16	10	1	1	2	2	1
LLIX28	234	130	191	285	176	18	10	1	2	2	2	1
LLIX29	55	42	59	94	54	11	6	1	1	1	1	1
LLIX30	124	76	117	210	120	12	6	1	1	1	1	1

Sample	*P*	*3-MP*	*2-MP*	*9+4-MP*	*1-MP*	*C_{20} Pregnane*	*C_{21} 20-Mpreg*	*C_{26} Chol (20S)*	*C_{26} Chol (20R) + C_{27} Ergost (20S)*	*C_{28} Stig (20S)*	*C_{27} Ergost*	*C_{28} Stig (20R)*
LLIX31	162	98	144	207	125	12	5	1	1	1	1	1
LLIX32	133	80	54	93	53	7	3	0	0	1	0	0
LLIX33	76	44	64	110	63	8	3	0	1	1	0	0
LLIX34	90	53	79	134	77	9	5	1	1	1	1	1
LLIX35	179	109	150	262	142	19	9	1	2	2	2	2
LLIX36	182	111	153	119	67	10	5	0	1	2	1	1
LLIX37	80	49	75	124	70	11	5	0	1	1	1	1

7.14.2. La Luna IA core

Sample	*P*	*3-MP*	*2-MP*	*9-MP*	*1-MP*	*C_{20} Pregnane*	*C_{21} 20-Mpreg*	*C_{26} Chol (20S)*	*C_{26} Chol (20R) + C_{27} Ergost (20S)*	*C_{28} Stig (20S)*	*C_{27} Ergost*	*C_{28} Stig (20R)*
LLIA1	14	521	681	1231	726	32	24	3	4	3	3	2
LLIA2	69	2553	3334	6028	3555	156	116	13	18	13	13	11
LLIA3	21	61	241	86	84	36	29	3	5	4	3	3
LLIA4	180	246	1403	1812	1487	4	3	0	1	0	0	0
LLIA5	2779	1496	2104	3991	2387	112	89	9	17	11	10	9
LLIA6	256	226	313	665	360	434	285	36	53	5	36	31
LLIA7	3180	2165	2906	5119	2796	157	103	13	19	13	13	11
LLIA8	1864	1128	1671	2817	1729	72	49	6	8	6	6	6
LLIA9	2881	1791	2546	4276	2669	122	78	11	14	10	9	9
LLIA10	1819	1144	1700	2901	1690	95	61	8	15	10	10	9

Sample	*P*	*3-MP*	*2-MP*	*9-MP*	*1-MP*	*C_{20} Pregnane*	*C_{21} 20-Mpreg*	*C_{26} Chol (20S)*	*C_{26} Chol (20R) + C_{27} Ergost (20S)*	*C_{28} Stig (20S)*	*C_{27} Ergost*	*C_{28} Stig (20R)*
LLIA11	1853	1173	1822	3156	1813	97	63	7	14	10	13	10
LLIA12	2642	1785	2653	4816	2769	138	96	9	24	16	17	15
LLIA13	967	585	823	1583	912	57	35	4	8	6	7	5
LLIA14	2036	1308	2065	3504	2094	107	66	7	16	11	12	9
LLIA15	1052	772	1164	2297	1312	83	59	8	20	11	13	10
LLIA16	794	600	846	1647	879	70	46	7	16	11	12	10
LLIA17	392	336	437	946	510	49	37	5	12	8	11	8
LLIA18	800	519	780	1481	832	53	39	6	16	11	11	11

7.14.3. La Luna IX core

Sample	*P*	*3-MP*	*2-MP*	*9-MP*	*1-MP*	*C_{20} Pregnane*	*C_{21} 20-Mpreg*	*C_{26} Chol (20S)*	*C_{26} Chol (20R) + C_{27} Ergost (20S)*	*C_{28} Stig (20S)*	*C_{27} Ergost*	*C_{28} Stig (20R)*
LLIS1	228	188	266	455	251	141	81	16	107	85	88	96
LLIS2	234	193	273	467	258	100	65	15	85	74	74	78
LLIS3	228	225	334	564	292	140	83	20	109	84	87	100
LLIS4	197	194	248	453	234	115	69	16	94	76	79	78
LLIS5	307	225	366	618	354	35	16	7	14	16	13	13
LLIS6	713	503	724	1244	676	205	122	22	145	106	112	129
LLIS7	506	438	630	1083	589	178	106	19	126	92	98	112
LLIS8	468	362	499	929	475	133	79	16	83	64	73	76
LLIS9	516	399	551	1024	524	147	87	18	92	70	81	84
LLIS10	713	571	711	1220	648	163	95	21	102	76	82	86

Sample	*P*	*3-MP*	*2-MP*	*9-MP*	*1-MP*	*C_{20} Pregnane*	*C_{21} 20-Mpreg*	*C_{26} Chol (20S)*	*C_{26} Chol (20R) + C_{27} Ergost (20S)*	*C_{28} Stig (20S)*	*C_{27} Ergost*	*C_{28} Stig (20R)*
LLIS11	286	281	397	740	376	167	98	20	106	85	84	88
LLIS12	286	245	322	562	317	103	63	13	54	45	43	49
LLIS13	247	561	753	1281	696	141	80	16	59	48	47	51
LLIS14	850	527	708	1205	654	133	76	15	55	45	44	48

7.14.4. La Luna stratotype

Sample	*P*	*3-MP*	*2-MP*	*9-MP*	*1-MP*	*C_{20} Pregnane*	*C_{21} 20-Mpreg*	*C_{26} Chol (20S)*	*C_{26} Chol (20R) + C_{27} Ergost (20S)*	*C_{28} Stig (20S)*	*C_{27} Ergost*	*C_{28} Stig (20R)*
Perija1	21	13	13	12	14	2	2	4	10	14	14	6
Perija2	14	9	9	8	10	2	2	2	7	9	9	4
Perija3	12	8	8	7	8	1	1	2	6	8	8	3
Perija4	14	9	9	8	10	2	2	2	7	10	10	4
Perija5	11	7	7	6	7	1	1	2	5	7	7	3
Perija6	13	8	8	7	9	1	1	2	6	9	9	4
Perija7	16	10	11	9	11	2	2	3	8	11	11	5
Perija8	11	7	7	6	8	1	1	2	5	7	7	3